

NASA CR-134799  
BCAC D6-42440-3



**PHASE II PROGRAM ON GROUND TEST  
OF REFANNED JT8D TURBOFAN ENGINES AND NACELLES  
FOR THE 727 AIRPLANE**

**Final Report**

**VOLUME III  
GROUND TESTS**

**December 1975**

**Boeing Commercial Airplane Company  
Seattle, Washington 98124**

**prepared for**

**NATIONAL AERONAUTICS AND SPACE ADMINISTRATION**

**NASA Lewis Research Center  
Contract NAS3-17842**



(NASA-CR-134799) PHASE 2 PROGRAM ON GROUND  
TEST OF REFANNED JT8D TURBOFAN ENGINES AND  
NACELLES FOR THE 727 AIRPLANE. VOLUME 3:  
GROUND TESTS Final Report (Boeing  
Commercial Airplane Co., Seattle) 350 p

N76-21189

HC \$10.00

Unclas  
25147

G3/05

1. Report No. NASA CR-134799		2. Government Accession No.		3. Recipient's Catalog No.	
4. Title and Subtitle PHASE II PROGRAM ON GROUND TEST OF REFANNED JT8D TURBOFAN ENGINES AND NACELLES FOR THE 727 AIRPLANE-- FINAL REPORT - VOLUME III GROUND TESTS				5. Report Date December 1975	
				6. Performing Organization Code	
7. Author(s)				8. Performing Organization Report No. D6-42440-3	
9. Performing Organization Name and Address BOEING COMMERCIAL AIRPLANE COMPANY P.O. Box 3707 SEATTLE, WASHINGTON 98124				10. Work Unit No.	
				11. Contract or Grant No. NAS3-17842	
				13. Type of Report and Period Covered Contractor Report	
12. Sponsoring Agency Name and Address National Aeronautics and Space Administration Washington, D.C. 20546				14. Sponsoring Agency Code	
15. Supplementary Notes V/STOL and Noise Division Chief, R. W. Schroeder NASA Lewis Research Center, Cleveland, Ohio 44135					
16. Abstract  The NASA Refan Program included full-scale performance and noise ground tests of both a current production (JT8D-15) and a refanned (JT8D-115) engine. This report is a description of the two ground tests and includes detailed propulsion, noise, and structural test results. The primary objectives of the total test program were comparison of JT8D-15 and JT8D-115 overall propulsion system performance and noise characteristics and determination of incremental component noise levels. Other objectives of the test program included: determination of acoustic treatment effectiveness; measurement of internal sound pressure levels; measurement of inlet and exhaust hardware performance; determination of center-engine surge margin; and evaluation of certain structural characteristics associated with the 727 refan center-engine inlet duct and JT8D refan engine exhaust system. The JT8D-15 and -115 tests were conducted at the Contractor's Boardman, Oregon test facility during September 1974 and January to March 1975, respectively. Analyses of the test data indicated that the JT8D-115, as compared to the JT8D-15, demonstrated a 12.5% to 13.2% reduction in static specific fuel consumption, and a reduction of 6 to 7 PNdB in a weighted average value of static tone corrected perceived noise level. Separated into noise components, a significant reduction was shown for the inlet fan, aft fan, exhaust duct flow, turbine, and jet noises; however, core noise was increased.					
17. Key Words (Suggested by Author(s)) JT8D refan Ground test Acoustic Component noise				18. Distribution Statement Unclassified - Unlimited	
19. Security Classif. (of this report) Unclassified		20. Security Classif. (of this page) Unclassified		21. No. of Pages 335	
				22. Price*	

\* For sale by the National Technical Information Service, Springfield, Virginia 22151



PHASE II PROGRAM ON GROUND TEST  
OF REFANNED JT8D TURBOFAN ENGINES AND NACELLES  
FOR THE 727 AIRPLANE

FINAL REPORT

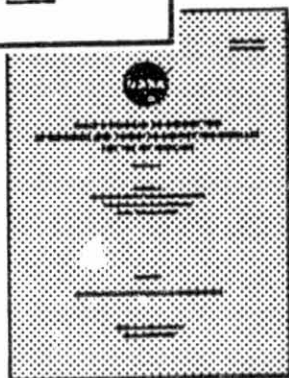
OVERALL REPORT ORGANIZATION



VOLUME I - SUMMARY (NASA CR-134797)



VOLUME II - HARDWARE DESIGN AND  
MANUFACTURING  
(NASA CR-134798)



VOLUME III - GROUND TESTS  
(NASA CR-134799)



VOLUME IV - AIRPLANE  
EVALUATION  
AND ANALYSIS  
(NASA CR-134800)

## CONTENTS

	Page
1.0 SUMMARY .....	1
2.0 INTRODUCTION .....	5
3.0 TEST DESCRIPTION .....	7
3.1 Test Objectives .....	7
3.2 Test Facility .....	7
3.3 Hardware .....	8
3.3.1 JT8D-15 .....	11
3.3.2 JT8D-115 .....	11
3.4 Instrumentation and Data Acquisition .....	18
3.4.1 Propulsion .....	18
3.4.2 Acoustic .....	28
3.4.3 Structural .....	28
3.5 Test Conditions .....	39
3.6 Test Procedures .....	43
3.6.1 Steady-State Propulsion Performance .....	43
3.6.2 JT8D-115 Surge Margin .....	43
3.6.3 Acoustic .....	45
3.6.4 Structural .....	47
4.0 TEST RESULTS .....	51
4.1 Propulsion .....	51
4.1.1 JT8D-15 Engine Test Results .....	51
4.1.2 JT8D-115 Engine Test Results .....	51
4.1.2.1 Engine Performance .....	51
4.1.2.2 Nozzle Match .....	57
4.1.2.3 Nozzle Performance .....	71
4.1.2.4 Side- and Center-Engine Inlet Steady-State Performance .....	81
4.1.2.5 Side- and Center-Engine Inlet Low Pressure Compressor Surge Margin Results .....	85
4.1.3 Data Quality .....	99
4.1.3.1 General .....	99
4.1.3.2 Results of Statistical Evaluation .....	99
4.2 Acoustic Results .....	101
4.2.1 Component Noise Evaluation .....	107
4.2.1.1 Inlet-Radiated Fan Noise: JT8D-15 Engine .....	108
4.2.1.2 Inlet-Radiated Fan Noise: JT8D-115 Engine .....	129
4.2.1.3 Discharge-Radiated Fan Noise: JT8D-15 Engine .....	152
4.2.1.4 Discharge-Radiated Fan Noise: JT8D-115 Engine .....	159
4.2.1.5 Turbine Noise: JT8D-15 Engine .....	165
4.2.1.6 Turbine Noise: JT8D-115 Engine .....	165

## CONTENTS (Concluded)

	Page
4.2.1.7 Jet Noise: JT8D-15 Engine.....	173
4.2.1.8 Jet Noise: JT8D-115 Engine.....	192
4.2.1.9 Core Noise: JT8D-15 Engine.....	196
4.2.1.10 Core Noise: JT8D-115 Engine.....	208
4.2.1.11 Exhaust Duct Flow Noise.....	212
4.2.1.12 Exhaust Duct Flow Noise: JT8D-15 Engine.....	213
4.2.1.13 Exhaust Duct Flow Noise: JT8D-115 Engine.....	218
4.2.2 Total Static Engine Noise.....	225
4.2.2.1 JT8D-15 Engine.....	225
4.2.2.2 JT8D-115 Engine.....	234
4.2.3 Acoustic Lining Attenuation.....	247
4.2.3.1 Side-Engine inlet Without Ring.....	247
4.2.3.2 Side-Engine Inlet With Ring.....	249
4.2.3.3 Center-Engine Inlet.....	253
4.2.3.4 Flyover Analysis Inputs.....	253
4.2.3.5 Hybrid Exhaust System.....	254
4.2.3.6 Flight-Type Exhaust System.....	254
4.2.4 Internal Microphone Data.....	259
4.2.4.1 Center-Engine Inlet Duct.....	259
4.2.4.2 Side-Engine Inlet (With and Without Ring).....	262
4.2.4.3 Exhaust System.....	263
4.2.5 Data Validity.....	263
4.2.5.1 Data Repeatability.....	263
4.2.5.2 Comparison of Ground-Level and Elevated Micro- phones.....	279
4.2.5.3 Acoustic Barrier Evaluation.....	284
4.3 Structural.....	292
4.3.1 Center-Engine Inlet Duct.....	292
4.3.2 Exhaust System.....	301
5.0 SUMMARY OF RESULTS AND CONCLUSIONS.....	313
5.1 Propulsion.....	313
5.2 Acoustic.....	313
5.3 Structural.....	314
APPENDIX.....	315
Symbols and Abbreviations.....	315
Definitions.....	323
Equations.....	325
Tables A-1 through A-12.....	329
REFERENCES.....	335



## FIGURES

No.		Page
1	JT8D-115 Ground Test—Total Noise . . . . .	3
2	Boardman Ground Test Facility Acoustic Range—JT8D-15 and -115 . . . . .	8
3	Boardman B2 Test Stand With JT8D-15 Engine . . . . .	9
4	Boardman B2 Test Stand With JT8D-115 Engine . . . . .	10
5	JT8D-115 Ground Test Side Inlet With Acoustic Ring . . . . .	12
6	JT8D-115 Center-Engine Inlet and Duct Assembly Test Setup . . . . .	13
7	JT8D-115 Flight-Type Exhaust System . . . . .	14
8	JT8D-15 and -115 Ground Test Inlet Bellmouth Configurations . . . . .	15
9	JT8D-15 and -115 Reference Exhaust Systems . . . . .	16
10	JT8D-115 Flight-Type and Hybrid Exhaust Systems . . . . .	17
11	727/JT8D-115 Center-Engine Inlet and Duct Crosswind Ground Test Configuration Schematic . . . . .	19
12	727/JT8D-115 Side-Engine Inlet Crosswind Ground Test Configuration Schematic . . . . .	20
13	JT8D-115 Center-Engine Crosswind Test Setup . . . . .	21
14	JT8D-115 Side-Engine Crosswind Test Setup . . . . .	22
15	JT8D-115—Configuration 1, Acoustic Lining Definition as Tested . . . . .	23
16	JT8D-115—Configuration 2, Acoustic Lining Definition as Tested . . . . .	24
17	JT8D-115 Center-Engine Inlet Duct Acoustic Lining Definition as Tested . . . . .	25
18	Propulsion Data Acquisition Flow Diagram . . . . .	26
19	JT8D-115 Full-Scale Ground Test Inlet Pressure Survey Rake . . . . .	27
20	JT8D-115 Side-Engine Inlet Flush-Mounted Microphone Locations . . . . .	30
21	JT8D-115 Center-Engine Inlet Duct Internal Microphone Locations . . . . .	31
22	JT8D-115 Exhaust System Flush-Mounted Microphone Locations . . . . .	32
23	Acoustic Data System Flow Diagram . . . . .	35
24	JT8D-115 Center-Engine Inlet Duct Test Setup . . . . .	36
25	JT8D-115 Ground Test—Center-Engine Inlet Duct Strain, Deflection, and Pressure Transducer Locations . . . . .	37
26	JT8D-115 Ground Test—Exhaust System Thermocouple Locations and Identification . . . . .	38
27	JT8D-15 and -115 Ground Test—Acoustic Baffle Arrangement for Isolation of Inlet Noise . . . . .	48
28	JT8D-115 Ground Test—Acoustic Baffle Arrangement for Shielding of Inlet and Exhaust Noise Components . . . . .	49
29	JT8D-15 and -115 Ground Tests—Acoustic Baffle Configurations for Component Noise Isolation . . . . .	50
30	JT8D-15 Ground Test—Low Pressure Compressor Rotor Speed Versus Engine Pressure Ratio . . . . .	52
31	JT8D-15 Ground Test—Airflow Versus Engine Pressure Ratio . . . . .	53
32	JT8D-15 Ground Test—Fan Pressure Ratio Versus Engine Pressure Ratio . . . . .	54
33	JT8D-15 Ground Test—Gross Thrust Versus Engine Pressure Ratio . . . . .	55
34	JT8D-15 Ground Test—Thrust Specific Fuel Consumption Versus Gross Thrust . . . . .	56

## FIGURES (Continued)

No.		Page
35	JT8D-115 Ground Test—Low Pressure Compressor Rotor Speed Versus Engine Pressure Ratio With Reference Hardware . . . . .	58
36	JT8D-115 Ground Test—Airflow Versus Engine Pressure Ratio With Reference Hardware . . . . .	59
37	JT8D-115 Ground Test—Fan Pressure Ratio Versus Engine Pressure Ratio With Reference Hardware . . . . .	60
38	JT8D-115 Ground Test—Thrust Versus Engine Pressure Ratio With Reference Hardware . . . . .	61
39	JT8D-115 Ground Test—Specific Fuel Consumption Versus Thrust With Reference Hardware . . . . .	62
40	JT8D-115 Ground Test—Low Pressure Compressor Rotor Speed Versus Engine Pressure Ratio, Side- and Center-Engine Inlet Configurations . . . . .	63
41	JT8D-115 Ground Test—Airflow Versus Engine Pressure Ratio, Side- and Center-Engine Inlet Configurations . . . . .	64
42	JT8D-115 Ground Test—Fan Pressure Ratio Versus Engine Pressure Ratio, Side- and Center-Engine Inlet Configurations . . . . .	65
43	JT8D-115 Ground Test—Thrust Versus Engine Pressure Ratio, Side- and Center-Engine Inlet Configurations . . . . .	66
44	JT8D-115 Ground Test—Specific Fuel Consumption Versus Thrust, Side- and Center-Engine Inlet Configurations . . . . .	67
45	JT8D-115 Engine Match Parameter Versus Nozzle Effective Area Relationships . . . . .	69
46	JT8D-115 Ground Test—Deviation From Nominal Engine Match Parameters Relative to the Reference Exhaust System . . . . .	70
47	JT8D-115 Ground Test—Thrust Versus Engine Pressure Ratio for the Reference, Flight-Type, and Hybrid Exhaust Systems . . . . .	74
48	JT8D-115 Ground Test—Airflow Versus Engine Pressure Ratio for the Reference, Flight-Type, and Hybrid Exhaust Systems . . . . .	75
49	JT8D-115 Ground Test—Fan Pressure Ratio Versus Engine Pressure Ratio for the Reference, Flight-Type, and Hybrid Exhaust Systems . . . . .	76
50	JT8D-115 Reference Exhaust System Performance . . . . .	77
51	JT8D-115 Flight-Type Exhaust System Performance . . . . .	78
52	JT8D-115 Hybrid Exhaust System Performance . . . . .	79
53	Correlation of Model and Full-Scale Nozzle Coefficients for JT8D-115 Reference Exhaust System . . . . .	80
54	JT8D-115 Side-Engine Inlet Static Performance . . . . .	82
55	JT8D-115 Side-Engine Inlet (Without Ring) Recovery Map and Engine Contractor's Distortion Parameters at $W_a \sqrt{\theta_{t2}/\delta_{t2}} = 470 \text{ lb/s (213 kg/s)}$ . . . . .	83
56	JT8D-115 Center-Engine Inlet (Production Lip) Static Performance . . . . .	84
57	JT8D-115 Center-Engine Inlet Recovery Map and Engine Contractor's Distortion Parameters at $W_a \sqrt{\theta_{t2}/\delta_{t2}} = 417 \text{ lb/s (189 kg/s)}$ . . . . .	86
58	JT8D-115 Center-Engine Inlet Recovery Map and Engine Contractor's Distortion Parameters at $W_a \sqrt{\theta_{t2}/\delta_{t2}} = 476 \text{ lb/s (216 kg/s)}$ . . . . .	87

## FIGURES (Continued)

No.		Page
59	JT8D-115 Ground Test—Calibration of Simulated Crosswind . . . . .	88
60	JT8D-115 Surge Margin Test Results . . . . .	91
61	JT8D-115 Surge Margin Versus Crosswind Velocity Correlation . . . . .	96
62	JT8D-115 Center-Engine Inlet Total Pressure Contours With Crosswind . . . . .	97
63	JT8D-115 Side-Engine Inlet (Without Ring) Total Pressure Contours Arriving at Verge-of-Surge Conditions by Increasing Crosswind Velocity ( $N_1/\sqrt{\theta_{t2}} \approx 6900$ rpm) . . . . .	98
64	JT8D-115 Side-Engine Inlet (Without Ring) Total Pressure Contours With Crosswind ( $N_1/\sqrt{\theta_{t2}} \approx 7400$ rpm) . . . . .	100
65	JT8D-15 and -115 Inlet Fan Noise Comparison at Ground Static Condition . . .	103
66	JT8D-15 and -115 Aft Fan Noise Comparison at Ground Static Conditions . . .	104
67	JT8D-15 and -115 Turbine Noise Comparison at Ground Static Conditions . . .	104
68	JT8D-15 and -115 Jet Noise Comparison at Ground Static Conditions . . . . .	105
69	JT8D-15 and -115 Core Noise Comparison at Ground Static Conditions . . . . .	105
70	JT8D-15 and -115 Exhaust Duct Flow Noise Comparison at Ground Static Conditions . . . . .	106
71	JT8D-15 and -115 Total Engine Noise Comparison at Ground Static Conditions .	106
72	JT8D-15 Ground Test—Narrow Band Spectra in Forward Quadrant, Approach Power ( $N_1/\sqrt{\theta_{t2}} = 6683$ ) . . . . .	111
73	JT8D-15 Ground Test—Narrow Band Spectra in Forward Quadrant, $40^\circ$ Directivity Angle . . . . .	112
74	JT8D-15 Ground Test—Inlet-Radiated First Fan Fundamental Tone Versus Fan Stage Pressure Rise . . . . .	113
75	JT8D-15 Ground Test—Inlet-Radiated First Fan Harmonic Tone Levels Relative to Fundamental Tone Level . . . . .	114
76	JT8D-15 Ground Test—Inlet-Radiated Fan Sumtone (1F1H + 2F1H) Versus Fan Stage Pressure Rise . . . . .	115
77	JT8D-15 Ground Test—Polar Directivity of First Fan Fundamental Tone . . . .	116
78	JT8D-15 Ground Test—Fan Peak Broadband Noise, Inlet-Radiated for 1st or 2nd Stage . . . . .	117
79	JT8D-15 Ground Test—Fan Broadband Noise Spectrum Shaping—All Directivity Angles . . . . .	118
80	JT8D-15 Ground Test—Inlet-Radiated Fan Broadband Noise Directivity for Either Fan Stage . . . . .	119
81	JT8D-15 Ground Test—Buzzsaw Noise Level of Peak at $0.30 \times$ BPF . . . . .	120
82	JT8D-15 Ground Test—Buzzsaw Noise Level of Peak at $0.50 \times$ BPF . . . . .	121
83	JT8D-15 Ground Test—Buzzsaw Noise Level of Peak at $0.75 \times$ BPF . . . . .	122
84	JT8D-15 Ground Test—Buzzsaw Noise Level of Peak at $1.30 \times$ BPF . . . . .	123
85	JT8D-15 Ground Test—Buzzsaw Noise Spectrum Shaping . . . . .	124
86	JT8D-15 Ground Test—Buzzsaw Directivity Characteristics for Peak Level at Spectrum Location of $0.30 \times$ BPF . . . . .	125
87	JT8D-15 Ground Test—Buzzsaw Directivity Characteristics for Peak Level at Spectrum Location of $0.50 \times$ BPF . . . . .	126



## FIGURES (Continued)

No.	Page
88 JT8D-15 Ground Test—Buzzsaw Directivity Characteristics for Peak Level at Spectrum Location of 0.75 x BPF . . . . .	127
89 JT8D-15 Ground Test—Buzzsaw Directivity Characteristics for Peak Level at Spectrum Location of 1.30 x BPF . . . . .	128
90 JT8D-15 Ground Test—Rotor-Stator Spacing Correction . . . . .	130
91 JT8D-115 Ground Test—Fan Noise Subcomponent Identification by 20 Hz Bandwidth Filter Analysis . . . . .	132
92 JT8D-115 Ground Test—Inlet Fundamental Fan Tone Basic Noise Level . . . . .	133
93 JT8D-115 Ground Test—Relationship Between Inlet-Radiated Second Harmonic and Fundamental Fan Tone . . . . .	134
94 JT8D-115 Ground Test—Inlet-Radiated First Stage Compressor Fundamental Tone Level . . . . .	135
95 JT8D-115 Ground Test—Inlet-Radiated Fan and First Stage Compressor Sumtone Basic Noise Level . . . . .	136
96 JT8D-115 Ground Test—Inlet-Radiated Fan Tone Directivity . . . . .	137
97 JT8D-115 Ground Test—Inlet-Radiated First Stage Compressor Tone Directivity . . . . .	138
98 JT8D-115 Ground Test—Inlet-Radiated Fan and First Stage Compressor Sumtone Directivity . . . . .	139
99 JT8D-115 Ground Test—Example of Method for Converting 20 Hz Bandwidth Data to 1/3 OB Level . . . . .	140
100 JT8D-115 Ground Test—Inlet-Radiated Fan Broadband Basic Noise Level . . . . .	141
101 JT8D-115 Ground Test—Inlet-Radiated Fan Broadband Noise Spectrum Shaping . . . . .	142
102 JT8D-115 Ground Test—Inlet-Radiated Fan Broadband Directivity . . . . .	143
103 JT8D-115 Ground Test—Inlet-Radiated Basic Buzzsaw Level at 0.25 x Fan Blade Passing Frequency . . . . .	144
104 JT8D-115 Ground Test—Inlet-Radiated Basic Buzzsaw Noise Level at 0.50 x Fan Blade Passing Frequency . . . . .	145
105 JT8D-115 Ground Test—Inlet-Radiated Basic Buzzsaw Noise Level at 0.75 x Fan Blade Passing Frequency . . . . .	146
106 JT8D-115 Ground Test—Inlet-Radiated Basic Buzzsaw Noise Level at 1.25 x Fan Blade Passing Frequency . . . . .	147
107 JT8D-115 Ground Test—Inlet-Radiated Buzzsaw Noise Spectrum Shaping . . . . .	148
108 JT8D-115 Ground Test—Inlet-Radiated Buzzsaw Directivity . . . . .	149
109 JT8D-115 Ground Test—Inlet-Radiated Fan Noise Correlated on Fan Pressure Ratio . . . . .	150
110 JT8D-115 Ground Test—Inlet-Radiated Fan Noise Correlated on Corrected $N_1$ . . . . .	151
111 JT8D-15 Ground Test—Sample Discharge-Radiated Narrow Band Spectra, 120° Directivity Angle . . . . .	153
112 JT8D-15 Ground Test—Discharge-Radiated First Fan Fundamental Tone Versus Fan Stage Pressure Rise . . . . .	154
113 JT8D-15 Ground Test—Discharge-Radiated First Fan Harmonics Relative to Fundamental Tone . . . . .	155

## FIGURES (Continued)

No.	Page
114 JT8D-15 Ground Test—Discharge-Radiated First Fan Fundamental Tone Directivity . . . . .	156
115 JT8D-15 Ground Test—Discharge-Radiated Fan Peak Broadband Noise for First- or Second-Stage . . . . .	157
116 JT8D-15 Ground Test—Discharge-Radiated Fan Broadband Noise Directivity for Either Fan Stage . . . . .	158
117 JT8D-115 Ground Test—Basic Noise Level of Discharge-Radiated Fundamental Fan Tone . . . . .	160
118 JT8D-115 Ground Test—Relationship Between Discharge-Radiated Second Harmonic and Fundamental Fan Tone . . . . .	161
119 JT8D-115 Ground Test—Discharge-Radiated Fan Tone Directivity . . . . .	162
120 JT8D-115 Ground Test—Discharge-Radiated Fan Broadband Basic Noise Level . . . . .	163
121 JT8D-115 Ground Test—Discharge-Radiated Fan Broadband Noise Directivity . . . . .	164
122 JT8D-115 Ground Test—Inlet Baffled Narrow Band Spectra for Various Power Settings at a Constant Directivity Angle ( $120^\circ$ Ground Microphone, 100 ft (30.48 m) Sideline) . . . . .	166
123 JT8D-115 Ground Test—Inlet Baffled Narrow Band Spectra for Various Directivity Angles at Constant Power Setting ( $N_1/\sqrt{\theta_{t2}} = 5077$ , 100 ft (30.48 m) Sideline, Ground Microphones) . . . . .	169
124 JT8D-115 Ground Test—Inlet Baffled Narrow Band Spectra for Various Directivity Angles at Constant Power Setting ( $N_1/\sqrt{\theta_{t2}} = 5492$ , 100 ft (30.48 m) Sideline, Ground Microphones) . . . . .	171
125 JT8D-115 Ground Test—Basic Turbine Tone Level Versus Corrected rpm . . . . .	174
126 JT8D-115 Ground Test—Turbine Tone Directivity Corrections . . . . .	174
127 JT8D-115 Ground Test—Peak Turbine Broadband Level Versus Corrected rpm . . . . .	175
128 JT8D-115 Ground Test—Turbine Broadband Directivity Corrections . . . . .	175
129 JT8D-15 Ground Test—Illustration of Jet Noise Analysis Technique . . . . .	176
130 JT8D-15 Ground Test—Normalized Jet Noise Spectrum Shapes for All Power Settings . . . . .	178
131 JT8D-15 Ground Test—Normalized Jet Noise Spectra, $130^\circ$ Directivity Angle for Several Power Settings . . . . .	181
132 JT8D-15 Ground Test—Normalized Jet Noise Spectra, $110^\circ$ Directivity Angle for Several Power Settings . . . . .	182
133 JT8D-15 Ground Test—Jet Noise Spectrum Shape Comparison, $130^\circ$ Directivity Angle . . . . .	183
134 JT8D-15 Ground Test—Jet Noise Spectrum Shape Comparison, $110^\circ$ Directivity Angle . . . . .	184
135 JT8D-15 Ground Test—Frequency of Jet Noise Peak Sound Pressure Level . . . . .	185
136 JT8D-15 Ground Test—Sample Working Plots for Determination of Jet Noise Peak Frequency . . . . .	186
137 JT8D-15 Ground Test—Peak Jet Noise Sound Pressure Levels . . . . .	187
138 JT8D-15 Ground Test—Sample Working Plot for Determination of Peak Jet Noise Level, $130^\circ$ Directivity Angle . . . . .	188

## FIGURES (Continued)

No.	Page
139 JT8D-15 Ground Test—Sample Working Plot for Determination of Peak Jet Noise Level, 110° Directivity Angle . . . . .	189
140 JT8D-15 Ground Test—Peak Jet Noise Velocity Exponent . . . . .	190
141 JT8D-109 Ground Test—Aft Quadrant Jet Spectrum Shapes, All Power Settings. . . . .	194
142 JT8D-109 Ground Test—Forward Quadrant Jet Spectrum Shapes, All Power Settings . . . . .	195
143 JT8D-109 Ground Test—Sample Plot of Frequency of Maximum Jet Noise Level Versus $\log V_{pri}$ . . . . .	197
144 JT8D-109 Ground Test—Sample Plot of Jet Noise Spectrum Peak Level Versus $\log V_{pri}$ . . . . .	199
145 JT8D-15 Ground Test—Sample Working Plot For Evaluation of Core Noise (Measured Total Noise Minus Predicted Jet Noise): 150 ft (45.72 m) Polar, Ground Microphones, Inlet Baffled . . . . .	202
146 JT8D-15 Ground Test—Normalized Core Noise Spectrum Shape, Average for All Angles and Power Settings . . . . .	205
147 JT8D-15 Ground Test—Normalized Core Noise Peak Sound Pressure Level. . . . .	206
148 JT8D-15 Ground Test—Normalized Peak Core Noise Directivity, Average for All Power Settings . . . . .	207
149 JT8D-109 Ground Test—Core Noise Basic Level . . . . .	210
150 JT8D-109 Ground Test—Core and Jet Noise Levels: 150 ft (45.72 m) Polar, Ground Microphone at 120° Directivity Angle . . . . .	211
151 JT8D-109 Ground Test—Core Noise Spectrum Shape, Average for All Angles and Power Settings . . . . .	212
152 JT8D-109 Ground Test—Core Noise Directivity, Average for All Power Settings. . . . .	213
153 JT8D-15 Ground Test—Normalized Spectra Showing Influence of Exhaust Duct Flow Noise, 140° Directivity Angle . . . . .	214
154 JT8D-15 Ground Test—Normalized Spectra Showing Influence of Exhaust Duct Flow Noise, 150° Directivity Angle . . . . .	215
155 JT8D-15 Ground Test—Jet and Exhaust Duct Flow Noise Comparison, 140° Directivity Angle . . . . .	216
156 JT8D-15 Ground Test—Jet and Exhaust Duct Flow Noise Comparison, 150° Directivity Angle . . . . .	217
157 JT8D-115 Ground Test—Evidence of Internal Noise Source at 500 Hz . . . . .	220
158 JT8D-115 Ground Test—Coherence Spectra Between Internal Exhaust Duct and External (140°) Ground Microphone at Various Power Settings . . . . .	221
159 JT8D-115 Ground Test—Sample Working Plot for Evaluation of Exhaust Duct Flow Noise, $N_1/\sqrt{\theta_{12}} = 7650$ . . . . .	222
160 JT8D-115 Ground Test—Exhaust Duct Flow Noise Basic Level . . . . .	223
161 JT8D-115 Ground Test—Exhaust Duct Flow Noise Spectrum Shape, Average for All Angles and Power Settings . . . . .	224
162 JT8D-115 Ground Test—Exhaust Duct Flow Noise Directivity, Average for All Power Settings . . . . .	224



## FIGURES (Continued)

No.	Page
163 JT8D-15 Ground Test—Predicted Static Component Noise Levels, Approach rpm . . . . .	226
164 JT8D-15 Ground Test—Predicted Static Component Noise Levels, Takeoff rpm . . . . .	230
165 JT8D-115 Ground Test—Predicted Static Component Noise Levels, Approach rpm . . . . .	235
166 JT8D-115 Ground Test—Predicted Static Component Noise Levels, Takeoff rpm . . . . .	239
167 JT8D-115 Ground Test—Total Engine Spectra for Various Nacelle Treatments: 150 ft (45.72 m) Polar, Ground Microphone, Approach rpm . . . . .	243
168 JT8D-115 Ground Test—Total Engine Spectra for Various Nacelle Treatments: 150 ft (45.72 m) Polar, Ground Microphone, Takeoff rpm . . . . .	245
169 JT8D-115 Ground Test—Measured Versus Predicted Lining Attenuation of Side-Engine Inlet Without Ring . . . . .	248
170 JT8D-115 Ground Test—Measured Versus Predicted Lining Attenuation of Side-Engine Inlet With Ring . . . . .	250
171 JT8D-115 Ground Test—Directivity of Acoustic Lining Attenuation for Treated Side-Engine Inlet With Ring . . . . .	252
172 JT8D-115 Ground Test—Comparison of Space Averaged SPL of Center-Engine Inlet and Side-Engine Inlet With Ring: Aft Baffled, 150 ft (45.72 m) Polar, Ground Microphones, Approach rpm . . . . .	253
173 JT8D-115 Ground Test—Differences in SPL Between the Hardwall Side-Engine Inlet Without Ring and the Treated Center-Engine Inlet at Approach, Cutback, and Takeoff rpm . . . . .	255
174 JT8D-115 Ground Test—Measured Versus Predicted Lining Attenuation Spectra of Hybrid Exhaust System . . . . .	256
175 JT8D-115 Ground Test—Measured Versus Predicted Lining Attenuation Spectra of Flight-Type Exhaust System . . . . .	257
176 JT8D-115 Ground Test—Center-Engine Inlet Internal Combination Tone SPL's . . . . .	260
177 JT8D-115 Ground Test—Center-Engine Inlet, Internal OASPL's . . . . .	261
178 JT8D-115 Ground Test—Center-Engine Inlet, Fan Tone Internal SPL's . . . . .	261
179 JT8D-115 Ground Test—SPL Versus Radial Distance at Fan Face, Side-Engine Inlet With Ring, Approach rpm . . . . .	264
180 JT8D-115 Ground Test—SPL Versus Radial Distance at Fan Face, Side-Engine Inlet With Ring, Cutback rpm . . . . .	265
181 JT8D-115 Ground Test—SPL Versus Radial Distance at Fan Face, Side-Engine Inlet With Ring, Takeoff rpm . . . . .	265
182 JT8D-115 Ground Test—Acoustic Repeatability, Side-Engine Inlet (Without Ring) and Hybrid Exhaust System: 100 ft (30.48 m) Polar, Ground Microphones, Approach rpm . . . . .	268
183 JT8D-115 Ground Test—Acoustic Repeatability, Side-Engine Inlet (Without Ring) and Hybrid Exhaust System: 100 ft (30.48 m) Polar, Ground Microphones, Takeoff rpm . . . . .	273

## FIGURES (Concluded)

No.	Page
184 JT8D-115 Ground Test--Time History of Inlet-Radiated Fan Tone Sound Pressure Level for Hardwall Side-Engine Inlet (Without Ring): 30° Directivity Angle, 100 ft (30.48 m) Polar, Ground Microphone, Approach rpm . . . . .	278
185 JT8D-115 Ground Test--Space-Averaged Fan Tone SPL Versus $N_1/\sqrt{\theta_{t2}}$ for Nine Repeatability Runs, Side-Engine Inlet (Without Ring), and Hybrid Exhaust System: 100 ft (30.48 m) Polar, Ground Microphones . . . . .	279
186 JT8D-15 Ground Test--Comparison of Elevated and Ground Level Microphone Acoustic Data: 100 ft (30.48 m) Polar . . . . .	280
187 JT8D-15 Ground Test--Direct Comparison of Elevated and Ground Level Microphone Spectra: 100 ft (30.48 m) Polar . . . . .	285
188 JT8D-15 Ground Test--Apparent Baffle Attenuation Spectra . . . . .	286
189 JT8D-15 Ground Test--Effect of Aft-Mounted Baffles on Forward Quadrant Noise: 100 ft (30.48 m) Polar, Ground Microphones . . . . .	290
190 JT8D-115 Ground Test--Estimated Attenuation of Inlet-Radiated Noise by Forward-Mounted Baffles, Average for All Power Settings . . . . .	291
191 JT8D-15 Ground Test--Estimated Attenuation of Discharge-Radiated Noise by Aft-Mounted Baffles, Average for All Power Settings . . . . .	291
192 JT8D-115 Ground Test--Center-Engine Inlet Duct Surge Strain Gage Trace, Multiple Peak Surge Condition at Takeoff Power . . . . .	293
193 JT8D-115 Ground Test--Front Spar Forging Surge Strain Gage Trace, Multiple Peak Surge Condition at Takeoff Power . . . . .	294
194 JT8D-115 Ground Test--Center-Engine Inlet Duct Surge Deflection Gage Trace, Multiple Peak Surge Condition at Takeoff Power . . . . .	295
195 JT8D-115 Ground Test--Multiple Surge Pressure Gage Traces, Multiple Peak Surge Condition at Takeoff Power . . . . .	296
196 JT8D-115 Ground Test--Typical Pressure Gage Traces for Single Surge Condition at Idle Power . . . . .	298
197 JT8D-115 Ground Test--Typical Strain and Deflection Gage Traces for Single Surge Condition at Idle Power . . . . .	299
198 JT8D-115 Ground Test--Center-Engine Inlet-Duct Pressure, Calculated and Test Data Correlation . . . . .	300
199 JT8D-115 Center-Engine Inlet Duct, Predicted, and Ground Test Gage Dynamic Response--Duct Upper Centerline Axial and Circumferential Stresses .	302
200 JT8D-115 Center-Engine Inlet Duct, Predicted, and Ground Test Gage Dynamic Response--Side and Lower Centerline Circumferential Stress . . . . .	303
201 Typical JT8D-115 Center-Engine Inlet Duct Surge Profile (for Multiple Peak Surge Condition at Takeoff Power) Showing Pressure, Stress and Deflection Versus Time Relationship . . . . .	304
202 JT8D-115 Ground Test--Exhaust System Assembly Thermocouple Temperature Trace--Idle to Takeoff to Idle . . . . .	307
203 JT8D-115 Ground Test--Fan/Primary Flow Divider Thermocouple Temperature Trace--Takeoff to Cruise and Idle to Engine Shutdown . . . . .	309
204 JT8D-115 Ground Test--Fan/Primary Divider Temperature Test--Analysis Correlation--Engine EPR = 1.93 . . . . .	310

## TABLES

No.		Page
1	Propulsion Data Accuracy . . . . .	22
2	JT8D-115 Refan Ground Test—Summary of Internal Microphone Locations . .	33
3	Performance and Acoustic Test Matrix—JT8D-15 Engine . . . . .	39
4	Performance Test Matrix—JT8D-115 Engine . . . . .	40
5	Acoustic Test Matrix—JT8D-115 Engine . . . . .	40
6	Acoustic Data Compilation—JT8D-115 Engine . . . . .	42
7	Structural Test Matrix . . . . .	43
8	Acoustic Test Power Settings . . . . .	46
9	LPC Operating Line Changes for JT8D-115 Engine With Reference Hardware .	90
10	Surge Margin Results for Center-Engine Inlet on JT8D-115 Engine Without Cross- wind . . . . .	93
11	Surge Margin Results for Center-Engine Inlet on JT8D-115 Engine with 90° Crosswind . . . . .	94
12	Surge Margin Results for Side-Engine Inlet (Without Acoustic Ring) on JT8D- 115 Engine with 90° Crosswind . . . . .	95
13	Results of Statistical Analysis of JT8D-115 Exhaust Systems at Takeoff Pressure Ratio . . . . .	102
14	JT8D-15 and -115 Ground Test—Guide to Locating Key Component Noise Curves by Figure Number . . . . .	109
15	JT8D-15 Ground Test—Jet Noise Spectrum Shapes: 150 ft (45.72 m) Polar, Ground Microphones . . . . .	191
16	JT8D-15 Ground Test—Band Number for 1/3 OB at which Jet Noise Spectrum SPL Peaks <sup>a</sup> . . . . .	192
17	JT8D-15 Ground Test—SPL of 1/3 OB at which Jet Noise Peaks <sup>a</sup> . . . . .	193
18	JT8D-109 Ground Test—Frequency of Peak Jet Noise (1/3-OB Number of Peak SPL) Versus Log $V_{pri}$ . . . . .	198
19	JT8D-109 Ground Test—Jet Noise Spectrum Peak SPL . . . . .	200
20	JT8D-109 Ground Test—Primary Velocity Exponent for Jet Peak SPL Relation- ship to Log $V_{pri}$ . . . . .	201
21	JT8D-15 Core Noise Empirical Model: 150 ft (45.72 m) Polar, Ground Microphones . . . . .	209
22	JT8D-115 Ground Test—SPL's at Various Surface Locations in the Center-Engine Inlet Duct for Various Values of $N_1$ <sup>a</sup> . . . . .	259
23	JT8D-115 Ground Test—SPL's at Various Locations in the Side-Engine Inlet for Various Values of $N_1$ . . . . .	262
24	JT8D-115 Ground Test - SPL's at Various Surface Locations in the Exhaust System at Values of $N_1$ Corresponding to the Approach Condition . . . . .	266
25	JT8D-115 Ground Test—Performance Data for Selected Conditions from Acoustic Repeatability Runs Plotted in Figures 182 Through 184 . . . . .	267
26	JT8D-115 Ground Test—Stabilized Engine Data for Structural Runs Analyzed and Illustrated . . . . .	300



## TABLES (Concluded)

No.		Page
27	Comparison of Ground Test and Predicted and Duct Design Average Pressure for the JT8D-115 Center-Engine Inlet Duct . . . . .	301
28	Comparison of Ground Test and Predicted Deflection Data for the JT8D-115 Center-Engine Inlet Duct . . . . .	305
29	JT8D-115 Ground Test--Stabilized Engine Data for Structural Runs Analyzed and Illustrated . . . . .	306
30	JT8D-115 Ground Test--Comparison of Test and Predicted Heat Transfer Coefficients, Engine EPR = 1.96 . . . . .	311
31	JT8D-115 Ground Test--Maximum Recorded Temperature on Titanium and Inconel Honeycomb, Engine EPR = 1.96 . . . . .	311
A-1	JT8D-15 Ground Test--Engine Performance Parameters Used in Noise Analysis . . . . .	329
A-2	JT8D-115 Ground Test--Engine Performance Parameters Used in Noise Analysis . . . . .	329
A-3	JT8D-15 Ground Test--1F1H First Fan BPF Inlet Radiated Noise at 150 ft (45.72 m) Polar . . . . .	330
A-4	JT8D-15 Ground Test--2F1H Second Fan BPF Inlet Radiated Noise at 150 ft (45.72 m) Polar . . . . .	330
A-5	JT8D-15 Ground Test--1F2H $\Delta$ First Fan (Second-First Harmonic) Inlet Radiated at 150 ft (45.72 m) Polar . . . . .	331
A-6	JT8D-15 Ground Test--2F2H $\Delta$ Second Fan (Second-First Harmonic) Inlet Radiated at 150 ft (45.72 m) Polar . . . . .	331
A-7	JT8D-15 Ground Test--1F1H + 2F1H Fans Sum-tone Inlet Radiated at 150 ft (45.72 m) Polar . . . . .	332
A-8	JT8D-15 Ground Test--1F1H First Fan BPF Discharge-Radiated Noise at 150 ft (45.72 m) Polar . . . . .	332
A-9	JT8D-15 Ground Test--2F1H Second Fan BPF Discharge-Radiated Noise at 150 ft (45.72 m) Polar . . . . .	333
A-10	JT8D-15 Ground Test--1F2H $\Delta$ First Fan (Second-First Harmonic) Discharge-Radiated Noise at 150 ft (45.72 m) Polar . . . . .	333
A-11	JT8D-15 Ground Test--2F2H Second Fan (Second-First Harmonic) Discharge-Radiated Noise at 150 ft (45.72 m) Polar . . . . .	334
A-12	JT8D-15 Ground Test--(1F1H + 2F1H) Fans Sum-Tone Discharge-Radiated Noise at 150 ft (45.72 m) Polar . . . . .	334

## 1.0 SUMMARY

The NASA Refan Program (contract NAS3-17842) included full-scale performance and noise ground tests of the JT8D-15 (baseline) and JT8D-115 (refan) engines. This document is a description of the two ground tests and includes detailed propulsion, noise, and structural test results.

The objectives of the full-scale ground tests were to determine the:

- Installed JT8D refan engine performance
- Component noise differences, as related to propulsion cycle parameters, between the JT8D (baseline) and the JT8D refan engines (in order to develop through analytical methods predicted in-flight noise increments that would be applied to a known flight data base)
- JT8D refan acoustic treatment effectiveness and internal sound pressure levels (SPL)
- Structural loads and deflection for the center-engine inlet duct; thermal environment for the exhaust duct and fan/primary flow divider.

The tests were conducted on the B-2 test stand at the Contractor's Boardman, Oregon test facility. The baseline test was conducted on a new JT8D-15 engine during the time period August 28, 1974 to September 13, 1974. Upon completion of the baseline test, the JT8D-15 was shipped to Pratt & Whitney Aircraft (P&WA) for conversion to a JT8D-115; this refanned engine was returned to Boardman for testing in the time period January 7, 1975 to March 28, 1975.

The propulsion testing of the JT8D-15 engine included both engine calibration with reference hardware and installed engine performance evaluation with production nacelle hardware. Propulsion testing of the JT8D-115 engine included test configurations to evaluate the performance characteristics associated with flight-type nacelle hardware elements; namely, the side-engine inlet both with and without an acoustically treated inlet ring; the center-engine inlet; and two exhaust system configurations (differing in the fan/primary flow divider geometry and amount of acoustic treatment). Inlet pressure surveys and crosswind testing were conducted to measure inlet recovery, inlet pressure distortion, and engine surge margin characteristics. In addition, the static (zero crosswind) surge margins were determined for the side-engine inlet (without ring) and the center-engine inlet. Surge margin characteristics were determined using the P&WA cross-bleed system. During the center-engine inlet testing, two vortex generator configurations were evaluated. Inlet duct deflections were measured at critical structural and aerodynamic areas. Normal engine instrumentation was utilized to monitor engine cycle parameters for both performance and acoustic tests.

The JT8D-115 center- and side-engine inlet total pressure recoveries were found to be as predicted from model scale tests. At a corrected takeoff airflow of 470 lb/s (213 kg/s), recoveries

(relative to the reference bellmouth inlet) for the center-engine inlet, the side-engine inlet with acoustic ring, and the side-engine inlet without ring were 0.984, 0.9925, and 0.995, respectively.

The static specific fuel consumption, at takeoff thrust, of the JT8D-115 is 12.5% to 13.2% lower than the JT8D-15 for the side-engine inlets with and without acoustic ring. The JT8D-115 center-engine inlet and side-engine inlet (without ring) gave a low pressure compressor (LPC) surge margin nearly the same as for the reference bellmouth inlet at static conditions. A 90° crosswind of 20 kn (10.3 m/s) degraded the LPC surge margin 4% relative to static conditions.

The flight-type exhaust system was matched at the upper limit (+0.5%) of P&WA's permitted effective area tolerance. The flight-type exhaust system and the reference exhaust system were found to have identical gross thrust coefficients over the full range of nozzle pressure ratios from 1.2 to 1.95. The flow coefficient of the flight-type nozzle was found to be 0.0035 higher than that of the reference nozzle.

Propulsion data accuracy and repeatability were close to those anticipated; with 95% confidence, mass flow accuracy was within 0.5% of full-scale and thrust accuracy within 0.25% of full-scale.

Acoustic testing of the JT8D-15 and -115 engines included the use of baffles to obtain far field component noise data. The JT8D-15 engine was tested with a hardwall production nacelle. The as-delivered treated JT8D-115 engine was tested with various nacelle hardware: hardwall inlet, treated inlet (both with and without treated ring); treated center-engine duct; and one hardwall and two treated exhaust systems. Internal sound pressure level (SPL) measurements were taken including flush-mounted microphones in the center duct, side inlet, and exhaust system, as well as a side inlet radial SPL survey.

Analysis of acoustic data showed that good acoustic repeatability was achieved for all noise components except inlet fan tones and buzzsaw, provided testing was restricted to accepted weather limits. The large variation in measured inlet fan tone levels is compatible with the Contractor's earlier test experience and is attributed to fluctuations in atmospheric turbulence ingested by the engine in a static mode. Studies of factors that affect inlet tone data scatter should have high priority for future ground test work.

Analysis of component noise data showed that the fully treated JT8D-115 produced a reduction of 5 to 11 PNdB in a weighted average value of tone corrected perceived noise level (PNLTW), relative to the JT8D-15 hardwall compared at equal static thrust as shown in figure 1. Separated into noise components, the JT8D-115 showed significant noise reduction in inlet fan noise, aft fan noise, exhaust duct flow noise, turbine noise, and jet noise relative to the JT8D-15; however, core noise was increased.

The side-engine inlet lining attenuation (approximately 12 dB at the fan tone frequency with the treated ring configuration at approach power) agreed well with pretest predictions; the center-engine inlet noise was reduced to a low SPL level relative to the side-engine inlet noise

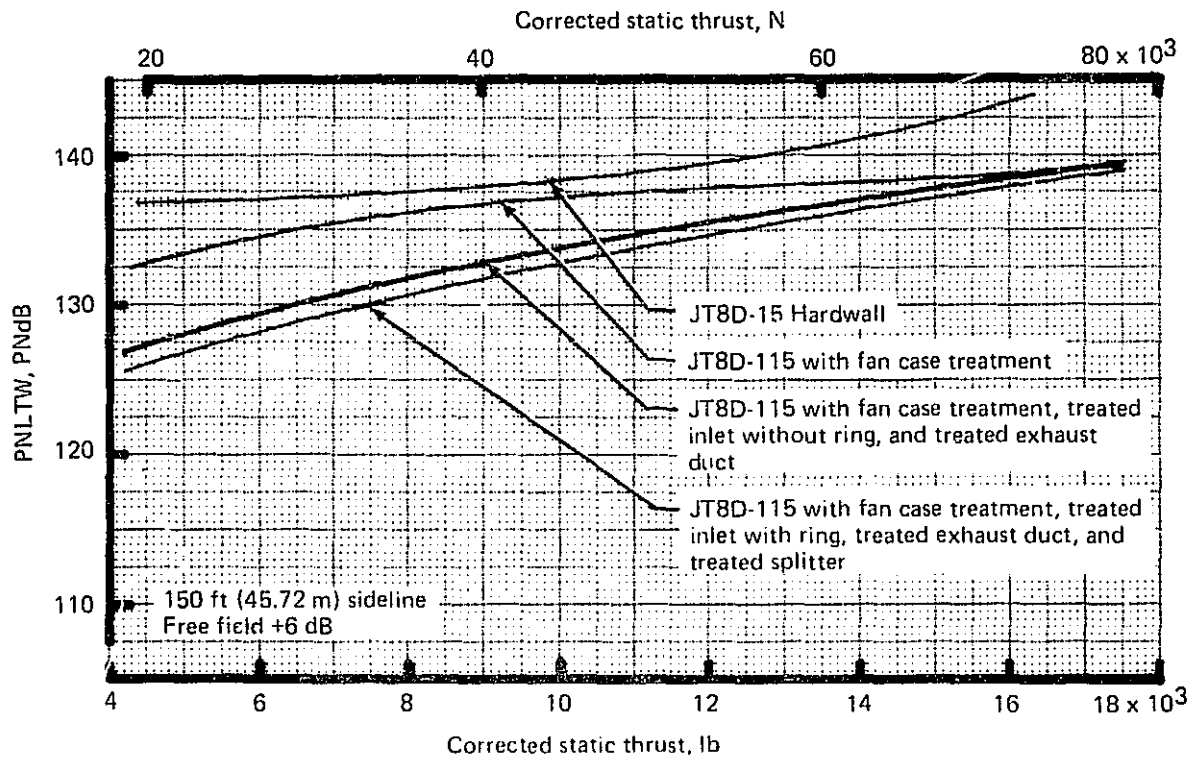


Figure 1.—JT8D-115 Ground Test—Total Noise

(approximately 24 dB at the fan tone frequency at approach power); and the exhaust treatment suppression was not as large as predicted (a peak attenuation of only 5 dB was measured compared to a pretest prediction of 10 dB). Internal SPL measurements provide a basis for possible improvements in inlet splitter locations and lining designs for both the inlet and exhaust system.

The test techniques employed in the JT8D-15 and -115 ground tests for acquisition of component noise information proved generally successful; indeed, these tests provided component noise information to a greater degree of detail than any existing JT8D acoustic data. The use of acoustic barriers for segregation of inlet and aft noise components provided essential information that could not have been obtained otherwise, and the use of ground level microphones at all directivity angles substantially improved the resolution of low-frequency acoustic data. The microphones mounted in the inlets and exhaust system of the JT8D-115 engine provided essential lining design information and yielded the clue that led to the definition of a new noise source: exhaust duct flow noise.

The component noise information extracted from the JT8D-15 and -115 ground test data generally agreed with predicted results with the exception of exhaust duct flow noise. The analysis of this noise source has thus far only been superficial. Much work, both analytical and experimental, is needed to clearly define this noise component.

One of the most interesting aspects of the ground tests resulted from the comparison of Contractor conducted acoustic ground tests on a JT8D-115 engine with P&WA acoustic

tests on a JT8D-109 engine. These two engines are identical throughout, except for the exhaust system hardware and the hot rematch. Curiously, the largest noise difference between the two engines was in the inlet fan noise component when correlated on fan pressure rise (the traditional fan noise parameter). However, when correlated on corrected rpm, the two sets of data agree quite well. From this cursory information, it appears that a detailed study of the relationship between fan noise and the fan operating map is needed in order to better understand inlet-guide-vane fan noise.

The center-engine inlet duct was instrumented to measure skin stresses, duct wall and engine seal deflections, and internal pressures. The structural test data were recorded for both stabilized and surge conditions concurrently with the center-engine inlet-duct surge margin evaluation testing. The exhaust duct and fan/primary flow divider surface temperatures were measured during cold start, maximum acceleration to takeoff power, and engine shutdown.

Analysis of center-engine inlet-duct wall pressure data indicated up to 3% lower stabilized pressures and up to 19% higher surge pressures than predicted by model tests and duct flow analyses. Measured exhaust system hardware temperatures were within the design structural limits.

## 2.0 INTRODUCTION

The NASA Refan Program included development of a JT8D refan engine (JT8D-100 series) by P&WA, and development of the associated 727-200 nacelle hardware by the Boeing Commercial Airplane Company (BCAC). The JT8D-100 series engines are derivatives of the basic JT8D turbofan engines, modified to incorporate a new larger-diameter higher airflow single-stage fan with a bypass ratio (BPR) of approximately 2.0 and two supercharging low-pressure compressor stages. The modification reduces jet noise, increases takeoff and maximum cruise thrust, and reduces static specific fuel consumption. The use of a JT8D refan engine on the 727 airplane requires new side-engine nacelles, center-engine inlet duct and engine installation hardware because of the increased engine diameter and increased engine airflow.

The NASA Refan Program included full-scale performance and noise ground testing of a baseline (JT8D-15) and refan (JT8D-115) engine. The JT8D-115 engine test included both a 727 side- and center-engine installation. This test also included extensive diagnostic and component noise testing, making use of flush-mounted internal microphones and sound shields (baffles). The JT8D-15 portion of the test considered only a side-engine installation with less extensive diagnostic and component noise testing.

The baseline test was conducted on a new JT8D-15 engine on the B-2 test stand at the Contractor's Boardman, Oregon test facility during the time period of August 28 to September 13, 1974. Upon completion of the baseline test, the JT8D-15 was shipped to the Engine Contractor for conversion to a JT8D-115, which was returned to Boardman and was tested during the time period of January 7, 1975 to March 28, 1975.

This volume of the final report presents a description of the two ground tests, describes the data analysis procedures, and presents detailed performance, acoustic, and structural test results. These results include JT8D-15 and -115 engine overall performance, inlet and exhaust system incremental performance relative to the reference hardware, and a component noise evaluation for both engines. The ultimate use of this ground test data was to support the performance and community noise evaluation of the 727-200 refan airplane described in Volume IV of this final report series "Airplane Evaluation and Analysis" (ref. 1).

The JT8D-9 was selected as the baseline in the analysis of the 727 refan airplane because of its wide usage in the current airplane fleet. A new JT8D-15 engine was used as the baseline in the full-scale ground tests due to availability from the Contractor's inventory at greatly reduced program costs compared to acquisition of a JT8D-9 engine. The JT8D-109 performance and noise characteristics were analytically derived from the JT8D-115 ground test data.

The Phase II program used the English system of measurements, with conversion to the International System of Units (SI) (ref. 2) for this report where applicable. The SI units will be found in parentheses following the English units, in additional columns, or as secondary scales where appropriate.

### 3.0 TEST DESCRIPTION

Full-scale ground tests were conducted on the JT8D-15 and -115 engines to acquire steady-state performance, engine surge margin, acoustic, and structural loads data. The test objectives and descriptions of the test facility, test hardware, test instrumentation and data acquisition systems, test conditions, and test procedures are presented in the following subsections.

#### 3.1 TEST OBJECTIVES

The propulsion performance objectives were: (1) to obtain JT8D-15 production nacelle installed engine characteristics that could be used for correlation with measured JT8D-15 noise levels; (2) to determine the side-engine inlet, center-engine inlet duct, and exhaust system performance with the JT8D-115 engine; (3) to investigate the compatibility of the side-engine inlet (with and without inlet ring) and center-engine inlet duct with the JT8D-115 engine; and (4) to obtain JT8D-115 engine characteristics for use in noise source correlations for the various acoustic configurations tested.

The acoustic objectives included determination of: (1) the incremental component noise levels of the JT8D-115 engine compared to the hardwall JT8D-15 engine; (2) the suppression afforded by the side-engine inlet and exhaust system acoustic treatment; (3) the internal sound pressure levels (SPL) in the nacelle; and (4) the incremental free-field noise differences between the side- and center-engine installations.

The structural objectives included: (1) determination of the effect of engine surges on the center-engine inlet duct structure and verification of analysis methods; (2) investigation of the thermal environment in the exhaust duct during critical engine operating conditions; and (3) determination of maximum temperature differentials across the fan/primary flow divider (splitter) during engine startup, acceleration, and shutdown.

#### 3.2 TEST FACILITY

The ground tests were conducted at the Contractor's Boardman, Oregon test facility. This facility has two full scale engine test stands and is equipped with test shop facilities and engineering data support buildings. Instrumentation and data reduction equipment, including an onsite computer, are located at the facility.

The B-2 test stand, which was used for this test, is situated on a large concrete pad and, therefore, is particularly well suited for acoustic testing. Figure 2 shows a sketch of the acoustic test range. The pad has a 250-ft (76.2-m) radius covering 90° of arc, mostly in the aft quadrant, and has a 110-ft (33.53-m) minimum radius in the forward quadrant. The concrete pad provides a uniform, level surface, making the use of ground level microphones possible thereby avoiding frequency-dependent interference pattern problems associated with elevated microphones. In order to minimize variability of acoustic data, the test stand and

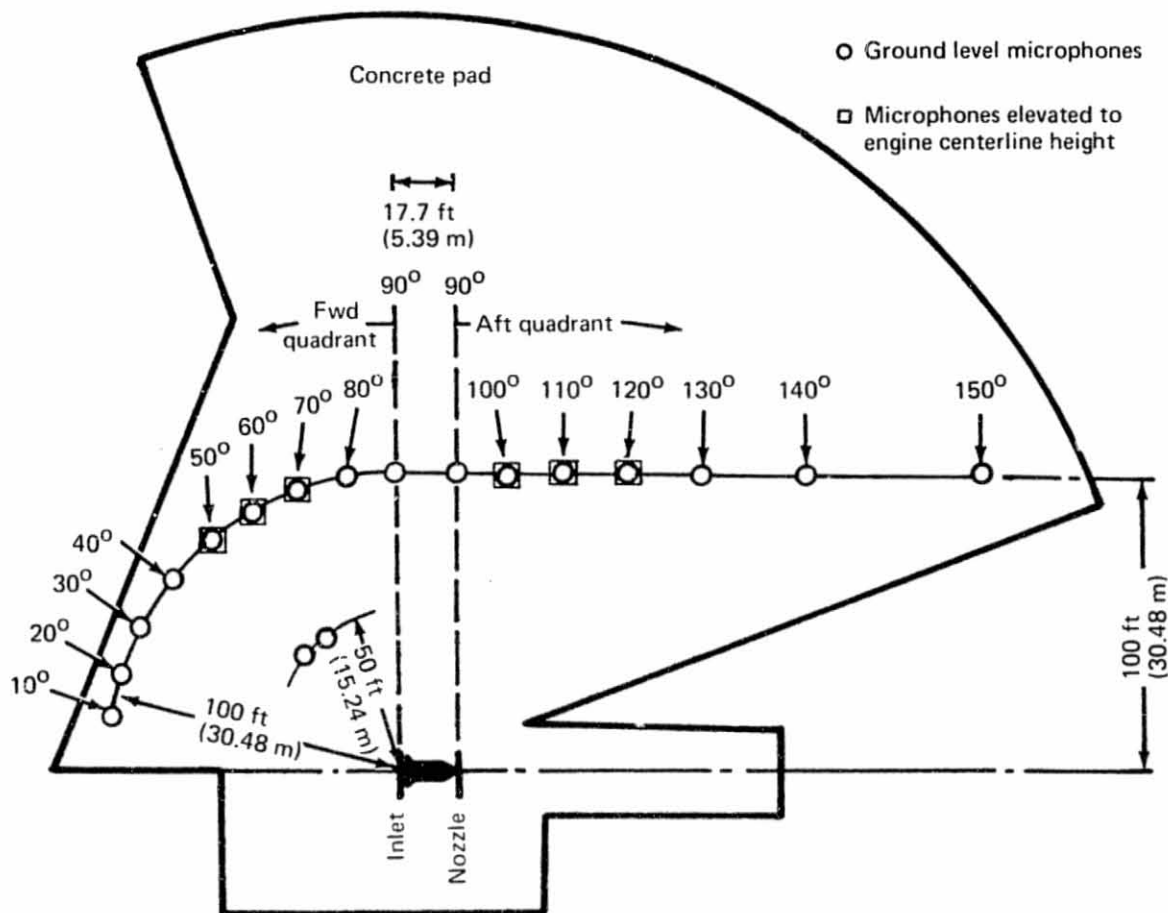


Figure 2.—Boardman Ground Test Facility Acoustic Range—JT8D-15 and -115

other characteristics of the facility were not changed between the JT8D-15 and -115 tests, with two exceptions: engine centerline height was reduced 4 in. (10.16 cm) to 11.7 ft (3.57 m) because of the increased engine diameter, and the side-engine mount system was changed to a top-mount system for the JT8D-115 portion of the testing. These differences were expected to have negligible impact on the ground microphone acoustic data. Photographs of the B-2 test stand with the JT8D-15 and -115 engines are shown in figures 3 and 4.

### 3.3 HARDWARE

The JT8D-15 engine was tested primarily using production hardwall nacelle hardware as well as the Engine Manufacturer's reference hardware. The JT8D-115 engine was tested as a fully treated engine equipped with a variety of acoustically treated nacelle hardware components. The following paragraphs describe the nacelle hardware for the two engines and present a detailed description of the JT8D refan nacelle acoustic linings.



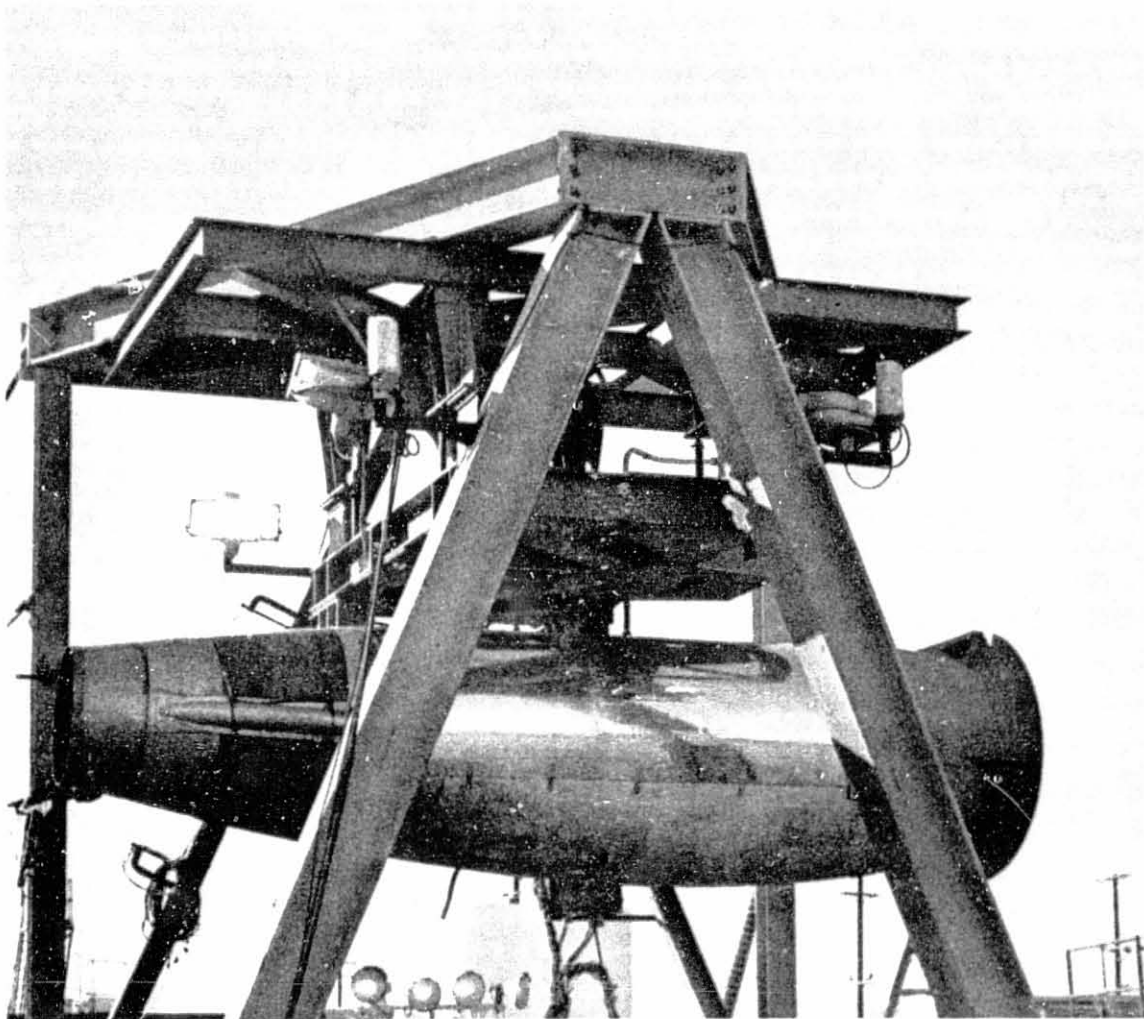


*Figure 3.—Boardman B2 Test Stand With JT8D-15 Engine*

REPRODUCIBILITY OF THE  
ORIGINAL PAGE IS POOR

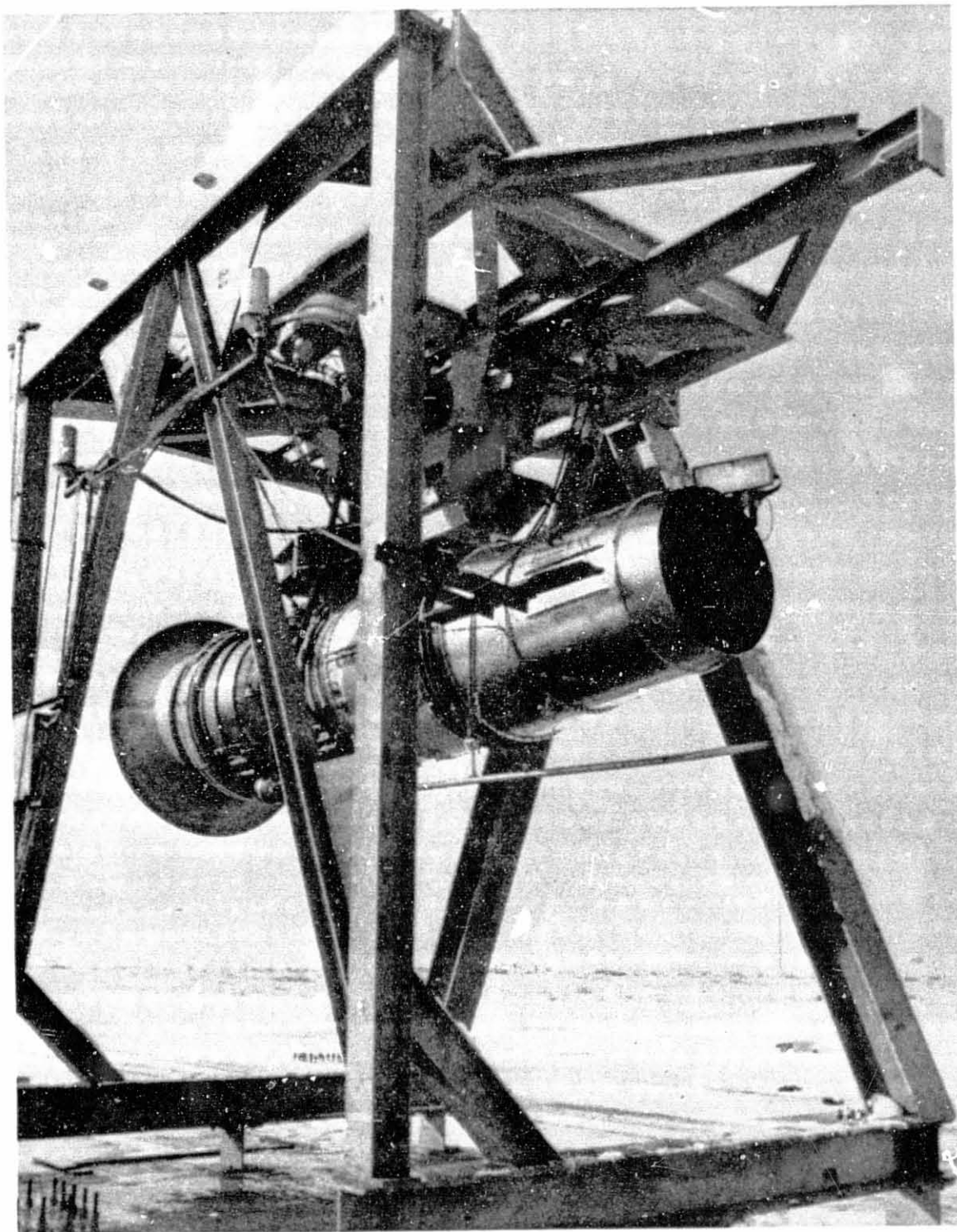


*Figure 4.—Boardman B2 Test Stand With JT8D-115 Engine*

### 3.3.1 JT8D-15

The JT8D-15 engine installation was tested as a 727 no. 3 side engine (i.e., right-hand side engine) and was equipped with a production "hardwall" side-engine inlet (the inlet had a small band of acoustic treatment on the diffuser wall and was judged to closely approximate a hardwall from an acoustic standpoint). This inlet had a flight diffuser and was fitted with a bellmouth lip to simulate the streamlines of a nonseparated flight-type inlet in low-speed flight. The engine was a production JT8D-15 installation except that the production fan case treatment known as BG-19 was replaced with hardwall panels, resulting in a completely hardwall engine. The hardwall production exhaust system included a thrust reverser and complete production cowling. The engine/nacelle configuration is acoustically identical to that used in the existing 727 flight test data base adopted for use in the Refan Program. At the beginning and end of the JT8D-15 ground testing, performance runs were made using a reference bellmouth and exhaust system (exhaust duct, plug, and splitter).

### 3.3.2 JT8D-115

The JT8D-115 engine was tested using a top mount system. This mount system was used instead of the JT8D-15 side mount system because of high stress levels experienced in the side mount test stand adapters during JT8D-15 testing.

The JT8D-115 engine was tested with both reference hardware and the Contractor's hardware which consisted of a side-engine inlet with and without an acoustic ring (fig. 5); a 727 center-engine inlet and duct (fig. 6); and an exhaust duct (wedge duct and nozzle), plug, and splitter assembly (fig. 7). The center- and side-engine inlets were tested with both bellmouth and flight lips. Surge margin data were obtained with flight lips only. The center-engine inlet, side-engine inlet, and flight-type exhaust duct had acoustic lining on the walls and were also tested as hardwall configurations (with tape covering the acoustic lining). Cowling was not used during the testing, but 1/8-in. (3.18-mm) lead sheets were wrapped around the engine during a portion of the testing to simulate the acoustic shielding of the cowl. The exhaust system did not incorporate a thrust reverser.

Details of the design and manufacture of the Contractor's hardware, with the exception of the bellmouth lips, are given in references 3 through 6, and are not repeated here. The flight-type bellmouth lips, reference bellmouth lip, and reference inlets are shown in figure 8. The center-engine inlet duct was shortened by 2.6 in. (6.6 cm) from that shown in reference 4. This was accomplished by reducing the length of the straight section just upstream of the engine face. The vortex generator (VG) configuration used during the JT8D-115 ground test are configurations 12 and 7 from reference 4. The VG's were the vane type used in the production 727 airplanes, consisting of a row of airfoils that project normal from the surface and are set at an angle of incidence to the local flow to produce single trailing vortices. The side-engine inlet acoustic-ring support struts are slightly shorter and thicker than those shown in reference 5. The flight-type exhaust duct plug and splitter are identical to configuration 11 from reference 6. The reference exhaust system, which did not utilize acoustic lining, is shown in figure 9.

Much of the JT8D-115 acoustic testing was conducted using an exhaust system that consisted of the reference plug and splitter and the flight-type exhaust duct. This configuration is referred to as the hybrid exhaust system throughout this report. Sketches of the flight-type exhaust system and the hybrid exhaust system are shown in figure 10.

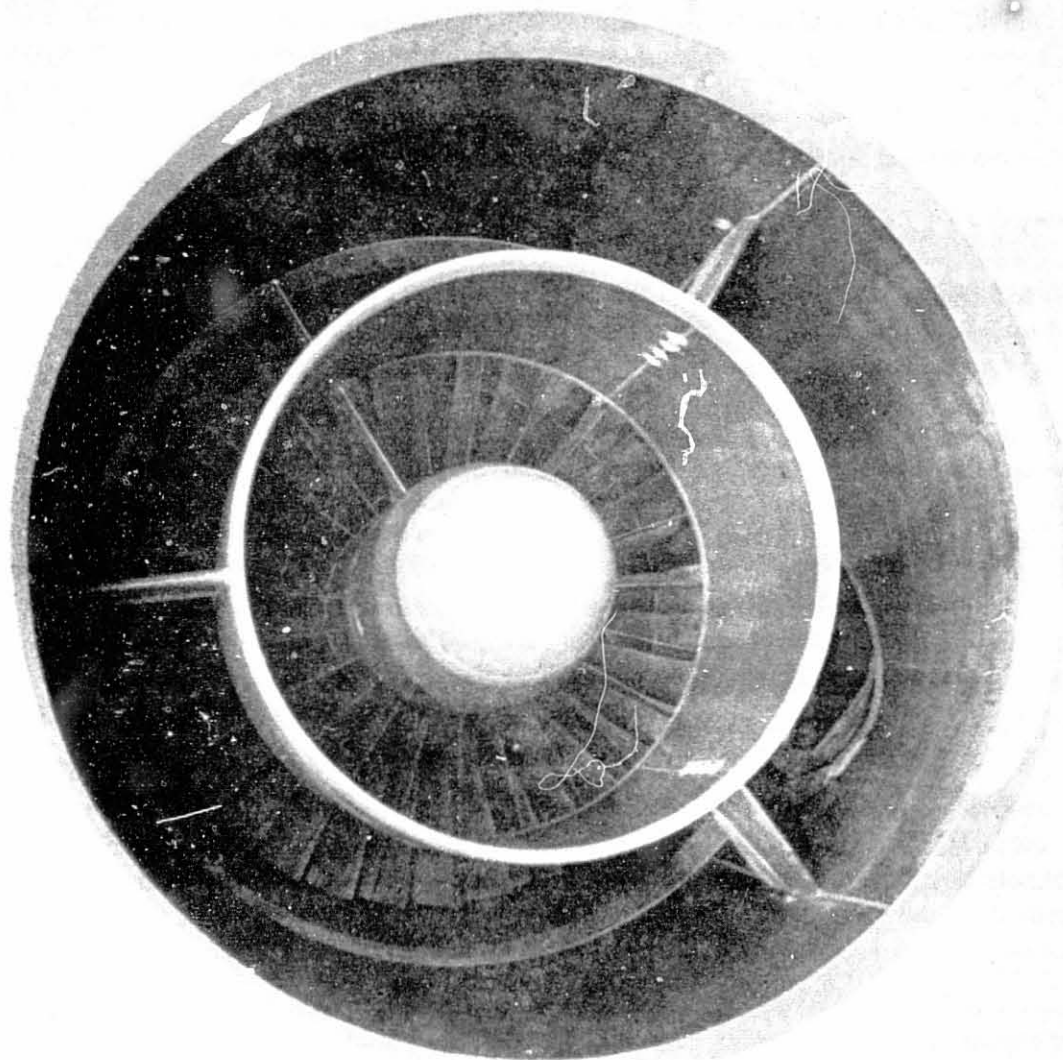


*Figure 5. -JT8D-115 Ground Test Side Inlet With Acoustic Ring*

REPRODUCIBILITY OF THE  
ORIGINAL PAGE IS POOR

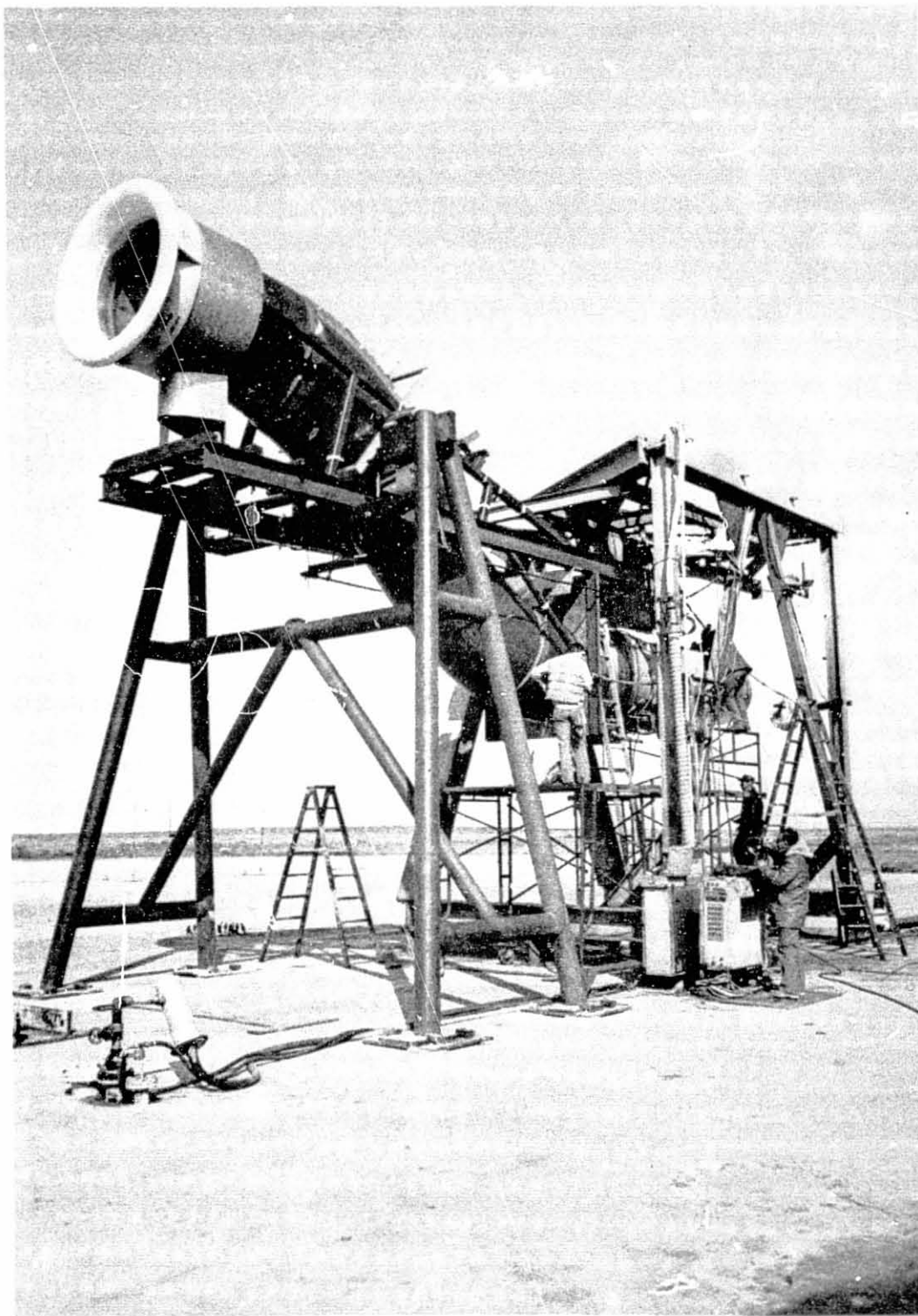


*Figure 6.—JT8D-115 Center-Engine Inlet and Duct Assembly Test Setup*





*Figure 7.— JT8D-15 Flight-Type Exhaust System*

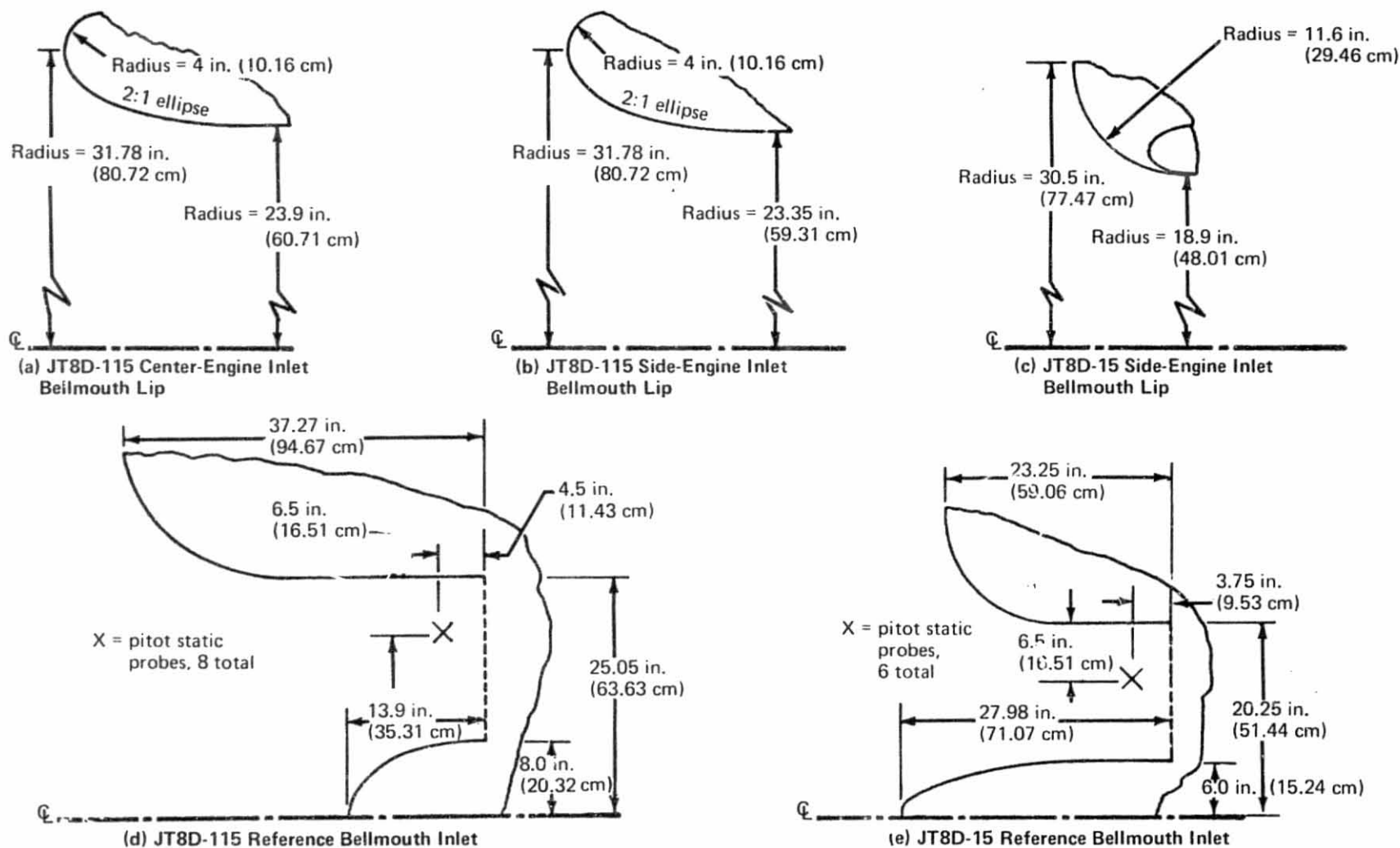
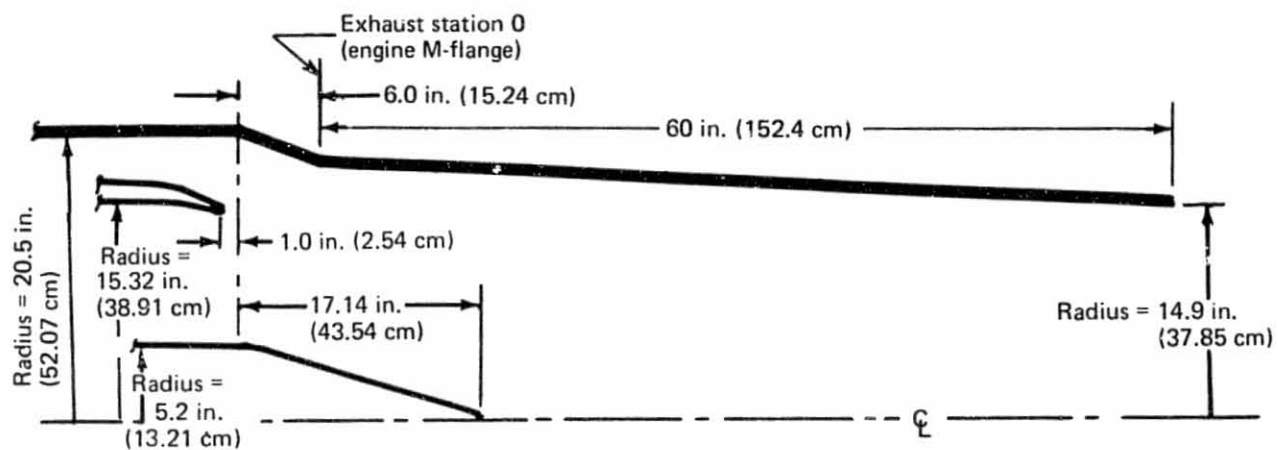
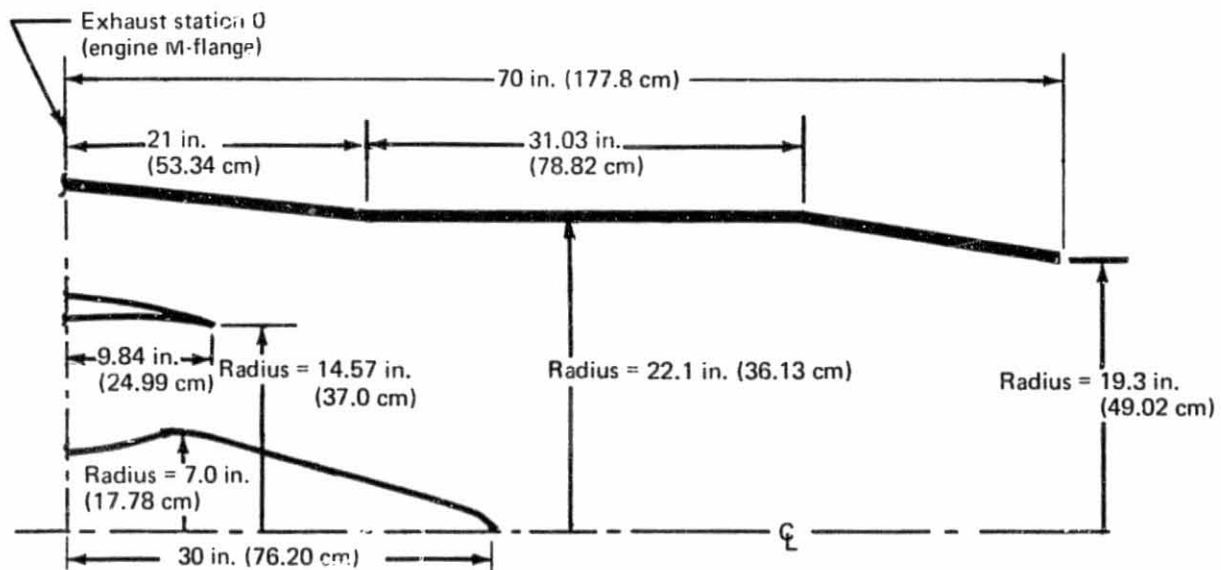


Figure 8.— JT8D-15 and -115 Ground Test Inlet Bellmouth Configurations



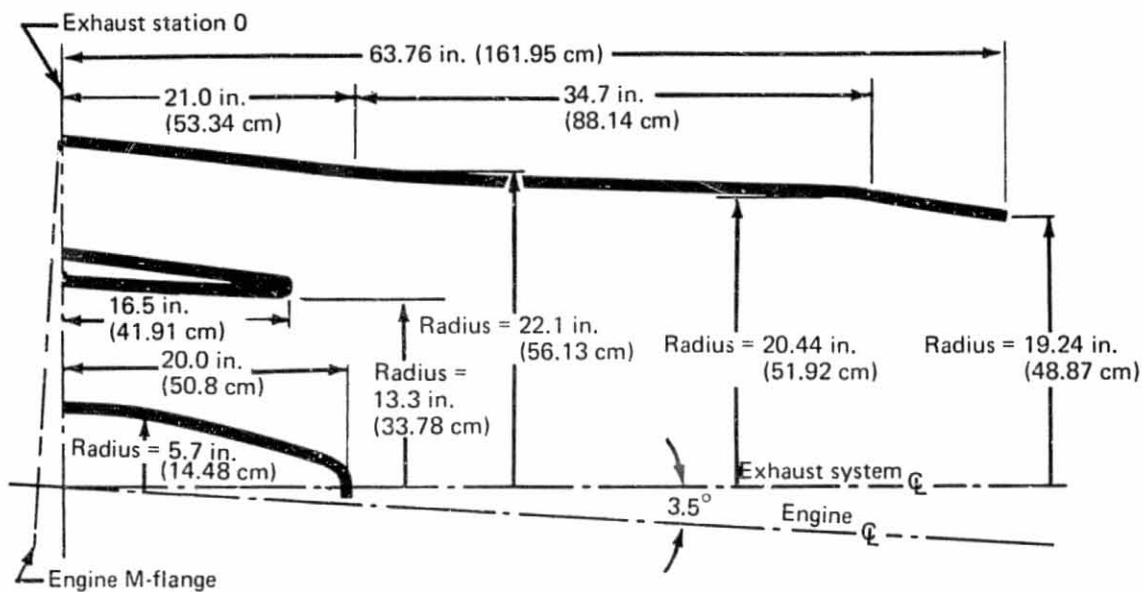
(a) JT8D-15 Reference Exhaust System



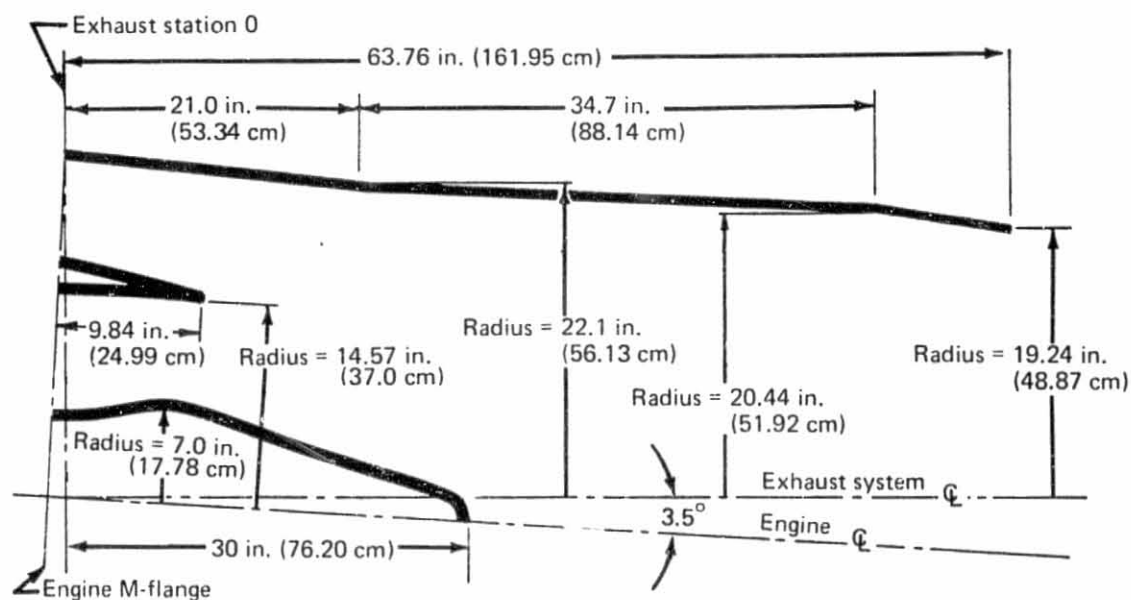
(b) JT8D-115 Reference Exhaust System

Figure 9.— JT8D-15 and -115 Reference Exhaust Systems





(a) JT8D-115 Flight-Type Exhaust System



(b) JT8D-115 Hybrid Exhaust System

Figure 10.—JT8D-115 Flight-Type and Hybrid Exhaust Systems

REPRODUCIBILITY OF THE  
ORIGINAL PAGE IS POOR

During the testing, the center- and side-engine inlets were tested under crosswind conditions, simulated by use of a R2800-31 engine driving a variable-pitch propeller (crosswind machine). To include the fuselage effect on the flowfield, an airplane fuselage section was used during all crosswind testing. Figures 11 through 14 show general details of the crosswind test setups.

Hardware representing two levels of acoustic lining was designed and tested on the JT8D-115 engine. The main features of the configurations were as follows: in configuration 1 (fig. 15), inlet acoustic treatment was applied to the inlet diffuser and nose dome; fan duct treatment was that prescribed by the Engine Contractor; and exhaust duct treatment was peripheral. In configuration 2 (fig. 16), the inlet treatment included, in addition to diffuser and nose dome treatment, a treated inlet ring; the fan duct treatment again was that prescribed by the Engine Contractor; and the exhaust duct treatment was peripheral. The fan/primary flow divider (splitter) acoustic treatment was applied to both the fan and primary flow sides of the splitter. The center-engine inlet was also fully treated (fig. 17).

Inlet, exhaust duct, and fan/primary flow divider acoustic treatments were designed for the JT8D-109 engine powering the 727-200. The design point was the FAR Part 36 approach point for a landing weight of 142 500 lb (64 637 kg). The aircraft was assumed to be in the landing configuration with 6310-lb (28 068-N) net thrust, 40° flap position, 139-kn (71.5-m/s) true airspeed, and 370-ft (113-m) altitude at the FAR Part 36 approach point. The inlet and exhaust system linings were tuned for the fan fundamental blade passage frequency, except for the inner surface of the fan/primary flow divider which was tuned for turbine tones.

### 3.4 INSTRUMENTATION AND DATA ACQUISITION

The JT8D-15 engine was tested with a minimum of performance instrumentation, an array of 24 far-field ground level and elevated microphones, and no structural instrumentation. The JT8D-115 engine was tested with more extensive performance and acoustic instrumentation and with structural instrumentation in the center-engine inlet, exhaust duct, and fan/primary flow divider. The following paragraphs describe the test instrumentation and data acquisition systems used to process and record the performance, acoustic, and structural test data.

#### 3.4.1 PROPULSION

Figure 18 shows a flow diagram of the propulsion data acquisition from the Contractor's Standard Digital Data System (SDDS) through the onsite computer to obtain quick-look tabulated data and plots as well as the transmission of the data to the Control Data Corporation (CDC-6600) digital computer for final processing of propulsion data in Renton, Washington. A backup computer was also available in Seattle, Washington. A digital mini-computer was used to obtain the onsite quick-look data.

During center-engine inlet performance and crosswind testing and during side-engine inlet crosswind testing, a fixed eight-arm pressure survey rake was used in the inlet to determine inlet performance. Ten probes were located on each arm at equal area centers (fig. 19).

REPRODUCIBILITY OF THE  
ORIGINAL PAGE IS POOR

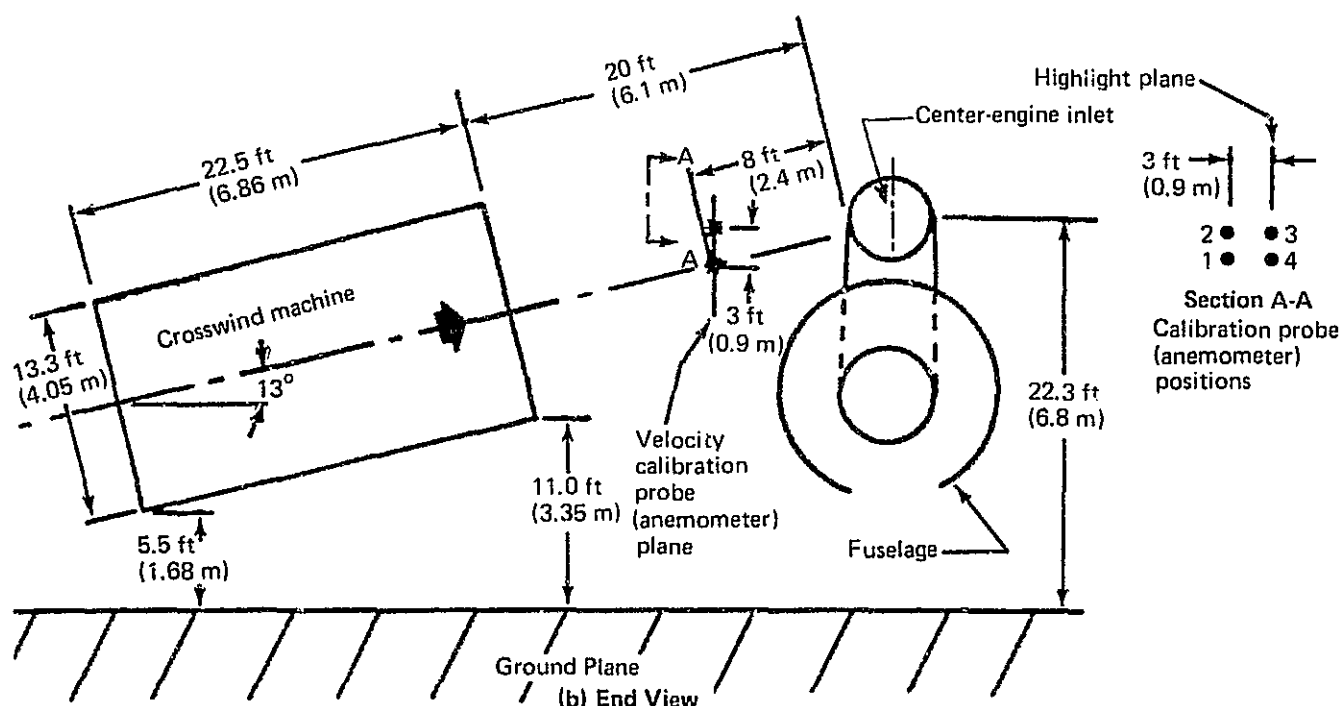
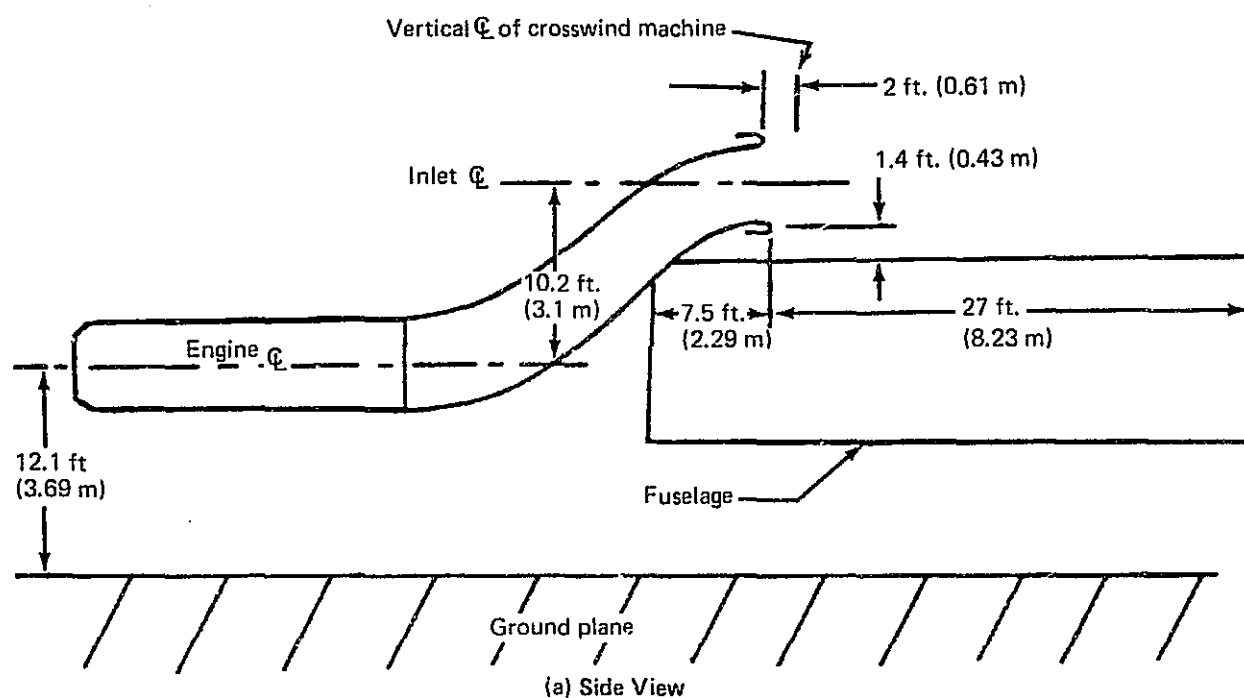


Figure 11.—727/JT8D-115 Center-Engine Inlet and Duct Crosswind Ground Test Configuration Schematic

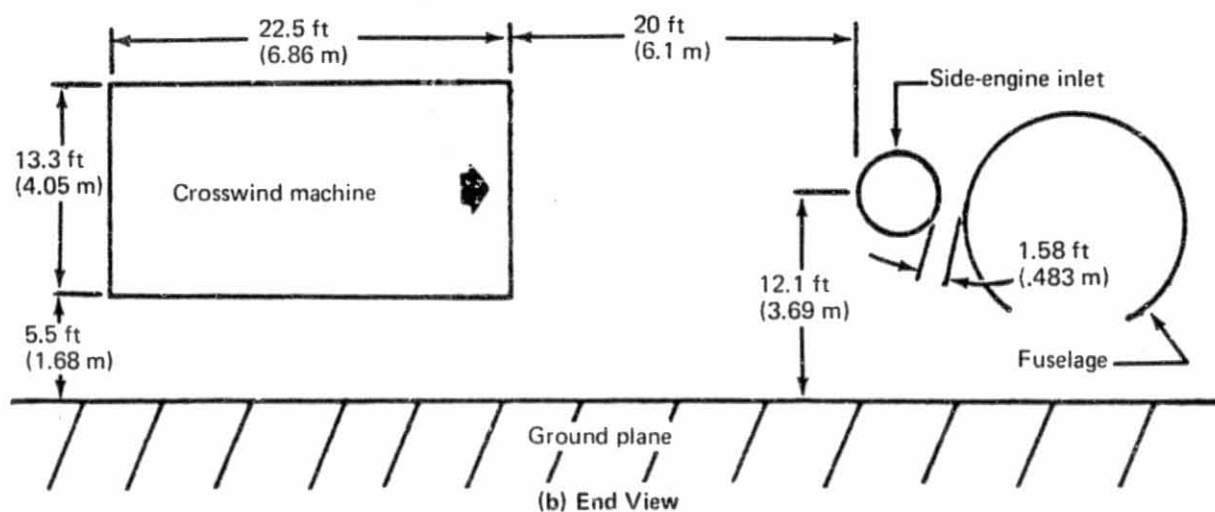
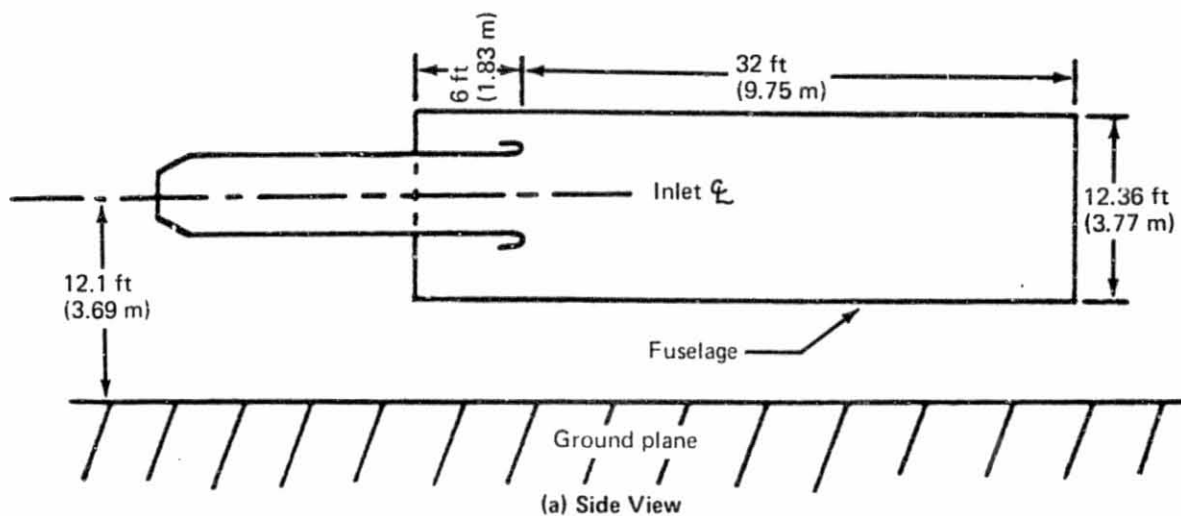
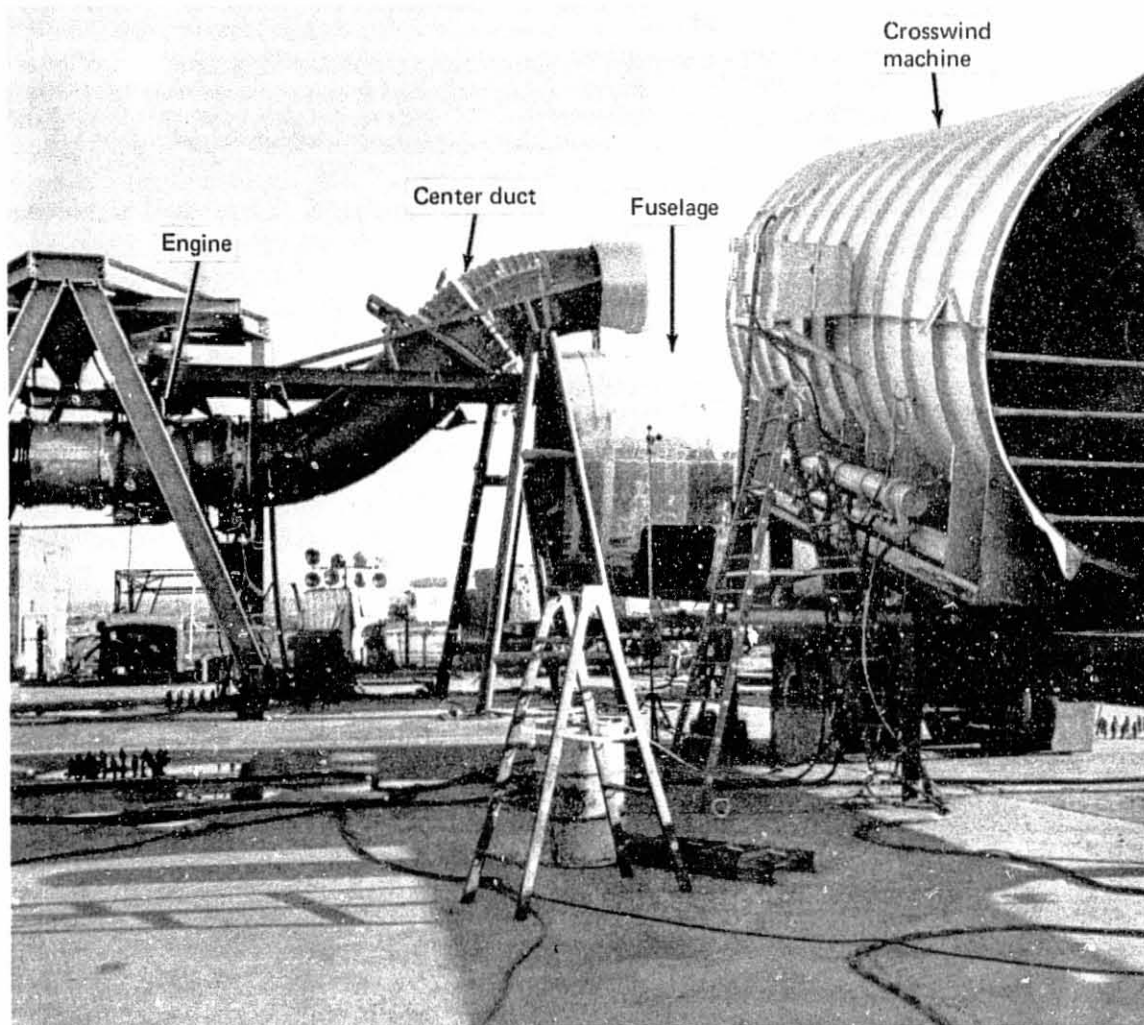


Figure 12.—727/JT8D-115 Side-Engine Inlet Crosswind Ground Test Configuration Schematic

REPRODUCIBILITY OF THE  
ORIGINAL PAGE IS POOR



*Figure 13.—JT8D-115 Center-Engine Crosswind Test Setup*

REPRODUCIBILITY OF THE  
ORIGINAL PAGE IS POOR

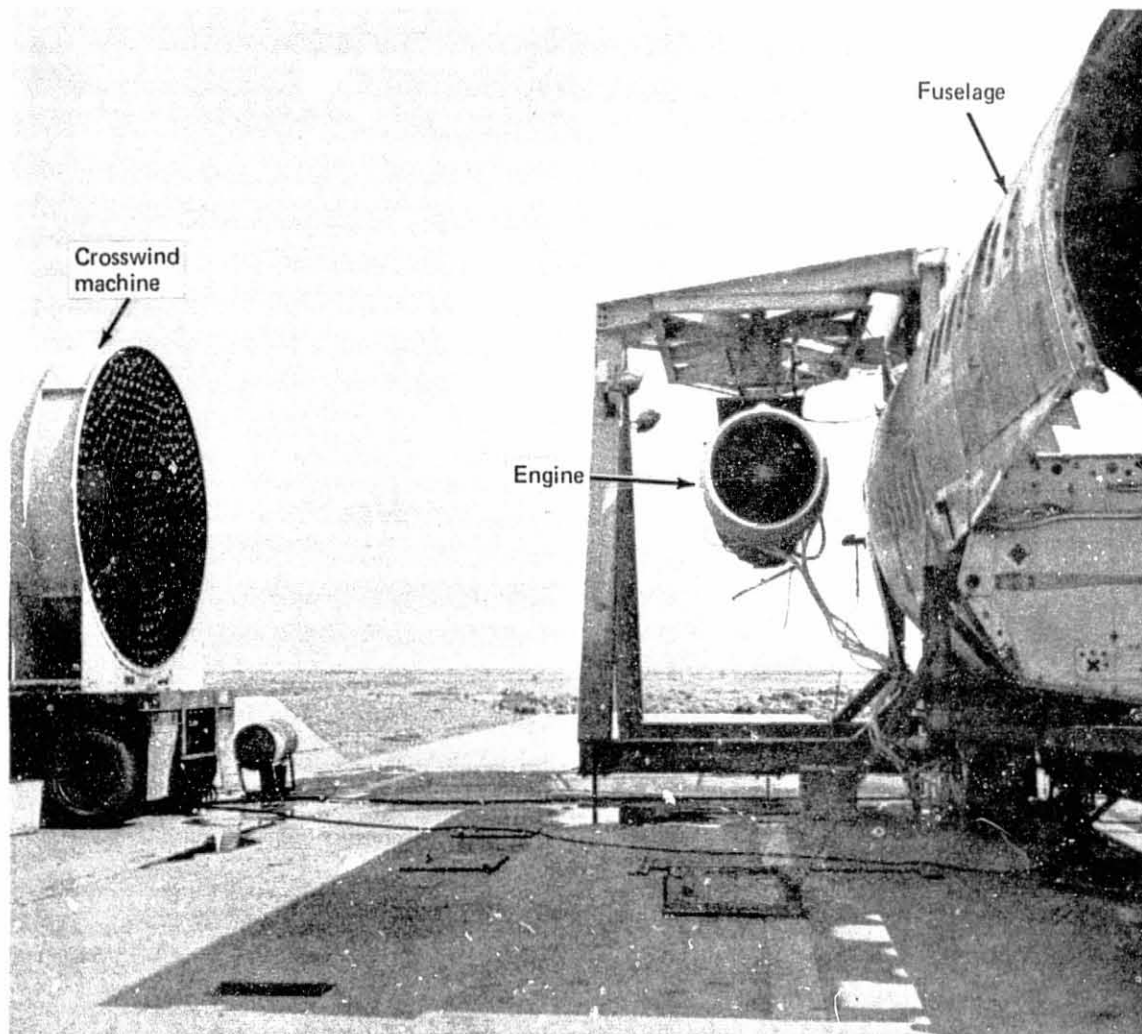
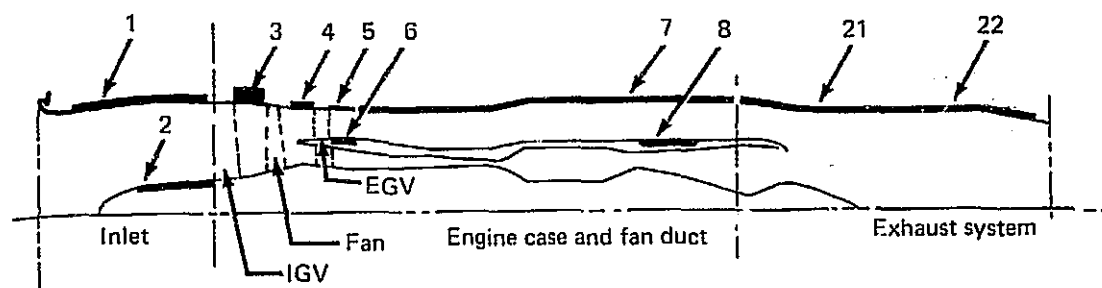


*Figure 14.—JT8D-115 Side-Engine Crosswind Test Setup*



Lining designation	Location	Face sheet type	Net active treatment area ft <sup>2</sup> (m <sup>2</sup> )	Core depth, in. (cm)	Cell size, in. (cm)	Undirectional flow resistance R/ρc at Vp/√θ, cm/s		Open area, %	Hole dia, in. (cm)	Face sheet thickness, in. (cm)
						1	2			
Inlet										
1	Diffuser	Polyimide ↓	29.9 (2.78)	0.30 (0.76)	0.375 (0.95)	2.16 + 15%	82.3			
2	Nose dome		4.3 (0.39)	0.30 (0.76)	0.375 (0.95)	2.16 + 15%	82.3			
Engine case and fan duct										
3	Fwd of fan	Perforated sheet ↓	7.6 (0.706)	1.00 (2.54)	0.375 (0.95)			20	0.045 to 0.060 (0.114 to 0.152)	0.016 (0.0406)
4	Aft of fan			6.3 (0.505)	0.50 (1.27)			12		
5	Aft of EGV			11.2 (1.04)	0.25 (0.635)					
6	Aft of EGV			6.12 (0.568)	0.25 (0.635)					
7	Outer wall aft			76.8 (7.13)	0.50 (1.27)					
8	Inner wall aft			7.5 (0.696)	0.50 (1.27)					
Exhaust system										
21	Wedge duct	Perforated titanium sheet ↓	20.0 (1.86)	0.50 (1.27)	0.375 (0.95)	1.46 { +0.48 -0.36	40	2.8	0.042 (0.107)	0.014 (0.035)
22	Nozzle		31.0 (2.89)	0.50 (1.27)	0.375 (0.95)	1.46 { +0.48 -0.36	40	2.8	0.042 (0.107)	0.014 (0.035)

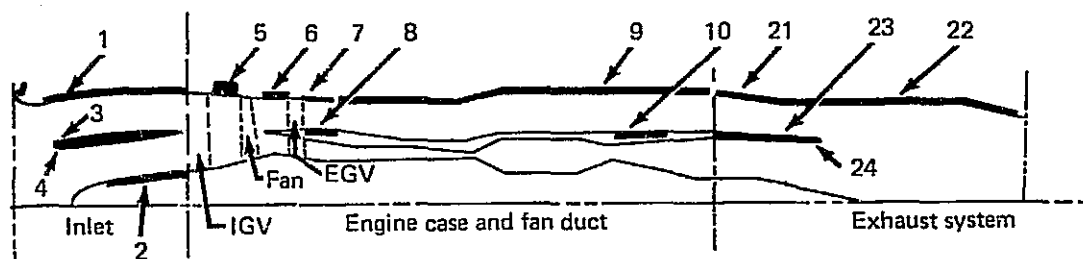


Undirectional flow resistance ratio after bonding with core where R = flow resistance of sample in N-sec/m<sup>3</sup> (MKS Rayls) and ρc = reference flow resistance in N-sec/m<sup>3</sup> (MKS Rayls).



Vp = particle velocity and θ = static temperature ratio T<sub>S</sub><sup>0</sup>R/519 (T<sub>S</sub>K/288) of air approaching sample in flow resistance test.

Figure 15.—JT8D-115—Configuration 1, Acoustic Lining Definition as Tested



Lining designation	Location	Face sheet type	Net active treatment area ft <sup>2</sup> (m <sup>2</sup> )	Core depth, in. (cm)	Cell size, in. (cm)	Unidirectional flow resistance R/ρc at Vp/θ cm/s		Open area, %	Hole dia, in. (cm)	Face sheet thickness, in. (cm)
						1	2			
Inlet										
1	Diffuser	Polyimide ↓	29.4 (2.73)	0.30 (0.76)	0.375 (0.95)	2.16 + 15%	82.3			
2	Nose dome		4.3 (0.39)	0.30 (0.76)	0.375 (0.95)	2.16 + 15%	82.3			
3	Ring (outer wall)		13.3 (1.23)	0.18 (0.46)	0.375 (0.95)	2.03 + 15%	77.4			
4	Ring (inner wall)		12.7 (1.18)	0.17 (0.43)	0.375 (0.95)	2.42 + 15%	64.8			
Engine case and fan duct										
5	Fwd of fan	Perforated sheet ↓	7.6 (0.706)	1.00 (2.54)	0.375 (0.95)			20	0.045 to 0.060 (0.114 to 0.152)	0.116 (0.0406)
6	Aft of fan		6.3 (0.585)	0.50 (1.27)				12		
7	Aft of EGV		11.2 (1.04)	0.25 (0.635)						
8	Aft of EGV		6.12 (0.568)	0.25 (0.635)						
9	Outer wall aft		76.8 (7.13)	0.50 (1.27)						
10	Inner wall aft		7.5 (0.696)	0.50 (1.27)						
Exhaust system										
21	Wedge duct	Titanium ↓	20.0 (1.86)	0.50 (1.27)	0.375 (0.95)	1.46 { +0.48 -0.36 ↓	40	2.8	0.042 (0.107)	0.014 (0.035)
22	Nozzle		31.0 (2.89)	0.50 (1.27)	0.375 (0.95)		40	2.8	0.042 (0.107)	0.014 (0.035)
23	Divider-fan flow side		19.4 (1.002)	1.0 (2.54)	0.375 (0.95)		40	2.8	0.042 (0.107)	0.014 (0.035)
24	Divider-primary flow side		Perforated Inconel	5.5 (0.511)	0.50 (1.27)		0.375 (0.95)	40	3.3	0.040 (0.10)



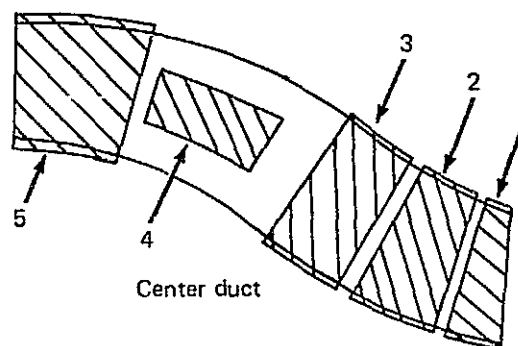
Unidirectional flow resistance ratio after bonding with core where R = flow resistance of sample in N. sec/m<sup>3</sup> (MKS Rayls) and ρc = reference flow resistance in N. sec/m<sup>3</sup> (MKS Rayls).



Vp = particle velocity and θ = static temperature ratio T<sub>S</sub><sup>0</sup>R/519 (T<sub>S</sub>K/288) of air approaching sample in flow resistance test.

Figure 16.—JT8D-115—Configuration 2, Acoustic Lining Definition as Tested





Lining designation	Location	Face sheet type	Net active treatment area ft <sup>2</sup> (m <sup>2</sup> )	Core depth, in. (cm)	Cell size, in. (cm)	Unidirectional flow resistance R/ρc at Vp/θ, cm/s		Open area, %	Hole dia, in. (cm)	Face sheet thickness, in. (cm)
						1	2			
1	Center-duct, lower-aft	Perforated aluminum sheet	22.2 (2.06)	1.25 { +10% (3.17) - 5%	0.375 (0.95)	4		26.3	0.050 (0.127)	0.040 (0.102)
2	Center-duct, lower-center		54.1 (5.02)	0.18 ± 5% (0.46)		0.46 ± 15%	340	14.8	0.040 (0.102)	0.032/0.025 (0.081/0.013)
3	Center-duct, lower-fwd		40.7	0.18 ± 5% (0.46)		0.75 ± 15%	117	7.1	0.040 (0.102)	0.032/0.025 (1.081/0.063)
4	Center duct, upper-aft		29.1 (2.70)	2.50 ± 5% (6.35)		1.37 ± 15%	36.3	3.5	0.040 (0.102)	0.020 (0.051)
5	Center-duct, upper-fwd		58.3 (5.42)	0.18 ± 5% (0.46)		1.65 ± 15%	30.1	3.5	0.040 (0.102)	0.028 (0.071)



Unidirectional flow-resistance ratio after bonding with core where  $R$  = flow resistance of sample in  $N \cdot \text{sec}/m^3$  (MKS Rayls) and  $\rho c$  = reference flow resistance in  $N \cdot \text{sec}/m^3$  (MKS Rayls).



$V_p$  = particle velocity and  $\theta$  = static temperature ratio  $T_s^0 R/519$  ( $T_s^0 K/288$ ) of air approaching sample in flow resistance test.



Based on open perforations in active treatment area after bonding with core.



Use skin perforation open area.



Face sheet is segmented. Gage of top and bottom sections is 0.032 in. (0.813 mm). Gage of side sections is 0.025 in. (0.635 mm). For attenuation predictions an average value of 0.028 in. (0.711 mm) was used.

Figure 17.—JT8D-115 Center-Engine Inlet Duct Acoustic Lining Definition as Tested

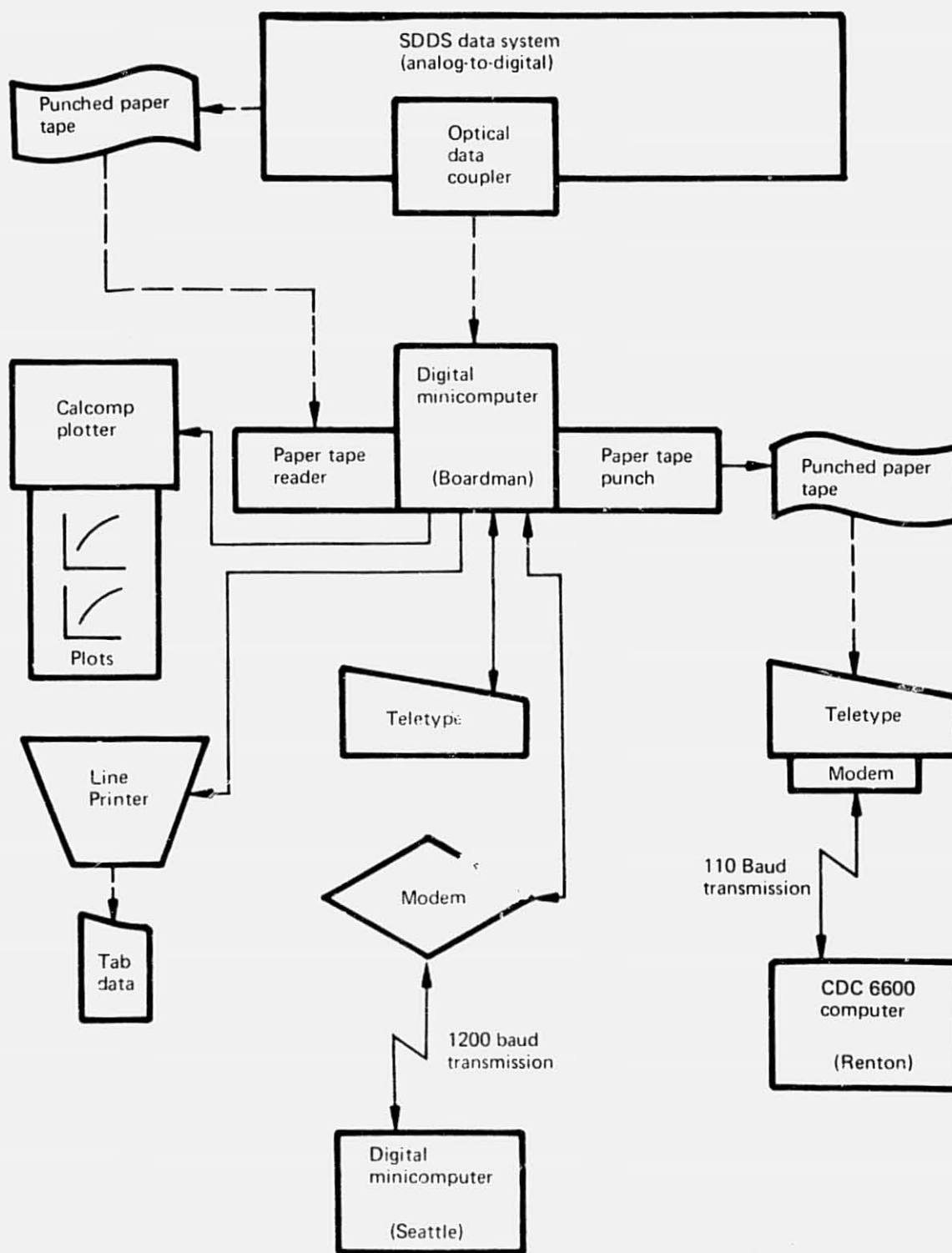


Figure 18.—Propulsion Data Acquisition Flow Diagram

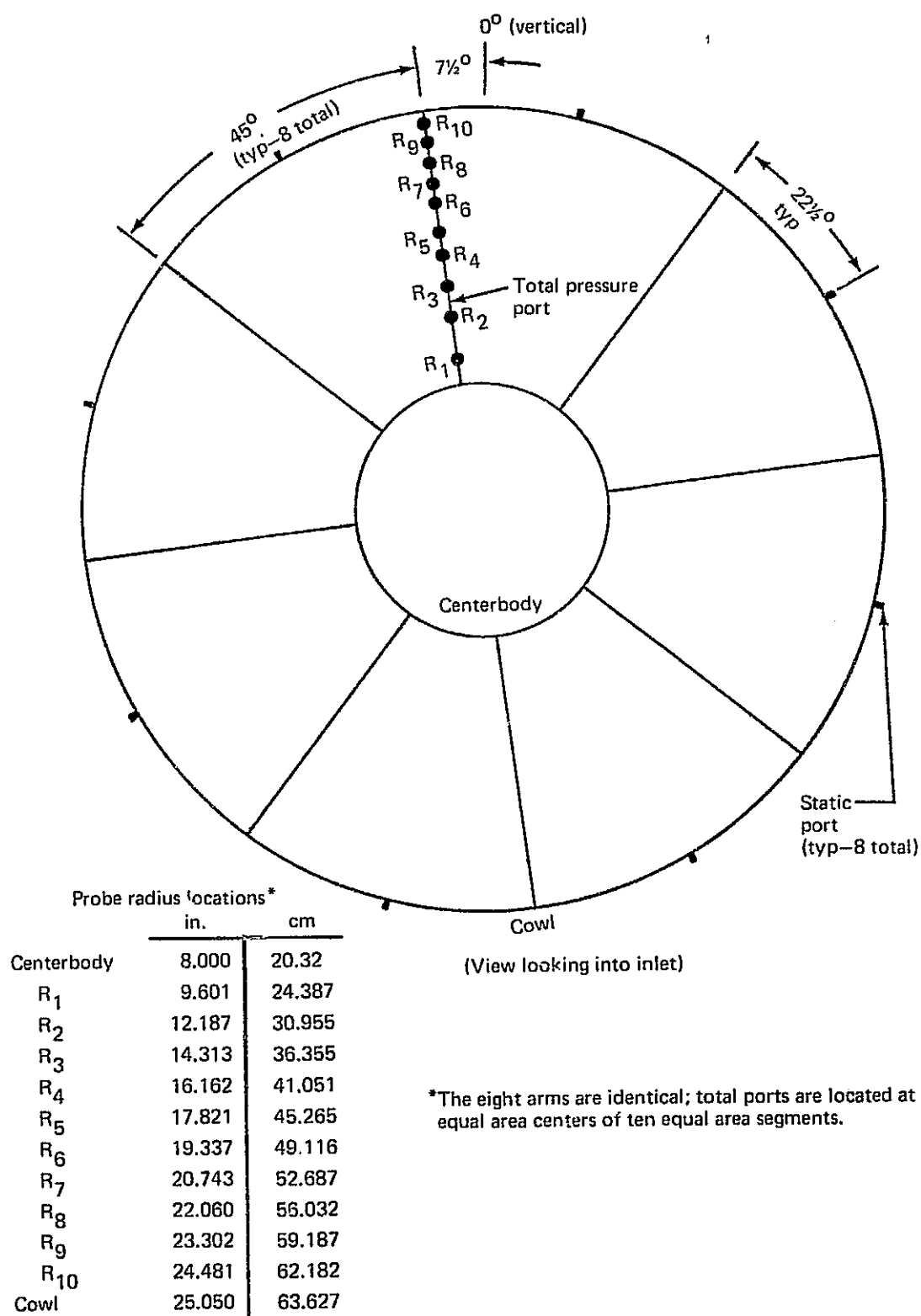


Figure 19.—JT8D-115 Full-Scale Ground Test Inlet Pressure Survey Rake

Output signals from the thrust load cell, pressure transducers, thermocouples, engine rotor speed tachometers, displacement transducers, as well as constants were properly sequenced and converted to digital values by the SDDS system. All propulsion steady-state data were sampled 10 times and averaged for each data point. Without recording the inlet compressor-face total pressure data, the system required 52 sec to record the propulsion data. Each of the 10 samples of data from the engine rotor speed tachometers was averaged over a 1-sec time period. Inlet compressor-face total pressure data was trapped at the beginning of the first sampling of the other propulsion data and then scanned at the completion of the tenth sampling. Additional time required to complete the inlet total pressure scan equalled 48 sec. Table 1 shows a list of the recorded propulsion parameters, their ranges, and accuracies.

### 3.4.2 ACOUSTIC

Instrumentation used for acquisition of acoustic data included ground level and engine centerline height far-field microphones together with flush-mounted and inlet survey internal microphones. The far-field microphones were located as shown in figure 2, and the internal microphones were located in the side-engine inlet, center-engine inlet, and exhaust system as shown in figures 20, 21, and 22, respectively. A summary of all internal microphone locations is given in table 2.

A flow diagram of the acoustic data system is shown in figure 23. All acoustic data was recorded on magnetic tape and was digitized in 1/3 octave bands (OB) after each test run. The original tape was then stored for selective follow-on analyses, such as narrow-band spectra, cross correlation functions, coherence, and time histories. Analog-to-digital conversion of recorded acoustic data was performed at the Boardman site using a root mean square (rms) detector and 1/3-OB filter set. Microphone frequency response corrections and formation of the digital data was handled by a mini-computer. Digital 1/3-OB data were transmitted by telephone line to the CDC-6600 computer in Renton, Washington, where it was stored in a data bank. Onsite reduced data included tabulated corrected spectra and 1/3-OB plots for selected microphones. Online data (taken during engine stabilization and prior to tape recorded data) consisted of 1/3-OB plots for up to six microphones. The online data included microphone system frequency corrections and were plotted by the minicomputer.

### 3.4.3 STRUCTURAL

The center-engine inlet duct was instrumented with strain, pressure, and deflection gages to record the dynamic response during stabilized and surge conditions. The center-engine inlet duct is shown set up in the ground test rig in figure 24.

Four axial strain gages were mounted on the vertical fin front spar fitting which supported the duct in the test rig (fig. 25, cross-section AA).

The center-engine inlet duct perforated aluminum inner skin was instrumented with four rosette strain gages located at the top, lower, and side centerlines (i.e., major and minor axes) on a section normal to the duct longitudinal axis at body station (B.S.) 1230 in. (3124.2 cm). To avoid interference with the holes in the skin, the gages were mounted on 2-in. (5.08-cm) square 0.004-in. (0.102-mm) thick 2219 aluminum foil which was bonded to the perforated

Table 1.—Propulsion Data Accuracy

Parameter	Range	Accuracy (95% confidence)
Thrust, $F_g$	$\pm 25\ 000$ lb	$\pm 0.2\%$ of full-scale reading
LPC rotor speed, $N_1$	0 to 8000 rpm	$\pm 0.6\%$ of full-scale reading
HPC rotor speed, $N_2$	0 to 12 250 rpm	$\pm 0.4\%$ of full-scale reading
LPC discharge press, $P_{s3}$	$\pm 100$ psig ( $\pm 6.89 \times 10^5$ N/m <sup>2</sup> )	$\pm 1.4\%$ of full-scale reading
HPC discharge press, $P_{s4}$	$\pm 400$ psig ( $\pm 2.75 \times 10^6$ N/m <sup>2</sup> )	$\pm 1/4\%$ of full-scale reading
Fan duct total press, $P_{tf7}$	$\pm 25$ psig ( $\pm 1.72 \times 10^5$ N/m <sup>2</sup> )	$\pm 1/4\%$ of full-scale reading
Turbine discharge total press, $P_{t7}$	$\pm 25$ psig ( $\pm 1.72 \times 10^5$ N/m <sup>2</sup> )	$\pm 1/4\%$ of full-scale reading
Fan duct total temp, $T_{tf7}$	0 to 530°F (255.4 to 549.8 K)	$\pm 2^\circ\text{F}$ ( $\pm 256.4$ K) of reading
Turbine discharge total temp, $T_{t7}$	530 to 1200°F (549.8 to 922 K)	$\pm 0.5\%$ of reading
Fuel flow, $W_f$	0 to 48 gpm (0 to 0.003 m <sup>3</sup> /s)	$\pm 0.5\%$ of reading
Fuel temp, $T_{fuel}$	-20 to 100°F (244.3 to 310.9 K)	$\pm 1^\circ\text{F}$ ( $\pm 255.9$ K) of reading
Fuel sp. gr., $F_{sg}$	0.77 to 0.83	$\pm 0.15\%$ of reading
Ambient press, $P_{amb}$	28 to 31 in. Hg abs (711 to 787 mmHg abs)	$\pm 0.1\%$ of reading
Ambient temp, $T_{amb}$	0 to 120°F (255.4 to 322 K)	$\pm 0.2^\circ\text{F}$ ( $\pm 255.5$ K) of reading
Relative humidity, RH	0 to 100%	$\pm 5\%$ of full-scale reading
Wind velocity, $V_w$	0 to 30 mph (0 to 13.4 m/s)	$\pm 1.7\%$ of full-scale reading
Wind direction, $D_w$	0 to 360°	$\pm 1.4\%$ of full-scale reading
Inlet static press, $P_{s2}$	$\pm 2.5$ psig ( $\pm 1.72 \times 10^4$ N/m <sup>2</sup> )	$\pm 1.4\%$ of full-scale reading
Inlet total press, $P_{t2}$	$\pm 5$ psig ( $\pm 3.44 \times 10^4$ N/m <sup>2</sup> )	$\pm 1/4\%$ of full-scale reading

REPRODUCIBILITY OF TEST  
ORIGINAL PAGE IS FOR

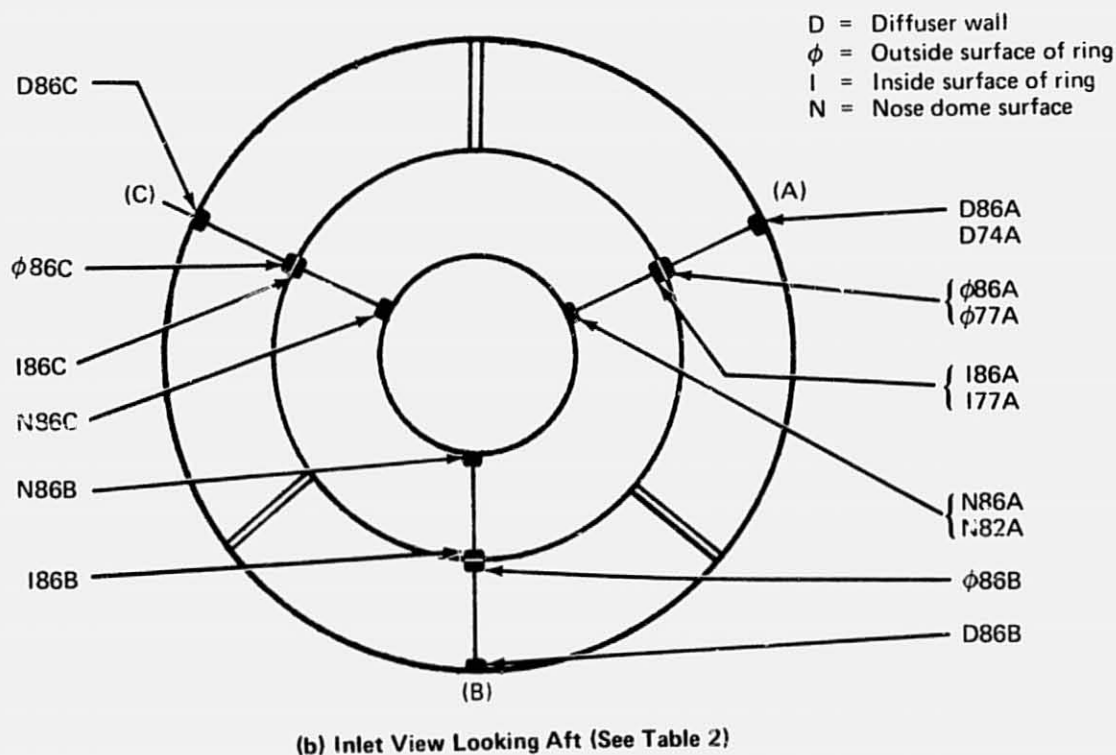
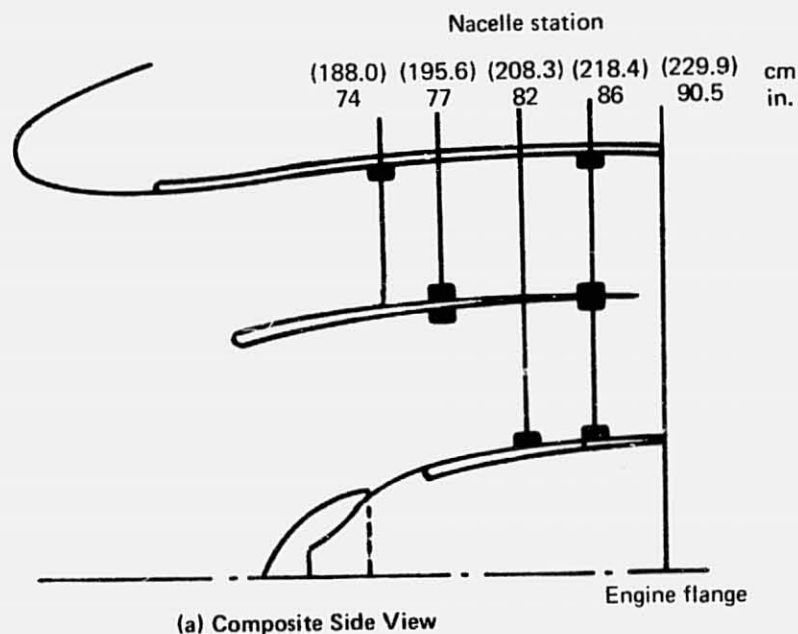


Figure 20.—JT8D-115 Side-Engine Inlet Flush-Mounted Microphone Locations

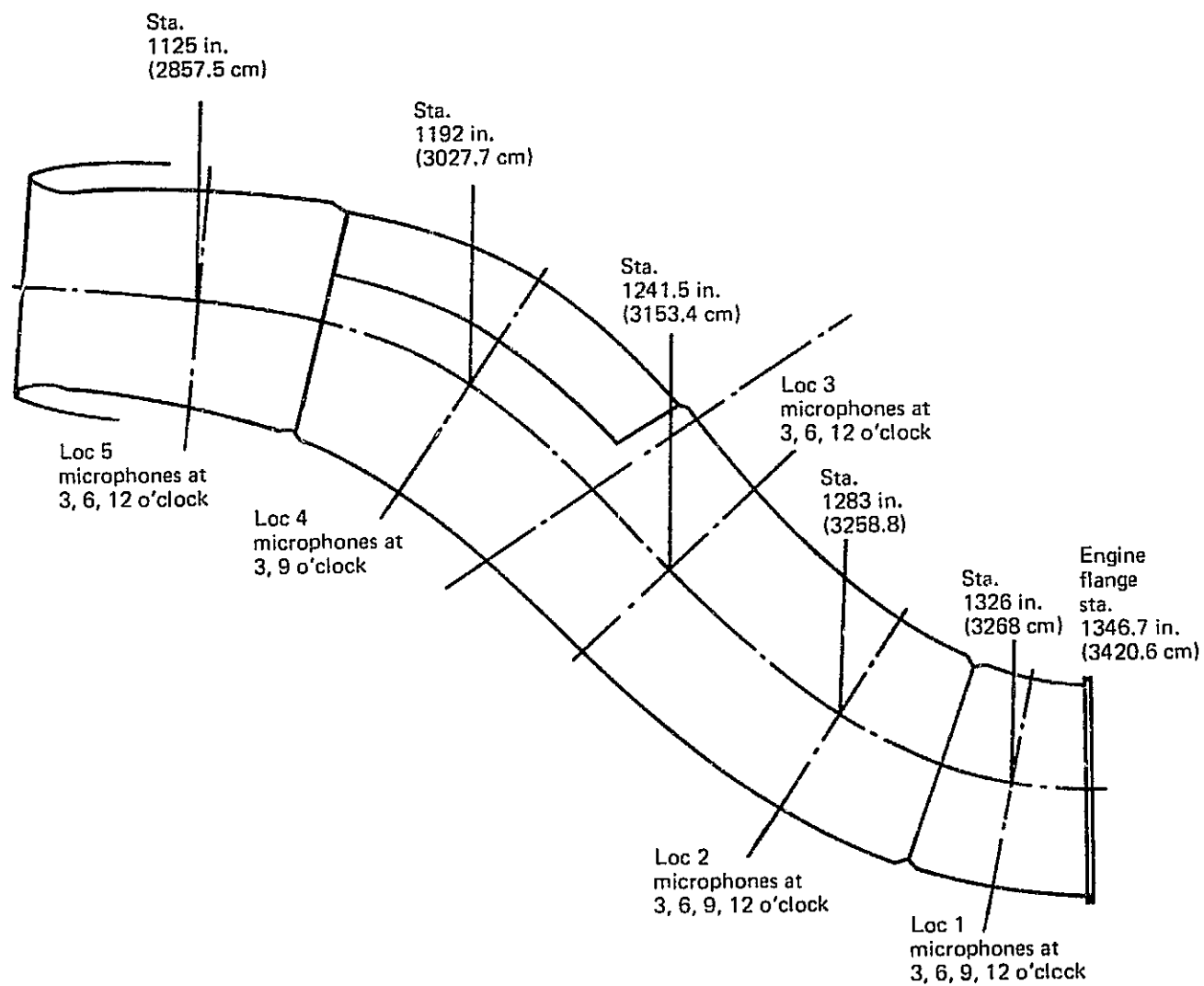


Figure 21.—JT8D-115 Center-Engine Inlet Duct Internal Microphone Locations

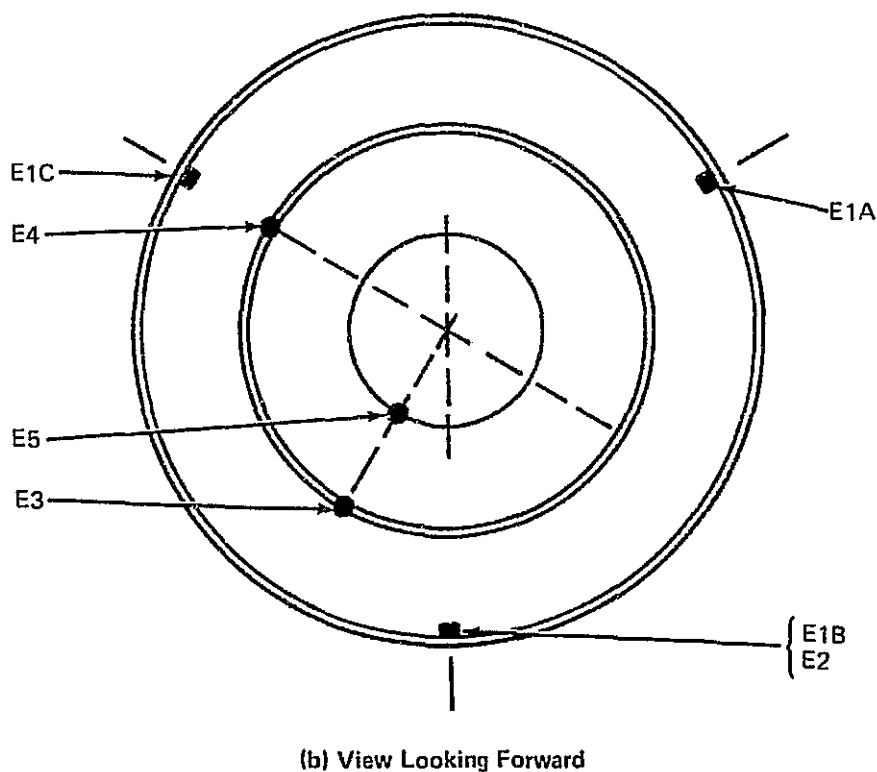
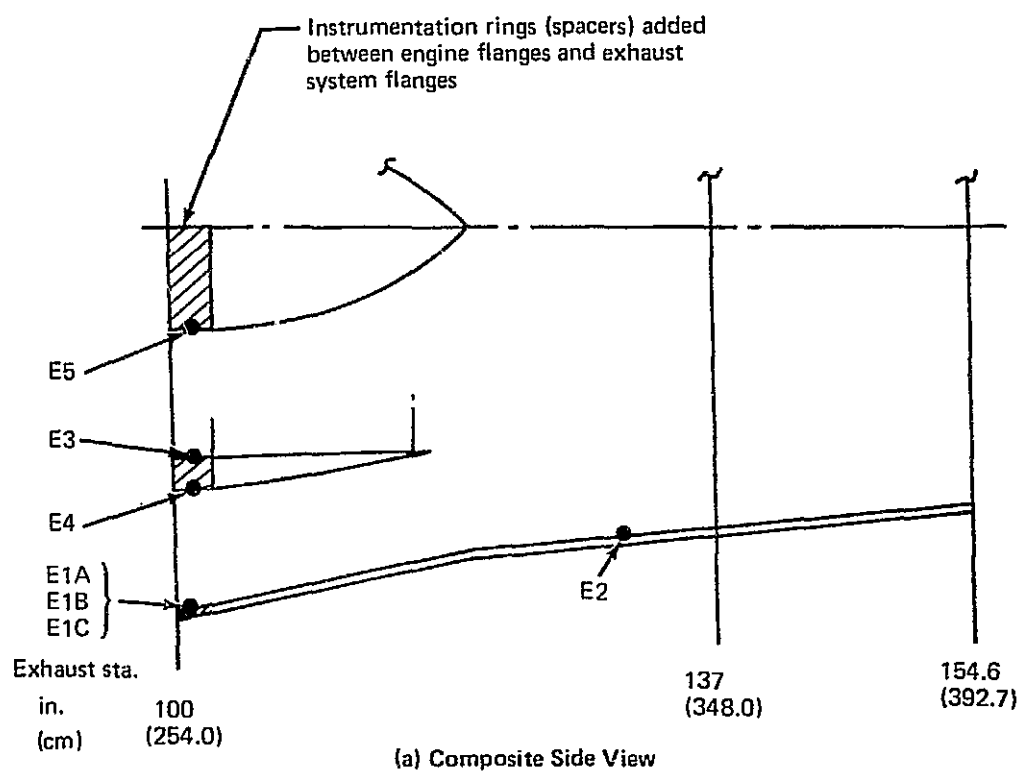


Figure 22.—JT8D-115 Exhaust System Flush-Mounted Microphone Locations



Table 2.—JT8D-115 Refan Ground Test—Summary of Internal Microphone Locations

Probe designation	Surface location	Axial station	Circumferential location
Side-engine inlet (26 microphones) (Fig. 20)		Nacelle station numbers, in. (cm)	Clock position
D86A	Diffuser wall	86 (218.4)	2
D86B	Diffuser wall	86 (218.4)	6
D86C	Diffuser wall	86 (218.4)	10
D74A	Diffuser wall	74 (188.0)	2
O86A	Outside surface of inlet ring	86 (218.4)	2
O86B	Outside surface of inlet ring	86 (218.4)	6
O86C	Outside surface of inlet ring	86 (218.4)	10
O77A	Outside surface of inlet ring	77 (195.6)	2
I86A	Inside surface of inlet ring	86 (218.4)	2
I86B	Inside surface of inlet ring	86 (218.4)	6
I86C	Inside surface of inlet ring	86 (218.4)	10
I77A	Inside surface of inlet ring	77 (195.6)	2
N86A	Nose dome surface	86 (218.4)	2
N86B	Nose dome surface	86 (218.4)	6
N86C	Nose dome surface	86 (218.4)	10
N82A	Nose dome surface	82 (208.3)	2
R1 through R10	10 equally spaced flush-mounted microphones on inlet radial strut	89 (226.1)	2
Center-engine inlet (16 microphones) (Fig. 21)		Body station numbers, in. (cm)	Clock position
S13	Center duct wall surface	1326 (3368.0)	3
S16	Center duct wall surface	1326 (3368.0)	6
S19	Center duct wall surface	1326 (3368.0)	9
S112	Center duct wall surface	1326 (3368.0)	12
S23	Center duct wall surface	1283 (3258.8)	3
S26	Center duct wall surface	1283 (3258.8)	6
S29	Center duct wall surface	1283 (3258.8)	9
S212	Center duct wall surface	1283 (3258.8)	12
S33	Center duct wall surface	1241 (3152.1)	3
S36	Center duct wall surface	1241 (3152.1)	6
S312	Center duct wall surface	1241 (3152.1)	12
S43	Center duct wall surface	1192 (3027.7)	3
S49	Center duct wall surface	1192 (3027.7)	9
S53	Center duct wall surface	1125 (2857.5)	3
S56	Center duct wall surface	1125 (2857.5)	6
S512	Center duct wall surface	1125 (2857.5)	12

ATRO PROPERTY OF THE  
ORIGINAL PAGE IS FOUR

Table 2.--(Concluded)

Probe designation	Surface location	Axial station	Circumferential location
Exhaust system (7 microphones) (Fig. 22)		Exhaust station numbers, in. (cm)	Clock position
E1A	Fan duct wall	100 (254.0)	10
E1B	Fan duct wall	100 (254.0)	6
E1C	Fan duct wall	100 (254.0)	2
E2	Exhaust duct wall	130 (330.2)	6
E3	Primary side of flow divider	100 (254.0)	7
E4	Fan side of flow divider	100 (254.0)	10
E5	Plug surface	100 (254.0)	7

skin. A fifth gage was located on the duct lower centerline on a section at B.S. 1200 in. (3048 cm) forward of the fin front spar fitting. The gages were oriented to measure the center-engine inlet duct circumferential and longitudinal strains, as shown in figure 25, cross-section BB.

The microphones used in the center-engine inlet duct acoustic evaluation were removed to prevent damage by the surge pressures during the duct surge margin testing. The vacated locations were used to install pressure transducers for a Contractor-sponsored duct internal pressure survey, running concurrently with the surge margin tests. The pressure data were used to correlate with the duct model tests and flow analysis and to enable a definitive analysis to be made of the stabilized and surge test stress and deflection data.

Linear potentiometer deflection gages were mounted on the test rig forward of the front spar forging to measure the major and minor axis deflections. They were also mounted at the engine seal on the duct vertical centerline to measure the fore and aft and vertical deflection. Deflection gage locations are shown in figure 25, cross-section CC.

All gage data, engine speed ( $N_1$ ), pressure ( $P_{17}$ ), and reference time were recorded on magnetic tape by analog instrumentation and subsequently plotted on strip charts using a computer-assisted data reduction system.

The exhaust system was instrumented with eight chromel/alumel sheathed thermocouples welded to the inner skin of the exhaust duct and 16 thermocouples welded to the fan/primary flow divider skin. Thermocouple locations are shown in figure 26.

Temperature data, engine speed ( $N_1$ ), and reference time were recorded directly onto oscillograph tracings, and during stabilized conditions, recorded on the SDDS system for printout with the quick look data.



REPRODUCIBILITY OF THE  
ORIGINAL PAGE IS POOR

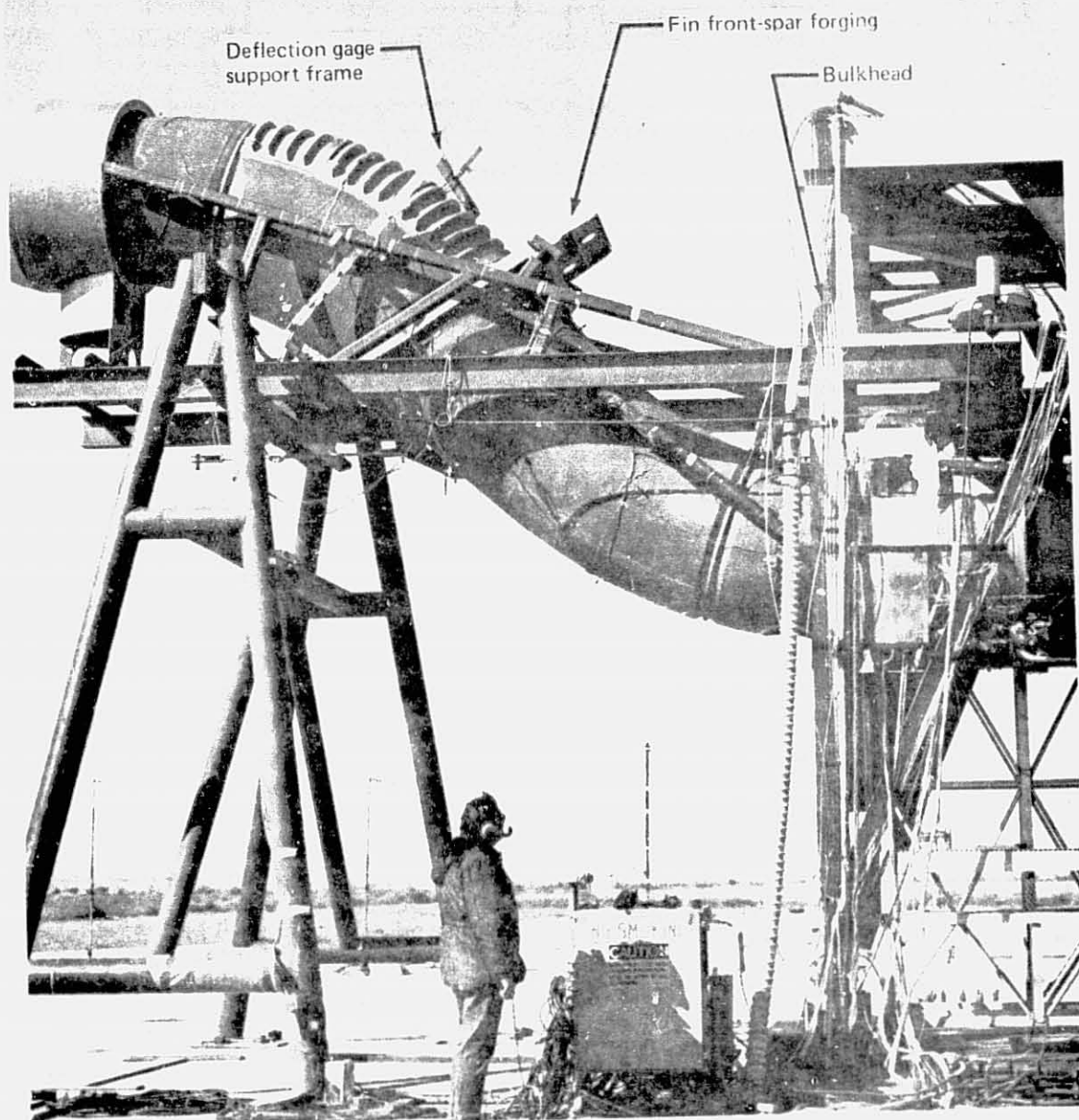


Figure 24.—JT8D-115 Center-Engine Inlet Duct Test Setup

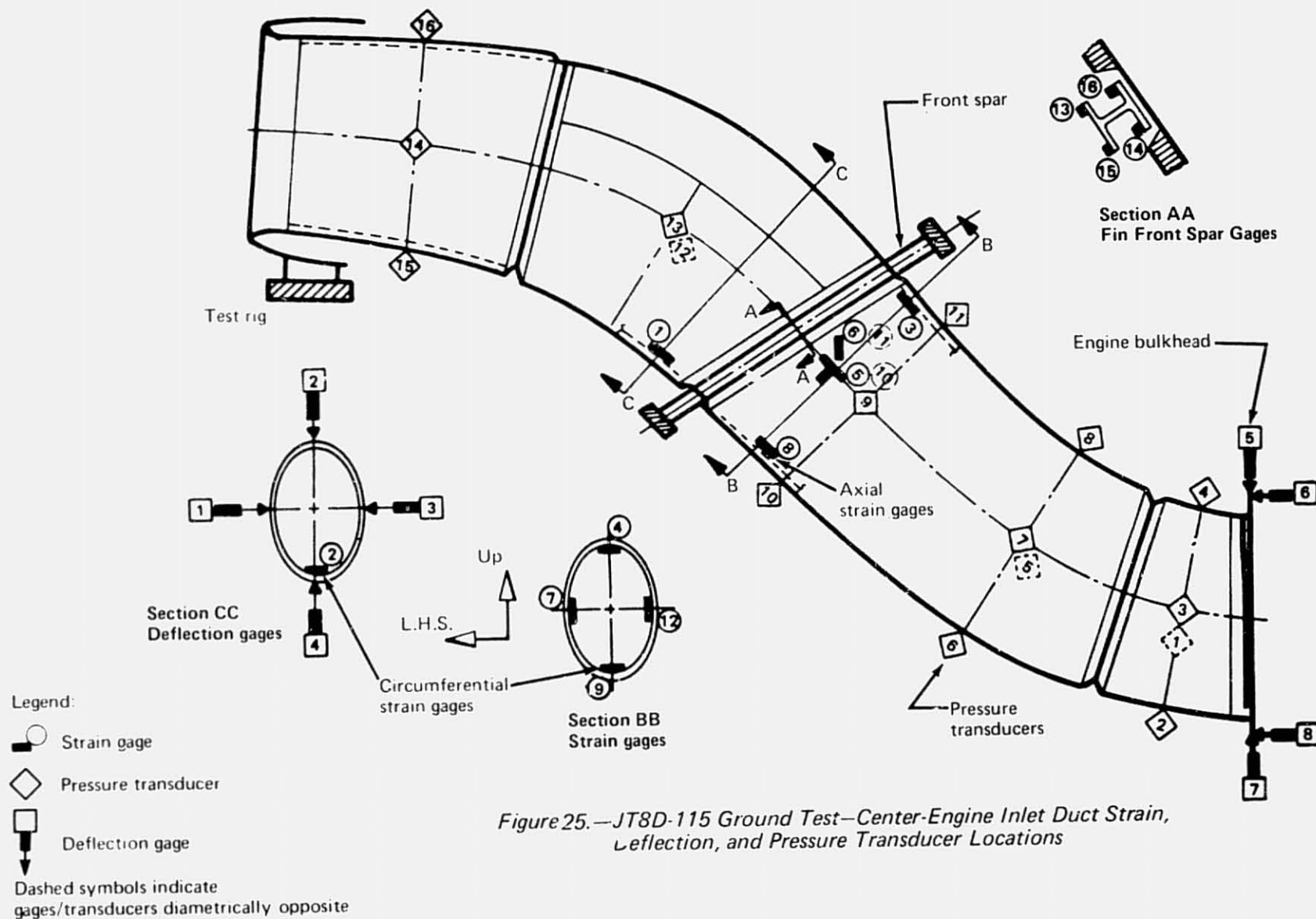


Figure 25.—JT8D-115 Ground Test—Center-Engine Inlet Duct Strain, Deflection, and Pressure Transducer Locations

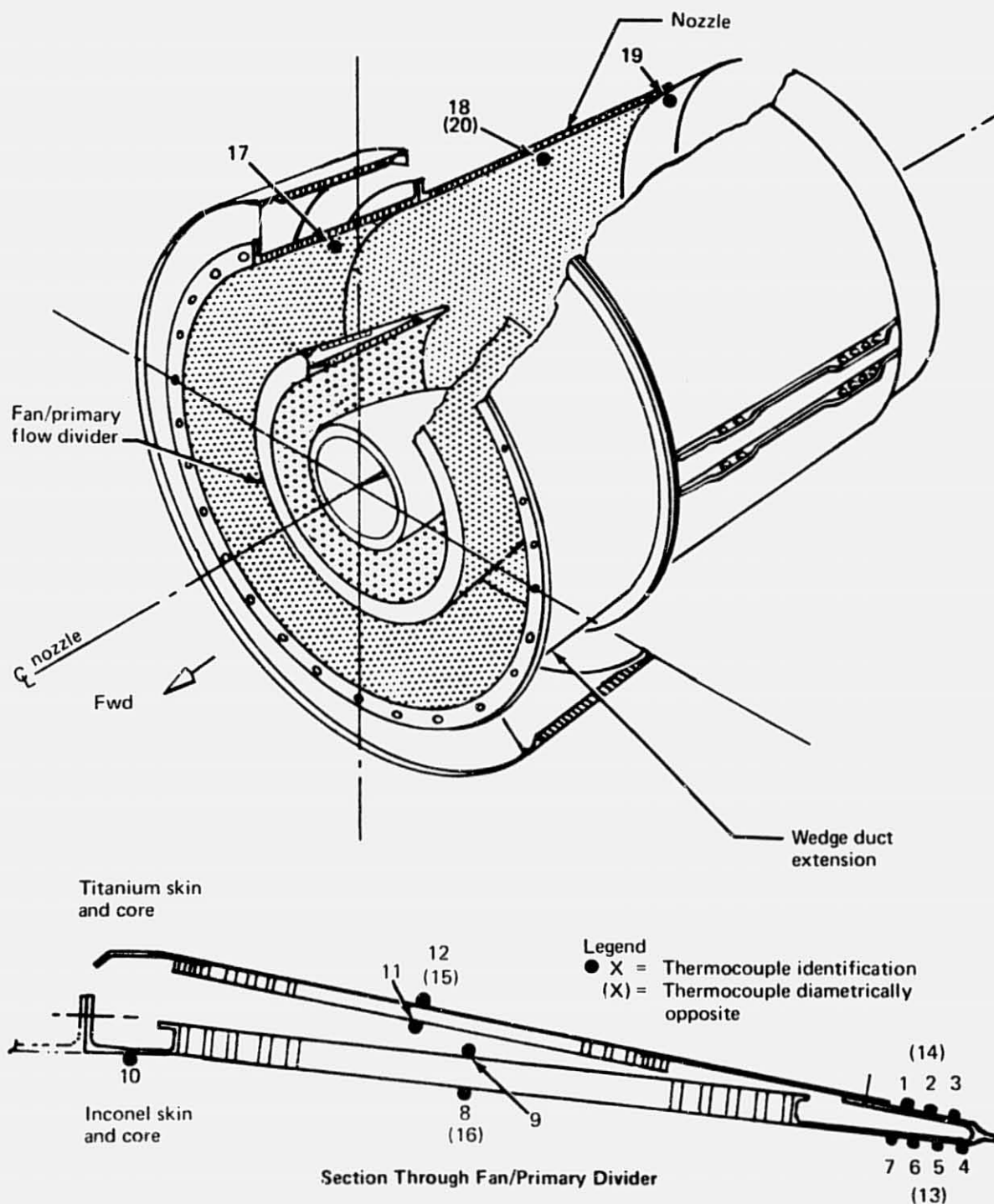


Figure 26.—JT8D-115 Ground Test—Exhaust System Thermocouple Locations and Identification

### 3.5 TEST CONDITIONS

The acoustic and performance test matrix for the JT8D-15 test is shown in table 3. A basic performance calibration of the engine was run with the Engine Contractor's reference inlet and exhaust system. The acoustic tests were conducted on a fully cowled hardwall JT8D-15 engine equipped with a production exhaust system and flight inlet with bellmouth lip. Various engine component noise sources were isolated one at a time to give a total of five acoustic configurations. Isolation of noise components was accomplished by positioning a set of baffles adjacent to the engine in locations appropriate to the component to be isolated. The technique of using baffles to isolate noise components is described in more detail in section 3.6.

*Table 3.—Performance and Acoustic Test Matrix — JT8D-15 Engine*

Test config no.	Objective	Inlet	Engine case	Exhaust system	Baffle config from figure 29
0	Performance baseline calibration	Reference bellmouth	Uncowled	Reference	—
1	Acoustic baseline and repeatability	727 side <sup>a</sup>	Cowled	Production hardwall	—
2	Inlet noise	727 side <sup>a</sup>	Cowled, baffled	Production hard-wall baffled	A
3	Aft noise	727 side <sup>a</sup> baffled	Cowled, baffled	Production hardwall	B
4	Engine case radiation	727 side <sup>a</sup> baffled	Cowled	Production hard-wall baffled	C
5	Engine case radiation	727 side <sup>a</sup> baffled	Cowled, baffled	Production hard-wall baffled	D

<sup>a</sup>Production hardwall inlet with bellmouth lip.

The performance test matrix for the JT8D-115 test is shown in table 4. Performance runs were made using both reference hardware and Contractor hardware, which consisted of a side-engine inlet with and without an acoustic ring, a 727 center-engine inlet and duct, and an exhaust duct, plug, and splitter assembly.

The acoustic test matrix for the JT8D-115 test is shown in table 5. A compilation of the data acquired as related to the test configuration number(s) is shown in table 6.

Table 4.--Performance Test Matrix -- JT8D-115 Engine

Test config no.	Objective	Inlet	Exhaust system
P1	Performance baseline calibration	Reference bellmouth	Reference
P2	Nozzle match	Reference bellmouth	Hybrid
P3	Nozzle calibration	Reference bellmouth	Hybrid
P4	727 side engine performance	a. 727 side, with ring <sup>a</sup> b. 727 side, without ring <sup>a</sup>	Hybrid
P5	Effect of vortex generators on center inlet performance	727 center <sup>a</sup>	Hybrid
P6	Center engine performance	727 center <sup>a</sup>	Hybrid
P7	Inlet pressure survey and surge margin evaluation with crosswind	727 center with fuselage	Hybrid
P8	Inlet pressure survey and surge margin evaluation with crosswind	727 side with fuselage	Hybrid
P9	Nozzle match and calibration	Reference bellmouth	Flight type

<sup>a</sup>With bellmouth lip.

Table 5.--Acoustic Test Matrix -- JT8D-115 Engine

Test config no.	Objective <sup>a</sup>	Inlet <sup>b</sup>	Exhaust system	Baffle config from figure 29
A1	Acoustic baseline-hardwall	727 side hardwall, without ring	Hybrid hardwall	—
A2	Inlet and exhaust system internal noise	727 side with ring	Flight type	—
A3	Center engine acoustic baseline and exhaust system internal noise	727 center	Hybrid	—
A4	Acoustic repeatability	727 side, without ring	Hybrid	—
A5	Inlet noise	727 side hardwall, without ring	Hybrid baffled	A

<sup>a</sup>See table 6 for comprehensive list of information obtained.

<sup>b</sup>All acoustic testing included the bellmouth lip except for configuration A20 which used the reference bellmouth.



Table 5.—(Concluded)

Test config no.	Objective <sup>a</sup>	Inlet <sup>b</sup>	Exhaust system	Baffle config from figure 29
A6	Inlet noise	727 side hardwall, with ring	Hybrid baffled	A
A7	Inlet noise	727 side, without ring	Hybrid baffled	A
A8	Inlet noise	727 side, with ring	Hybrid baffled	A
A9	Aft noise	727 side, without ring, baffled	Hybrid hardwall	B
A10	Aft noise	727 side, with ring, baffled	Hybrid	B
A11	Aft noise	727 side, with ring, baffled	Hybrid hardwall	B
A12	Inlet noise	727 center	Hybrid baffled	E
A13	Total engine noise	727 side, with ring	Hybrid	—
A14	Engine case radiation	727 side, with ring, baffled	Hybrid baffled	D
A15	Engine case radiation	727 side, with ring, baffled	Hybrid baffled	C
A16	Aft noise	727 side, with ring, baffled	Flight type	B
A17	Total engine noise	727 side, without ring	Flight type	—
A18	Aft noise	727 side, without ring, baffled	Hybrid	B
A19	Total engine noise	727 side, with ring	Flight type	—
A20	Core noise	Reference bellmouth, baffled	Reference, 30% over area	B

<sup>a</sup>See table 6 for comprehensive list of information obtained.

<sup>b</sup>All acoustic testing included the bellmouth lip except for configuration A20 which used the reference bellmouth.

Table 6.—Acoustic Data Compilation — JT8D-115 Engine

Test data	Test config no.
Total Engine Noise	
Hardwall nacelle	A1
Peripheral nacelle treatment	A4
Treated side-engine inlet (with ring) and treated hybrid exhaust system	A13
Center-engine inlet with hybrid exhaust system	A3
Treated side-engine inlet (without ring) and flight-type exhaust system	A17
Treated side-engine inlet (with ring) and flight-type exhaust system	A19
Inlet levels	
Without ring	
Untreated	A5
Treated	A7
With ring	
Untreated	A6
Treated	A8
Center duct—Treated	A12
Inlet attenuation	
Without ring	A5, A7
With ring	A6, A8
Exhaust levels	
Without inlet ring	
Hardwall hybrid exhaust system	A9
Treated hybrid exhaust system	A18
With inlet ring	
Hardwall hybrid exhaust system	A11
Treated hybrid exhaust system	A10
Treated flight-type exhaust system	A16
Center duct	
Treated hybrid exhaust system	A3
Effect of side-engine inlet acoustic ring	A9, A11
Exhaust attenuation	
Hybrid exhaust splitter	A10, A11
Flight-type exhaust splitter	A11, A16
Internal SPL's	
Flush-mounted	
Inlet	
Without ring	A5(hardwall)
With ring	A4(treated)
Center duct	A2(treated)
Exhaust	A6(hardwall)
Center-engine inlet duct	A3(treated)
Side-engine inlet with inlet ring	A2(treated)
Side-engine inlet SPL survey	A2
Fan case radiation	A14, A15
Repeatability	A4
Core noise	A20

The acoustic tests were conducted on an acoustically treated JT8D-115 engine equipped with a flight-type exhaust system and inlets with bellmouth lips. Various component noise sources were isolated one at a time to give a total of 20 acoustic configurations. Isolation of noise components was accomplished as described in section 3.6. Because of the late availability of the flight-type exhaust plug and splitter, much of the acoustic test was run with the flight-type exhaust duct matched to the reference plug and splitter (hybrid exhaust system). This hybrid exhaust system is believed to be a valid substitute for the flight-type exhaust system within the limits of acoustic data repeatability.

Center-engine inlet duct and exhaust system structural test data were recorded for the JT8D refan configuration only. Table 7 presents the structural test matrix.

*Table 7.—Structural Test Matrix*

Test config no.	Objective	Inlet	Exhaust system
S1	Center inlet structural evaluation during steady-state and surge conditions	727 center	Hybrid
S2	Exhaust system temperature survey	727 side	Flight type

### 3.6 TEST PROCEDURES

Various techniques were used to acquire steady-state performance, engine surge margin, acoustic, and structural loads data. These test procedures are discussed in the following paragraphs.

#### 3.6.1 STEADY-STATE PROPULSION PERFORMANCE

During all steady-state performance testing a standard engine operating procedure was followed. After 5 min of engine warmup at idle, data were taken on the way up the powerline. A performance powerline consisted of 9 to 12 data points per run. Three min of stabilization time were allowed prior to each data point. To obtain repeat data points, the engine was taken back to idle prior to doing another performance powerline run. Generally, three runs were made for each performance configuration. During both the JT8D-15 and -115 testing, one run was made using a 4-min stabilization period to check the influence of stabilization time on the data.

#### 3.6.2 JT8D-115 SURGE MARGIN

The low-pressure compressor (LPC) stall or surge margin was determined for the JT8D-115 engine using the P&WA cross-bleed duct hardware and their test procedures. However, when the 727 refan center-engine inlet and the 727 refan side-engine inlet were tested with a 90° crosswind, the P&WA surge margin test procedures were slightly modified. This section discusses the basic principle of the P&WA cross-bleed procedure.

The cross-bleed stall procedure involves the use of high pressure air, available at the 13th-stage compressor discharge, to back-pressure the low-pressure compressor thereby raising the low-pressure compressor operating line (O.L.). (Note: The 13th-stage of the JT8D-15 becomes the 14th-stage of the JT8D-115 engine.) The equipment consists of tubing to connect the 13th-stage bleed ports to the 6th-stage bleed ports (referred to as cross-bleed ducts) on each side of the engine with an electrically operated shutoff valve in each tube. Provisions are also available for installing plates with orifices of various sizes to control the flow rate recirculating from the 13th-stage discharge to the 6th-stage port, thus controlling the back pressure at the LPC discharge. Based on full-scale tests and engine analyses, P&WA generates a relationship of percentage increase in the LPC operating line versus engine LPC corrected rotor speed ( $N_1/\sqrt{\theta_{t2}}$ ) for specific orifice sizes in the cross-bleed ducts. The percentage increase in LPC operating line is defined at a constant LPC corrected airflow by the following equation:

$$\text{Percent LPC O.L. increase} = \frac{(P_{t3}) \text{ cross-bleed O.L.} - (P_{t3}) \text{ normal O.L.}}{(P_{t3}) \text{ cross-bleed O.L.}} \times 100, \quad (1)$$

where  $P_{t3}$  represents the total pressure at the LPC exit.

The P&WA surge margin test procedure is to first idle the engine for 5 min with the cross-bleed system shutoff valves closed and then slowly accelerate to a specified stabilization  $N_1$  speed for the orifice diameter being used. After stabilizing the engine for 1 min, the cross-bleed valves are opened and the drop-in  $N_1$  rpm is noted to check for proper valve operation. Following a 10-min stabilization period, the engine is accelerated slowly over a period of approximately 2 min or more, until the engine surges, a corrected  $N_1$  speed of 7400 rpm is reached, or the engine exhaust temperature (EGT) limit is reached. If no surge occurs, the engine is stabilized for 10 min at the corrected  $N_1$  speed of 7400 rpm or just below the exhaust gas temperature limit, whichever occurs first; then a full scan of engine data is recorded. Also, when no surge is encountered, the engine is shut down, and a larger diameter orifice is installed in the cross-bleed ducts, and the procedure is repeated until the engine does surge near the corrected  $N_1$  speed of 7400 rpm. When the engine does surge, the  $N_1$  speed is noted and the bleed valves are immediately closed without changing the power setting. The  $N_1$  speed is then reduced by 100 rpm, and after the engine is allowed to stabilize for 1 min, the bleed valves are opened. If no surge occurs, the engine is stabilized for 10 min and a full scan of engine data is recorded. This point is called the "verge-of-surge" condition. If a surge is encountered before the completion of the 10-min stabilization period, the bleed valves are closed, and the  $N_1$  speed is reduced by 50 rpm. The engine is stabilized for 1 min before the bleed valves are opened to try again for the engine to operate at that condition without surging for 10 min. This procedure of reducing the  $N_1$  speed by 50 rpm increments is repeated if there is a surge at any time during a 10-min stabilization period. Throughout these procedures, care must be taken to not exceed the 7400-rpm corrected  $N_1$  speed with the bleed valves open and not to exceed the maximum  $N_1$  speed, engine exhaust gas temperature, or the allowed time above the maximum continuous thrust rating, with or without the bleed valves open.

With a simulated 90° crosswind, the procedure for determining the LPC surge margin with the 727 refan center-engine inlet or the 727 refan side-engine inlet was established by first trying to hold a constant crosswind velocity and then using the above mentioned P&WA

procedures for establishing the verge-of-surge condition. At high crosswind velocities, however, the engine would surge immediately upon opening the cross-bleed valves. As experience was gained with crosswind surge margin testing, it became apparent that the following procedure was the best method to determine the LPC surge margin with a 90° crosswind.

A low crosswind velocity was set across the inlet and the P&WA procedure was followed until the engine would run surge-free for 10 min with the bleed valves open at or near 7400-rpm corrected  $N_1$  speed. A full scan of engine data was recorded at this point. Slowly, the crosswind velocity was increased until an engine surge was encountered and the crosswind velocity or the speed of the crosswind engine was noted; immediately the bleed valves were closed and the crosswind velocity reduced.

The  $N_1$  speed was reduced below the maximum continuous thrust rating for approximately 5 min allowing the engine to cool down. The engine power was reset to 7400-rpm corrected  $N_1$  speed with a low crosswind velocity and stabilized for 1 min. The crosswind velocity was increased to a value 2 or 3 kn (1 to 2 m/s) lower than the noted crosswind velocity at the time of engine surge; i.e., about 100-rpm lower crosswind engine speed than at surge. If no surge was encountered during the 10 min of stabilization, this point was designated a verge-of-surge condition. Two or three engine data scans were recorded during the 10-min period. If a surge was encountered at any time during the 10-min period, the cross-bleed valves were immediately closed and the above procedure was repeated [with crosswind velocity reduced another 2 or 3 kn (1 to 2 m/s)] until the engine could run surge-free for 10 min. Once the verge-of-surge condition with crosswind was determined at the JT8D-115 corrected  $N_1$  speed of 7400 rpm, the procedure was repeated at lower  $N_1$  speeds where the surge margin is of interest. In order to obtain a verge-of-surge condition at higher crosswind velocity, a smaller diameter orifice was used in the cross-bleed ducts; conversely, for a lower crosswind velocity, a larger orifice was needed.

How much crosswind a particular engine inlet can endure without causing the engine to surge with the cross-bleed valves closed is also of interest. This was accomplished by stabilizing the JT8D-115 engine at the corrected  $N_1$  speed of interest for approximately 2 min. Then the crosswind engine was set to produce the minimum crosswind velocity of interest. After approximately 2 min on condition, a full scan of engine data was recorded. The crosswind engine speed was increased by 200 rpm, and data were again recorded. This procedure was repeated until either the engine surged or the maximum crosswind engine capability was reached.

### 3.6.3 ACOUSTIC

For each acoustic test configuration listed in tables 3 and 5, acoustic data were obtained according to the following procedure. When weather conditions (described in next paragraph) were determined to be acceptable for acquisition of acoustic data, the test engine was cycled through the ground static power conditions listed in table 8. At each power setting, the engine was allowed to stabilize for 3 min, and acoustic and performance data were recorded during the following 2 min. At least two such acoustic runs were made for each configuration.

*Table 8.—Acoustic Test Power Settings*

Nominal corrected rpm ( $N_1/\sqrt{\theta_{t2}}$ )	
JT8D-15 (baseline)	JT8D-115 (refan)
Idle	Idle or 3000 (alternate runs)
3600	3700
4800	4300
5600	4800
6200	5200
6700	5500
7200	5800
7700	6100
8100	6400
Max power	6800
	7200
	Max power

The following weather window defined acceptable acoustic testing conditions:

Wind speed	Less than 8 kn (14.8 km/hr)
Temperature	25° to 86°F (269.3 to 303.2 K)
Relative humidity	30% to 90%
Precipitation	None

For purposes of isolation of engine noise components, a set of seven acoustic baffles, each 8-ft (2.44-m) wide by 20-ft (6.10-m) high, were arranged alongside the engine in such a way as to shield one end of the engine (either inlet or exhaust) from radiating directly into the acoustic arena while allowing the other end to radiate freely. For the fan case radiation test,

both ends were shielded and the center portion was exposed, allowing fan case radiated noise to propagate into the acoustic arena. These data were compared with data measured with total engine shielding to determine fan case radiated noise. The baffles of steel frame construction with 2-in. (5.08-cm) plywood facing covered with 2 in. (5.08 cm) of fiberglass blanket are shown in the aft-shielded configuration in figure 27. The baffle arrangements for inlet and aft noise shielding are shown in figure 28. Installation of the baffles provided noise reduction at a given angle up to the limit determined by one or the other of the following limitations: (1) the maximum attenuation of the baffles determined by transmission through the baffles and diffraction around and over the baffles; (2) the noise floor from the unbaffled source. In this way inlet-radiated fan noise could be separated from discharge-radiated fan noise, jet noise could be separated from inlet-radiated fan broadband noise, and so on. Sketches of the various baffle arrangements used during the tests are shown in figure 29.

#### 3.6.4 STRUCTURAL

Strain gage, deflection, and pressure data were recorded during surge margin evaluation testing of the center-engine inlet duct representing idle-to-takeoff power conditions. The test procedures were described in section 3.6.2.

Exhaust system temperatures were recorded during three runs for the following engine conditions.

1. Cold start cycle

Cold start to idle  
(Stabilize idle 5 min)

2. Maximum acceleration

Idle-to-takeoff power in 15 sec  
(Stabilize takeoff power 3 min)  
Decelerate to idle  
(Stabilize idle 3 min)

3. Maximum deceleration

Takeoff to cruise

4. Shutdown cycle

Idle-to-engine shutdown  
(Stabilize shutdown 5 min)

REPRODUCIBILITY OF THE  
ORIGINAL PAGE IS POOR

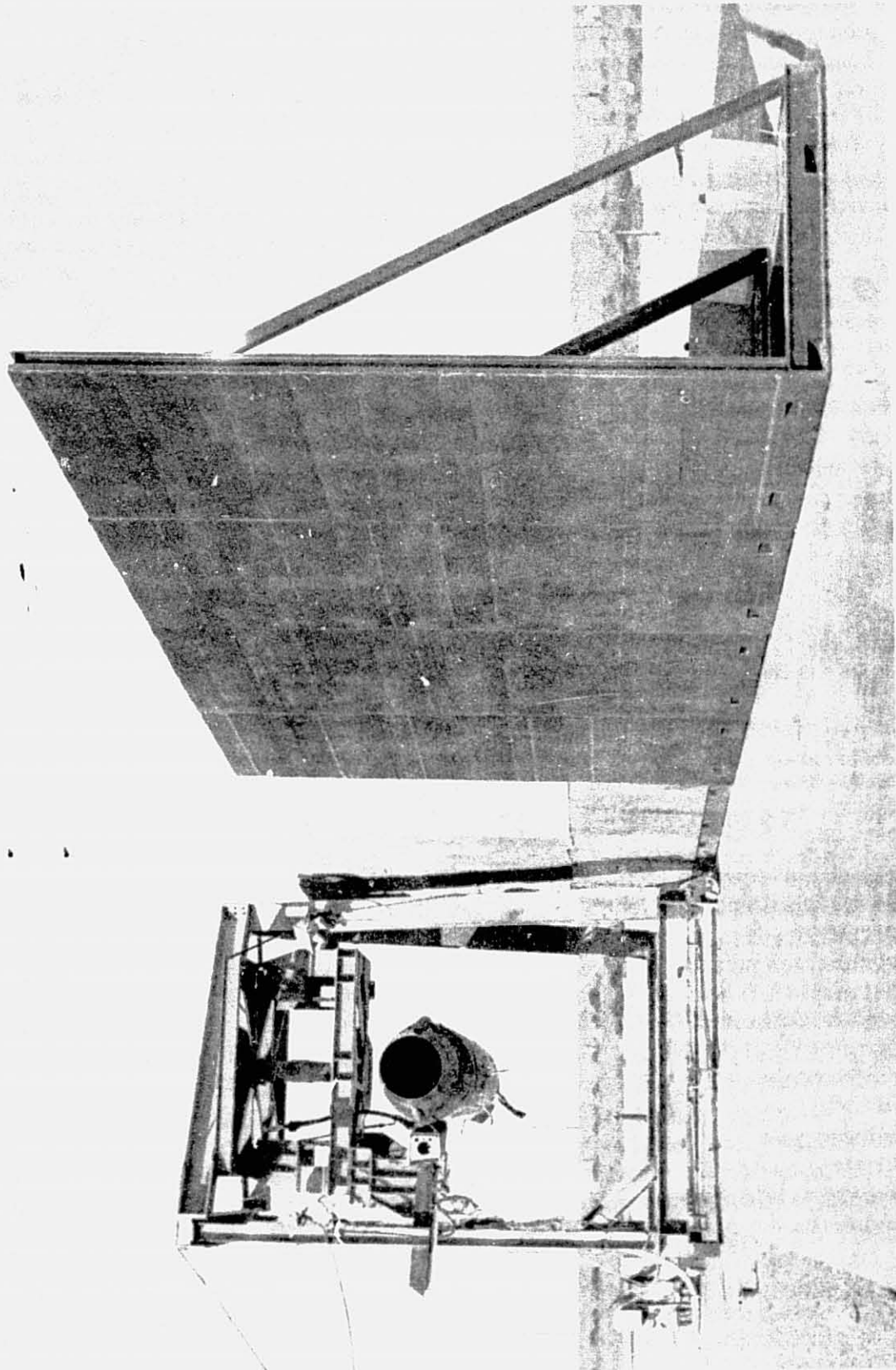
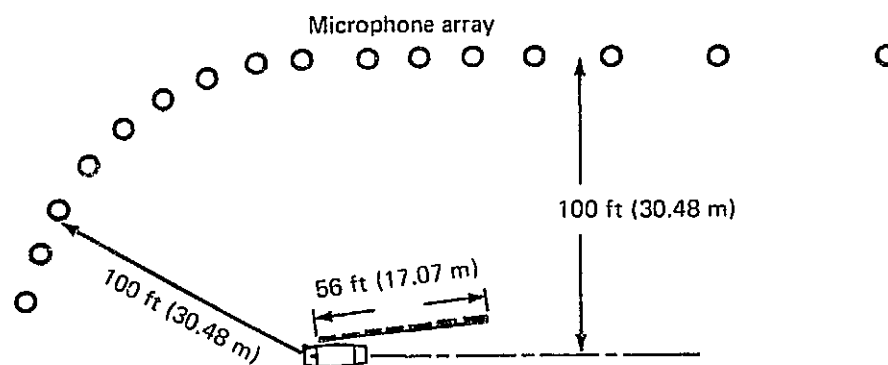
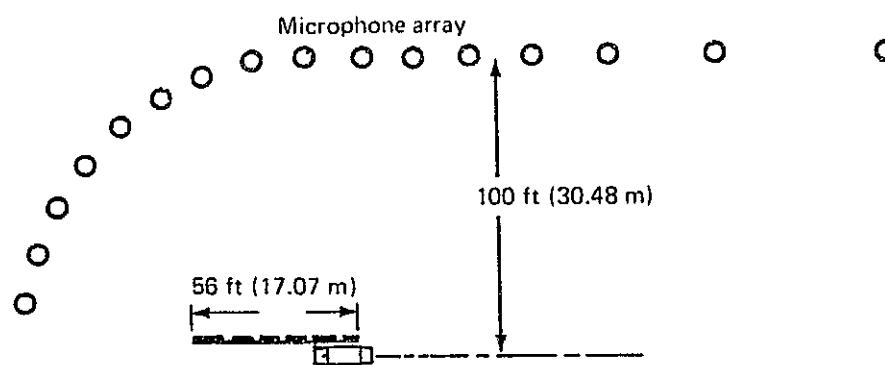


Figure 27.—JT8D-15 and -115 Ground Test — Acoustic Baffle Arrangement  
for Isolation of Inlet Noise



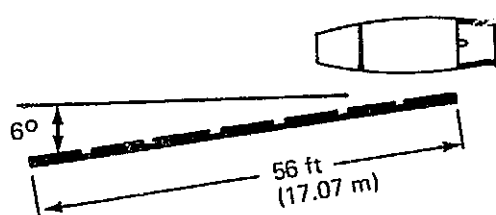


(a) Aft Shielded Configuration

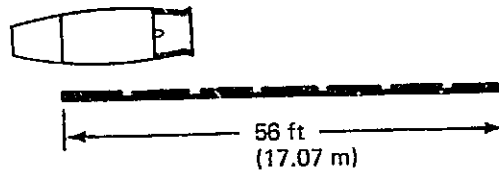


(b) Inlet Shielded Configuration

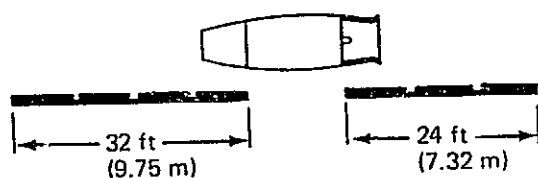
Figure 28.—JT8D-115 Ground Test—Acoustic Baffle Arrangement for Shielding of Inlet and Exhaust Noise Components



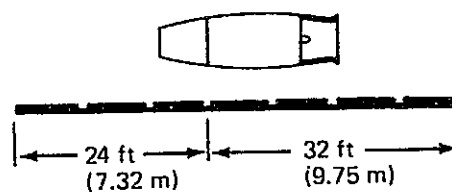
(a) Side-Engine Inlet Noise Isolation



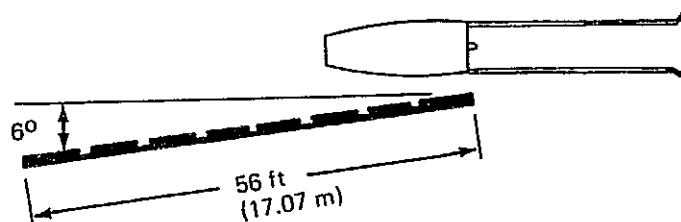
(b) Exhaust Noise Isolation



(c) Engine Case Radiation Isolation



(d) Total Engine Shielding



(e) Center-Engine Inlet Noise Isolation

*Figure 29.—JT8D-15 and -115 Ground Tests—Acoustic Baffle Configurations for Component Noise Isolation*

## 4.0 TEST RESULTS

### 4.1 PROPULSION

Propulsion test results are discussed under three major headings: JT8D-15 Engine Test Results, JT8D-115 Engine Test Results, and Data Quality. This information is ultimately used in determining the flight performance benefit of the refan engine [see Volume IV of this final report, "Airplane Evaluation and Analysis," (ref. 1)].

All measured engine parameters presented in this report are an average of 10 data samples taken for each test condition. Calculated engine parameters are defined in the appendix. Symbols and abbreviations used in this report are found in the appendix.

#### 4.1.1 JT8D-15 ENGINE TEST RESULTS

Engine performance parameters were obtained during the JT8D-15 testing of the reference hardware and the 727/JT8D production hardware. See section 3.3.1 for a description of the production hardware. Figures 30 through 34 present the propulsion test data obtained for the two configurations. Figures 30 and 31 show less than 1% difference in the LPC rotor speed and total airflow between the reference and the 727/JT8D production hardware at the takeoff engine pressure ratio (EPR). The total airflow for the production hardware was obtained from an LPC rotor speed versus total airflow relationship generated during the reference hardware testing, which utilized a calibrated bellmouth inlet. In order to do this, it was assumed that the inlet total pressure recovery for the reference bellmouth and the production inlet with a bellmouth lip were equivalent. Thus, the difference in airflows is essentially due to the difference in LPC rotor speed for a given EPR. Figure 32 shows that the fan pressure ratio (FPR) is identical for both configurations for any given EPR. Figure 33 shows the gross thrust for the production hardware to be 0.6% lower than the reference hardware. Figure 34 shows that the specific fuel consumption (SFC) for the production hardware is 1.8% higher than for the reference hardware at the takeoff rated thrust, 15 500 lb (68 951 N). This difference is about twice as large as what was expected based on previous Contractor tests. Since the baseline testing was primarily an acoustic performance test, additional testing was not conducted to ascertain the reason for the SFC difference.

#### 4.1.2 JT8D-115 ENGINE TEST RESULTS

##### 4.1.2.1 Engine Performance

*Reference Hardware.*—A total of 17 runs were made using the reference bellmouth and exhaust system installed on the JT8D-115 engine. These reference hardware runs were made at the beginning of the test, at various intervals during the test, and near the end of the test. The reference hardware runs near the end of the test were obtained after the LPC surge

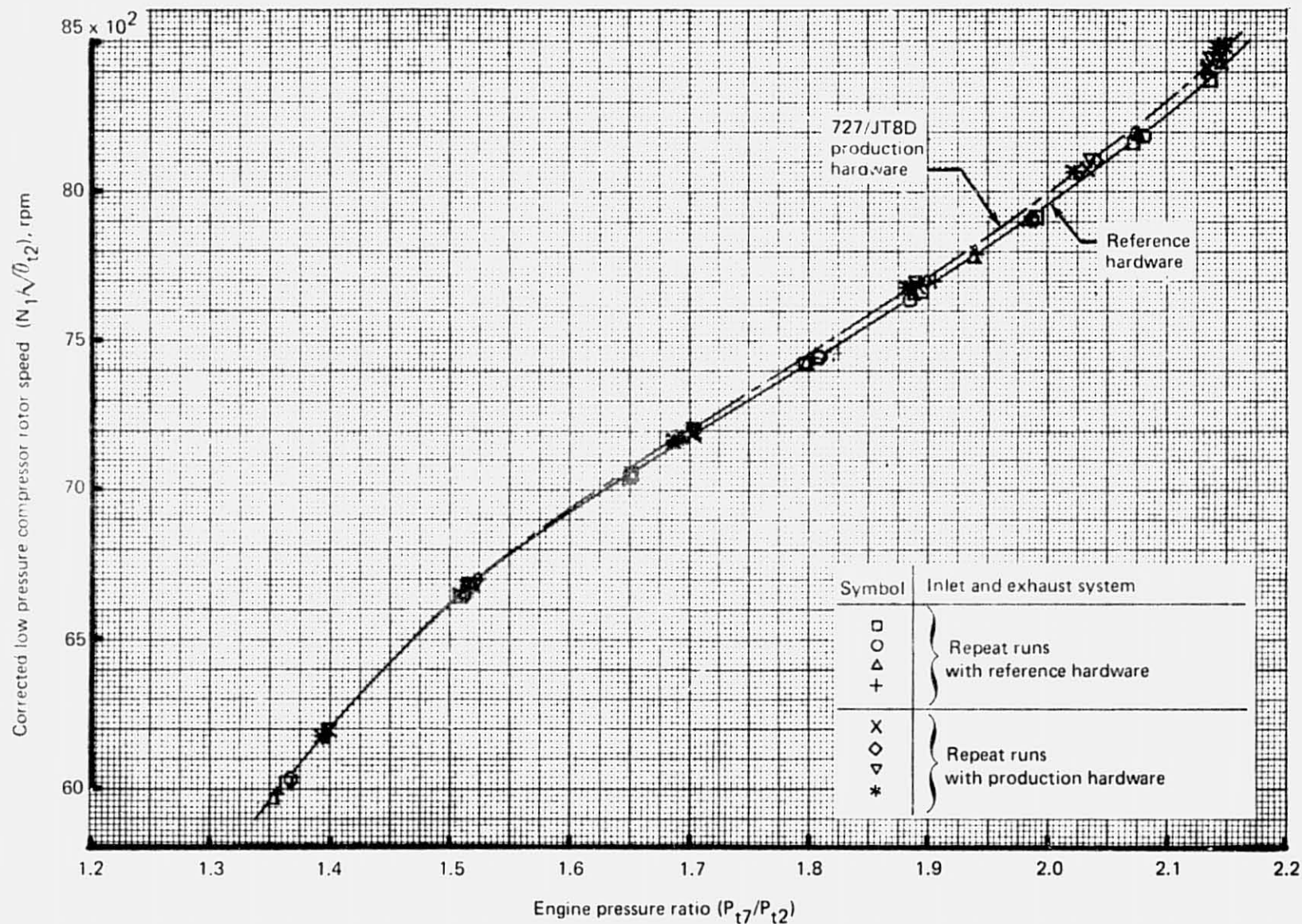


Figure 30.—JT8D-15 Ground Test—Low Pressure Compressor Rotor Speed Versus Engine Pressure Ratio

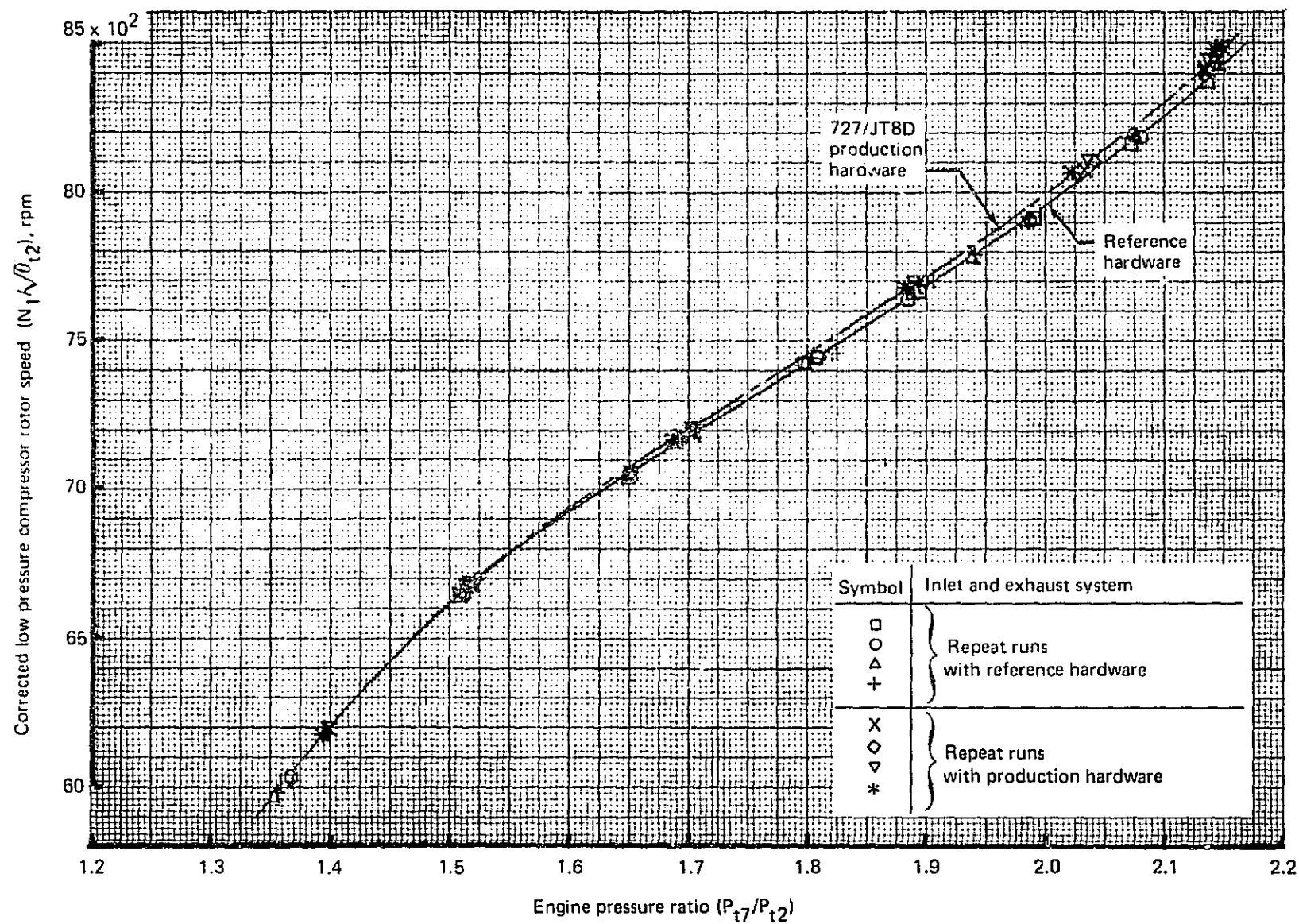


Figure 30.—JT8D-15 Ground Test—Low Pressure Compressor Rotor Speed Versus Engine Pressure Ratio

REPRODUCIBILITY OF THE  
ORIGINAL PAGE IS POOR

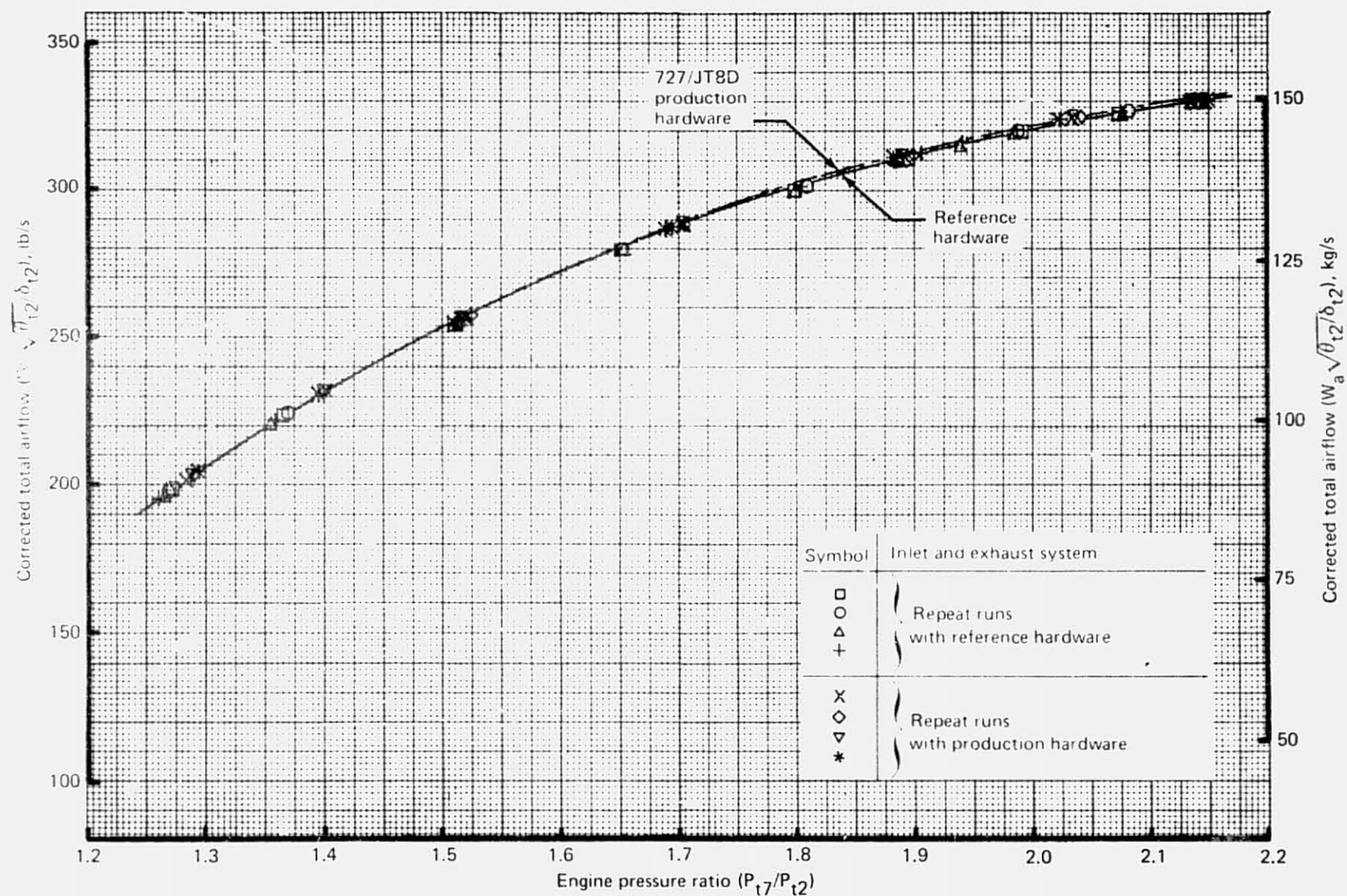


Figure 31.—JT8D-15 Ground Test—Airflow Versus Engine Pressure Ratio



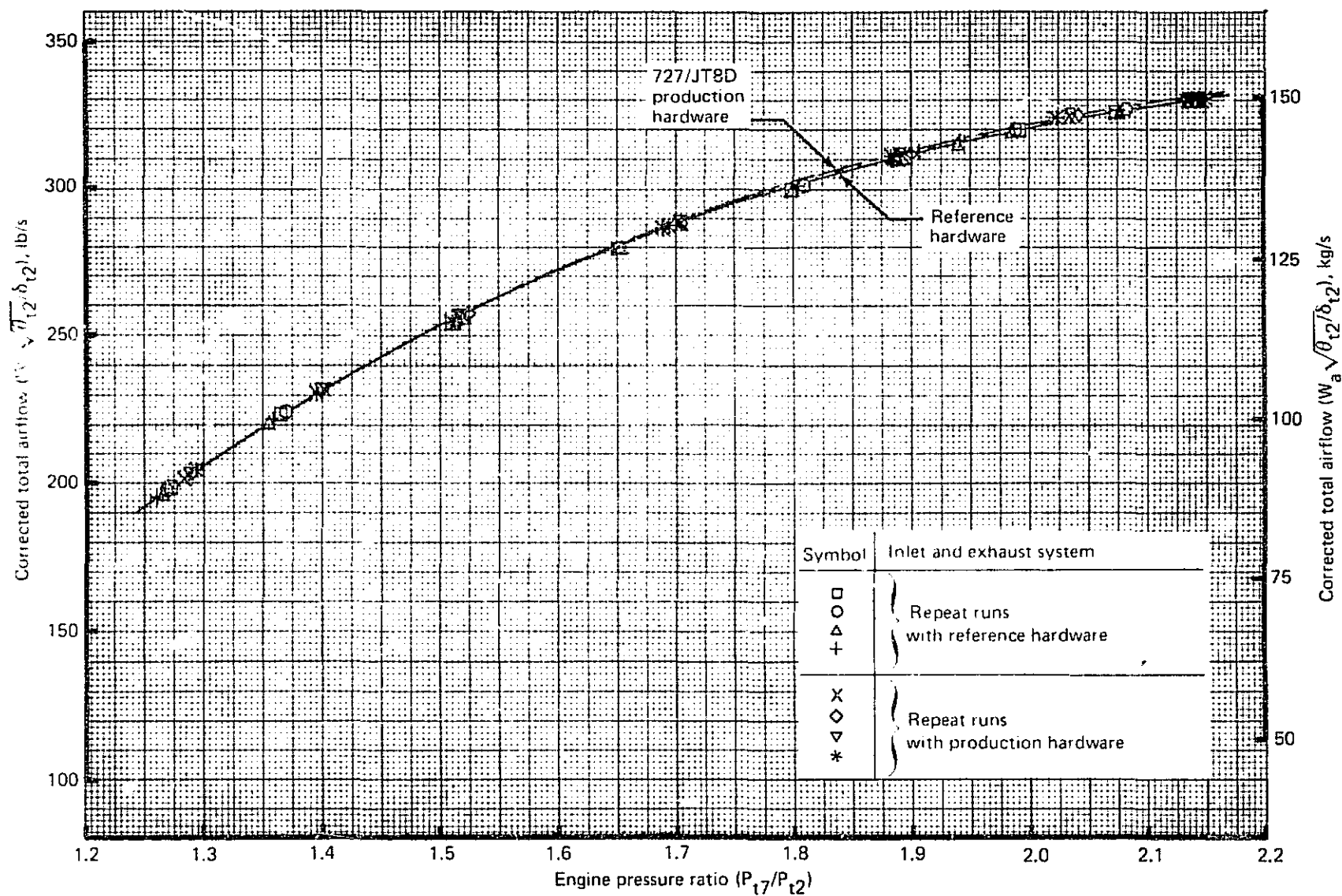


Figure 31.—JT8D-15 Ground Test—Airflow Versus Engine Pressure Ratio

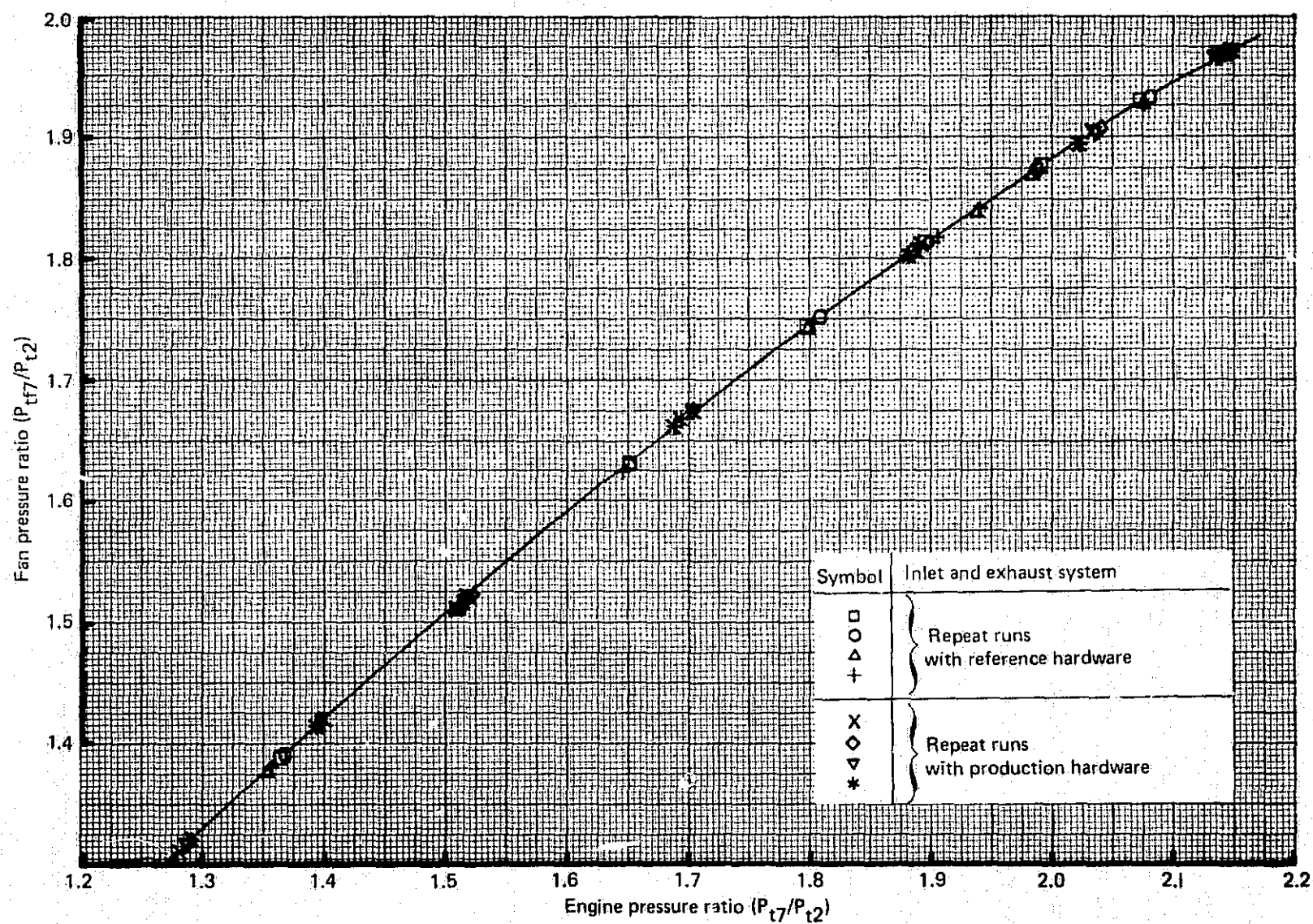


Figure 32.—JT8D-15 Ground Test—Fan Pressure Ratio Versus Engine Pressure Ratio



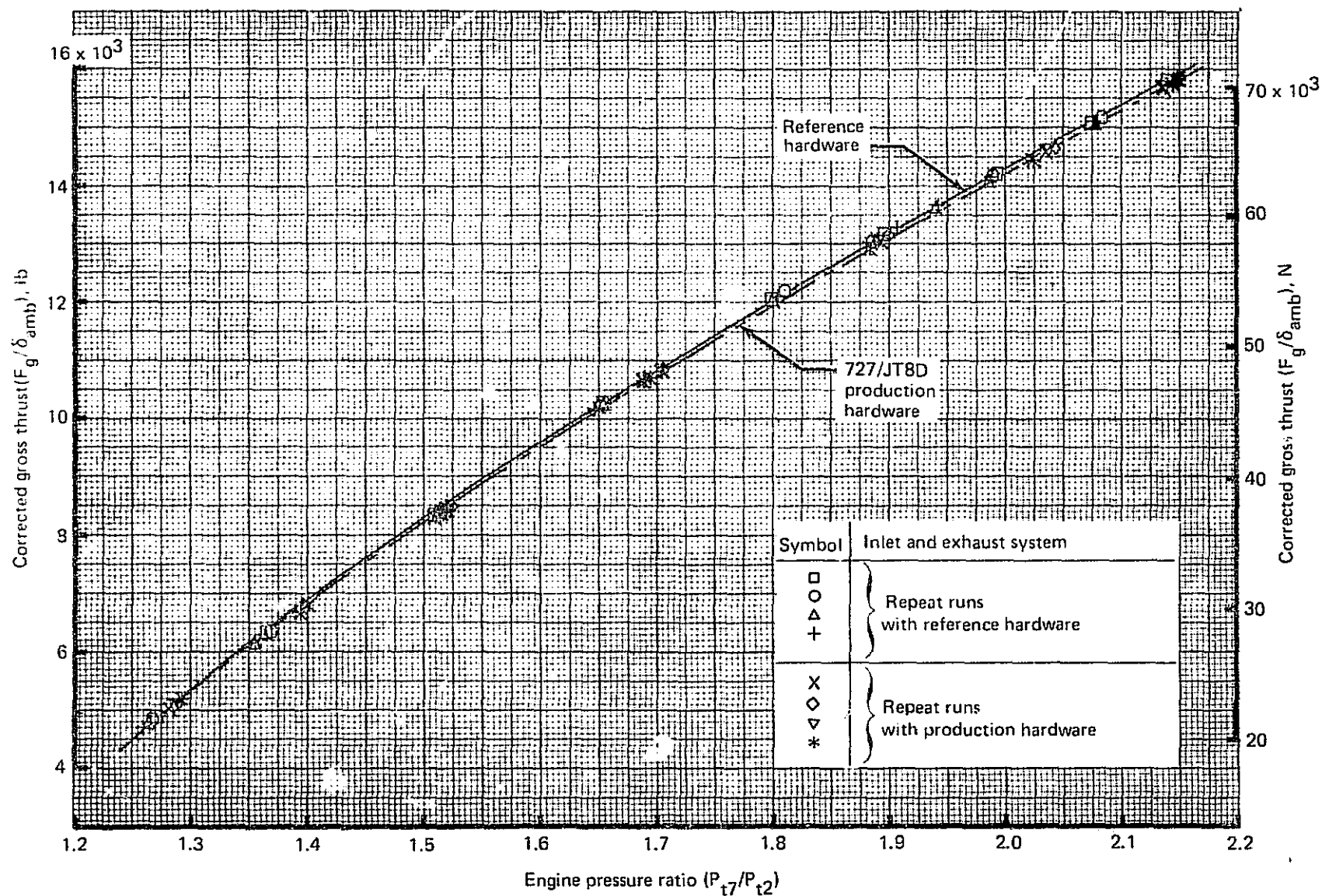


Figure 33.—JT8D-15 Ground Test—Gross Thrust Versus Engine Pressure Ratio

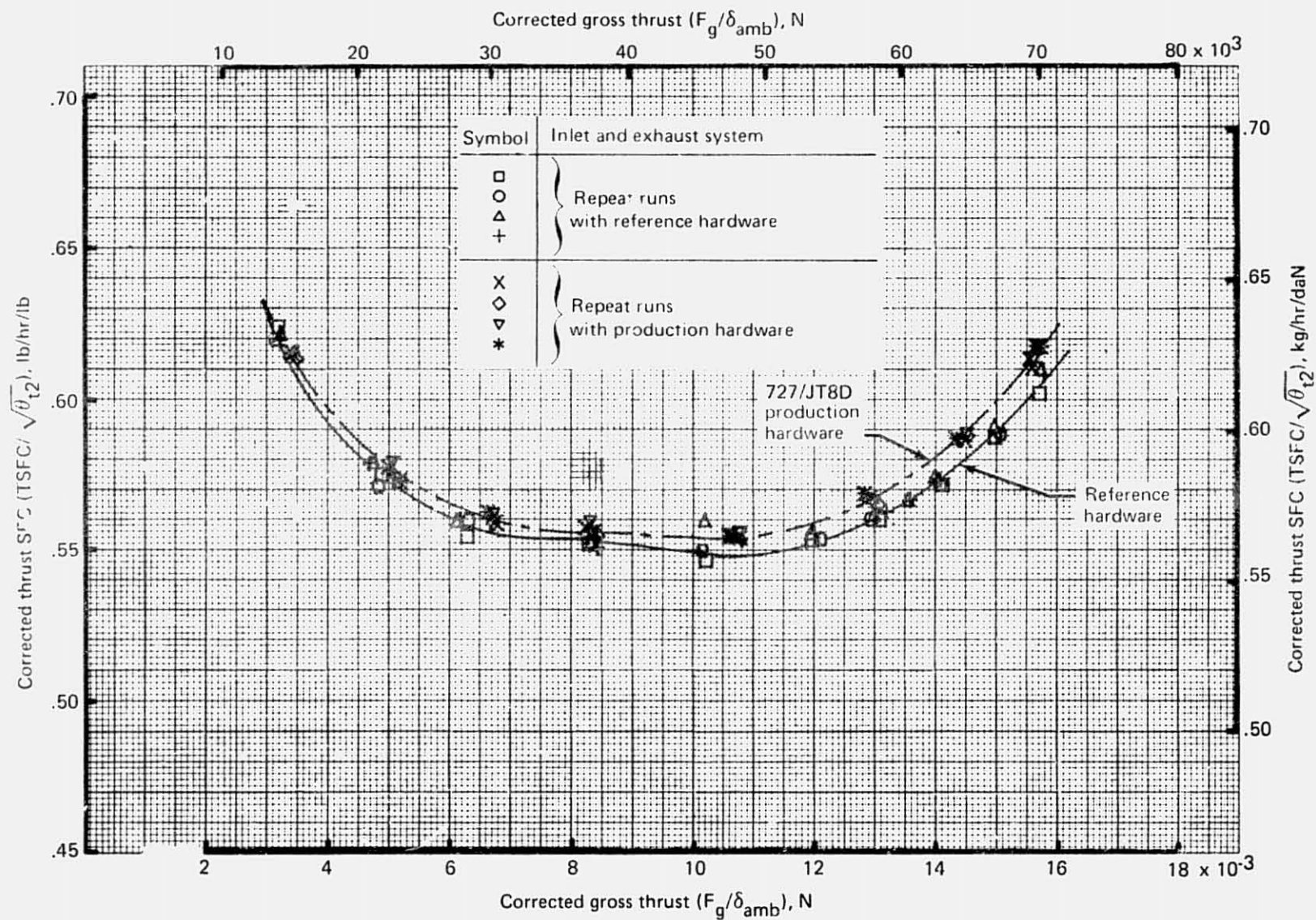


Figure 34.—JT8D-15 Ground Test—Thrust Specific Fuel Consumption Versus Gross Thrust

margin testing with the reference hardware and the center-engine inlet hardware but before the LPC surge margin testing with the side-engine inlet without acoustic ring. Figures 35 through 39 present the test results for a portion of the reference hardware runs. The total airflow, FPR, and gross thrust, plotted versus EPR, did not vary significantly as is shown by figures 36, 37, and 38, respectively. The LPC rotor speed, also plotted against EPR, increased slightly after the surge testing and is shown in figure 35, though only one line has been drawn through all the data. Thrust SFC was increased significantly (about 1%) after the surge testing as shown in figure 39. A discussion of data quality is presented in section 4.1.3.

Computer simulations were assembled to match 11 of the tested configurations on the JT8D-115 engine. The results from these simulations were used as inputs to the noise prediction procedures. These computer simulations, in general, match the test data shown in figures 35 through 39 within 0.5% of the measured engine parameters. Simulation of test data to within 0.5% of measured engine parameters is considered good agreement for noise analysis work.

*Contractor Inlet and Exhaust Hardware.*—The majority of testing to evaluate engine performance with the inlet and exhaust system installed was conducted jointly with acoustic tests. The hybrid exhaust system (described in sec. 3.3) with various inlet configurations was used for most engine performance evaluations. Figures 40 through 43 show the effect of the center-engine inlet and duct and the side-engine inlet with and without ring on low pressure compressor rotor speed, total airflow, fan pressure ratio, and gross thrust. These inlets all had a bellmouth lip installed to simulate the inlet streamlines at low-speed flight conditions. Figure 44 shows the thrust SFC comparison of the test inlets with the hybrid exhaust system installed. The JT8D-15 engine performance is also shown in the figure for comparison to the JT8D-115 engine. At takeoff thrust, the JT8D-115 shows 12.5% to 13.2% reduction in static SFC for the side-engine inlets with and without ring. This comparison is valid even though it was made with the JT8D-115 hybrid exhaust system, and it will be pointed out in section 4.1.3 that the thrust performances of the hybrid and flight-type exhaust systems were statistically equal. In general, figure 44 shows that as inlet recovery decreases, SFC increases.

#### 4.1.2.2 Nozzle Match

*Definition of Nozzle Match.*—An engine is said to be matched when certain pressures, temperatures, and engine rotor speeds fall into some predetermined optimum relationships as determined by the engine operating with the engine manufacturer's reference hardware. The engine manufacturer requires the effective nozzle area of any other configuration to be matched within  $\pm 0.5\%$  of the reference hardware. In mixed flow engines such as the JT8D-115, three flow areas have considerable influence on these pressure, temperature, and rotor speed relationships. These areas are: (1) primary flow area at primary/secondary mixing plane; (2) fan flow area at primary/secondary mixing plane; and (3) nozzle exit plane area.

The reference exhaust system (fig. 9) had a geometric nozzle area of  $1170.14 \text{ in.}^2$  ( $754.927 \text{ cm}^2$ ) measured at  $40^\circ\text{F}$  ( $277.6 \text{ K}$ ).

*Nozzle Configurations.*—Nozzle match had to be determined for the hybrid exhaust system and the flight-type exhaust system on the JT8D-115 engine. Figure 10 shows a sketch of

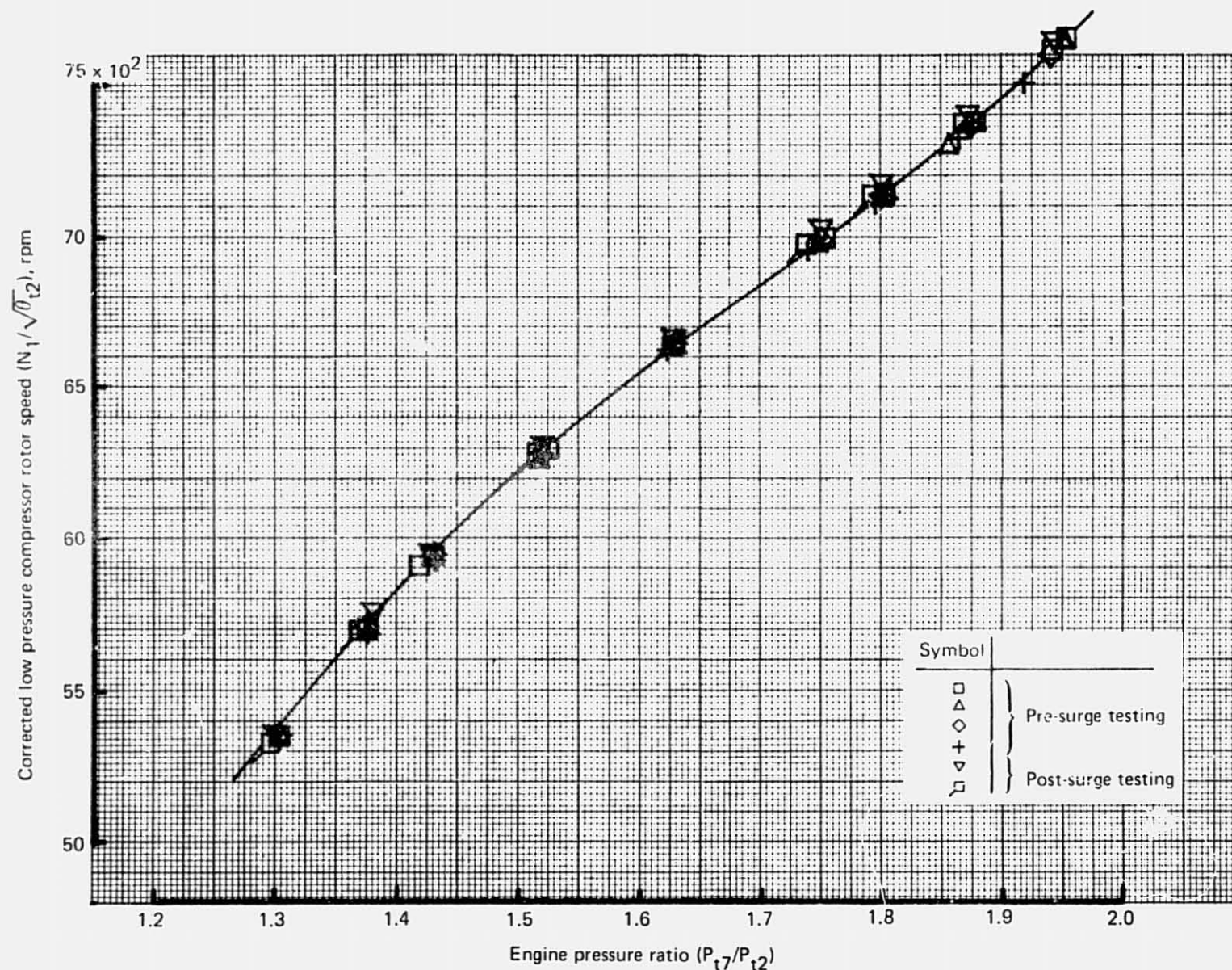


Figure 35.—JT8D-115 Ground Test—Low Pressure Compressor Rotor Speed Versus Engine Pressure Ratio With Reference Hardware



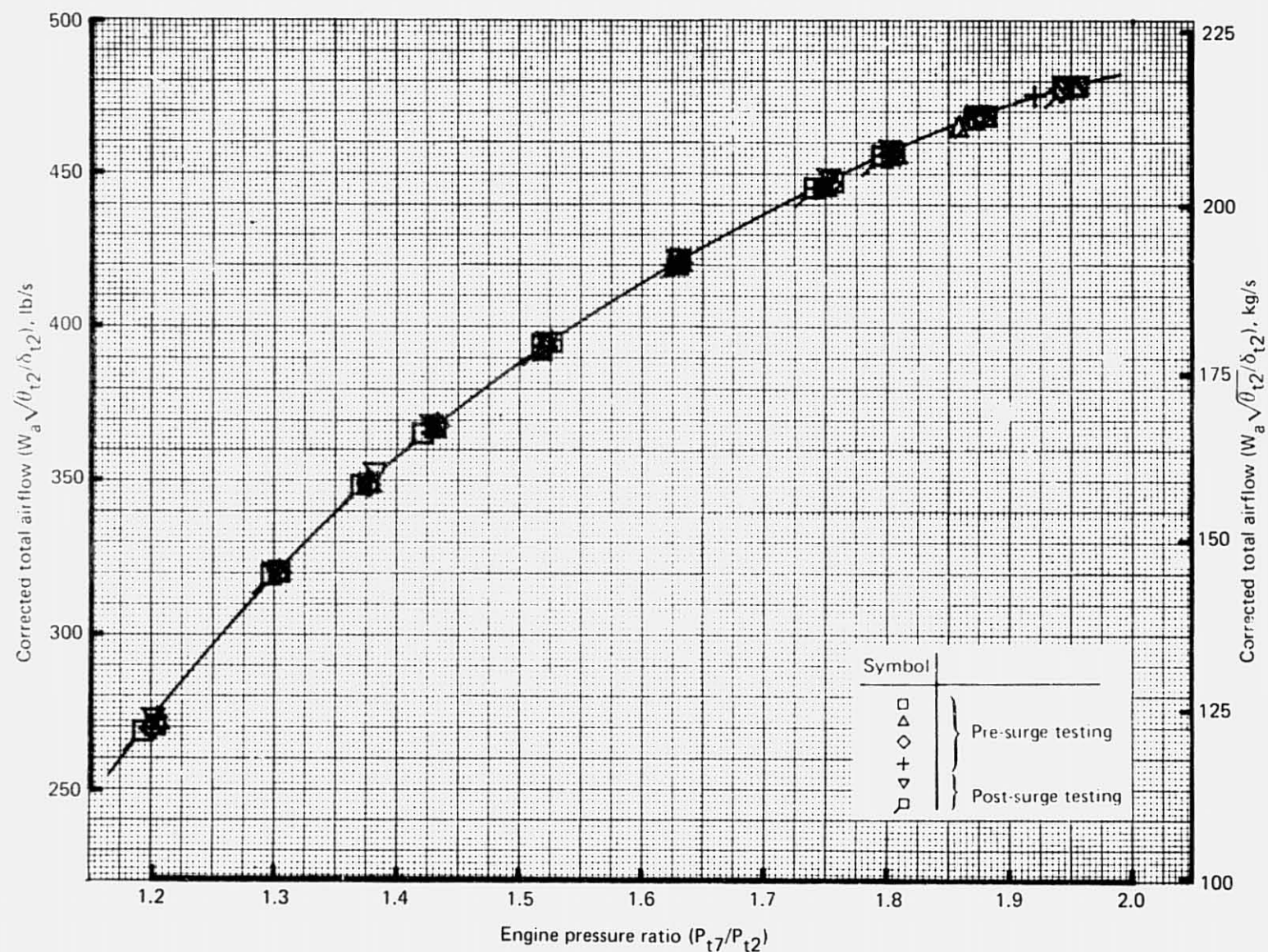


Figure 36.—JT8D-115 Ground Test—Airflow Versus Engine Pressure Ratio With Reference Hardware

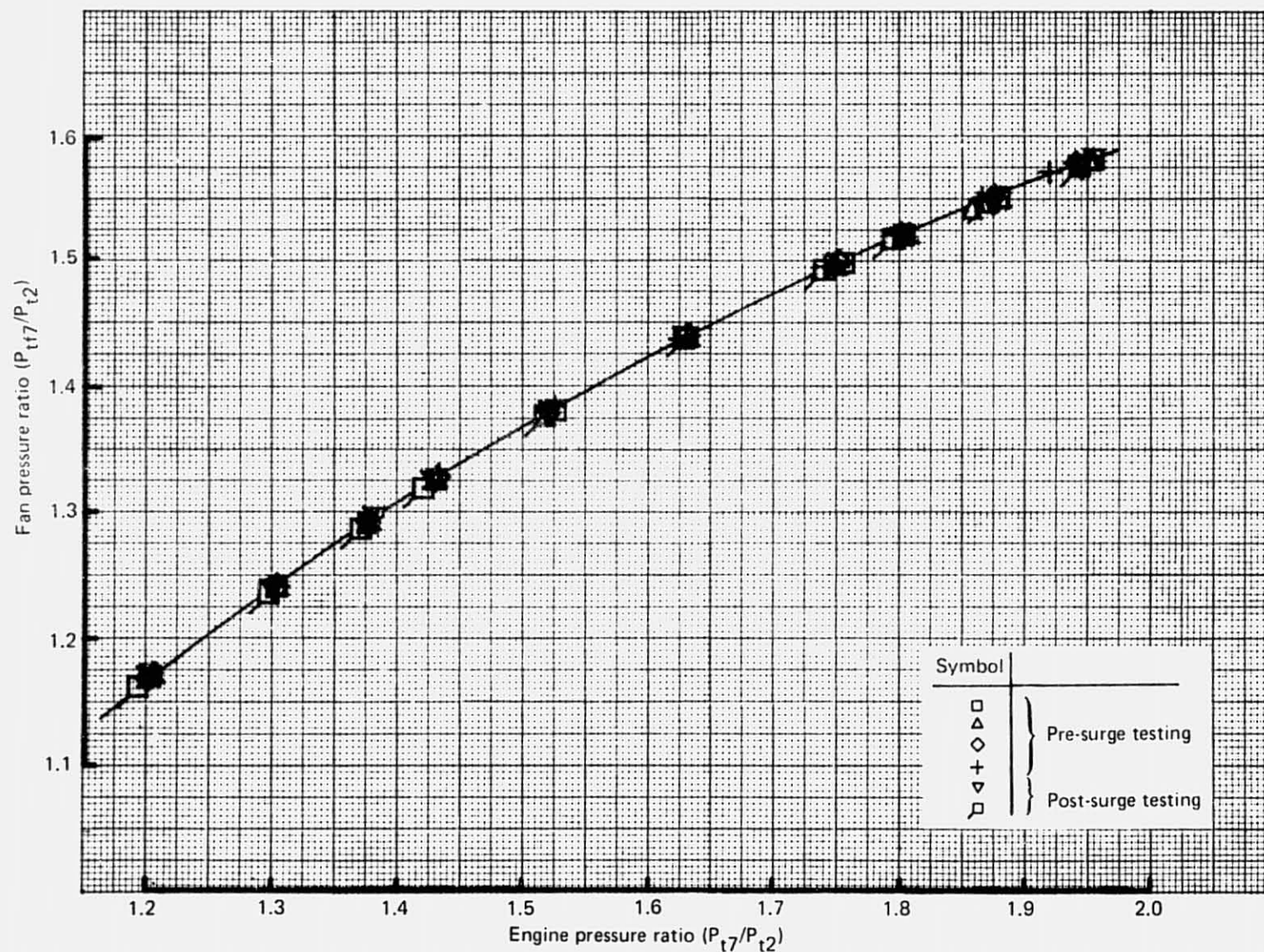


Figure 37.—JT8D-115 Ground Test—Fan Pressure Ratio Versus Engine Pressure Ratio With Reference Hardware

REPRODUCIBILITY OF THIS  
ORIGINAL PAGE IS POOR

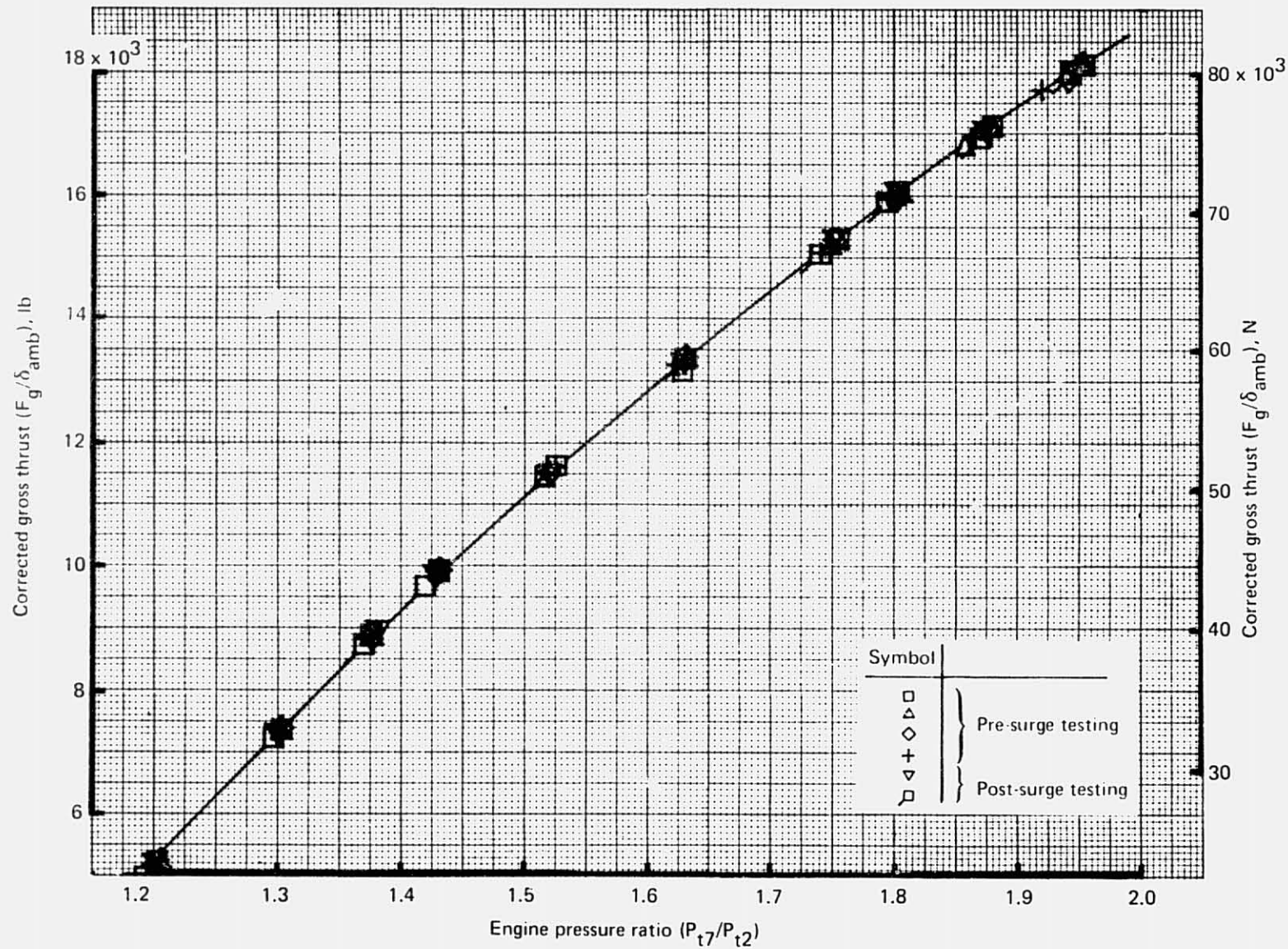


Figure 38.—JT8D-115 Ground Test—Thrust Versus Engine Pressure Ratio With Reference Hardware

REPRODUCIBILITY OF THE  
ORIGINAL PAGE IS POOR



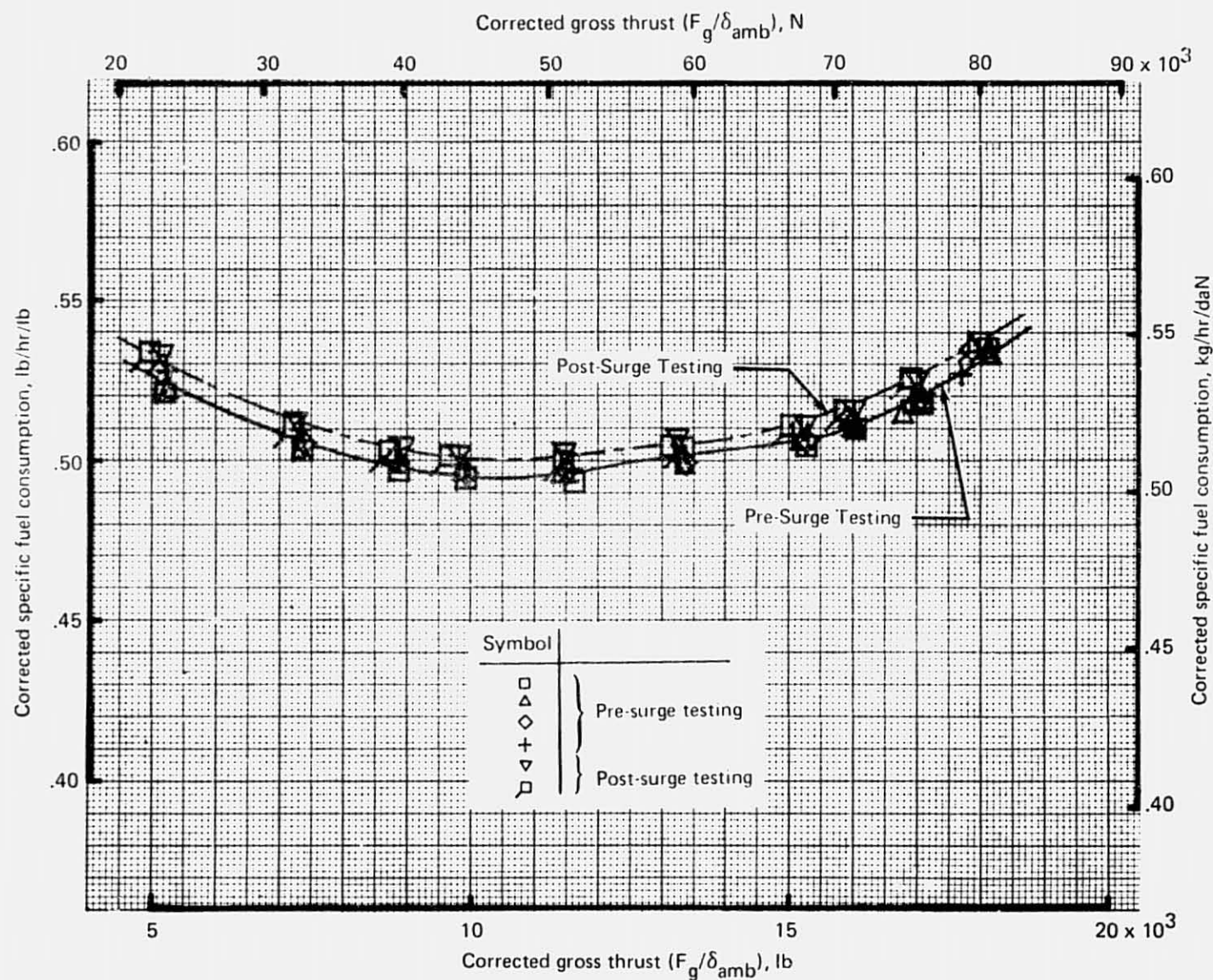


Figure 39.—JT8D-115 G Round Test—Specific Fuel Consumption Versus Thrust With Reference Hardware



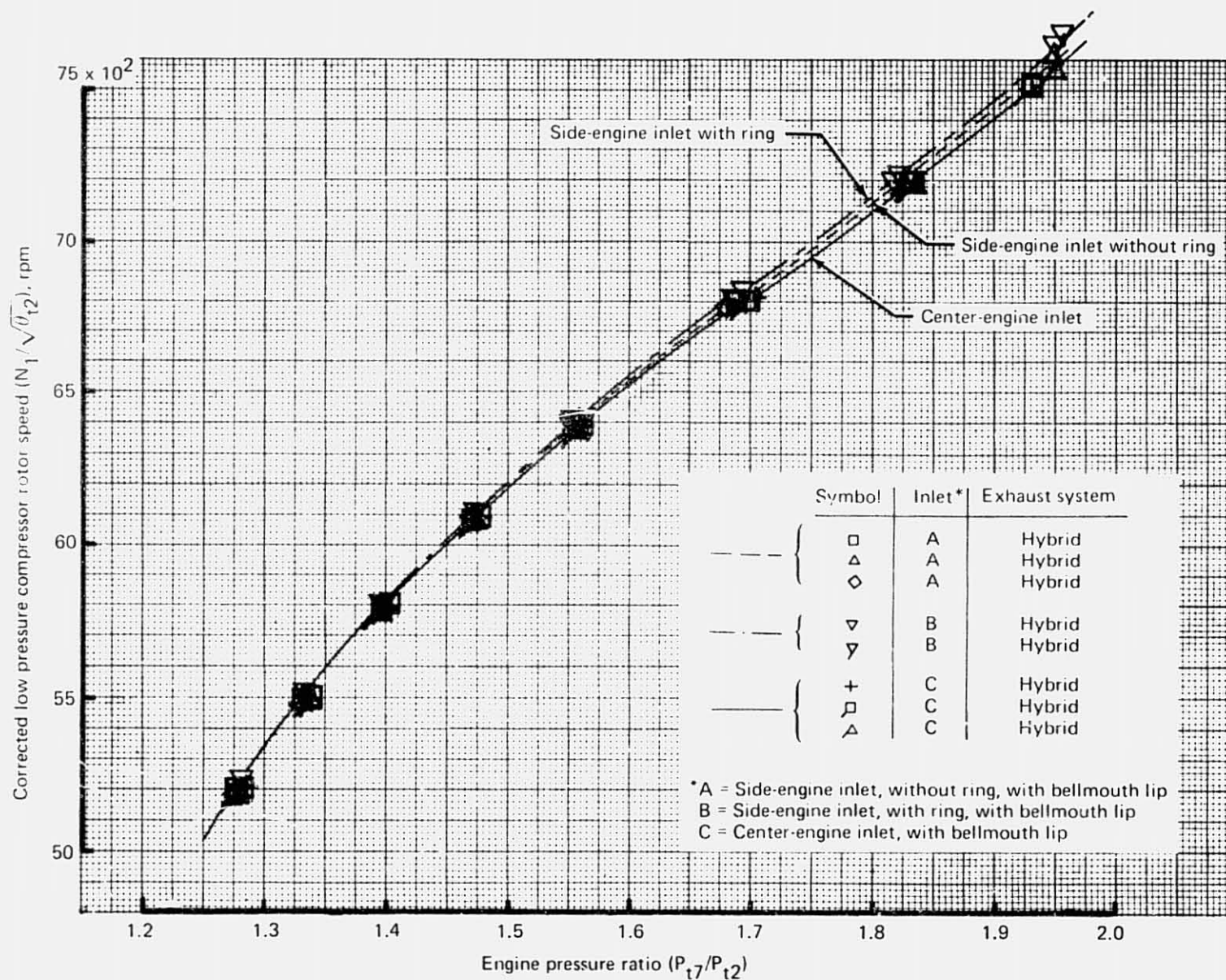


Figure 40.—JT8D-115 Ground Test—Low Pressure Compressor Rotor Speed Versus Engine Pressure Ratio, Side- and Center-Engine Inlet Configurations

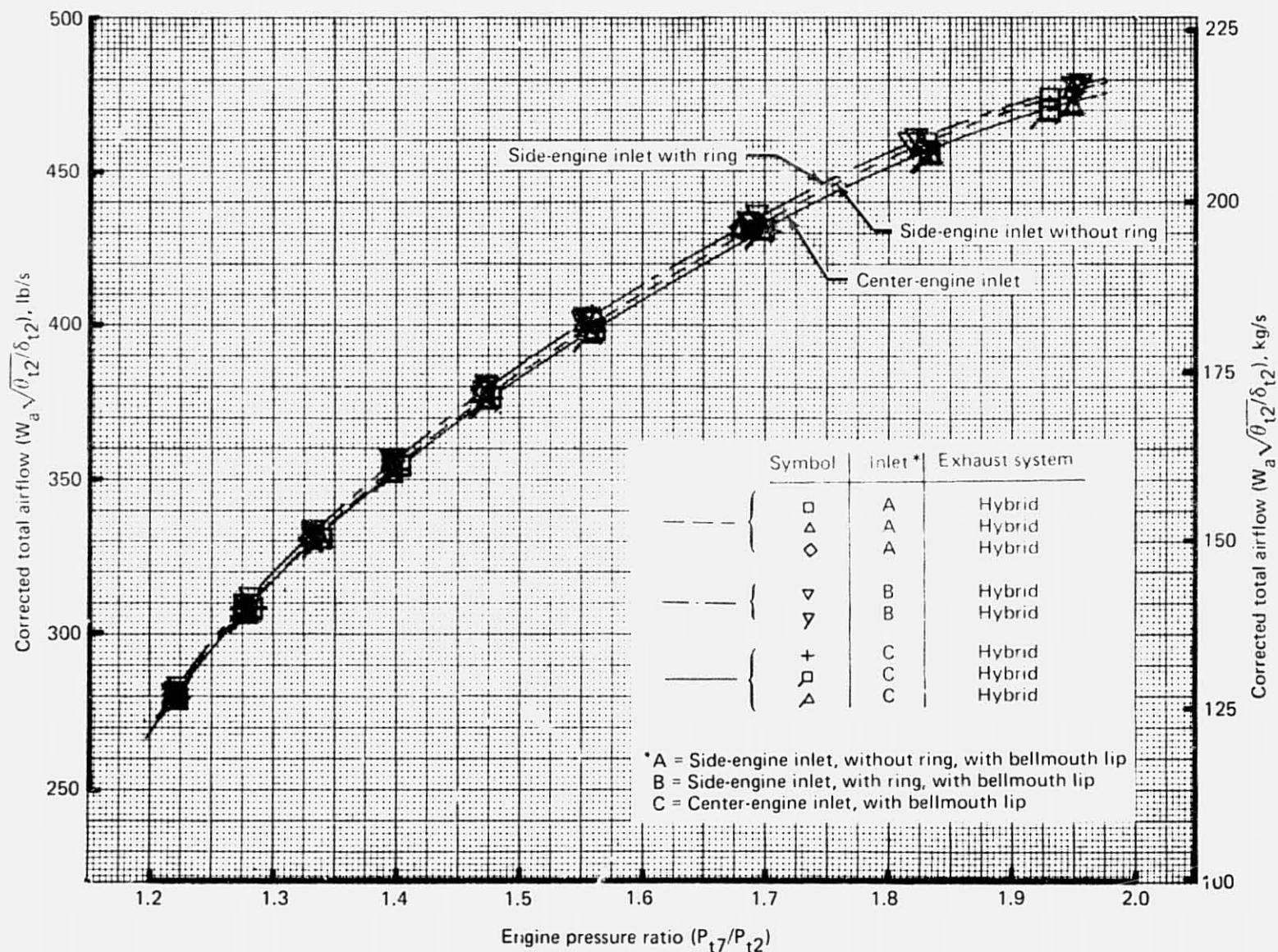


Figure 41.—JT8D-115 Ground Test—Airflow Versus Engine Pressure Ratio, Side- and Center-Engine Inlet Configurations

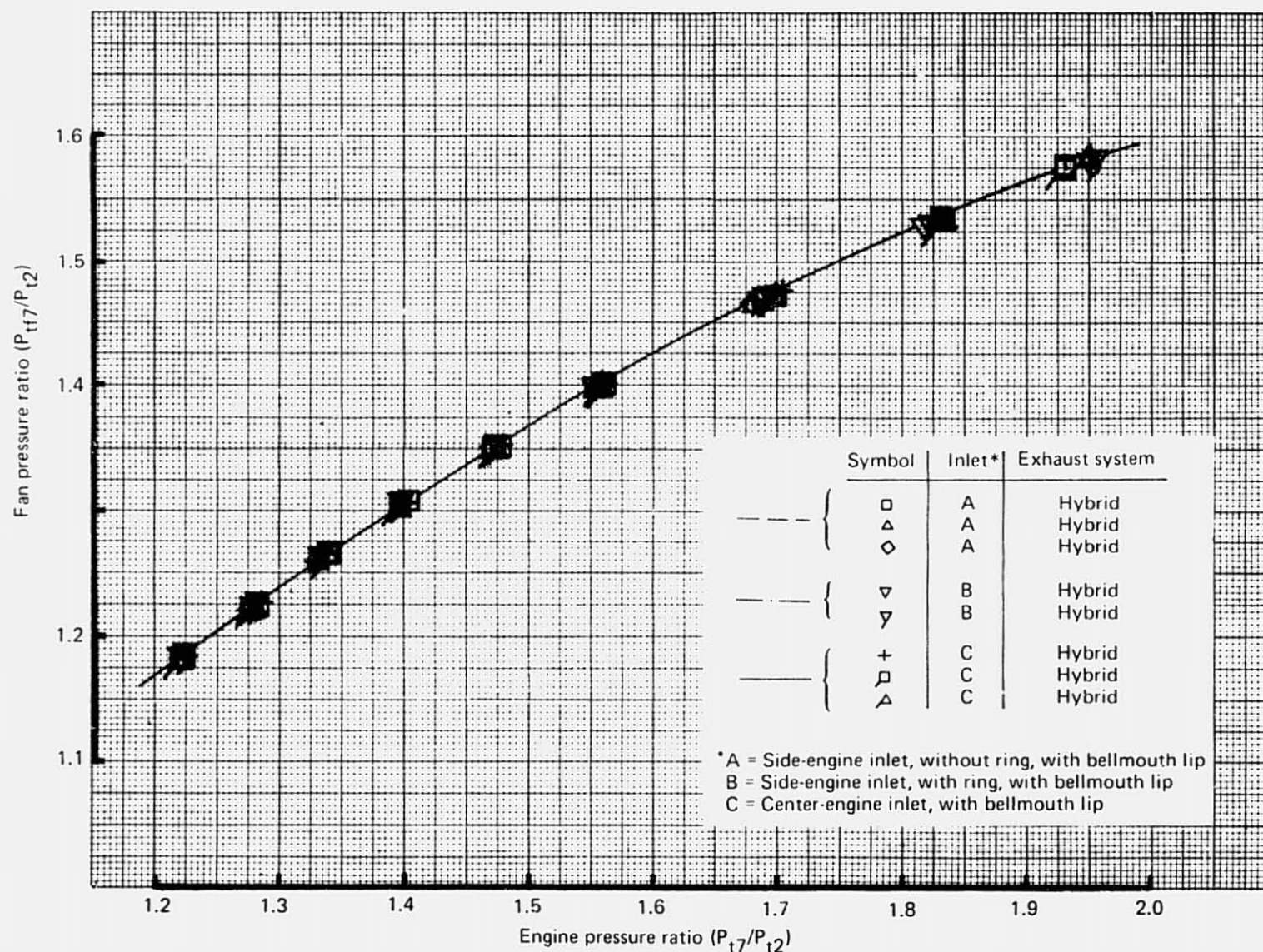


Figure 42.—JT8D-115 Ground Test —Fan Pressure Ratio Versus Engine Pressure Ratio,  
Side- and Center-Engine Inlet Configurations



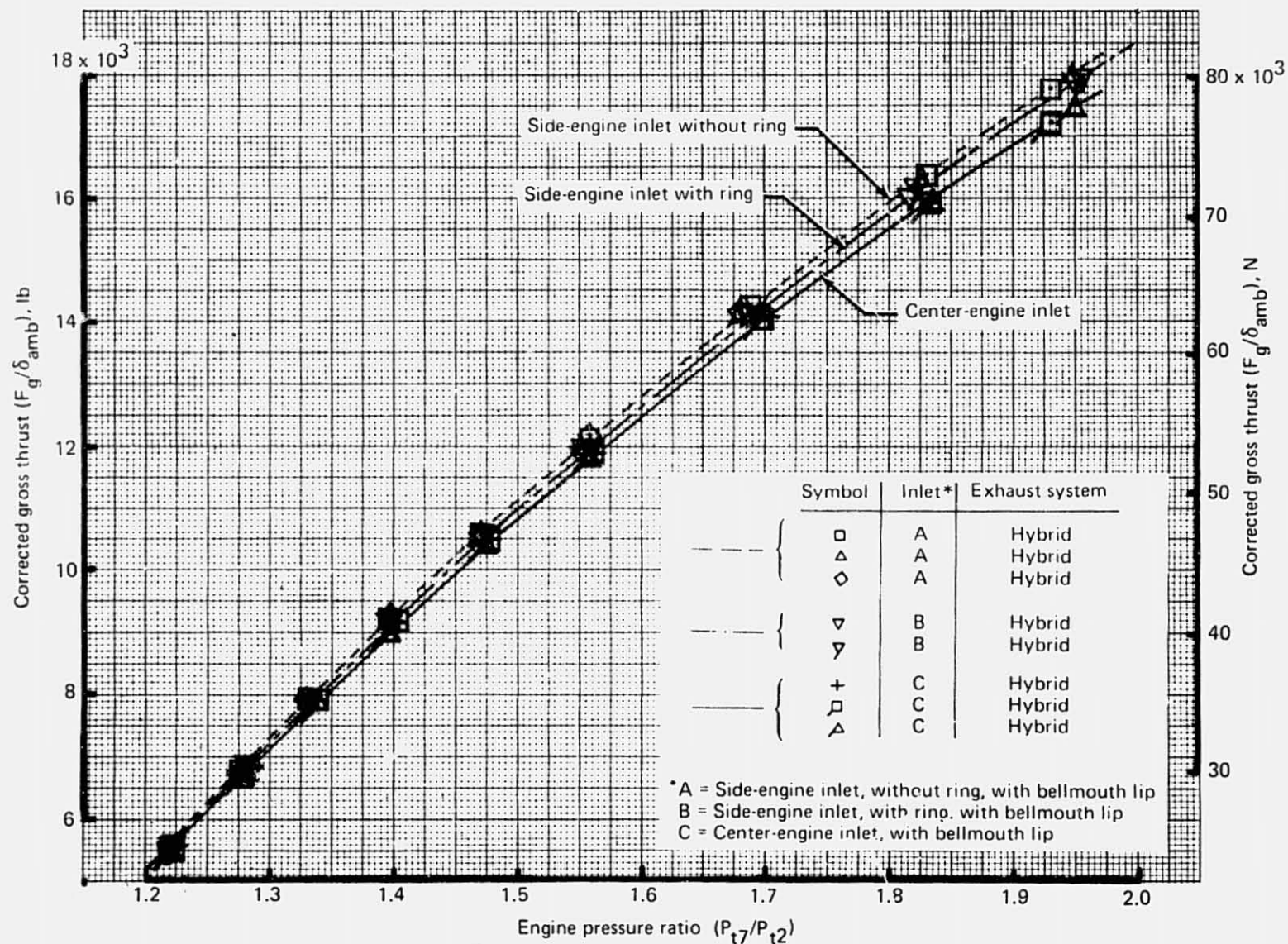


Figure 43.—JT8D-115 Ground Test—Thrust Versus Engine Pressure Ratio, Side-and Center-Engine Inlet Configurations

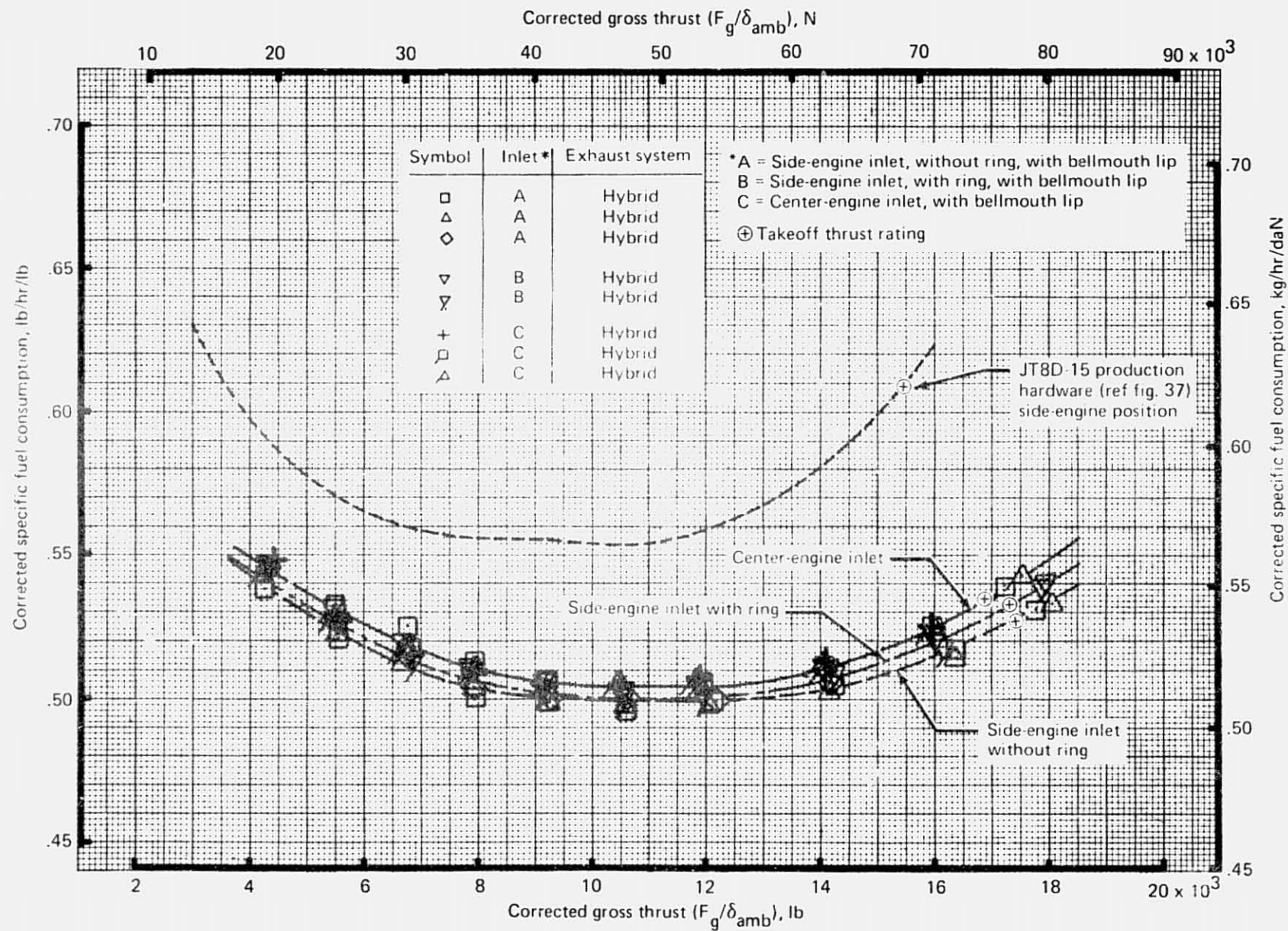


Figure 44.—JT8D-115 Ground Test—Specific Fuel Consumption Versus Thrust, Side- and Center-Engine Inlet Configurations

these two configurations. The sizing of the flight-type exhaust duct had to be accomplished with the reference fan/primary flow divider and plug because of a delay in manufacture of the flight-type fan/primary flow divider.

Since both the hybrid and flight-type exhaust systems use the same treated exhaust duct, a study was undertaken to determine the best procedure to match both configurations within the specified  $\pm 0.5\%$  effective nozzle area. This study indicated that the hybrid exhaust system should be matched at a nozzle area  $0.5\%$  below the nominal value, permitting the flight-type exhaust system to fall within the tolerance band, probably on the high side. This difference was due to the discharge coefficient difference of the flight-type exhaust system, with its different fan/primary flow divider and plug configurations. No change in the mixing plane performance was expected for the hybrid exhaust system relative to the reference exhaust system since both use common geometry up to the mixing plane, although the flight-type exhaust duct had a  $3.5^\circ$  cant relative to the axial reference fan/primary flow divider and plug.

*Matching Procedure.* Nozzle match was determined by comparing the JT8D-115 engine match parameters ( $P_{s4}/P_{t7}$ ,  $P_{s3}/P_{t2}$ , and  $N_1/\sqrt{\theta_{t2}}$ ) for the hybrid or the flight-type exhaust system to those for the reference exhaust system. Then using figure 45, the deviation from nominal nozzle effective area was determined for each of the three engine match parameters. The three values of effective nozzle area deviation were then averaged to establish the match point of the nozzle. This procedure was based upon the P&WA match procedure for the basic JT8D engine.

Engine match parameter relationships with respect to nozzle effective areas (fig. 45) had to be established during this test program because the Engine Contractor had not tested different nozzle areas on the JT8D-115 engine. However, the Engine Contractor did provide the nozzle match parameter relationship, which they had determined from their JT8D-109 engine tests, in order to establish the initial value of nozzle mismatch. The flight-type nozzle for the JT8D-115 engine was purposely manufactured underarea to allow trimming back the nozzle exit to match the reference nozzle effective area. After the first trimming of the flight-type nozzle, it was discovered that the JT8D-109 engine match relationships were not valid for the JT8D-115 engine. Two additional nozzle trims were needed to match the hybrid exhaust system within the  $\pm 0.5\%$  tolerance band allowed by the Engine Contractor. Figure 46 is the result of a statistical analysis of the reference and hybrid exhaust system runs. The flight-type nozzle area after the final cut was  $1163.14 \text{ in.}^2$  ( $750411 \text{ cm}^2$ ) measured at  $33^\circ\text{F}$  ( $273.7 \text{ K}$ ).

*Exhaust System Match Results.* Figure 46 shows the percent deviation from nominal of the three engine match parameters for the hybrid and flight-type exhaust systems as determined from a statistical analysis of the test data. Also shown is the one standard deviation ( $1.0 \sigma$ ) about the statistically best estimate of the mean value of the engine parameter. Using the data shown in figures 45 and 46, the final match of these two exhaust systems relative to the reference exhaust system on the JT8D-115 engine was determined to be as follows:



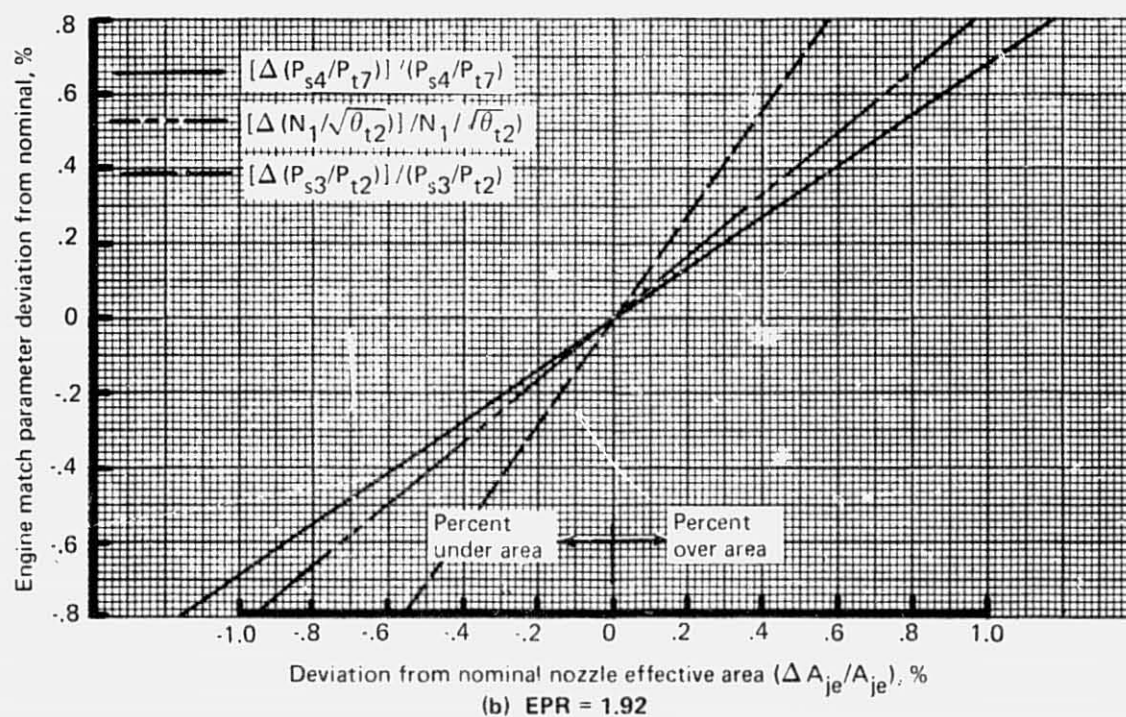
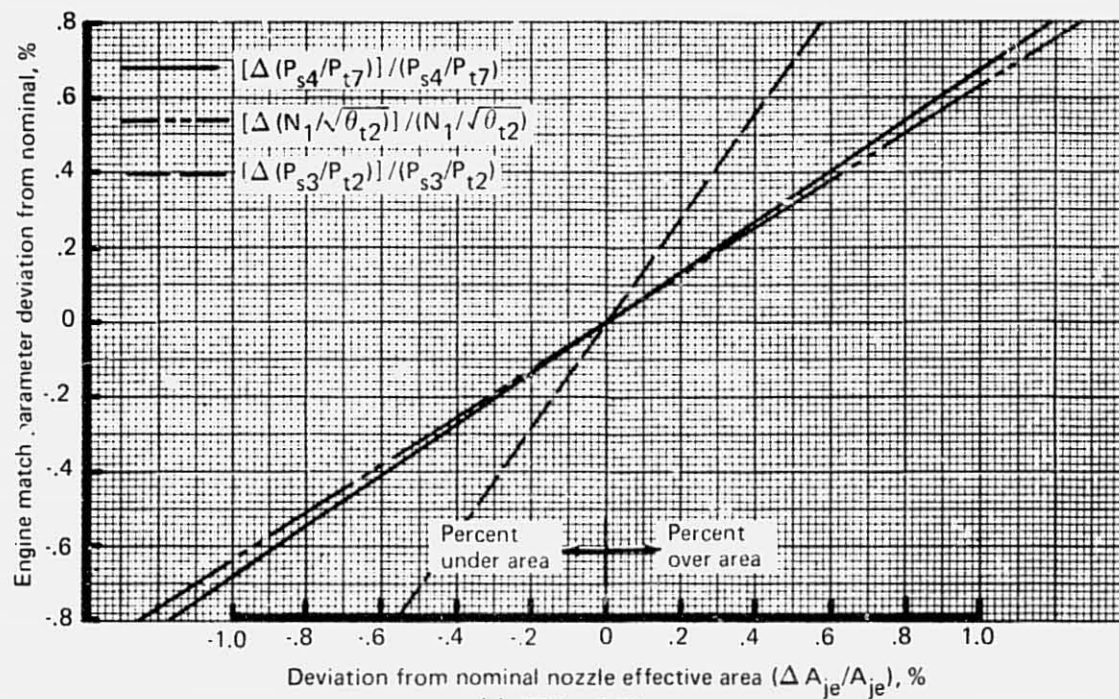


Figure 45.—JT8D-115 Engine Match Parameter Versus Nozzle Effective Area Relationships

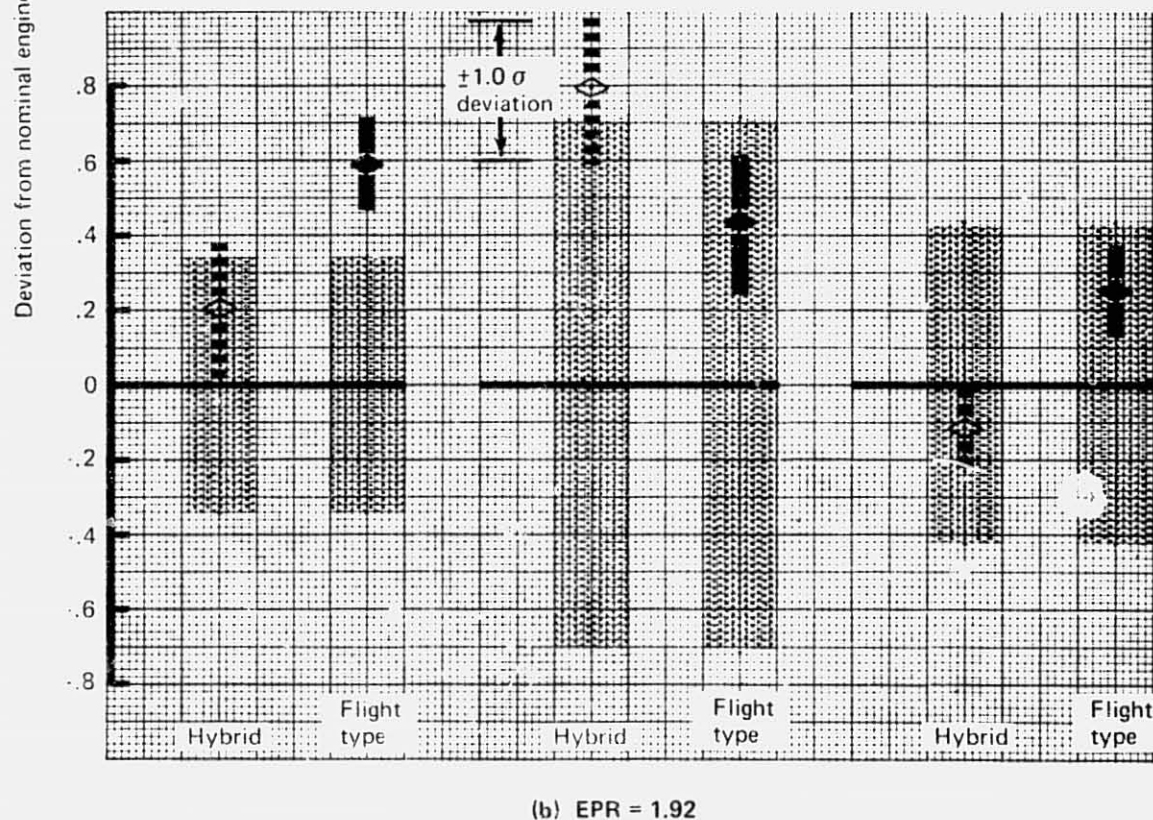
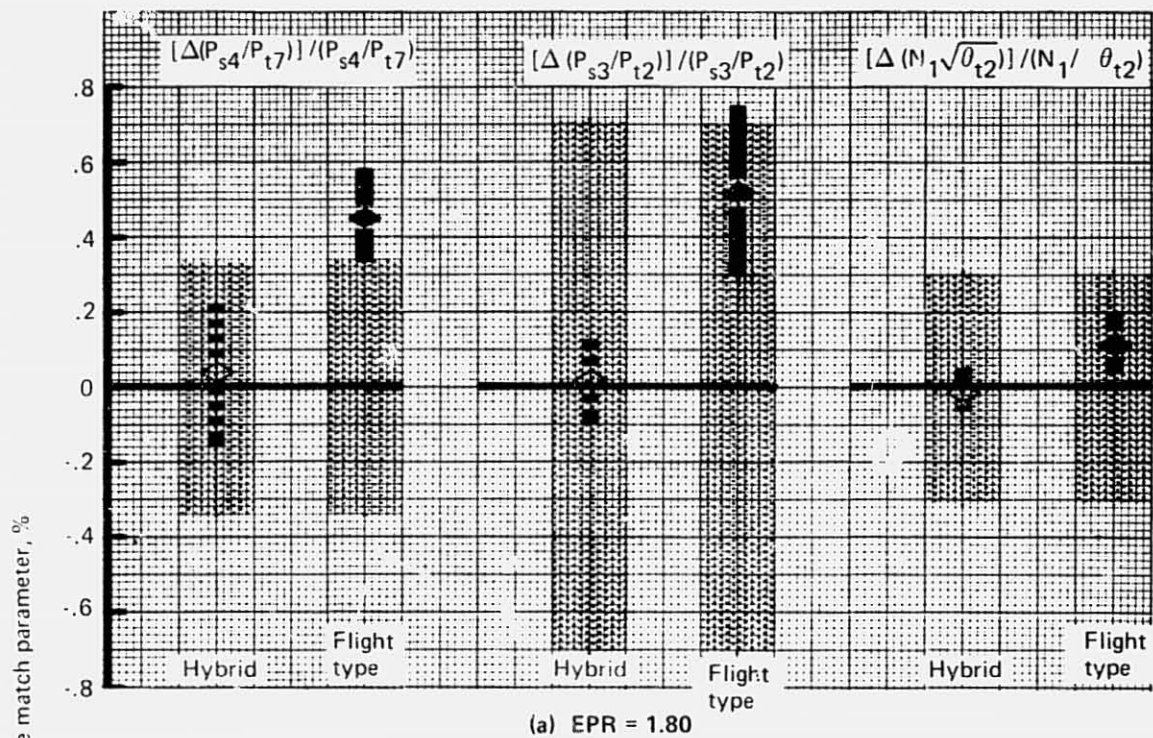


Figure 46.—JT8D-115 Ground Test—Deviation From Nominal Engine Match Parameters Relative to the Reference Exhaust System



Configuration	Engine pressure ratio	
	1.80	1.92
Hybrid exhaust system	Matched	0.24% overarea
Flight-type exhaust system	0.46% overarea	0.50% overarea

The match results for the flight-type exhaust system should be interpreted with caution. Test data indicated that the fan pressure ratio,  $P_{t7}/P_{t2}$ , was approximately 0.45% higher at a given EPR than with the reference exhaust system. This indicates that the effective fan-to-primary area ratio ( $A_F/A_P$ ) at the mixing plane was slightly different from the reference exhaust system. Therefore, the engine is not at the same operating point with the flight-type exhaust system as with the reference exhaust system. There was no provision in the test schedule to modify the flight-type fan/primary flow divider to match the reference effective  $A_F/A_P$ . If this had been done, any modification to the nozzle exit area would depend on the inter-relationship of  $A_F/A_P$  and the nozzle exit area.

#### 4.1.2.3 Nozzle Performance

*Nozzle Types.*—Nozzle performance for the following exhaust systems was obtained during the JT8D-115 ground tests: (1) reference exhaust system (fig. 9); (2) flight-type exhaust system (fig. 10); and (3) hybrid exhaust system (fig. 10).

*Nozzle Performance Data Presentation.*—Nozzle performance in terms of gross thrust, velocity, and discharge coefficients for mixed flow engines was calculated based on a mixed total pressure and temperature of the fan and primary flow streams from the engine. Mixed flow conditions for the nozzles were determined using two methods: (1) an empirical relationship derived from test data and (2) a theoretical 100% thermodynamic mixed relationship. The empirical relationship was used because of its ease in calculating thrust of an airplane in flight by measuring relatively few engine parameters, whereas the 100%-theoretical mixed relationship was used in engine-airplane-noise analyses that required a computer simulation of the engine and were used for comparing model-to-full-scale test results. Computer simulations of the JT8D-115 engine use nozzle performance coefficients that are based on the 100%-theoretical mixed flow conditions. A discussion of the methods for determining the mixed flow conditions is presented herein.

The Engine Contractor uses the following empirical relationship for determining the JT8D-15 and -115 mixed flow total pressure ( $P_{tm7}$ ) of the fan and primary streams:

$$P_{tm7} = \frac{P_{t7} + X P_{t7}}{(1 + X)} \quad (2)$$

The X-factor is the value required to provide nozzle performance coefficients as unique functions of the mixed pressure ratio ( $P_{tm7}/P_{amb}$ ) for all pressures and temperatures encountered during normal engine operations throughout the airplane flight envelope. For the JT8D-15 engine, this value was determined by the Engine Contractor from model tests to be 0.8. The model scale tests of the reference and flight-type exhaust systems (ref. 6), accomplished by the Contractor provided sufficient information to determine that the value of the X-factor

for the JT8D-115 engine was 1.35. This value was used to calculate  $P_{tm7}$  for the ground testing of the reference, flight-type, and hybrid exhaust systems.

The mixed total temperature ( $T_{tm7}$ ) that is used with the empirical mixed pressure to determine the nozzle performance coefficients is based on the thermodynamic relationship that the heat added is equal to the difference in enthalpy across the engine, since the internal work of the compressors and turbines cancel out. The resulting equation for  $T_{tm7}$  is:

$$T_{tm7} = \frac{W_a C_{p2} T_{t2} + W_f C_{pf} T_{t2} + W_f (H_v) N_c}{(W_a + W_f) C_{p7}} \quad (3)$$

where:  $C_{p2}$  = specific heat at constant pressure of air evaluated at  $T_{t2}$  temperature  
 $C_{pf}$  = specific heat at constant pressure of fuel evaluated at  $T_{t2}$  temperature  
 $C_{p7}$  = specific heat at constant pressure of air evaluated at  $T_{tm7}$  temperature  
 $N_c$  = efficiency of combustion (assumed to be equal to 1.0)  
 $H_v$  = fuel lower heating value

Since  $C_{p7}$  is a function of the  $T_{tm7}$  temperature, the unknown quantity, it requires an iterative process (by a computer program) to solve for  $T_{tm7}$ .

The measured primary and secondary temperatures and mass flow rates were used to calculate the mixed temperature for the model test (ref. 6). This method could not be used for the full-scale test since the primary/secondary flow split was not determined. This resulted in different mixed temperatures for the model test and full-scale test. Therefore, the nozzle performance coefficients presented in this report will not agree with the nozzle coefficients used in reference 6. Since the calculated values of the nozzle coefficients are consistent within themselves, they can, however, be used for comparing nozzle configurations.

Calculation of nozzle performance coefficients based upon 100% theoretical mixed total pressures and temperatures requires a knowledge of the flow properties for both the fan and primary streams at the mixing plane. Using these flow stream properties, the 100% theoretical mixed flow pressure and temperature ( $P_{tm8}$  and  $T_{tm8}$ , respectively) can be calculated by simultaneously solving the momentum, energy, and continuity equations for a constant-area mixing process and satisfying the condition of equal static pressures for both streams at the mixing plane. In order to determine the flow properties entering the mixing process from the measured engine parameters (i.e., total airflow, fuel flow,  $P_{t7}$ ,  $T_{t7}$ ,  $P_{tf7}$  and  $T_{tf7}$ ), the total pressure losses for both the fan and primary streams from the probe measurement station to the mixing plane, the BPR, and any probe measurement errors must be known. A comparison of the full-scale test data obtained by the Engine Contractor on the JT8D-109 engine with the associated computer program simulation of the same engine was used to derive a correction to the measured engine total temperature ( $T_{t7}$ ) to arrive at the best estimate of the thermodynamic total temperature. The total pressure losses from the probe measurement station to the mixing plane were determined by forcing agreement between the

model and full-scale nozzle performance coefficients corrected to the same station (i.e., the mixing plane). These total pressure losses will be discussed later in this section in the paragraph concerning the correlation of model and full-scale nozzle performance test results. The BPR was determined using the measured JT8D-115 engine parameters obtained from the ground testing of the reference exhaust system and an analysis program that iterated on BPR until the 100%-theoretical mixed total temperature agreed with  $T_{tm7}$  as determined by equation (3). Using the above mentioned relationships for BPR,  $T_{t7}$ , and total pressure loss for the fan and primary streams, the 100%-theoretical mixed total pressure ( $P_{tm8}$ ) and temperature ( $T_{tm8}$ ) were calculated for use in determining the nozzle performance coefficients.

*Nozzle Performance Results.*—Figures 47 through 49 show the measured engine parameters of corrected thrust, corrected engine airflow, and fan total pressure ratio versus EPR for the reference, the flight-type, and the hybrid exhaust systems tested on the JT8D-115 engine. The data for the reference exhaust system are from typical test runs taken at the beginning, midway, and near the end of the test program. Figure 50 shows the nozzle performance coefficients for the reference exhaust system obtained at the three different periods during the ground test. Statistically, there is a detectable difference between the three sets of nozzle coefficients for the reference exhaust system. However, considering the errors which affect the variables in determining the nozzle coefficients, these three sets of reference exhaust system data were considered to be equal.

Figures 51 and 52 show the nozzle performance coefficients for the flight-type and hybrid exhaust systems, respectively. The hybrid exhaust system test runs followed the first set of reference exhaust system runs (fig. 50a) and the flight-type exhaust system runs were between the four runs shown in figure 50c. No difference in gross thrust or velocity coefficients is detectable when the hybrid and flight-type exhaust systems are compared to their respective adjacent reference runs or with all of the reference runs (see sec. 4.1.3). The discharge coefficient for the flight-type exhaust system is statistically the same as the adjacent reference runs but significantly different when compared with all of the reference runs. The hybrid exhaust system discharge coefficient is different from either the adjacent or all of the reference runs. The preceding comparisons were made at the takeoff  $P_{tm7}$ .

*Correlation of Model and Full-Scale Nozzle Performance.*—Figure 53 shows the model and full-scale nozzle performance coefficients for the reference exhaust system using the 100%-theoretical mixed total pressure ( $P_{tm8}$ ) and total temperature ( $T_{tm8}$ ) for calculating the ideal thrust, airflow, and velocity. The model scale test results are from the tests (ref. 6) conducted by the Contractor with a correction applied to account for the total pressure losses from the model probe measurement station to the mixing plane of the fan and primary stream. As mentioned previously, the full-scale test results for the JT8D-115 reference exhaust system used total pressure losses from the measurement station to the mixing plane which forced agreement with the model scale test results. Since the full-scale total pressure losses required to close the nozzle performance coefficients were in reasonable agreement to those used by the Engine Contractor in their JT8D-115 engine computer simulation, the model and full-scale nozzle coefficient correlation was considered valid. These nozzle performance coefficients for the reference exhaust system were used in the Contractor's simulation of the JT8D-115 engine. After simulating the JT8D-115 engine, nozzle coefficient increments

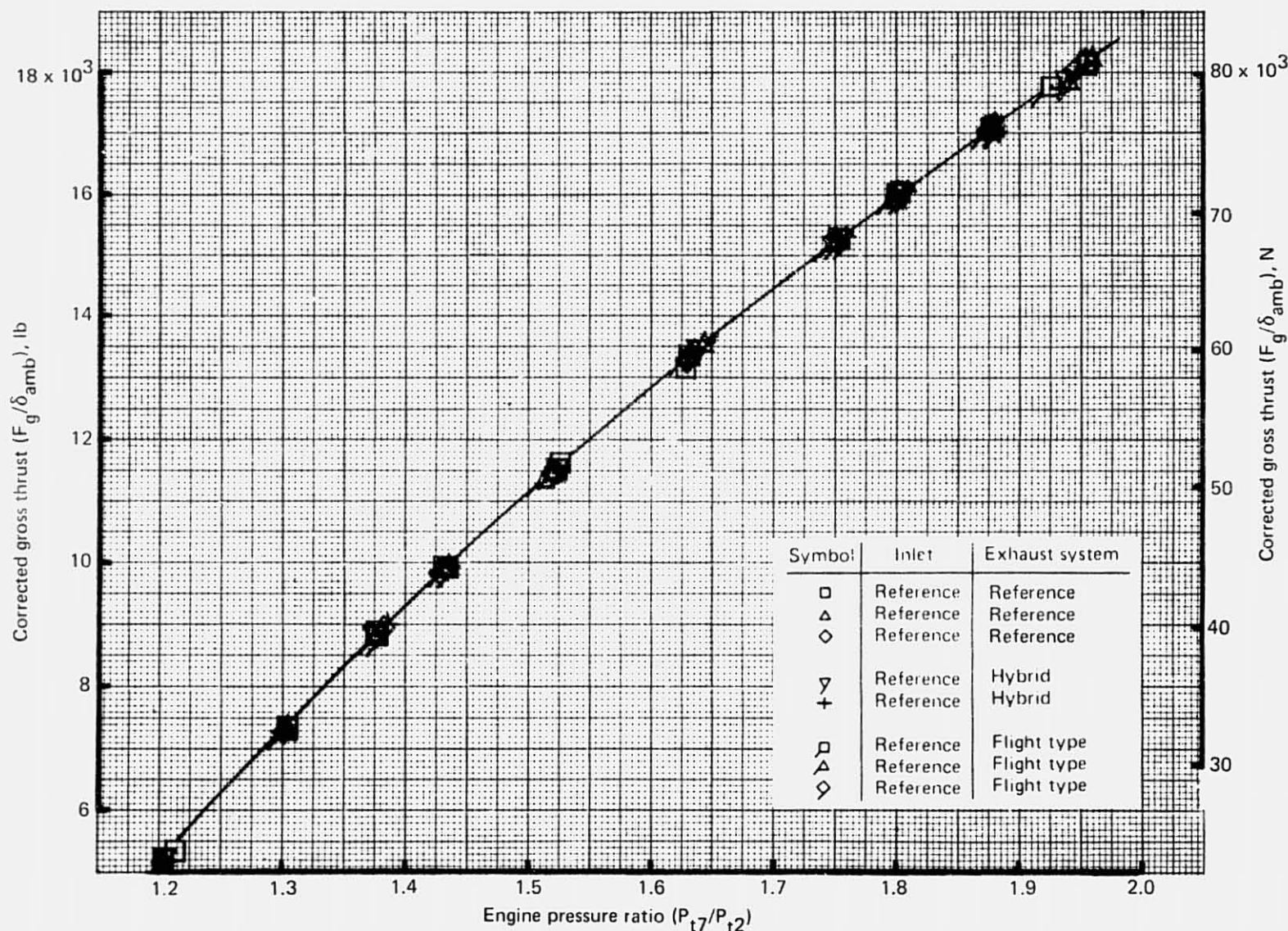


Figure 47.—JT8D-115 Ground Test—Thrust Versus Engine Pressure Ratio for the Reference, Flight-Type, and Hybrid Exhaust Systems

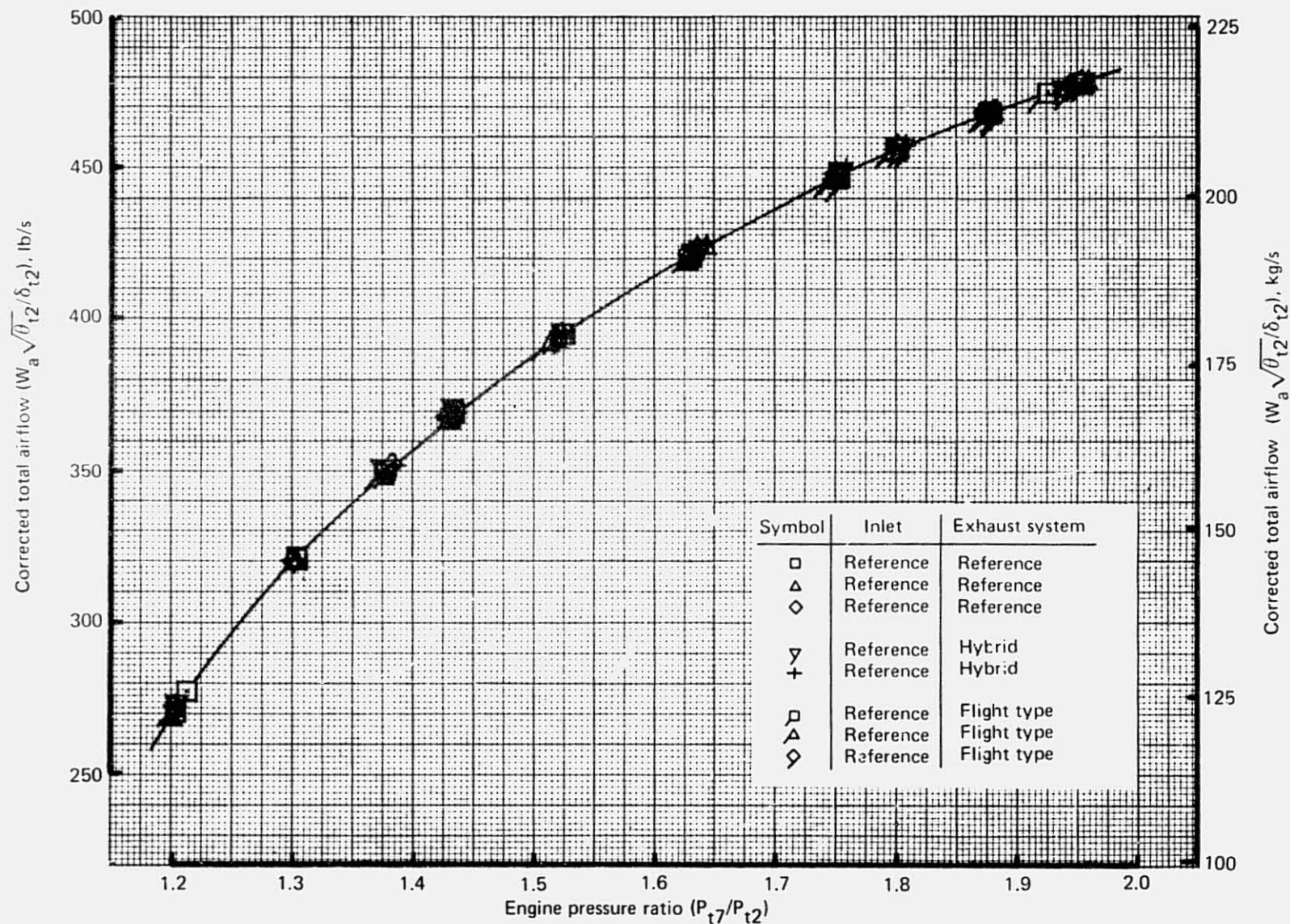


Figure 48.—JT8D-115 Ground Test—Airflow Versus Engine Pressure Ratio for the Reference, Flight-Type, and Hybrid Exhaust Systems



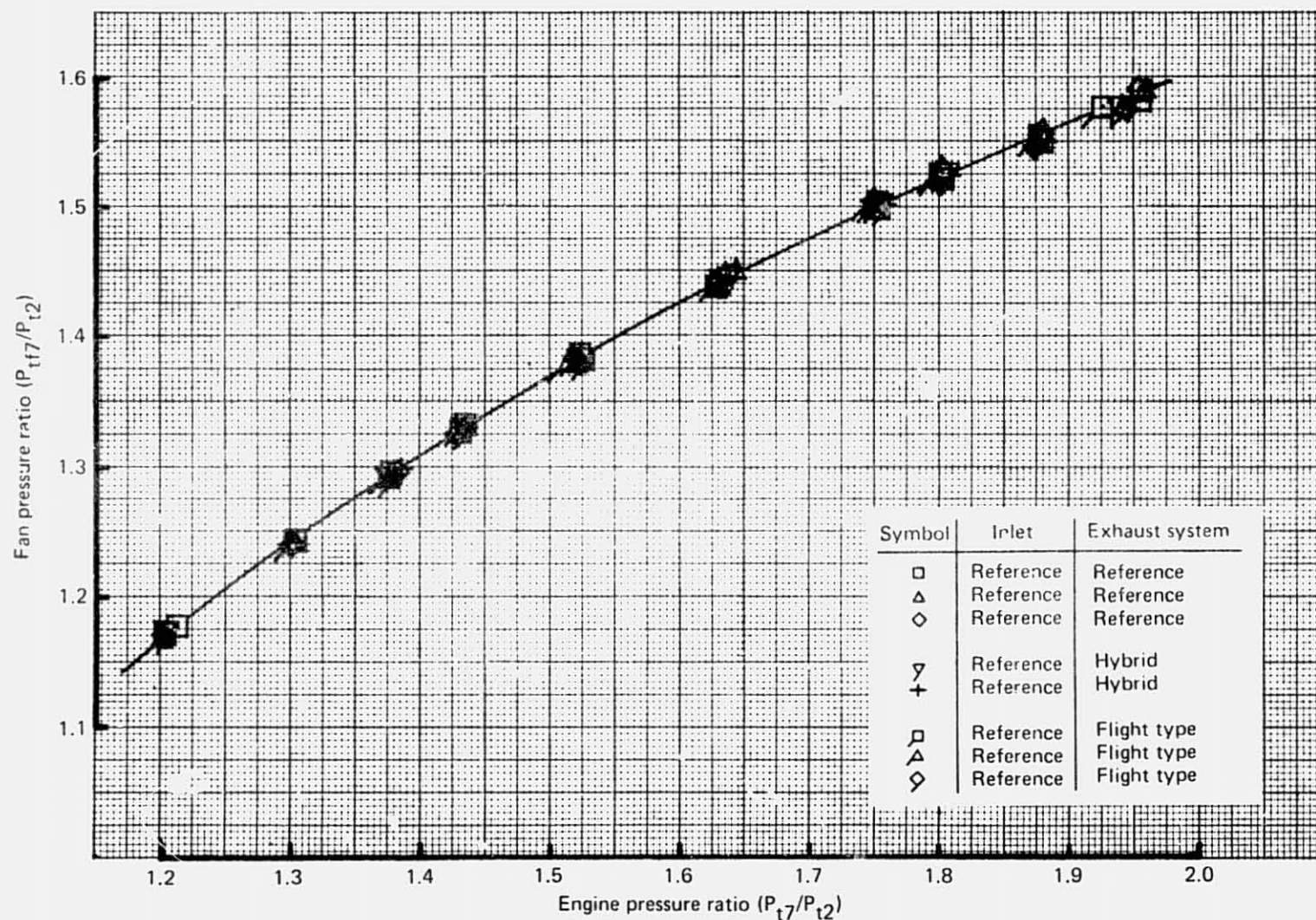
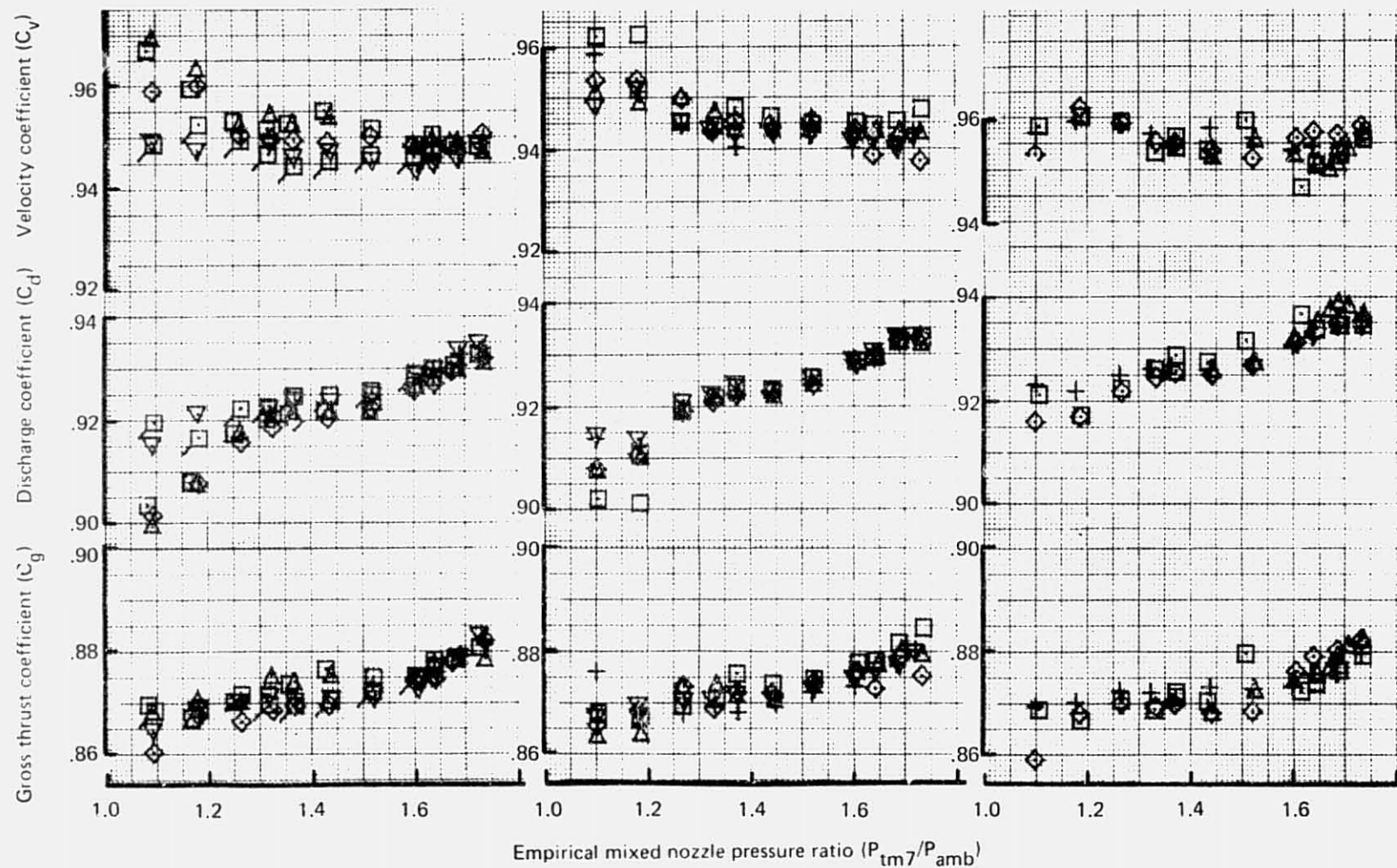


Figure 49.—JT8D-115 Ground Test—Fan Pressure Ratio Versus Engine Pressure Ratio for the Reference, Flight-Type, and Hybrid Exhaust Systems



(a) Typical Test Runs Taken at the Beginning of the Test Program

(b) Typical Test Runs Taken Midway in the Test Program

(c) Typical Test Runs Taken Near the End of the Test Program

Figure 50.— JT8D-115 Reference Exhaust System Performance

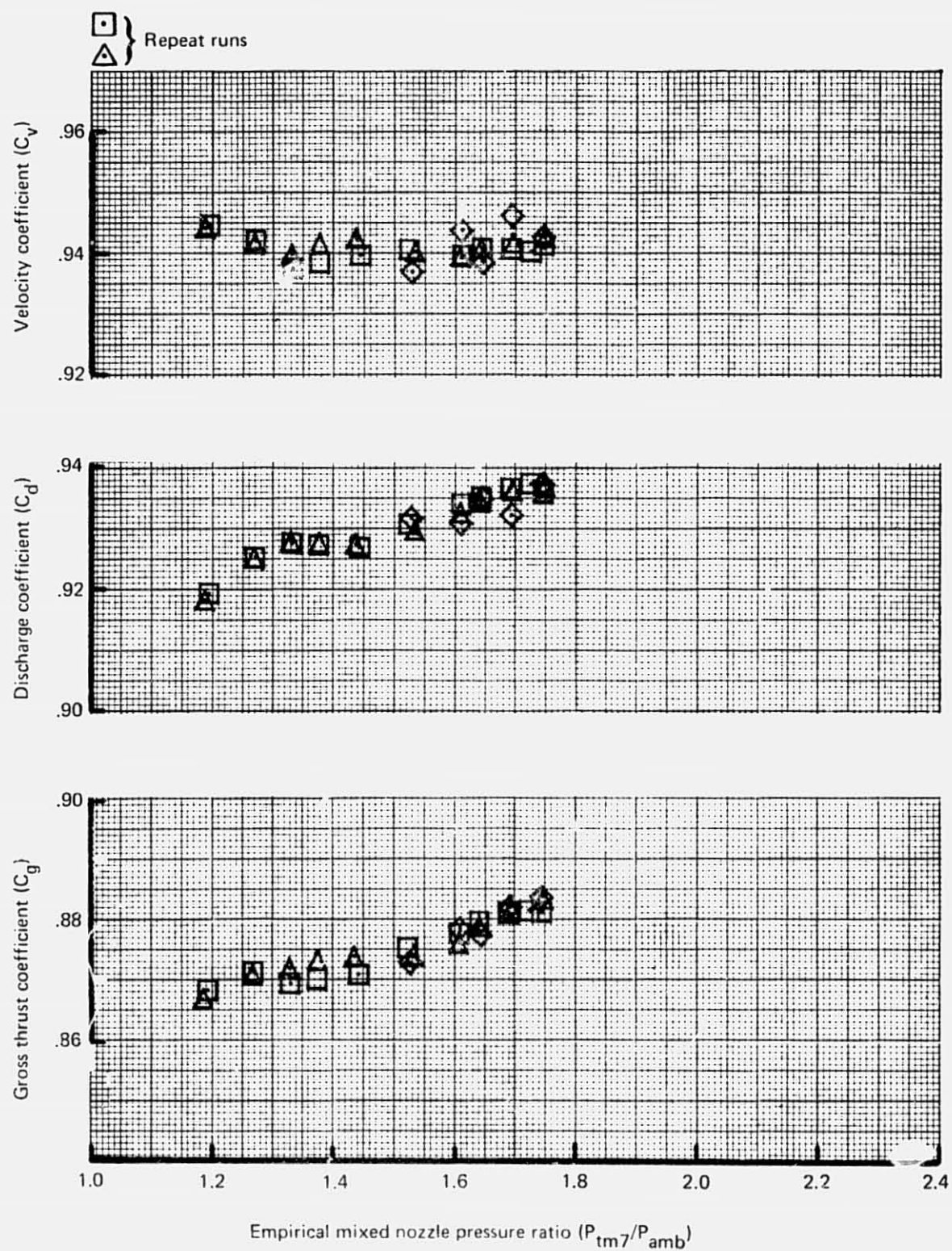


Figure 51.—JT8D-115 Flight-Type Exhaust System Performance



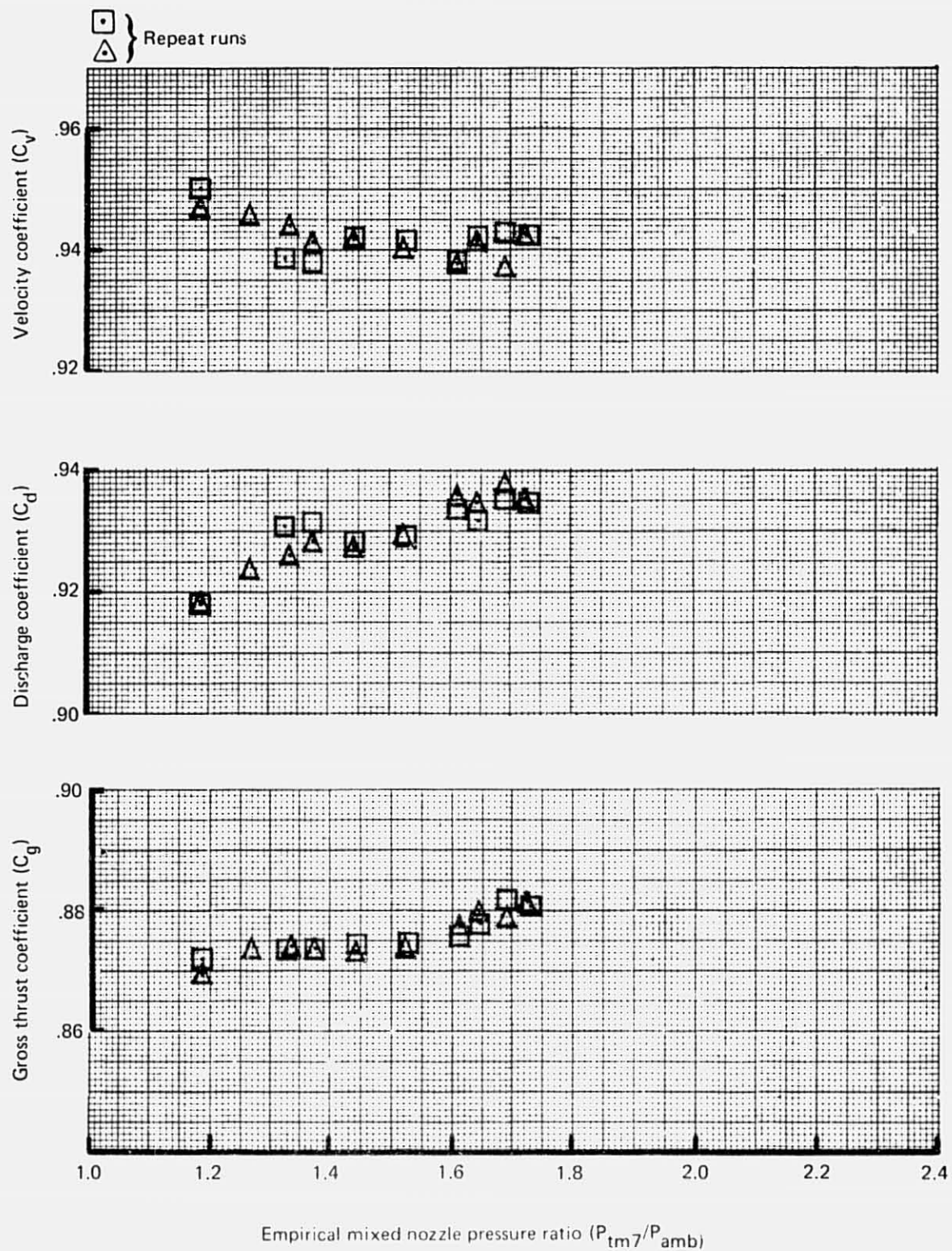


Figure 52.—JT8D-115 Hybrid Exhaust System Performance

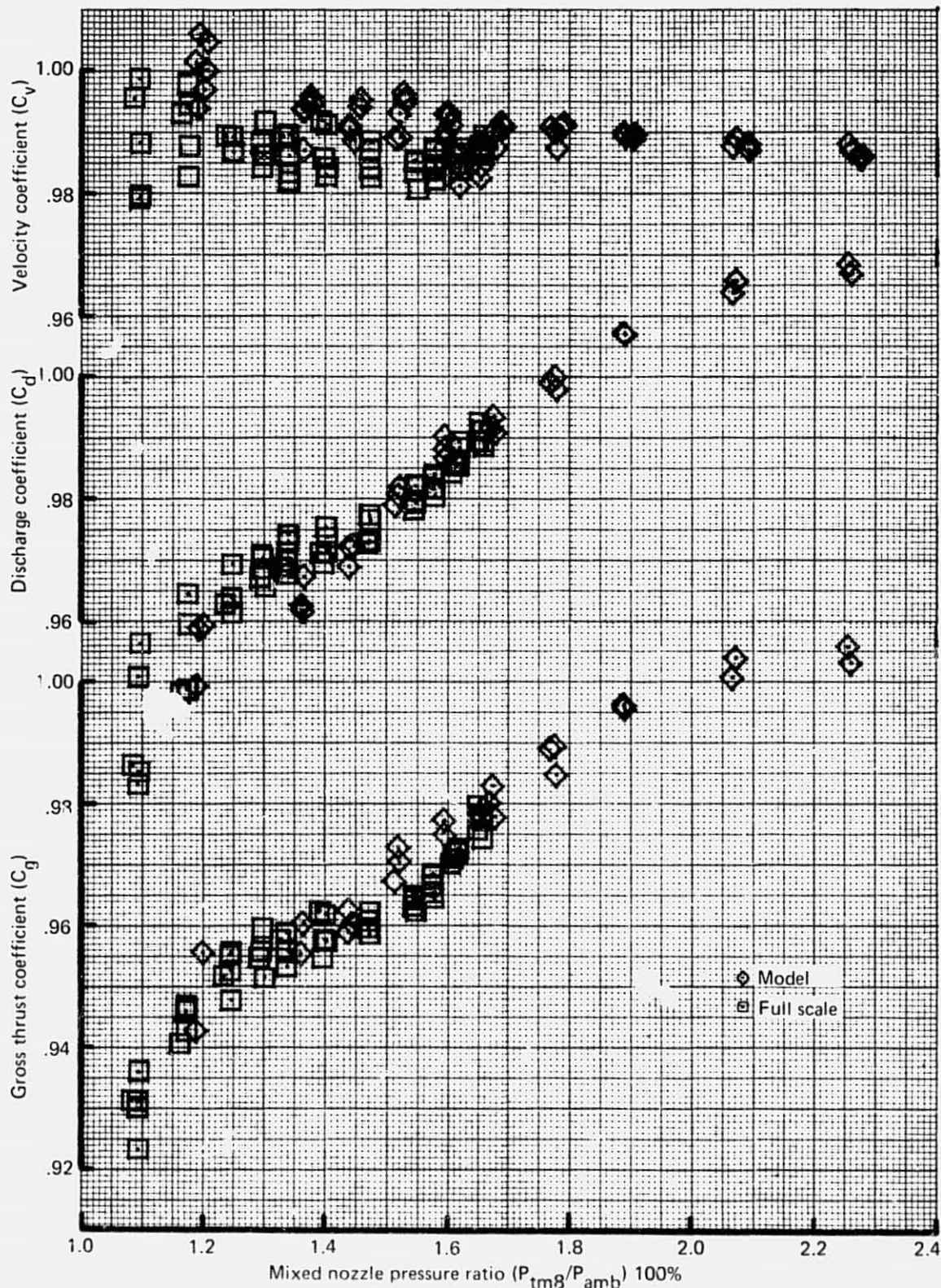


Figure 53.—Correlation of Model and Full-Scale Nozzle Coefficients for JT8D-115 Reference Exhaust System

were applied to the reference exhaust system coefficients to simulate the JT8D-115 with the flight-type and hybrid exhaust systems for noise analyses.

#### 4.1.2.4 Side- and Center-Engine Inlet Steady-State Performance

The side-engine inlets with and without acoustic ring and the center-engine inlet were each tested with the hybrid exhaust system on the JT8D-115 engine. The airflows for the JT8D-115 ground tests with side- and center-engine inlets installed were derived from a corrected airflow versus corrected LPC rotor speed relationship determined from the reference bellmouth inlet and reference exhaust system testing. This relationship was used in spite of an independent analysis indicating about 1.5% more airflow at takeoff power than indicated by the Engine Contractor.

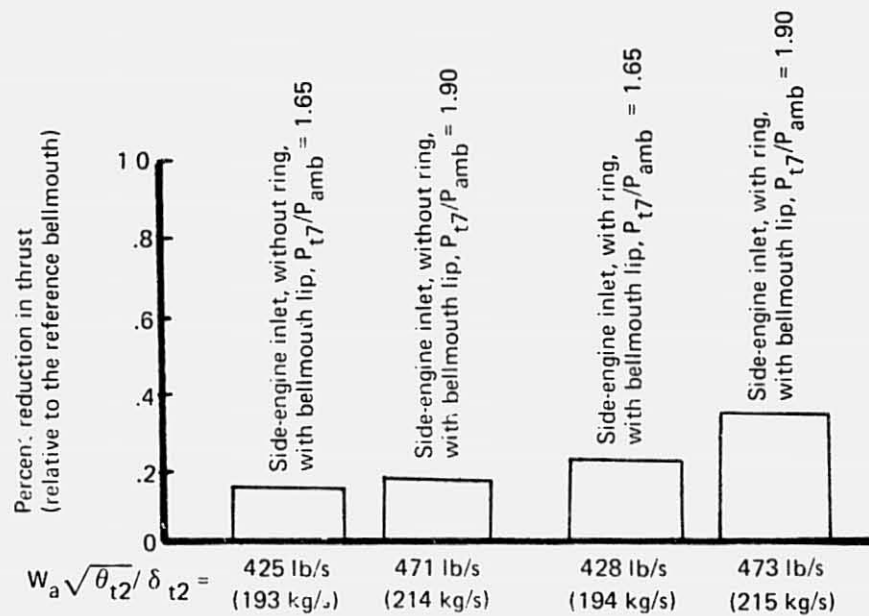
Inlet performance can be determined by installing an inlet total pressure survey rake at the inlet exit station or by evaluating the change in engine performance due to the addition of the inlet. Side-engine inlet performance was evaluated based on the change in engine performance. The center-engine inlet evaluation was based both on the change in engine performance and an inlet total pressure survey.

Side-engine inlet performance is summarized in figure 54. The percent reductions in thrust shown were obtained from test measurements. These thrust reductions were combined with sensitivity factors obtained from the Engine Contractor's JT8D-115 computer simulation to obtain the total pressure recovery plotted in the lower half of the figure. The inlet lip loss is based on the model scale data in reference 5. During the LPC surge margin testing (without crosswind), two sets of inlet total pressure rake data were obtained with the side-engine inlet without acoustic ring, while the engine was at steady-state conditions. These total pressure recovery data measured by the rake are also shown in figure 54. The total pressure recovery map along with values for the Engine Contractor's distortion parameters for one of the test conditions is shown in figure 55. The recovery and distortion parameters are defined in the appendix under Equations. The inlet total pressure loss is seen to pass through the fan portion of the inlet. This fact had to be used in determining the previously mentioned JT8D-115 computer sensitivity factors.

Generally, it can be stated that the side-engine inlet test results are comparable to model scale results (adjusted to exclude the boundary layer loss similar to the reference bellmouth) reported in reference 5.

The center-engine inlet performance is summarized in figure 56. The changes in LPC rotor speed ( $N_1$ ) and fan duct total pressure ( $P_{tf7}$ ) were obtained from test measurements. These changes were combined with the sensitivity factors obtained from the Engine Contractor's JT8D-115 computer simulation to obtain the total pressure recovery plotted in figure 56. Originally, it was planned to base the total pressure recovery on the thrust reduction as was done with the side-engine inlets. However, data analyses indicated that the center-engine inlet thrust measurements, taken when the inlet pressure survey rake was not installed, were suspect. Therefore, the technique using the parameters  $N_1$  and  $P_{tf7}$  was selected. The results presented thus far are for both VG configurations (configurations 12 and 7 from reference 4), as the engine performance was not influenced by the change in vortex generators.





Total corrected airflow ( $W_a \sqrt{\theta_{t2}} / \delta_{t2}$ ), kg/sec

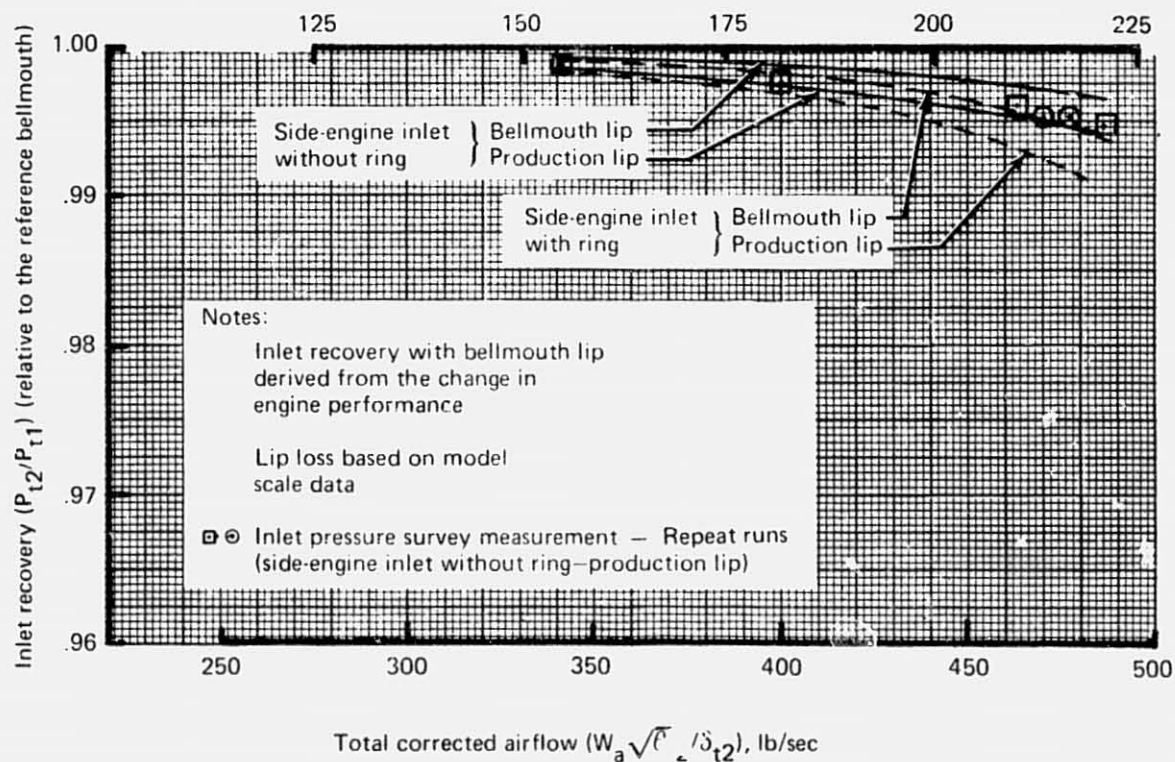
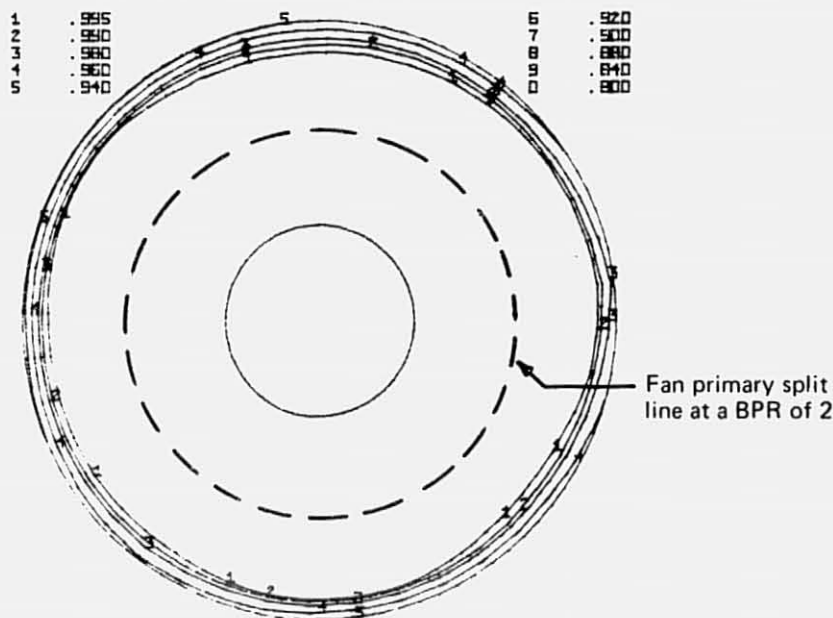


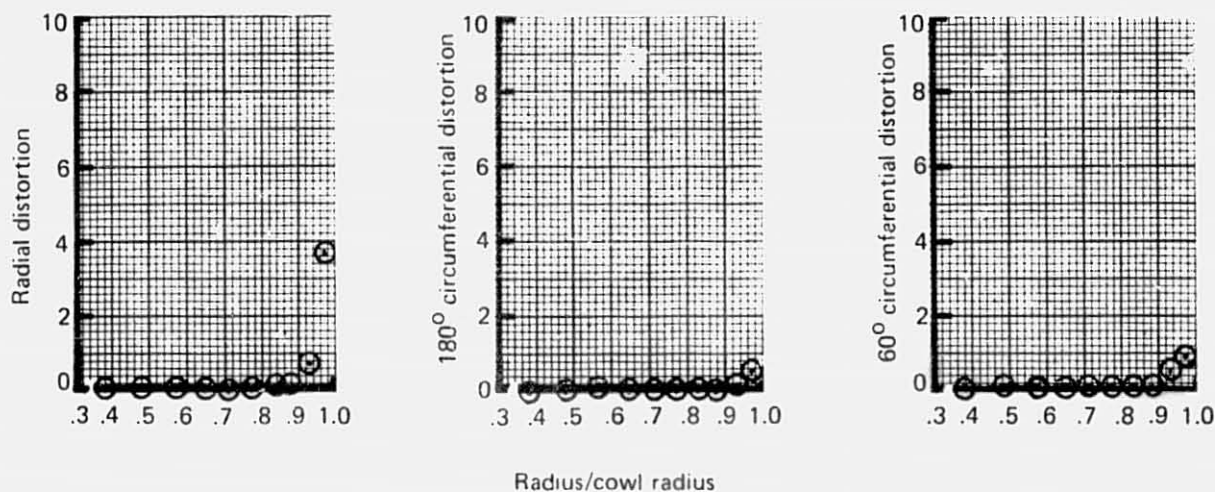
Figure 54.—JT8D-115 Side-Engine Inlet Static Performance

NASA JT8D REFAN PROGRAM  
JT8D-115 ENGINE GROUND TEST AT BOARDMAN, OREGON - 1975  
P00 ENGINE FLIGHT INLET PRESSURE RECOVERY MAP



TEST NO.	2468	TEST DATE	32675	CALC. DATE	03/27/75
RUN NO.	114	RECOVERY	.9922	DISTORTION	4.1482
COND. NO.	15	CERT. RECV.	.9957	CERT. DIST.	4.1653
WCAZ	470 LB/SEC	WIND DIR.	-125.4 DEG	WIND VEL.	8.4 MPH

(a) Engine Compressor Face Recovery ( $P_{t2}/P_{t1}$ ) Map



(b) Engine Contractor's Distortion Parameters

Figure 55.—JT8D-115 Side-Engine Inlet (Without Ring) Recovery Map and Engine Contractor's Distortion Parameters at  $W_a \sqrt{\theta_{t2}} / \delta_{t2} = 470 \text{ lb/s (213 kg/s)}$

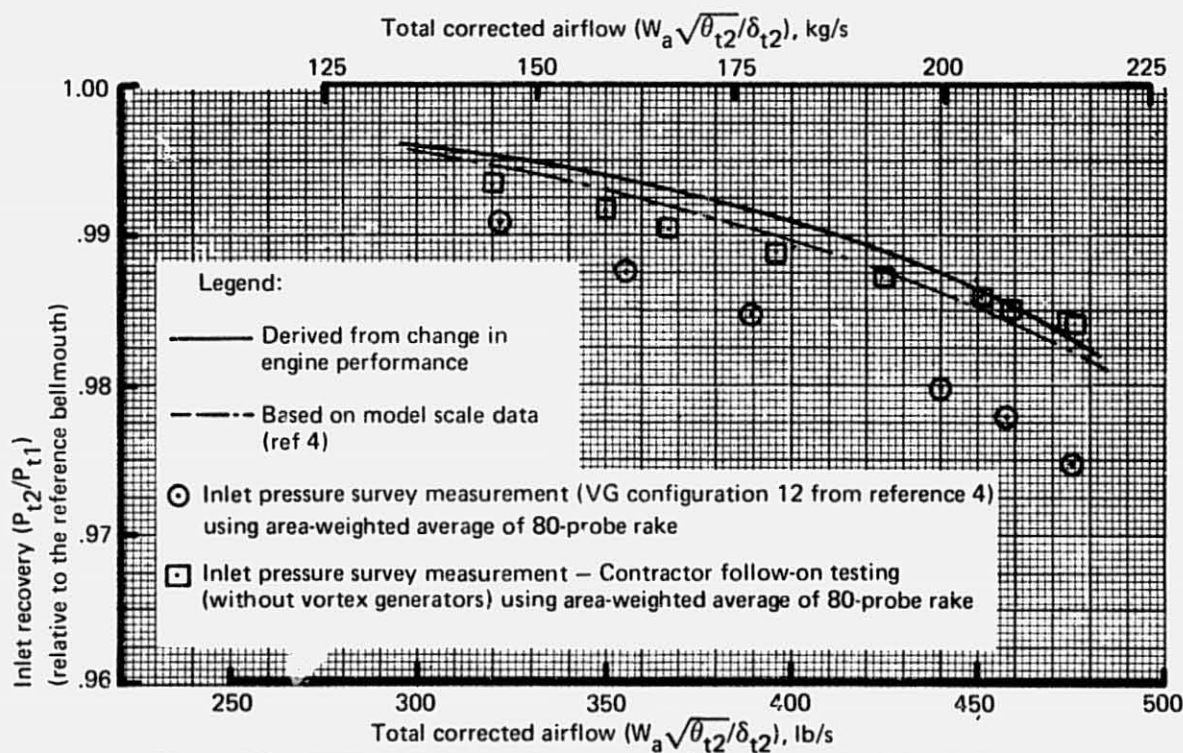
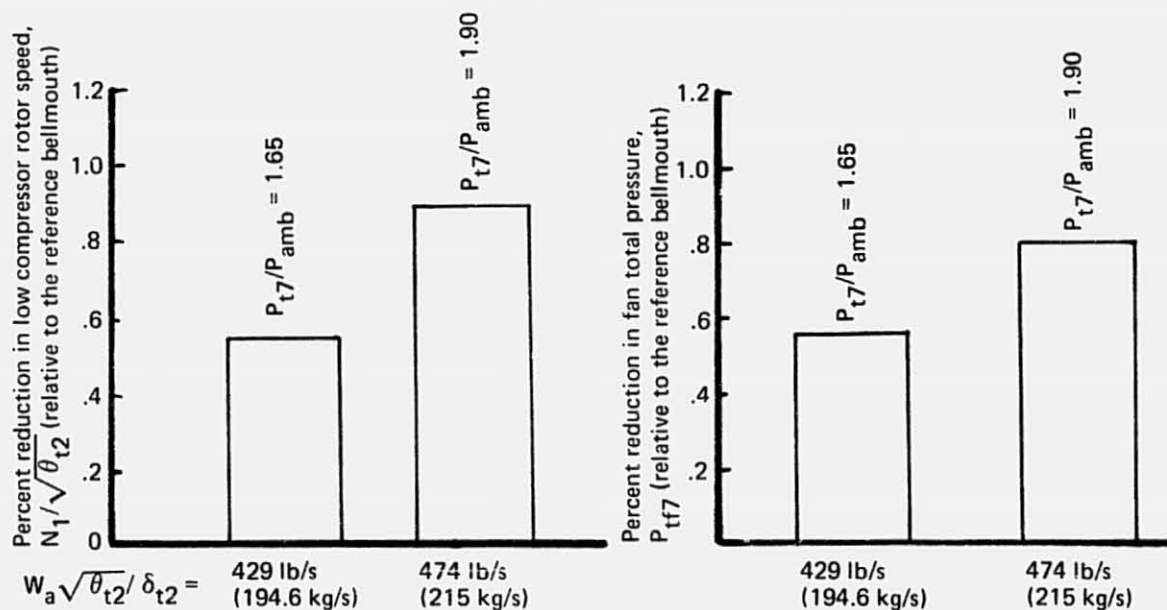


Figure 56.—JT8D-115 Center-Engine Inlet (Production Lip) Static Performance

During some tests the center-engine inlet recovery was measured using the inlet total pressure survey rake. The results are included on the recovery plot of figure 56. The center-engine total pressure recovery map and the P&WA distortion parameters calculated from the survey rake data for two power conditions are shown in figures 57 and 58. The recovery level measured with the survey rake is somewhat lower than that derived from the change in engine performance; the latter agrees with model test data as shown in figure 56. The lower indicated recovery is assumed to be due to a local interference of the upper wall VG wakes with the measuring probes. Vortex generators create an extremely nonuniform flowfield in close proximity to their trailing edges. Average total pressure measurements are very sensitive to the orientation of the pressure instrumentation relative to the local flow and to the number of data points in the survey. The model scale and ground test total pressure recovery difference is partly due to the ground test survey rakes being rotated  $7.5^\circ$  from the top centerline and recorded in  $45^\circ$  increments and the model scale pressure survey starting at the top centerline and recorded in  $10^\circ$  increments. The model scale test results for the center-engine inlet (ref. 4) showed a similar total pressure profile as that shown in figure 58 obtained during the ground test, but the model data did not have as large a depression at the upper wall region. Subsequent Contractor-funded testing using the survey rake and JT8D-115 engine with a slightly modified JT8D refan center-engine inlet duct measured a higher pressure recovery level without vortex generators as shown in figure 56. The difference between the pressure recoveries from the initial and follow-on testing cannot be attributed solely to the absence or presence of vortex generators. Reference 4 showed only a 0.2% reduction in recovery due to the vortex generators at a corrected airflow of 470 lb/s (213 kg/s).

Generally, it can be stated that the center-engine inlet ground test results are comparable to the model scale results obtained during the reference 4 testing. The lower indicated pressure recoveries obtained from the pressure surveys are attributed to probe placement relative to the VG wakes.

#### 4.1.2.5 Side- and Center-Engine Inlet Low-Pressure Compressor Surge Margin Results

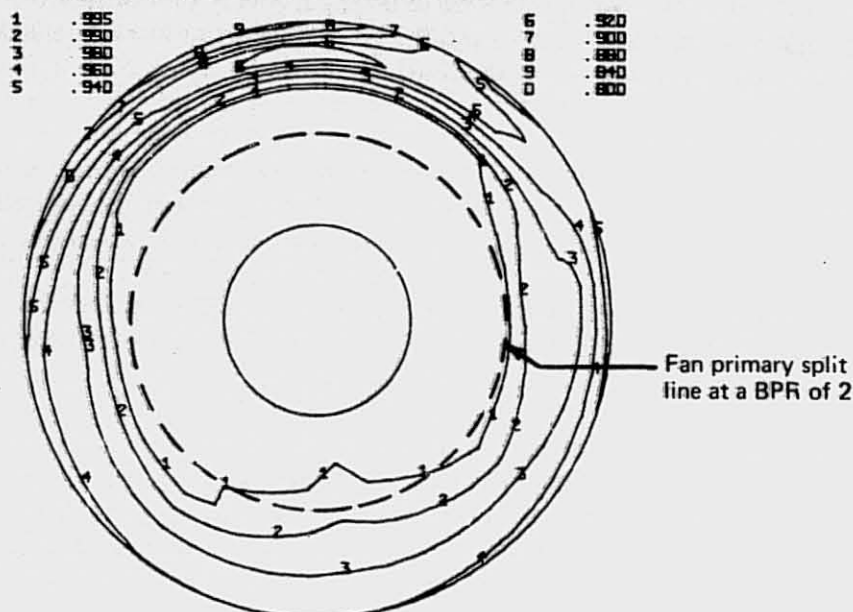
LPC surge margins were determined with the center- and side-engine inlets (without acoustic ring) installed on the JT8D-115 engine with a  $90^\circ$  crosswind blowing across the inlet. The LPC surge margin was also determined for the reference bellmouth inlet and the center-engine inlet on the JT8D-115 without crosswind. No surge margin testing was conducted with the JT8D-15 engine during this NASA program.

The measured crosswind velocities versus crosswind engine speed are shown by the solid symbols in figure 59. When the compressor face total pressures at the exit plane of the center-engine inlet obtained during this ground test program were compared to the model test results (ref. 5), the total pressure distortions were lower for the ground test than for the model test at the same crosswind velocities; i.e., for the same distortion level, the indicated crosswind velocities for the ground test were twice as high as those for the model test. It appeared that the crosswind velocity calibration for the ground rig testing was in error because inlet lip geometries like those found on the test inlets normally separate around 20 kn (8.8 m/s) rather than at twice that value as was indicated if the crosswind engine

REPRODUCIBILITY OF THE  
ORIGINAL PAGE IS POOR

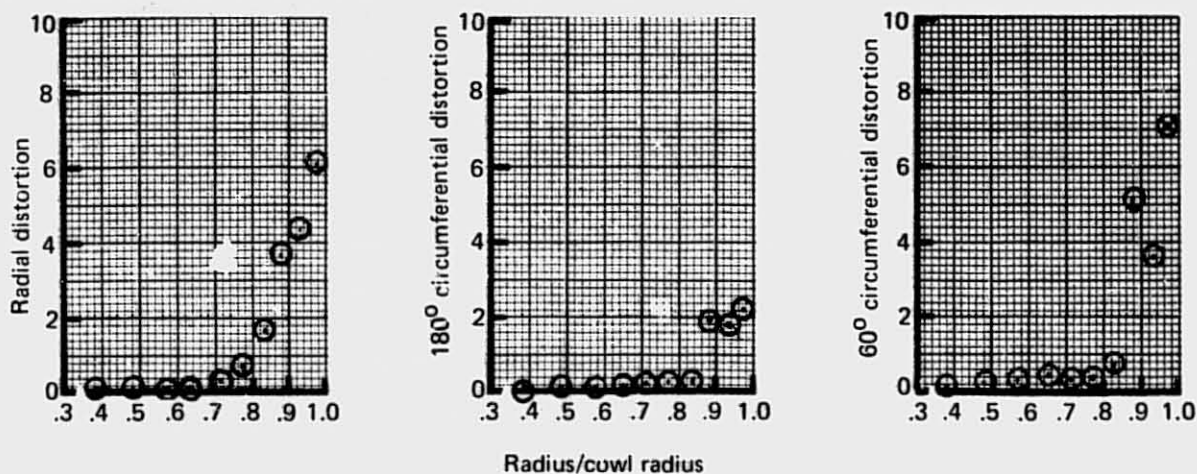
Note: VG configuration = configuration 12 from reference 4

NASA JT8D REFAN PROGRAM  
JT8D-115 ENGINE GROUND TEST AT BOARDMAN, OREGON - 1975  
CENTER ENGINE INLET AND DUCT PRESSURE RECOVERY MAP



TEST NO.	2468	TEST DATE	31475	CALC. DATE	04/01/75
RUN NO.	83	RECOVERY	.9789	DISTORTION	12.7293
COND. NO.	10	CERT. RECOV.	.9812	CERT. DIST.	12.9309
WCAZ	417 LB/SEC	WIND DIR.	-45.4 DEG	WIND VEL.	14.5 MPH

(a) Engine Compressor Face Recovery ( $P_{t2}/P_{t1}$ ) Map



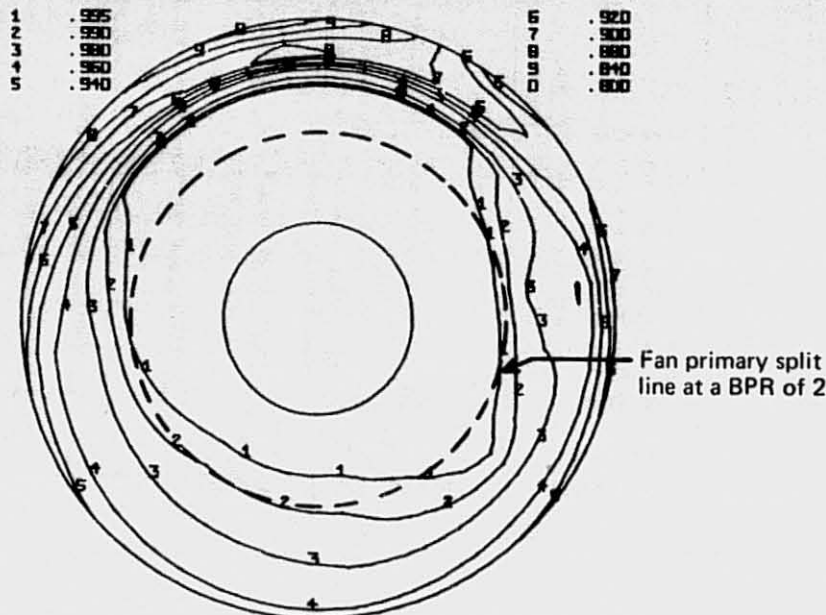
(b) Engine Contractor's Distortion Parameters

Figure 57.—JT8D-115 Center-Engine Inlet Recovery Map and Engine Contractor's Distortion Parameters at  $W_{a\sqrt{\theta}}/b_{t2} = 417 \text{ lb/s (189 kg/s)}$



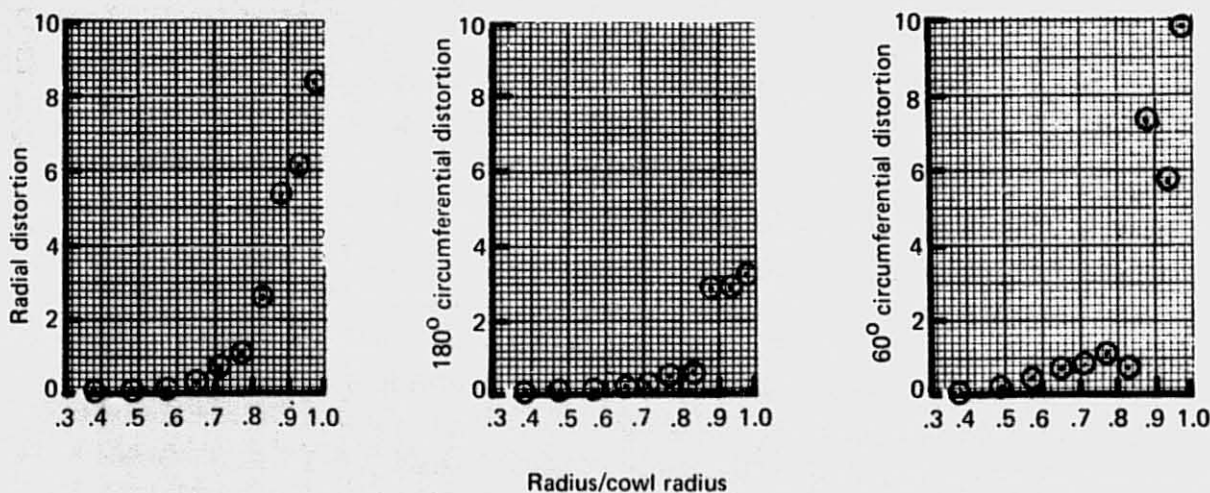
Note: VG configuration = configuration 12 from reference 4

NASA JT8D REFAN PROGRAM  
JT8D-115 ENGINE GROUND TEST AT BOARDMAN, OREGON - 1975  
CENTER ENGINE INLET AND DUCT PRESSURE RECOVERY MAP



TEST NO.	2468	TEST DATE	31475	CALC. DATE	04/01/75
RUN NO.	83	RECOVERY	.9707	DISTORTION	17.2553
COND. NO.	11	CERT. RECOV.	.9739	CERT. DIST.	17.5655
WCAZ	476 LB/SEC	WIND DIR.	-22.3 DEG	WIND VEL.	13.5 MPH

(a) Engine Compressor Face Recovery ( $P_{t2}/P_{t1}$ ) Map



(b) Engine Contractor's Distortion Parameters

Figure 58.— JT8D-115 Center-Engine Inlet Recovery Map and Engine Contractor's Distortion Parameters at  $W_{a\sqrt{\theta}}/t_2/\delta_{t2} = 476 \text{ lb/s (216 kg/s)}$

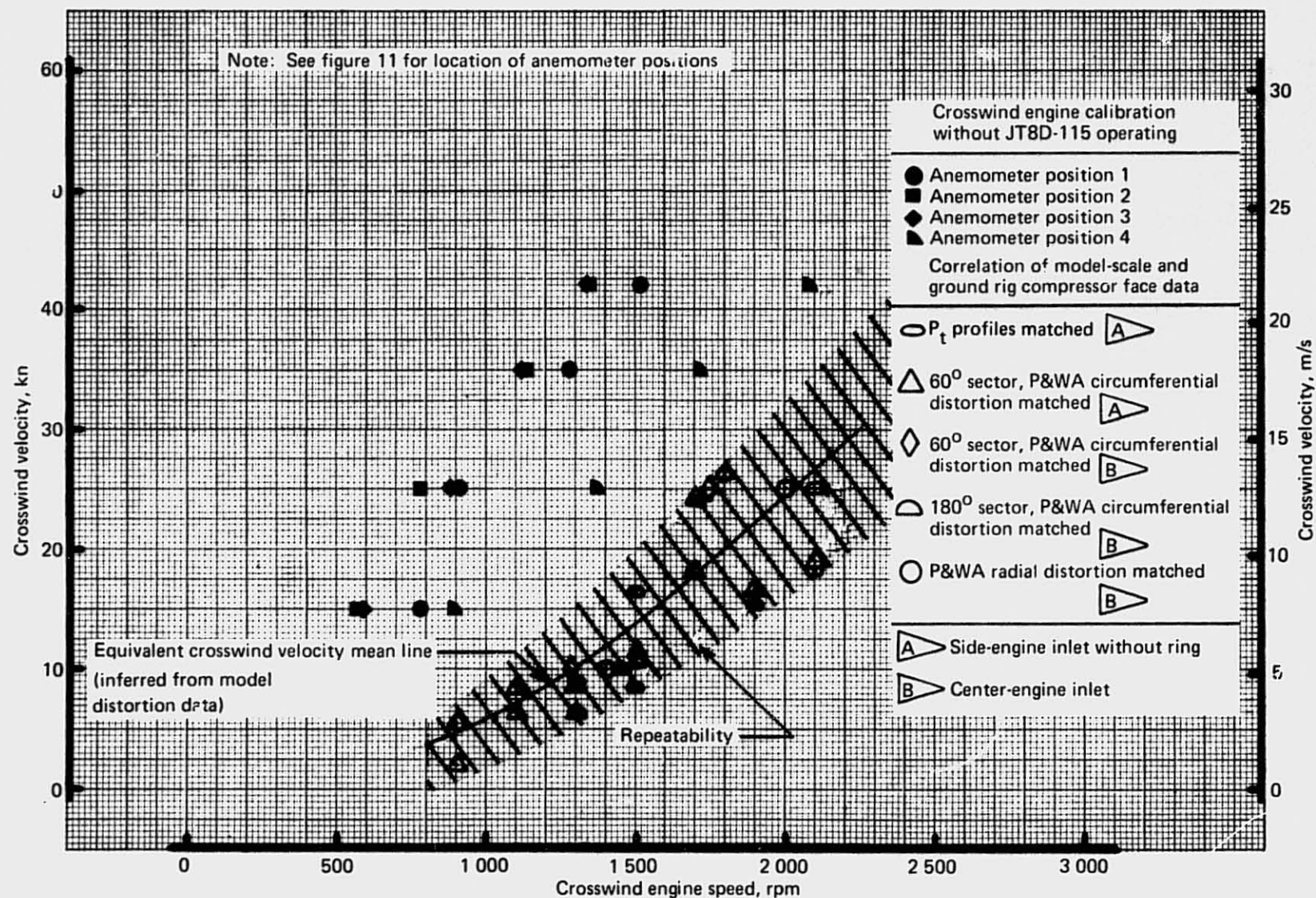


Figure 59.—JT8D-115 Ground Test—Calibration of Simulated Crosswind

calibration were to be believed. The discrepancy could be caused by the crosswind produced by the R2800 engine installation not being a good representation of an infinite wind source. Additionally, the cup-shaped anemometer may not have recorded the average velocity of the flowfield because of axial and radial gradients in the plane of measurement. It was, therefore, decided to correlate the ground test compressor face total pressure data to that of the wind tunnel model scale tests and to use the wind tunnel crosswind velocity as the ground test equivalent crosswind velocity. The three distortion definitions and the total pressure profiles for the ground tests were matched to the wind tunnel model scale test data for both the center-engine inlet (ref. 4) and side-engine inlet without acoustic ring (ref. 5). These results are also shown in figure 59 as open symbols. However, the data are repeatable only within  $\pm 7$  kn ( $\pm 3.6$  m/s) at the 1800 rpm crosswind engine speed. The mean line shown through these data points was used for correlating the LPC surge margin test results with crosswind.

LPC surge margin testing on the JT8D-115 engine (without crosswind) was accomplished with the reference bellmouth inlet and the reference exhaust system. The compressor face total pressure survey rake was installed between the bellmouth and the engine front flange in order to compare LPC surge results with the center- and side-engine inlets with the effect of the survey rake installed. However, compressor face total pressures were not recorded during the LPC surge margin tests of the reference hardware. The P&WA test procedures mentioned in section 3.6.2 were used to locate the verge-of-surge conditions for the reference hardware. Table 9 lists all conditions where stabilized engine data were obtained with the cross-bleed valves open. The percentage change in LPC operating line for a given corrected  $N_1$  speed and the orifice size was determined from the lines that were provided by the Engine Contractor shown in figure 60. One verge-of-surge condition was identified at 5134-rpm corrected  $N_1$  speed with a 1.80-in. (4.57-cm) orifice. However, this point was determined with a tailwind component; i.e., with a wind direction more than  $90^\circ$  from the engine inlet centerline. Further testing was accomplished without a tailwind, and a verge-of-surge condition could not be repeated near the 5100-rpm speed, even without an orifice in the cross-bleed ducts. This provided evidence that LPC surge margin testing should not be done with a tailwind component.

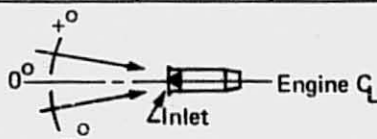
With the cross-bleed valves open and without any restrictor orifice in the ducts, the engine was stabilized at 5511-rpm corrected  $N_1$  speed for 10 min without surging. With the bleed valves still open, the engine was then slowly accelerated to 6684-rpm corrected  $N_1$  speed where the engine surged. Inadvertently, a verge-of-surge condition was not obtained at this higher  $N_1$  speed. However, based on other verge-of-surge conditions, 6400 rpm was estimated to be the verge-of-surge corrected  $N_1$  speed for the reference hardware with the cross-bleed valves open and without an orifice in the bleed ducts. This value is shown as an estimated verge-of-surge point in figure 60. This figure also shows the Engine Contractor's LPC surge line measured in a test rig with a bellmouth inlet. These ground test JT8D-115 engine verge-of-surge data confirm the Engine Contractor's LPC rig surge data up to 5100-rpm corrected  $N_1$  speed. The estimated verge-of-surge condition does not agree well with the Engine Contractor's LPC rig data at higher  $N_1$  speeds. It was impossible to confirm the LPC rig 14.5% surge margin on the JT8D-115 engine at 6000-rpm corrected  $N_1$  speed, because the cross-bleed ducts were not large enough to provide the LPC back pressure required for surge.



Table 9.—LPC Operating Line Changes for JT8D-115 Engine With Reference Hardware

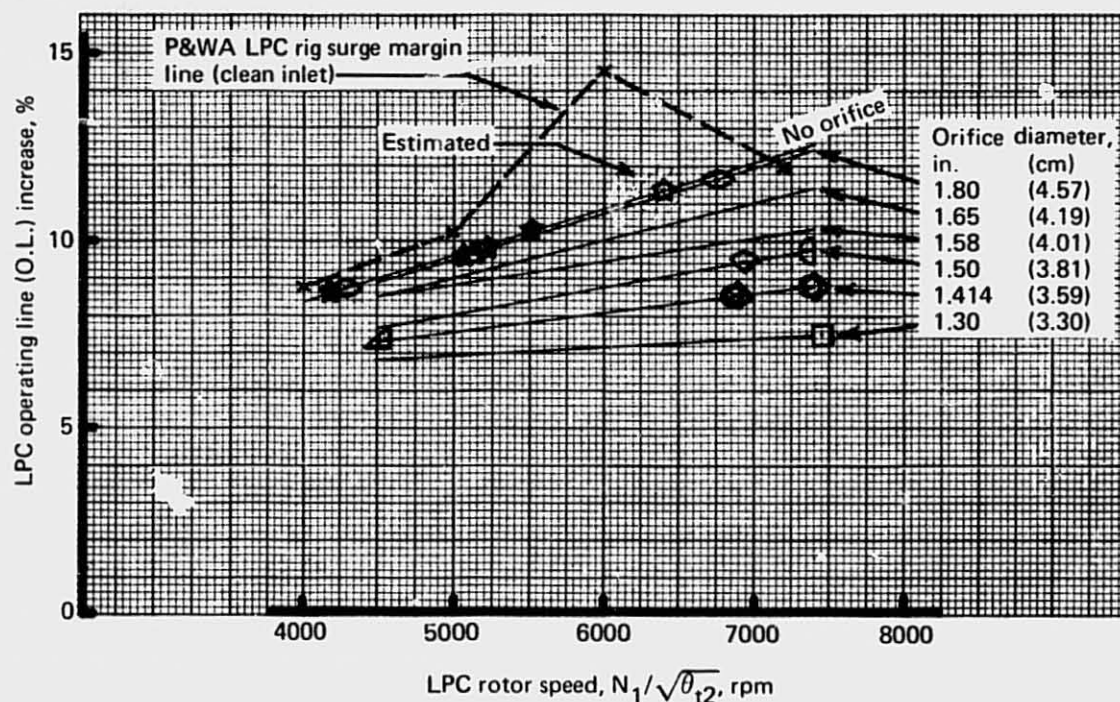
Orifice Size, in. (cm)	$N_1/\sqrt{\theta_{t2}}$ , rpm	$W_a\sqrt{\theta_{t2}/\delta_{t2}}$ , lb/s (kg/s)	LPC O.L. increase, %	Natural wind velocity, kn (m/s)	Natural wind direction, <sup>a</sup> deg	Verge-of-surge condition
1.58 (4.013)	7294	466 (211.4)	10.25	4.6 (2.4)	-38	No
1.65 (4.191)	7397	467 (211.8)	11.40	2.0 (1.0)	-12	No
1.80 (4.572)	5134	302 (137.0)	9.75	4.2 (2.1)	+150	Yes
1.80 (4.572)	5069	286 (129.7)	9.68	2.5 (1.3)	-80	No
1.80 (4.572)	5221	296 (134.3)	9.86	3.7 (1.9)	-88	No
1.80 (4.572)	5338	305 (138.3)	9.97	2.2 (1.1)	-57	No
1.80 (4.572)	5466	315 (142.9)	10.12	1.5 (0.8)	+55	No
1.80 (4.572)	7210	449 (203.7)	12.20	3.0 (1.5)	-62	No
None	4188	231 (104.8)	8.65	2.0 (1.0)	+48	No
None	4278	236 (107.0)	8.78	4.6 (2.4)	+36	No
None	5511	317 (143.8)	10.24	9.0 (4.6)	+40	No <sup>b</sup>

<sup>a</sup>Natural wind direction in degrees as related to engine centerline.



<sup>b</sup>The engine was slowly accelerated to  $N_1/\sqrt{\theta_{t2}} = 6634$  rpm when the engine surged. No verge-of-surge condition was determined near this point, but it was estimated to be at 6400 rpm.

REPRODUCIBILITY OF THE  
ORIGINAL PAGE IS POOR



JT8D-115 engine configuration	Symbols						
	Equivalent crosswind velocity, kn (m/s)						
	0 (0)	5 (2.6)	9 (4.6)	10 (5.1)	12 (6.2)	14 (7.2)	20 (10.3)
Reference bellmouth	★	—	—	—	—	—	—
Center-engine inlet and duct	○	△	—	—	—	◇	□
Side-engine inlet (without ring)	—	—	◐	◑	○	◒	—

Notes: 1. Dark symbols not a verge-of-surge condition.  
2. Excludes verge-of-surge points determined with natural wind directions greater than  $\pm 90^\circ$ , except with reference bellmouth configuration.

$$\% \text{ LPC O.L. INCR} = \frac{(P_{t3}) \times \text{BLEED} - (P_{t3}) \text{ NORMAL}}{(P_{t3}) \times \text{BLEED}} \times 100$$

$$\text{at } W_a \sqrt{\theta_{t2}} / \delta_{t2} = \text{CONSTANT}$$

Figure 60.—JT8D-115 Surge Margin Test Results

Surge margin testing of the center-engine inlet installed on the JT8D-115 engine, without a simulated crosswind, was accomplished using the P&WA procedures mentioned in section 3.6.2. Compressor face total pressure data were also recorded using the inlet total pressure rakes defined in section 3.4.1. The hybrid exhaust system was installed on the aft flanges of the engine during these tests. All verge-of-surge points obtained for the 727 center-engine inlet are listed in table 10, including those points obtained during tailwind conditions. Based on the surge margin testing with the reference bellmouth inlet, the verge-of-surge points obtained during tailwind conditions were not utilized in further analyses; the remaining points from table 10 are also shown in figure 60. This figure shows that the center-engine inlet without crosswind produces nearly the same surge margin as the reference bellmouth inlet.

The center-engine inlet was also subjected to crosswinds up to 20 kn (10.3 m/s) to measure the degradation of LPC surge margin due to a simulated crosswind. The method used is described in section 3.6.2. Table 11 lists the verge-of-surge conditions determined for the center-engine inlet subjected to 90° crosswinds. These points are also shown in figure 60.

Surge margin testing of the side-engine inlet without acoustic ring installed on the JT8D-115 engine exposed to a 90° crosswind was accomplished using the same test procedures established for the center-engine inlet (see sec. 3.6.2). Compressor face total pressure data were also recorded along with the normal engine performance data. During this testing, the hybrid exhaust system was installed on the engine. Table 12 lists all verge-of-surge points that were determined for the side-engine inlet without acoustic ring during simulated 90° crosswind conditions. These data points are also shown in figure 60. No verge-of-surge data were obtained without crosswind for the side-engine inlet because of test time limitations.

The LPC surge margin data obtained for the center-engine inlet and the side-engine inlet were correlated to the equivalent crosswind velocity and are shown in figure 61. This figure shows that the engine surge margin data for both inlets at  $N_1$  speeds between 6400 and 7400 rpm are nearly the same (i.e., within  $\pm 1.5\%$ ) for the crosswind velocities tested. It also shows that the LPC surge margins for these two inlets converge to a value of 11.4%, the same value as for the reference bellmouth inlet at zero crosswind. Figure 61 shows that a 20-kn (10.3-m/s) crosswind degrades the surge margin by 4% from the zero crosswind value. The LPC surge margin for the center-engine inlet at 4300- to 4500-rpm corrected  $N_1$  speeds is shown to be about 3% lower than that for the 6400- to 7400-rpm range.

Testing was also accomplished with the cross-bleed valves closed to determine how much crosswind the center-engine inlet and the side-engine inlet without acoustic ring could endure without causing the JT8D-115 engine to surge. With the center-engine inlet, the JT8D-115 engine was set at 7550-rpm corrected  $N_1$  speed, and then the crosswind engine speed was increased in steps to 24-kn (12.3-m/s) equivalent crosswind velocity without encountering LPC surge. Compressor face total pressure contour plots are shown in figure 62 as the crosswind velocity was increased across the center-engine inlet. Similar testing was accomplished with the side-engine inlet without acoustic ring and the JT8D-115 engine power set at 6900- and 7400-rpm corrected  $N_1$  speeds. Figure 63 shows the compressor face total pressure contours as the 90° crosswind was increased in steps until the engine, at 6900-rpm  $N_1$  speed, reached a verge-of-surge condition at 20-kn (10.3-m/s) equivalent crosswind velocity. There was

Table 10.—Surge Margin Results for Center-Engine Inlet on JT8D-115 Engine Without Cross-wind

Orifice size, in. (cm)	$N_1/\sqrt{\theta_{t2}}$ rpm	$W_a\sqrt{\theta_{t2}}\delta_{t2}$ lb/s (kg/s)	LPC OL increase, %	Certification <sup>a</sup> inlet recovery	Certification <sup>b</sup> inlet distortion, %	Natural wind velocity, kn (m/s)	Natrual wind <sup>c</sup> direction, deg
1.58 (4.013)	7118	455 (206.6)	10.14	0.9782	16.69	2.9 (1.5)	-113
1.65 (4.191)	7265	463 (210.4)	11.29	0.9760	18.29	5.0 (2.6)	-107
1.80 (4.572)	6742	429 (194.7)	11.72	0.9807	14.56	3.2 (1.6)	-80
1.80 (4.572)	6762	431 (195.4)	11.74	0.9801	14.85	3.6 (1.9)	-75
None	4279	245 (111.2)	8.79	0.9942	3.96	5.1 (2.6)	+23

Note: All points are considered to be verge-of-surge conditions.

<sup>a</sup>Certification recovery =  $P_{t2}/P_{t1}$

Where  $P_{t2}$  = area-weighted average of the 80-probe rake

<sup>b</sup>Certification distortion =  $(P_{t2} - P_{t \min})/P_{t2}$

Where  $P_{t \min}$  = lowest total pressure measured by the 80-probe rake

<sup>c</sup>Natural wind direction in degrees as related to engine centerline.

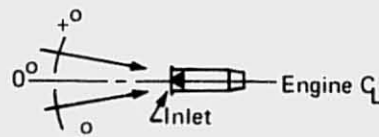




Table 11.—Surge Margin Results for Center-Engine Inlet on JT8D-115 Engine with 90° Crosswind

Orifice size, in. (cm)	$N_1/\sqrt{\theta_{t2}}$ rpm	$W_a\sqrt{\theta_{t2}}\delta_{t2}$ lb/s (kg/s)	LPC O.L. increase, %	Certification <sup>a</sup> inlet recovery	Certification <sup>b</sup> inlet distortion, %	Natural wind velocity, m/s	Natural wind direction, deg	Equivalent crosswind velocity, kn (m/s)
1.414 (3.592)	4521	262 (118.8)	7.4	0.9954	4.20	7.0 (3.6)	+23	5 (2.6)
1.300 (3.302)	7446	472 (214.1)	7.4	0.9735	16.83	8.7 (4.5)	+21	20 (10.3)
1.414 (3.592)	7400	470 (213.2)	8.7	0.9745	15.71	6.1 (3.1)	-10	14 (7.2)
1.414 (3.592)	6898	441 (200.0)	8.5	86	13.81	8.7 (4.5)	-13	14 (7.2)

Note: All points are considered to be verge-of-surge conditions.

<sup>a</sup>Certification recovery =  $P_{t2}/P_{t1}$

Where  $P_{t2}$  = area-weighted average of the 80-probe rake

<sup>b</sup>Certification distortion =  $(P_{t2} - P_{t \min})/P_{t2}$

Where  $P_{t \min}$  = lowest total pressure measured by the 80-probe rake

<sup>c</sup>Natural wind direction in degrees as related to engine centerline.



Table 12.—Surge Margin Results for Side-Engine Inlet (Without Acoustic Ring) on JT8D-115 Engine with 90° Crosswind

Orifice size, in. (cm)	$N_1/\sqrt{\theta_{t2}}$ rpm	$W_a\sqrt{\theta_{t2}/\delta_{t2}}$ lb/s (kg/s)	LPC O.L. increase, %	Certification <sup>a</sup> inlet recovery	Certification <sup>b</sup> inlet distortion, %	Natural wind velocity, kn (m/s)	Natural wind <sup>c</sup> direction, deg	Equivalent crosswind velocity, kn (m/s)
1.414 (3.592)	7340	468 (212.3)	8.67	0.9956	6.59	7.0 (3.6)	-124	6 (3.1)
1.414 (3.592)	6900	441 (200.0)	8.45	0.9969	4.40	4.3 (2.2)	-3	10 (5.1)
1.580 (4.013)	7100	455 (206.4)	10.15	0.9965	4.71	7.0 (3.6)	-134	6 (3.1)
1.500 (3.810)	7350	470 (213.2)	9.65	0.9958	4.88	3.5 (1.8)	-17	9 (4.1)
1.500 (3.810)	6920	442 (200.5)	9.39	0.9973	5.07	1.7 (0.9)	-7	14 (7.2)
1.414 (3.592)	7360	468 (212.3)	8.68	0.9965	5.65	2.6 (1.3)	-66	12 (6.2)
1.414 (3.592)	6870	437 (198.2)	8.44	0.9976	4.80	6.1 (3.1)	-72	12 (6.2)

Note: All points are considered to be verge-of-surge conditions.

<sup>a</sup>Certification recovery =  $P_{t2}/P_{t1}$

Where  $P_{t2}$  = area-weighted average of the 80-probe rake

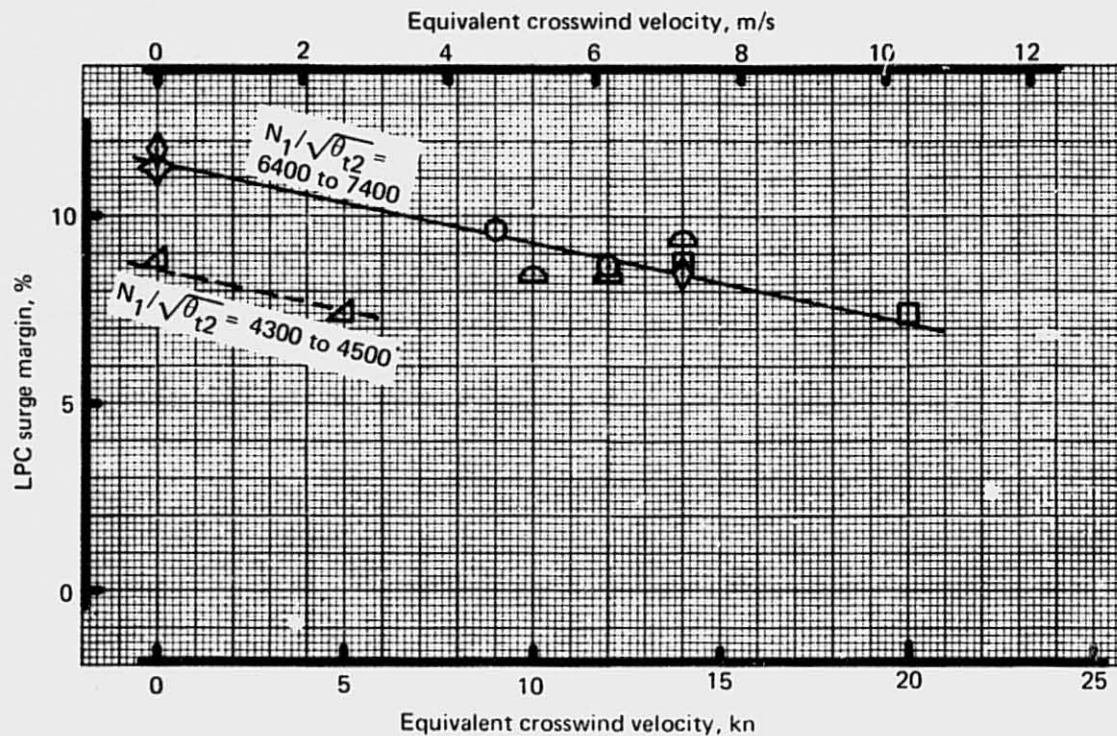
<sup>b</sup>Certification distortion =  $(P_{t2} - P_{t \min})/P_{t2}$

Where  $P_{t \min}$  = lowest total pressure measured by the 80-probe rake

<sup>c</sup>Natural wind direction in  
degrees as related to engine  
centerline.



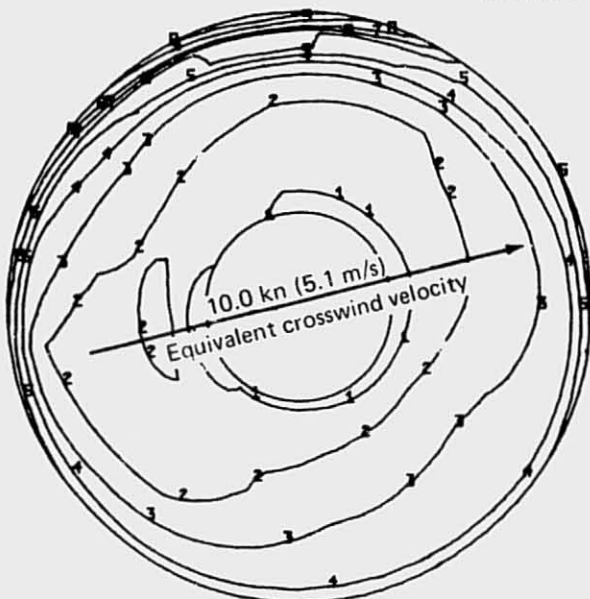
REPRODUCIBILITY OF THE  
ORIGINAL PAGE IS POOR



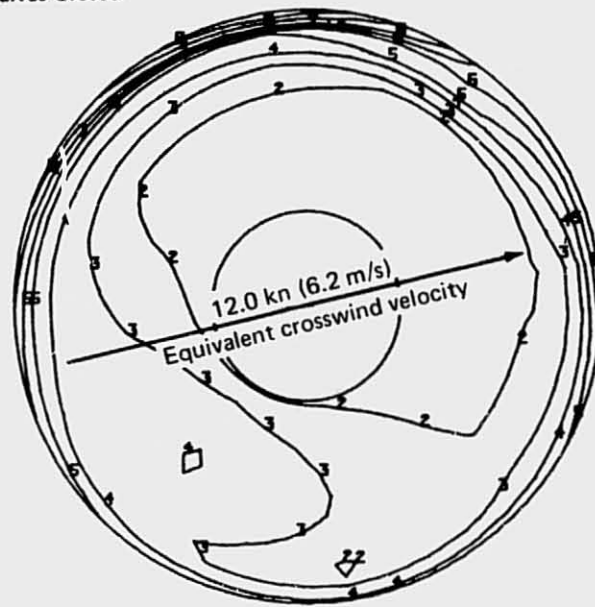
JT8D-115 engine configuration	Symbols			
	Approximate LPC rotor speed ( $N_1/\sqrt{\theta}t_2$ ),			
	4400	6400	6900	7400
Reference bellmouth	—	◇	—	—
Center-engine inlet	△	—	◇	□
Side-engine inlet (without ring)	—	—	△	○
Excludes surge points determined with natural wind direction greater than $\pm 90^\circ$ .				

Figure 61.—JT8D-115 Surge Margin: Versus Crosswind Velocity Correlation

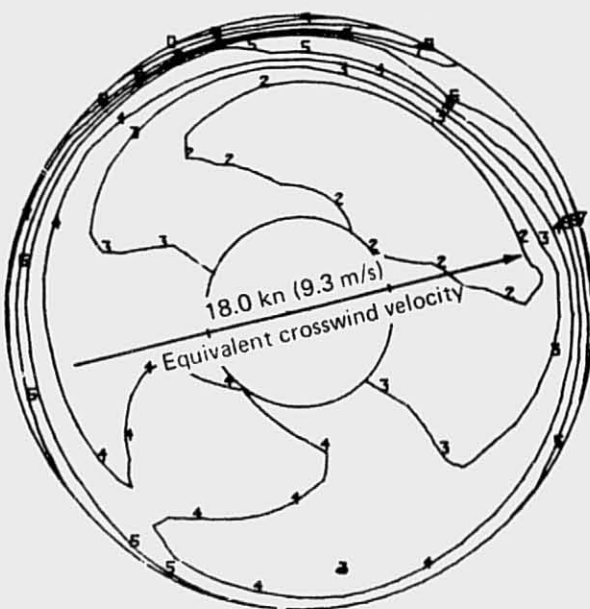
Crossbleed Valves Closed



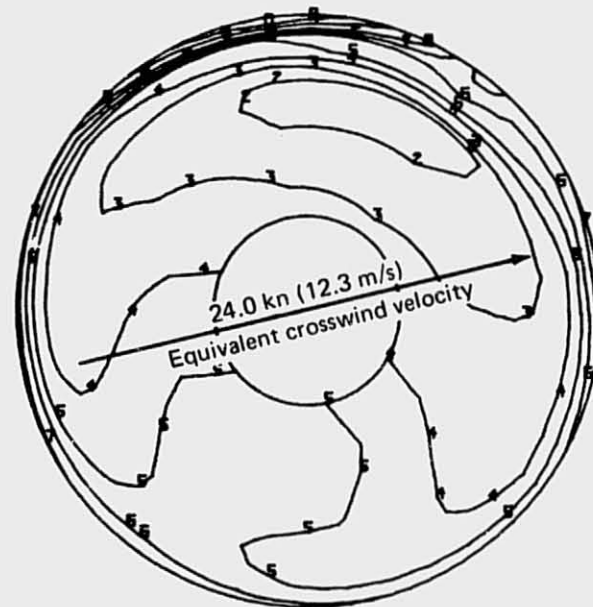
(a)  $N_1/\sqrt{\theta_{t2}} = 7556$  rpm



(b)  $N_1/\sqrt{\theta_{t2}} = 7546$  rpm



(c)  $N_1/\sqrt{\theta_{t2}} = 7556$  rpm



(d)  $N_1/\sqrt{\theta_{t2}} = 7536$  rpm

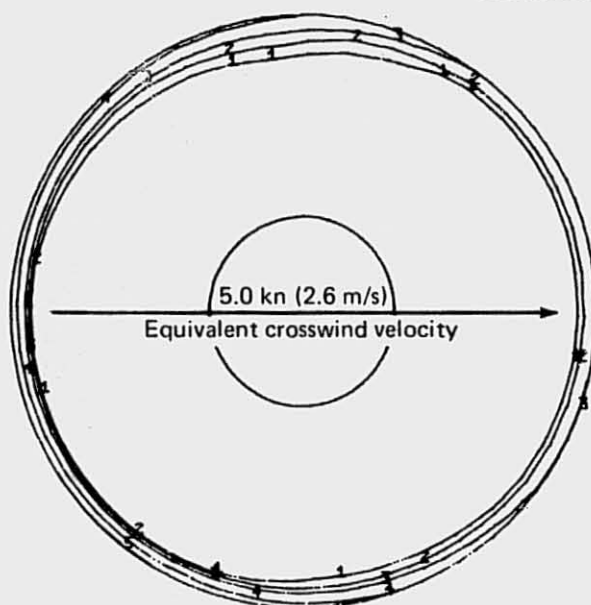
$P_{t2}/P_a$  contour code:

1	0.995	4	0.960	7	0.900
2	0.990	5	0.940	8	0.880
3	0.980	6	0.920	9	0.840

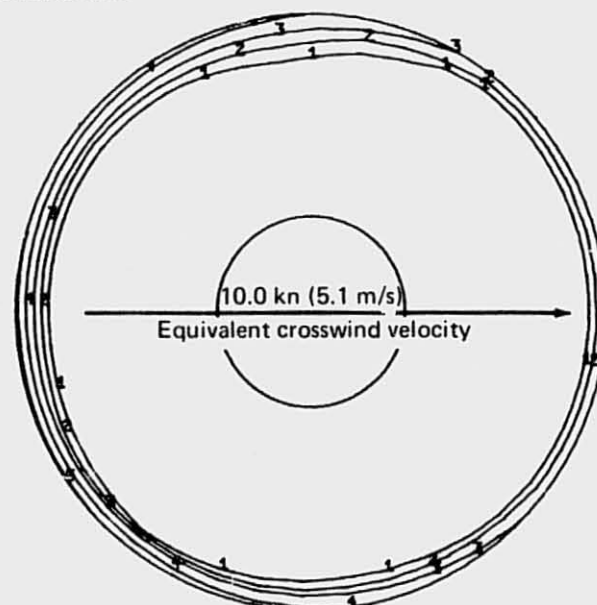
Figure 62.—JT8D-115 Center-Engine Inlet Total Pressure Contours With Crosswind



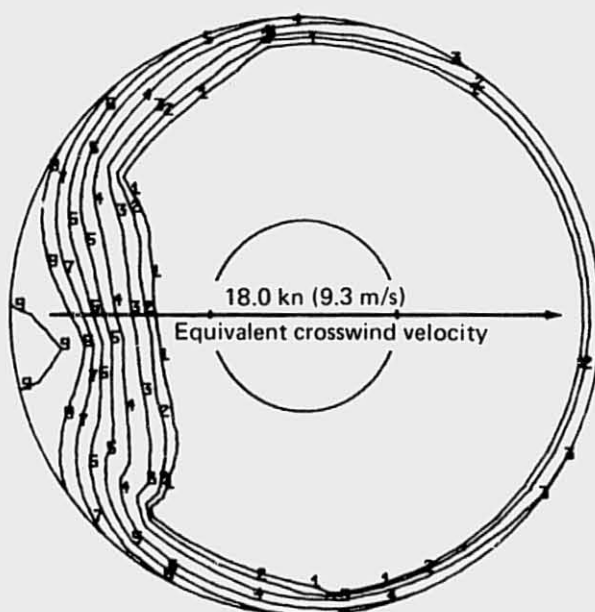
Crossbleed Valves Closed



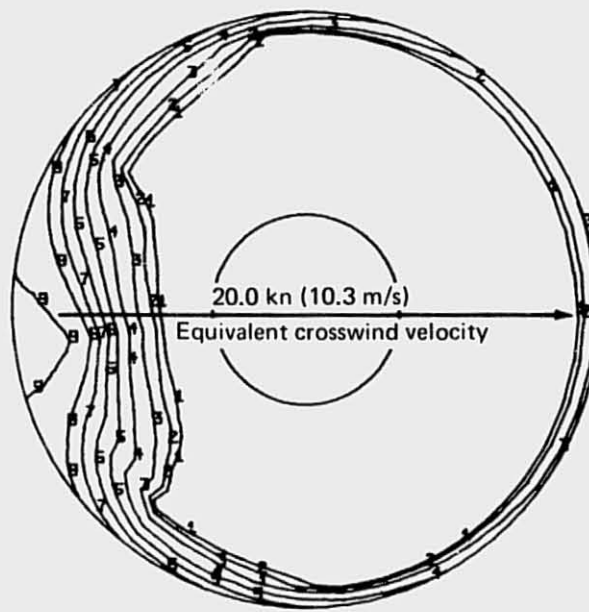
(a)  $N_1/\sqrt{\theta_{t2}} = 6845$  rpm



(b)  $N_1/\sqrt{\theta_{t2}} = 6884$  rpm



(c)  $N_1/\sqrt{\theta_{t2}} = 6901$  rpm



(d)  $N_1/\sqrt{\theta_{t2}} = 6917$  rpm  
(Verge-of-surge condition)

$P_{t2}/P_a$  contour code:

1 0.995	4 0.960	7 0.900
2 0.990	5 0.940	8 0.880
3 0.980	6 0.920	9 0.840

Figure 63.—JT8D-115 Side-Engine Inlet (Without Ring) Total Pressure Contours Arriving at Verge-of-Surge Conditions by Increasing Crosswind Velocity ( $N_1/\sqrt{\theta_{t2}} \approx 6900$  rpm)

another contour plot obtained at 14-kn (7.2-m/s) crosswind, but because the side-engine inlet lip had not separated, it showed a similar contour to the 10-kn (5.1-m/s) contours. At 7400-rpm corrected  $N_1$  speed, the crosswind engine could not cause the side-engine inlet without acoustic ring to surge. The compressor face total pressure contours at four equivalent crosswind velocities across the side-engine inlet without acoustic ring are shown in figure 64. Figures 63 and 64 show that the compressor face total pressure contour plots for the 6900- and 7400-rpm corrected  $N_1$  speeds for the same crosswind velocity are very similar.

### 4.1.3 DATA QUALITY

#### 4.1.3.1 General

One of the most important aspects of any test is an assessment of the data quality to determine whether the test was able to fulfill the original objectives.

An existing statistical analysis computer program was used to examine the data for each individual run (11 data points per run in the majority of cases). A least-squares curve was fitted through each set of data points for a run. Then all the runs for each configuration were examined to determine the within-configuration variances.

The statistical analysis was also used to compare the performance of configurations (i.e., flight-type inlet versus reference bellmouth, flight-type exhaust system versus reference exhaust system, etc.) to determine what differences in performance can be defined statistically. A statistical "F test," which tests the hypothesis that the performance of the configurations being compared are the same at the 95% confidence level, was used for the comparisons. Acceptance of the hypothesis that the performance is the same means there is a 95% probability that the assumption is correct.

In addition, the statistical analysis was used to identify the probability of detecting a given increment in the test data or, conversely, to identify the detectable increments associated with a given level of probability. This application of statistics provides assurance in the estimated performance differences between configurations and a measure of the data quality of the test.

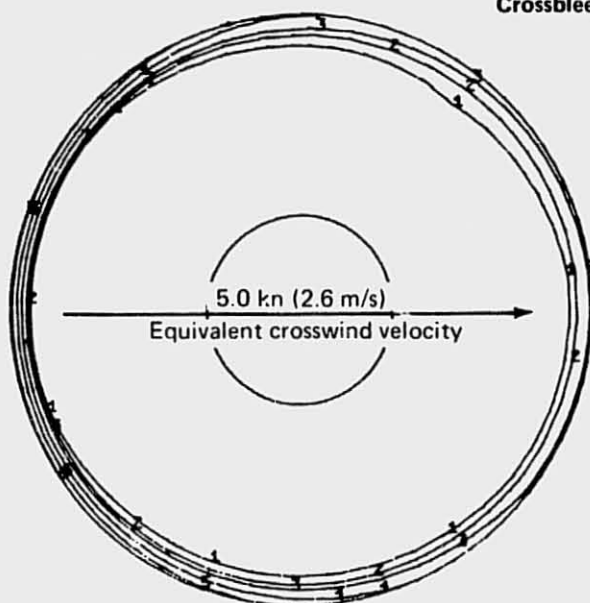
#### 4.1.3.2 Results of Statistical Evaluation

Not all the results of the statistical analysis will be presented, since to do so would require a lengthy discussion and numerous graphical presentations. Instead, some typical examples will be used to demonstrate the use and the results of the analysis.

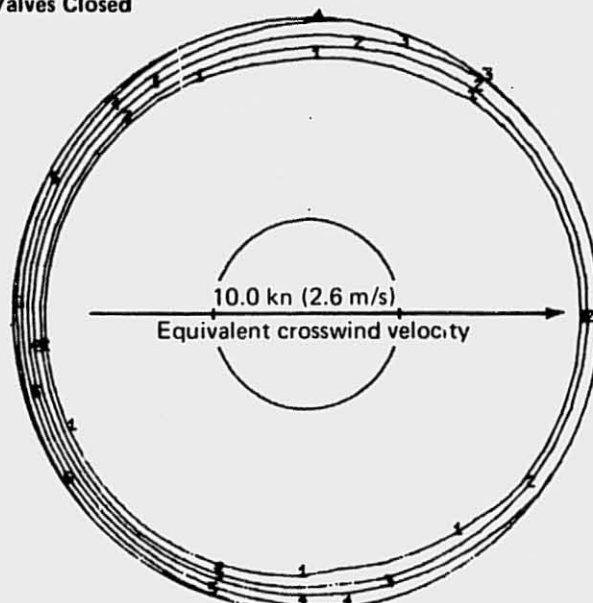
During the JT8D-115 ground test program, the following three exhaust systems were tested with the reference bellmouth inlet installed on the JT8D-115:



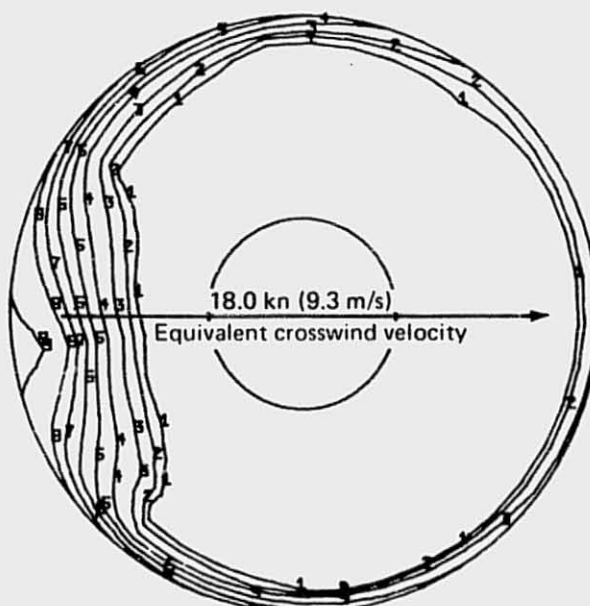
Crossbleed Valves Closed



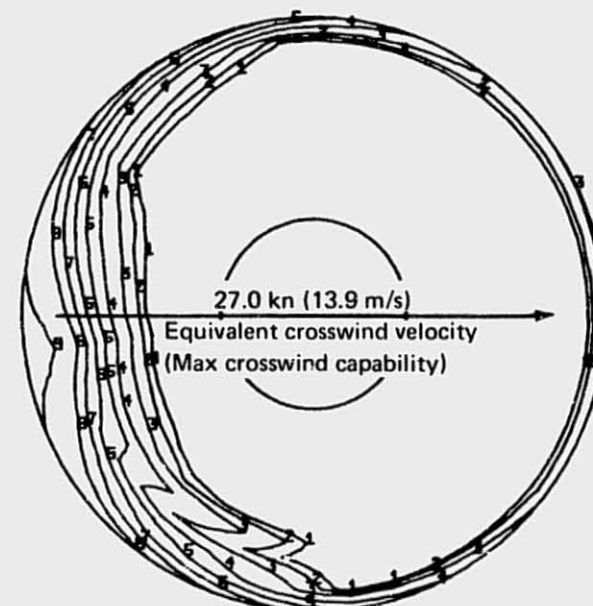
(a)  $N_1/\sqrt{\theta_{t2}} = 7386$  rpm



(b)  $N_1/\sqrt{\theta_{t2}} = 7370$  rpm



(c)  $N_1/\sqrt{\theta_{t2}} = 7420$  rpm



(d)  $N_1/\sqrt{\theta_{t2}} = 7487$  rpm

$P_{t2}/P_a$  contour code:

1 0.995	4 0.960	7 0.900
2 0.990	5 0.940	8 0.880
3 0.980	6 0.920	9 0.840

Figure 64.—JT8D-115 Side-Engine Inlet (Without Ring) Total Pressure Contours  
With Crosswind ( $N_1/\sqrt{\theta_{t2}} \approx 7400$  rpm)

1. Reference exhaust system
2. Hybrid exhaust system
3. Flight-type exhaust system

These configurations were previously described in section 3.3.

One application of the statistical analysis was to compare for sameness the nozzle coefficients ( $C_g$ ,  $C_V$ ,  $C_d$ ) and many of the measured engine parameters (thrust, airflow, fuel flow, etc.) for these three configurations. In addition, the detectable differences in the fore-mentioned parameters at the 50% and 95% probability levels were determined for the three exhaust systems. The comparisons were made at various values of the independent test variable (i.e., engine pressure ratio or nozzle pressure ratio), and the results varied as a function of the independent variable (the acceptance or rejection of the sameness hypothesis and the detectable differences depend on engine power setting).

Table 13 shows only the results of the analysis at the takeoff power setting. As shown in table 13, only gross thrust coefficient and velocity coefficient have been accepted for sameness for all three exhaust systems. It may seem contradictory to have two of the coefficients accepted for sameness while the third is rejected, since  $C_g$  is the product of  $C_d$  and  $C_V$ . This can be explained by comparing the within-configuration standard deviations. The velocity coefficient data have about twice the variance as that data for the other coefficients. This large variance hinders the ability to discern a difference.

The distribution of the independent test variables used is such that the maximum precision occurs at pressure ratios lower than takeoff. Therefore, the increments in the test parameters with 50% and 95% probability of detection are shown for both the takeoff condition and the point of maximum data quality.

Overall data accuracy and repeatability were close to that anticipated. Both airflow and thrust exhibited within-configuration variances, including within-run and between-run variances, which showed 95% confidence limit accuracies generally within the  $\pm 0.5\%$  of full-scale reading for airflow and  $\pm 0.25\%$  of full-scale reading for thrust.

## 4.2 ACOUSTIC RESULTS

Analysis of the acoustic data from the JT8D-15 and -115 ground tests was carried out with the principal objectives of providing component noise information for both engines and providing lining attenuation characteristics for the JT8D-115 nacelle. This information was ultimately used in an airplane flyover noise analysis to determine the acoustic benefit of the refan engine (see ref. 1, Vol. IV of this final report document series, "Airplane Evaluation and Analysis" (NASA CR-134800)).

The ground test data analysis effort was subdivided into five main areas of interest: (1) description of noise component characteristics, (2) examination of the impact of noise components on total static engine noise levels, (3) description of the JT8D-115 nacelle acoustic

Table 13.—Results of Statistical Analysis of JT8D-115 Exhaust Systems at Takeoff Pressure Ratio

Parameter Independent variable	Exhaust systems compared	Sameness hypothesis acceptance or rejection at 95% confidence	Maximum increments when hypothesis rejected	Average within-config standard deviation	Increments with 50%/95% probability of detection	Increments 50%/95% probability of detection at point of maximum data quality
Gross thrust ( $F_g$ ) Engine Pressure Ratio (EPR)	Reference (R) Hybrid (H) Flight type ( $\bar{r}$ )	Rejection	F-R = 24.0 lb (106.8 N) H-R = -88.0 lb (-391.4 N) F-H = -112.0 lb (-498.2 N)	$\pm 26.0$ lb ( $\pm 115.7$ N)	28.0/80.0 lb (124.6/355.9 N)	16.0/54.0 lb (71.2/240.2 N)
Total corrected airflow ( $W_{at}$ ) Corrected LPC rotor speed ( $N_1/\sqrt{\theta_{t_2}}$ )	Reference (R) Hybrid (H) Flight type (F)	Rejection	F-R = -1.6 lb/s (-0.7 kg/s) H-R = -0.7 lb/s (-0.3 kg/s) F-H = -0.9 lb/s (-0.4 kg/s)	$\pm 0.8$ lb/s ( $\pm 0.4$ kg/s)	0.0/2.8 lb/s (0.4/1.3 kg/s)	0.6/1.65 lb/s (0.3/0.75 kg/s)
Gross thrust coefficient ( $C_g$ ) Nozzle mixed press. ratio, $P_{tm7}/P_a$	Reference (R) Hybrid (H) Flight type (F)	Acceptance	—	$\pm 0.0012$	0.0013/0.0041	0.0012/0.0038
Discharge coefficient ( $C_d$ ) Nozzle mixed press. ratio, $P_{tm7}/P_a$	Reference (R) Hybrid (H) Flight type (F)	Rejection	F-R = 0.0032 H-R = 0.0031 F-H = 0.0001	$\pm 0.0015$	0.0019/0.0051	0.0017/0.0047
Velocity coefficient ( $C_v$ ) Nozzle mixed press. ratio, $P_{tm7}/P_a$	Reference (R) Hybrid (H) Flight type (F)	Acceptance	—	$\pm 0.0024$	0.0027/0.0080	0.0017/0.0053

lining attenuation characteristics, (4) definition of the sonic environment in the treated areas of the nacelle, and (5) examination of the data for repeatability and validity of test technique. The results of this analysis are presented in the following sections.

Throughout this section the terms approach rpm ( $N_1$ ), cutback rpm ( $N_1$ ), and takeoff rpm ( $N_1$ ) are used repeatedly to describe static engine power settings at which acoustic data are being presented. These terms equate the ground static engine-operating conditions to approach, cutback, or takeoff flight conditions for a 727-200 airplane equipped with the appropriate engine (JT8D-15 or -115) through the low-pressure rotor speed ( $N_1$ ). It must be remembered, however, that engine parameters and component noise levels are different statically and in flight; therefore, ground static noise data given for a specified flight operating condition (such as approach) are not necessarily representative of the noise data at the equivalent flight power setting. The designations of approach, cutback, and takeoff are intended only as indicators of nominal power setting ranges rather than as specific operating points.

For purposes of examining the order of magnitude of component noise reductions achieved by refanning the JT8D engine, the component noise empirical models developed from the analyses described in the following sections were used to generate ground static component noise levels for the JT8D-15 and -115 engines. Noise characteristics for the six noise components and total engine noise are compared on an equal static thrust basis in figures 65 through 71.

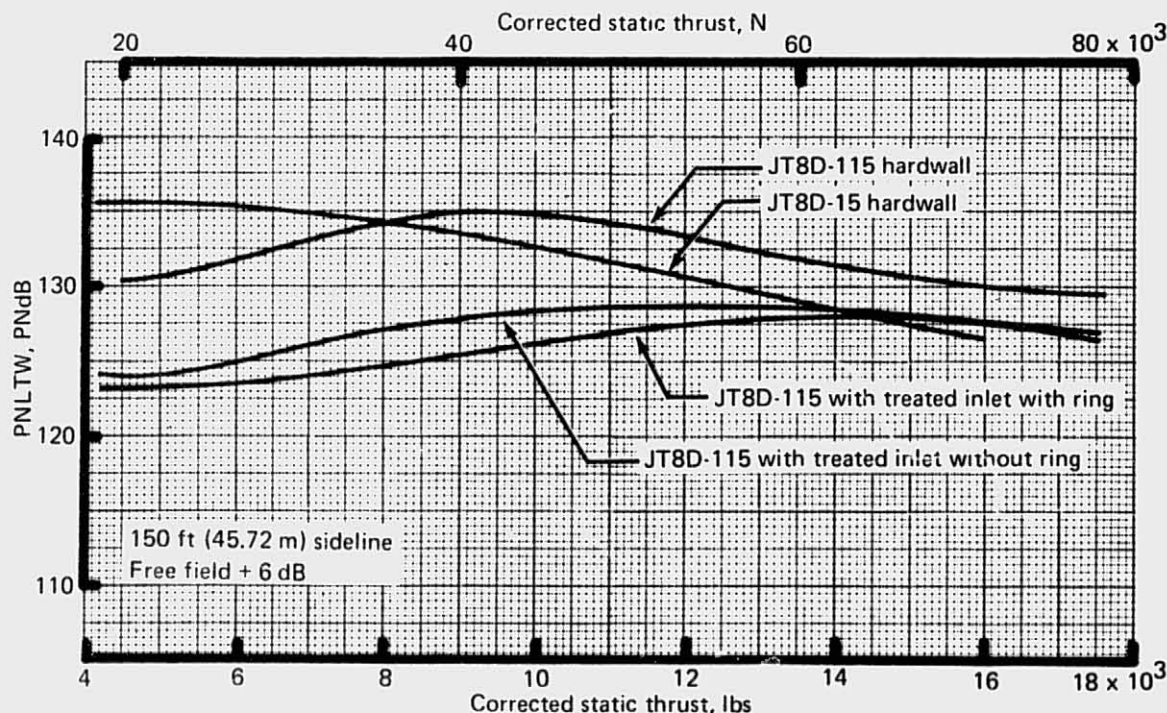


Figure 65.—JT8D-15 and -115 Inlet Fan Noise Comparison at Ground Static Conditions



REPRODUCIBILITY OF THE  
ORIGINAL PAGE IS POOR

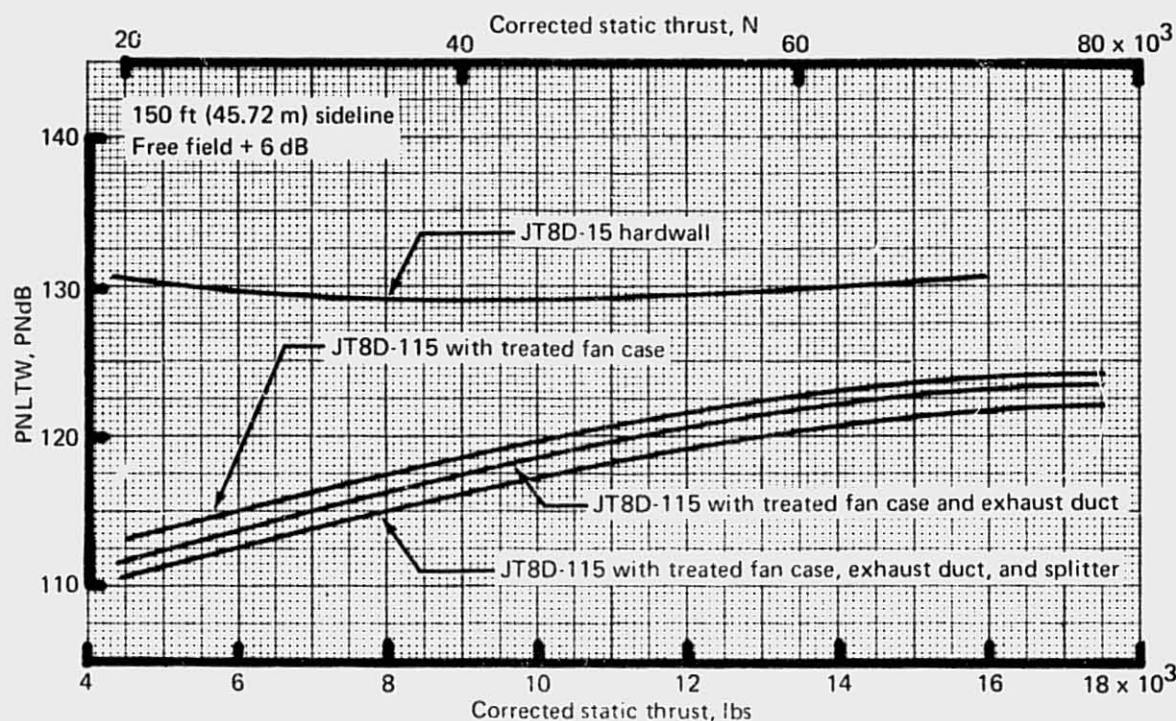


Figure 66.—JT8D-15 and -115 Aft Fan Noise Comparison at Ground Static Conditions

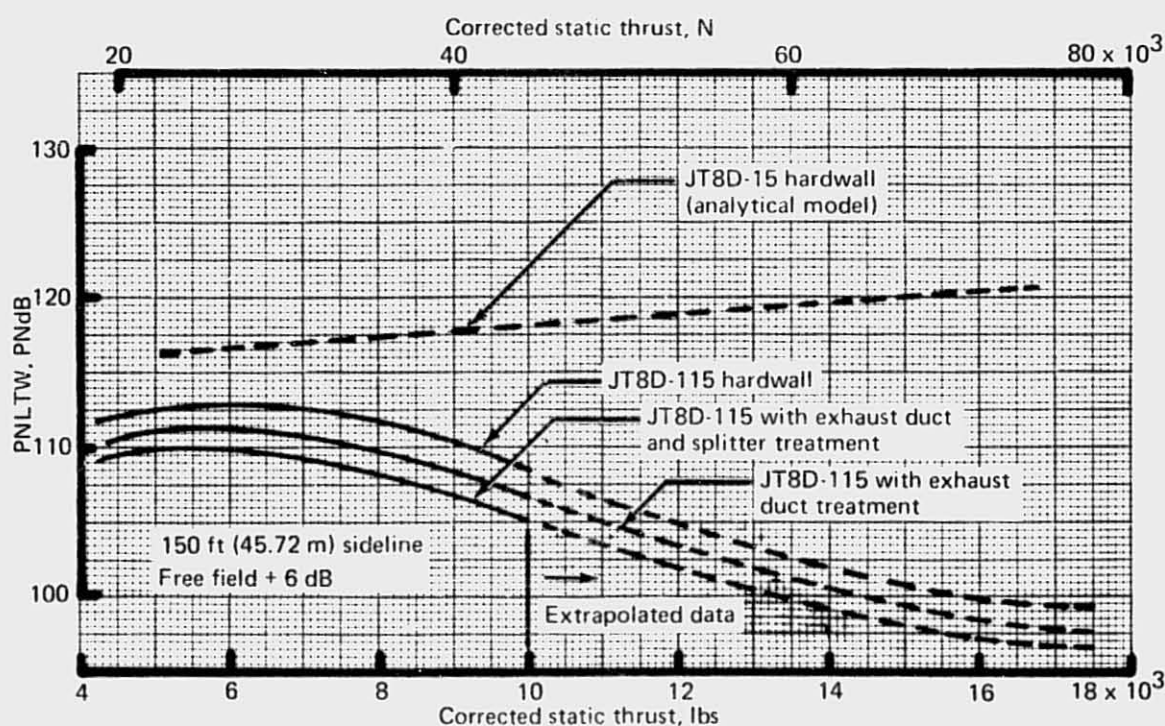


Figure 67.—JT8D-15 and -115 Turbine Noise Comparison at Ground Static Conditions

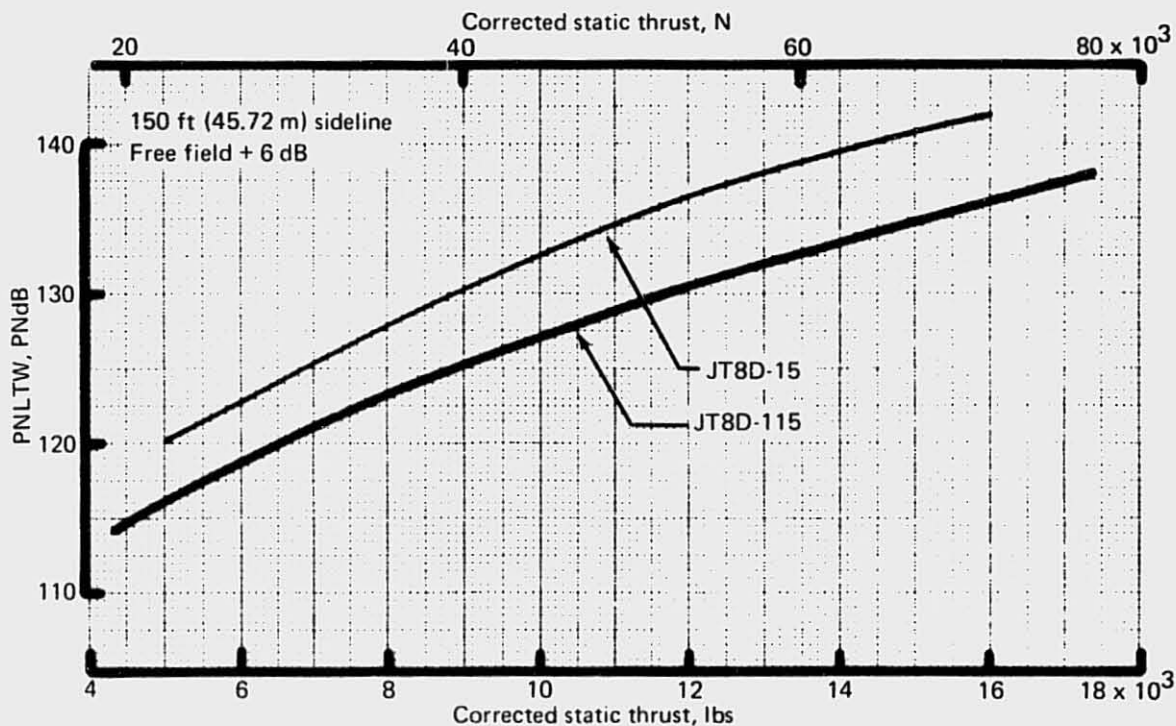


Figure 68.—JT8D-15 and -115 Jet Noise Comparison at Ground Static Conditions

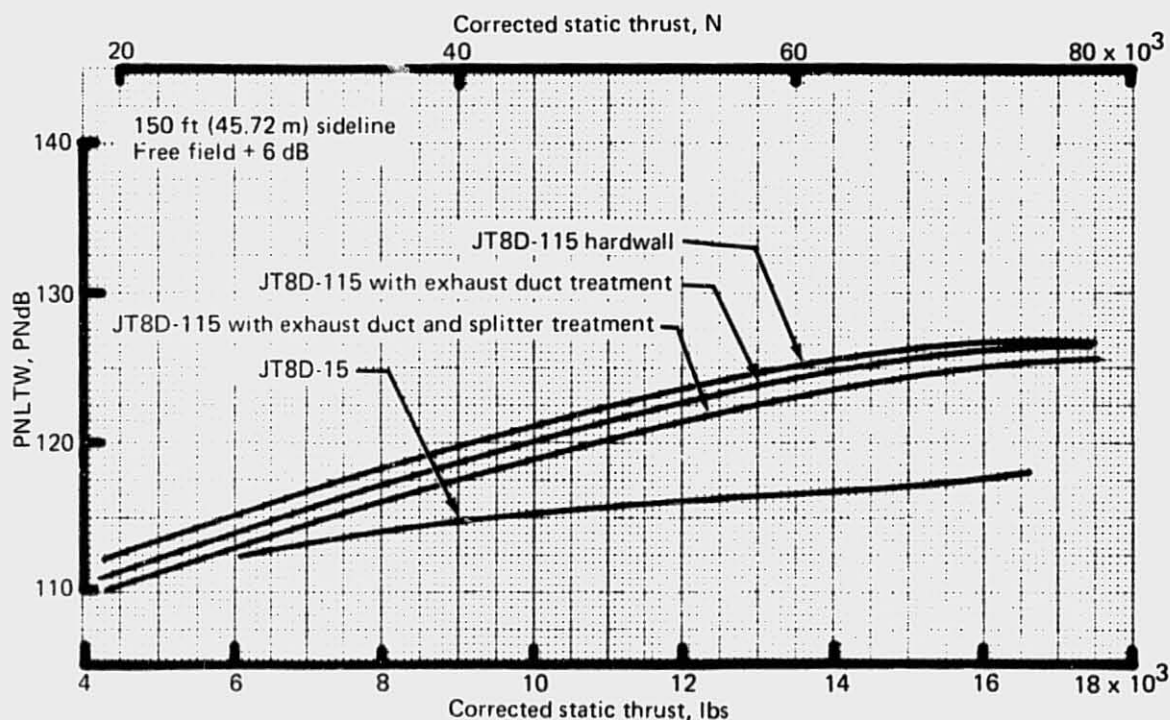


Figure 69.—JT8D-15 and -115 Core Noise Comparison at Ground Static Conditions



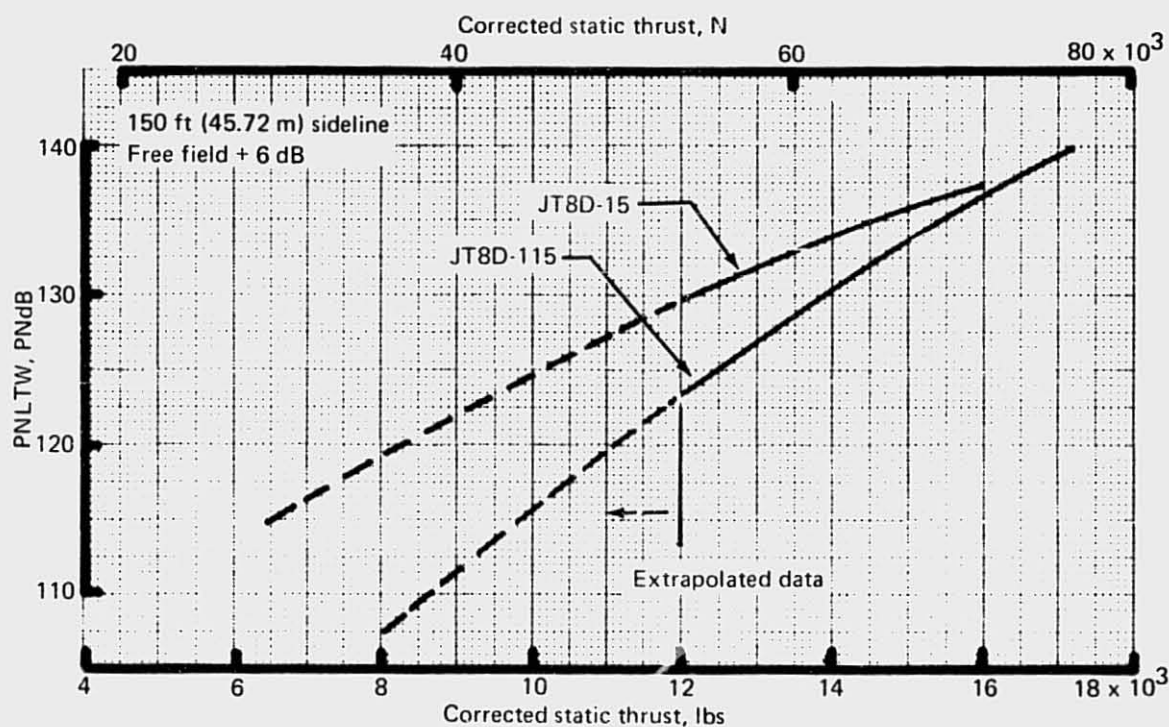


Figure 70.—JT8D-15 and -115 Exhaust Duct Flow Noise Comparison at Ground Static Conditions

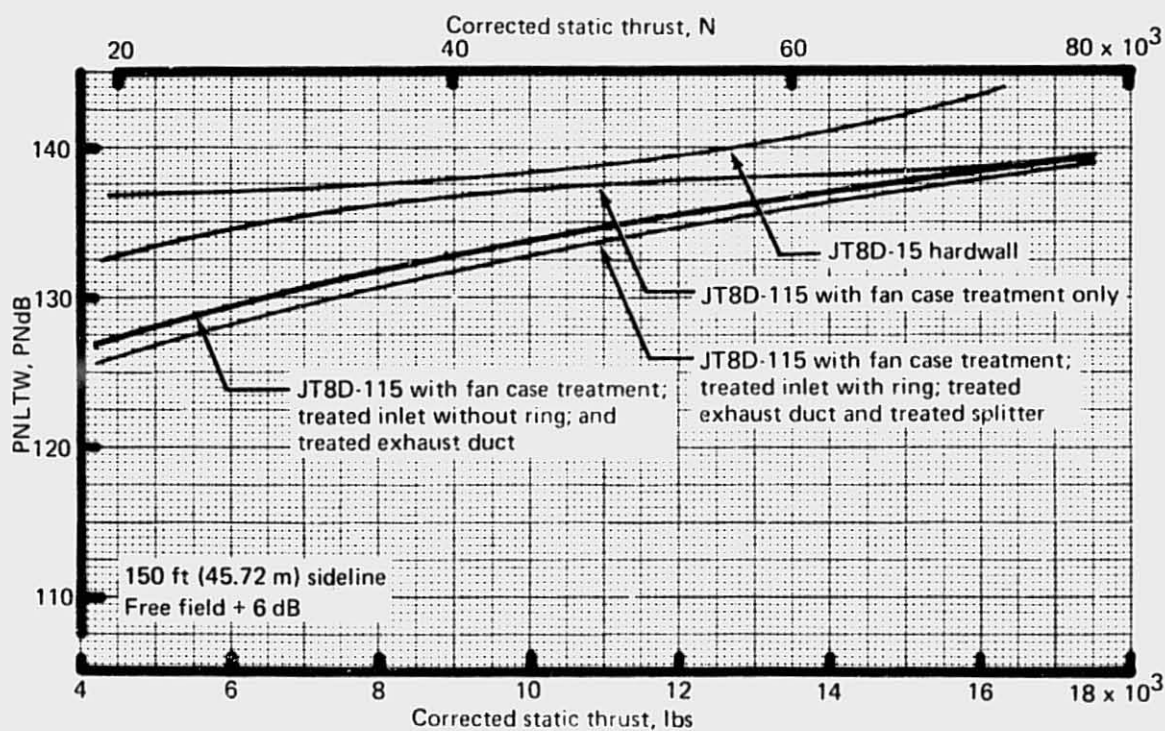


Figure 71.—JT8D-15 and -115 Total Engine Noise Comparison at Ground Static Conditions

These comparisons are valid representations of the static noise characteristics of the JT8D and JT8D refan engines, but they cannot be used directly to determine the JT8D refan noise benefit in flight, because forward motion affects the various engine cycle parameters differently on the two engines. For example, the JT8D-115 has a higher airflow than the JT8D-15 at equal static thrust and, therefore, suffers a larger ram drag penalty. The noise parameter used in figures 65 through 71, weighted average value of tone-corrected perceived noise level (PNLTW) (defined mathematically in the appendix), is a measurement of the contribution of each noise component to the total noise with an angular weighting that is the same as that used implicitly in computation of airplane flyover effective perceived noise level (EPNL).

Scanning through figures 65 through 71, one can see the important component noise differences between the JT8D-15 and -115 engines. The hardwall JT8D-115 produces an increase in inlet-radiated fan noise over most of the operational power range (fig. 65) with a difference ranging from 0.0 PNdB at 8 000-lb (35 584-N) thrust to 3.5 PNdB at 16 000-lb (71 168-N) thrust. However, with the treated side-engine inlet with ring, the JT8D-115 inlet noise is 9.5 PNdB lower at 8 000-lb (35 584-N) thrust and 1.0 PNdB higher at 16 000-lb (71 168-N) thrust than the JT8D-15. The JT8D-115 shows a large reduction in aft-radiated fan noise (fig. 66). The JT8D-115/-15 delta ranges from 11.5 PNdB at 8 000-lb (35 584-N) thrust to 6.5 PNdB at 16 000-lb (71 168-N) thrust, but most of this reduction is because of the extensive fan case treatment on the JT8D-115 engine. The exhaust system treatments provide an additional 2.5 PNdB reduction in aft-fan noise. Turbine noise measured on the JT8D-115 engine is much lower than that assumed for the JT8D-15 (fig. 67); i.e., the delta ranges from 6.0 PNdB at 8 000-lb (35 584-N) to 17.5 PNdB at 16 000-lb (71 168-N) thrust. The exhaust system treatments provide an additional 3- to 3.5-PNdB reduction in turbine noise. Static jet noise is substantially reduced by the JT8D-115 cycle modification (fig. 68) with a delta ranging from 5 to 6 PNdB at 8 000-lb (35 584-N) to 16 000-lb (71 168-N) thrust. The JT8D-115 produces a substantial increase in core (burner) noise (fig. 69) with the delta ranging from 4 PNdB at 8000-lb (35 584-N) thrust to 8.5 PNdB at 16 000-lb (71 168-N) thrust. The exhaust system treatments reduce this increment by 1 to 2 PNdB. Exhaust duct flow noise is substantially higher on the JT8D-15 than the JT8D-115 at low power settings, but the delta decreases to zero near maximum power. Finally, the total noise reduction achieved by the JT8D-115 with fan case treatment only is seen to range from 1 to 5 PNdB at 8 000-lb (35 584-N) to 16 000-lb (71 168-N) thrust (fig. 71). With the fully treated nacelle, the refan benefit is 6 to 7 PNdB across the entire power range.

#### 4.2.1 COMPONENT NOISE EVALUATION

Past experience has shown that satisfactory correlations between ground and flight data can only be achieved on a noise component basis; i.e., each individual noise component is subject to a different ground-to-flight increment that depends on a combination of effects including (1) airplane installation effects such as wing shielding and fuselage reflections, (2) engine cycle match changes due to the inlet ram effect, (3) reduced ingested turbulence levels in flight due to improved inlet aerodynamics, and (4) relative velocity effects on jet noise. Up to the time of the Refan Program ground tests, five engine noise components had been identified as significant contributors to JT8D total engine noise: (1) inlet radiated fan noise, (2) discharge radiated fan noise, (3) core engine or burner noise, (4) turbine noise, and (5) jet noise. Analysis of the acoustic data from the JT8D-15 and -115 ground tests was

carried out with the objective of extracting the detailed characteristics of these five noise components from the total engine noise.

During the analysis of the JT8D-15 and -115 ground test data it was found that the characteristics of the aft-quadrant noise at high power settings for both engines did not conform to previously established concepts of either jet noise or core (burner) noise. On the JT8D-15 engine, this anomaly shows up as a broadband "bulge" in the spectrum peaking at 800 Hz; on the JT8D-115 the spectral characteristics are similar except that the peak occurs at about 500 Hz. Correlation studies between far-field and internal microphones indicate that this noise is probably generated in the mixing region of the exhaust duct, and it has been designated as exhaust duct flow noise. This source has been treated as a separate noise component in this report, but unfortunately it was discovered too late to be included in detail in the computerized airplane flyover noise prediction models. For the purpose of flyover predictions, the effect of this source has been recognized by correcting the jet noise so that the jet noise contribution includes both jet and exhaust duct flow noise.

The following sections describe the analysis techniques used to separate noise components from the measured total engine noise levels. The resulting component noise empirical models are described for the JT8D-15 and -115 engines. These models provide component noise information to a greater degree of detail than any previous JT8D or JT8D refan data.

Each of the noise components and/or subcomponents is described by curves and tables that show: (1) basic noise level of the component as a function of its correlating engine parameter\*; i.e., fan pressure rise for fan tones, primary jet velocity for jet noise, etc.; (2) spectral characteristics for the component if applicable; and (3) directivity characteristics. This order of presentation is preserved throughout this section for each of the noise components with the exception of jet noise, where the logic of the analysis process dictates that spectrum shapes be determined as the first step. An index for locating key component noise figures is given in table 14.

All of the component noise SPL information presented in this section is given as 150-ft (45.72-m) polar arc data (except for the sample narrow band spectra which are shown at the as measured distances). Inlet fan, aft fan, and turbine component levels are expressed as free field +3 dB, while jet, core, and exhaust duct flow levels are expressed as free field +6 dB (ground plane microphones). Inlet fan tones and broadband noise have been normalized to 300% rotor/stator spacing and to a 1-ft (0.3048-m) fan diameter; aft fan tones and broadband noise have been normalized to 300% rotor/stator spacing and to a discharge area of 1 ft<sup>2</sup> (0.093 m<sup>2</sup>).

#### **4.2.1.1 Inlet-Radiated Fan Noise: JT8D-15 Engine**

The following paragraphs outline the methods utilized to segregate inlet fan noise components from total noise spectra and to establish noise/power relationships required for fan noise prediction.

\*Tables A-1 and A-2 relating the various engine cycle parameters used in noise analysis are given in the appendix for the purpose of relating component noise information to engine cycle parameters other than those given in this section.

Table 14.—JT8D-15 and -115 Ground Test—Guide to Locating Key Component Noise Curves by Figure Number

Component or Subcomponent	JT8D-15 engine				JT8D-115 engine			
	Basic level	Spectrum shape	Directivity	Peak frequency	Basic level	Spectrum shape	Directivity	Peak frequency
Inlet								
Fan tone	74	—	77	—	92	—	96	—
Harmonic	75	—	77	—	93	—	96	—
Sumtone	75	—	77	—	95	—	98	—
Compressor tone	—	—	—	—	94	—	97	—
Broadband	78	79	80	—	100	101	102	—
Buzzsaw	81	85	86	—	103	107	108	—
Aft fan								
Fan tone	112	—	114	—	117	—	119	—
Harmonic	113	—	114	—	118	—	119	—
Broadband	115	79	116	—	120	101	121	—
Turbine								
Tones	—	—	—	—	125	—	126	—
Haystack	—	—	—	—	127	—	128	—
Jet	137	130	137	135	144	141	Table 19	143
Core	147	146	148	—	149	151	152	—
Exhaust duct flow	155	—	—	—	160	161	162	—



Inlet fan noise characteristics were determined primarily from narrow band analyses (20-Hz bandwidth filter, figs. 72 and 73) performed on the far-field noise data measured by the forward arc ground microphones.

*Fan Tones.*—The JT8D-15 engine has a two-stage fan with 27 and 40 blades, respectively. The noise levels of the blade passing frequency tone and harmonics for each fan stage have been tabulated separately, since each exhibits a different directivity and amplitude relationship to power setting.\* Figure 74 is a sample plot of the power setting dependence of inlet-radiated fan tone SPL. A sample plot of the relationship between the fundamental and the harmonic tone levels is shown in figure 75.

*Sumtone of Two Fans.*—At idle power a sumtone of the fundamental tones from both fans is a dominant spike in the spectrum. This tone equals or exceeds both fundamental tones at an engine setting of 2600 rpm. In the forward quadrant, it decreases in level as power setting is increased until it is masked by buzzsaw and broadband noise at about 6700 rpm. A sample plot of sumtone level is shown in figure 76.

*Fan Tone Directivities.*—Inlet fan noise did not follow a smooth spatial distribution pattern, and the data indicated directivity would vary markedly with power setting without showing a simple correlation. A sample directivity plot for the first-stage fan fundamental tone is shown in figure 77.

*Fan Broadband Noise.*—Fan broadband noise was observed to peak at the 1/3 OB containing the fan second harmonic. The basic broadband peak level as a function of fan stage pressure rise is shown in figure 78 for both fan stages.

*Fan Broadband Noise Spectrum Shaping.*—Twenty Hz narrow band spectrum plots showed that the fan broadband spectrum shape used in earlier NASA Refan Program predictions agreed with the JT8D-15 engine fan noise at approach rpm. Below approach rpm, test data from the forward quadrant showed a steeper noise decline toward the low frequency end of the spectrum, and higher power settings indicated that more noise energy is found at the low frequency end of the spectrum. Data indicated that the barriers did not totally exclude jet noise from contaminating the noise measurements in the inlet quadrant; thus, the measured shape of broadband noise at 40° became less representative of isolated fan broadband noise as power setting was increased beyond approach power. The spectrum shape shown in figure 79 has been accepted as applicable to all directivity angles.

\*These tabulations (tables A-3 through A-7) are included in the supplementary data in the appendix.

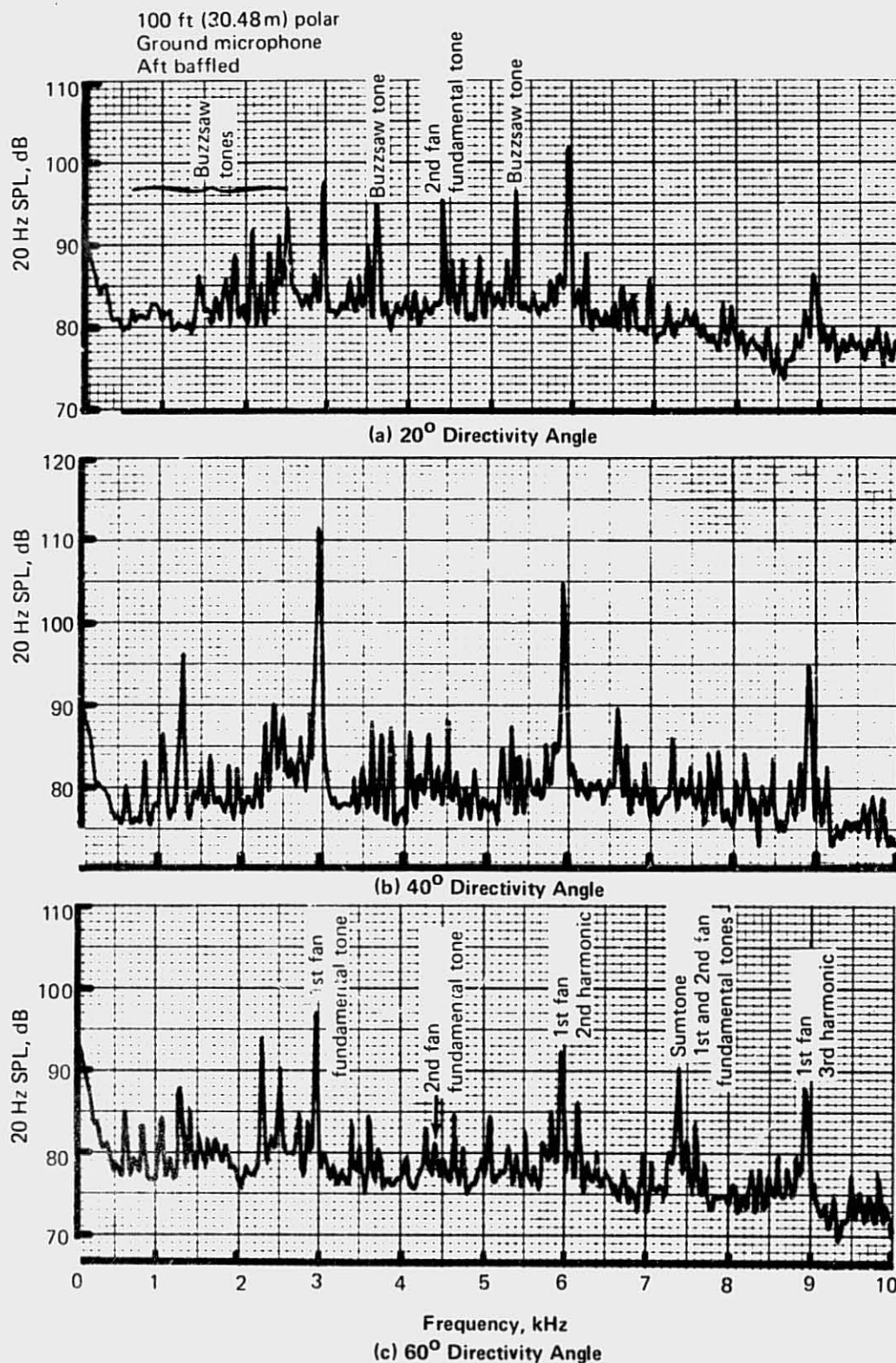


Figure 72. —JT8D-15 Ground Test—Narrow Band Spectra in Forward Quadrant,  
Approach Power ( $N_1/\sqrt{\theta_{t2}} = 6683$ )



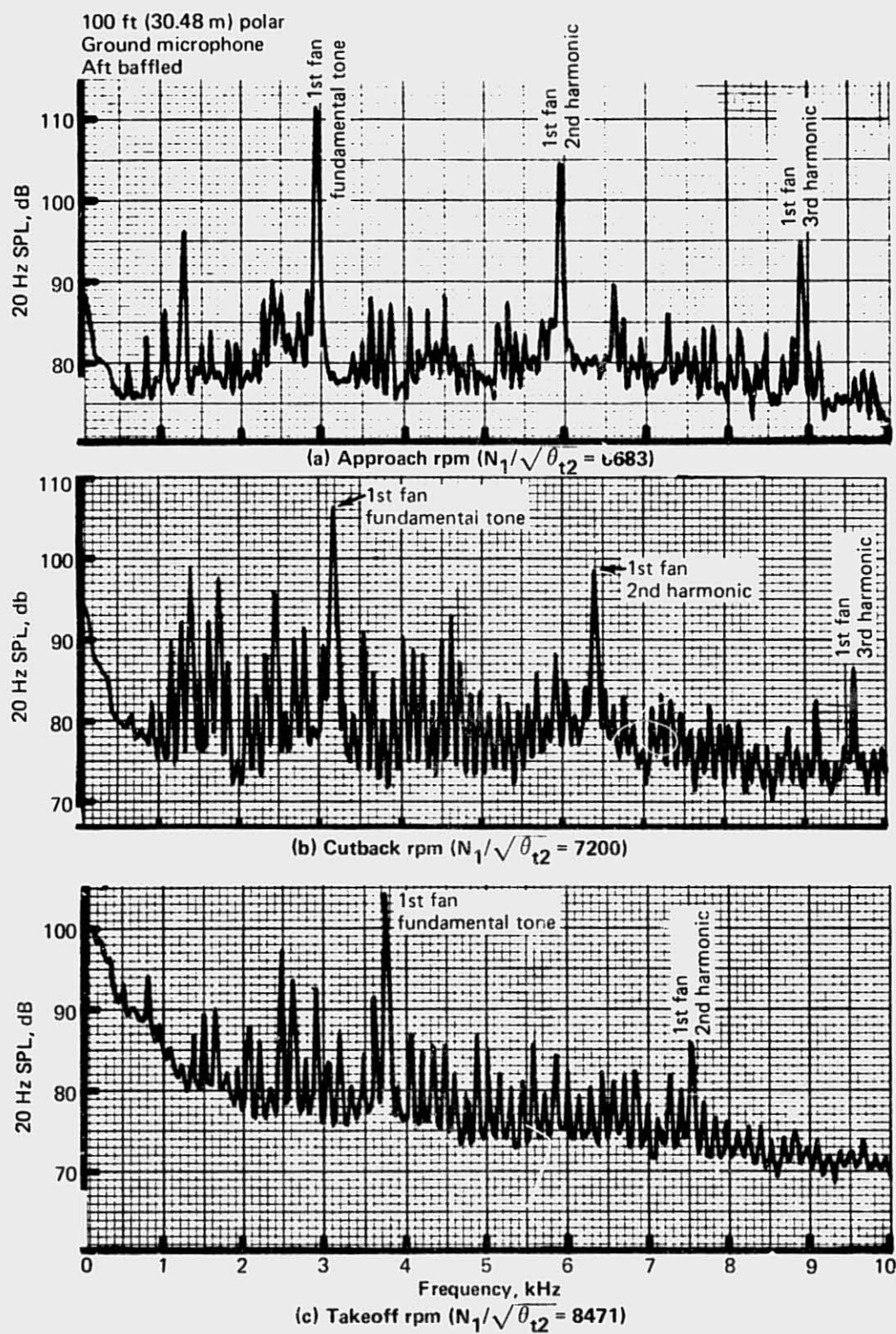


Figure 73.—JT8D-15 Ground Test—Narrow Band Spectra in Forward Quadrant,  $40^\circ$  Directivity Angle

REPRODUCIBILITY OF  
ORIGINAL PAGE IS POOR

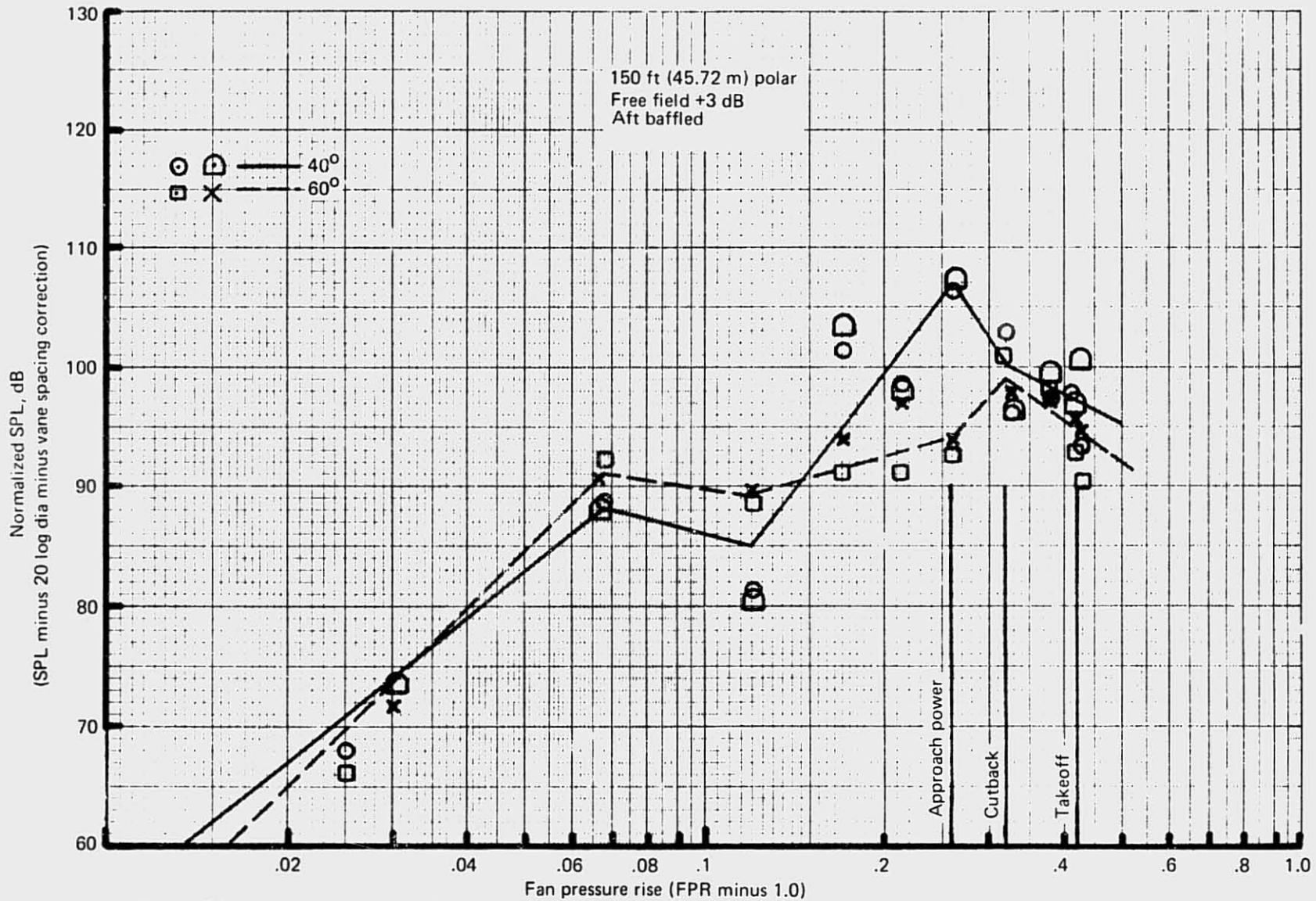


Figure 74.—JT8D-15 Ground Test—Inlet-Radiated First Fan Fundamental Tone Versus Fan Stage Pressure Rise

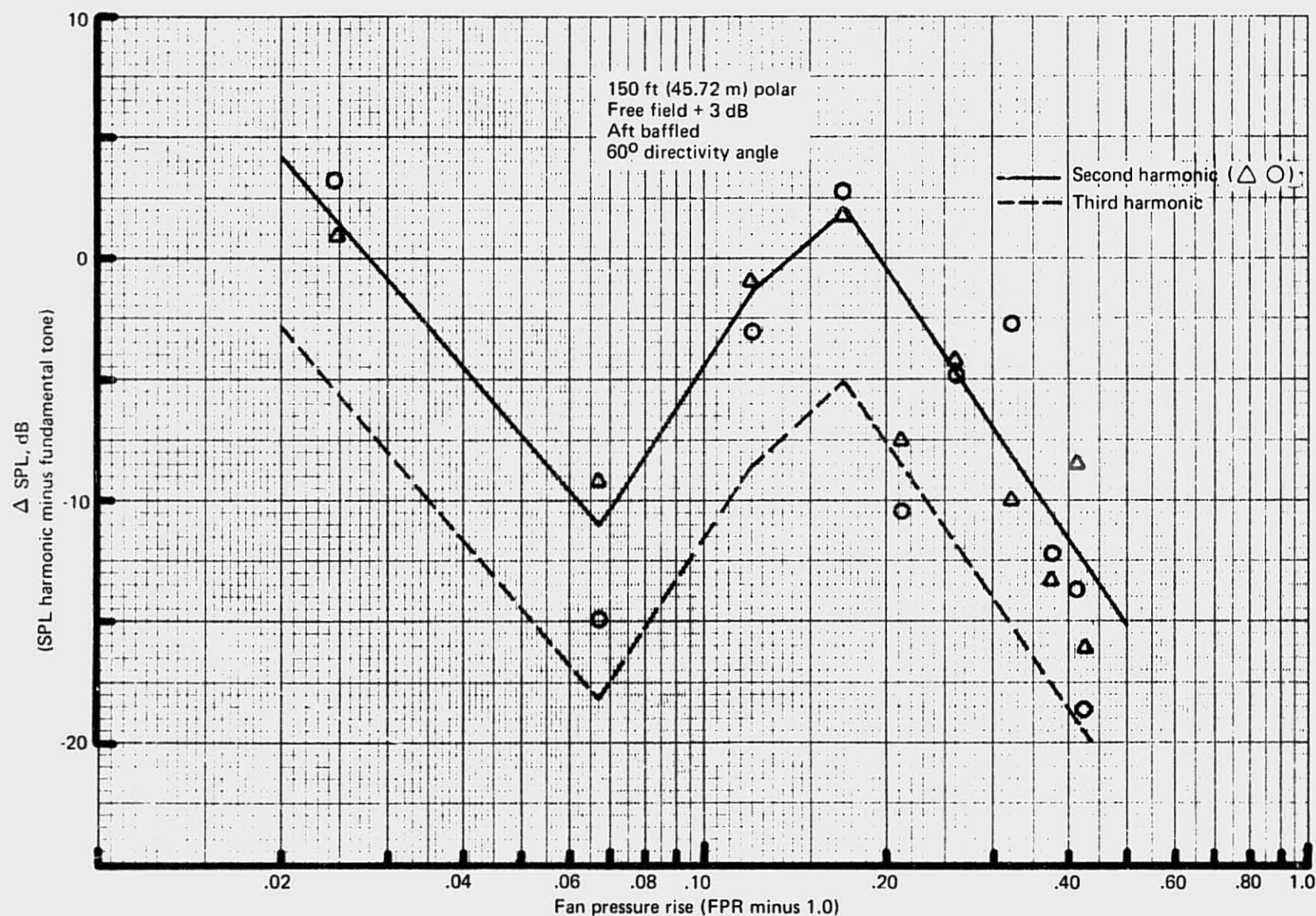
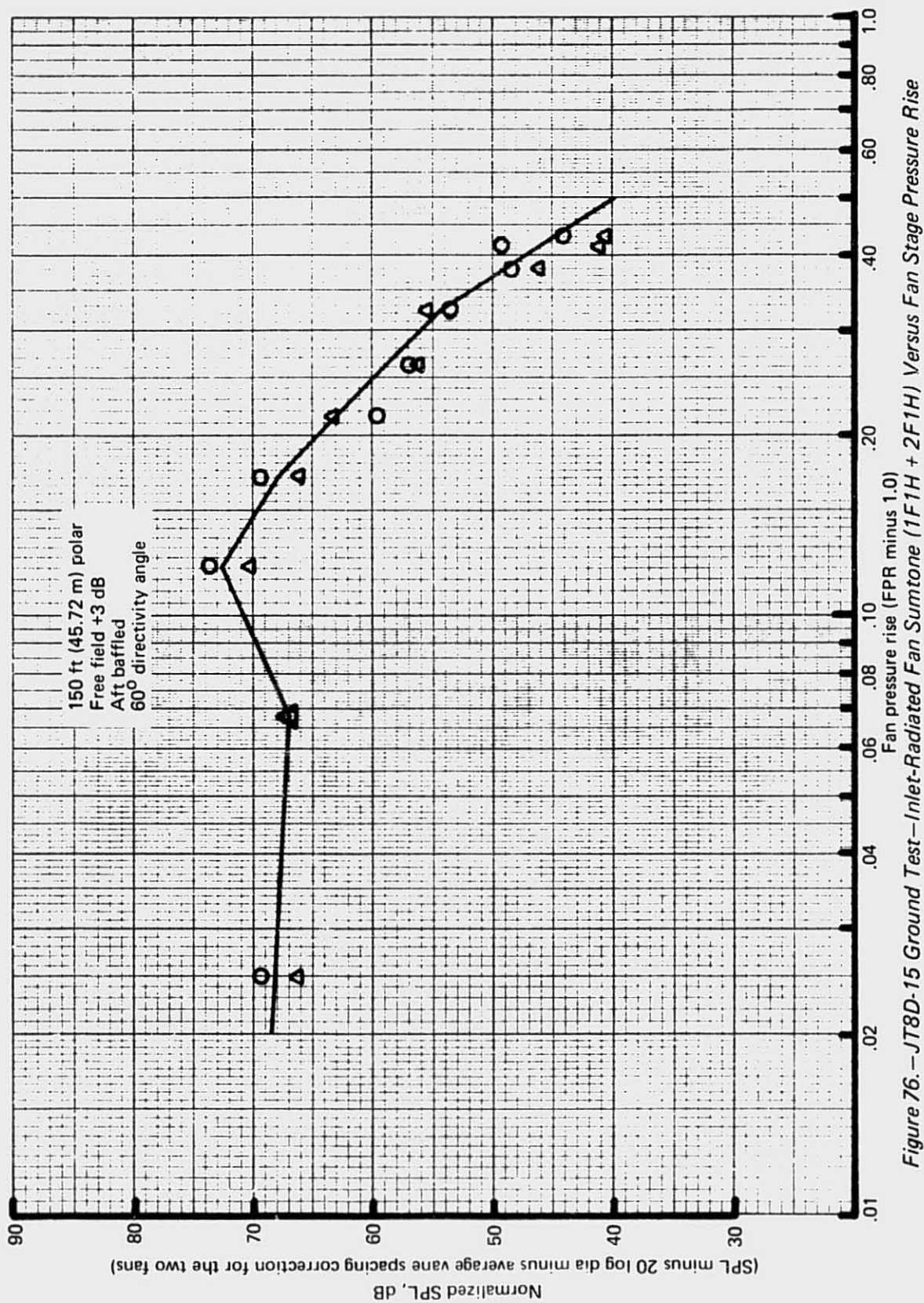


Figure 75.—JT8D-15 Ground Test—Inlet-Radiated First Fan Harmonic Tone Levels Relative to Fundamental Tone Level





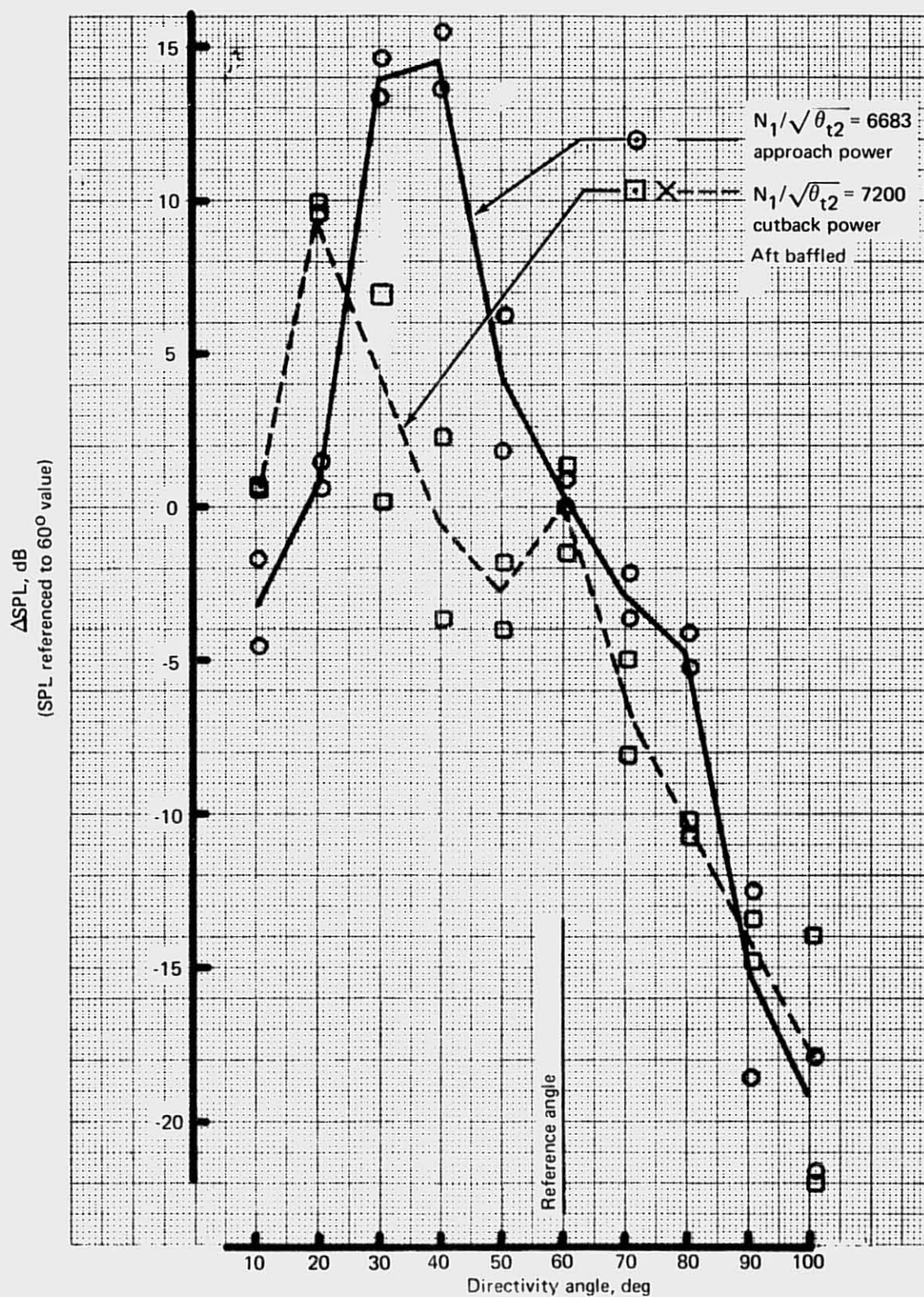


Figure 77.—JT8D-15 Ground Test—Polar Directivity of First Fan Fundamental Tcne

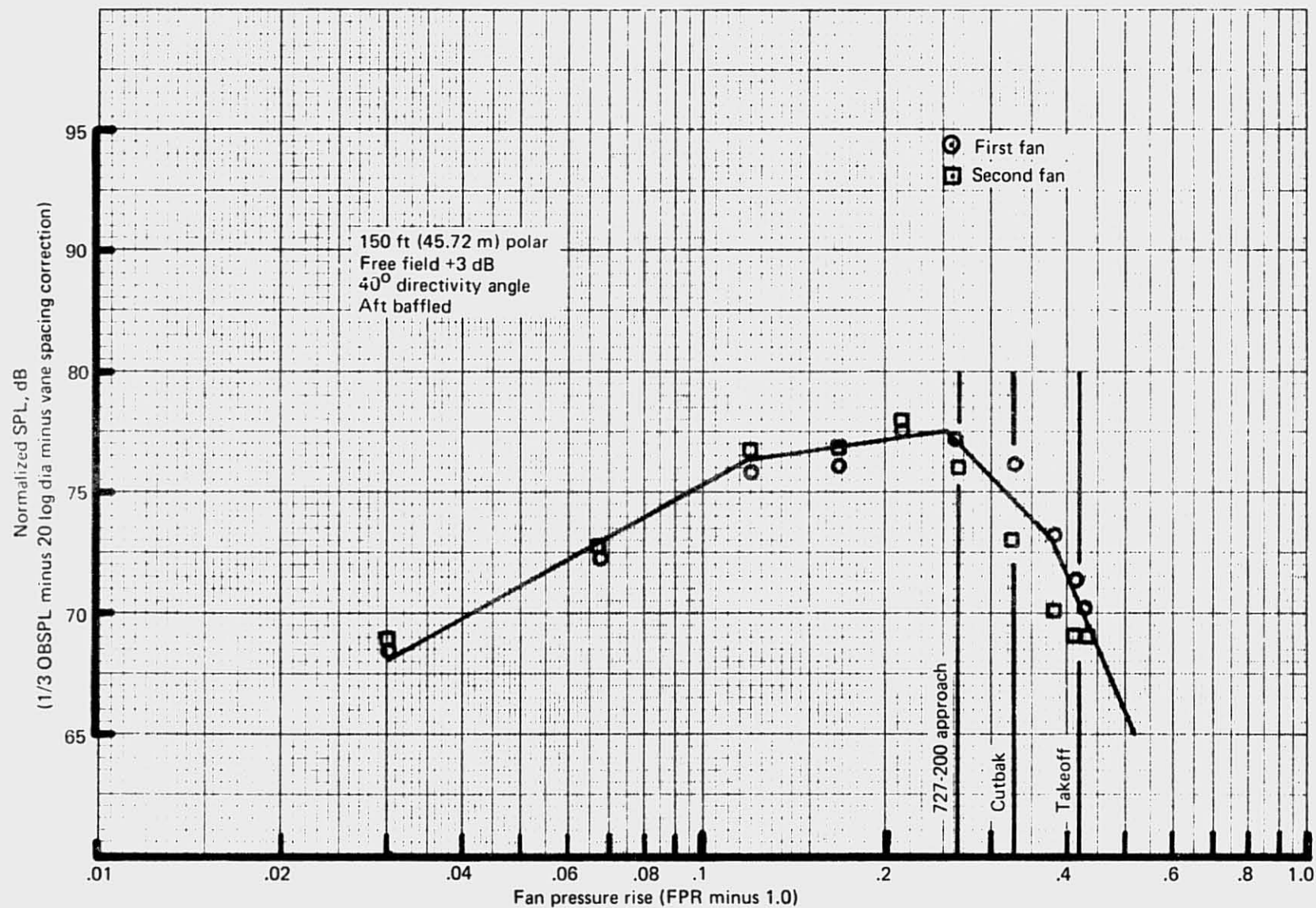


Figure 78.—JT8D-15 Ground Test—Fan Peak Broadband Noise, Inlet-Radiated for 1st or 2nd Stage



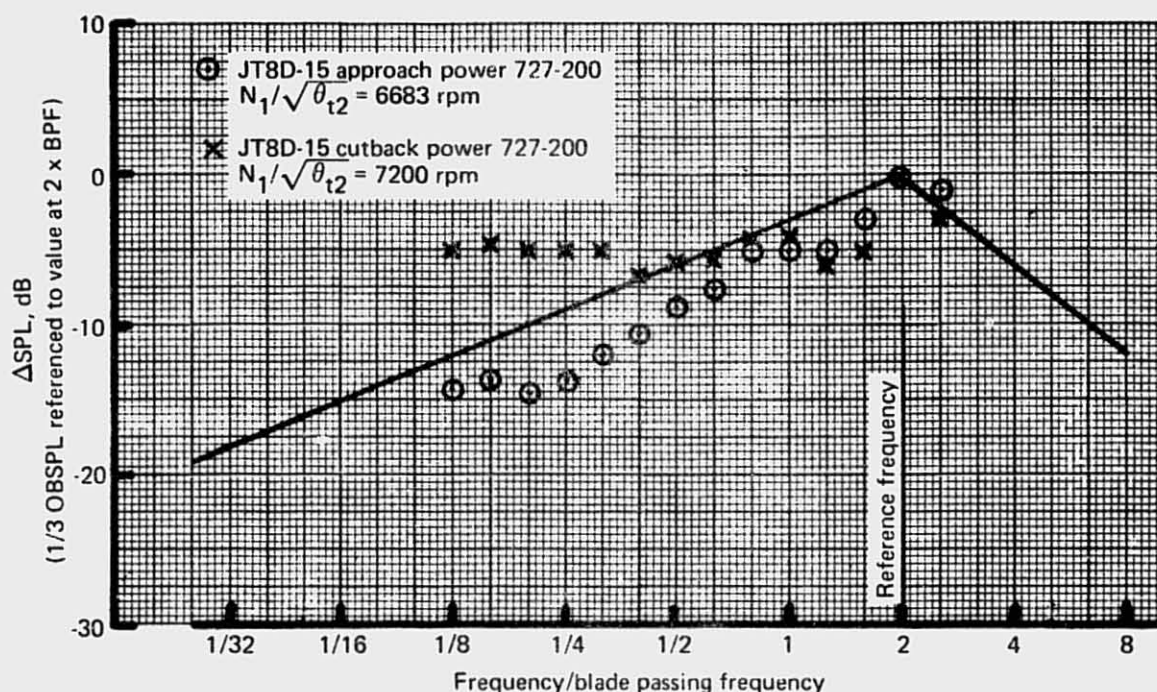


Figure 79.—JT8D-15 Ground Test—Fan Broadband Noise Spectrum Shaping—All Directivity Angles

**Fan Broadband Noise Directivity.**—Broadband noise directivity also showed some variation with power setting. The recommended curve was obtained by taking an average of that obtained at approach, cutback, and takeoff power. Directivities for the inlet-radiated broadband fan noise are shown in figure 80.

**Buzzsaw Noise.**—Buzzsaw noise on the JT8D-15 was clearly measurable at approach rpm (6700 rpm), where the fan tip relative Mach number was 1.01. At cutback rpm the SPL of the fan blade passing frequency dominated over the highest buzzsaw spike except for the 50° location. Peak buzzsaw spikes at several angles approach the level of fan tone at take-off power, where the fan tone tends to decrease with power setting near the top of the power curve. These noise spike comparisons were made on the basis of narrow band plots from an analyzer that utilized a 20-Hz bandwidth filter. Fan tone remained the dominant forward arc tone on the basis of 1/3-OB data comparisons and it also had the highest noise level and was consequently the major contributor to community noise.

Buzzsaw noise was second to the fan fundamental tone in noise contribution to perceived noise level (PNL) in the forward quadrant for the power settings where buzzsaw noise existed.

Figures 81 through 83 show the peak buzzsaw noise levels at three frequency locations below the first-stage fan tone. Figure 84 shows the level of a fourth spike at a frequency of 1.3 times blade passing frequency (BPF) throughout the operating range.

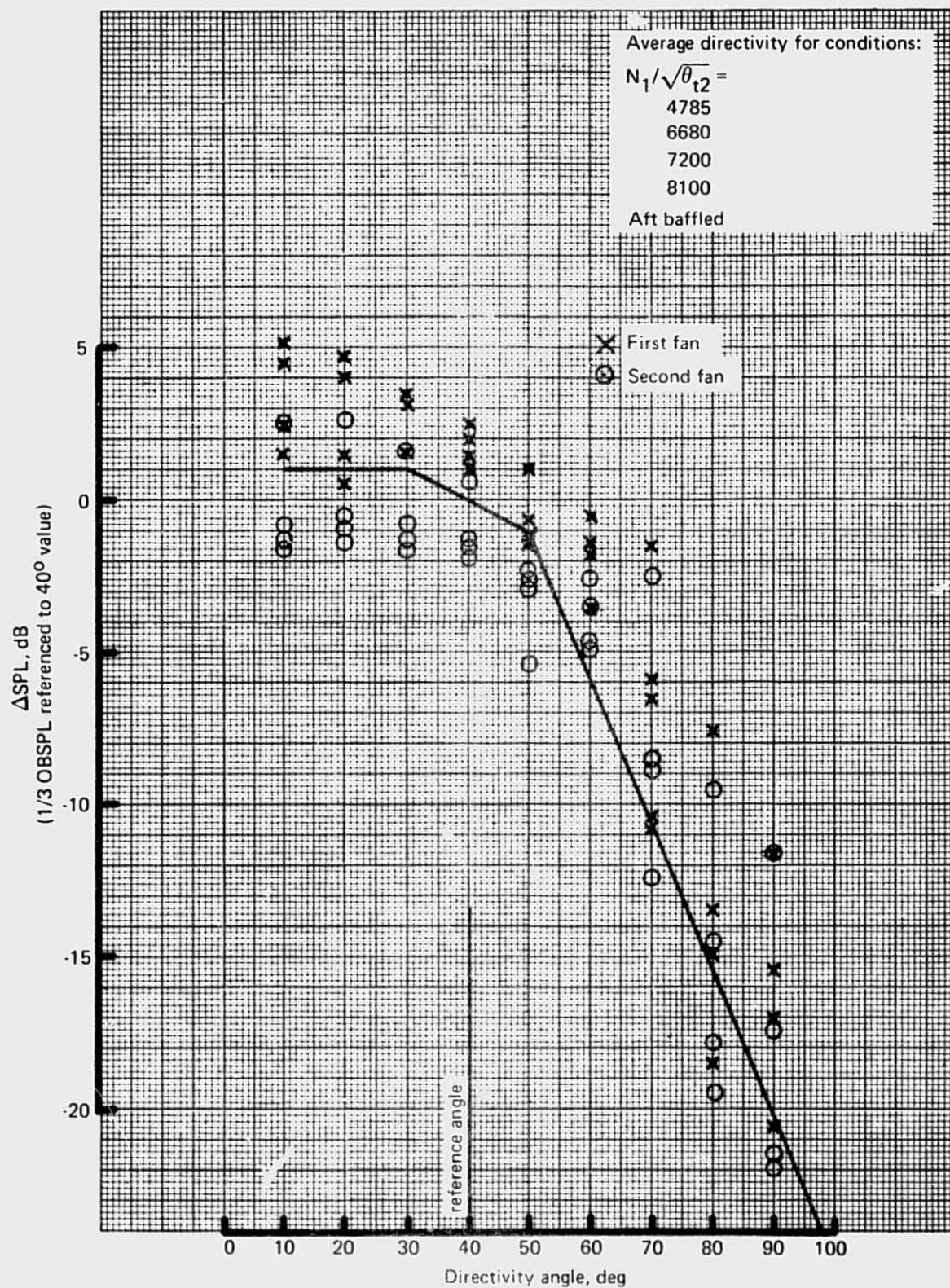


Figure 80.—JT8D-15 Ground Test—Inlet-Radiated Fan Broadband Noise Directivity for Either Fan Stage

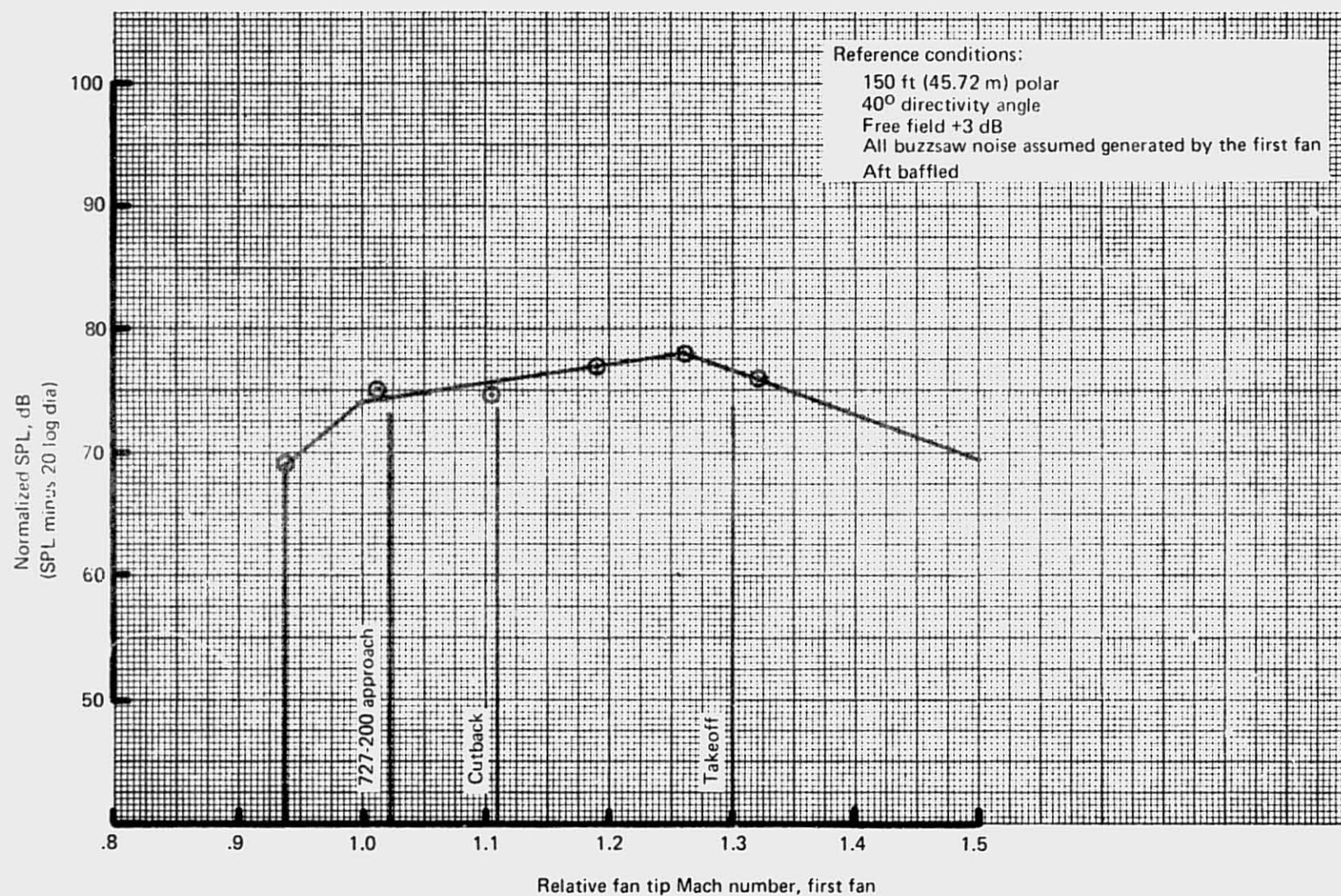


Figure 81.—JT8D-15 Ground Test—Buzzsaw Noise Level of Peak at  $0.30 \times \text{BPF}$



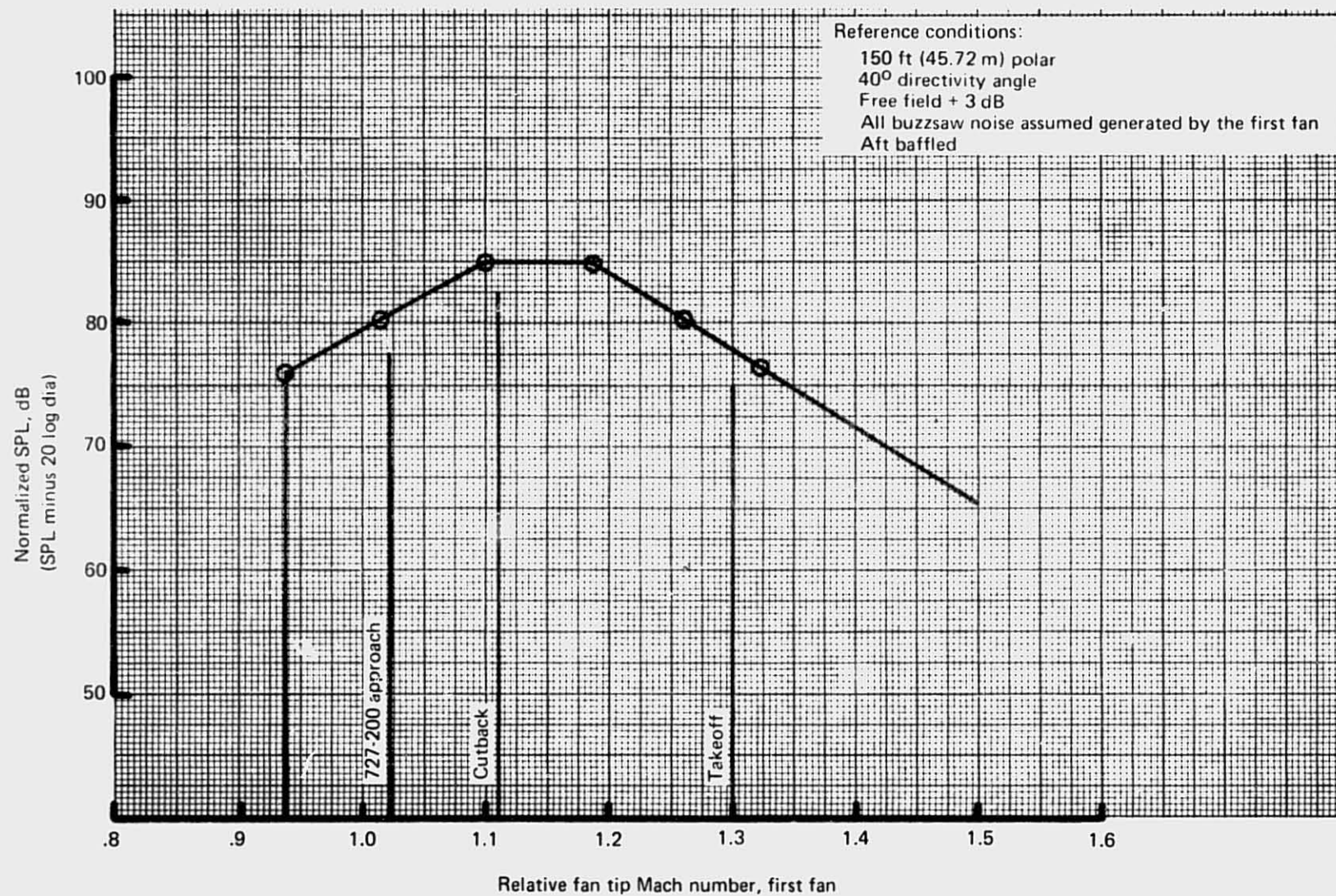


Figure 82.—JT8D-15 Ground Test—Buzzsaw Noise Level of Peak at  $0.50 \times \text{BPF}$

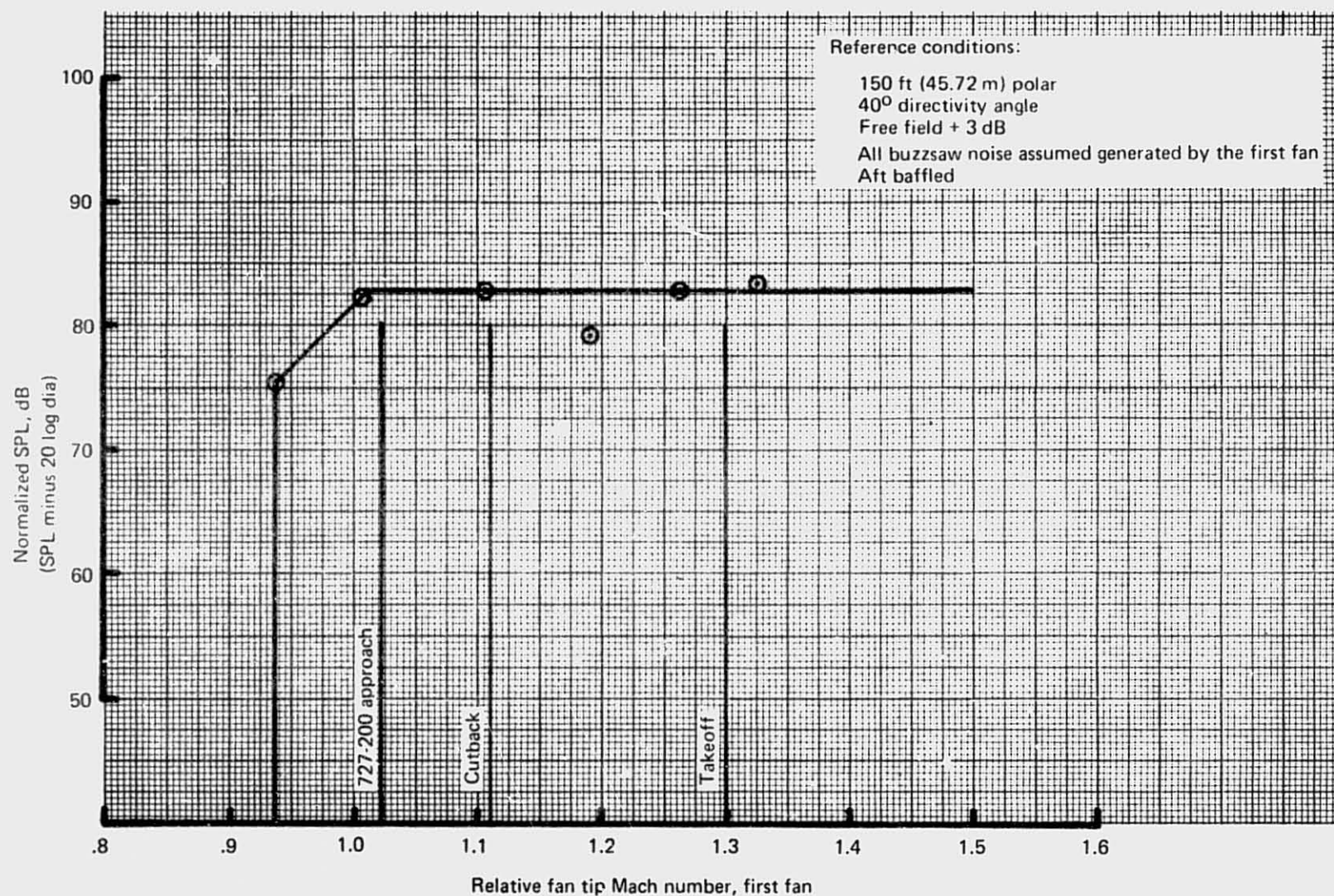


Figure 83.—JT8D-15 Ground Test—Buzzsaw Noise Level of Peak at  $0.75 \times BPF$



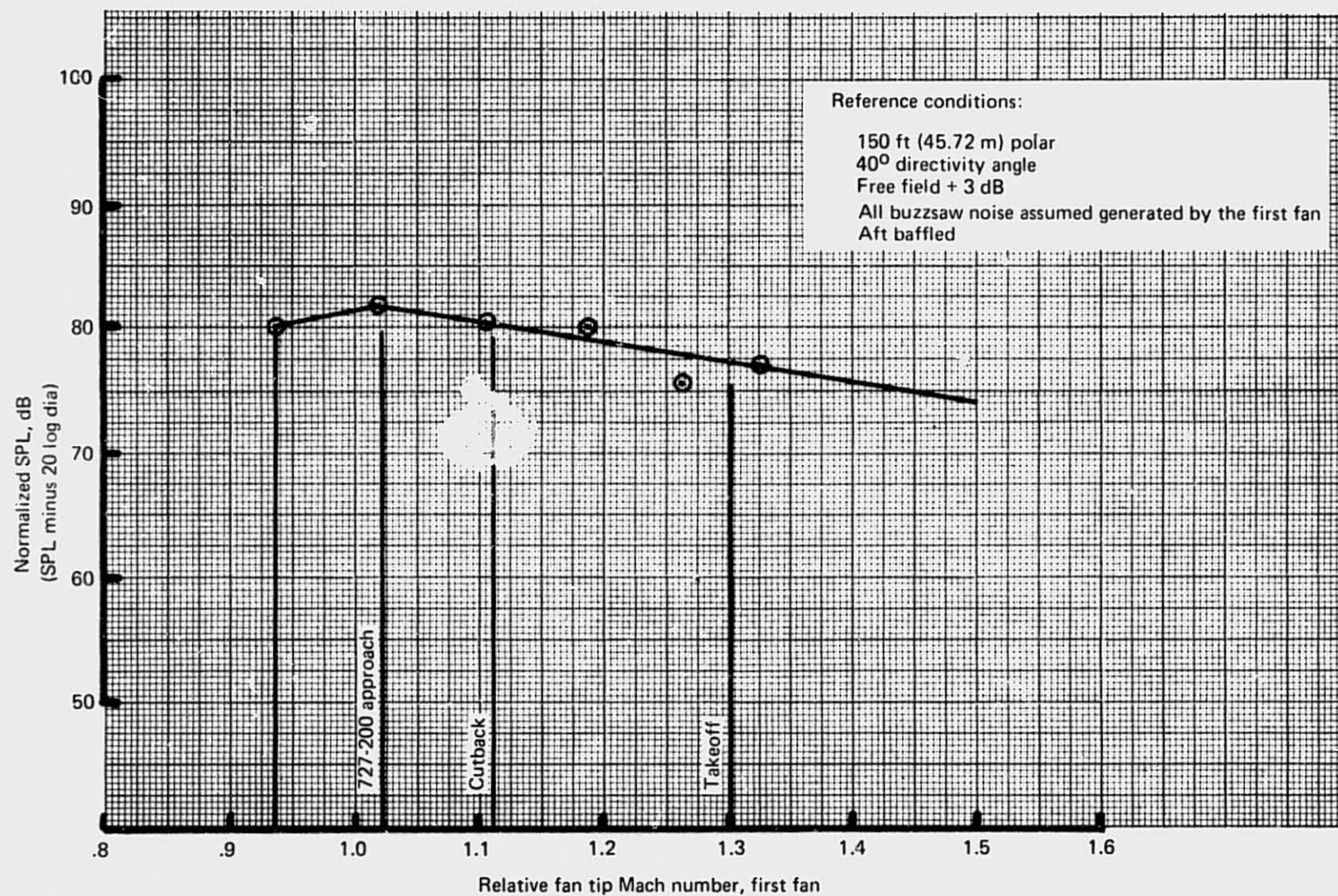


Figure 84.—JT8D-15 Ground Test—Buzzsaw Noise Level of Peak at  $1.30 \times \text{BPF}$

Buzzsaw levels presented here have been normalized to a 1-ft (0.3048-m) diameter fan according to the following formula:  $SPL_{normalized} = SPL_{measured} - 20 \log(\text{fan dia. in feet})$

This correction amounts to -10.6 dB relative to measured data.

**Buzzsaw Noise Spectrum Shaping.**—Shaping associated with peak noise areas of the buzzsaw spectrum is shown in figure 85. This shaping utilized spectrum shapes determined from earlier engines. Details of buzzsaw spectrum shaping were not specifically investigated for the JT8D-15. Data interpretation efforts were focused on establishing the noise levels of buzzsaw peak areas. Spectrum shaping has been shown only for the first three peak buzzsaw regions below the first fan fundamental tone.

**Buzzsaw Noise Directivity.**—Buzzsaw noise directivity variation with power setting revealed a behavior even more erratic than other tones produced by the fans. The selected directivity curves for the four major buzzsaw frequencies (figs. 86 through 89) represent average trends for all power settings where all measured directivities were normalized to  $40^\circ$ .

**Vane Spacing Correction.**—Fan noise bears a strong relationship to the spacing between the fan and the guide vanes (either inlet or exit) nearest the fan, and it is common practice to normalize fan noise to a reference fan/guide-vane spacing. This spacing is generally expressed as the ratio of the spacing to the fan chord length at 95% of the tip radius. All SPL values for tones and broadband noise in this section have been normalized to 300% vane spacing,

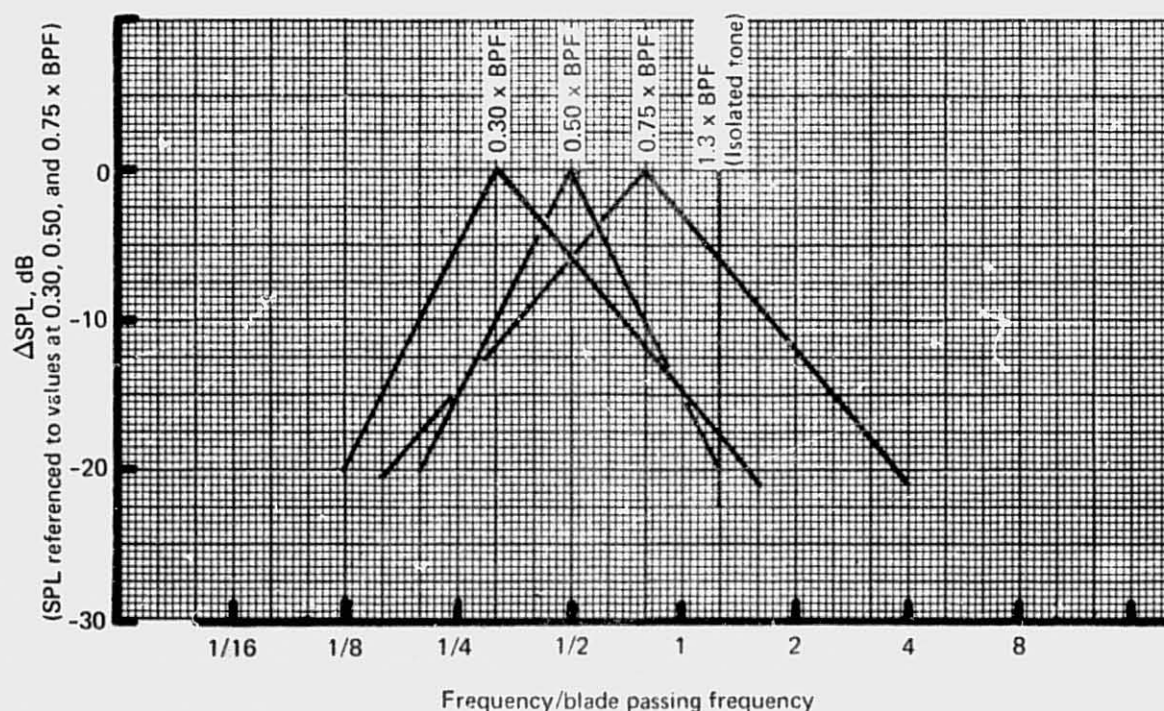


Figure 85.—JT8D-15 Ground Test—Buzzsaw Noise Spectrum Shaping

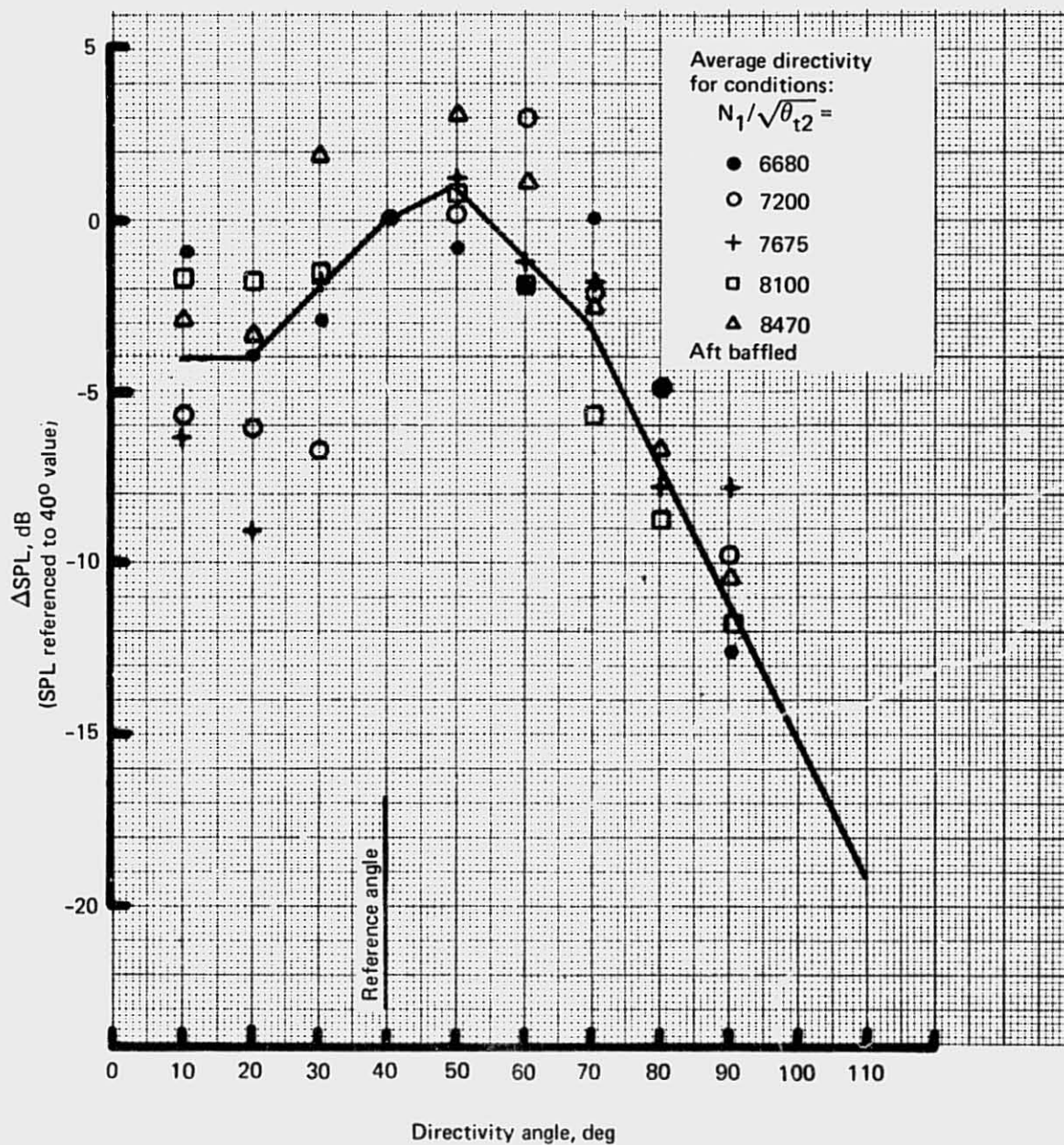


Figure 86.—JT8D-15 Ground Test—Buzzsaw Directivity Characteristics for Peak Level at Spectrum Location of  $0.30 \times \text{FPF}$



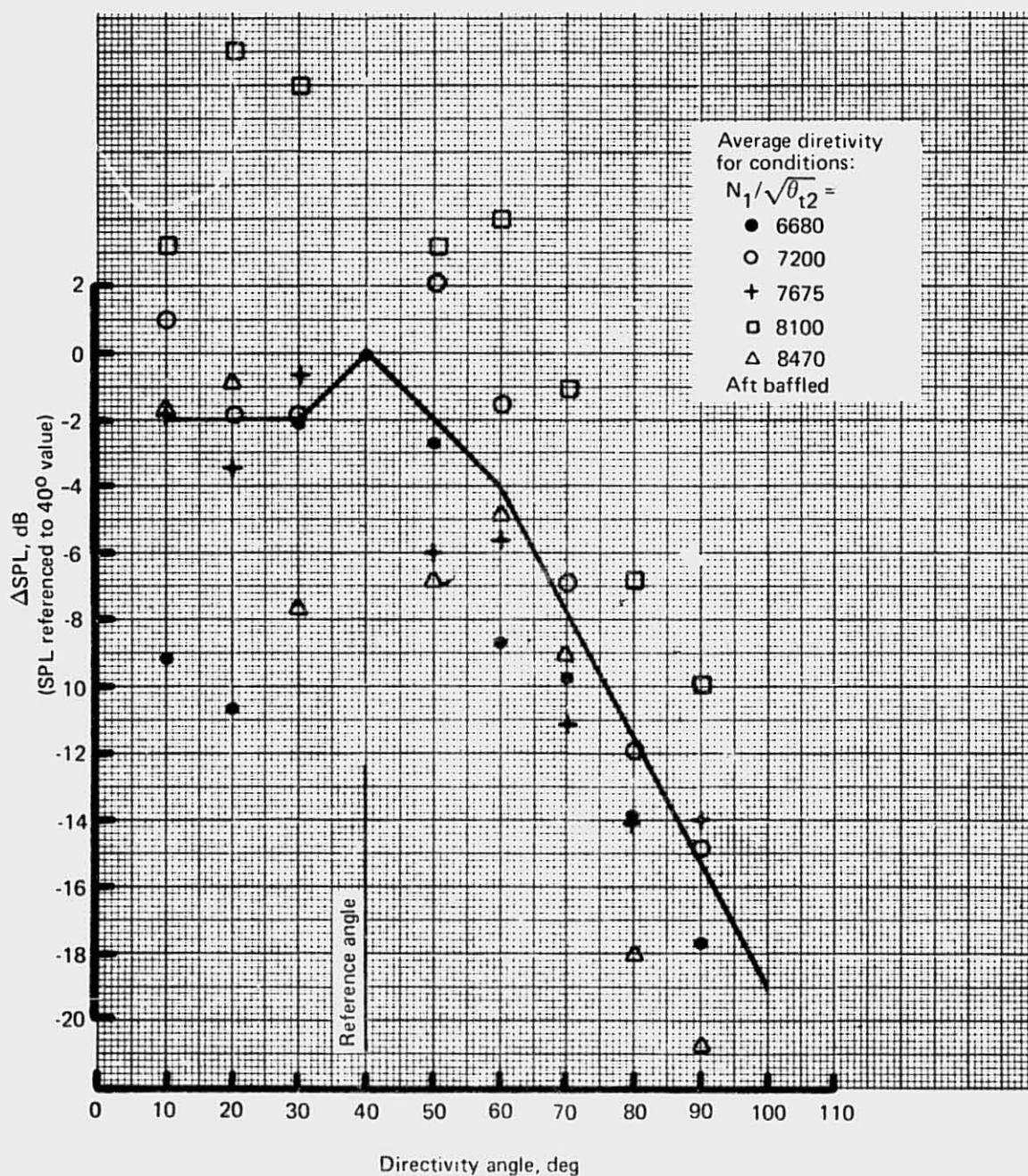


Figure 87.—JT8D-15 Ground Test—Buzzsaw Directivity Characteristics for Peak Level at Spectrum Location of  $0.50 \times \text{BPF}$

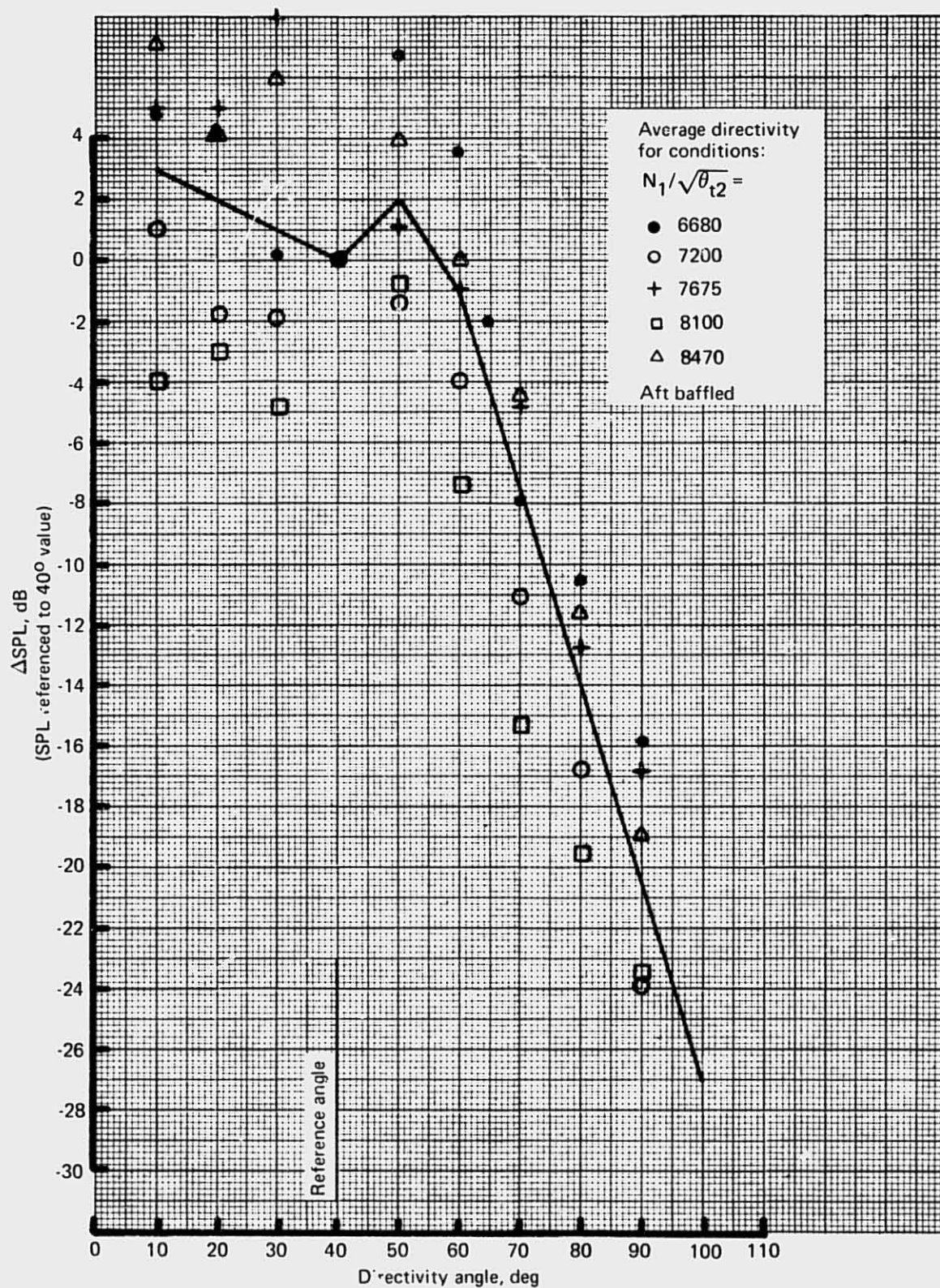


Figure 88.—JT8D-15 Ground Test—Buzzsaw Directivity Characteristics for Peak Level at Spectrum Location of 0.75 x BPF



REPRODUCIBILITY OF THE  
ORIGINAL PAGE IS POOR

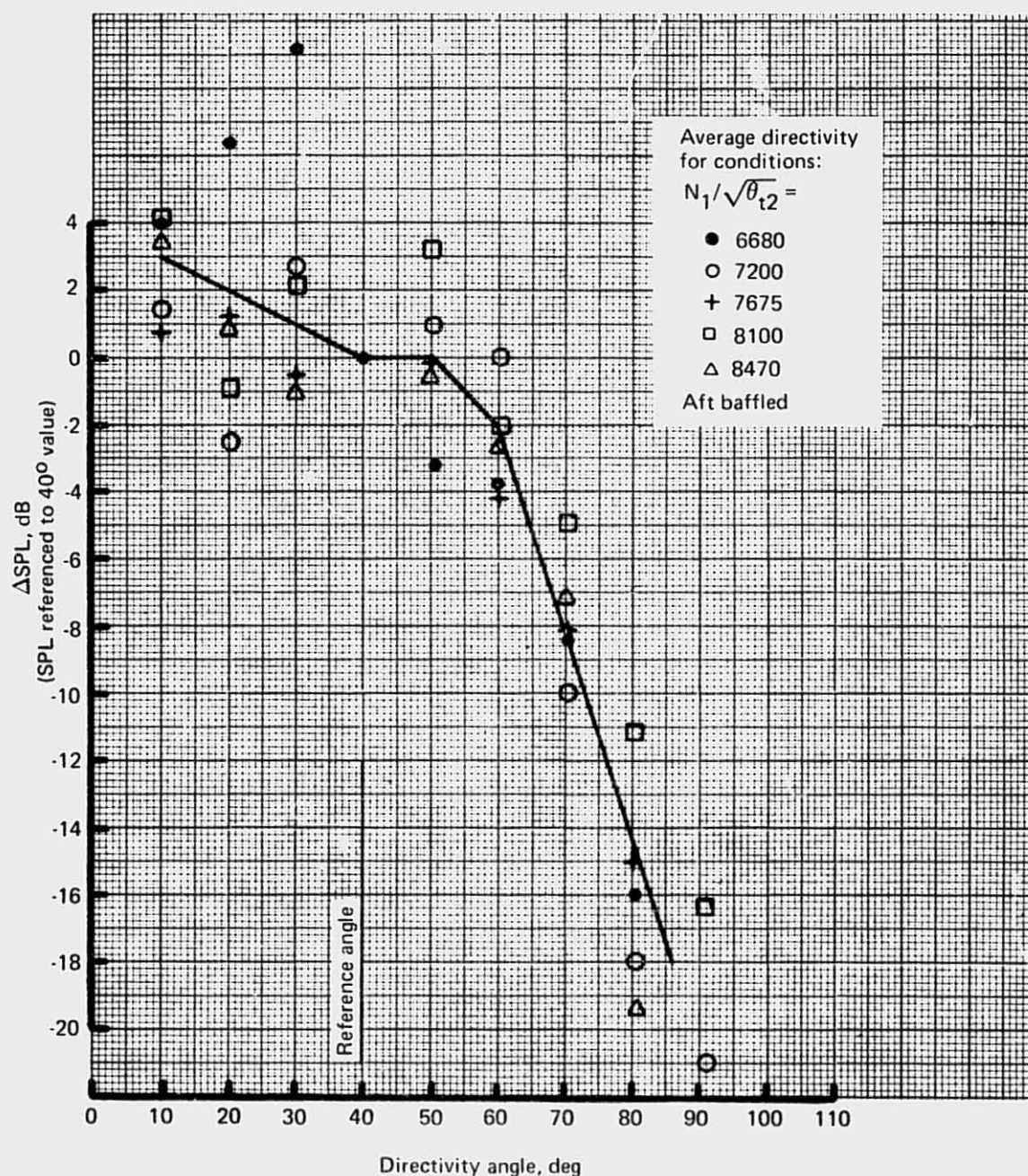


Figure 89.—JT8D-15 Ground Test—Buzzsaw Directivity Characteristics for Peak Level at Spectrum Location of  $1.30 \times \text{BPF}$

based on the guide vane row closest to the rotor of interest. Figure 90 shows how proximity of fan airfoil rows in prior turbomachinery tests affected fan tones and broadband noise emitted in both the forward and aft quadrant. These corrections have the following values for the JT8D-15 engine.

	<u>First-stage fan</u>	<u>Second-stage fan</u>
Tones	-6.5 dB	-7.5 dB
Broadband noise	-3.2 dB	-3.8 dB

#### 4.2.1.2 Inlet-Radiated Fan Noise: JT8D-115 Engine

The major difference between the JT8D-115 engine and its baseline counterpart is in the fan section of the engine. The JT8D-115 has a single-stage fan with inlet guide vanes, while the JT8D-15 has a two-stage fan with inlet guide vanes and generally operates at higher tip speeds and stage pressure ratios. The axial spacing between airfoils on the JT8D-15 fan is less than one-third of that on the JT8D-115. Consequently, the fan noise characteristics of the two engines are dramatically different. With the single higher-pressure-ratio fan stage and the reduced jet noise, fan noise becomes a more dominant noise component on the JT8D-115. The first-stage low pressure compressor also contributes some noise energy to the inlet noise spectrum. The fan and first low pressure primary compressor have 34 and 42 blades, respectively.

For the most part, the fan noise analysis for the JT8D-115 was carried out by methods similar to those used in the JT8D-15 fan noise analyses. One-third octave band and 20-Hz narrow band analyses were used to separate fan noise subcomponents. All data were measured with ground microphones and were averaged over three separate runs for inlet fan noise analysis. Checks made at several power settings ensured that the 1/3-OB and narrow band analyzer gave similar sound pressure levels for the 1/3-OB of interest.

Inlet fan tone and broadband noise data were normalized to 300% rotor/stator spacing. All other inlet subcomponents were predicted for a 200% rotor/stator spacing (the actual spacing on the JT8D-115 engine) as no standard normalizing procedure exists for these subcomponents (buzzsaw, sumtone, etc.). These corrections have the following values for the JT8D-115 engine:

	<u>Diameter correction</u>	<u>Rotor/stator spacing</u>
Fan tones	-12.4 dB	-1.8 dB
Broadband	-12.4 dB	-1.0 dB
Other subcomponents	-12.4 dB	-0 dB

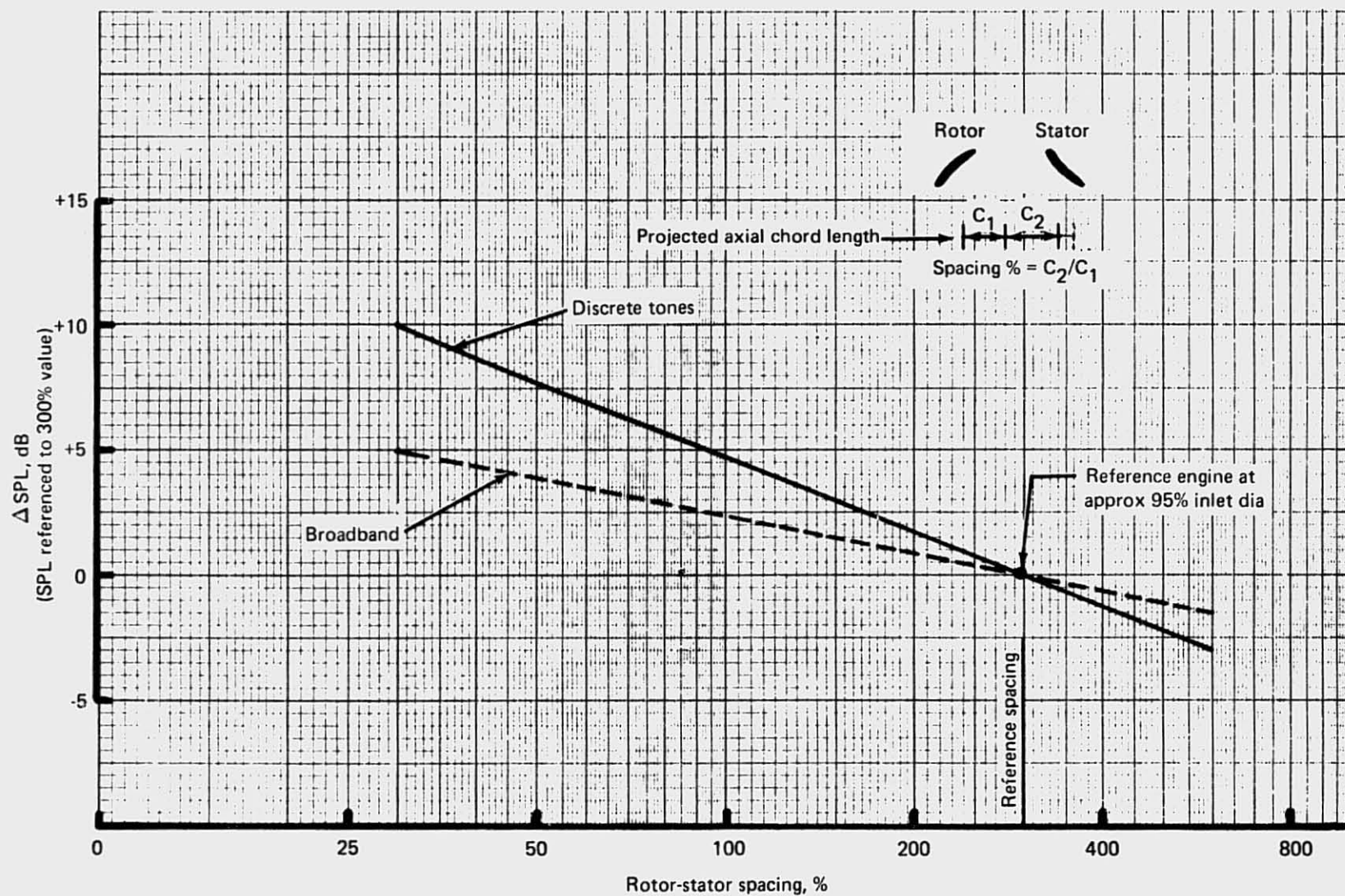


Figure 90.—JT8D-15 Ground Test—Rotor-Stator Spacing Correction

*Fan Tones.*—At low powers, accurate estimates of fan tone levels were possible by subtracting broadband noise (calculated from the 20-Hz narrow band data over the 1/3-OB frequency range containing the fan blade passing frequency) from the total 1/3-OBSPL. However, at approach rpm and above, buzzsaw becomes evident in the narrow band data. Therefore, the fan tone levels were taken directly from the narrow band spectra. Figure 91 shows how narrow-band data were used to identify discrete tones and broadband noise.

The sumtone of the fan and first-stage compressor blade passing frequencies was a sub-component of inlet-radiated noise at approach power which fell off rapidly at higher powers. Basic noise levels as a function of fan pressure rise for fan tone fundamental and second harmonic, compressor tone, and fan/compressor sumtone are shown in figures 92 through 95, respectively.

*Fan Tone Directivities.*—All directivity curves were plotted with reference to the basic sub-component noise level at 60°. Figure 96 shows the directivity pattern of the fan tone radiating from the inlet. This curve also serves as the directivity for the fan second harmonic. Substantial fluctuations in fan tone level at any given angle present a problem in establishing definite directivity characteristics at individual power settings. Therefore, one average directivity curve has been established which takes into account the fan tone levels from three runs of the same configuration at power settings varying from a FPR of 1.200 to maximum. As previously stated, the first-stage compressor tone is only apparent at low power settings; therefore, its directivity characteristics have been based on data taken at low power (fig. 97). The sumtone directivity is shown in figure 98. As with the first-stage compressor tone alone, the sumtone directivity was derived from power settings at and below approach power.

*Broadband Noise.*—Figure 99 shows a typical 20-Hz narrow-band spectrum and the method of determining the broadband noise level over the 1/3-OB frequency range of interest. Basic noise levels for inlet fan broadband noise versus fan pressure rise are shown in figure 100.

*Fan Broadband Noise Spectrum Shaping.*—The test data showed peak 1/3-OB broadband SPL's occurring at twice the fundamental fan blade passing frequency for power settings below FPR = 1.550. At higher power settings, the inlet broadband noise peaks at the fan fundamental blade passing frequency. Spectrum shaping is shown in figure 101.

*Fan Broadband Noise Directivity.*—Inlet broadband peak noise directivity is shown in figure 102. As with the fan tone, one directivity pattern covers all power settings. There is far less data scatter than was observed in the fan tone.

*Buzzsaw Noise.*—Buzzsaw noise was determined by subtracting the broadband level from the total 1/3-OB level. Basic buzzsaw noise levels for four key frequencies (stated as a percentage of fundamental blade passing frequency) are shown in figures 103 through 106 as a function of fan relative tip Mach number.

*Buzzsaw Noise Spectrum Shaping.*—As stated in the previous paragraph, buzzsaw noise levels are predicted at four 1/3-OB frequencies as a function of the fan fundamental blade passage frequency (0.25, 0.5, 0.75, and 1.25 times the fan blade passing frequency). Spectrum shaping is then applied relative to each of the four frequencies as shown in figure 107.



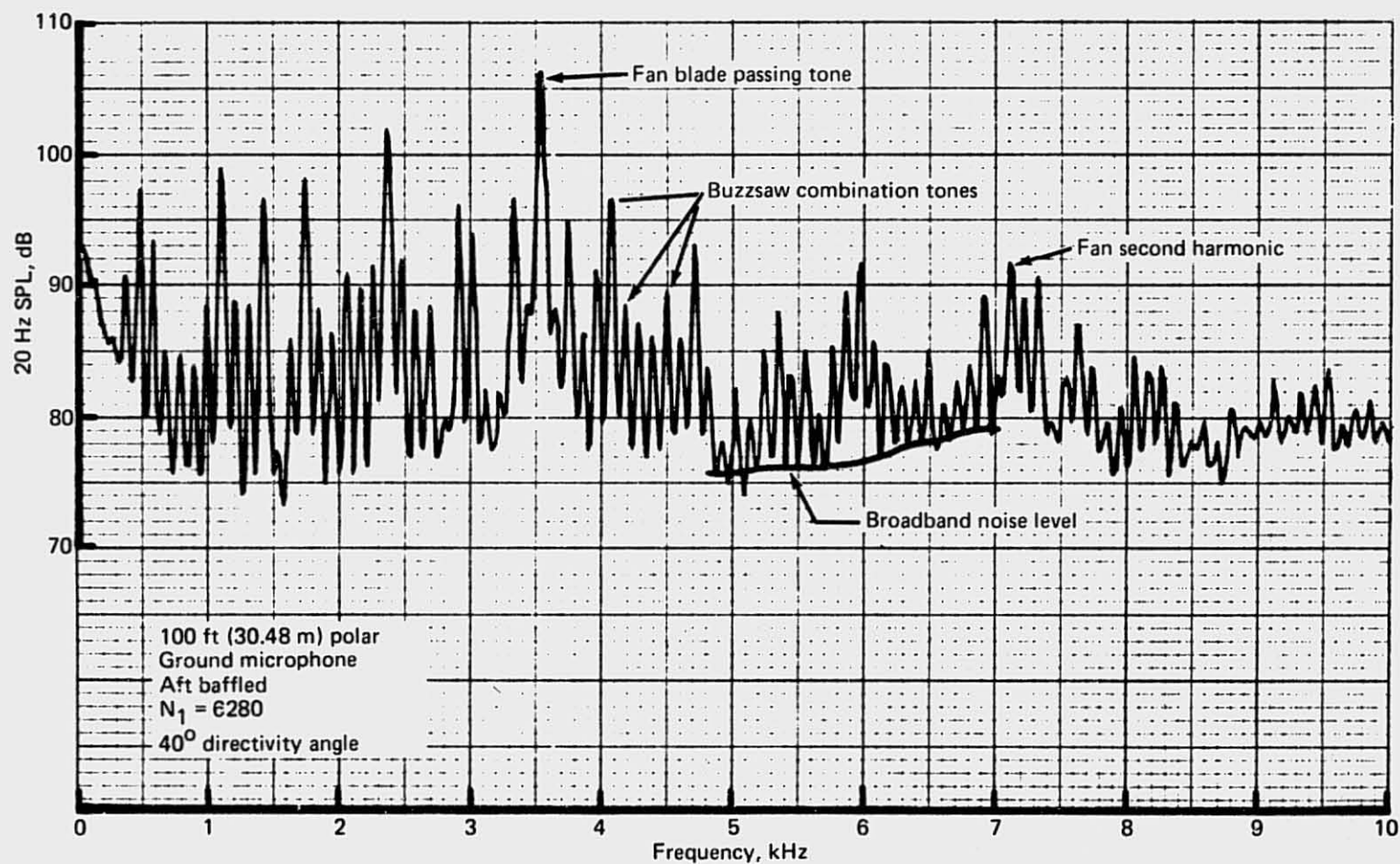


Figure 91.—JT8D-115 Ground Test—Fan Noise Subcomponent Identification by 20 Hz Bandwidth Filter Analysis



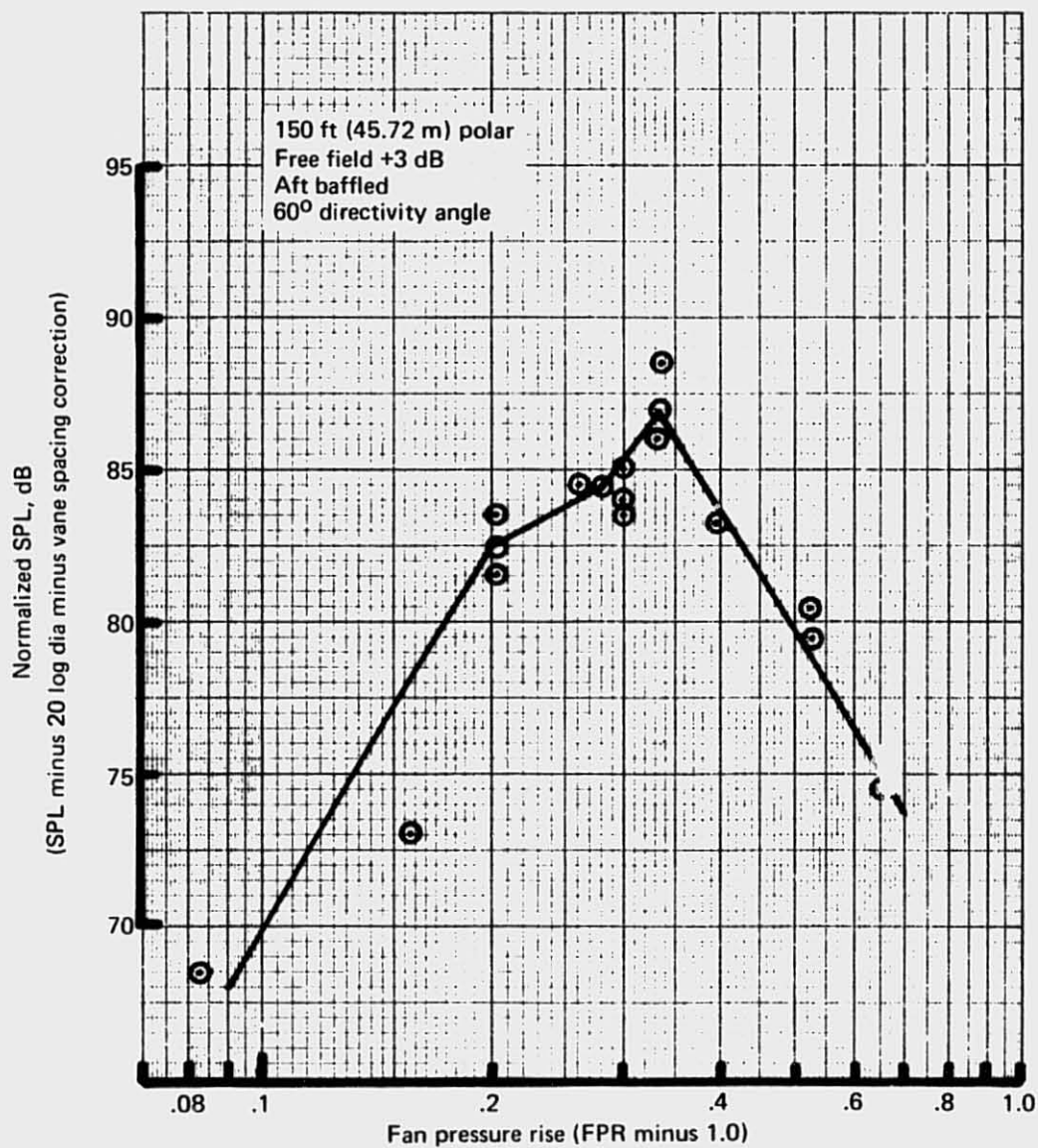


Figure 92.—JT8D-115 Ground Test—Inlet Fundamental Fan Tone Basic Noise Level

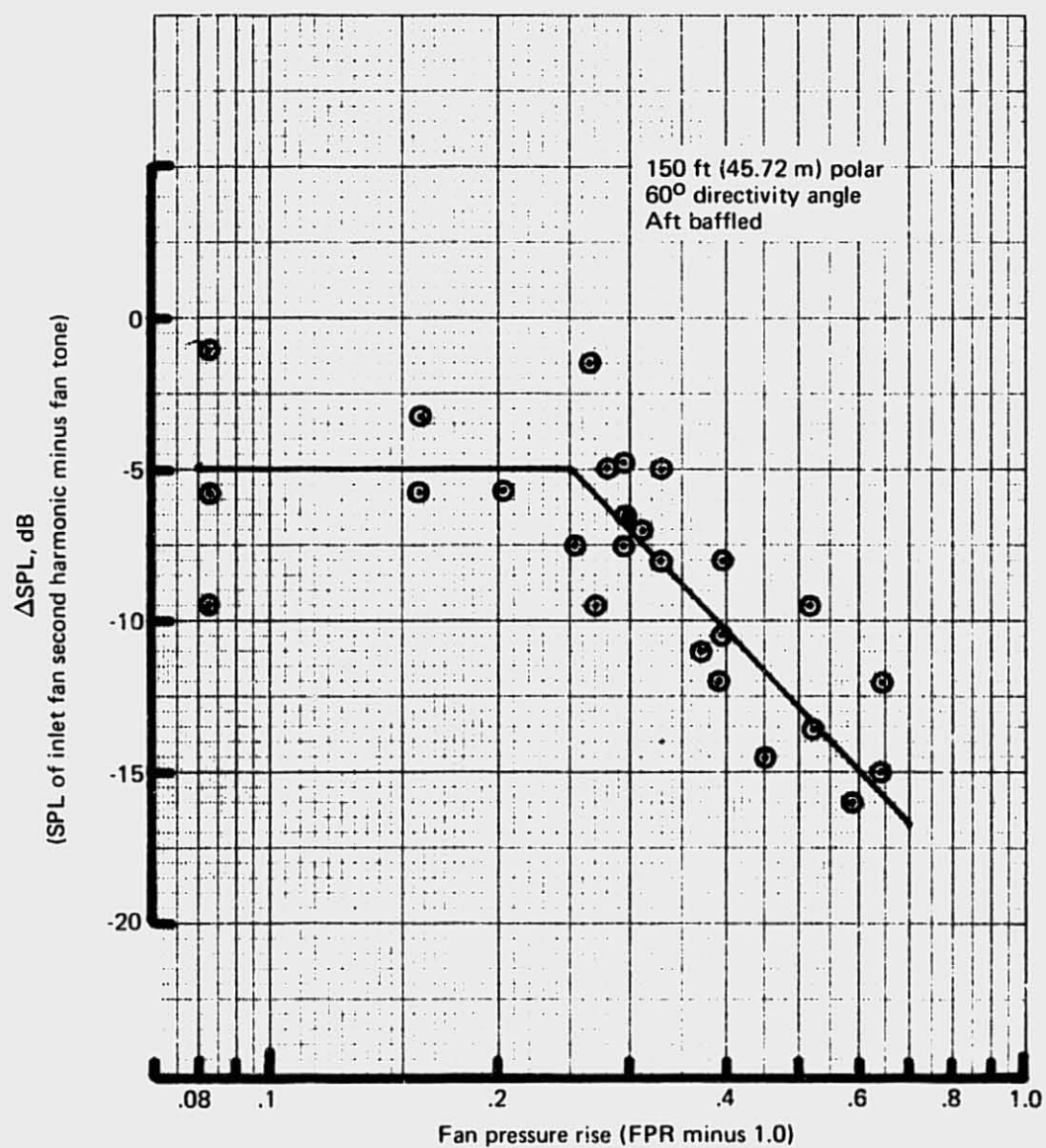


Figure 93.—JT8D-115 Ground Test—Relationship Between Inlet-Radiated Second Harmonic and Fundamental Fan Tone

REPRODUCIBILITY OF THE  
ORIGINAL PAGE IS POOR

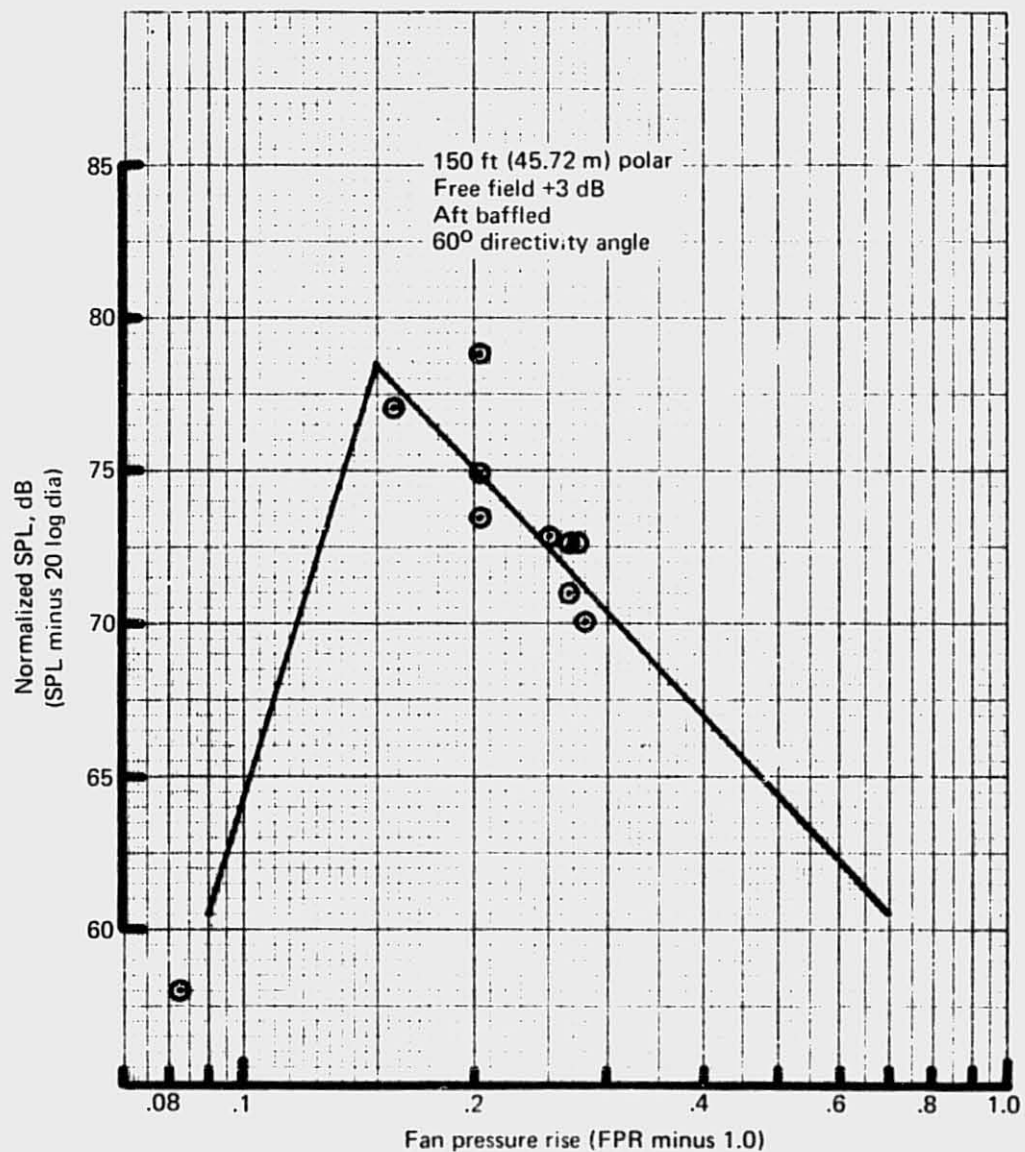


Figure 94.—JT8D-115 Ground Test—Inlet-Radiated First Stage Compressor  
Fundamental Tone Level

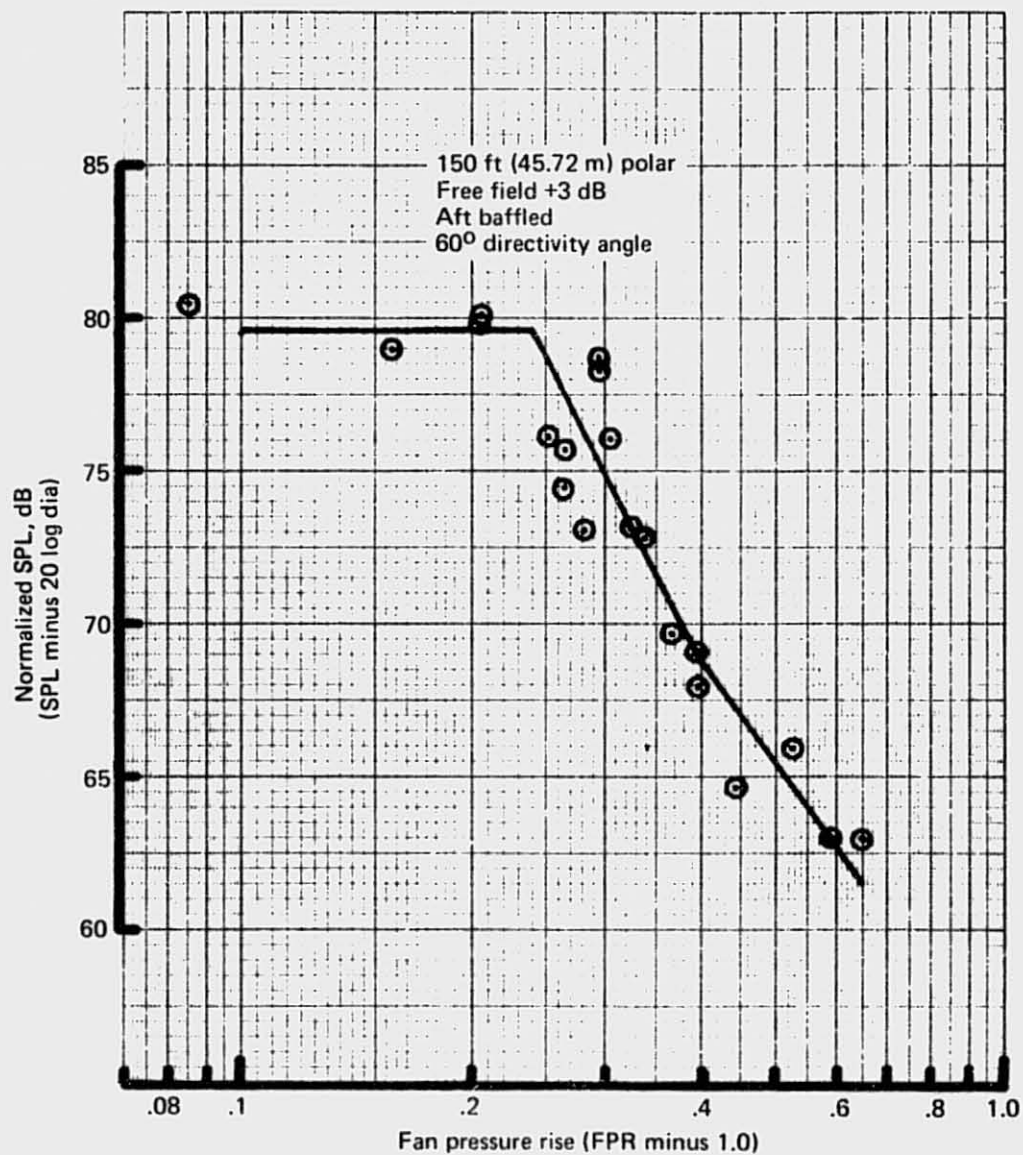


Figure 95—JT8D-115 Ground Test—Inlet-Radiated Fan and First Stage Compressor  
Sumtone Basic Noise Level

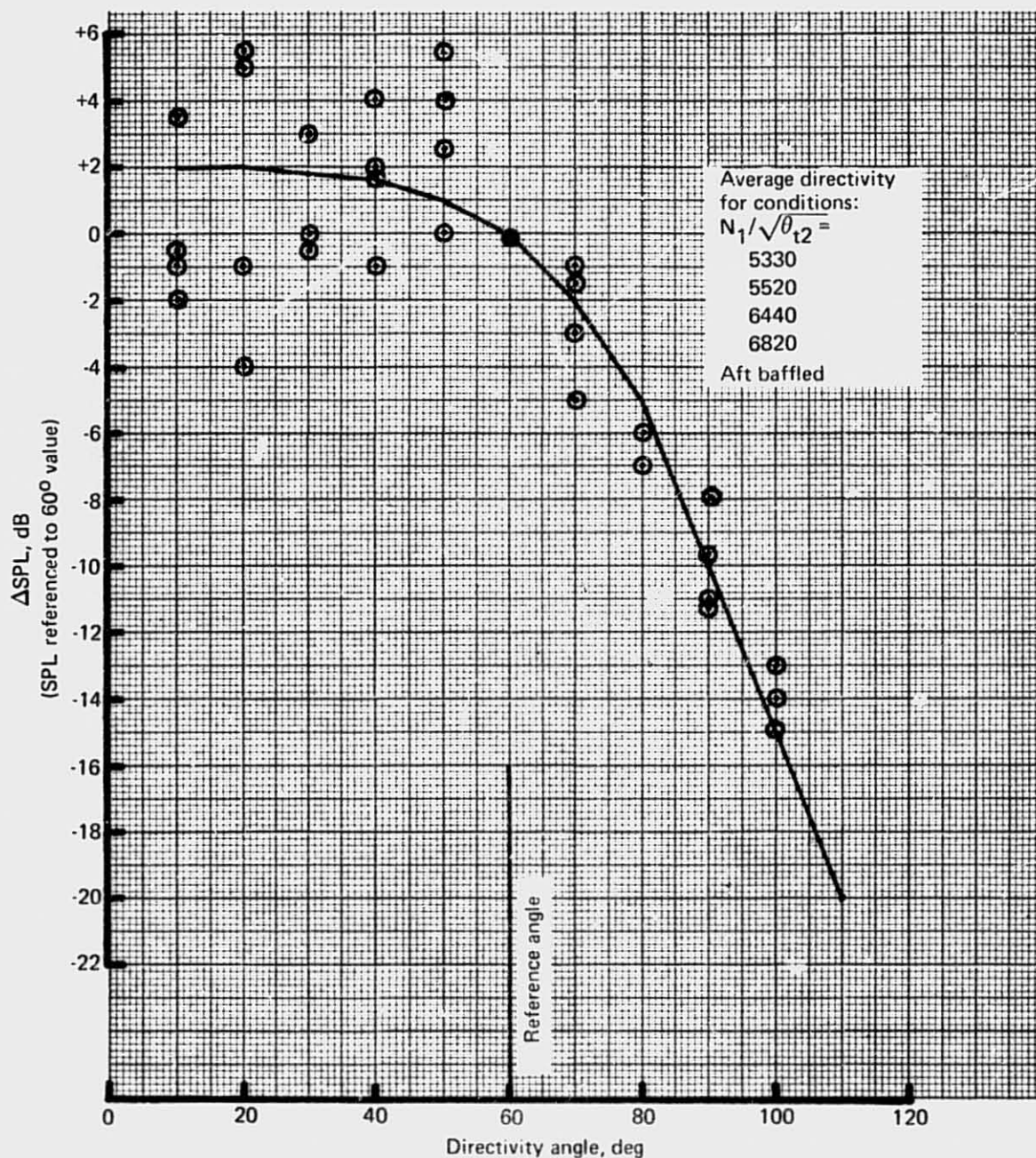


Figure 96.—JT8D-115 Ground Test—Inlet-Radiated Fan Tone Directivity



REPRODUCIBILITY OF THE  
ORIGINAL PAGE IS POOR

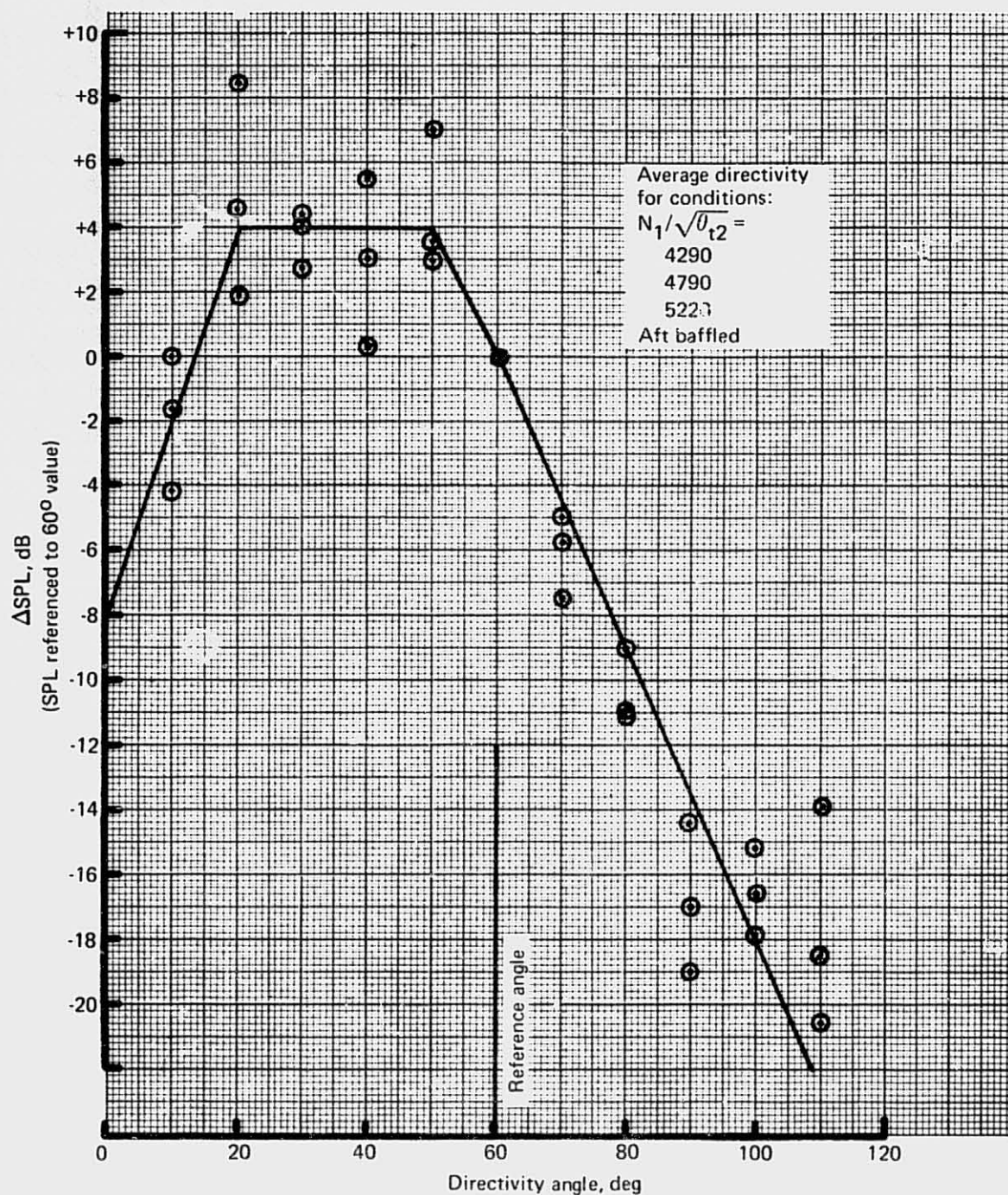


Figure 97.—JT8D-115 Ground Test—Inlet-Radiated First Stage Compressor Tone Directivity

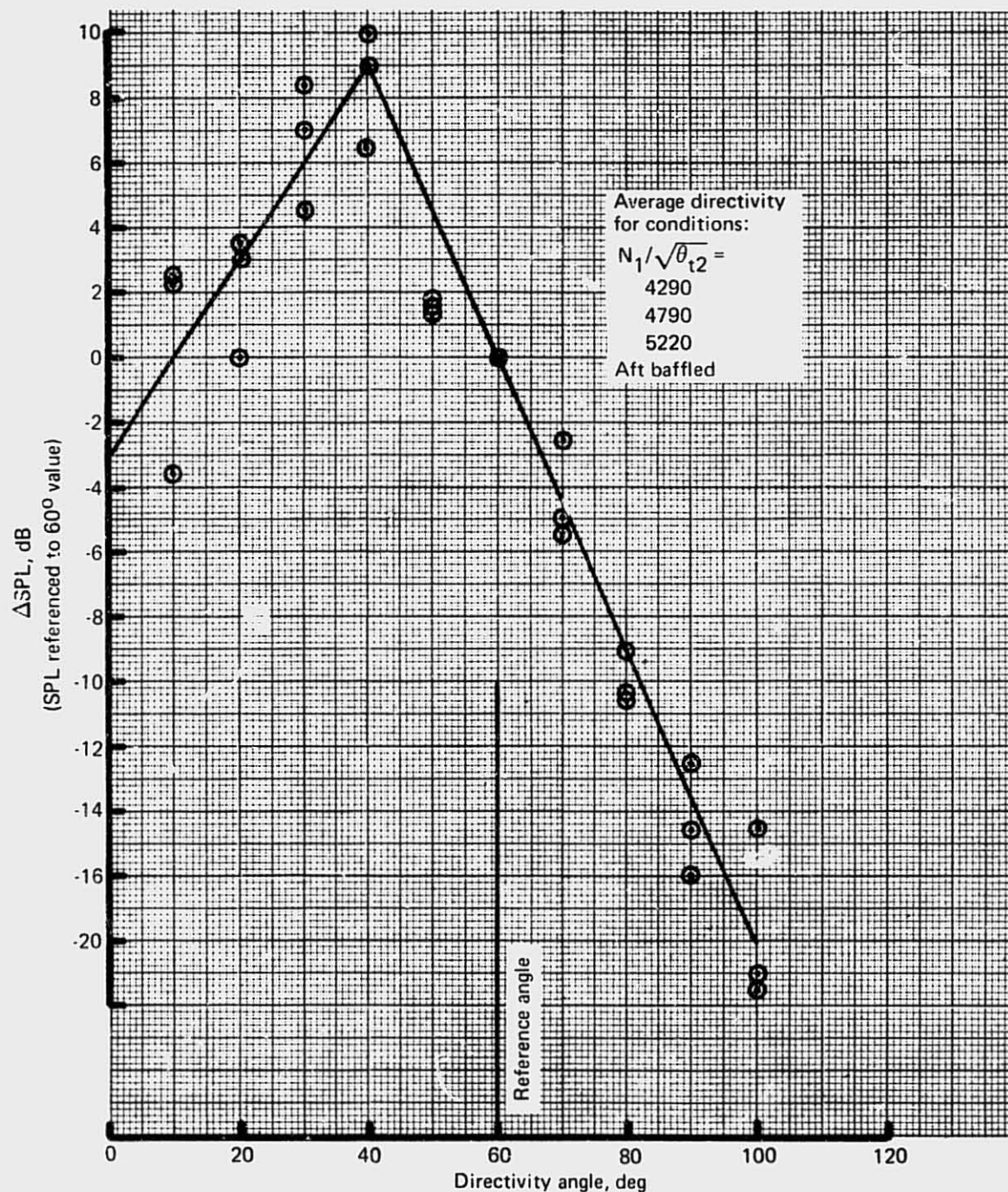


Figure 98.—JT8D-115 Ground Test—Inlet-Radiated Fan and First Stage Compressor Sumtone Directivity

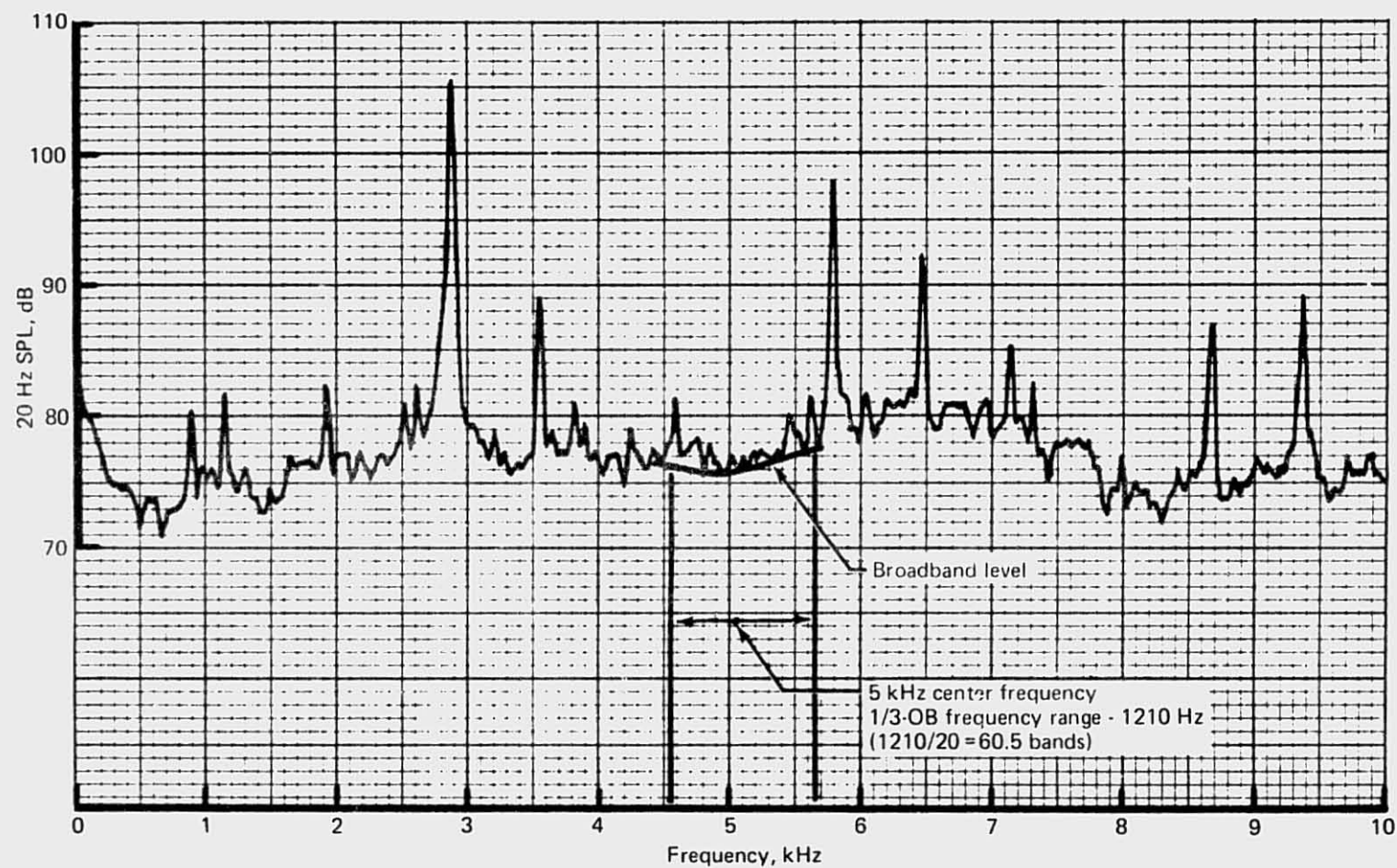


Figure 99. — JT8D-115 Ground Test—Example of Method for Converting  
20 Hz Bandwidth Data to 1/3 OB Level



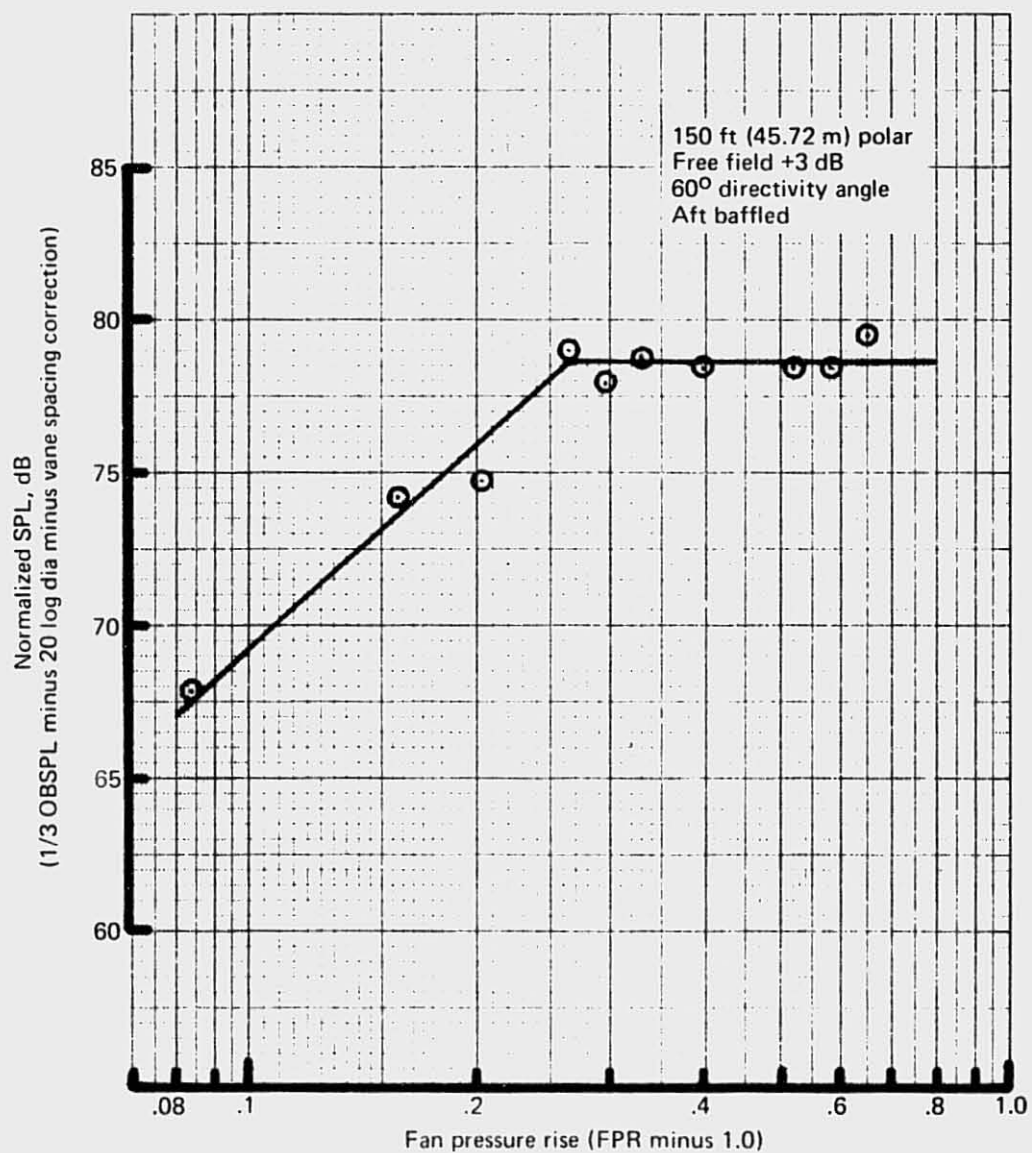


Figure 100.—JT8D-115 Ground Test—Inlet-Radiated Fan Broadband Basic Noise Level

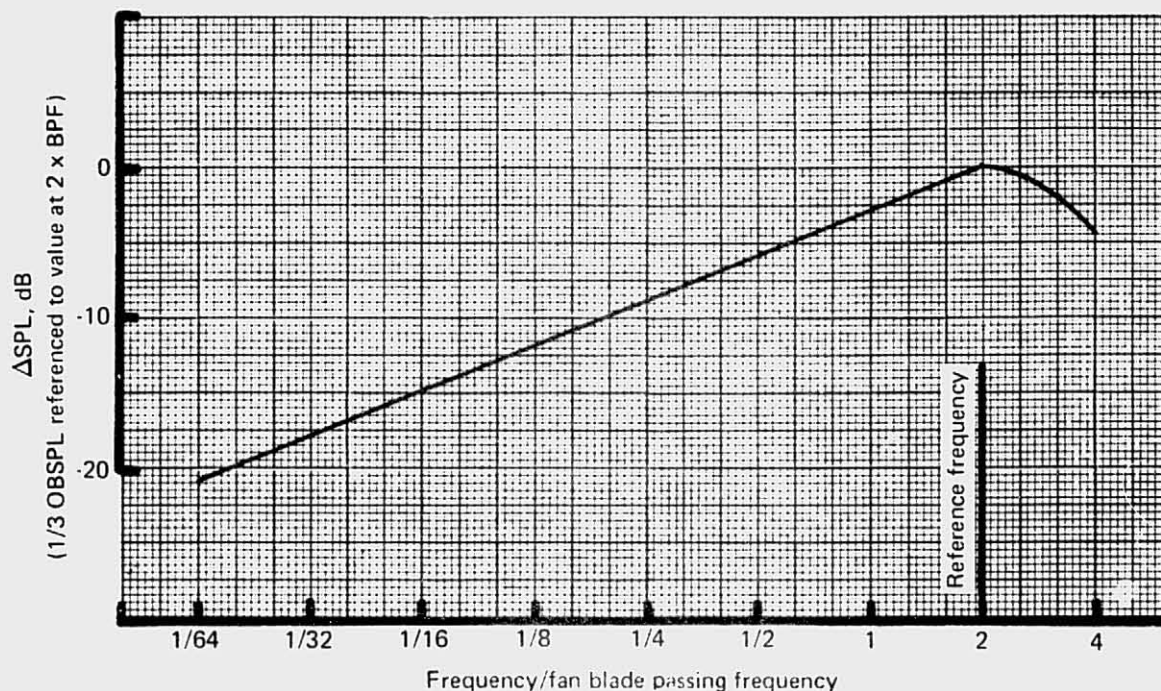


Figure 101.—JT8D-115 Ground Test—Inlet-Radiated Fan Broadband Noise Spectrum Shaping

**Buzzsaw Directivity.**—Buzzsaw (combination tone) levels showed a similar fluctuation from run to run as the fan tone levels. An average directivity curve was selected as representative of all power settings and frequencies and is shown in figure 108.

**Fan Noise Correlating Parameter.**—All fan tone and fan broadband noise levels presented in this section have been correlated on fan pressure rise, the historically accepted fan noise correlating parameter. In theory, these curves of fan noise versus fan pressure rise can be used in conjunction with a rotor/stator spacing correction and a fan diameter correction to predict the tone and broadband noise levels of any similar fan. However, comparisons of acoustic data from the JT8D-115 ground test with JT8D-109 acoustic data obtained by P&WA showed that the two sets of inlet fan noise data did not agree when plotted against fan pressure rise (fig. 109). The fans on these two engines are identical, but the JT8D-109 has a higher fan operating line (higher FPR at a given fan mass flow). Further analysis showed that the two sets of fan noise data did agree when plotted against corrected low pressure rotor speed ( $N_1$ ) (fig. 110). This result came as a surprise and indicates the need for a detailed study of the relationship between fan noise and the fan operating map in order to better understand inlet-guide-vane fan noise. Because of these findings, the JT8D-109 flyover noise predictions reported in Volume IV of this final report series made use of the JT8D-115 fan noise empirical model using corrected rpm ( $N_1$ ) as the correlating parameter, rather than using fan pressure rise as had been planned.



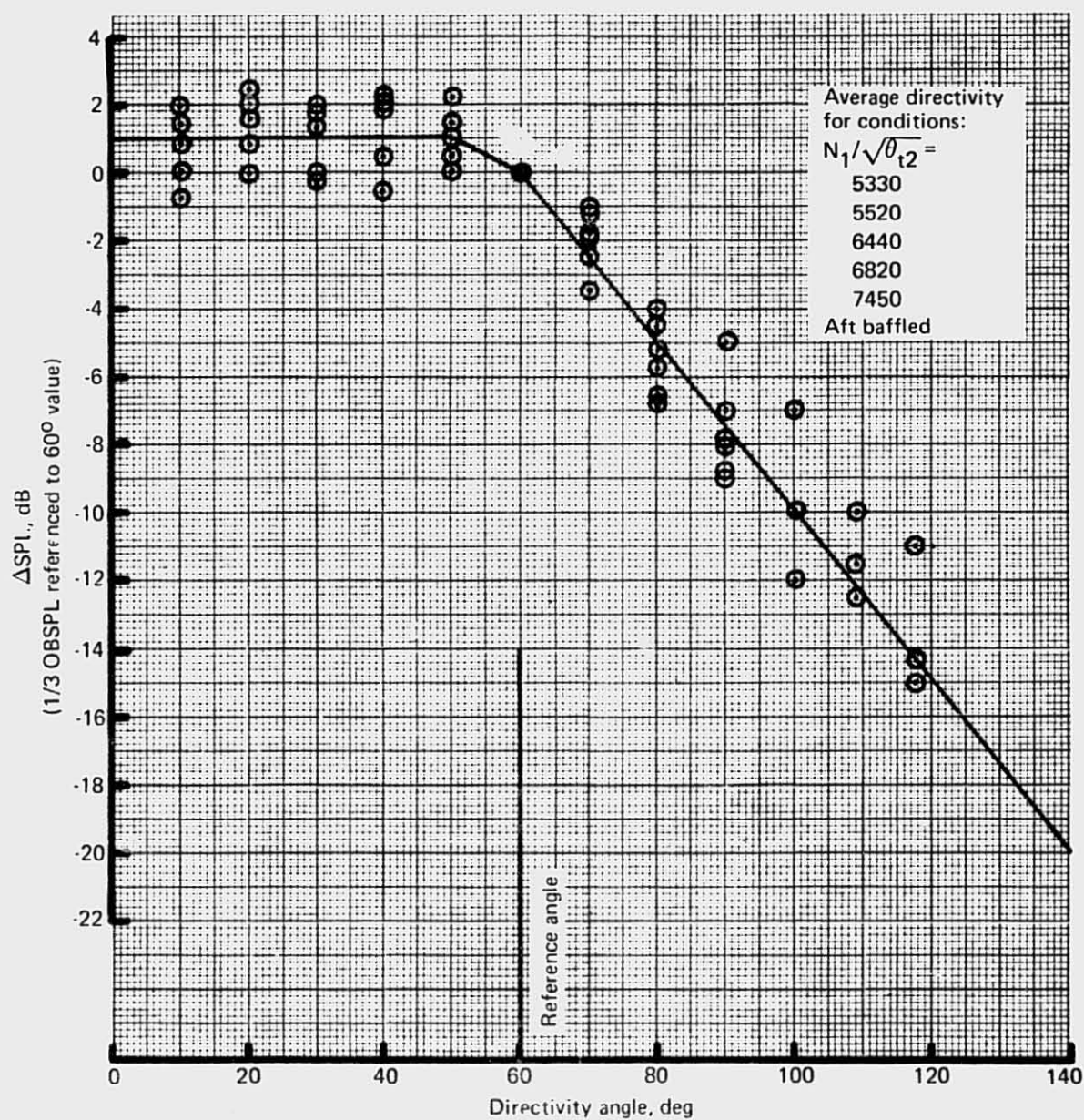


Figure 102.—JT8D-115 Ground Test—Inlet-Radiated Fan Broadband Directivity

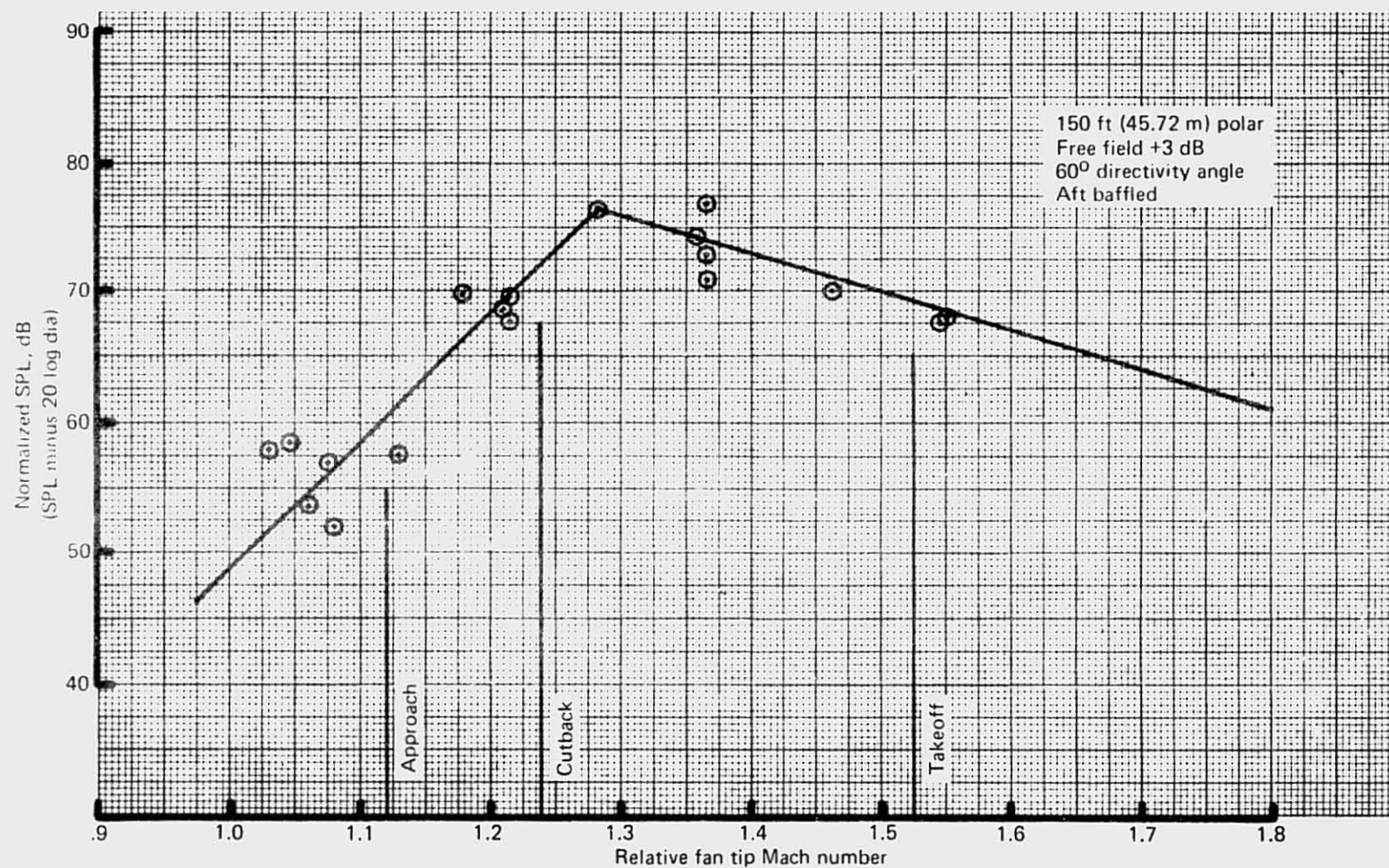


Figure 103.—JT8D-115 Ground Test—Inlet-Radiated Basic Buzzsaw Level at  $0.25 \times$  Fan Blade Passing Frequency

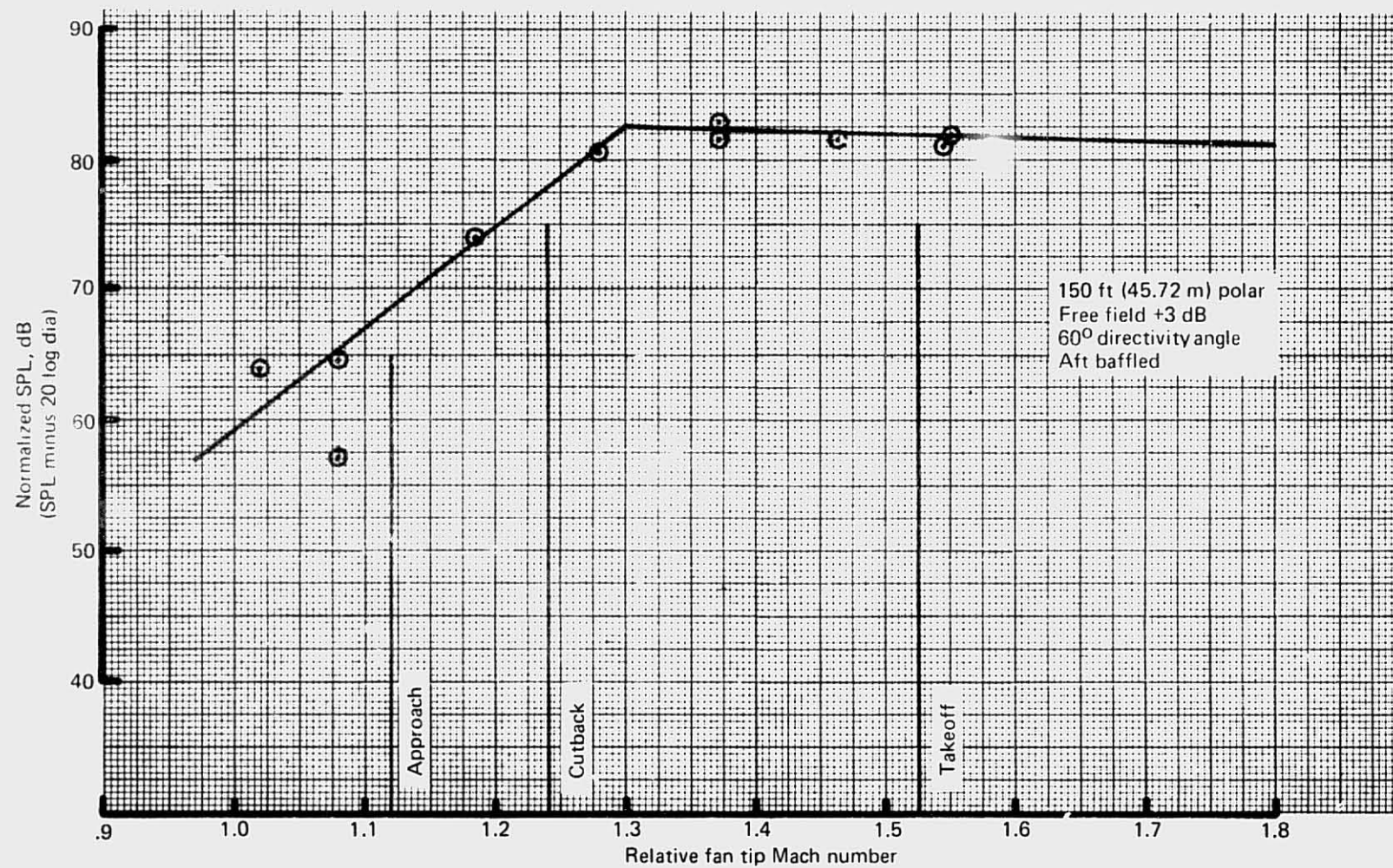


Figure 104.—JT8D-115 Ground Test—Inlet-Radiated Basic Buzzsaw Noise Level at 0.50 x Fan Blade Passing Frequency



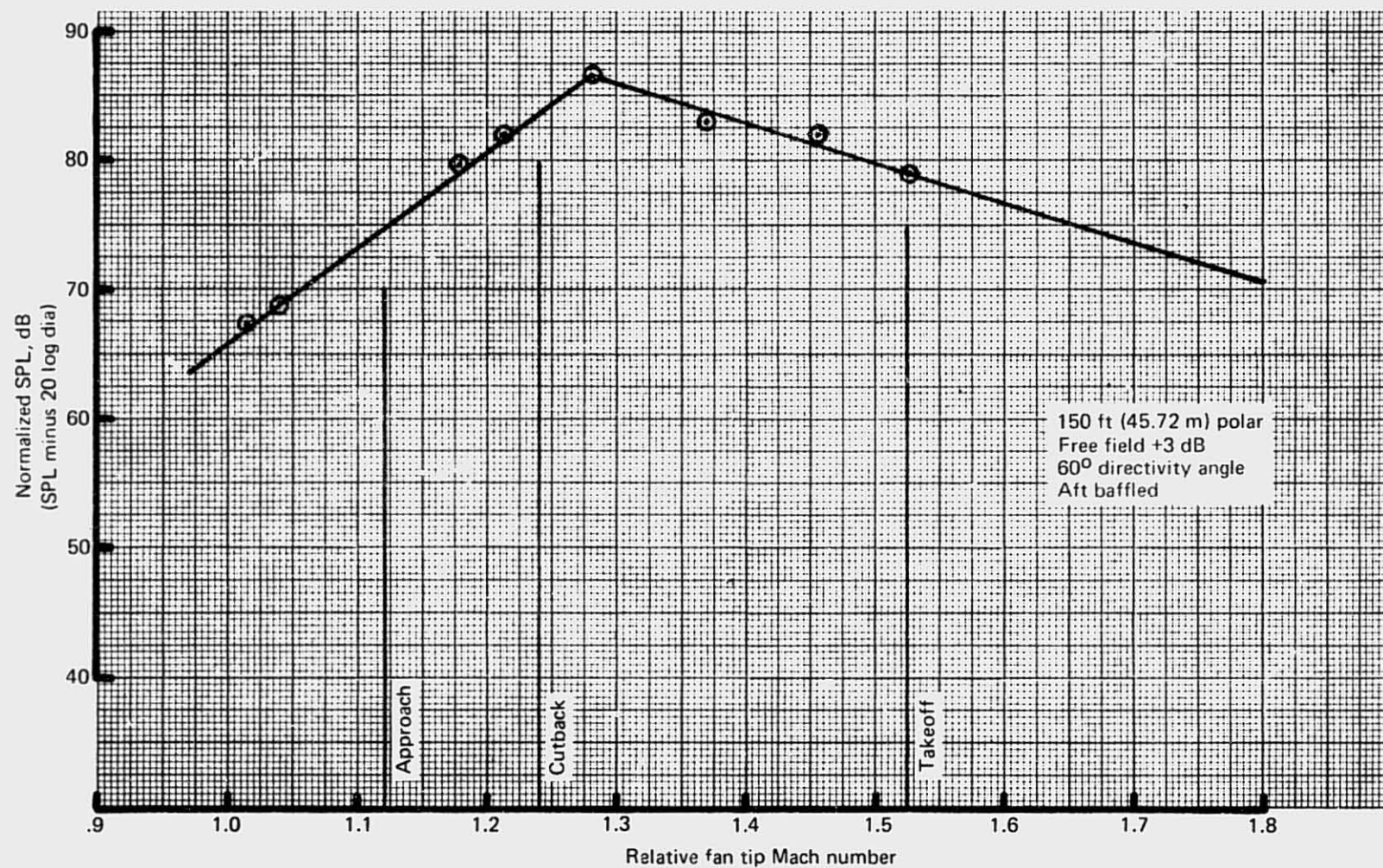


Figure 105.—JT8D-115 Ground Test—Inlet-Radiated Basic Buzzsaw Noise Level at  $0.75 \times$  Fan Blade Passing Frequency

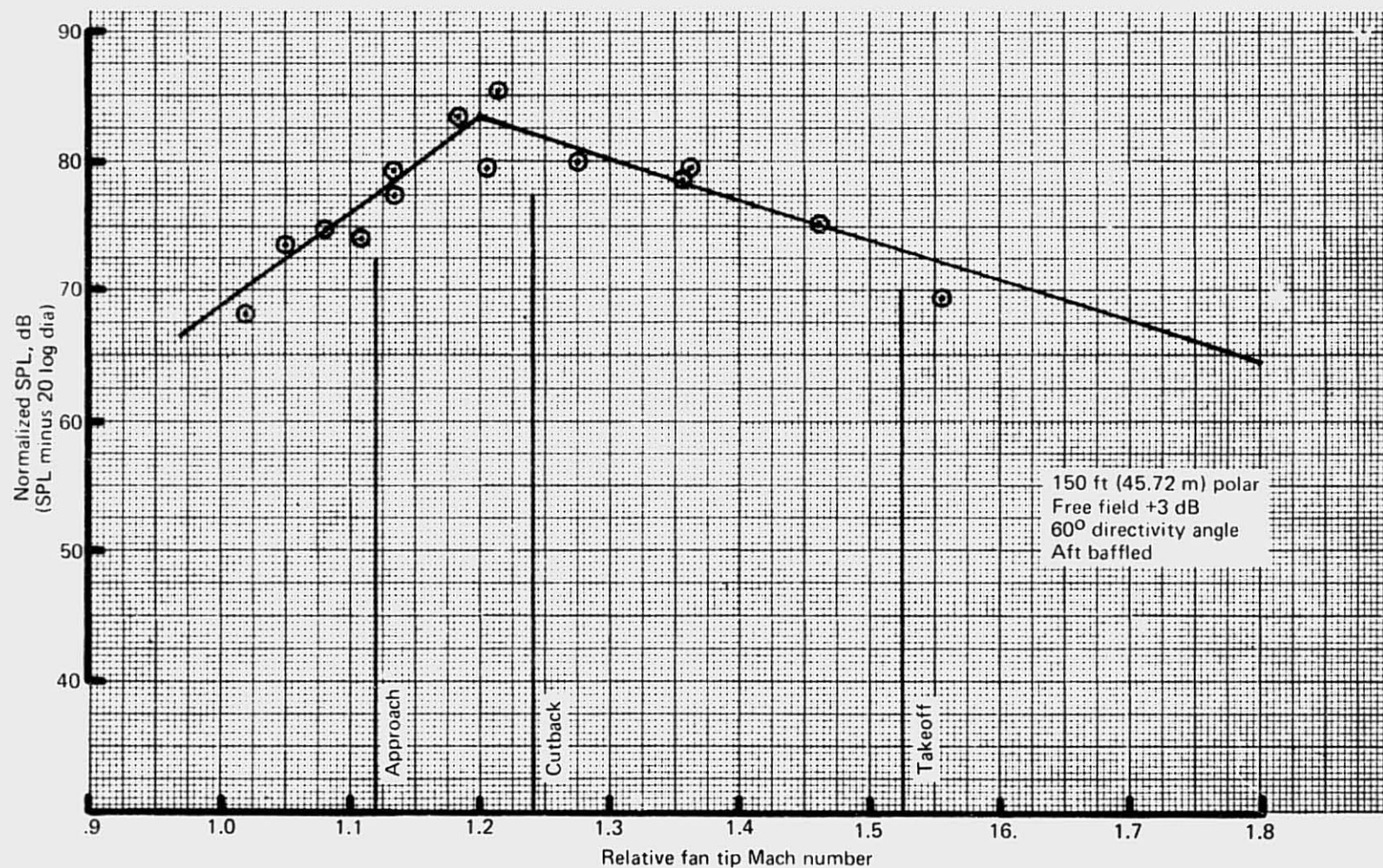


Figure 106.—JT8D-115 Ground Test—Inlet-Radiated Basic Buzzsaw Noise Level at  $1.25 \times$  Fan Blade Passing Frequency



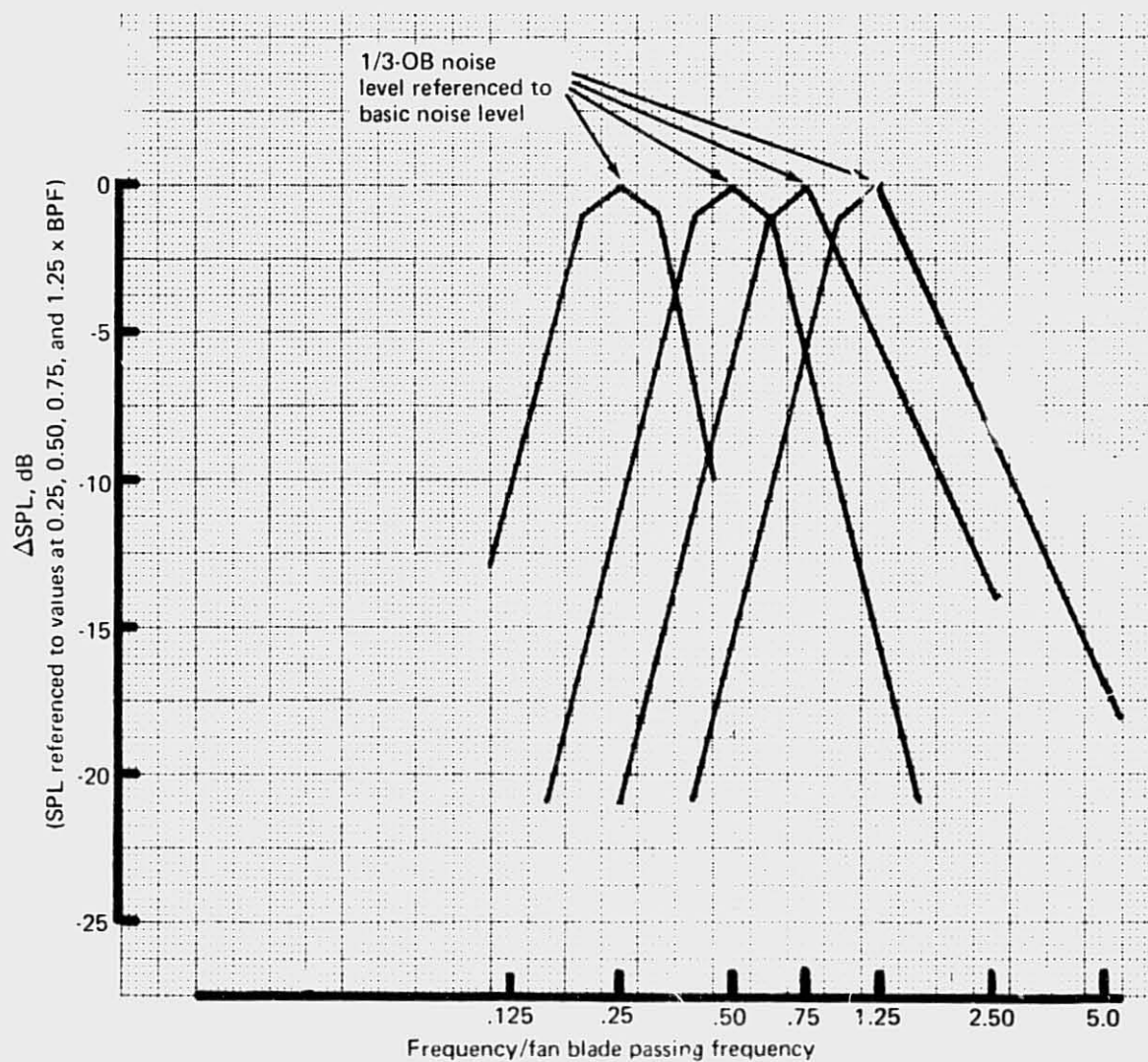


Figure 107.—JT8D-115 Ground Test—Inlet-Radiated Buzzsaw Noise Spectrum Shaping

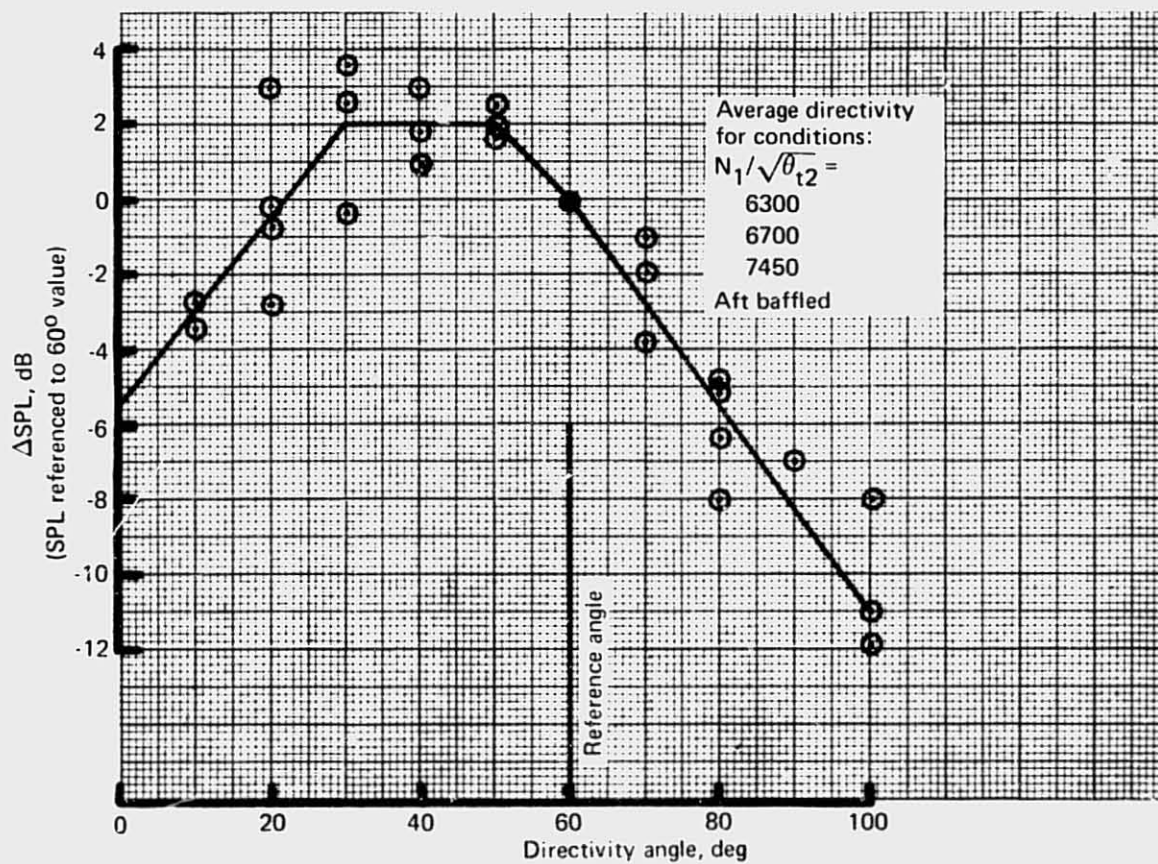


Figure 108.—JT8D-115 Ground Test -Inlet-Radiated Buzzsaw Directivity

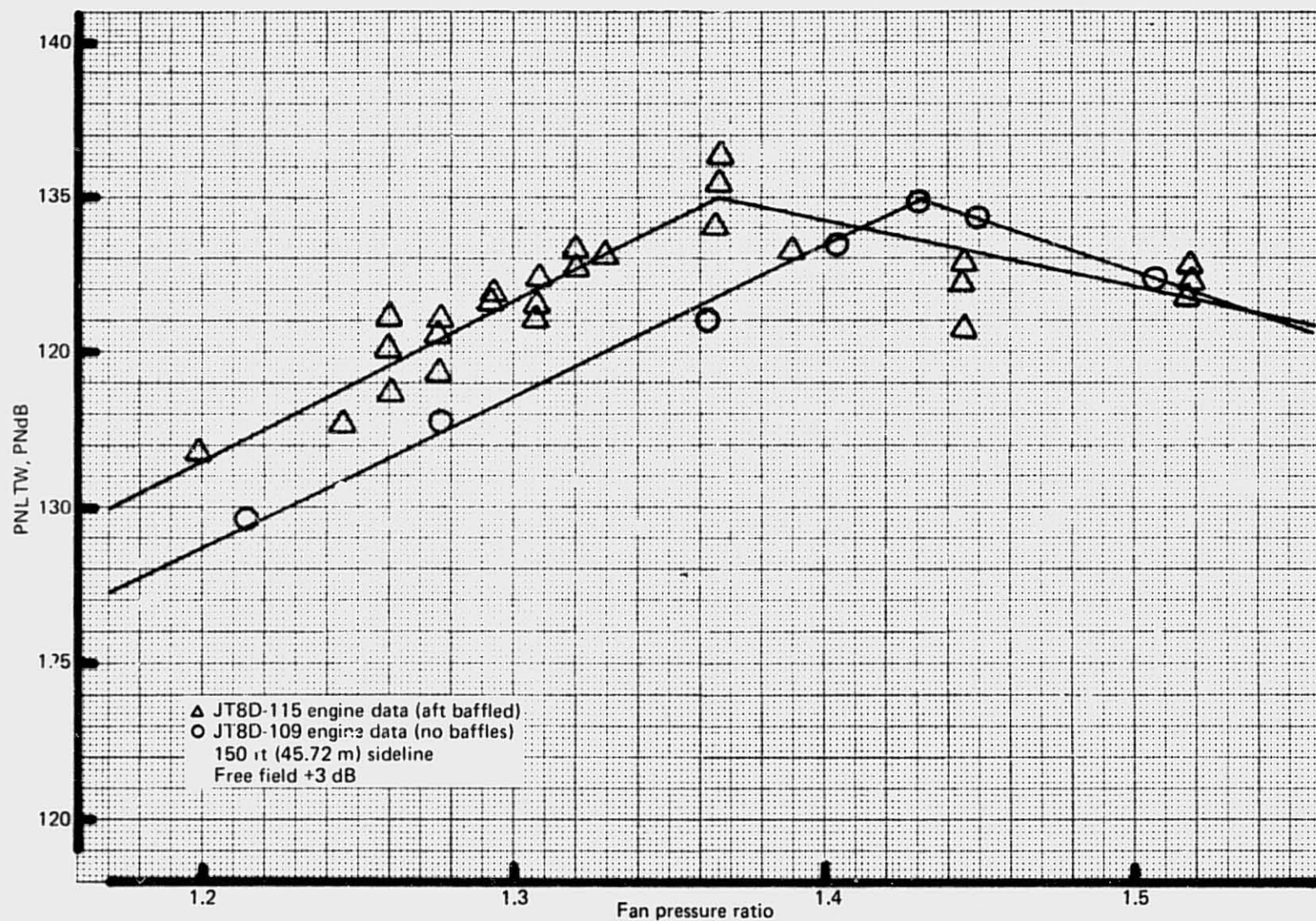


Figure 109.—JT8D-115 Ground Test—Inlet-Radiated Fan Noise Correlated on Fan Pressure Ratio



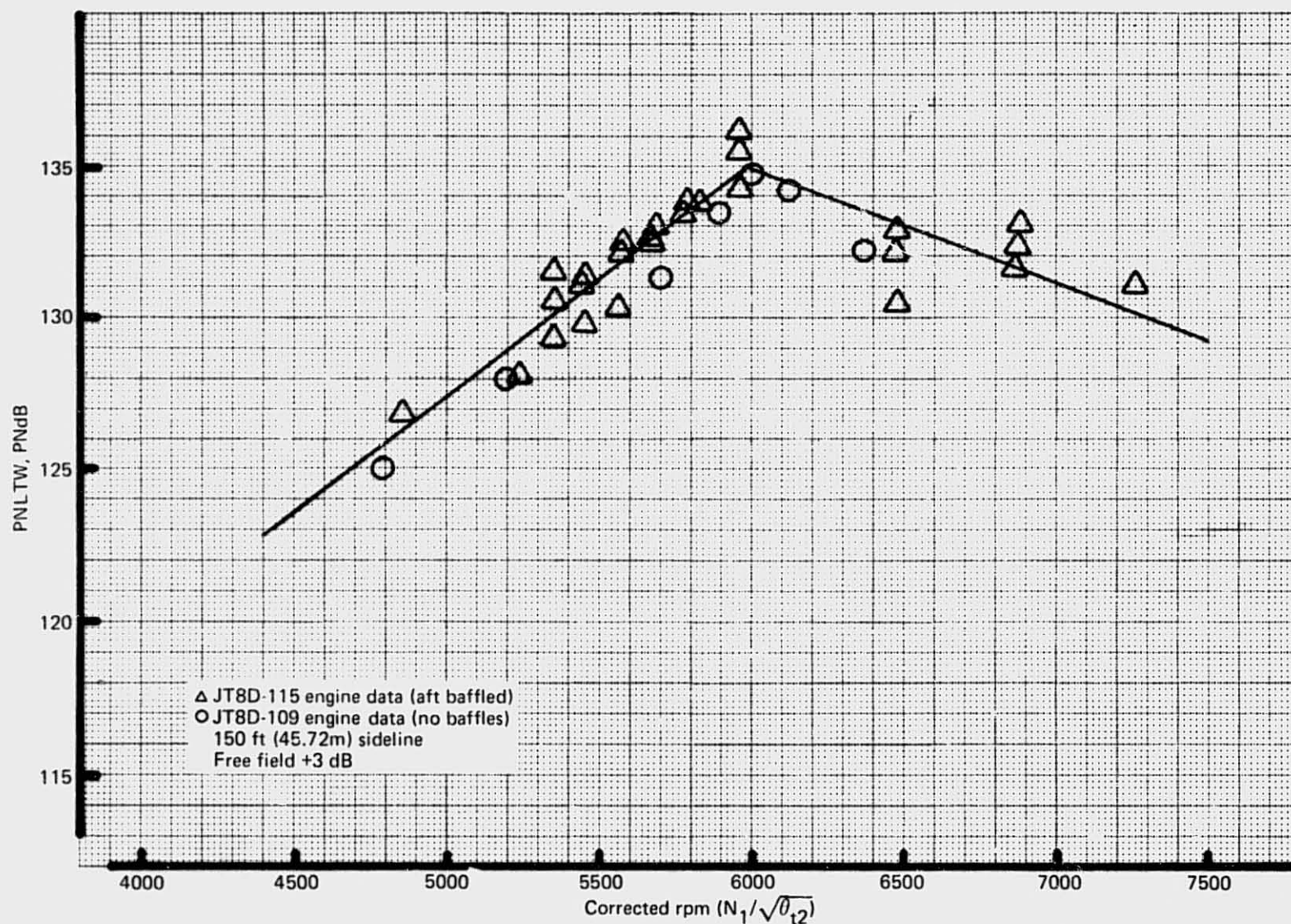


Figure 110.—JT8D-115 Ground Test—Inlet-Radiated Fan Noise Correlated on Corrected  $N_1$

#### 4.2.1.3 Discharge-Radiated Fan Noise: JT8D-15 Engine

Discharge-radiated fan noise characteristics for the JT8D-15 engine were analyzed in a manner similar to that used on the inlet radiated fan noise with a similar breakdown of subcomponents. Sample plots of discharge-radiated narrow-band spectra are shown in figure 111.

*Fan Tones.*—The noise levels of the blade passing frequency and harmonics for each fan stage were tabulated separately, since each exhibits a different directivity and amplitude relationship to power setting.\* Discharge fan tone levels were normalized to a discharge nozzle area of  $1 \text{ ft}^2 (0.0929 \text{ m}^2)$  and an airfoil spacing of 300% consistent with the procedure for inlet radiated tones. This correction has a value ranging from -2.9 to -3.6 dB over the operating range of the engine. Figure 112 is a sample plot of the directivity and throttling characteristics for discharge-radiated fan tone. A sample plot of the relationship between the fundamental and the harmonic tone levels is shown on figure 113 for discharge-radiated fan noise.

*Fan Tone Directivity.*—Discharge-radiated fan noise did not follow a smooth spatial distribution, and the data indicated directivity to vary markedly with power setting. Sample directivity curves for discharge fan tone are shown in figure 114.

*Fan Broadband Noise.*—Discharge-radiated broadband noise was established by a procedure similar to inlet-radiated noise prediction, except base noise levels (fig. 115) were given for 100%, and SPL levels were normalized to a discharge area of  $1.0 \text{ ft}^2 (0.0929 \text{ m}^2)$  (normalized  $\text{SPL} = \text{measured SPL} - 10 \log [\text{fan nozzle area, ft}^2 (\text{m}^2) - \text{rotor/stator spacing adjustment}]$ ). This correction amounts to -2.9 to -3.6 dB over the power range. Methods of extracting the data were identical to those used for inlet noise except that discharge-radiated broadband noise from the second fan was somewhat of an approximation. The second harmonic of the second fan was in the same spectrum location as turbine tones, and it was difficult to segregate the second fan broadband from that caused by the turbines. The basic noise level curve that was finally chosen for the second-stage fan discharge-radiated broadband noise is the same as that used for the first-stage fan, as shown in figure 115.

*Broadband Noise Spectrum Shaping.*—Discharge-radiated broadband fan noise was determined to have the same spectrum shape as for inlet-radiated noise (fig. 79).

*Fan Broadband Noise Directivity.*—Broadband noise directivity also showed some variation with power setting, and the resulting curve (fig. 116) was obtained by taking an average of that obtained at approach, cutback, and takeoff power.

*Vane Spacing Correction.*—All SPL values for discharge radiation tones and broadband noise have been normalized to 300% vane spacing as was done with inlet-radiated fan noise.

\*These tabulations (tables A-8 through A-12) are included in the supplementary data in the appendix.



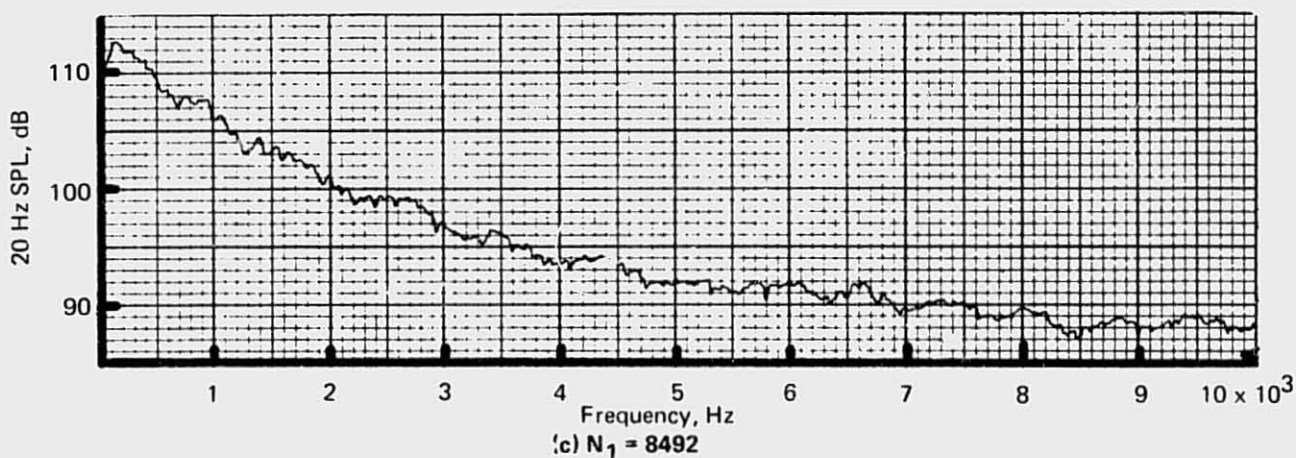
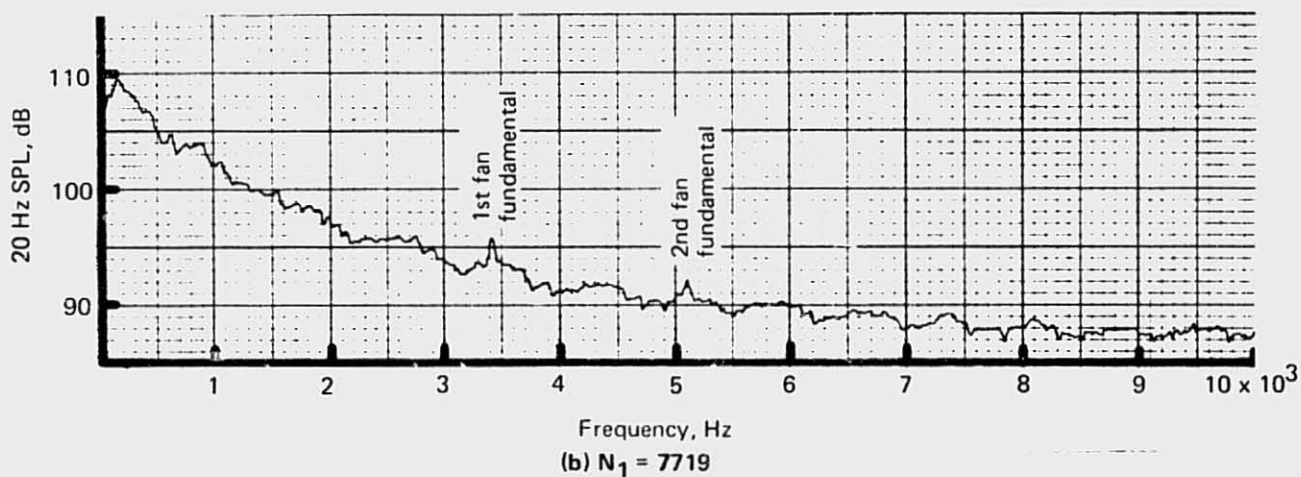
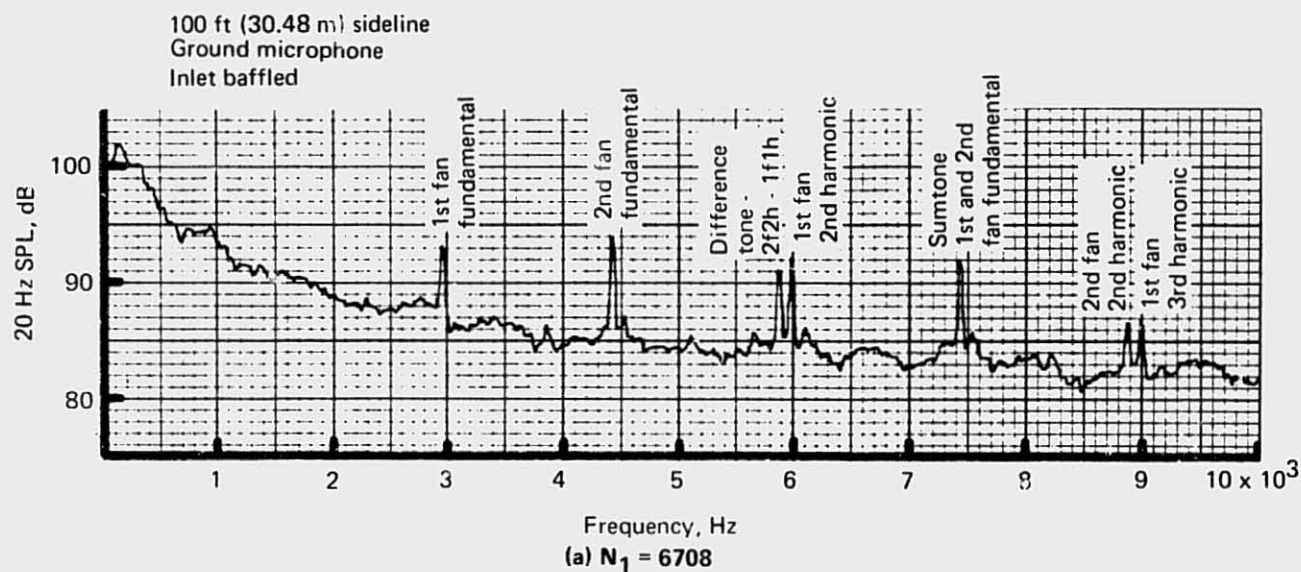


Figure 111.—JT8D-15 Ground Test—Sample Discharge-Radiated Narrow Band Spectra,  $120^\circ$  Directivity Angle

REPRODUCIBILITY OF THE  
ORIGINAL PAGE IS POOR

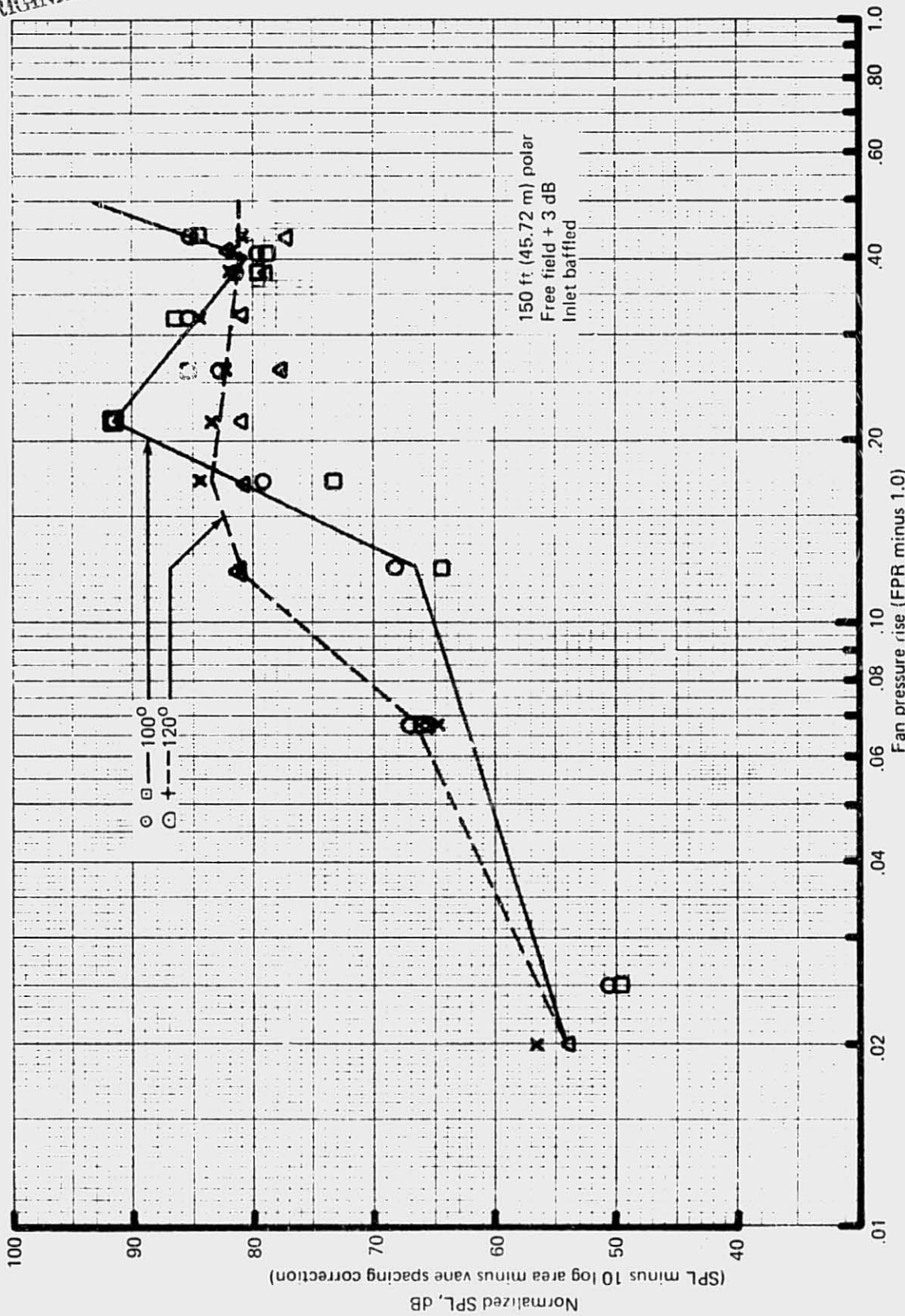


Figure 112.—JT8D-15 Ground Test—Discharge-Radiated First Fan Fundamental Tone Versus Fan Stage Pressure Rise

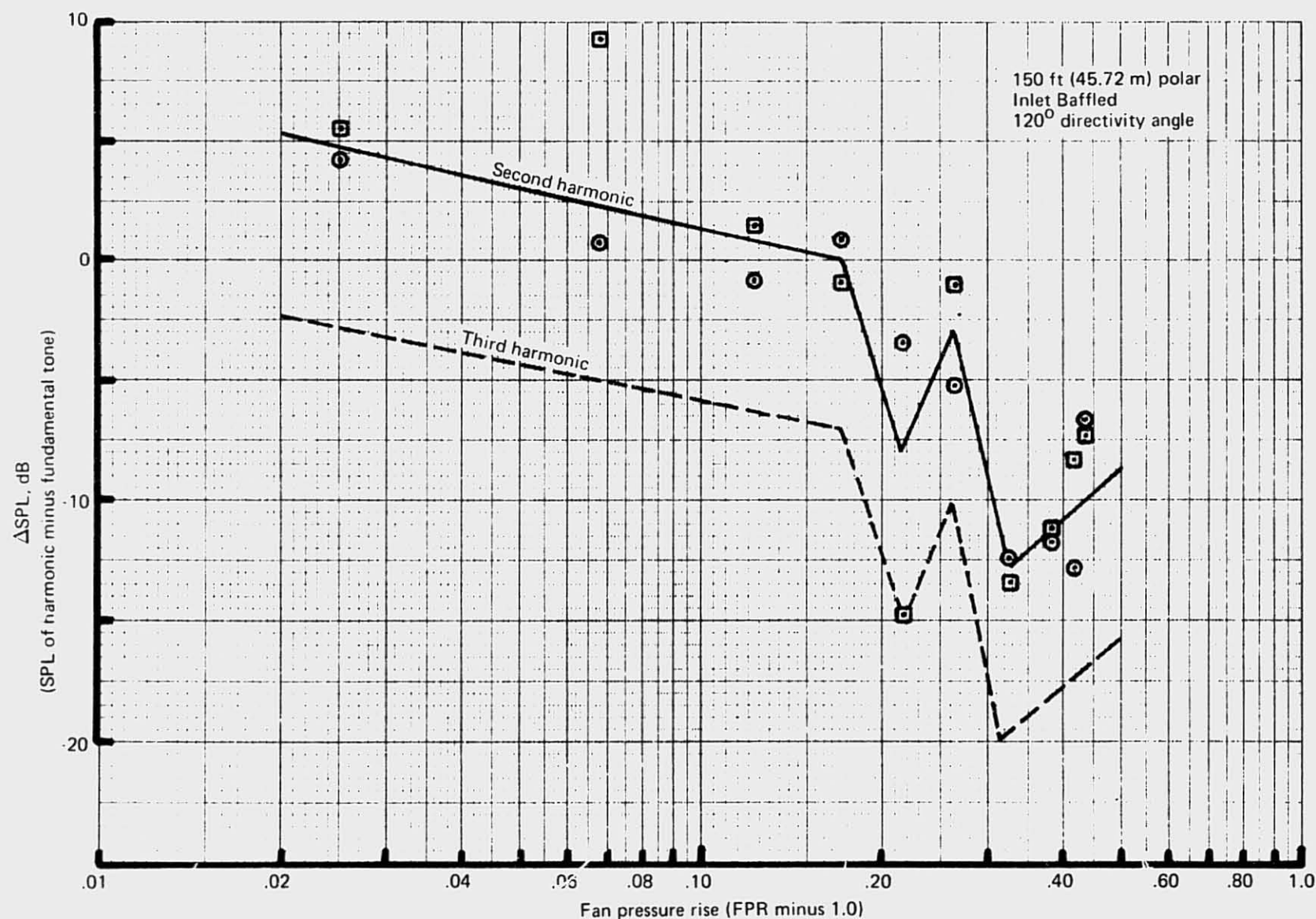


Figure 113.—JT8D-15 Ground Test—Discharge-Radiated First Fan Harmonics  
Relative to Fundamental Tone

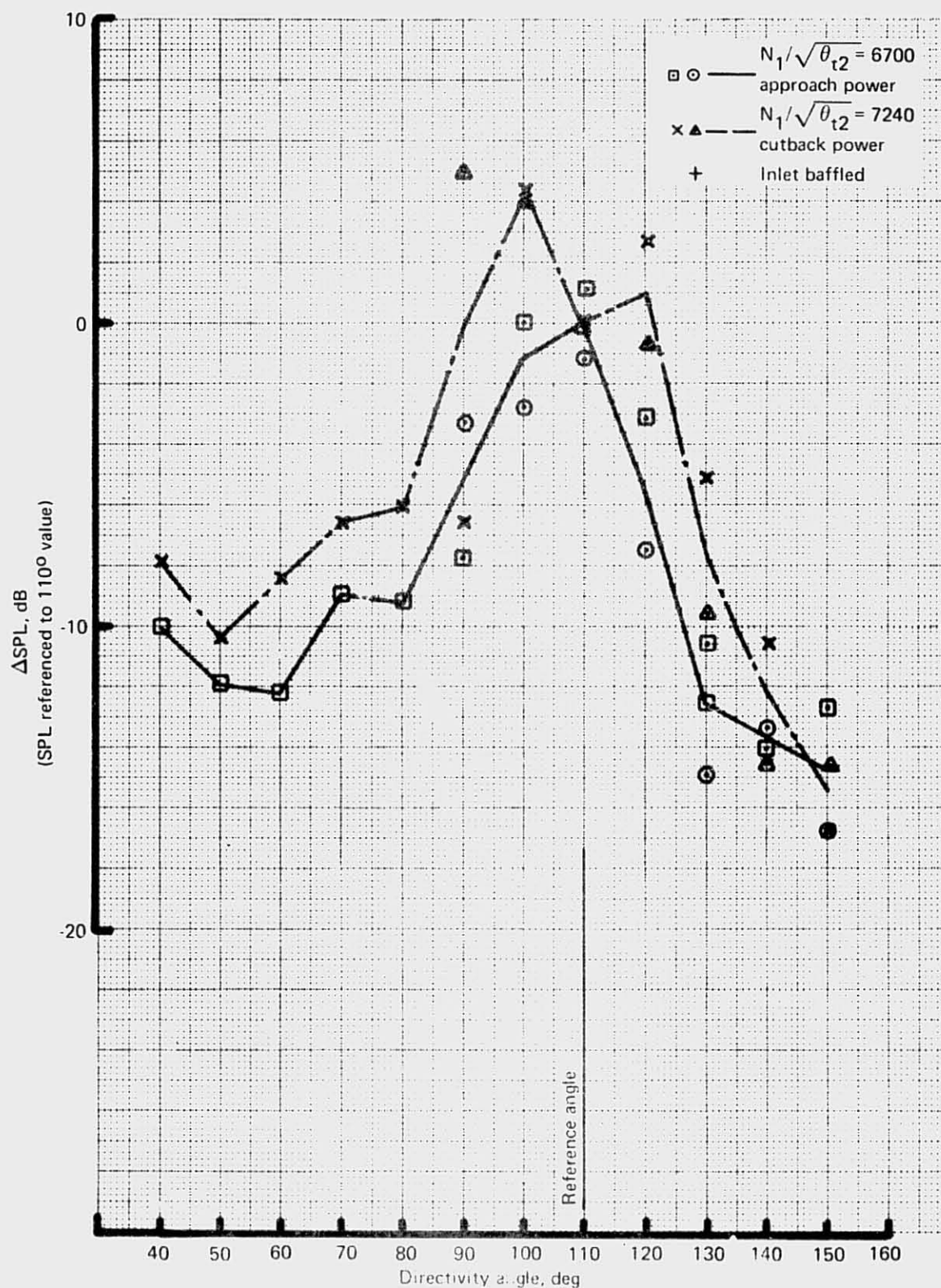


Figure 114.— JT8D-15 Ground Test—Discharge-Radiated First Fan Fundamental Tone Directivity



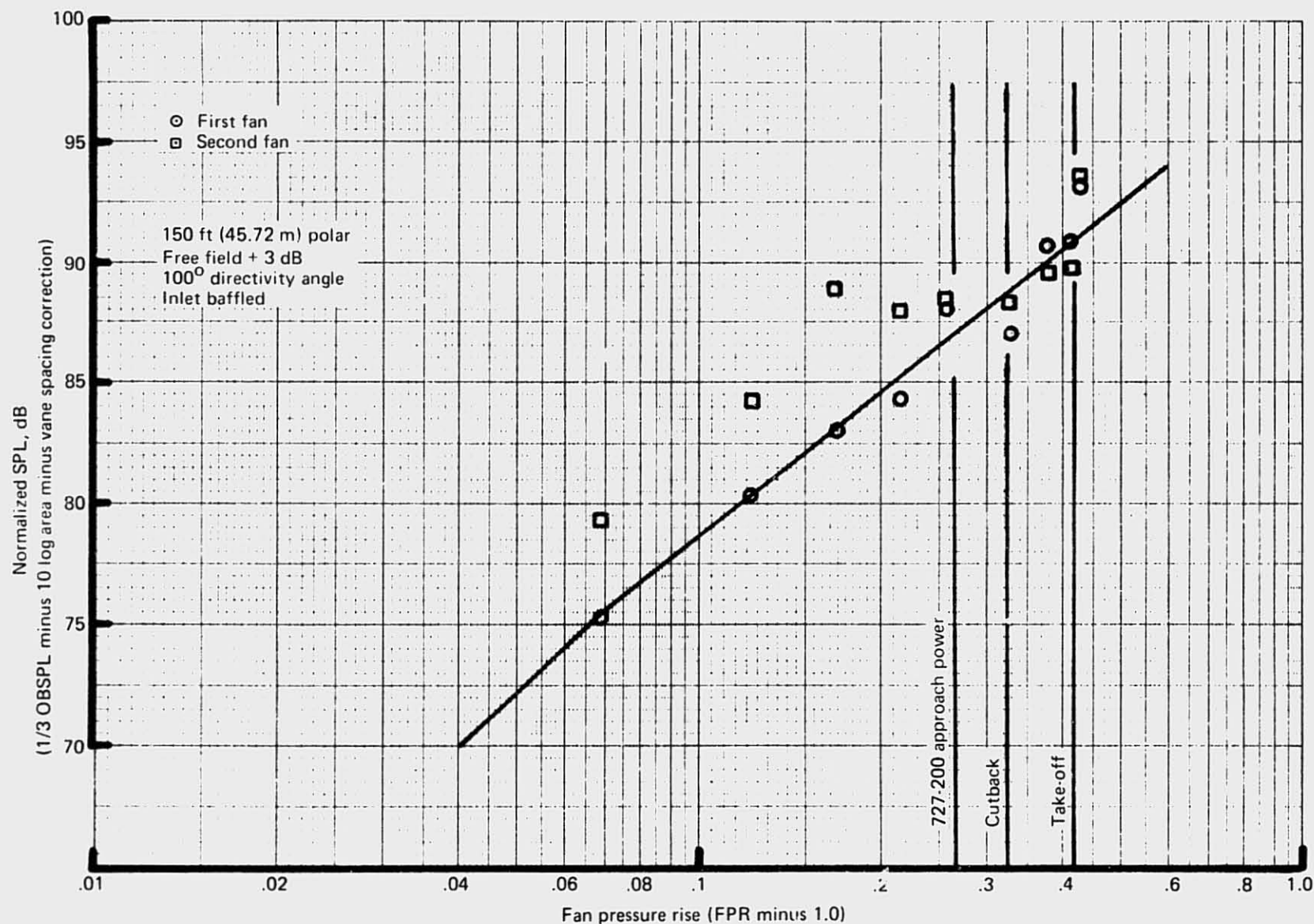


Figure 115—JT8D-15 Ground Test—Discharge-Radiated Fan Peak Broadband Noise  
for First- or Second-Stage



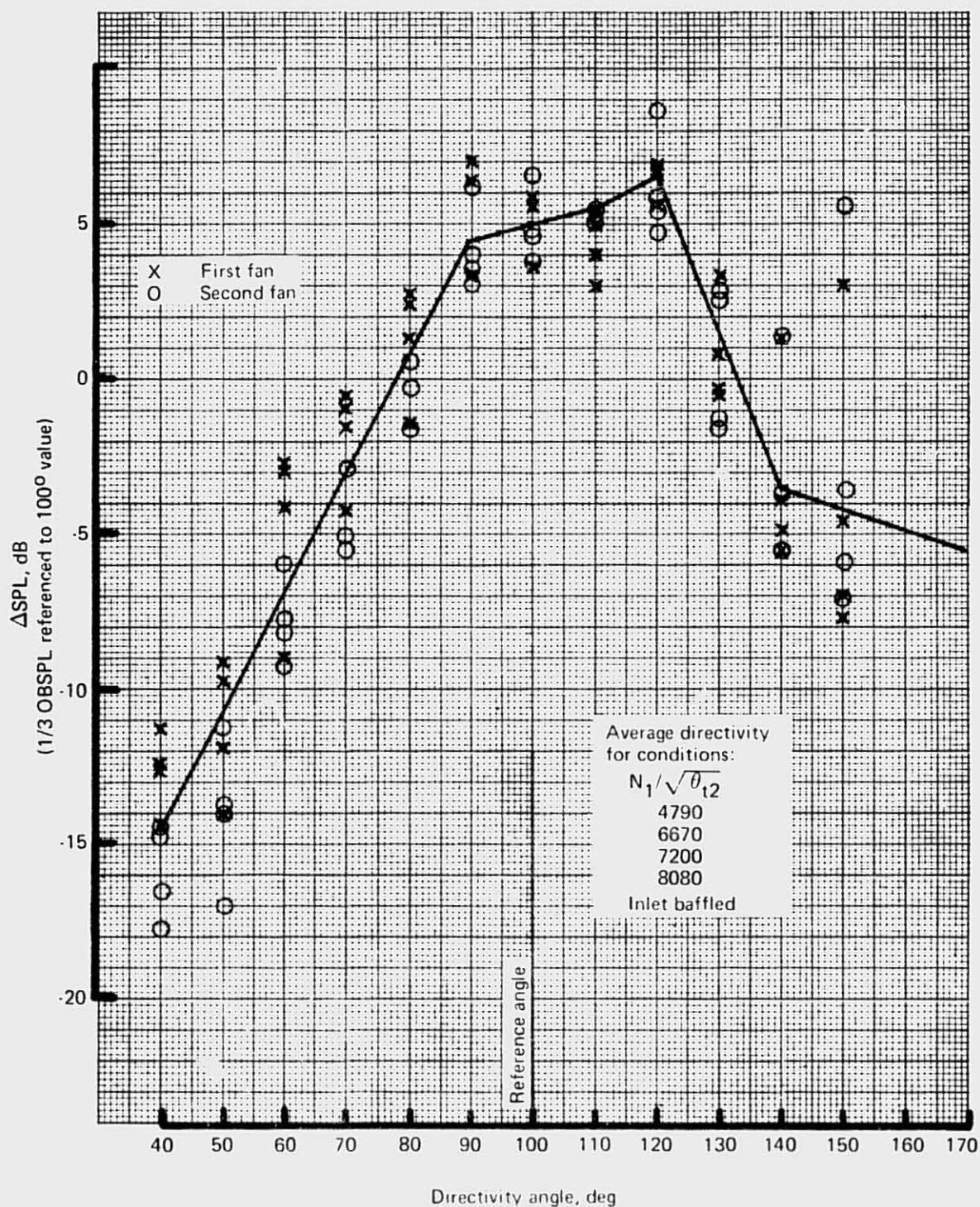


Figure 116.—JT8D-15 Ground Test—Discharge-Radiated Fan Broadband Noise Directivity for Either Fan Stage

#### 4.2.1.4 Discharge-Radiated Fan Noise: JT8D-115 Engine

The JT8D-115 engine as tested included a heavily treated fan case; consequently, discharge-radiated fan noise made only a minor contribution to total engine noise. Analysis of discharge-radiated fan noise was carried out in a similar manner to that used for inlet noise. Discharge-radiated fan noise predictions have been normalized as follows: (1) noise levels at 150-ft (45.72-m) polar arc, (2) noise levels at  $110^\circ$  from engine centerline, (3)  $1\text{-ft}^2$  ( $0.0929\text{-m}^2$ ) fan discharge area, (4) free field plus 3 dB, and (5) 300% rotor/stator spacing. These corrections have the following values for the JT8D-115 engine:

	<u>Discharge area correction</u>	<u>Rotor/stator spacing</u>
Tones	-6.7 to -7.0 dB	-1.8 dB
Broadband noise	-6.7 to -7.0 dB	-1.0 dB

*Fan Tones.* – Basic noise levels for the discharge-radiated fundamental fan tone and second harmonic are shown in figures 117 and 118, as a function of fan pressure rise. The fundamental tone level is presented at the reference angle of  $110^\circ$ , while the second harmonic level is given as an increment from the fundamental.

*Fan Tone Directivities.* – The discharge-radiated fan tone is subject to the same kind of fluctuation as the inlet fan tone at lower powers, but is almost undetectable above approach power. Therefore, one curve which has been established from data taken at low power settings (fig. 119) is used to define tone directivity at all power settings.

*Fan Broadband Noise.* – Basic noise levels for discharge-radiated fan broadband noise are given in figure 120 as a function of fan pressure rise at the reference directivity angle of  $110^\circ$ .

*Fan Broadband Noise Spectrum Shaping.* Discharge-radiated fan broadband noise is difficult to separate from other discharge noise components. For example, at low power settings (approach power and below), core and turbine noise are dominant noise sources. Since core noise peaks around 400 or 500 Hz, it does not present too great a problem. However, turbine noise, which is characterized by considerable “haystack” broadband noise above and below the extreme discrete frequencies of the turbine stages, masks the fan broadband noise. Therefore, in the turbine frequency range, fan broadband noise levels were estimated by interpolating between the levels above and below the turbine haystack.

At high power settings, core noise becomes less significant, and the turbine haystack is less prominent. On the other hand, jet noise is the major contributor to the total discharge-radiated noise at frequencies up to 2 kHz. Thus, broadband fan noise can only be definitely identified at frequencies above 2 kHz in the cutback and takeoff power range.

A single spectrum shaping was ultimately derived, which is the same as the inlet broadband shaping (see fig. 101).

*Fan Broadband Noise Directivity.* – Discharge-radiated broadband noise has, on average, a similar directivity pattern at all power settings (fig. 121).

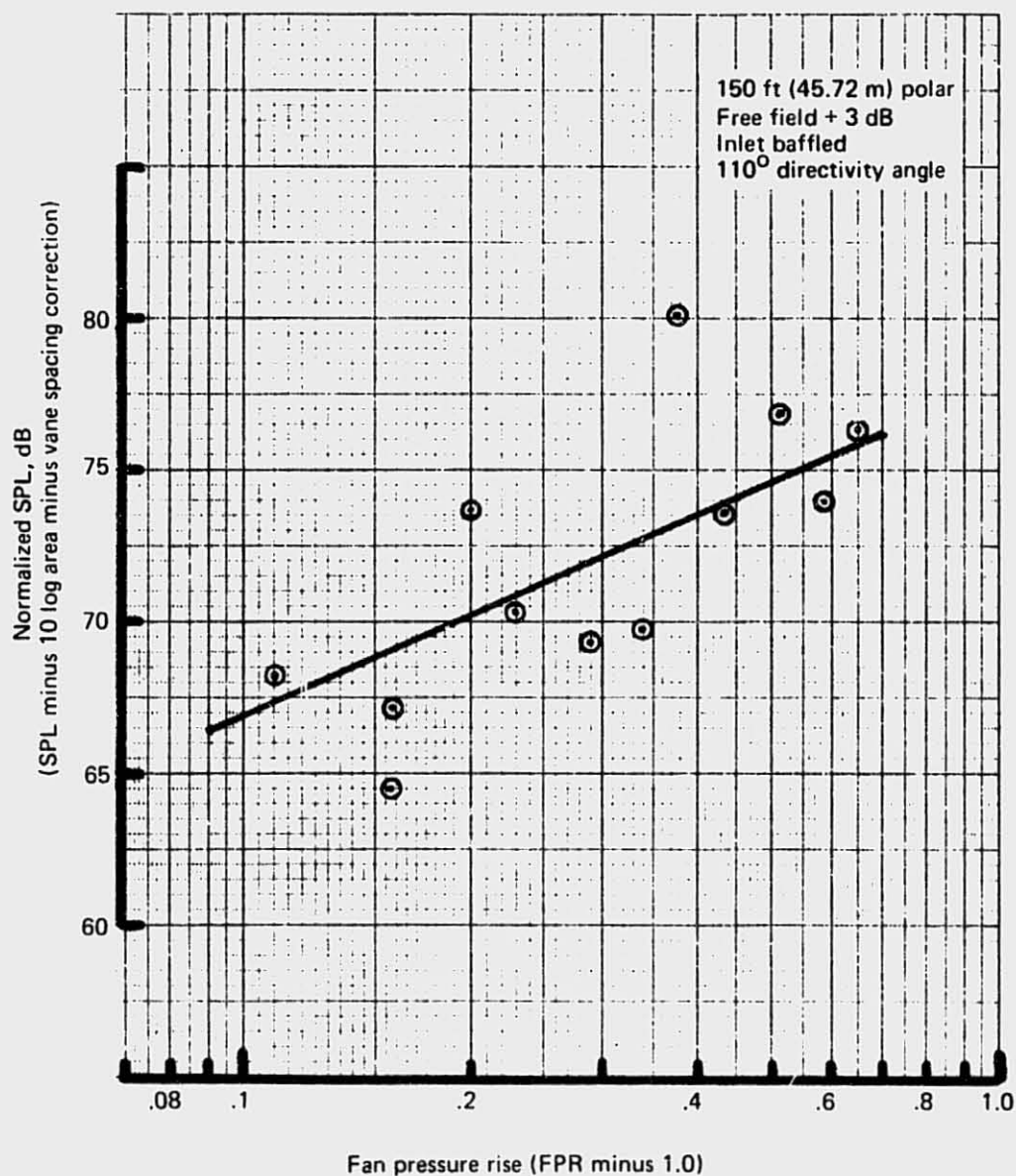


Figure 117.—JT8D-115 Ground Test—Basic Noise Level of Discharge-Radiated Fundamental Fan Tone

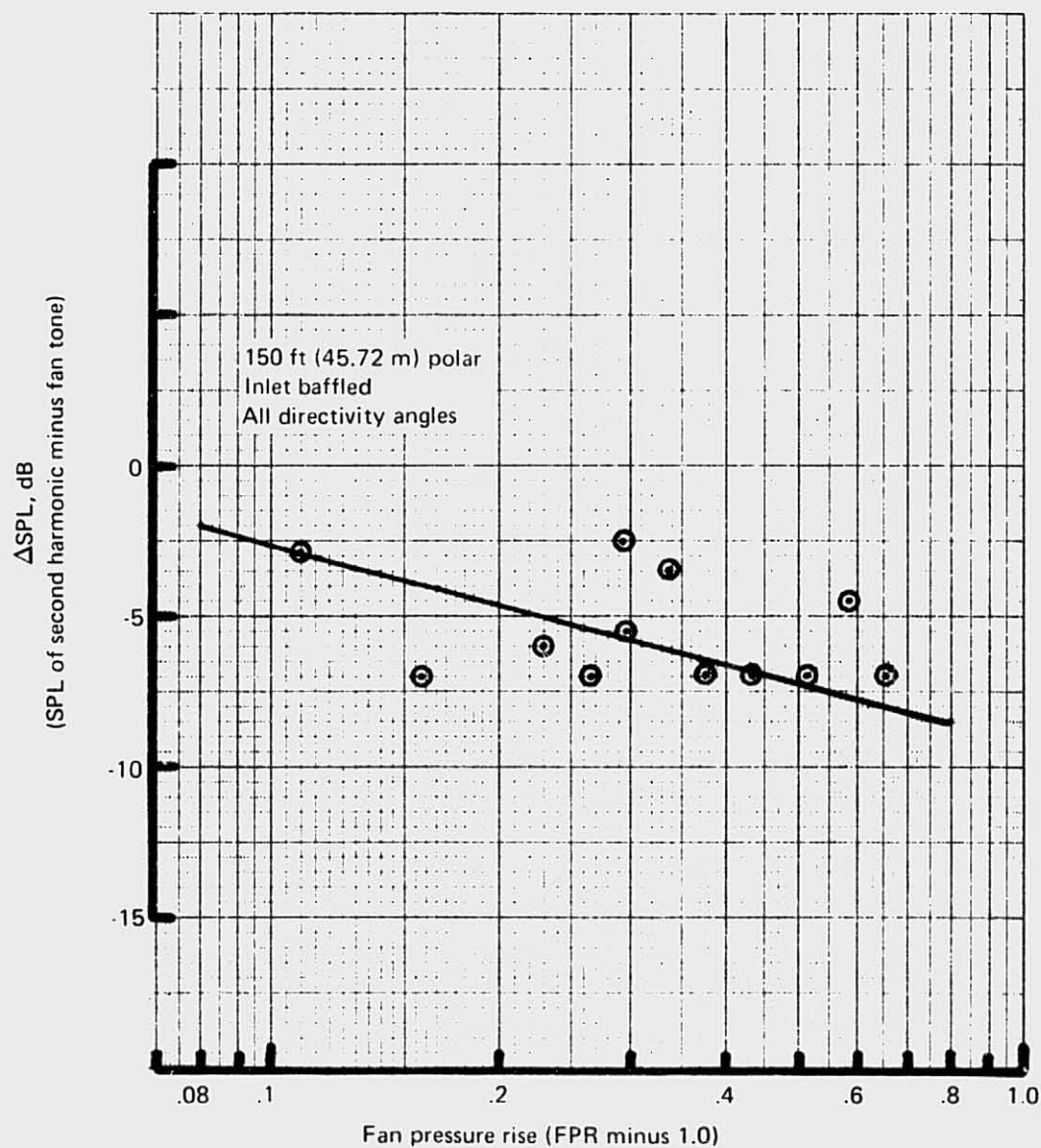


Figure 118.—JT8D-115 Ground Test—Relationship Between Discharge-Radiated Second Harmonic and Fundamental Fan Tone



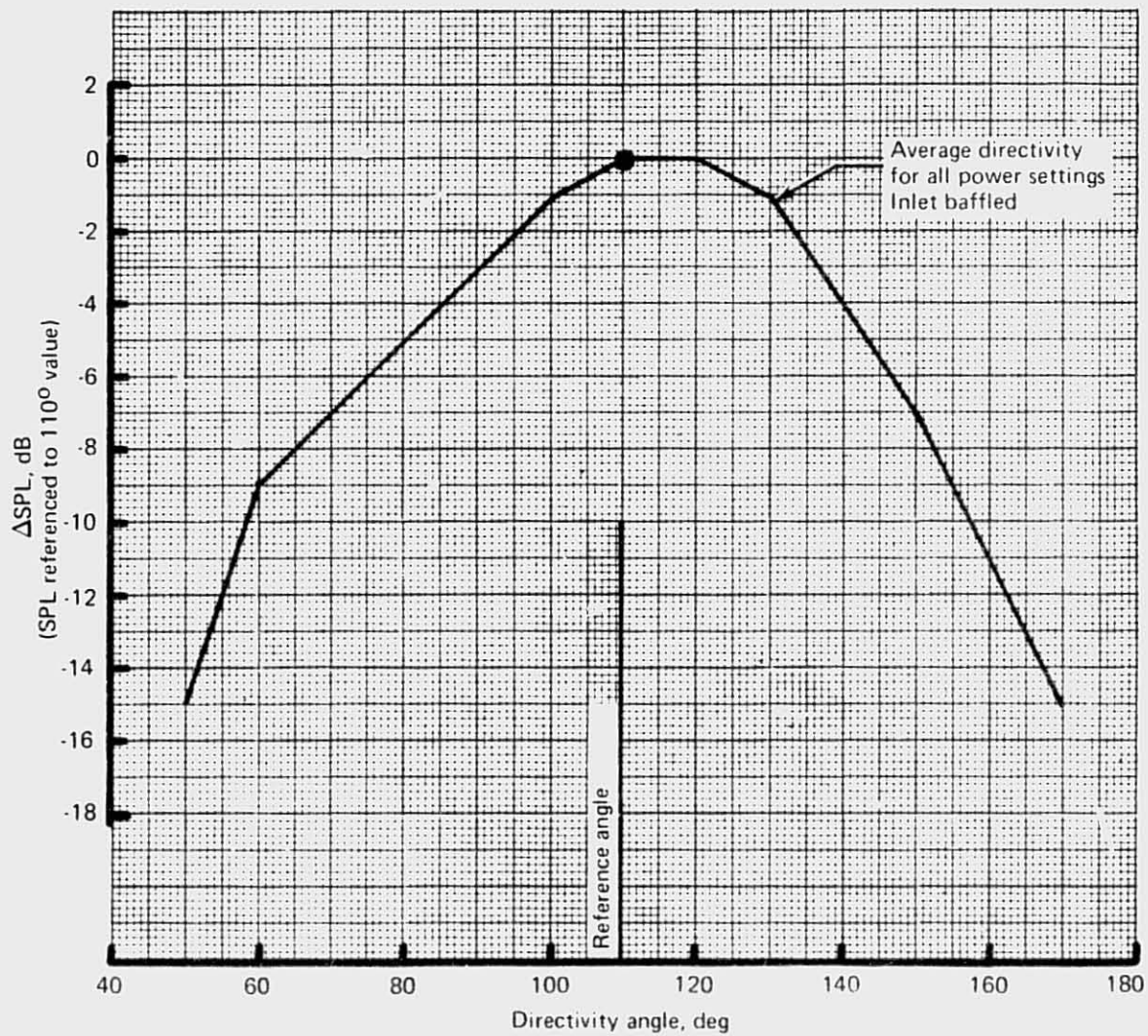


Figure 119.—JT8D-115 Ground Test—Discharge-Radiated Fan Tone Directivity



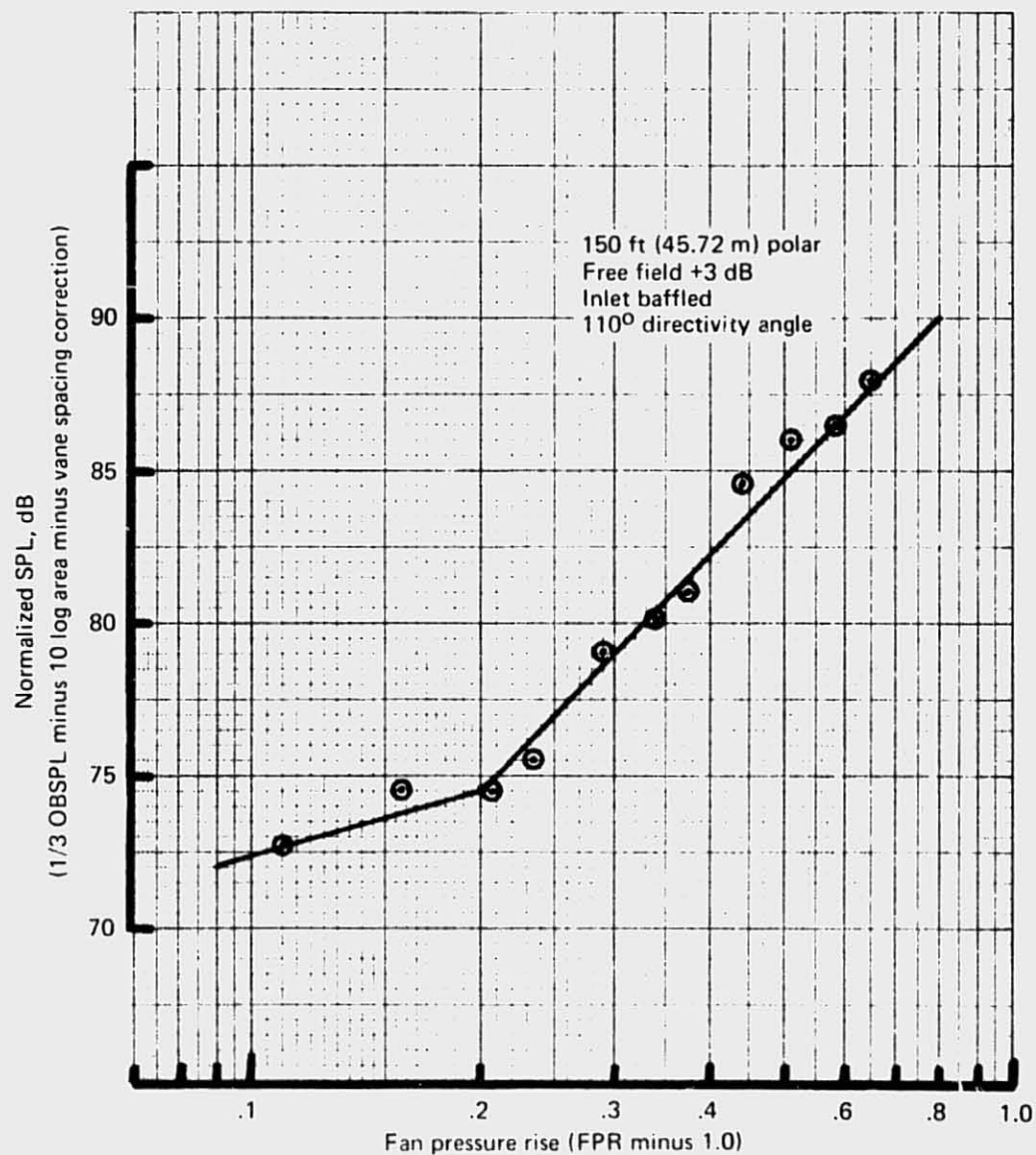


Figure 120.—JT8D-115 Ground Test—Discharge-Radiated Fan Broadband Basic Noise Level

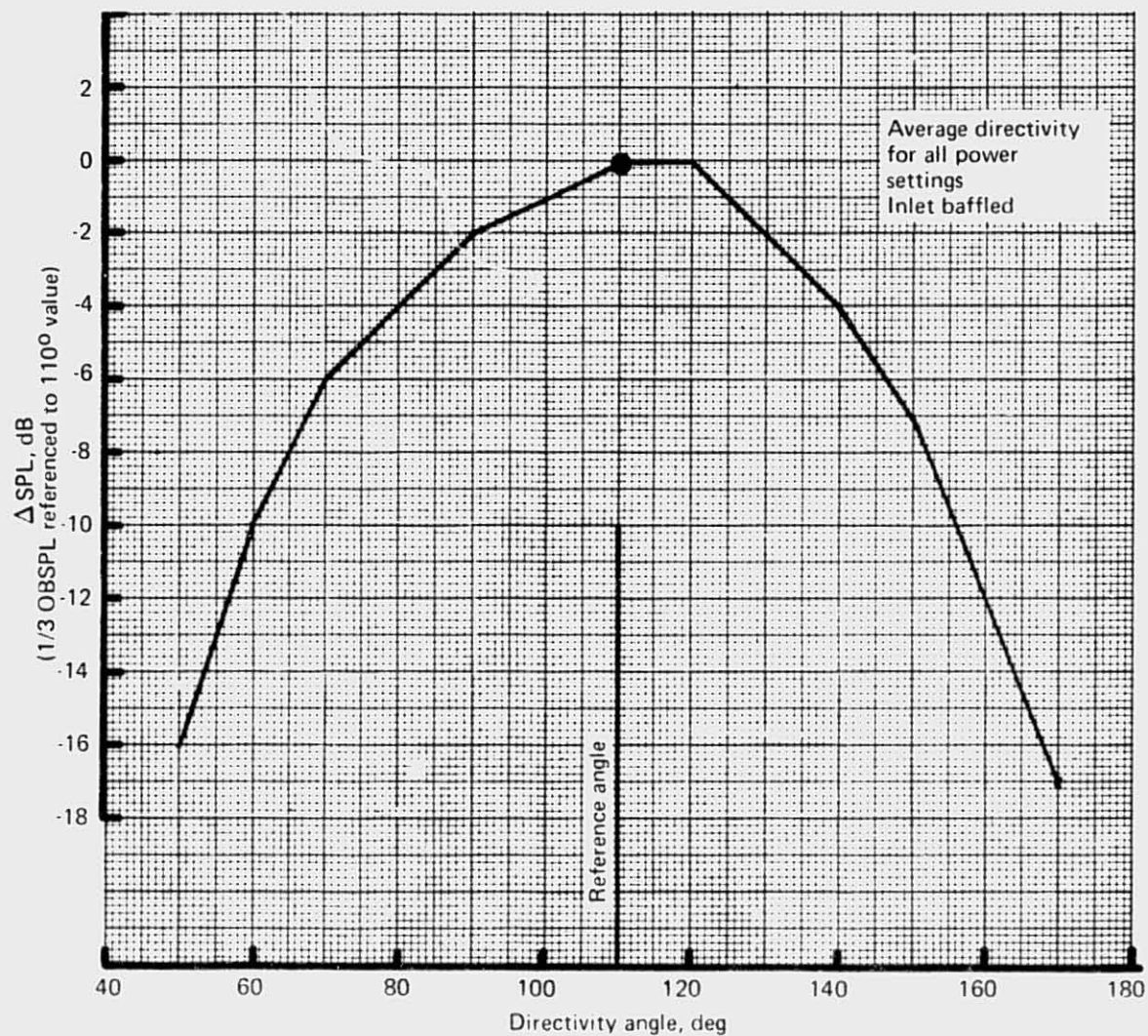


Figure 121.—JT8D-115 Ground Test—Discharge Radiated Fan Broadband Noise Directivity

#### 4.2.1.5 Turbine Noise: JT8D-15 Engine

Turbine noise makes only a minor contribution to total engine noise on the JT8D-15 engine because of the jet noise dominance of the total noise. Consequently, no attempt has been made to analyze the JT8D-15 engine turbine noise, but rather predictions have been made using an existing analytical model for turbine noise. This analysis is not presented here, but the turbine noise prediction results can be seen in section 4.2.2.1 along with other component predictions based on the ground test data analysis.

#### 4.2.1.6 Turbine Noise: JT8D-115 Engine

Analysis of the JT8D-115 test results showed that turbine noise is a significant contributor to the total noise of the refan engine because of reduced jet noise particularly in the approach power range. The JT8D-115 turbine has four turbine stages: one high-pressure stage and three low-pressure stages. The blade numbers of each stage are:

- First stage (HP1) - 80 Blades
- Second stage (LP2) - 88 Blades
- Third stage (LP3) - 92 Blades
- Fourth stage (LP4) - 74 Blades

In the analysis it was found that only the three low-pressure stages (LP2, LP3, and LP4) could be identified as contributing to the turbine noise. Because of the similarity of the blade numbers, the fundamental blade passing frequency tones of LP2 and LP3 occur close together and are often in the same 1/3-OB. Similarly, the fundamental blade passing frequency tone of LP4 and the fan second harmonic tone generally occur in the same 1/3-OB. These phenomena make it difficult to identify the individual turbine stage contribution to the 1/3-OB sound pressure level.

Far-field turbine noise consists of high-frequency tones, corresponding to the turbine blade passing frequencies, superimposed on a strong broadband noise floor which peaks near each of the tone frequencies. The peaking broadband, called the turbine haystack, is evident at low power settings and frequencies of 7 to 8 kHz in the narrow band data included in this section (fig. 122). The far-field turbine noise peaks in the aft quadrant at a directivity angle between  $100^\circ$  and  $120^\circ$ . A reference directivity of  $120^\circ$  was chosen for use in the prediction procedure. Narrow band acoustic data (20-Hz bandwidth) revealed a steady increase in turbine noise with increasing power setting, from a low at idle to a peak near approach power. With further increases in power settings, the turbine noise decreases until it disappears in the noise floor produced by the jet and fan sources.

*Turbine Tones.*—Examination of the sample narrow band spectral plots in figures 123 and 124 for directivity angles  $90^\circ$  through  $160^\circ$  and two power settings shows that turbine tones are generally identifiable above broadband noise, but often the tones contribute little to the total 1/3-OB level. Basic turbine tone levels extracted from the narrow band

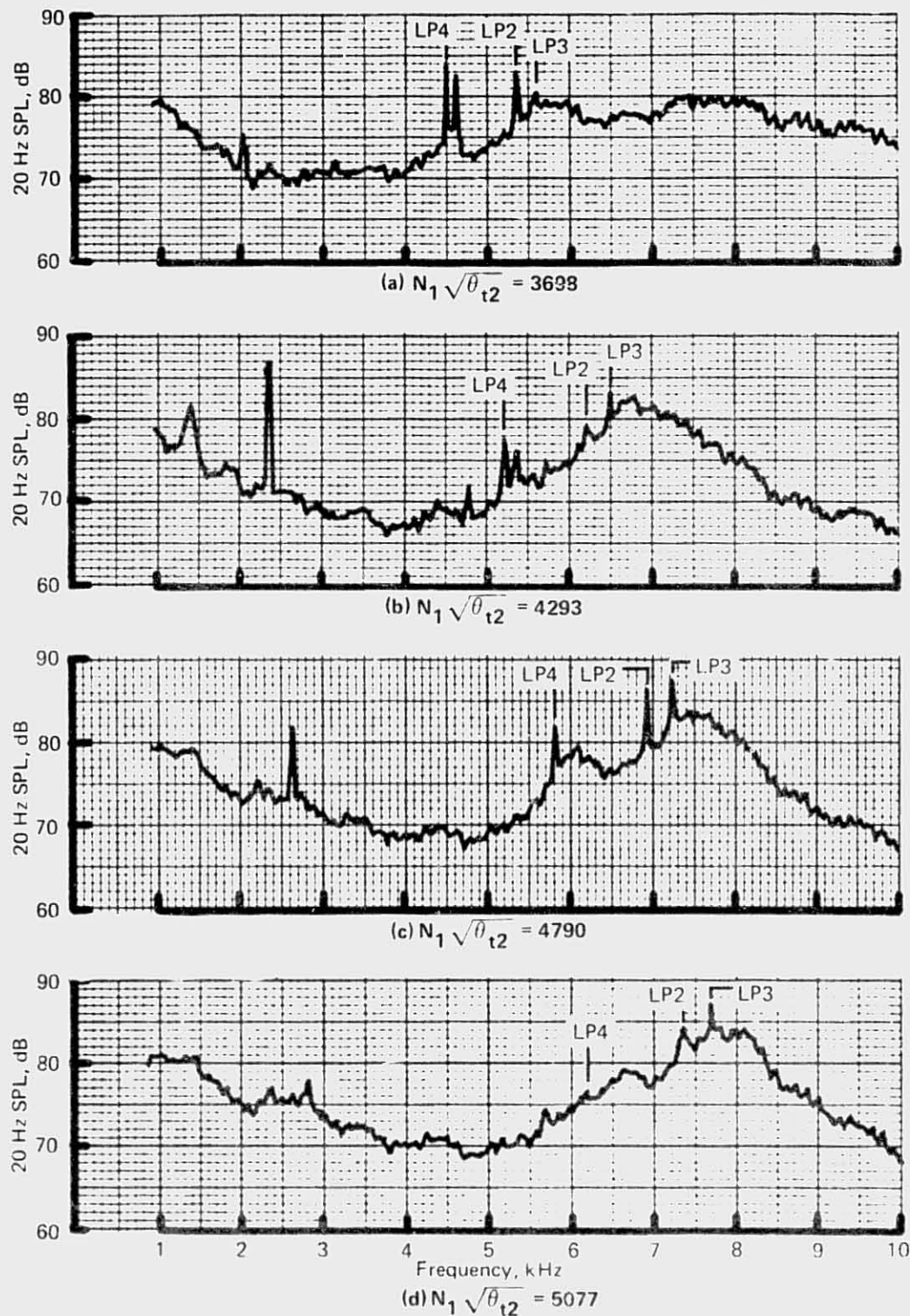


Figure 122.—JT8D-115 Ground Test—Inlet Baffled Narrow Band Spectra for Various Power Settings at a Constant Directivity Angle ( $120^\circ$  Ground Microphone, 100 ft (30.48 m) Sideline)

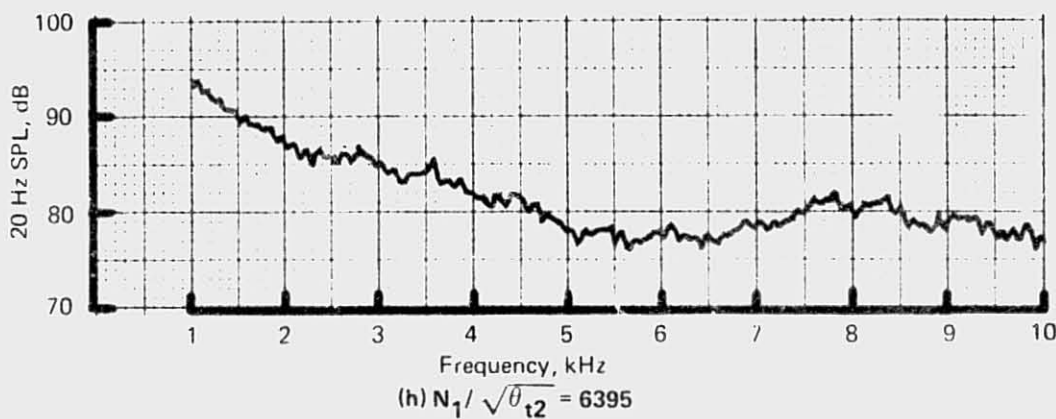
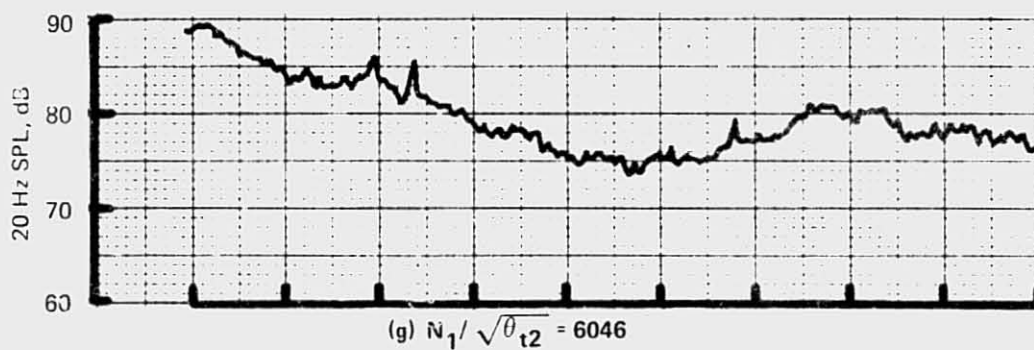
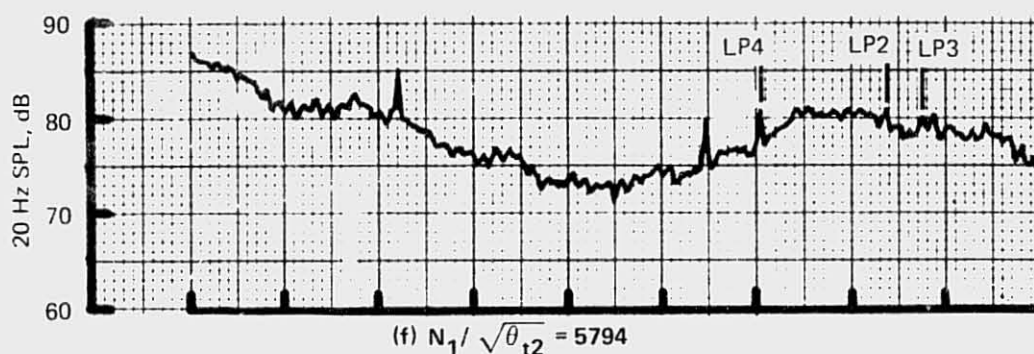
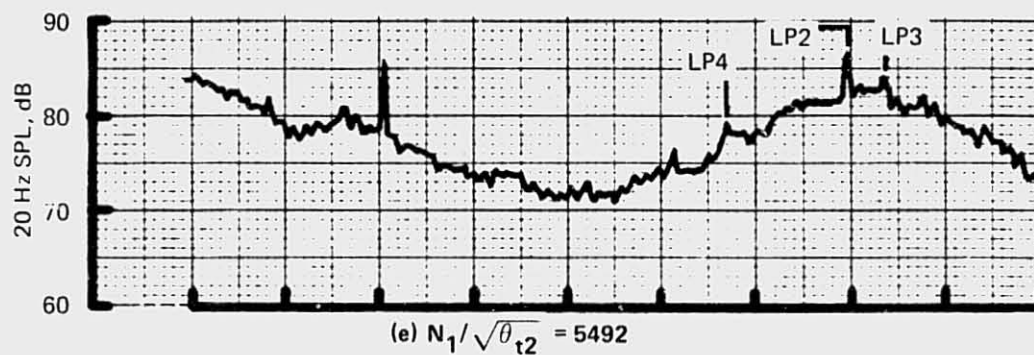


Figure 122.—(Continued)



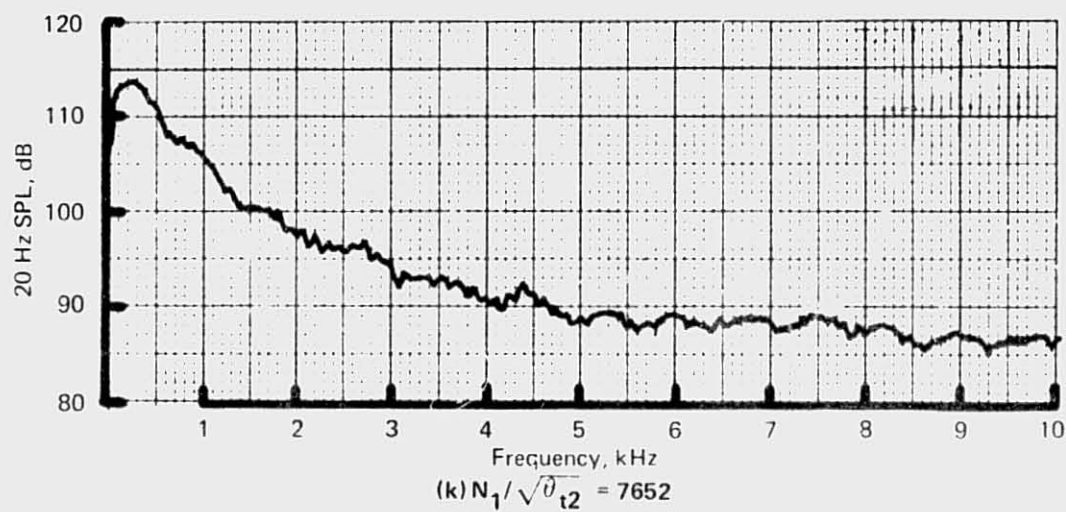
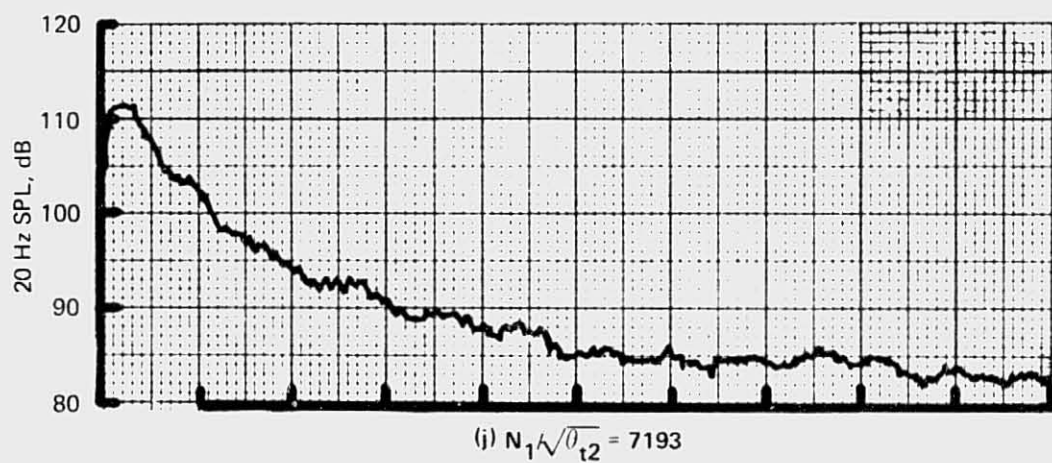
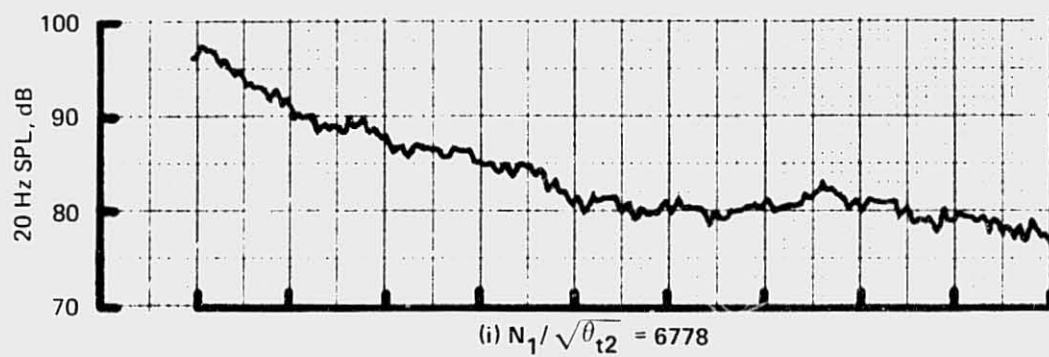


Figure 122.—(Concluded)

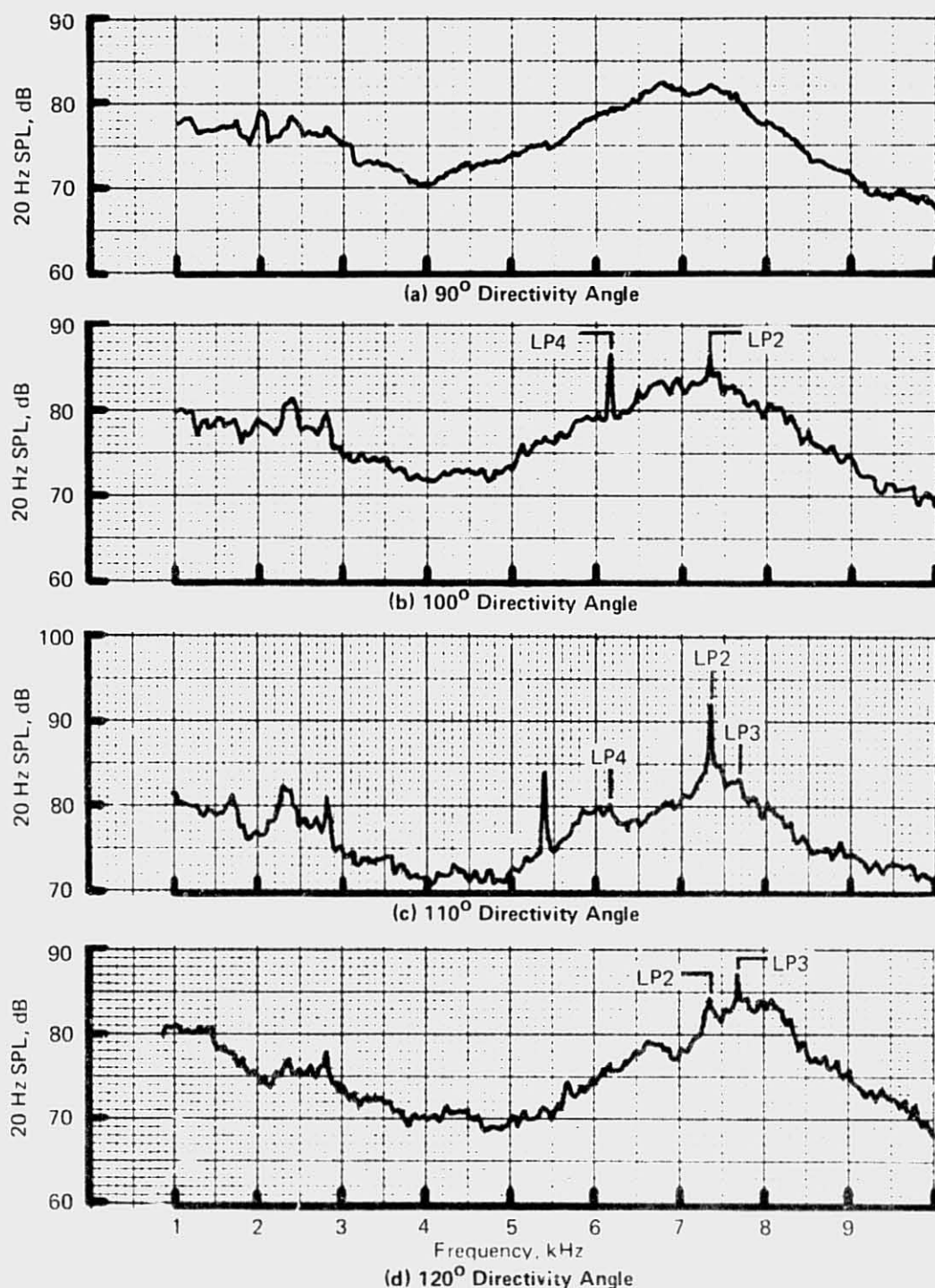
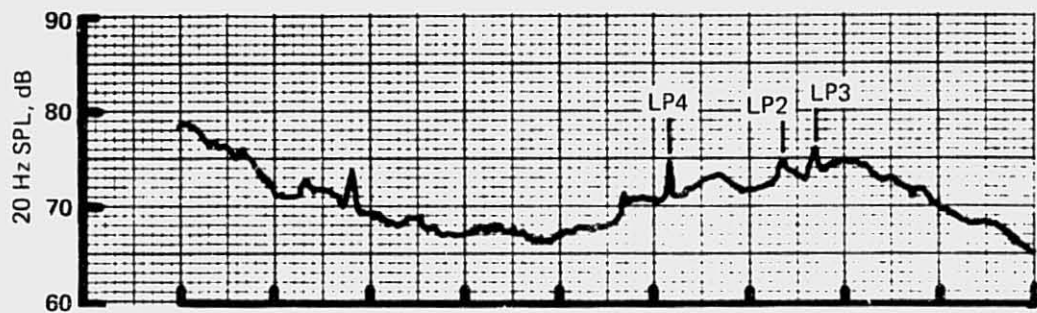
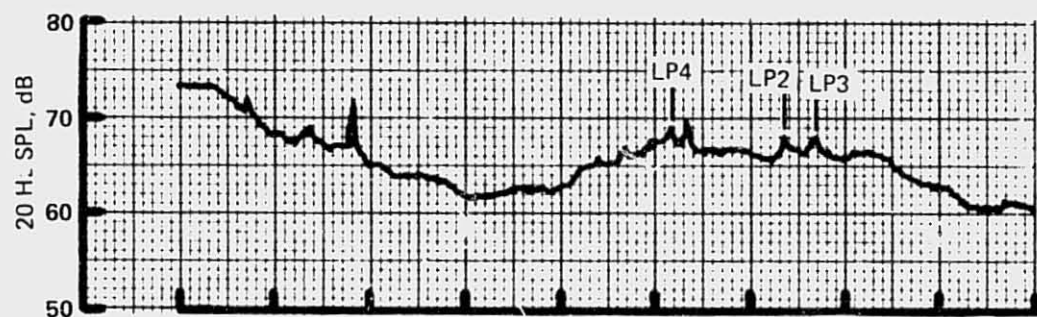


Figure 123.—JT8D-115 Ground Test—Inlet Baffled Narrow Band Spectra for Various Directivity Angles at Constant Power Setting ( $N_1/\sqrt{\theta}t_2 = 5077$ , 100 ft (30.48 m) Sideline, Ground Microphones)

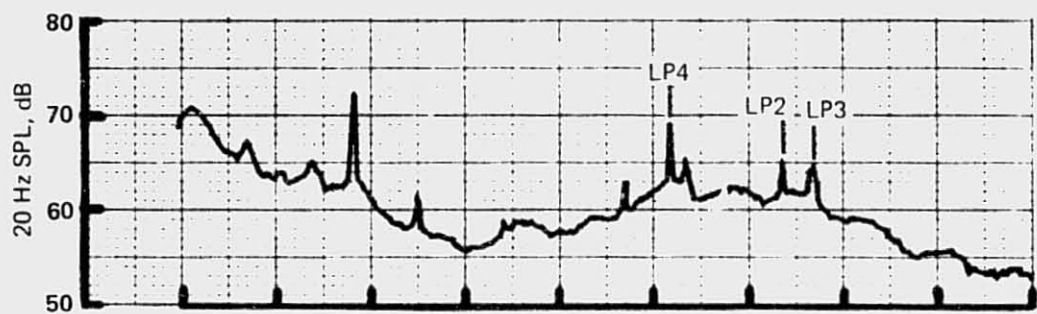
REPRODUCIBILITY OF THE  
ORIGINAL PAGE IS POOR



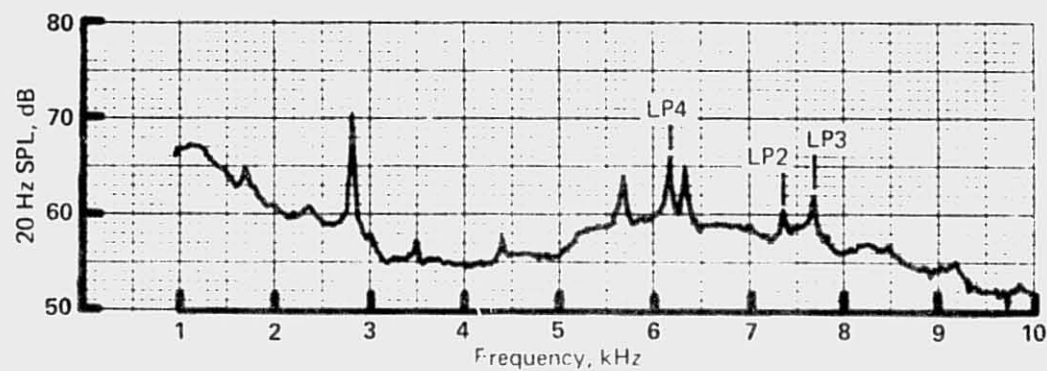
(e) 130° Directivity Angle



(f) 140° Directivity Angle



(g) 150° Directivity Angle



(h) 160° Directivity Angle, 200 ft (60.96 m) Polar

Figure 123.—(Concluded)

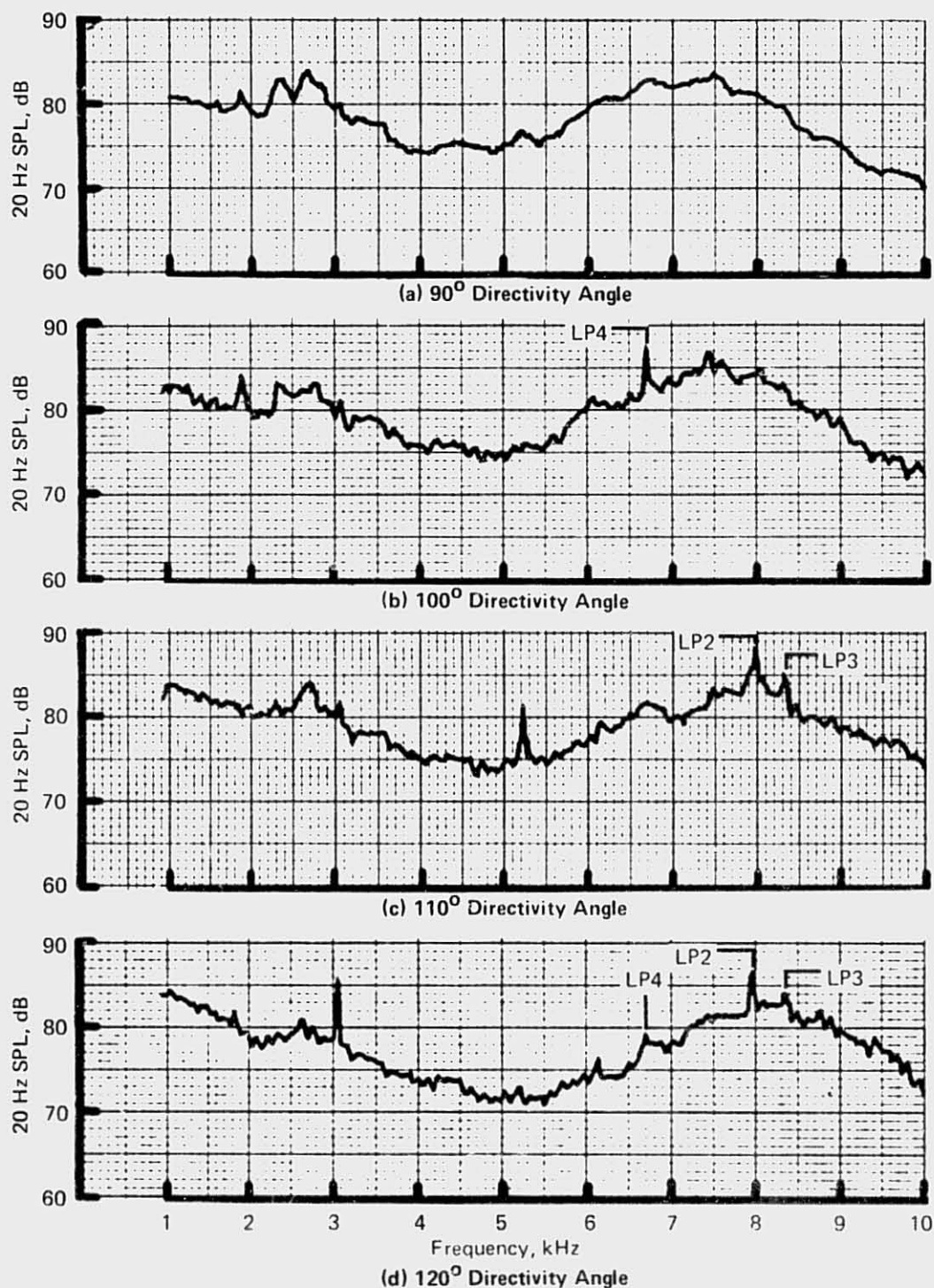
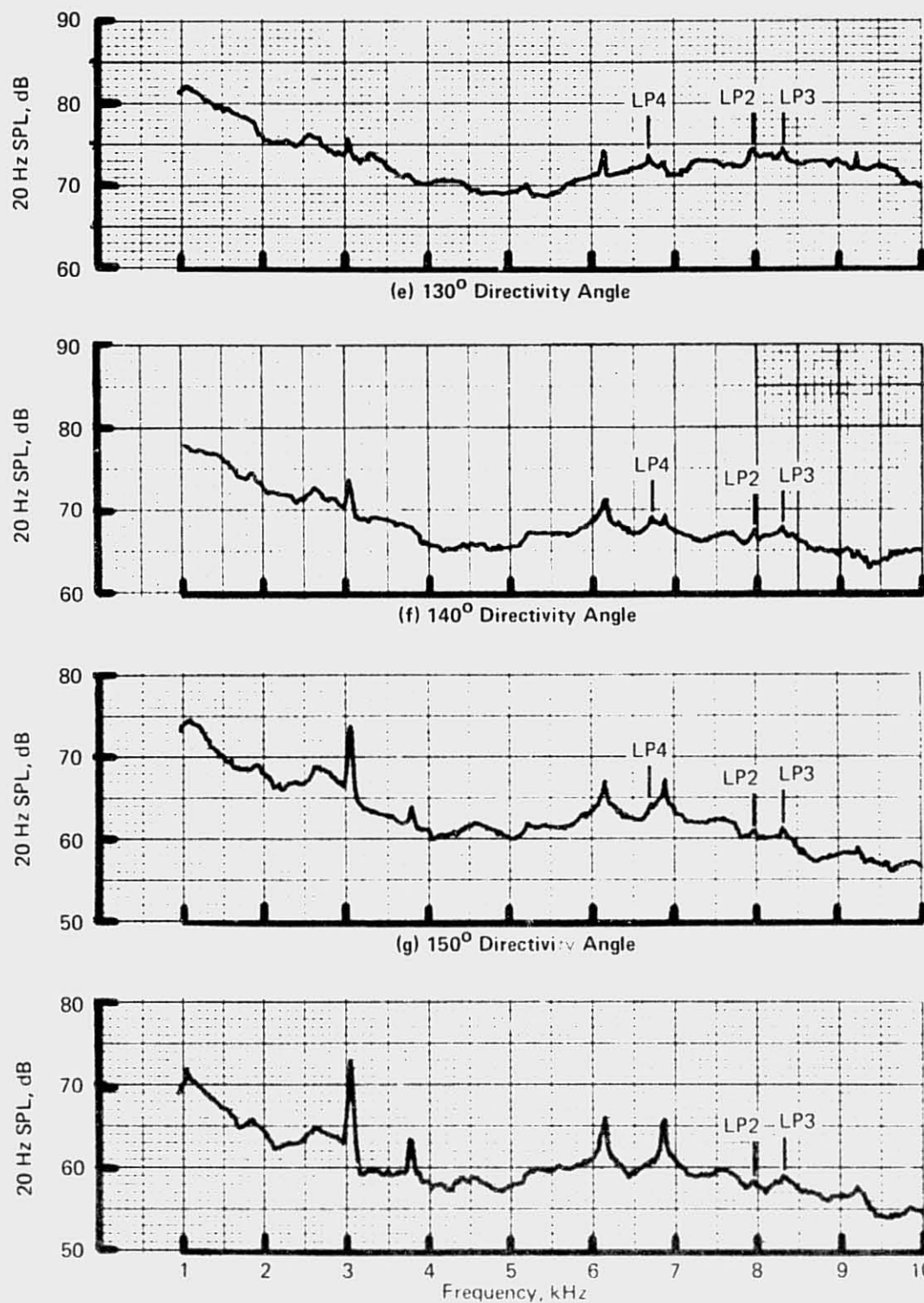


Figure 124.—JT8D-115 Ground Test—Inlet Baffled Narrow Band Spectra for Various Directivity Angles at Constant Power Setting ( $N_1/\sqrt{\theta_{t2}} = 5492$ , 100 ft (30.48 m) Sideline, Ground Microphones)



(h) 160° Directivity Angle, 200 ft (60.96 m) Polar

Figure 124. - (Concluded)



data are shown in figure 125. Entering with log of corrected rpm, the appropriate curve gives the 1/3-OBSPL for the fundamental blade passing frequency tone of a given stage. The level is assigned to the 1/3-OB containing the fundamental blade passing frequency.

*Turbine Tone Directivity.*—Turbine tone directivities were obtained by arithmetically averaging all data from the three turbine stages at all power settings where turbine tones were identifiable. A single directivity curve was derived for all three turbine stages applicable to all power settings (fig. 126).

*Turbine Haystack Broadband Noise.*—Peak haystack broadband levels were determined for each turbine stage from the narrow band data at the intersection of the stage tone and the turbine haystack. The resulting peak levels are shown in figure 127. Entering with log of corrected rpm, the appropriate curve gives the peak 1/3-OBSPL for the broadband noise of a given stage. This level is also assigned to the 1/3-OB containing the fundamental blade passing frequency.

*Turbine Haystack Broadband Spectrum Shape.*—The spectrum shaping chosen for the turbine haystack broadband is one in which the level decreases at the rate of 10 dB per 1/3-OB from the blade passing frequency in both the high and low frequency directions for all three turbine stages.

*Turbine Haystack Broadband Directivities.*—Haystack broadband directivities are shown in figure 128. The curves were derived by arithmetically averaging broadband data from several power conditions at each of the measurement directivity angles. Levels are referenced to the 120° directivity angle.

#### 4.2.1.7 Jet Noise: JT8D-15 Engine

The jet noise evaluation procedure makes use of the observation that the jet noise spectrum shape at a given radiation angle is nearly independent of engine power setting. Figure 129 schematically demonstrates the analysis procedure:

1. For a given radiation angle, the SPL spectra measured at high power settings ( $V_{pri} \geq 1000$  ft/s (340.8 m/s)) are shifted in level and frequency until they overlay one another.
2. The SPL and 1/3-OB frequency of the spectral peaks (excluding tones and obvious buzzsaw) are plotted versus  $\log V_{pri}$ .
3. This process is repeated for all radiation angles, resulting in a family of curves with directivity angle as a parameter.

The success or failure of the normalization procedure gives a measure of the relative importance of the jet-generated noise to the total measured noise levels. For example, in the present JT8D-15 engine noise analysis, the normalization was very successful for  $V_{pri} \geq 1000$  ft/s (340.8 m/s),  $f \leq 2$  kHz, and  $90^\circ \leq \theta \leq 130^\circ$ . At power conditions for which  $V_{pri} < 1000$  ft/s (340.8 m/s), low frequency core or burner noise obscured jet noise; turbomachinery noise masked frequencies greater than 2 kHz; forward of  $90^\circ$ , buzzsaw noise tended to mask certain portions of the low frequency spectrum; and aft of  $130^\circ$ , the effects of an unexpected noise source were observed.

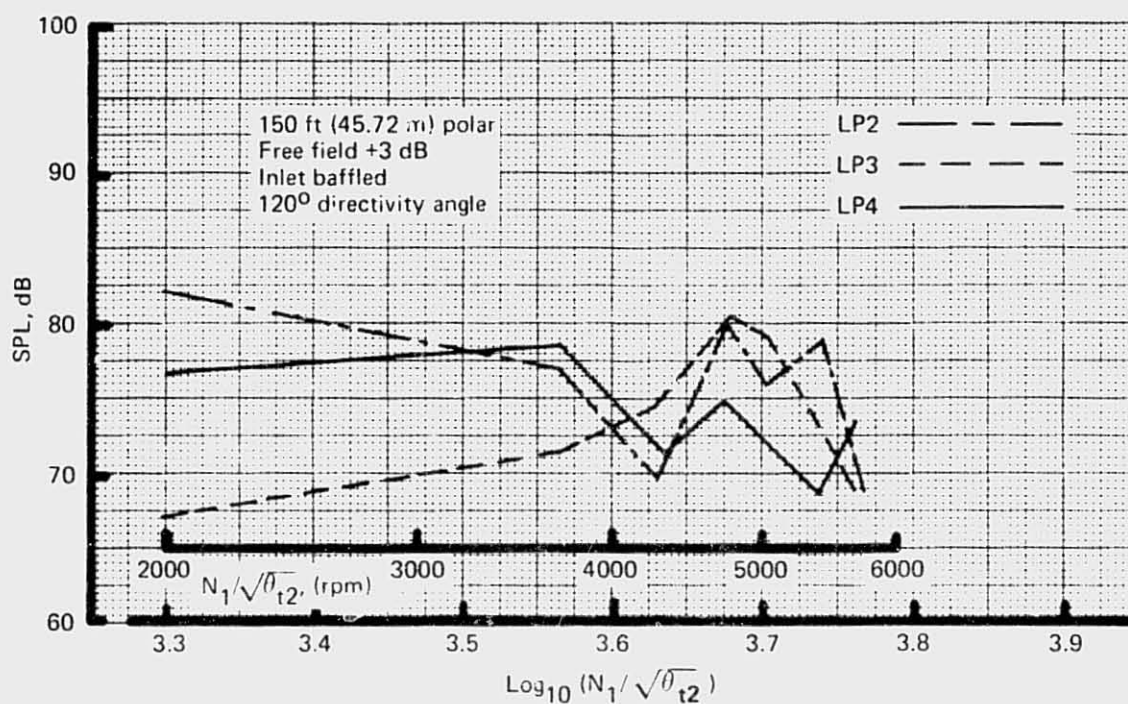


Figure 125.—JT8D-115 Ground Test—Basic Turbine Tone Level Versus Corrected rpm

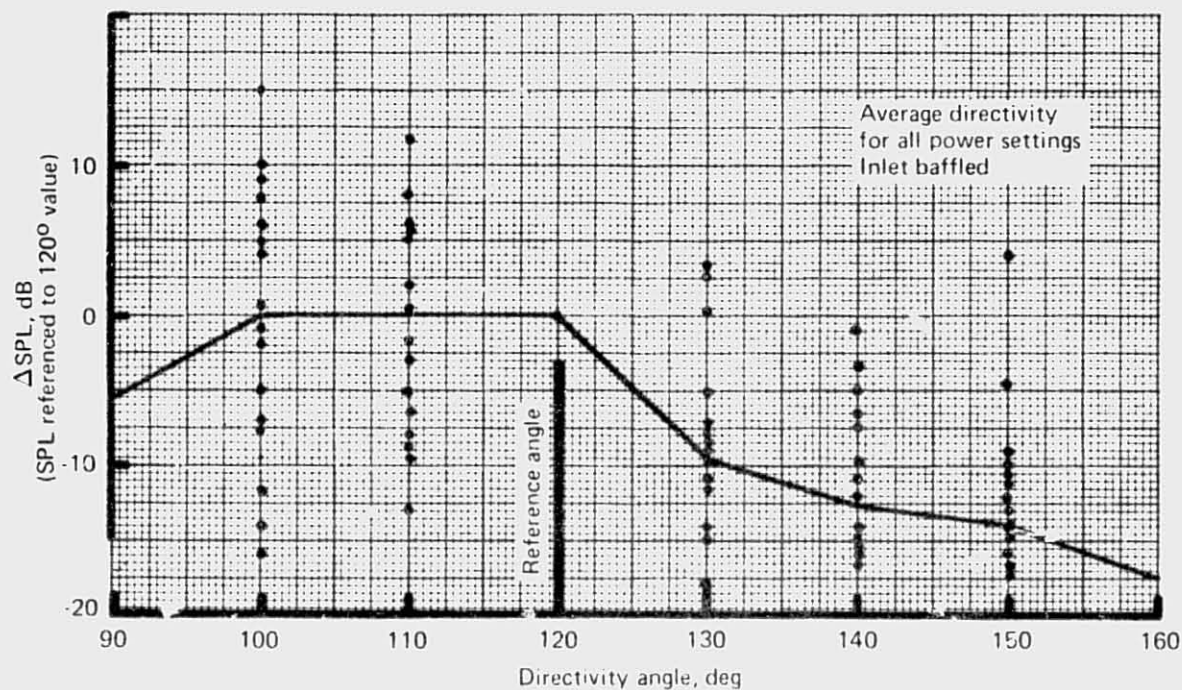


Figure 126.—JT8D-115 Ground Test—Turbine Tone Directivity Corrections

REPRODUCIBILITY OF THE  
ORIGINAL PAGE IS POOR

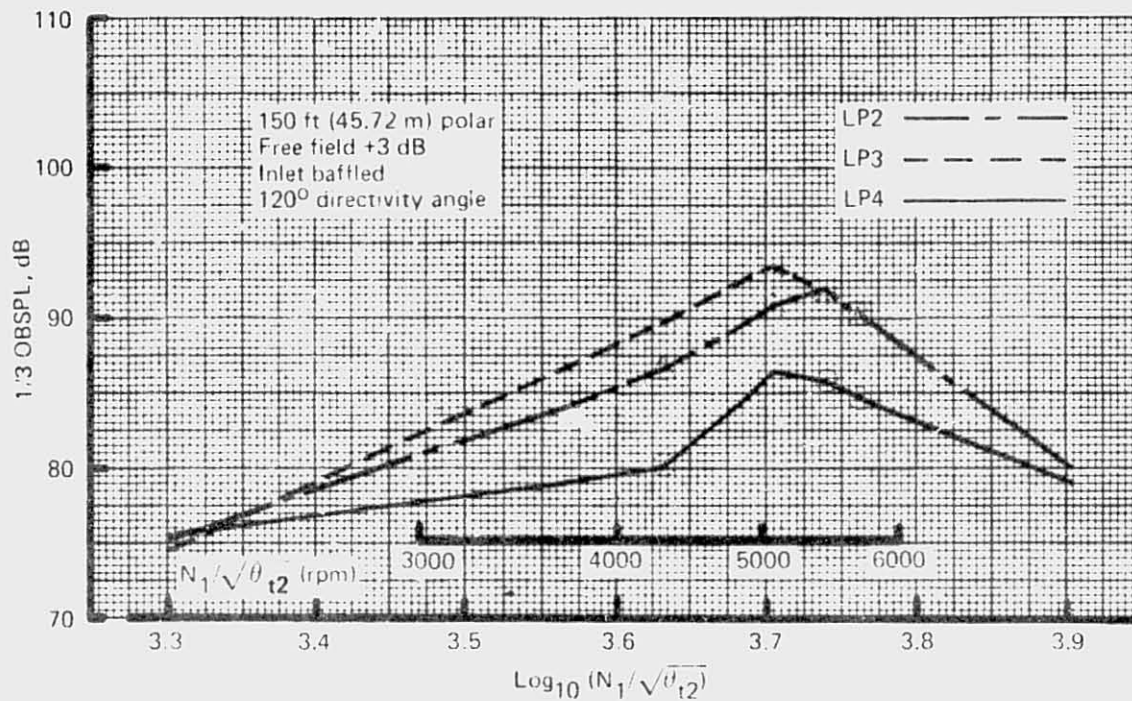


Figure 127.—JT8D-115 Ground Test—Peak Turbine Broadband Level Versus Corrected rpm

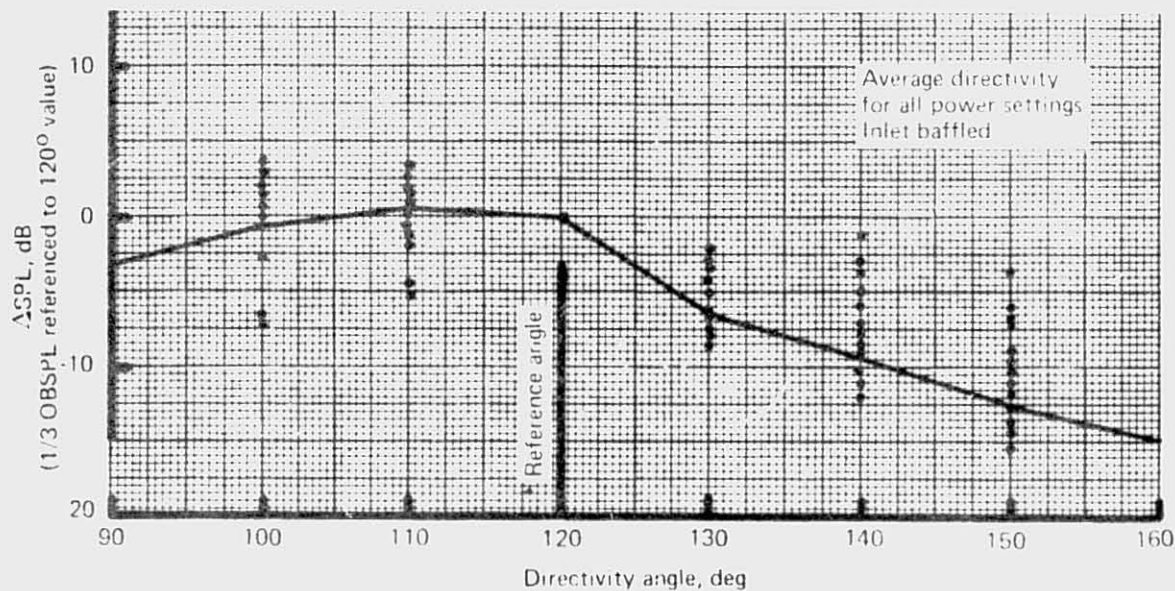


Figure 128.—JT8D-115 Ground Test—Turbine Broadband Directivity Corrections

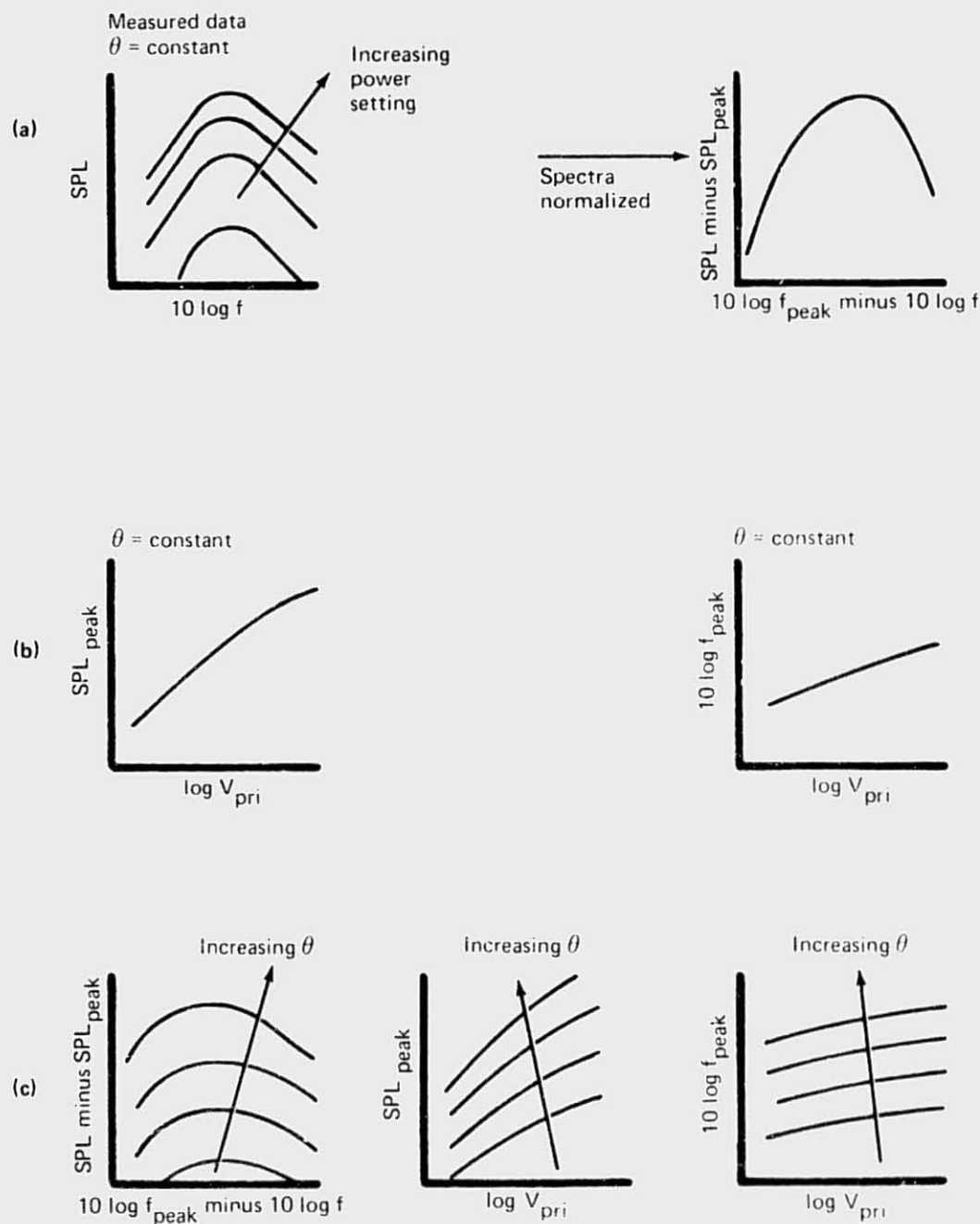


Figure 129.—JT8D-15 Ground Test—Illustration of Jet Noise Analysis Technique



*Jet Noise Spectrum.*—The normalized spectra resulting from the analysis of the JT8D-15 data are shown in figure 130 for  $10^\circ$  through  $150^\circ$  at  $10^\circ$  increments. Figures 131 and 132 show examples of how well the actual jet noise data normalized for  $130^\circ$  and  $110^\circ$ , respectively. The scatter of  $\pm 1$  dB is typical for those cases where no other noise source was thought to be contributing. Figures 133 and 134 compare the derived spectrum shapes for  $130^\circ$  and  $110^\circ$  with spectra shapes from the Contractor's jet prediction procedure based on model-scale jet noise data. The model data show that the assumption of consistency of spectrum shape with engine power setting is good for primary jet speeds above approximately 1000 ft/s (340.8 m/s) and only fair,  $\pm 2$  to 3 dB, when jet speeds over a range 400 to 1000 ft/s (121.9 to 340.8 m/s) are considered.

*Jet Noise Peak Frequency.*—Derived curves showing the frequency at which the spectra of figure 130 a, b, and c reach peak SPL are shown in figure 135 for  $90^\circ \leq \theta \leq 150^\circ$ . These curves represent linear fits to data points for jet velocities greater than 1000 ft/s (340.8 m/s). At high power conditions, peak frequency decreases with decreasing jet velocity and increasing angle. However, below  $V_{pri} = 1000$  ft/s (340.8 m/s) the curves tend to cross one another resulting in an irregular variation of peak frequency versus radiation angle. This indicates that the peak frequencies may be in error by + one 1/3-OB when these curves are used to predict jet noise for jet velocities below 1000 ft/s (340.8 m/s). This is not considered a substantial error since it can be seen in figure 130 a through g that the SPL varies by less than 1 dB per one 1/3 OB either side of the peak for all radiation angles shown except  $150^\circ$ .

Figure 136 gives examples of the data which were used to determine the curves shown in figure 135. The examples shown are for  $130^\circ$  and  $110^\circ$  radiation angles. Included in these figures are peak frequency points calculated by the Contractor's jet noise prediction procedure previously discussed, as well as the linear fit to the ground test data plotted in figure 135. The points from the prediction procedure were used as a guide in fitting a line to the data points.

*Jet Noise Levels.*—The final step in jet noise definition process is to define the variation of SPL with jet velocity. Figure 137 shows the resulting curves of SPL peak versus  $\log(V_{pri})$  for  $40^\circ$  and for  $80^\circ$  through  $150^\circ$ . Angles forward of  $40^\circ$  have the same slope curve as  $40^\circ$  with level decreasing as the angle decreases. These curves represent linear fits to the engine data for jet speeds above 1000 ft/s (340.8 m/s). Most of the curves behave in a reasonable manner with the exception of the  $130^\circ$  line. The crossover of this curve through the  $90^\circ$  to  $120^\circ$  curves below 1000 ft/s (340.8 m/s) is not felt to be accurate but no rationale could be found from the data to change this behavior. Figures 138 and 139 are examples of the data plots used to develop the curves in figure 137. In addition to the high power setting engine data, low power setting data as well as points from the Contractor's prediction procedure are shown. The final linear fit to the data chosen to describe the jet noise behavior was made so as not to be inconsistent with the low power setting data points. Figure 140 is a plot of the velocity exponent "n" defined by the relationship

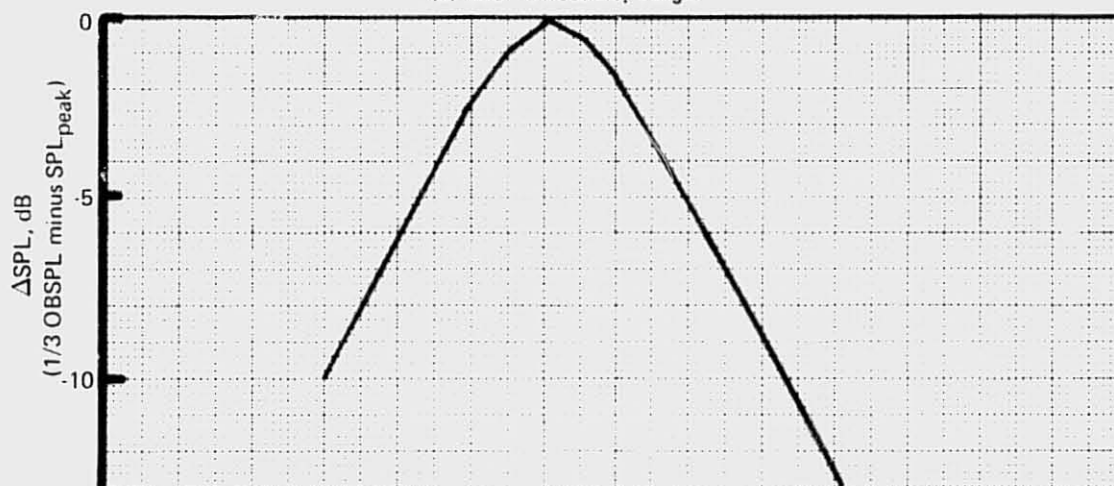
$$\text{SPL peak} = 10 \log \left[ (V_{pri})^n \right] + (\text{constant})$$

calculated from the slopes of the curves in figure 137. Also shown are velocity exponents from the prediction procedure.

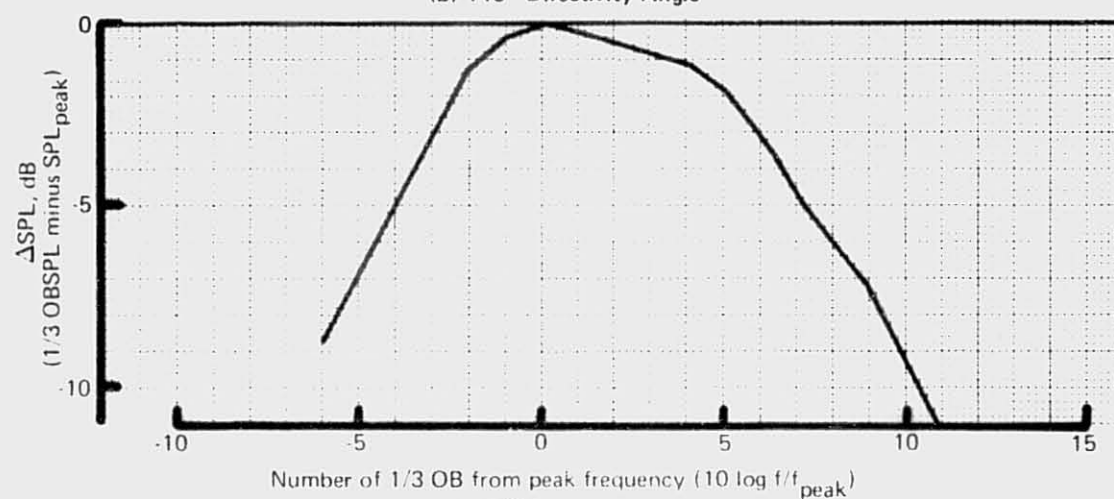




(a) 150° Directivity Angle



(b) 140° Directivity Angle

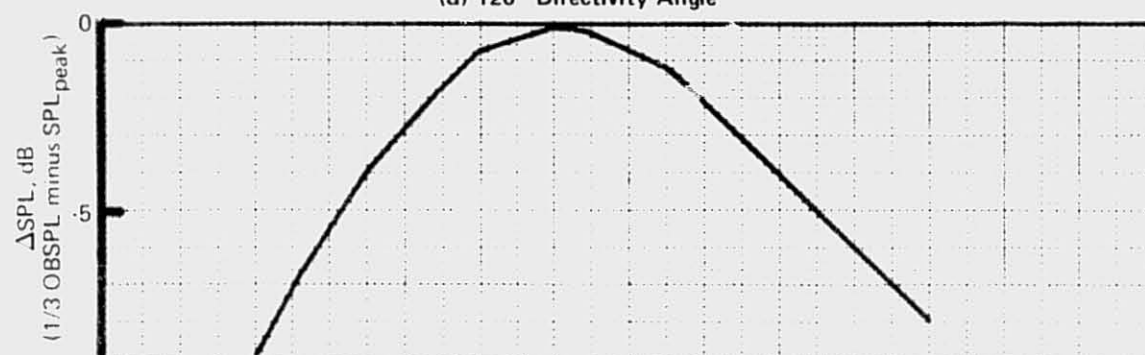


(c) 130° Directivity Angle

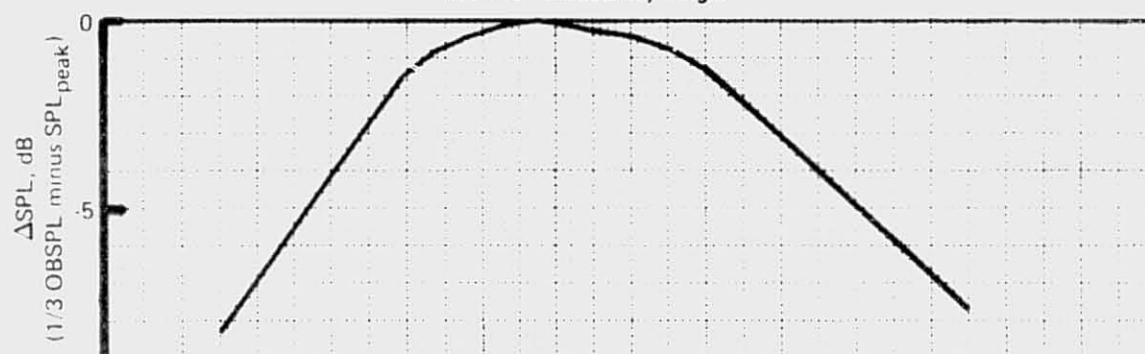
Figure 130.—JT8D-15 Ground Test—Normalized Jet Noise Spectrum Shapes for All Power Settings



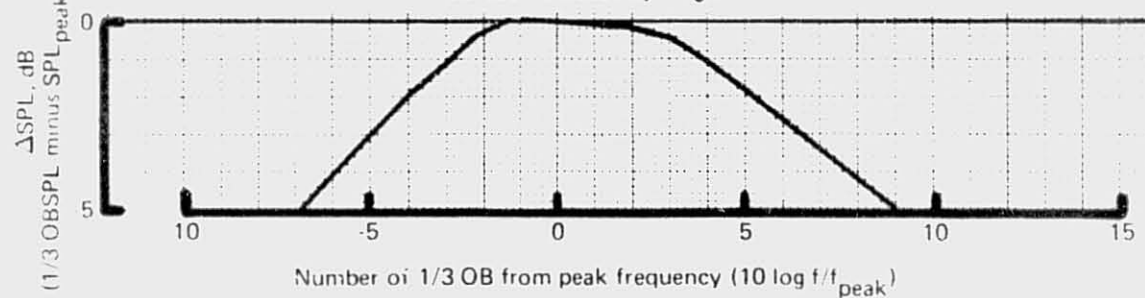
(d) 120° Directivity Angle



(e) 110° Directivity Angle



(f) 100° Directivity Angle



(g) 90° Directivity Angle

Figure 13D.-(Continued)

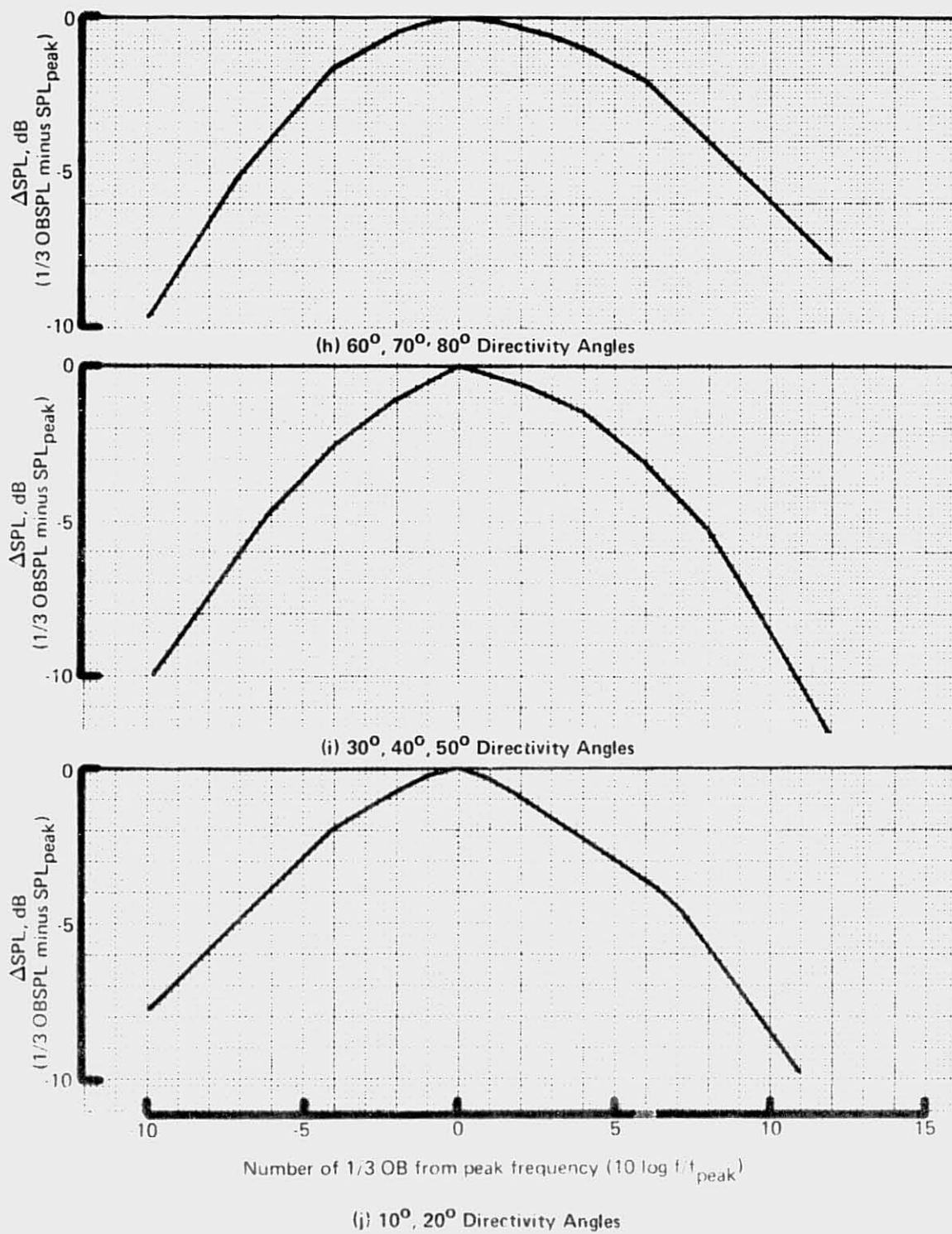


Figure 130. (Concluded)

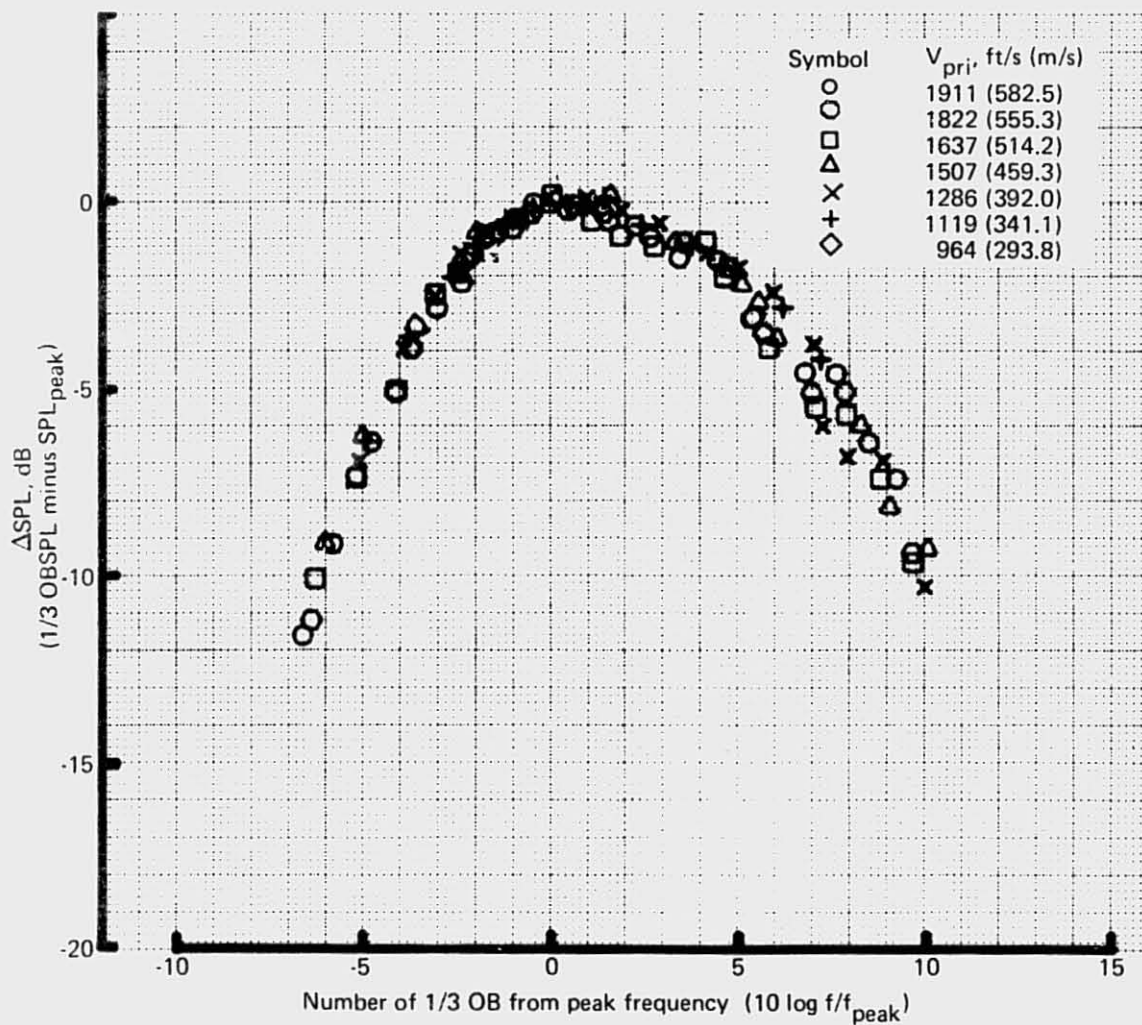


Figure 131.—JT8D-15 Ground Test—Normalized Jet Noise Spectra,  $130^\circ$  Directivity, Angle for Several Power Settings

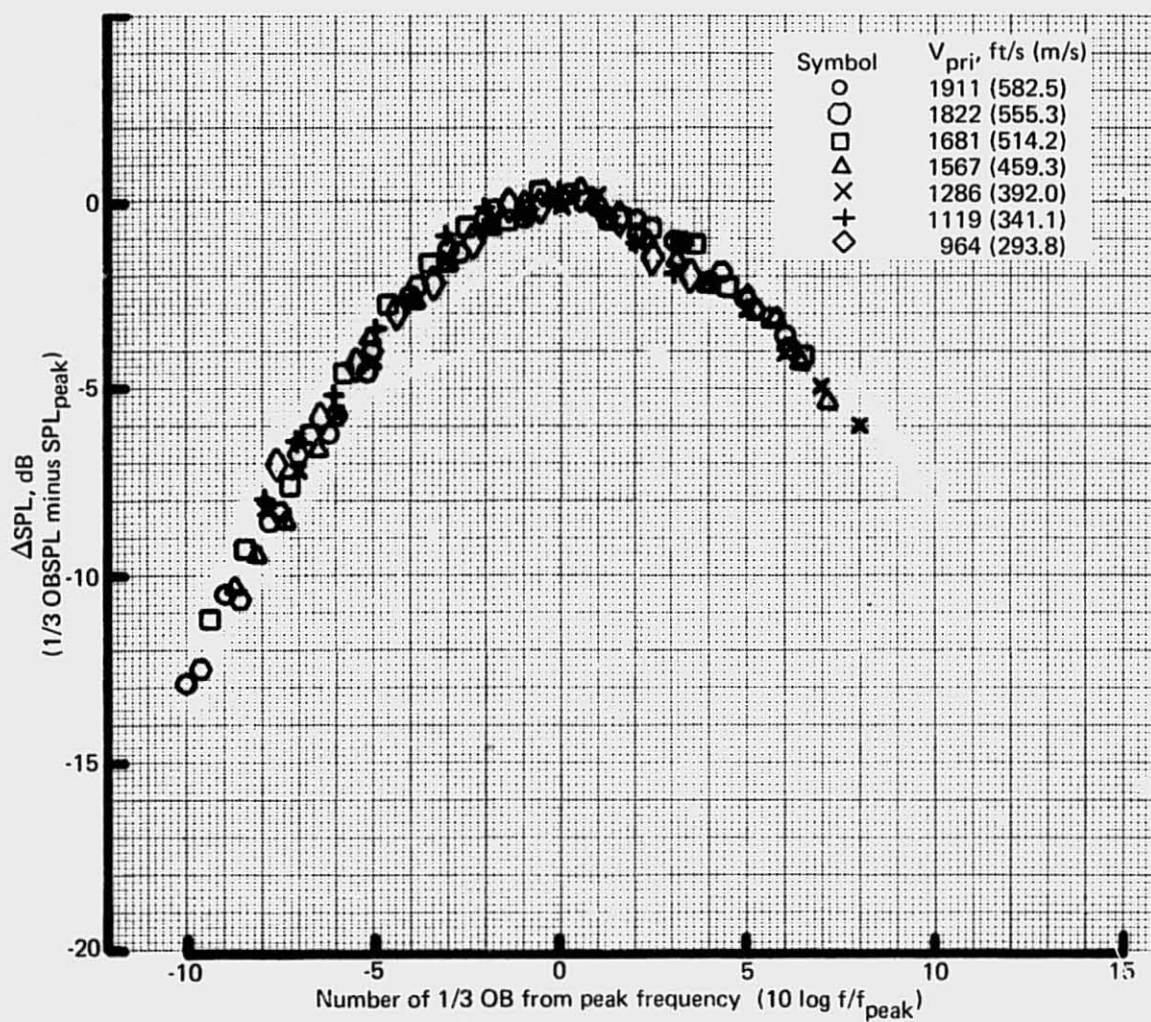


Figure 132.—JT8D-15 Ground Test—Normalized Jet Noise Spectra, 110° Directivity Angle for Several Power Settings



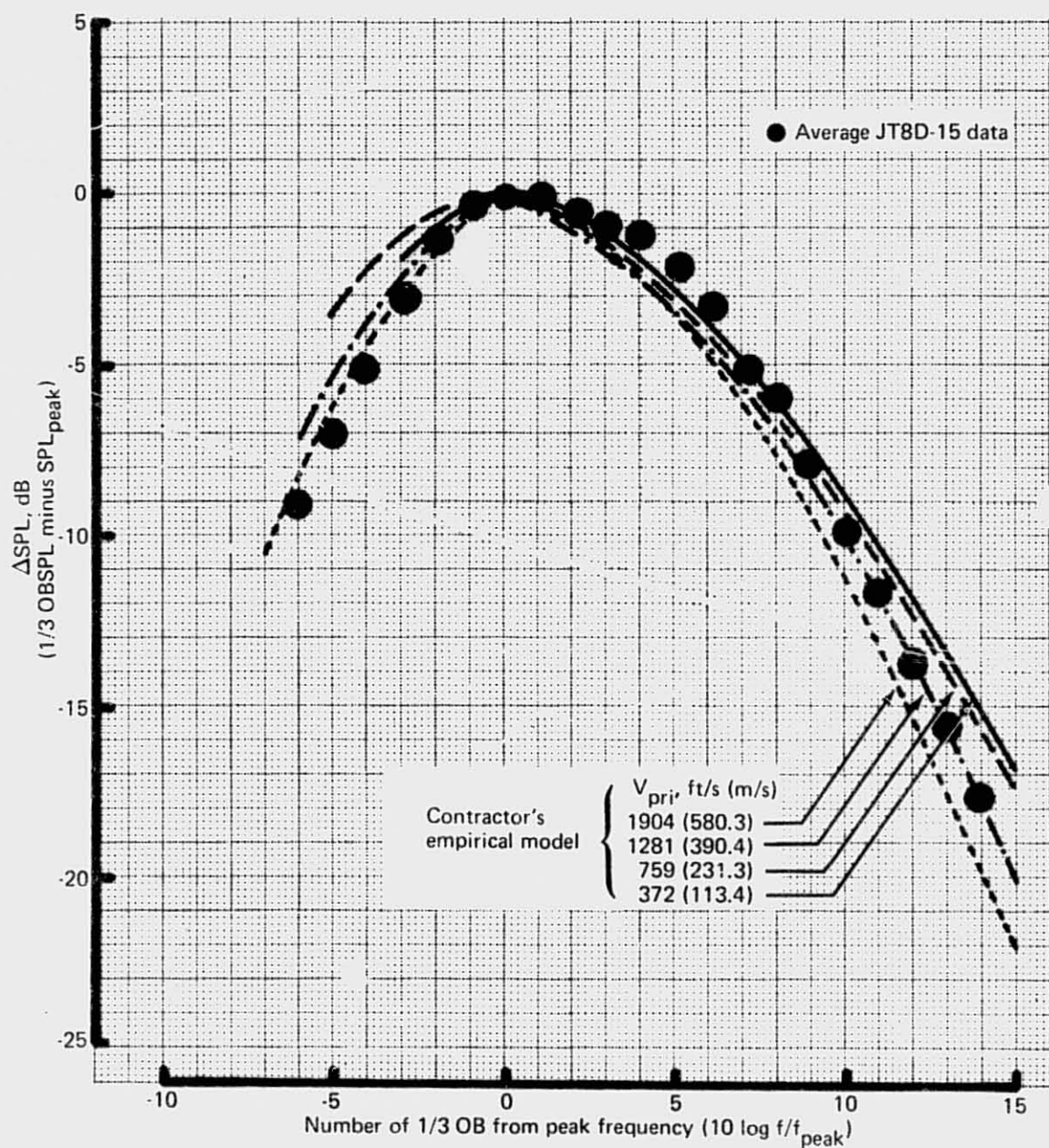


Figure 133.—JT8D-15 Ground Test—Jet Noise Spectrum Shape Comparison,  $130^\circ$  Directivity Angle

REPRODUCIBILITY OF THE  
ORIGINAL PAGE IS POOR

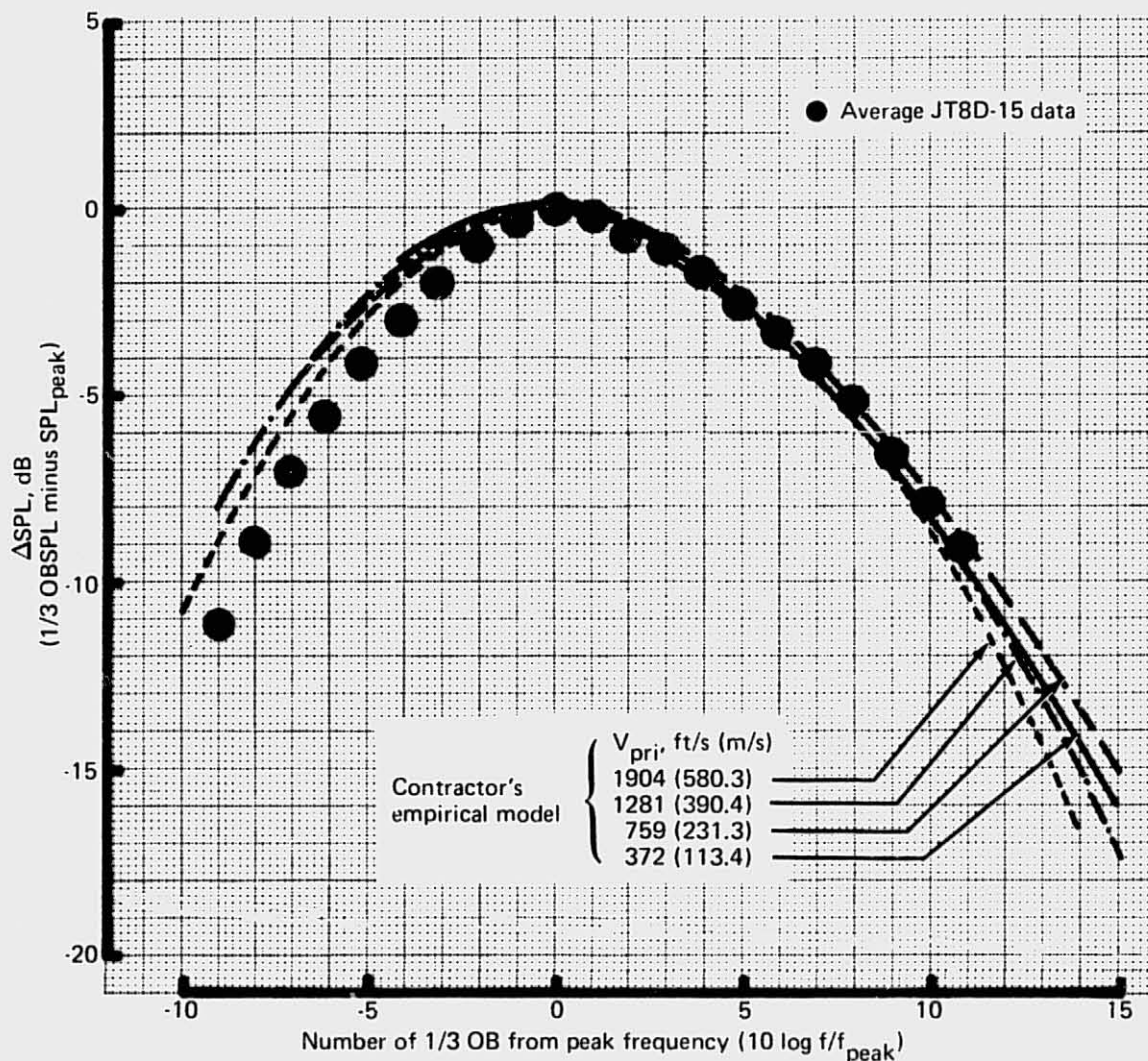


Figure 134.—JT8D-15 Ground Test—Jet Noise Spectrum Shape Comparison,  
110° Directivity Angle

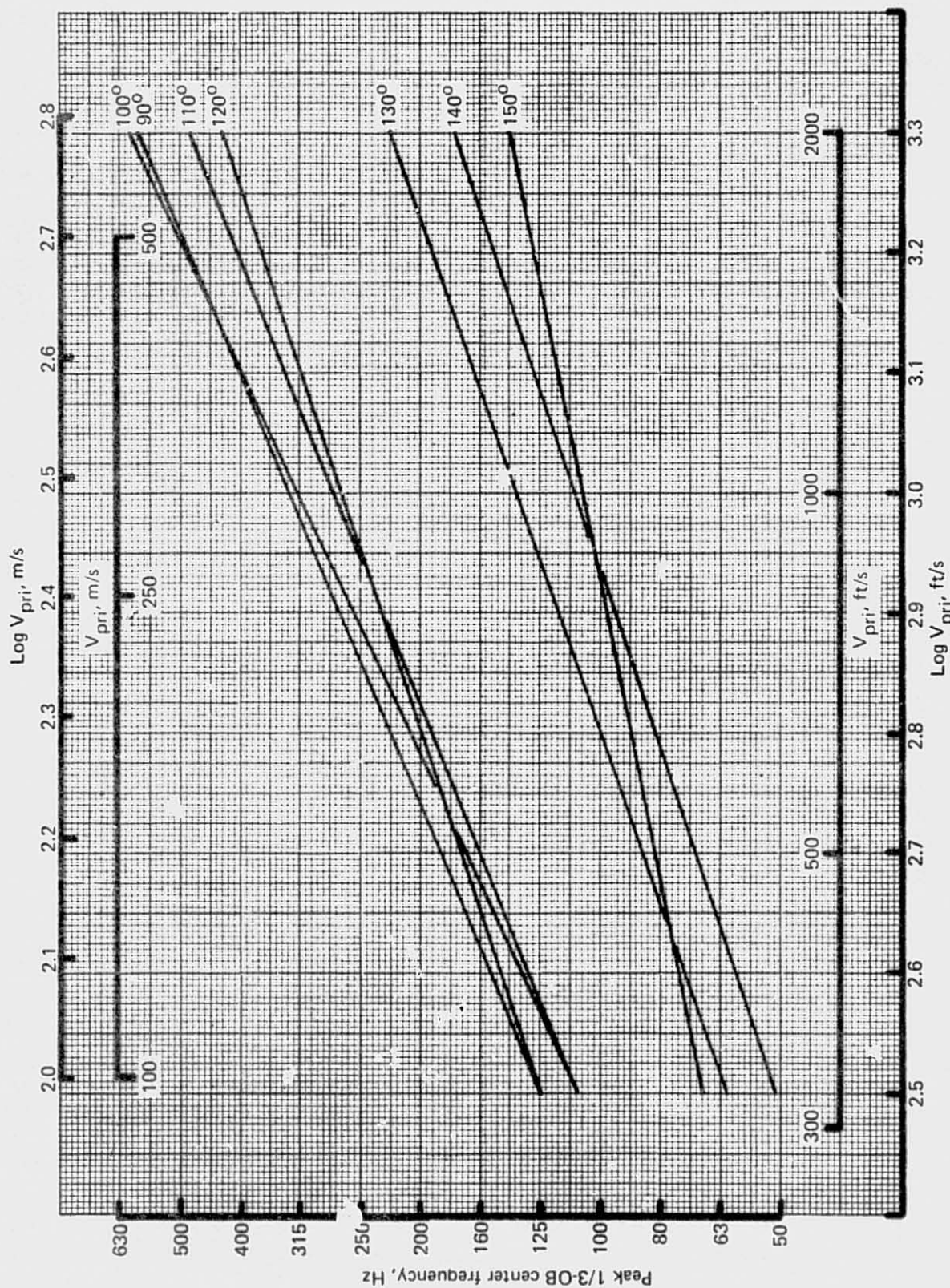
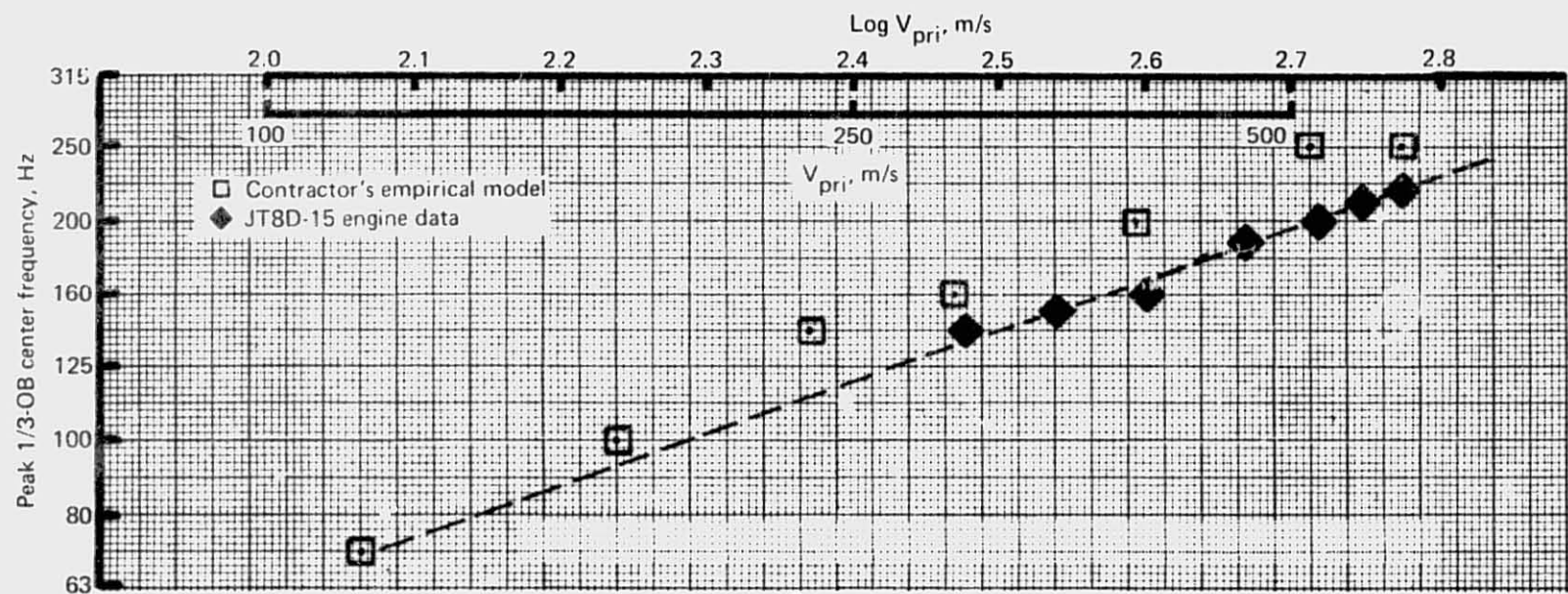
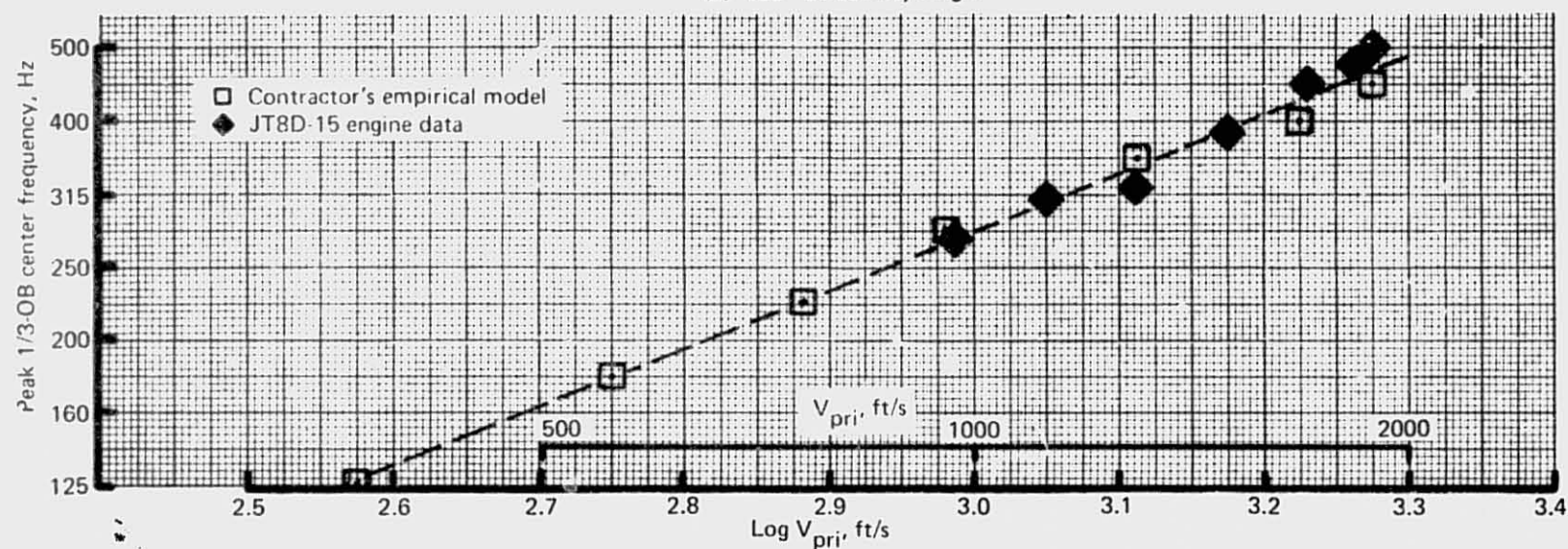


Figure 135.—JT8D-15 Ground Test—Frequency of Jet Noise Peak Sound Pressure Level





(a) 130° Directivity Angle



(b) 110° Directivity Angle

Figure 136.—JT8D-15 Ground Test—Sample Working Plots for Determination of Jet Noise Peak Frequency

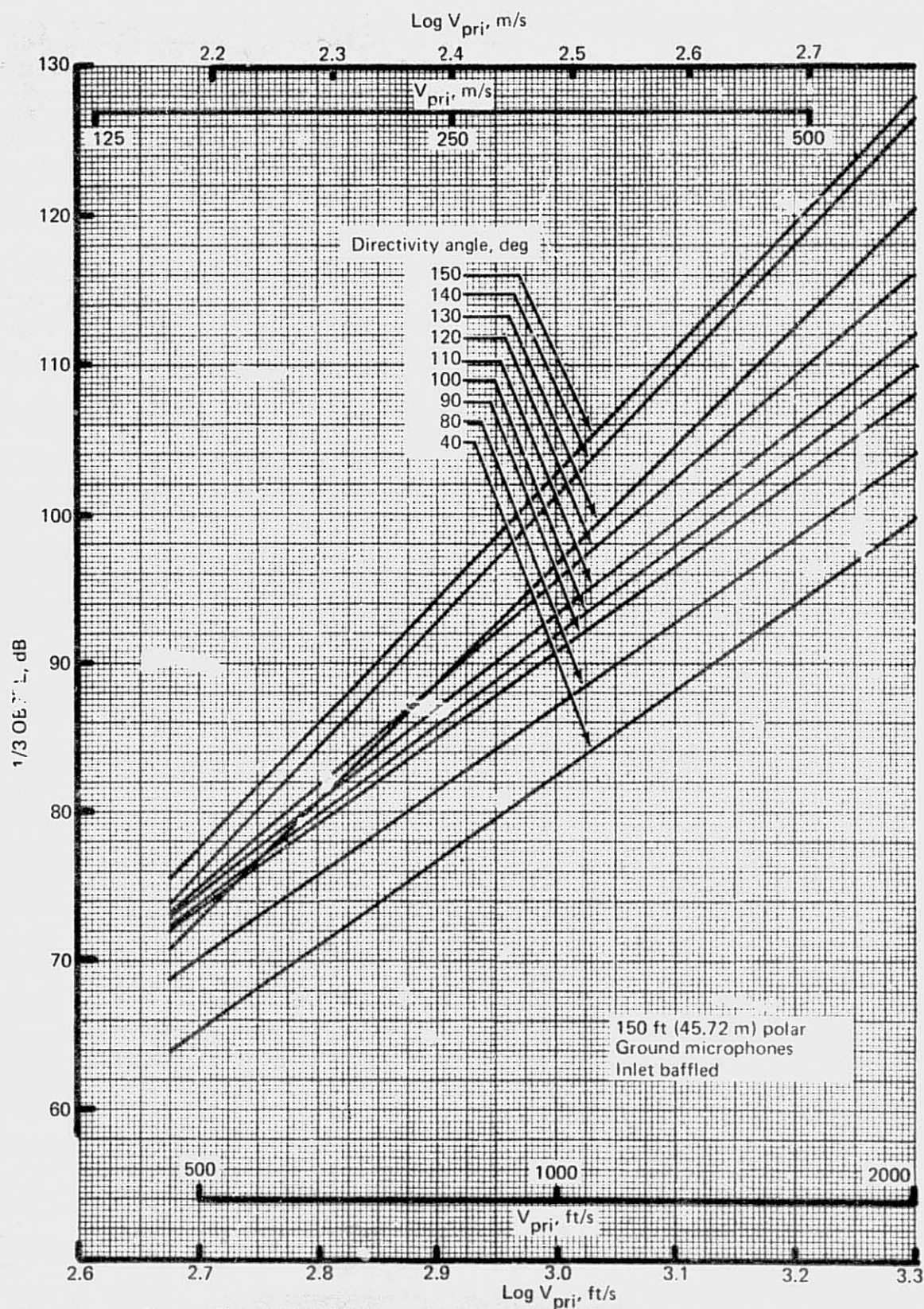


Figure 137.—JT8D-15 Ground Test—Peak Jet Noise Sound Pressure Levels



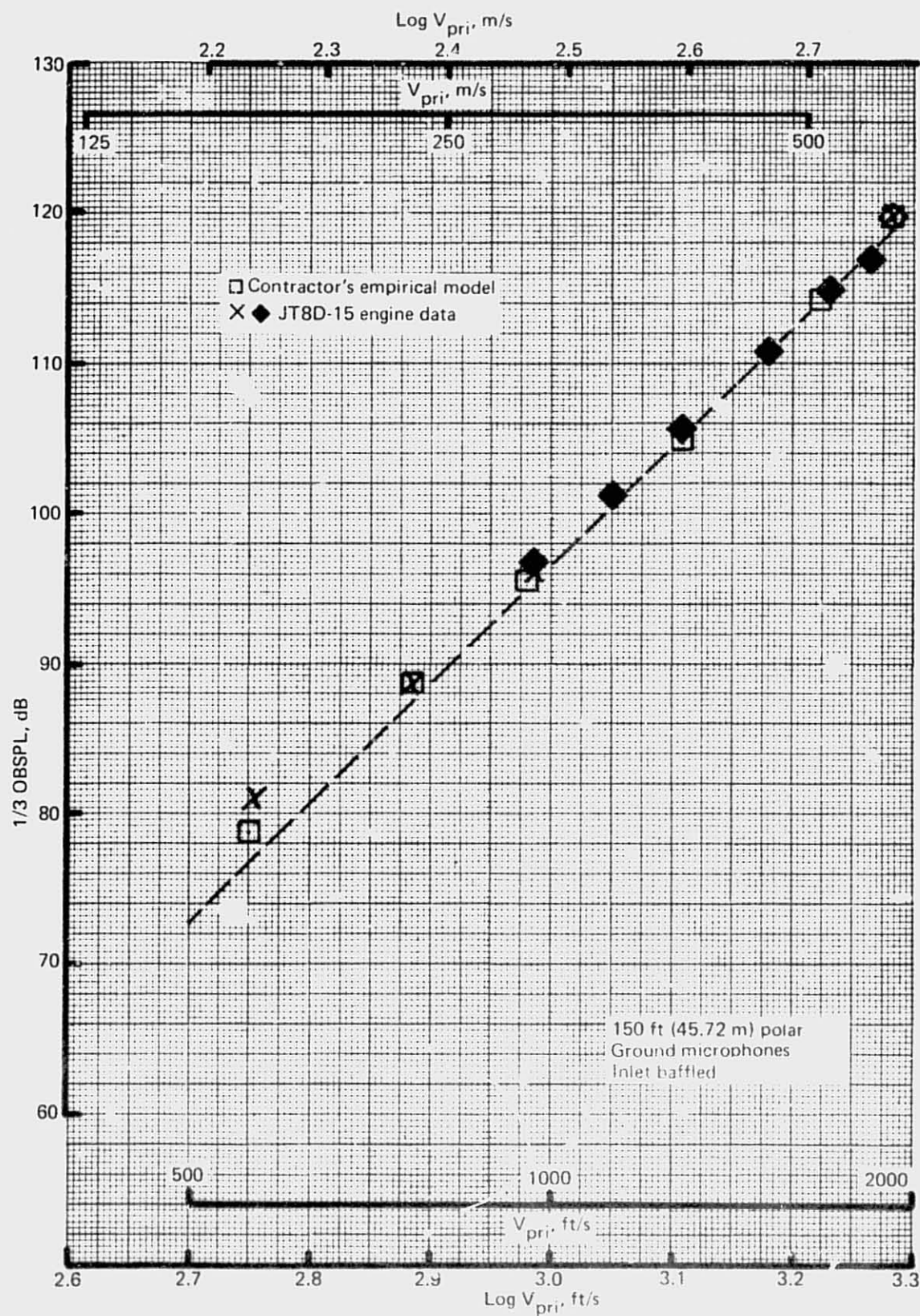


Figure 138.—JT8D-15 Ground Test—Sample Working Plot for Determination of Peak Jet Noise Level, 130° Directivity Angle

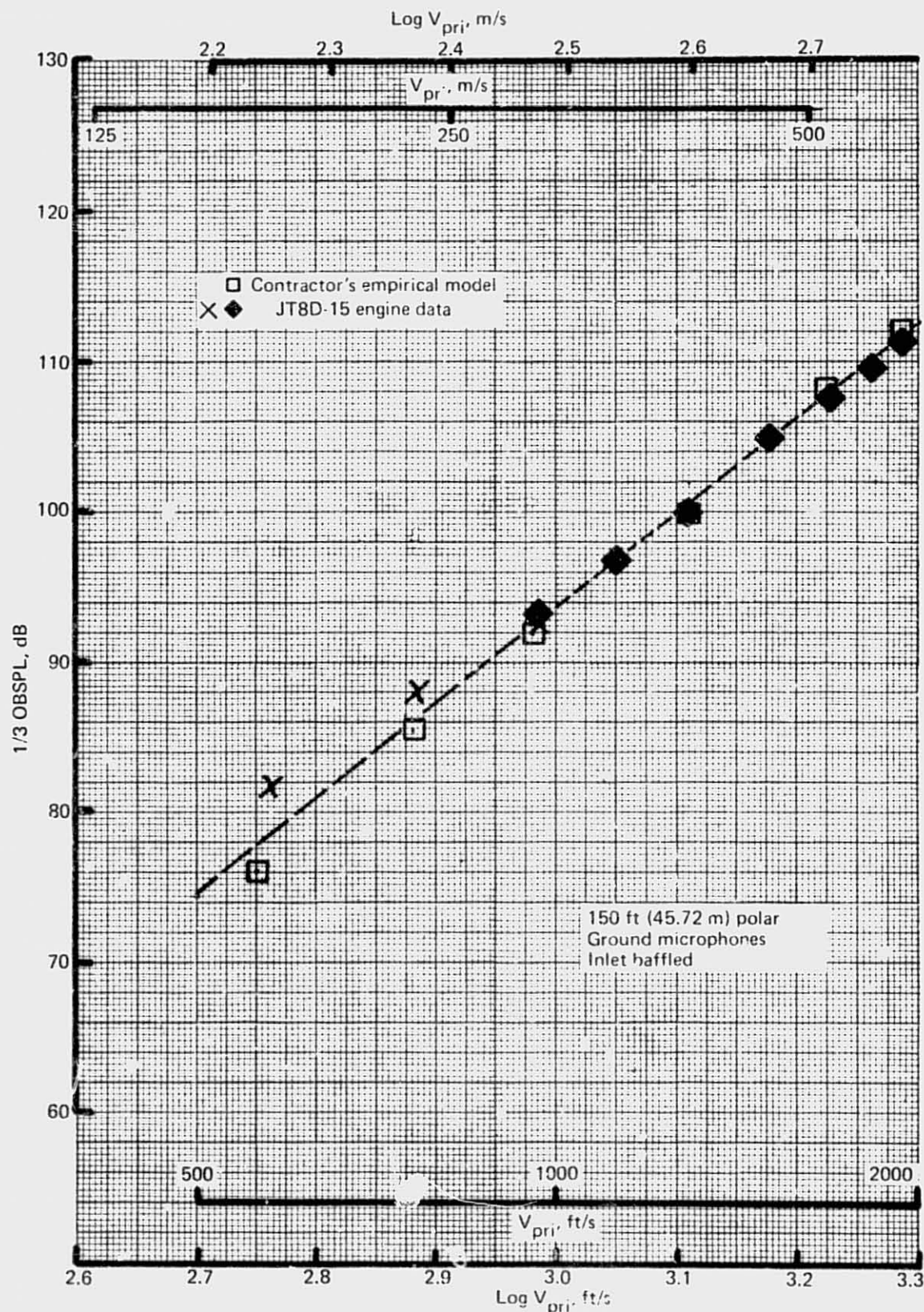


Figure 139.—JT8D-15 Ground Test—Sample Working Plot for Determination of Peak Jet Noise Level, 110° Directivity Angle

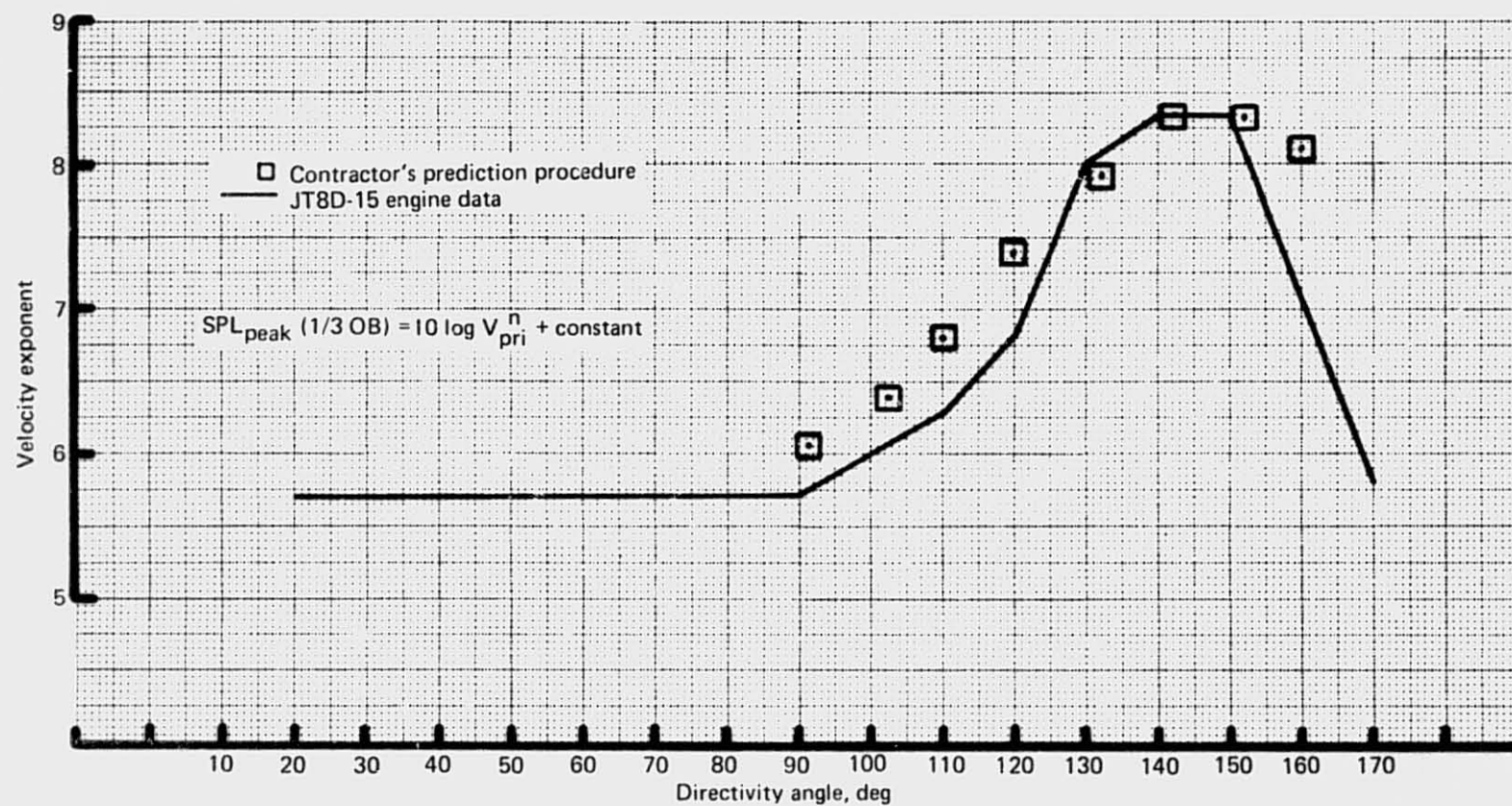


Figure 140.—JT8D-15 Ground Test—Peak Jet Noise Velocity Exponent



*Tabulated Curves.*—The curves shown in figures 130, 135, and 137 form the basis for a procedure for calculating JT8D-15 jet noise as a function of primary jet velocity,  $V_{pri}$ . The spectra shapes are tabulated in table 15. For a given angle “ $\theta$ ,” the frequency of the SPL peak is determined by:

$$10 \log f_{peak} = M(\theta) \log V_{pri} + B(\theta) \quad (5)$$

where  $M(\theta)$  and  $B(\theta)$  are given in table 16. The SPL for the 1/3-OB centered at the determined frequency is given by the relationship:

$$SPL_{peak} = N(\theta) \log V_{pri} - C(\theta) \quad (6)$$

where  $N(\theta)$  and  $C(\theta)$  are tabulated in table 17.

*Table 15.—JT8D-15 Ground Test — Jet Noise Spectrum Shapes: 150 ft (45.72 m)  
Polar, Ground Microphones*

10 log f minus 10 log f <sub>peak</sub>	Directivity angle, deg									
	150 160 170	140	130	120	110	100	90	60 70 80	30 40 50	10 20
	SPL minus SPL <sub>peak</sub> , dB									
-10	-25.0	-18.1	-17.0	-12.9	-13.0	-9.9	-9.5	-9.8	-10.3	-8.0
-9	-22.4	-16.1	-15.0	-10.9	-11.0	-8.4	-8.0	-8.3	-9.3	-7.0
-8	-19.8	-14.1	-13.0	-9.4	-9.0	-7.0	-6.5	-6.8	-7.7	-6.0
-7	-17.2	-12.1	-11.0	-7.9	-7.0	-5.5	-5.3	-5.1	-6.3	-5.0
-6	-14.6	-10.1	-9.0	-5.6	-5.6	-4.1	-4.0	-3.8	-4.9	-4.0
-5	-11.8	-8.1	-7.0	-4.0	-4.0	-2.6	-3.0	-2.7	-3.8	-3.0
-4	-9.2	-6.1	-5.0	-2.9	-2.6	-1.3	-2.0	-1.6	-2.6	-2.0
-3	-6.6	-4.1	-2.9	-1.6	-1.5	-0.6	-1.0	-1.0	-1.7	-1.3
-2	-4.0	-2.2	-1.3	-0.65	-0.6	-0.3	-0.3	-0.5	-1.0	-0.8
-1	-1.4	-0.7	-0.3	-0.2	-0.1	-0.1	-0.1	-0.1	-0.5	-0.2
0	0	0	0	0	0	0	0	0	0	0
1	-1.6	-0.5	-0.2	-0.1	-0.2	-0.3	-0.1	-0.1	-0.1	-0.2
2	-5.0	-1.6	-0.6	-0.9	-0.8	-0.4	-0.2	-0.3	-0.4	-0.8
3	-8.0	-3.5	-0.8	-2.0	-1.1	-0.7	-0.4	-0.6	-0.7	-1.3
4	-11.0	-5.5	-1.0	-2.5	-2.0	-1.4	-1.1	-1.0	-1.2	-2.0
5	-14.0	-7.1	-2.0	-3.6	-3.0	-2.3	-1.7	-1.5	-2.0	-2.7
6	-17.0	-8.6	-3.3	-4.8	-4.0	-3.2	-2.5	-2.1	-2.9	-3.3
7	-20.0	-11.6	-5.0	-5.9	-5.0	-4.1	-3.3	-3.0	-4.0	-4.1
8	-23.0	-13.1	-6.0	-6.8	-6.0	-5.0	-4.1	-4.0	-5.0	-5.4
9	-25.0	-15.6	-7.6	-8.2	-7.0	-5.9	-4.9	-5.0	-6.7	-6.7
10	-28.0	-18.1	-9.6	-9.6	-8.0	-6.8	-5.7	-6.0	-8.4	-8.0

Table 16.—JT8D-15 Ground Test—Band Number for 1/3 OB at which Jet Noise Spectrum SPL Peaks<sup>a</sup>

Directivity angle	Empirical constants for band no. equation <sup>b</sup>	
$\theta$	M ( $\theta$ )	B ( $\theta$ )
170°	3.64	6.04
160°	3.64	7.04
150°	4.01	8.26
140°	6.57	0.62
130°	6.93	0.57
120°	6.66	4.39
110°	6.99	3.83
100°	9.27	-2.79
90°	8.37	0.13
80°	8.37	0.13
70°	8.37	0.13
60°	8.37	-0.87
50°	8.37	-0.87
40°	8.37	-0.87
30°	8.37	-1.87
20°	8.37	-1.87
10°	8.37	-1.87

<sup>a</sup>150 ft (45.72 m) polar, Ground microphones

<sup>b</sup>Band no. (peak) =  $10 \log f_{\text{peak}} = M(\theta) \log V_{\text{pri}} + B(\theta)$ ,  $V_{\text{pri}}$  in ft/s (m/s)

#### 4.2.1.8 Jet Noise: JT8D-115 Engine

Noise spectra measured in the aft quadrant at high power settings on the JT8D-115 engine showed spectral characteristics which did not conform to previously established concepts of either jet noise or core (burner) noise. Specifically at directivity angles of 140° and 150°, a pronounced "bump" appeared in the spectrum with a center frequency of about 500 Hz. Noise data measured by P&WA on a JT8D-109 engine showed a much less pronounced bump in the noise spectrum under similar conditions, and for this reason the JT8D-109 acoustic data were used to derive the core and jet noise component empirical models for the JT8D-109 engine. The JT8D refan engine jet noise characteristics described here are the results of the Contractor's analysis of the P&WA JT8D-109 acoustic data.

Isolated jet noise was defined for a JT8D-109 engine with a hardwall exhaust duct and fan/primary flow divider (splitter). The jet noise description was compiled from test data measured from JT8D-109 noise tests conducted by the Engine Contractor. The core noise component as described in section 4.2.1.10 was applied together with the JT8D-109 fan and



Table 17.—JT8D-15 Ground Test — SPL of 1/3 OB at which Jet Noise Peaks<sup>a</sup>

Directivity angle	Empirical constants for peak SPL equation <sup>b</sup>	
$\theta$	$N(\theta)$	$C(\theta)$
170°	69.7	-107.2
160°	69.7	-105.2
150°	83.5	-147.7
140°	75.7	-149.6
130°	68.3	-142.5
120°	63.0	-109.5
110°	60.0	- 95.6
100°	57.0	- 88.1
90°	57.0	- 80.4
80°	57.0	- 83.4
70°	57.0	- 84.7
60°	57.0	- 86.2
50°	57.0	- 97.2
40°	57.0	- 88.4
30°	57.0	- 91.5
20°	57.0	- 95.0
10°	57.0	- 98.3

<sup>a</sup>150 ft (45.72 m) polar, Ground microphones

<sup>b</sup> $SPL_{peak} = N(\theta) \log V_{pri} - C(\theta)$ ,  $V_{pri}$  in ft/s (m/s)

turbine noise prediction models to calculate a composite spectrum of *all* noise components *except* the jet. These calculated spectra were subtracted from the total noise spectra for this reference engine configuration to calculate the jet noise.

**Jet Noise Spectrum Shape.**—The shapes of jet spectra resulting from a subtraction of all other engine noise components from the total measured spectra were somewhat irregular for all angles except 130° through 160° where jet noise strongly dominated the spectrum. Because of the nature of the sound energy subtraction process, small errors in predicted noise components (fan, turbine, and core) lead to erratic shapes in the resulting jet spectra. Each angular position around the engine was treated as a separate case; jet spectra were faired to a smooth curve and overlaid for shape comparison for all 15 engine power conditions tested. Good agreement was found for the spectrum region between 50 Hz and 1000 Hz, and it was decided that spectrum shape would be considered as independent of engine power setting for each 10° angular position. This is in agreement with a similar conclusion for the JT8D-15 jet noise described in section 4.2.1.7.

The average spectrum shape for each angle for the isolated jet noise component is shown in figures 141 and 142.

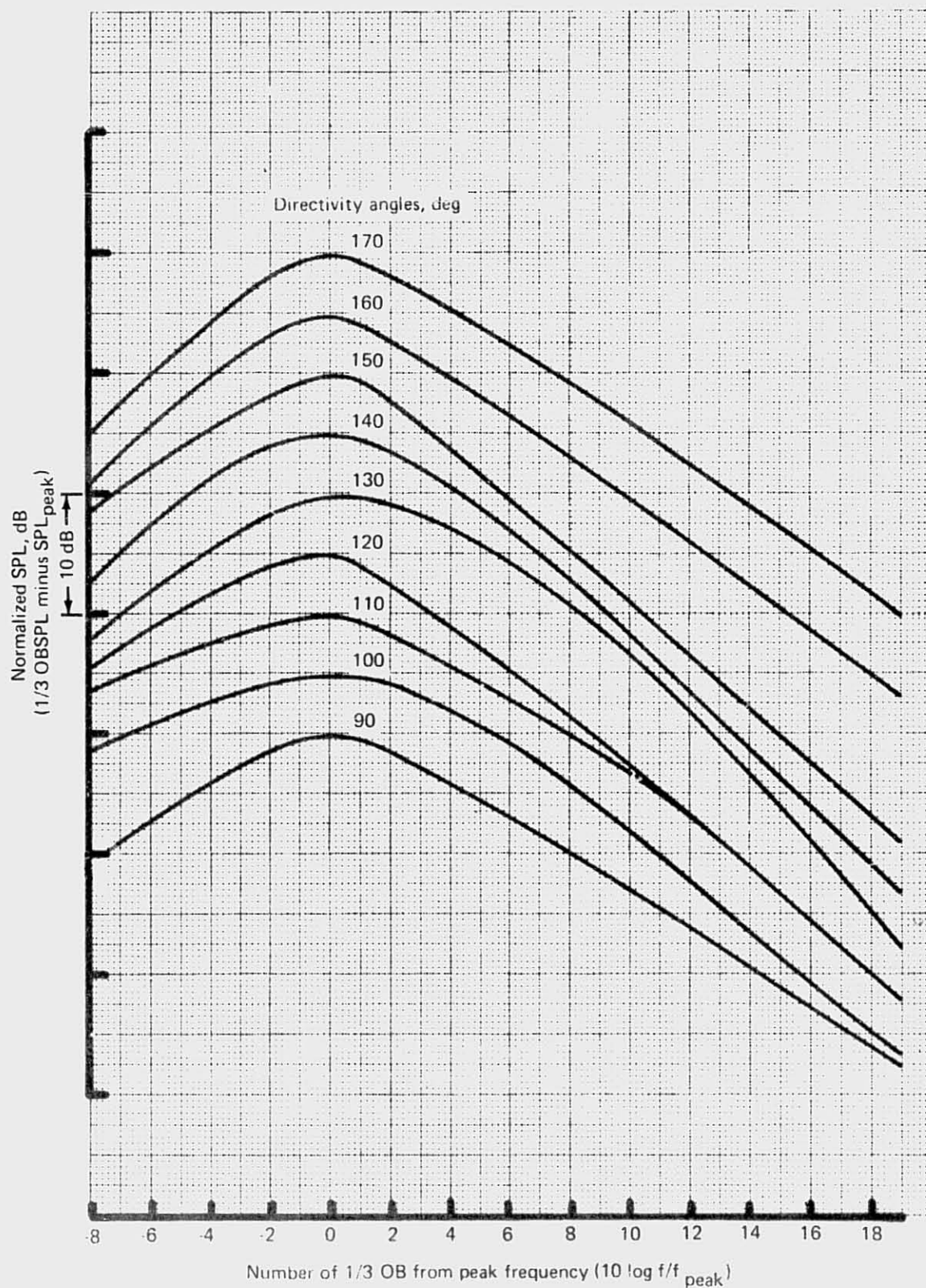


Figure 141.—JT8D-109 Ground Test—Aft Quadrant Jet Spectrum Shapes, All Power Settings

REPRODUCIBILITY OF THE  
ORIGINAL PAGE IS POOR

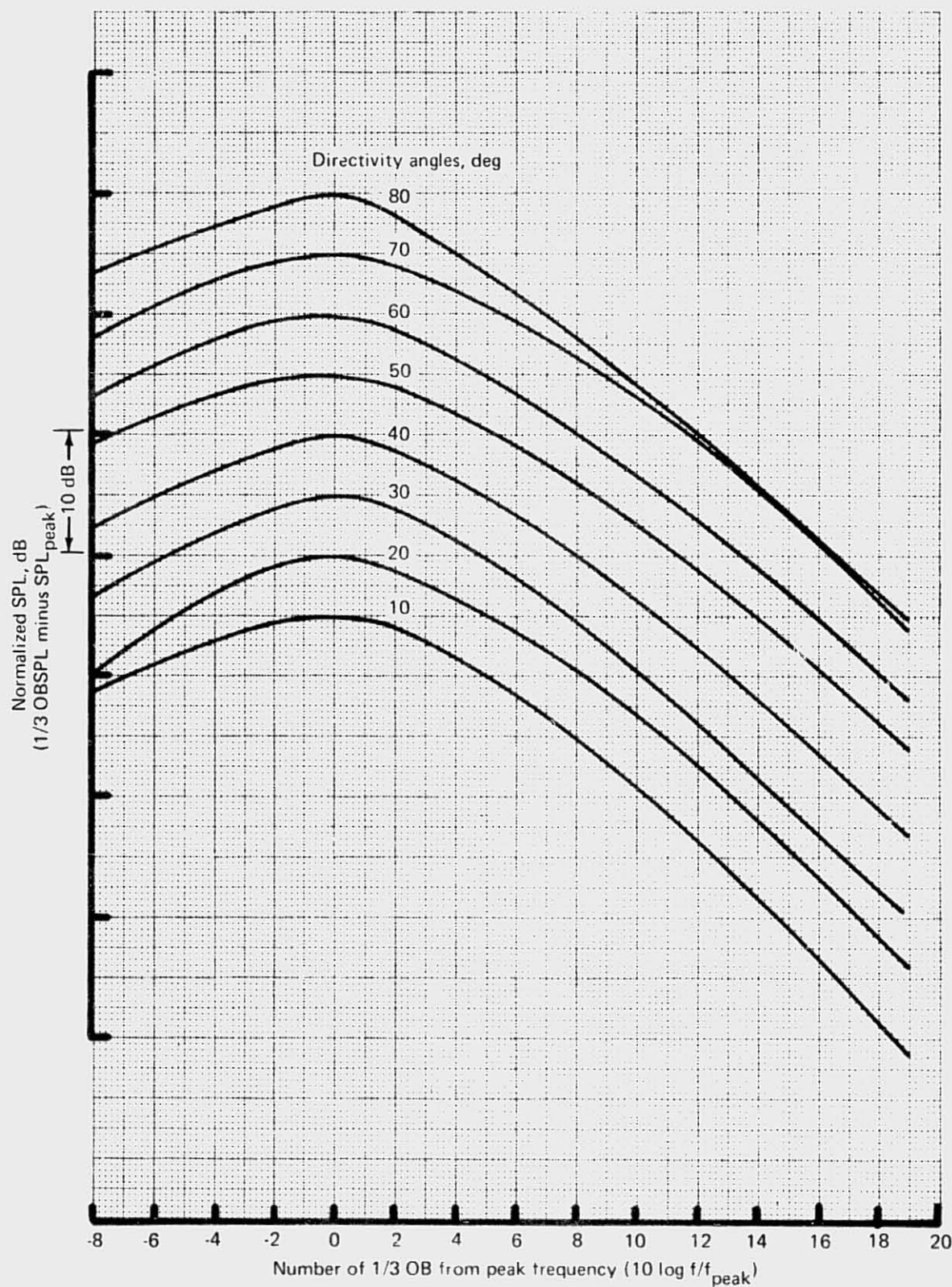


Figure 142.—JT8D-109 Ground Test—Forward Quadrant Jet Spectrum Shapes,  
All Power Settings

*Frequency Band of Peak Noise Level.*—The peak noise level in the jet spectrum tended to occur at higher frequencies as jet velocity was increased, as shown in figure 143. This peak frequency relationship to jet velocity was somewhat different for each angular location. Table 18 was constructed to show this information for 17 locations around the engine at increments of  $10^\circ$  intervals. The increase in peak frequency with jet velocity became less pronounced at the extreme aft angles ( $130^\circ$  and rearward).

*Spectrum Peak Sound Pressure Level.*—Peak SPL in the 1/3-OB jet spectra was defined for each of the 17 angles around the engine. The relationship between jet spectrum peak noise level and primary jet velocity is plotted in figure 144 for the  $120^\circ$  location.

The jet noise level and velocity relationship was different at each angular location, so the results for each angle were summarized in table 19. The region where  $\log V_{\text{pri}}$  is 2.92 (V is in ft/s) or greater (2.40 or greater if V is in m/s) represented the envelope of flight interest, so the upper portion of the curve in figure 144 was used in calculation of the velocity exponent. Table 20 was included to tabulate the velocity exponent for all 17 angular locations for the power regime of flight interest.

#### 4.2.1.9 Core Noise: JT8D-15 Engine

*Core Noise Evaluation Technique.*—The jet noise curves defined in section 4.2.1.7 were used to estimate the jet noise contribution to the total low frequency noise level at low engine power settings. The measured low frequency noise, which could not be accounted for as jet noise, was assumed to be primarily low frequency core engine noise.

The characteristics of the low frequency core noise calculated in this manner were used to update the Contractor's empirical core noise model. According to this model, the SPL level of the core noise is determined by the relationship:

$$\text{SPL} = 10 \log \left[ (T_{t5})^2 (P_{t5}/P_{t7})^2 \left( \frac{W_{\text{pri}} \sqrt{\theta_5}}{\delta_5} \right)^2 \right] + \text{constant} \quad (7)$$

where  $T_{t5}$  is the combustion exit temperature;  $P_{t5}/P_{t7}$  is the pressure ratio across both stages of the turbine;  $W_{\text{pri}}$  is the core engine airflow;  $\theta_5 = T_{t5}/519$ ; and  $\delta_5 = P_{t5}/2116$ .

*Core Noise Spectra.* Examples of derived core noise spectra resulting from subtracting calculated jet noise (on an energy basis) from total measured low frequency noise at low engine power settings are shown in figure 145 for  $100^\circ$ ,  $120^\circ$ , and  $140^\circ$ . It should be noted that the two lowest jet velocity conditions were the only conditions for which the calculated jet noise was at least 6 dB below the total measured noise across the entire spectrum. When the jet noise and the total measured noise are nearly the same level, minor errors in the assumed jet noise level or measured data will cause a magnified error in the derived core noise. Although tones are apparent in the derived spectra at 125 Hz and possibly 250 Hz, the major feature of the low frequency portion of the derived core noise spectrum is a broadband peak in the 250- to 315-Hz region. It is this feature that was taken to be representative of the core noise spectrum. The generalized spectrum chosen for the core noise prediction procedure is shown in figure 146.



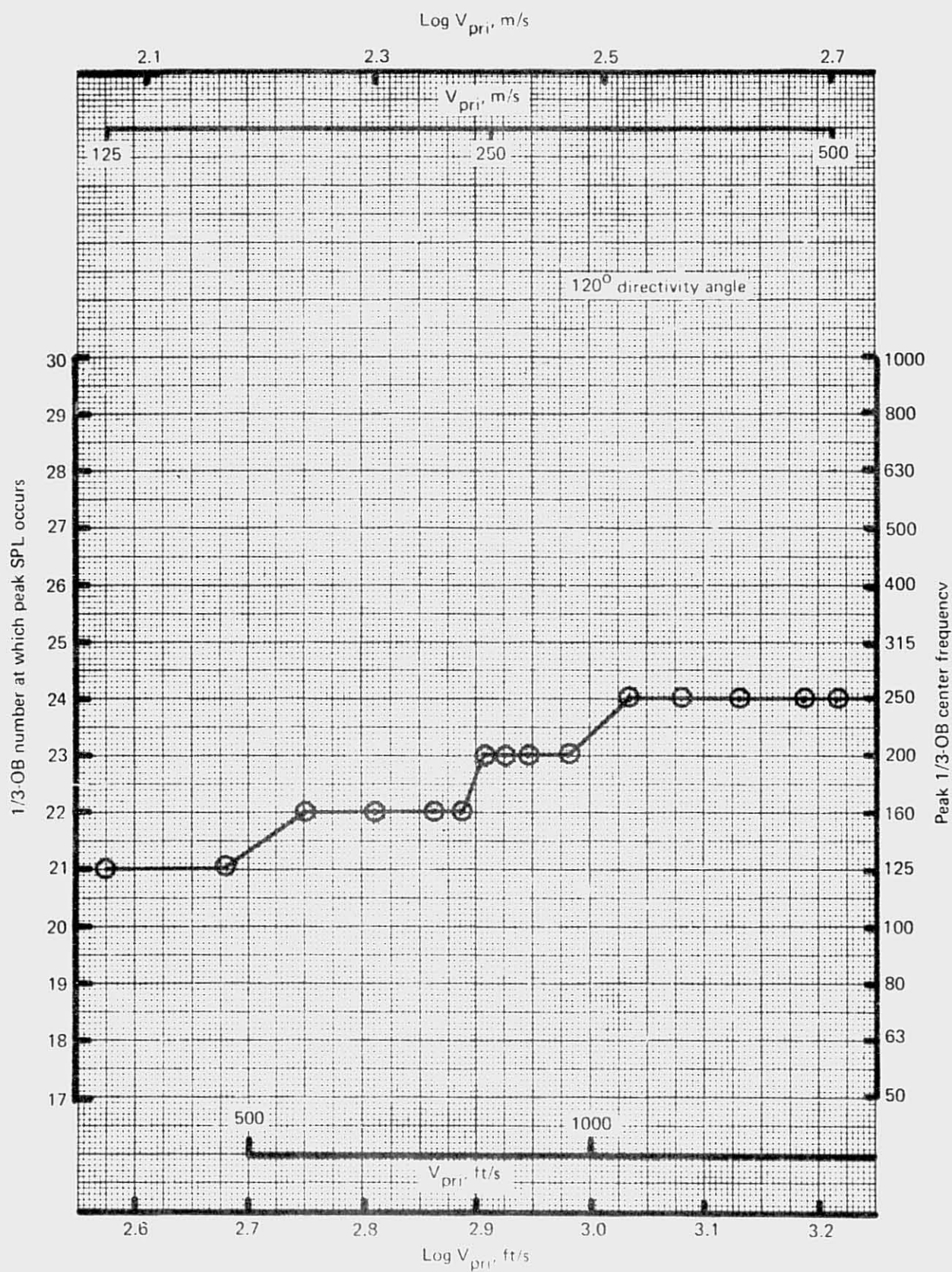


Figure 143. -JT8D-109 Ground Test - Sample Plot of Frequency of Maximum Jet Noise Level Versus Log  $V_{pri}$



Table 18.—JT8D-109 Ground Test—Frequency of Peak Jet Noise (1/3-OB Number of Peak SPL) Versus Log  $V_{pri}$ 

$V_{pri}$ ft/s (m/s)	Log $V_{pri}$ ft/s (m/s)	1/3-OB Number of Peak SPL, deg																
		Angle from inlet $\phi$																
		10	20	30	40	50	60	70	80	90	100	110	120	130	140	150	160	170
375 (114)	2.574 (2.058)	22	20	21	18	22	21	21	20	22	22	21	21	24	22	18	18	18
478 (146)	2.679 (2.163)	22	20	21	18	22	21	21	20	22	22	21	21	24	22	18	18	18
568 (173)	2.754 (2.238)	22	20	21	20	22	22	22	20	22	22	21	22	22	21	18	17	17
656 (200)	2.817 (2.301)	21	20	22	22	22	22	23	20	22	22	22	22	22	19	18	17	17
735 (224)	2.866 (2.350)	21	20	23	22	23	22	23	22	23	22	23	22	22	19	18	17	17
773 (236)	2.888 (2.372)	21	21	23	22	23	22	23	23	23	23	23	22	22	19	18	17	17
805 (245)	2.906 (2.390)	22	22	23	22	23	22	23	23	23	23	23	23	22	19	19	17	17
841 (256)	2.925 (2.409)	22	22	23	22	23	22	23	23	23	23	23	23	22	19	19	17	17
881 (269)	2.945 (2.429)	23	22	23	22	23	23	23	23	22	23	23	23	21	19	19	17	17
959 (292)	2.982 (2.466)	23	23	23	22	23	23	23	23	22	23	23	23	20	19	19	17	17
1076 (328)	3.032 (2.516)	23	23	23	23	23	23	23	23	22	23	23	24	20	19	19	17	17
1211 (369)	3.083 (2.567)	23	23	23	23	23	23	23	23	23	23	23	24	20	19	20	17	17
1361 (415)	3.134 (2.618)	24	23	23	24	24	24	23	23	24	23	24	24	20	19	20	17	17
1524 (465)	3.183 (2.667)	24	24	24	24	24	24	24	24	24	25	25	24	21	21	20	17	17
1644 (501)	3.216 (2.700)	24	24	24	24	24	24	24	24	24	25	25	24	21	21	20	17	17

REPRODUCIBILITY OF THE  
ORIGINAL PAGE IS POOR

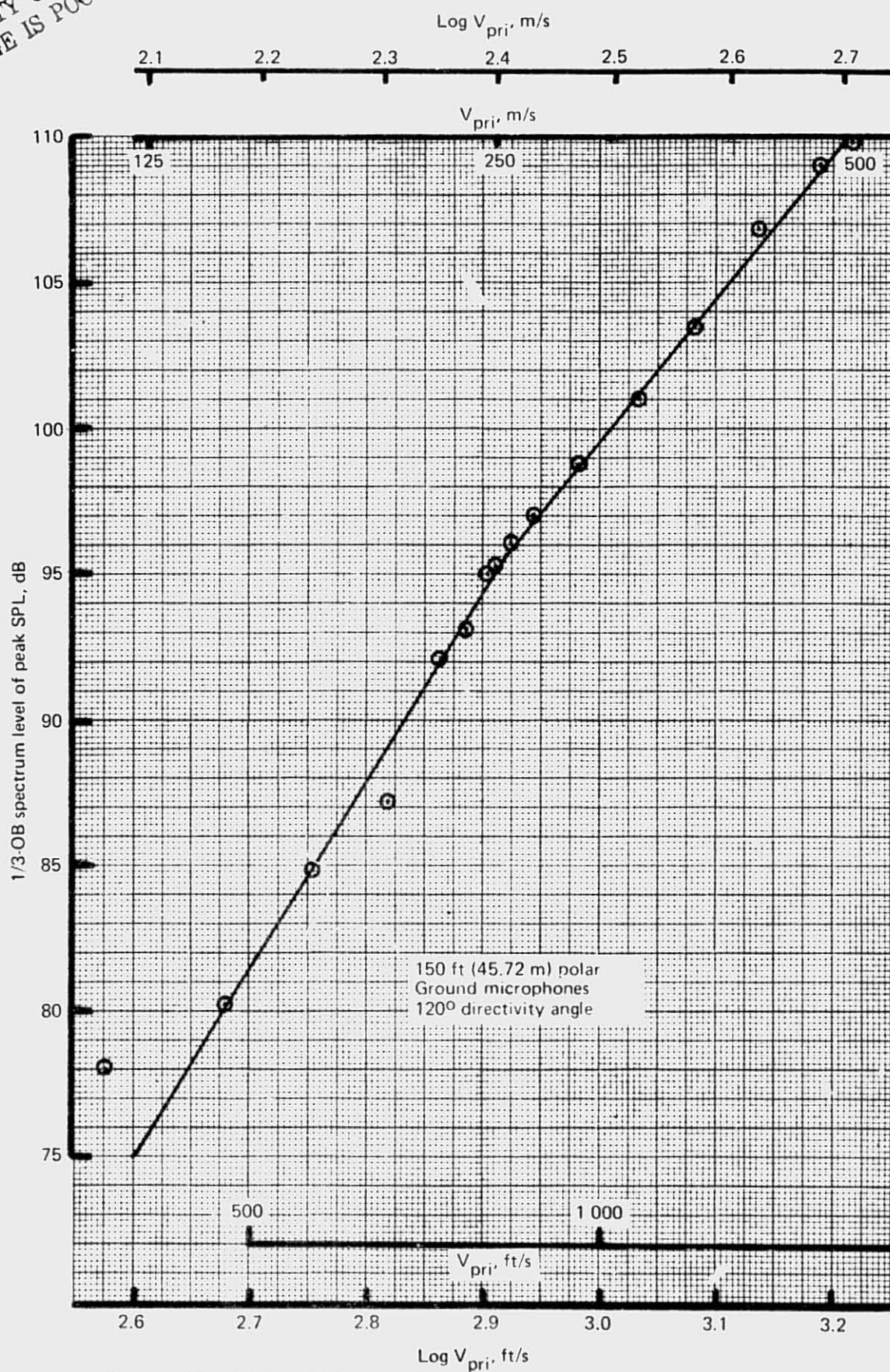


Figure 144. - JT8D-109 Ground Test—Sample Plot of Jet Noise Spectrum  
Peak Level Versus  $\text{Log } V_{pri}$

Table 19.—JT3D-109 Ground Test — Jet Noise Spectrum Peak SPL

Ground microphone noise levels [150 ft (45.72 m) polar]

(Use linear interpolation between given coordinates)

Directivity angle, deg	Log V <sub>prj</sub> , ft/s (m/s)		Jet spectrum peak level, dB
10	2.60	(2.084)	68.0
	3.25	(2.734)	98.8
20	2.60	(2.084)	71.7
	3.25	(2.734)	100.1
30	2.60	(2.084)	72.0
	3.25	(2.734)	101.0
40	2.60	(2.084)	68.9
	3.25	(2.734)	102.1
50	2.60	(2.084)	69.6
	3.25	(2.734)	102.6
60	2.60	(2.084)	67.7
	3.25	(2.734)	101.8
70	2.60	(2.084)	69.3
	3.25	(2.734)	102.0
80	2.60	(2.084)	71.7
	3.25	(2.734)	102.4
90	2.60	(2.084)	73.9
	2.95	(2.434)	93.7
	3.25	(2.734)	105.9
100	2.60	(2.084)	76.0
	2.93	(2.414)	93.0
	3.25	(2.734)	106.3
110	2.60	(2.084)	76.0
	2.91	(2.394)	93.2
	3.25	(2.734)	110.3
120	2.60	(2.084)	75.0
	2.92	(2.404)	95.6
	3.25	(2.734)	111.9
130	2.60	(2.084)	80.6
	3.25	(2.734)	116.5
140	2.60	(2.084)	76.9
	3.05	(2.534)	110.0
	3.25	(2.734)	121.2
150	2.60	(2.084)	76.4
	3.04	(2.524)	112.0
	3.25	(2.734)	123.0
160	2.60	(2.084)	76.8
	3.02	(2.504)	110.4
	3.25	(2.734)	118.9
170	2.60	(2.084)	79.8
	3.01	(2.494)	110.0
	3.25	(2.734)	119.4

Table 20.—JT8D-109 Ground Test — Primary Velocity Exponent for  
Jet Peak SPL Relationship to Log  $V_{pri}$

Directivity angle, deg	Velocity exponent <sup>a</sup> , n
10	4.74
20	4.37
30	4.46
40	5.11
50	5.01
60	5.25
70	5.03
80	4.72
90	4.07
100	4.16
110	5.03
120	4.94
130	5.52
140	5.60
150	5.24
160	3.70
170	3.92

<sup>a</sup>For primary jet velocities greater than 1000 ft/s (340.8 m/s).

**Core Noise Level.**—The SPL of the derived core noise for the 1/3-OB with center frequency of 315 Hz is plotted in figure 150 for 120°, 130°, and 140°. The SPL's are normalized by the factor  $(20 \log T_{t5} + 10 \log W_{pri} \sqrt{\theta_5/\delta_5})$  and plotted versus  $10 \log P_{t5}/P_{t7}$ . The lines chosen to represent the core noise levels are also shown in figure 147. It is seen that the same slope was used for each angle. The relationship for 130° is:

$$\text{SPL}_{130^\circ} = 20 \log T_{t5} + 10 \log \frac{W_{pri} \sqrt{\theta_5}}{\delta_5} + 20 \log P_{t5}/P_{t7} + 0.5 \quad (8)$$

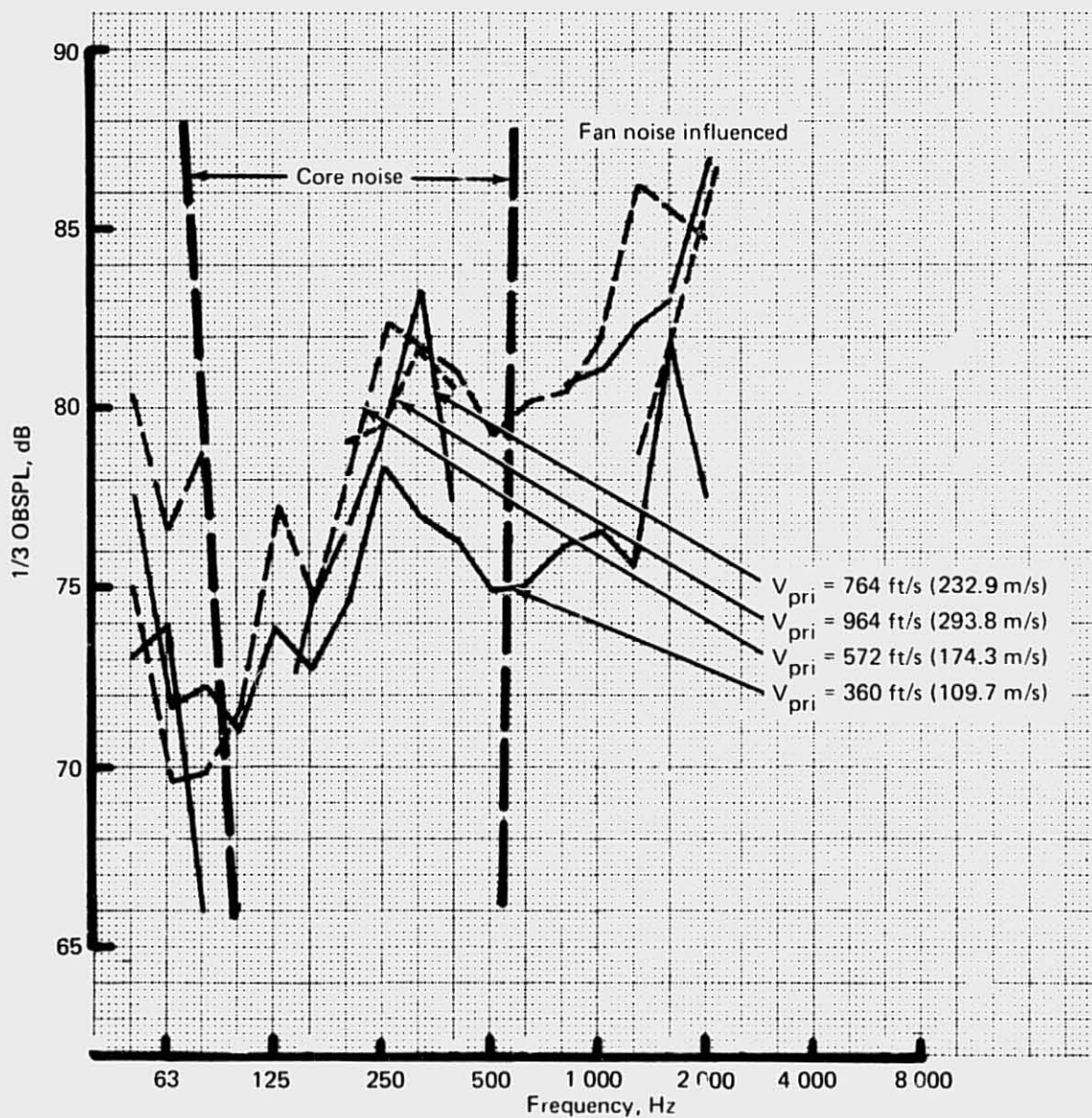
<sub>315 Hz, 1/3-OB</sub>  
<sub>150-ft (45.72-m) polar</sub>  
<sub>grd mic</sub>

The SPL for the remaining angles are related to the 130° SPL by an additive constant. This constant is termed the directivity factor  $D(\theta)$  defined by:

$$D(\theta) = \text{SPL}_{315 \text{ Hz}}(\theta) - \text{SPL}_{315 \text{ Hz}}(130^\circ) \quad (9)$$

**Core Noise Directivity.**—Since the core noise SPL slopes and spectrum shapes are the same at all angles, the directional characteristics of the core noise are independent of power setting. Figure 148 shows the curve of directivity factor  $D(\theta)$  versus radiation angle. The peak is seen to occur at 130° from the inlet axis. Since the same spectrum shape is assumed for each angle, this curve applies to all 1/3-OB center frequencies.



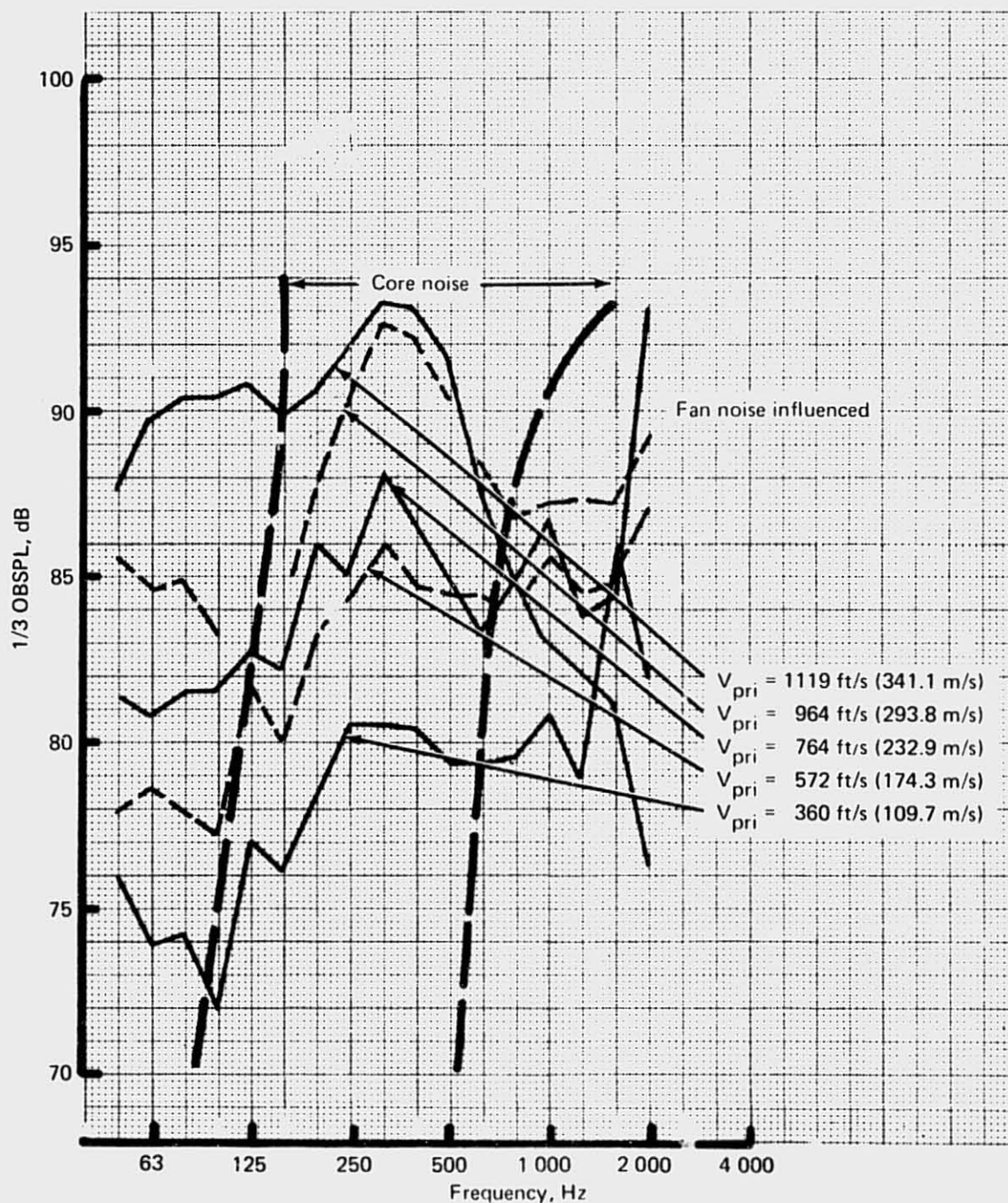


(a)  $100^\circ$  Directivity Angle

Figure 145.—JT8D-15 Ground Test—Sample Working Plot For Evaluation of Core Noise (Measured Total Noise Minus Predicted Jet Noise): 150 ft (45.72 m) Polar, Ground Microphones, Inlet Baffled

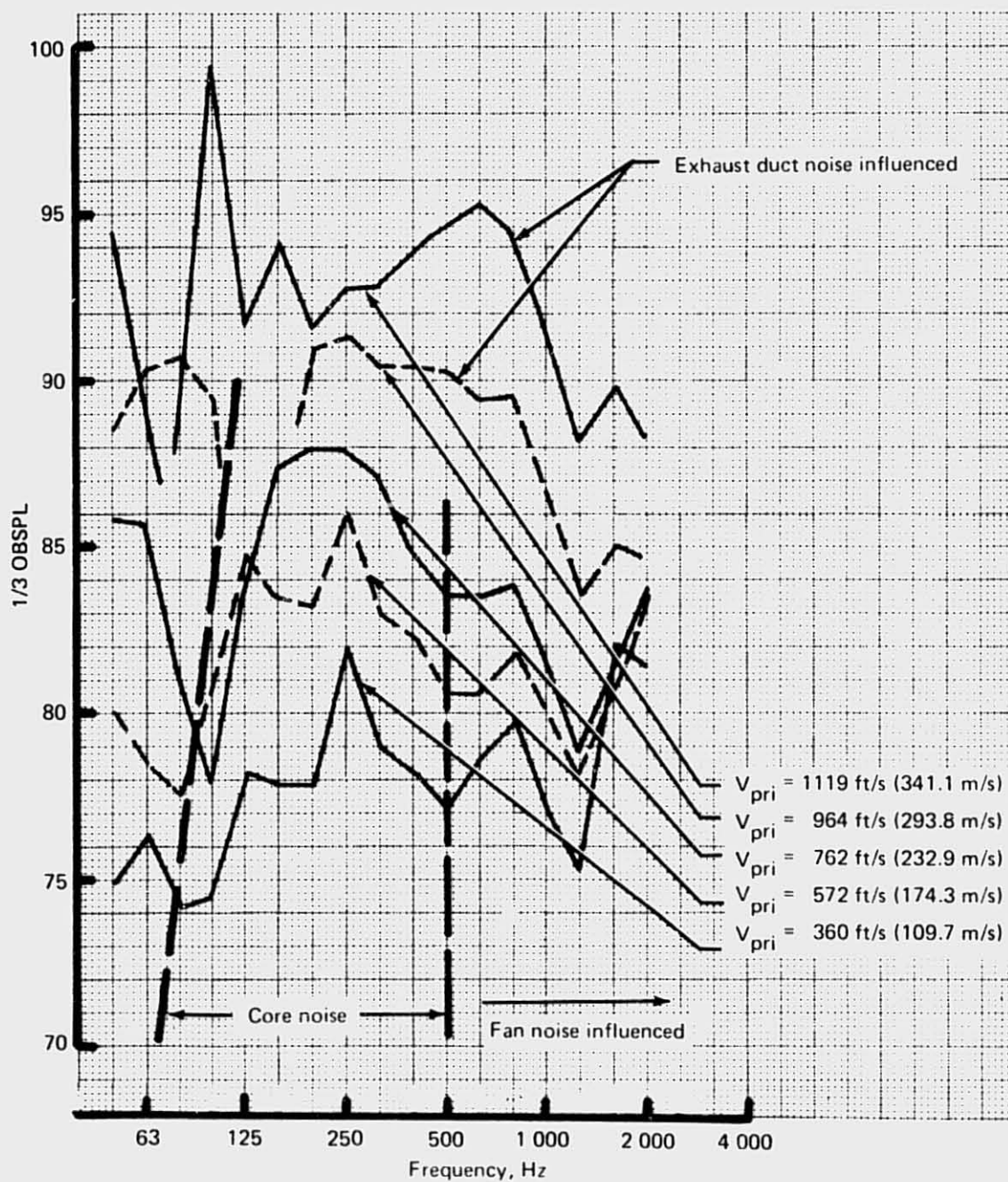


REPRODUCIBILITY OF THE  
ORIGINAL PAGE IS POOR



(b) 120° Directivity Angle

Figure 145.—(Continued)



(c)  $140^\circ$  Directivity Angle

Figure 145.—(Concluded)

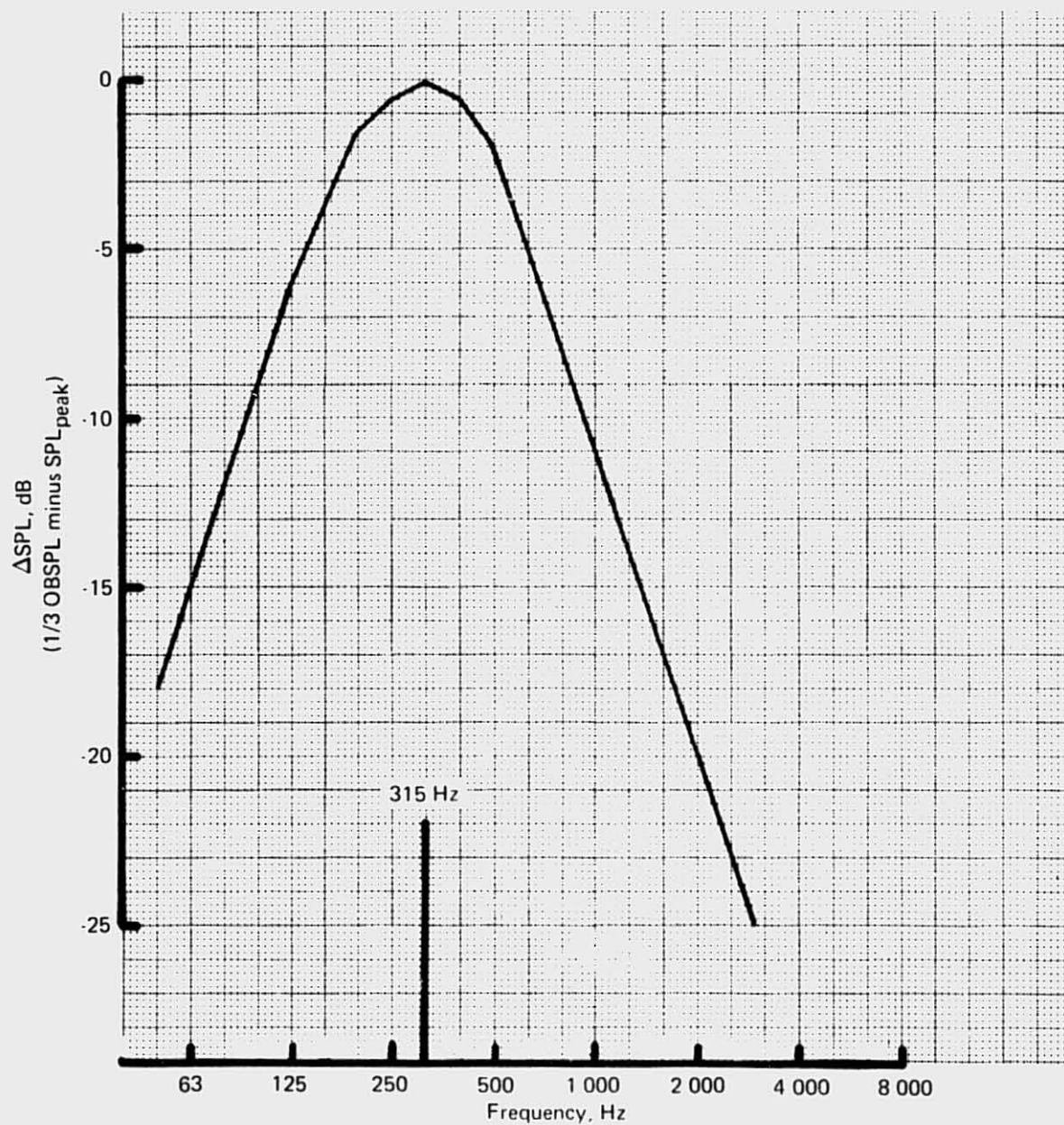


Figure 146.—JT8D-15 Ground Test—Normalized Core Noise Spectrum Shape, Average for All Angles and Power Settings



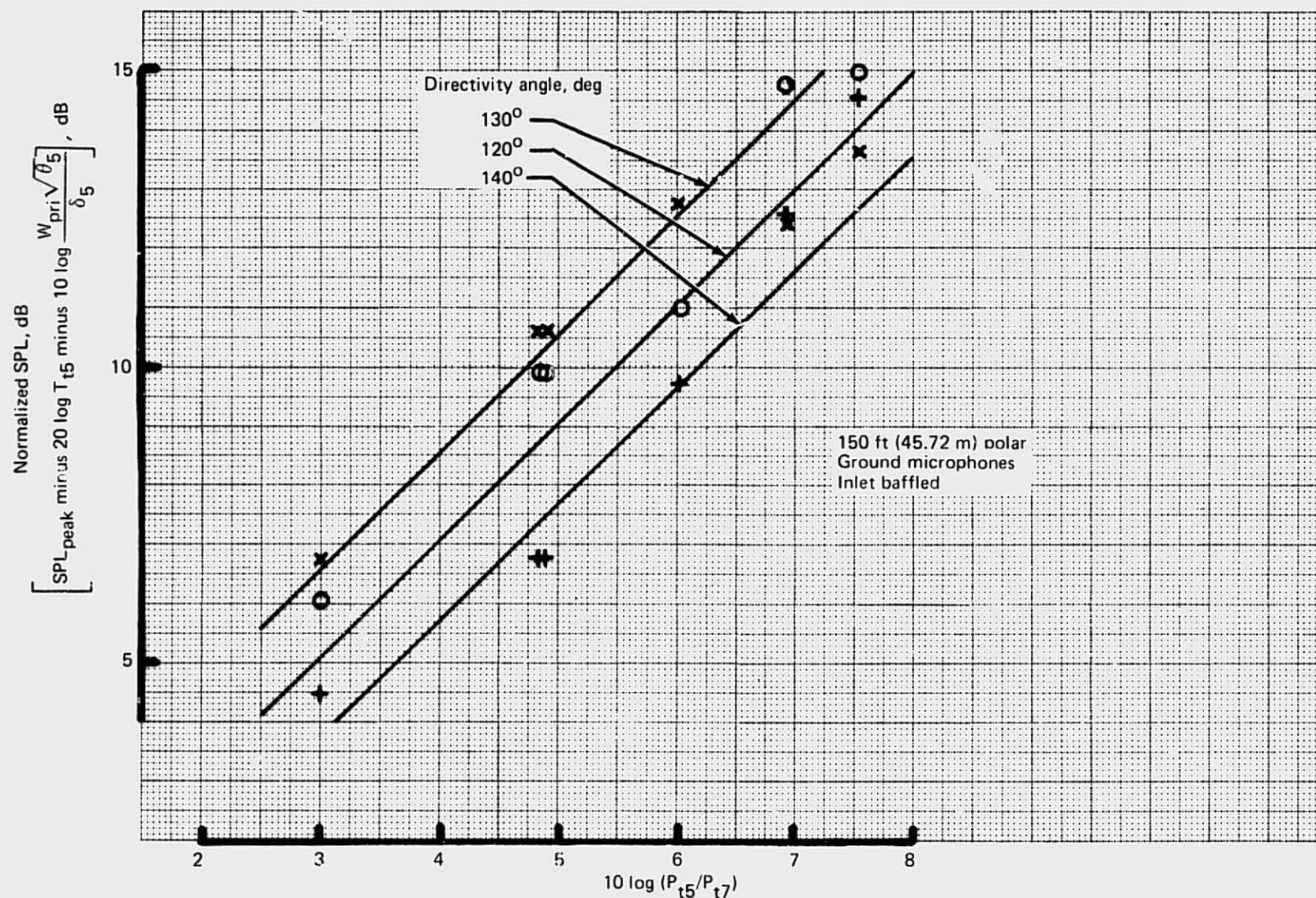


Figure 147.—JT8D-15 Ground Test—Normalized Core Noise Peak Sound Pressure Level

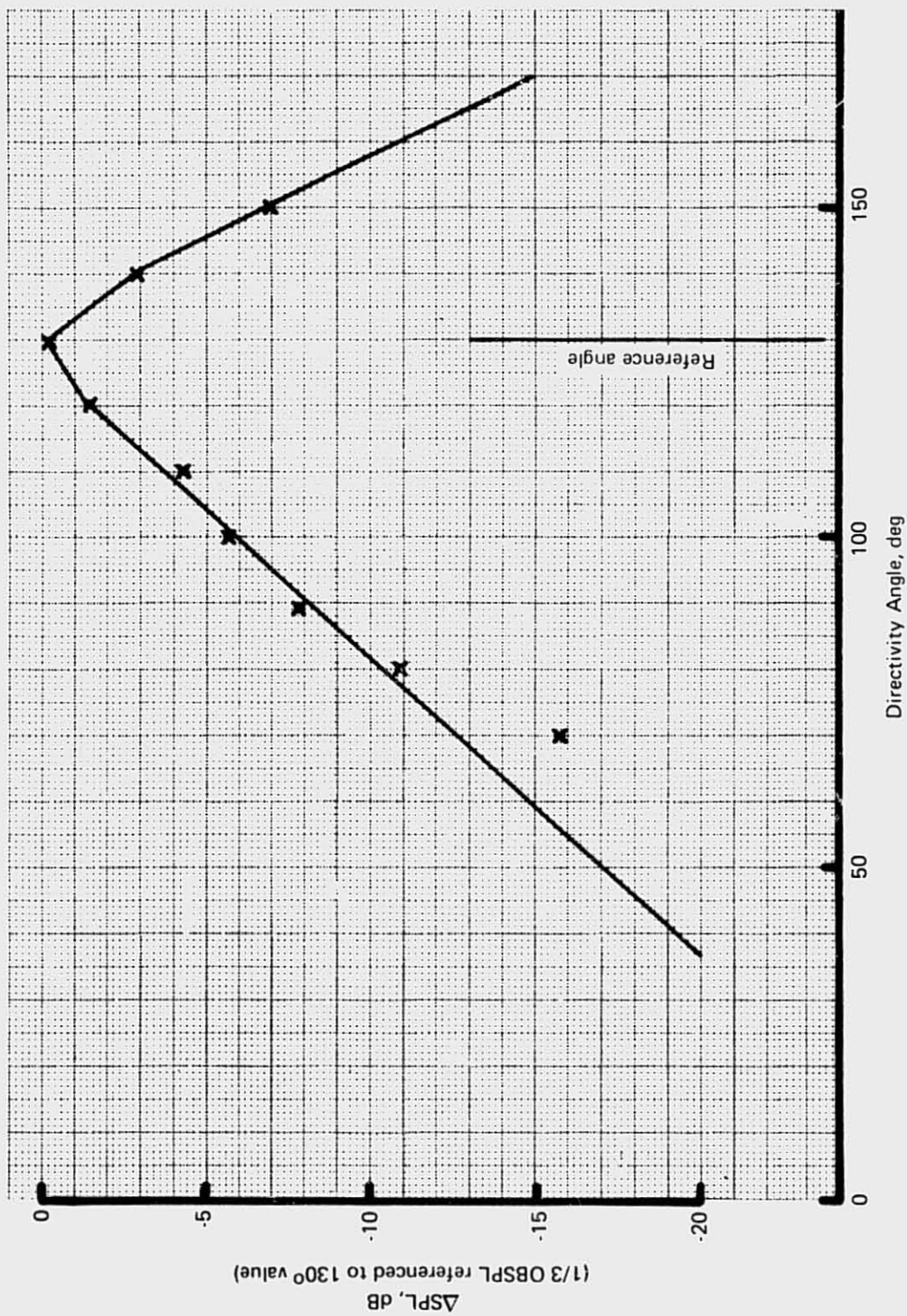


Figure 148. — JT8D-15 Ground Test—Normalized Peak Core Noise Directivity, Average for All Power Settings



**Tabulated Curves.**—The curves shown in figures 146 through 148 are the basis for a prediction procedure for low frequency core noise for the JT8D-15 engine. The SPL for a core noise 1/3-OB center frequency at any angle is determined by

$$\text{SPL}(f, \theta) = \text{SPL}_{130^\circ, 315 \text{ Hz}} + D(\theta) + [\text{SPL}(f) - \text{SPL}(315 \text{ Hz})] \quad (10)$$

where

$$\text{SPL}_{130^\circ, 315 \text{ Hz}} = 20 \log T_{t5} + 10 \log \frac{W_{\text{pri}} \sqrt{\theta_5}}{\delta_5} + 20 \log P_{t5}/P_{t7} + 0.5 \quad (11)$$

$D(\theta)$  is shown in figure 147 and tabulated in table 21 and  $[\text{SPL}(f) - \text{SPL}(315 \text{ Hz})]$  is shown in figure 146 and tabulated in table 21.

#### 4.2.1.10 Core Noise: JT8D-115 Engine

Core noise levels for the JT8D refan engine were established from acoustic data taken on a JT8D-109 engine test conducted by P&WA (ref. 7). Predicted jet noise SPL levels were logarithmically subtracted from measured total noise spectra to yield core noise spectrum shapes.

The core noise empirical model that resulted from the P&WA JT8D-109 test has been adopted for use also for the JT8D-115 engine and for the Contractor's airplane flyover noise analysis. It is this core noise model that is reported here rather than results of the JT8D-115 test data analysis. However, comparisons of predictions made using this model with measured JT8D-115 data show no contradictions (as shown later in sec. 4.2.2.2) and, at this point, there is no reason to believe that the JT8D-109 core noise model is not also applicable to the JT8D-115.

**Resulting Core Noise Empirical Model.**—Details of the core noise empirical model established by P&WA were changed only slightly in format by the Contractor for computer programming purposes. The JT8D-109 core noise component calculated for the final refan program airplane flyover noise analysis was computed by the method outlined in the following paragraph. It should be noted this model was developed specifically for the JT8D-109 and can not be directly applied to noise predictions of different types of engines.

**Core Noise Basic Level.**—Sound pressure level of the peak (400 Hz) band was correlated with a core noise parameter:

$$\log_{10} \left[ \sqrt{W_{\text{pri}}} \left( \frac{P_{t4}^{14.7}}{T_{t4}^{519}} \right) (T_{t5} - T_{t4}) \right] \quad (12)$$

Figure 149 was used to define the basic noise level of the core noise spectrum at any angular location.

Table 21.—JT8D-15 Core Noise Empirical Model: 150 ft (45.72 m) Polar,  
Ground Microphones

Directivity factor $\theta$ , deg $D(\theta)$ , dB		Spectrum shape f, Hz    SPL (f) - SPL (315 Hz), dB	
170	-15.0	50	-18.0
160	-11.0	63	-15.0
150	- 6.9	80	-12.0
140	- 2.9	100	- 9.0
130	0	125	- 6.0
120	- 1.5	160	- 3.5
110	- 3.8	200	- 1.5
100	- 5.9	250	- 0.5
90	- 8.2	315	0
80	-10.5	400	- 0.5
70	-12.7	500	- 2.0
60	-14.9	630	- 5.0
50	-17.1	800	- 8.0
40	-19.3	1000	-11.0
30	-21.5	1250	-14.0
20	-23.7	1600	-17.0
10	-25.9	2000	-20.0
		2500	-23.0
		3150	-26.0
		4000	-29.0
		5000	-32.0
		6300	-35.0
		8000	-38.0
		10 000	-41.0

$$SPL_{315 \text{ Hz}} = 20 \log T_{t5} + 10 \log \frac{W_{pri} \sqrt{\theta_5}}{\delta_5} + 20 \log \frac{P_{t5}}{P_{t7}} + 0.5$$

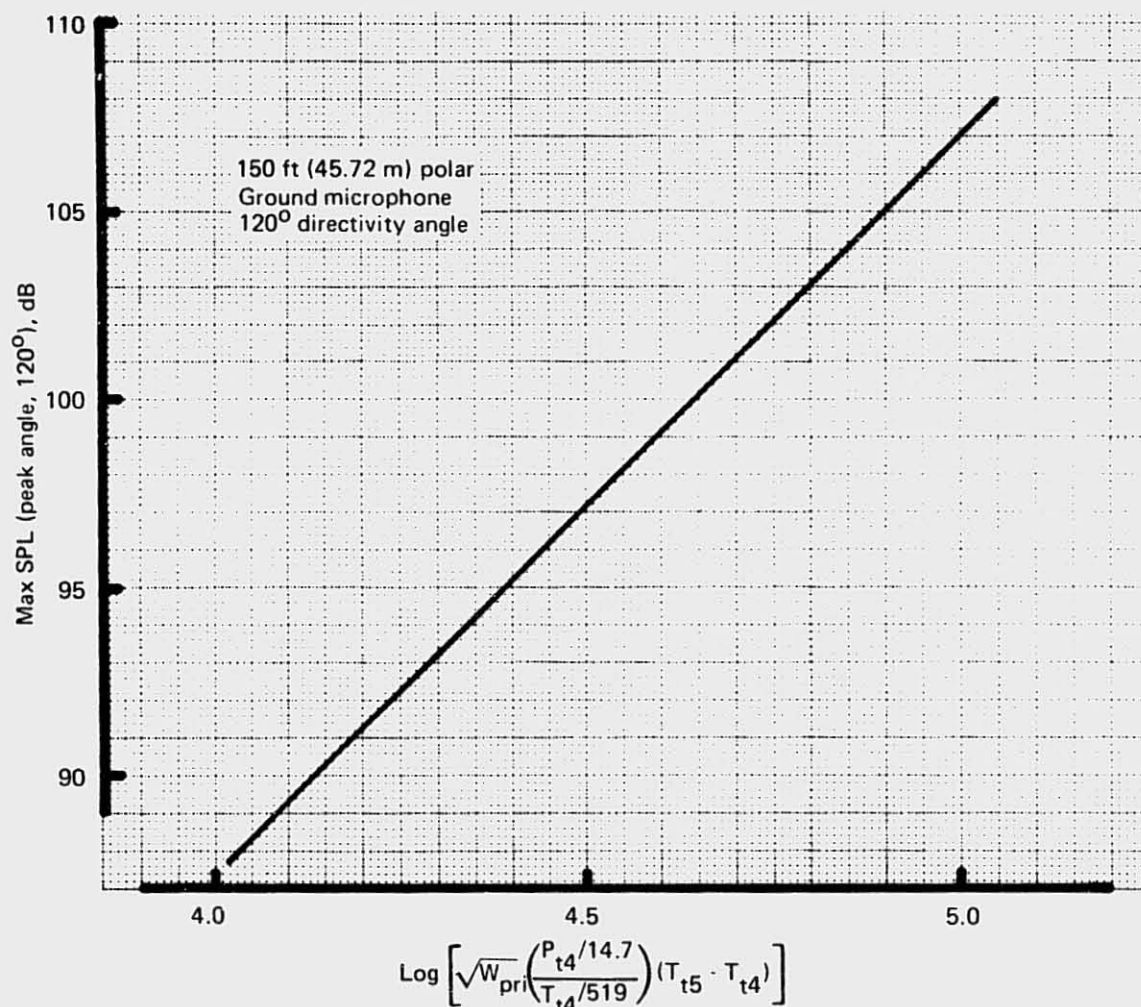
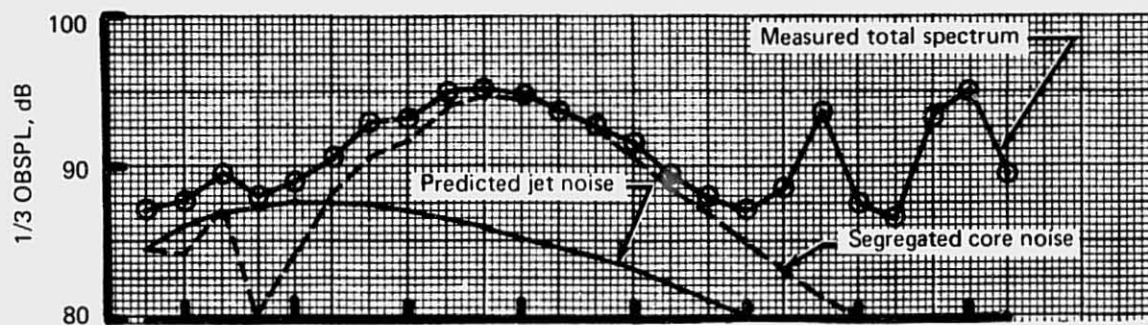


Figure 149.—JT8D-109 Ground Test—Core Noise Basic Level

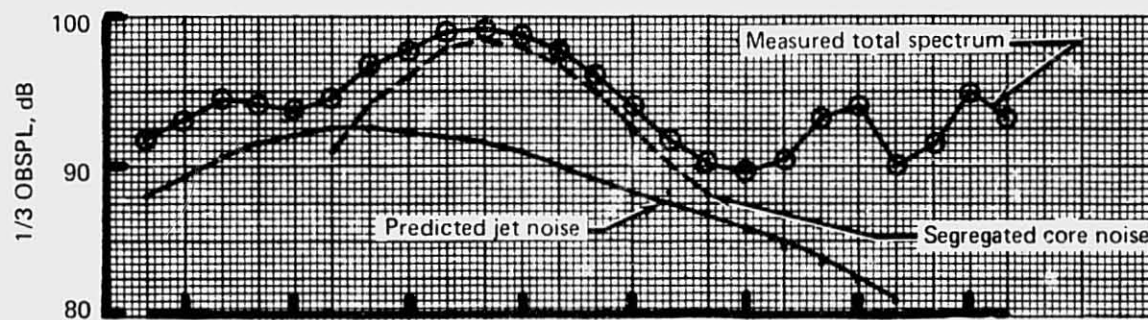
**Core Noise Spectrum Shape.**—The spectrum shape shown for the core noise component in figure 150 is very similar for the three different power settings shown. Consistency of spectrum shape for all angles in the aft quadrant was similarly evident, so one spectrum shape was adopted as an average. It was used to define core noise at all power settings and all locations in both the forward and aft quadrant (fig. 151). It was noted that for all conditions the spectrum peak noise occurred at the 400-Hz band in the 1/3-OB spectrum.

**Core Noise Directivity.**—Maximum noise levels from the core noise source were found to occur at 120° from the inlet axis as shown in figure 152. This curve was intended for use in establishing the SPL of the peak (400 Hz) in the spectrum for all locations other than 120° from the inlet axis.

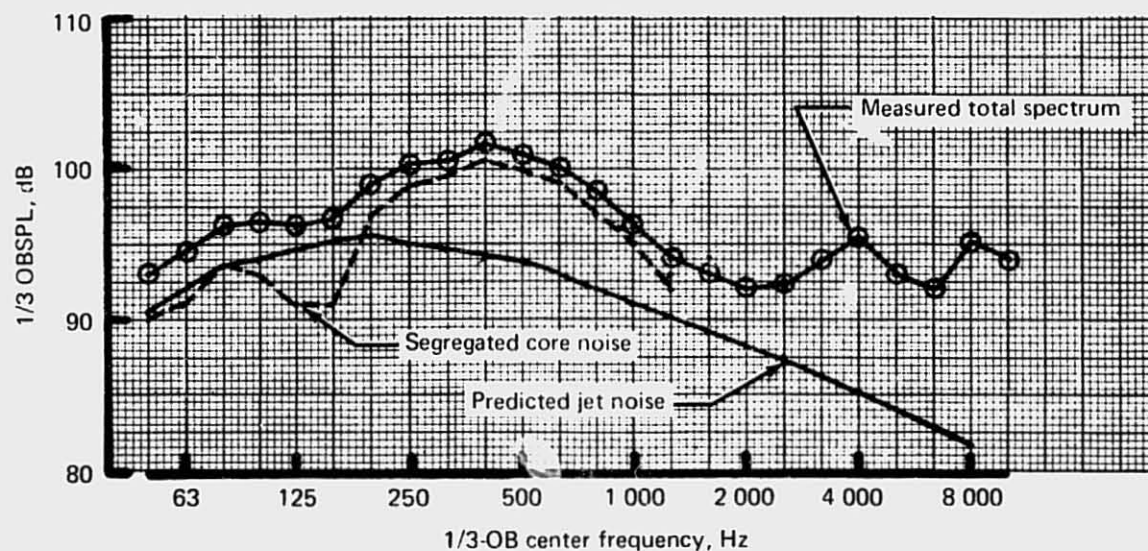
REPRODUCIBILITY OF THE  
ORIGINAL PAGE IS POOR



(a)  $N_1/\sqrt{\theta_{t2}} = 5199$



(b)  $N_1/\sqrt{\theta_{t2}} = 5783$



(c)  $N_1/\sqrt{\theta_{t2}} = 6096$

Figure 150.—JT8D-109 Ground Test—Core and Jet Noise Levels: 150 ft (45.72 m) Polar, Ground Microphone at 120° Directivity Angle



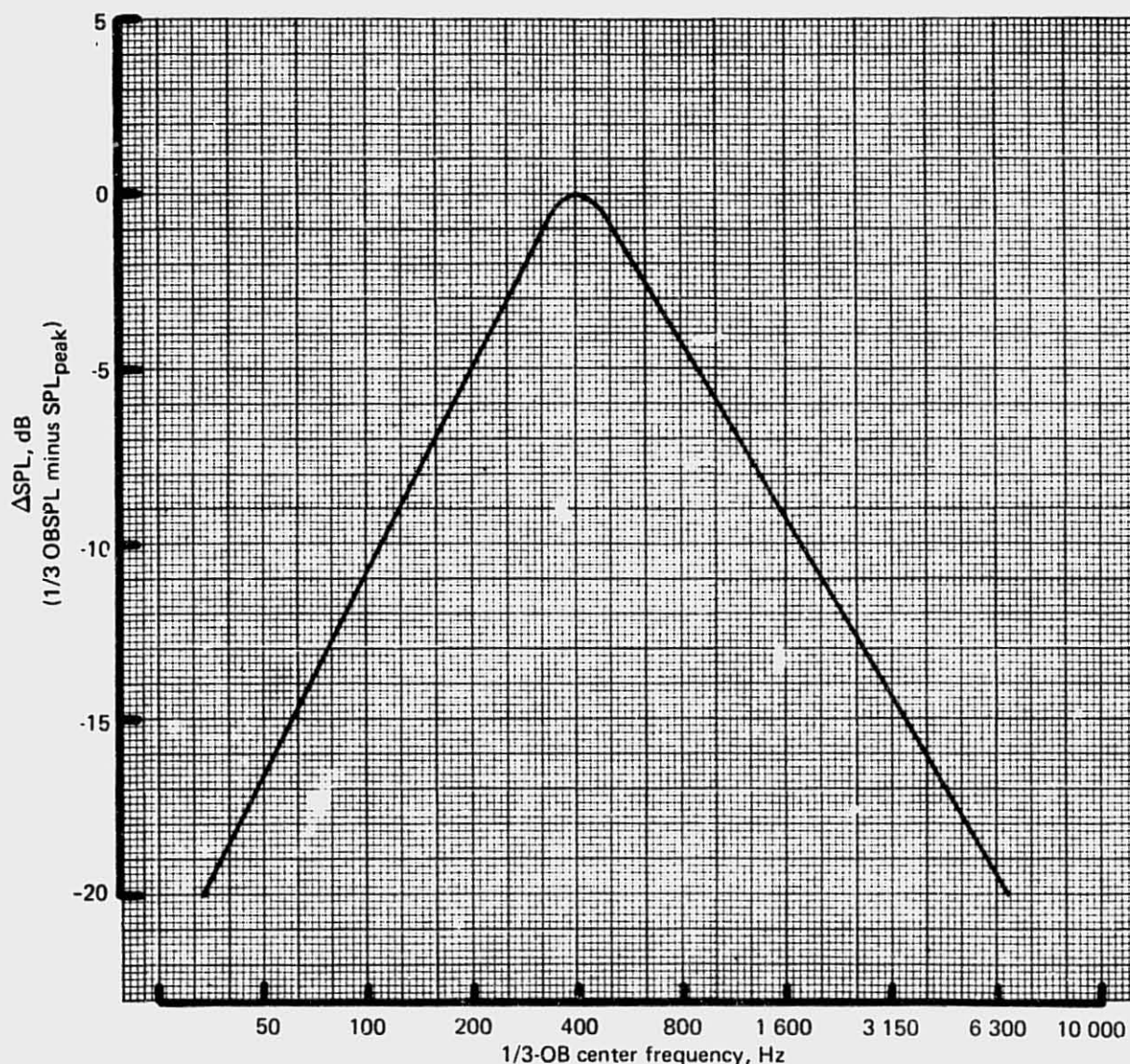


Figure 151.—JT8D-109 Ground Test—Core Noise Spectrum Shape,  
Average for All Angles and Power Settings

#### 4.2.1.11 Exhaust Duct Flow Noise

The source, which has been given the name exhaust duct flow noise, was not anticipated in the acoustic data of either the JT8D-15 or -115 ground tests. It shows up as a bump in the spectra measured in the aft quadrant at high power settings, peaking at 800 Hz on the JT8D-15 and at 500 Hz on the JT8D-115 engine. During the early stages of data analysis, the source of this spectrum bump was entirely speculative. It was attributed at various times to jet noise, to burner noise, and even to facility irregularities. It was not until late in the JT8D-115 data analysis that cross correlation studies between far-field microphones and flush-mounted microphones in the exhaust duct showed that this noise was generated in the mixing region of the exhaust duct. The following sections describe the analysis of the noise data relating to this source and describe its level, spectral, and directivity characteristics to the extent that the present data will permit. However, much work remains to be done to fully understand this new noise source.



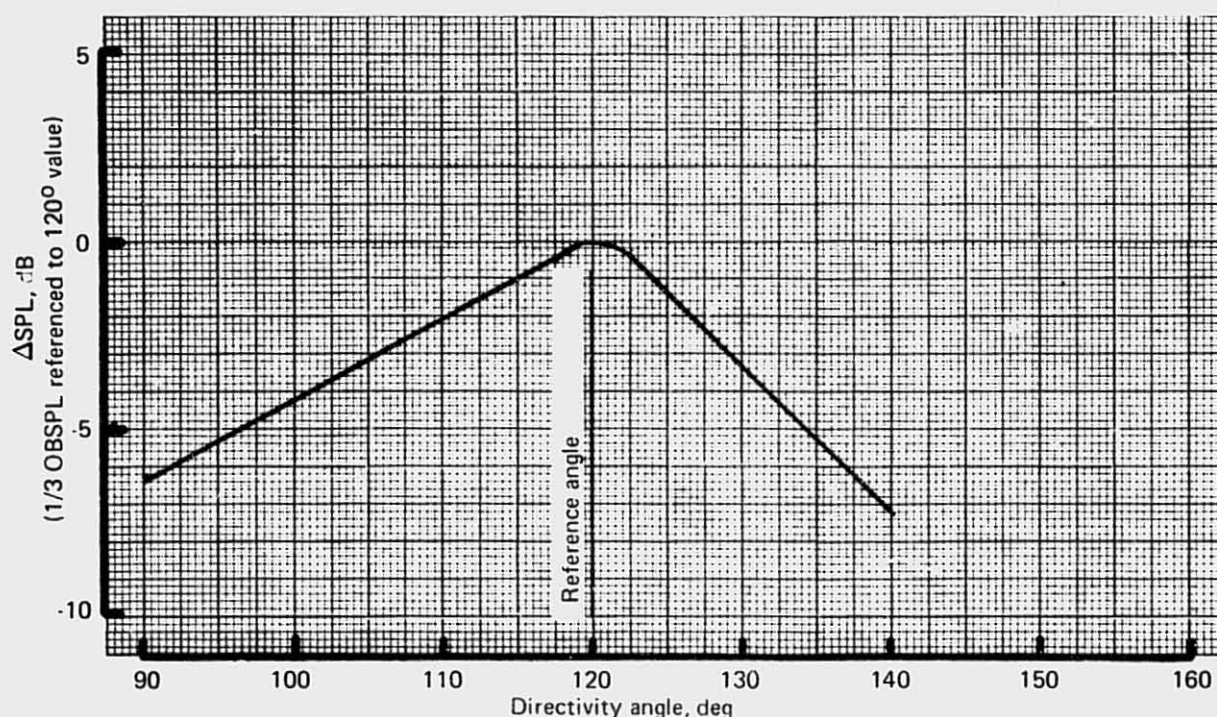


Figure 152 —JT8D-109 Ground Test—Core Noise Directivity,  
Average for All Power Settings

#### 4.2.1.12 Exhaust Duct Flow Noise: JT8D-15 Engine

The jet noise evaluation procedure discussed in section 4.2.1.7 was based on the independence of the jet noise spectrum shape with engine power setting variations. Examples were given demonstrating the ability to match the measured high power setting low frequency spectra at a given angle onto one curve with proper shifting of the SPL and frequency coordinates. However, this procedure was not successful at angles close to the jet axis ( $140^{\circ}$  to  $160^{\circ}$ ). When the spectra at one of these angles were normalized so that the region in which the peak SPL's occurred overlaid, it was evident that the frequency ranges 600 to 800 Hz for all three angles and also those for 250 Hz at  $150^{\circ}$  and  $160^{\circ}$  followed a different power setting dependence. The resulting curves are shown in figures 153 and 154 for  $140^{\circ}$  and  $150^{\circ}$ . The peak SPL regions of the spectra are considered to be jet noise controlled and were used to define the peak frequency and peak SPL versus  $\log V_{pri}$  relationships in the jet noise prediction procedure. Curves showing the variation of the 800-Hz 1/3 OBSPL with  $\log V_{pri}$  compared with the peak SPL region are shown in figures 155 and 156. The velocity exponent for the 800-Hz region is seen to be approximately 10 compared to the approximately eighth-power relationship for the peak region. This behavior is very similar to the 500-Hz noise observed with the JT8D-115 engine, discussed in section 4.2.1.13. It is believed that the generation mechanism is the same for both engines. As discussed in section 4.2.2, this noise is probably generated within the exhaust duct of the engine. The increased engine diameter associated with the JT8D refan engine probably accounts for the change in frequency of this noise. The ratio of peak frequencies for the two engines (800 Hz/500 Hz) is within the range of ratios of total diameters, primary diameters, and secondary annulus diameters.

REPRODUCIBILITY OF THE  
ORIGINAL PAGE IS POOR

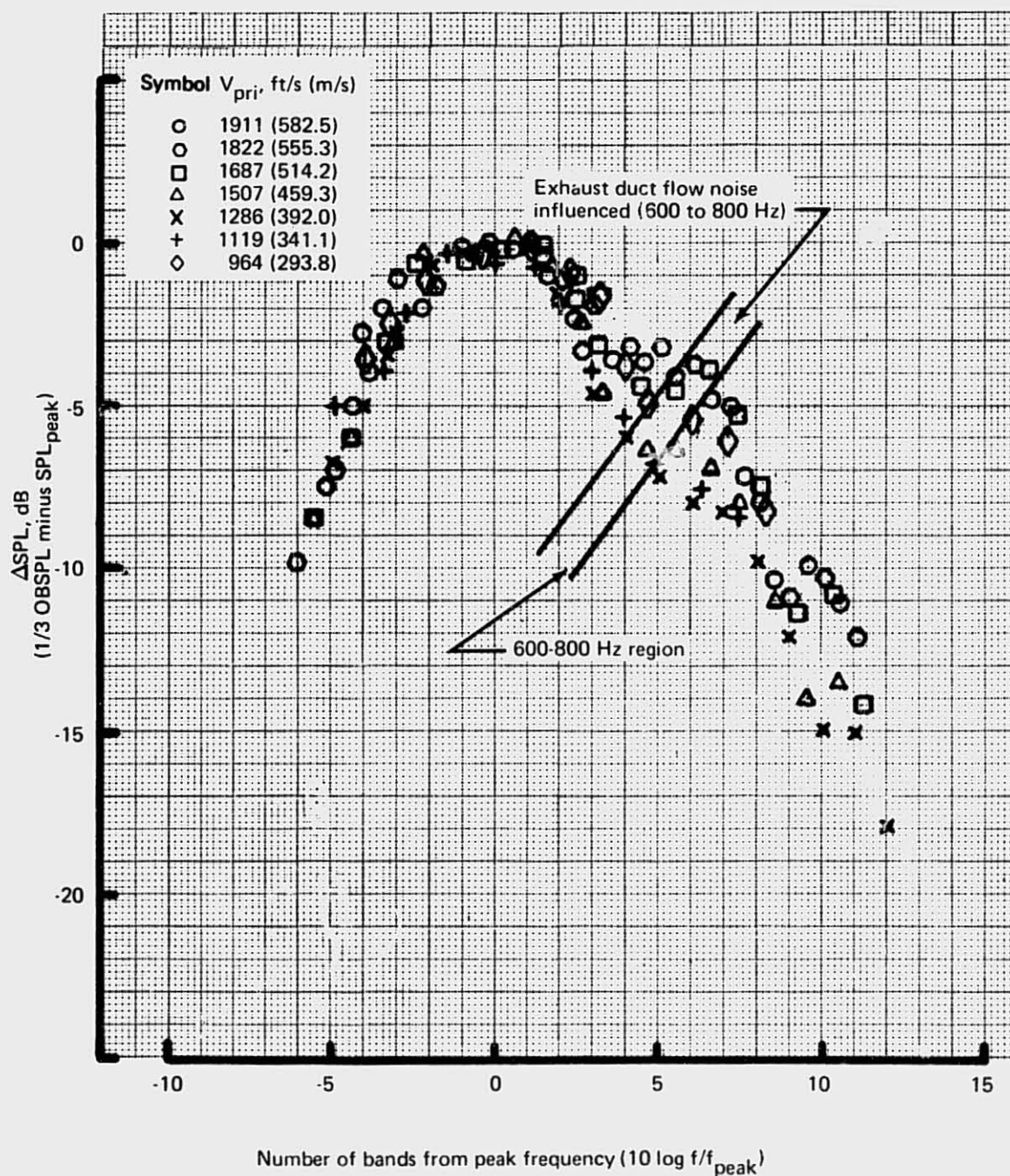


Figure 153.—JT8D-15 Ground Test—Normalized Spectra Showing Influence of Exhaust Duct Flow Noise,  $140^\circ$  Directivity Angle

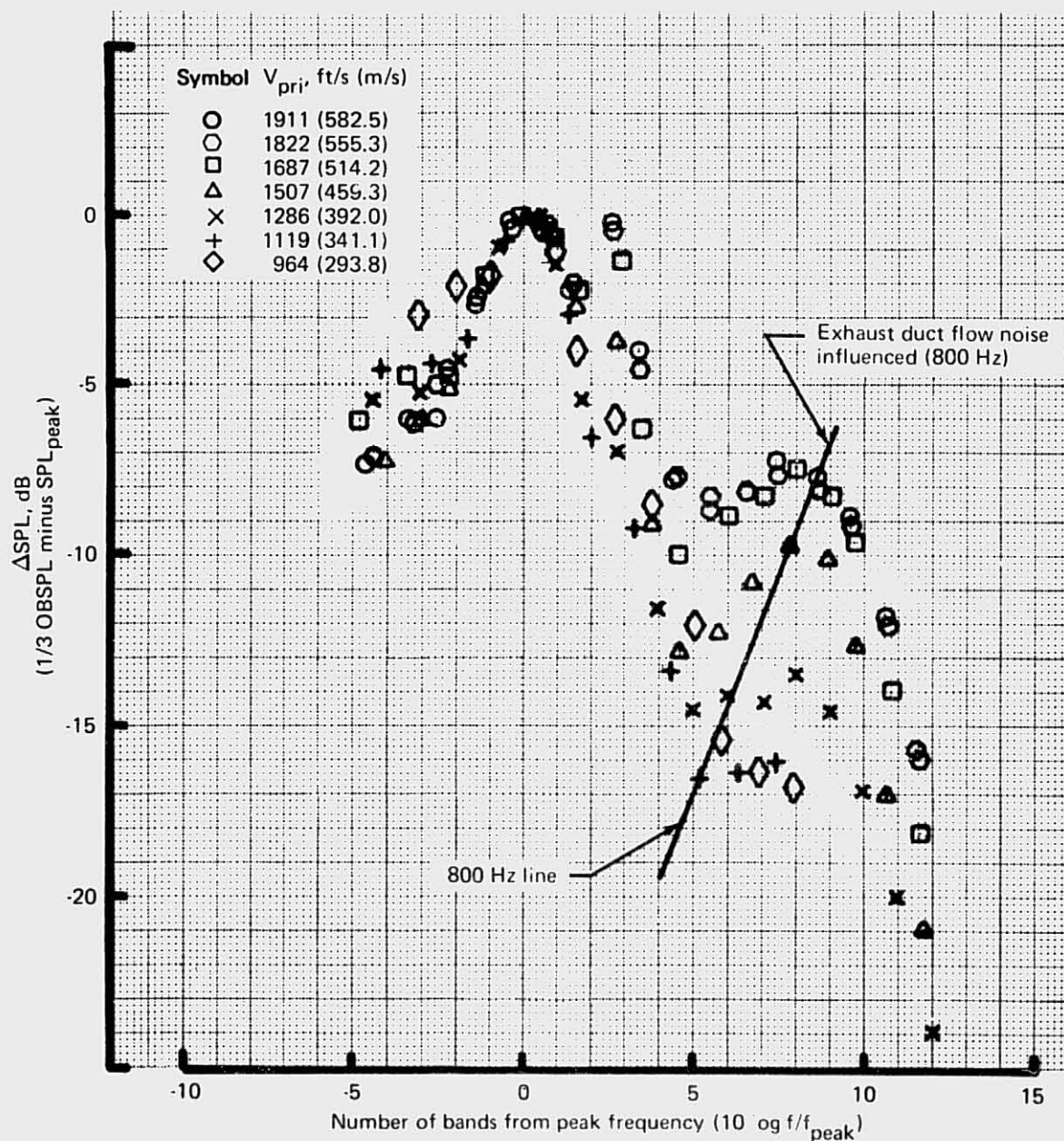


Figure 154.—JT8D-15 Ground Test—Normalized Spectra Showing Influence of Exhaust Duct Flow Noise,  $150^\circ$  Directivity Angle



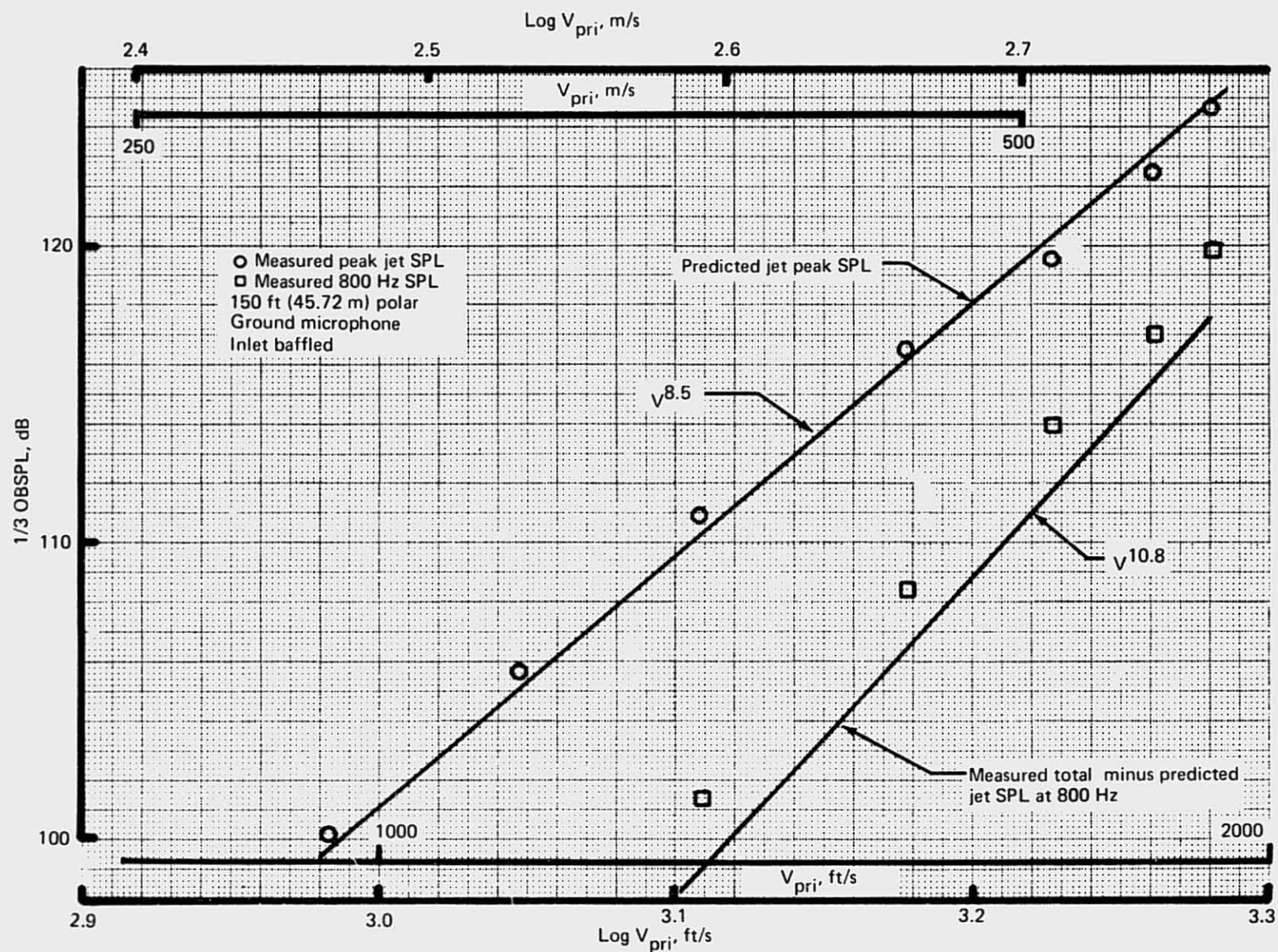


Figure 155.—JT8D-15 Ground Test—Jet and Exhaust Duct Flow Noise Comparison,  $140^\circ$  Directivity Angle

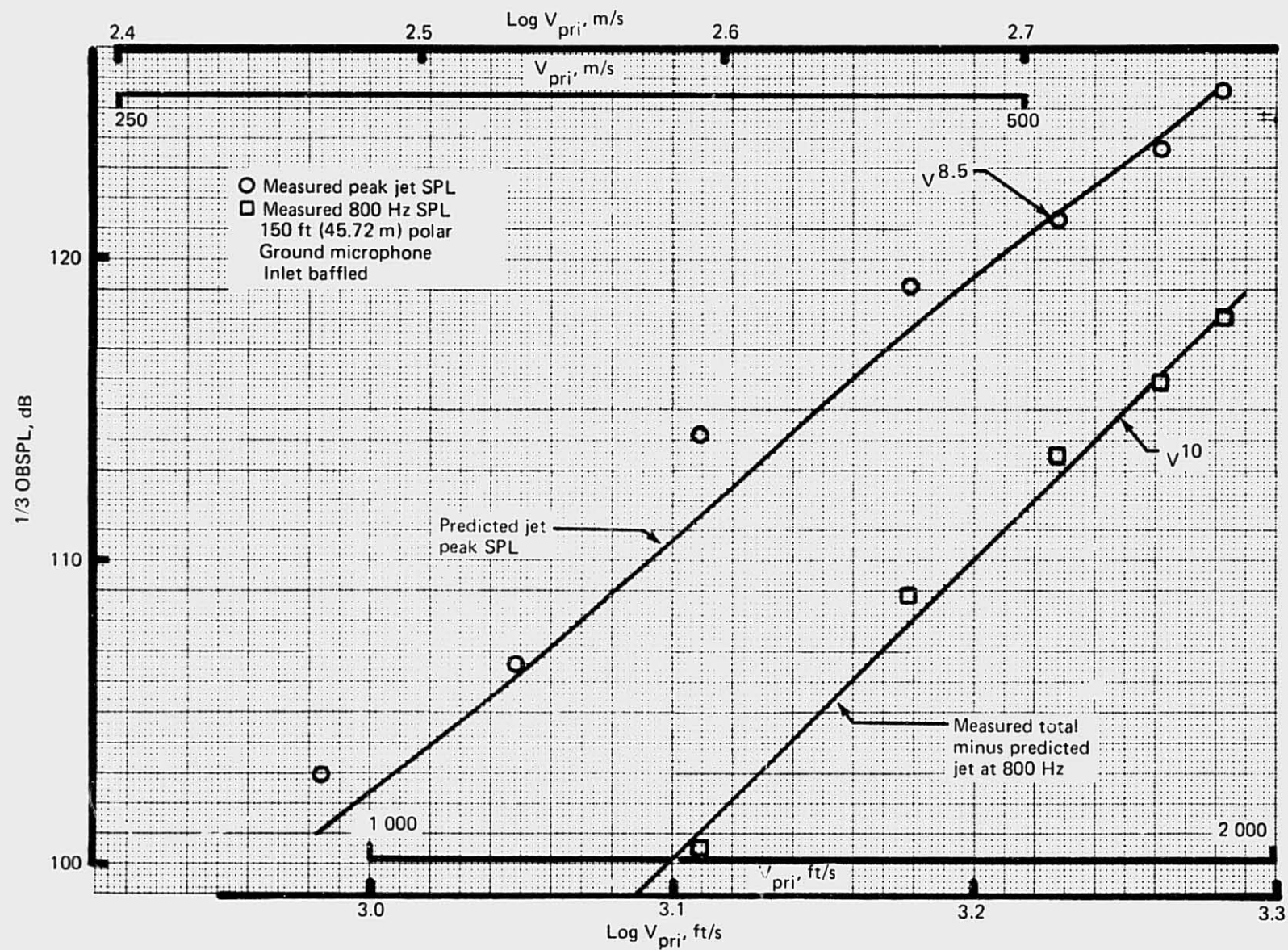


Figure 156.—JT8D-15 Ground Test—Jet and Exhaust Duct Flow Noise Comparison, 150° Directivity Angle



#### 4.2.1.13 Exhaust Duct Flow Noise: JT8D-115 Engine

Two methods of noise data analysis were used to determine the internal noise component in the measured aft arc far-field spectra from the JT8D-115 ground test. In one, a direct cross correlation and coherence function technique was applied to internal exhaust duct and external ground microphone data. In the other, a predicted jet and core noise spectrum (obtained from JT8D-109 data) was subtracted from the measured total noise. The two methods show good agreement on the level and directivity of internal noise but differ on the spectrum shape. These analyses indicate that the internal noise component dominating the aft arc spectra at engine takeoff power results from a turbulent flow process in the exhaust duct.

*Correlation Analysis.*—Internal exhaust duct noise measurements were obtained as part of the diagnostic testing to identify the internal noise component. Internal microphone locations for the exhaust system are shown in figure 22. These data were directly correlated with external ground microphone data. Two correlation functions were used in the analysis; cross correlation, defined as:

$$\varphi_{xy}(\tau) = \lim_{T \rightarrow \infty} \frac{1}{2T} \int_{-T}^T f_x(t) f_y(t + \tau) dt \quad (13)$$

and coherence:

$$r^2 = \frac{[\overline{P_{xy}(\omega)}]^2}{P_{xx} P_{yy}} \quad (14)$$

where  $P_{xy}(\omega)$ , the Fourier transform of  $\varphi_{xy}(\tau)$ , is the cross power spectral density function:

$$P_{xy}(\omega) = \frac{1}{2\pi} \int_{-\infty}^{\infty} \varphi_{xy}(\tau) e^{-i\omega\tau} d\tau \quad (15)$$

For noise measurements at a source  $x$  and receiving point  $y$ , the coherence function yields a number which is equal to or less than the fraction of the power at  $y$  due to the source at  $x$ . For example, a 100% coherence implies that all energy at  $y$  has a common origin with the energy at  $x$ , a 50% coherence implies that at least half the energy is common, and so on. If the signal at  $x$  is totally dominated by the source of interest, the coherence yields the exact fraction of the energy at  $y$  due to the source of  $x$ , but the presence of a high noise floor, locally reverberant field, or nonradiating fluctuating pressures at point  $x$ , will diminish the measured coherence.

Coherence spectra between different microphones were examined: pairs of internal microphones, and pairs of internal and external microphones. Significant coherence was obtained from 50 to 800 Hz for plug and exhaust duct microphone combinations, but no conclusions regarding the source reaching the far field can be drawn from these data. Between internal

and external microphones, no coherence was found between fan duct and far-field ground positions, and only small coherence was obtained between the plug and far field. Low coherence between internal and far-field microphones may be due to insufficient precomputation delay time; i.e., a limitation of the electronic equipment coupled with the fact that transit time is a significant portion of sample length.

The highest coherence values found were between a measurement at the exhaust duct exit and the 140° near-field aft arc ground microphone. Figure 157 shows a comparison of the two measured spectra and the coherence spectrum at takeoff power. These data indicate that between 400 and 700 Hz there is more than 50% common power between the two points. The measured coherence spectra decrease rapidly with decreasing power setting as shown in figure 158, which shows smooth curves formed through the coherence spectra at several power settings. This trend with power setting is consistent with the decreasing importance of the 500-Hz bump in the 140° far-field spectrum.

Using the measured coherence spectra, the internal noise component was separated from the total noise as shown in figure 159. The internal noise, so identified, ranges from 300 to 1000 Hz with a peak at 500 Hz. These spectra represent a lower limit on the exhaust duct flow noise source.

*Exhaust Duct Flow Noise Basic Level.*—Basic noise levels for the exhaust duct flow noise component determined by the two techniques (coherence spectra and component decomposition) show substantial agreement (fig. 160) at the highest power settings. At lower power settings the coherence technique gives only a slightly lower level than does the component decomposition technique. The correlating parameter, which has been used here for exhaust duct flow noise, is the same one that is used for core (burner) noise, and predicted core noise curves are shown in the same plot (fig. 160). This shows that the exhaust duct flow noise has substantially different throttling characteristics from burner noise. It is believed that there should exist a better correlating parameter which relates the exhaust duct flow noise to the physics of the noise-generating mechanism. Further work is needed to find this appropriate correlating parameter.

*Exhaust Duct Flow Noise Spectrum Shape.*—Spectrum shapes for the exhaust duct flow noise determined by the two techniques are compared in figure 161. The broader spectrum shape determined by component decomposition is probably more nearly true than the coherence spectrum shape, because the coherence spectrum is based on the assumption that the signal at the internal microphone is totally saturated by exhaust duct flow noise while the far-field microphone signal is a mixture of exhaust duct flow noise and noise from other sources. While this condition is probably met near the peak frequency, at other frequencies the signal at the internal microphone is likely to be affected by other sources, thus, reducing the coherence level and narrowing the coherence spectrum.

*Exhaust Duct Flow Noise Directivity.*—Directivity characteristics for exhaust duct flow noise determined by the two methods are shown in figure 162.

REPRODUCIBILITY OF THE  
ORIGINAL PAGE IS POOR

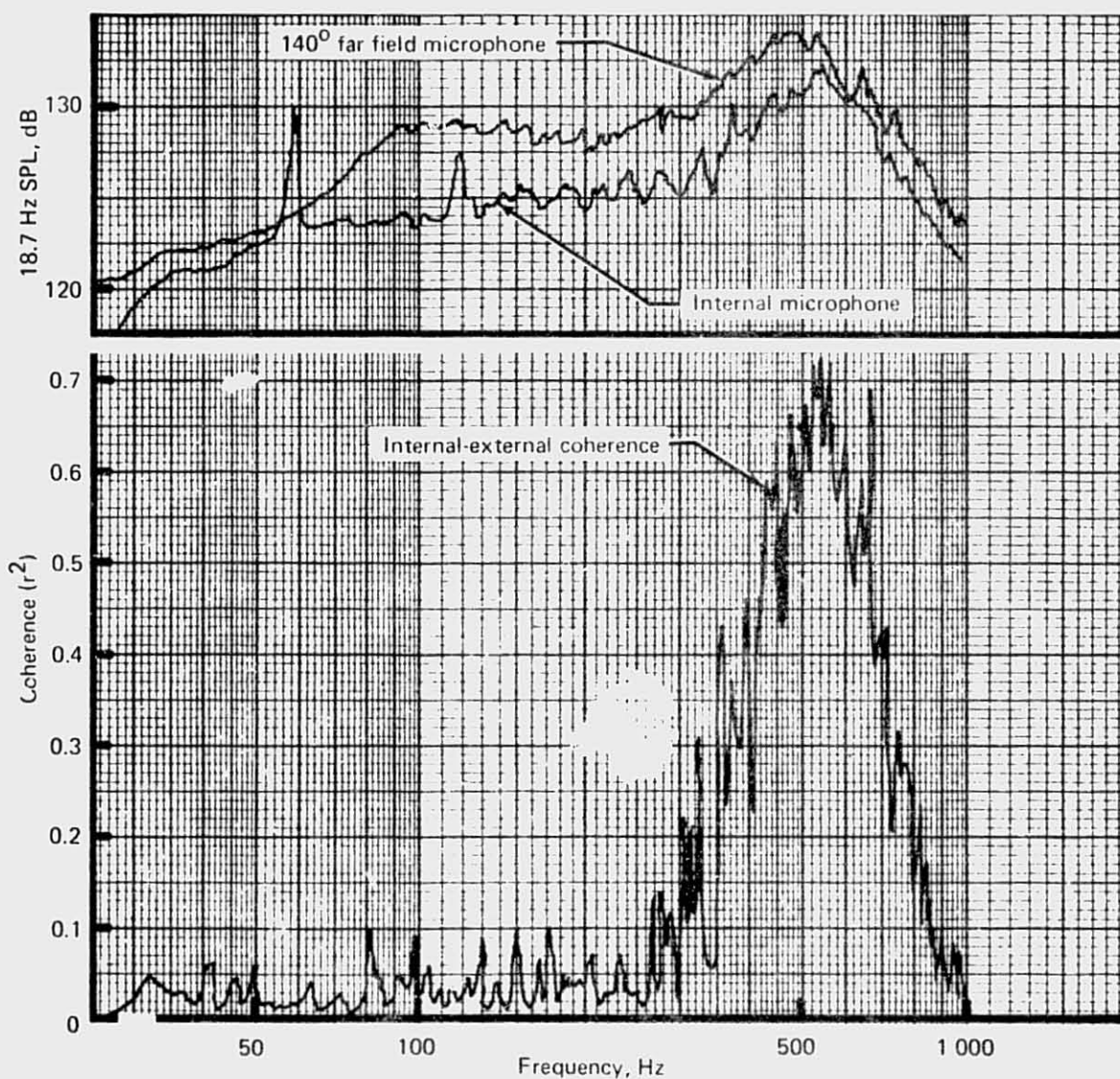


Figure 157.—JT8D-115 Ground Test—Evidence of Internal Noise Source at 500 Hz

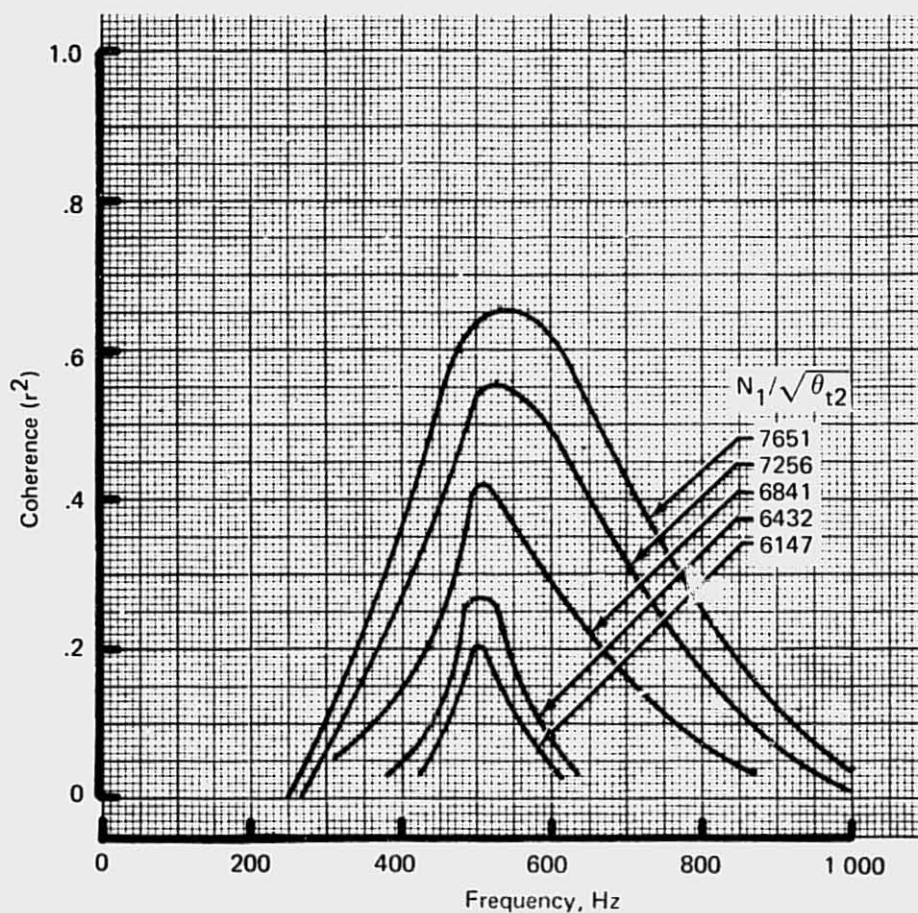


Figure 158.—JT8D-115 Ground Test—Coherence Spectra Between Internal Exhaust Duct and External (140°) Ground Microphone at Various Power Settings



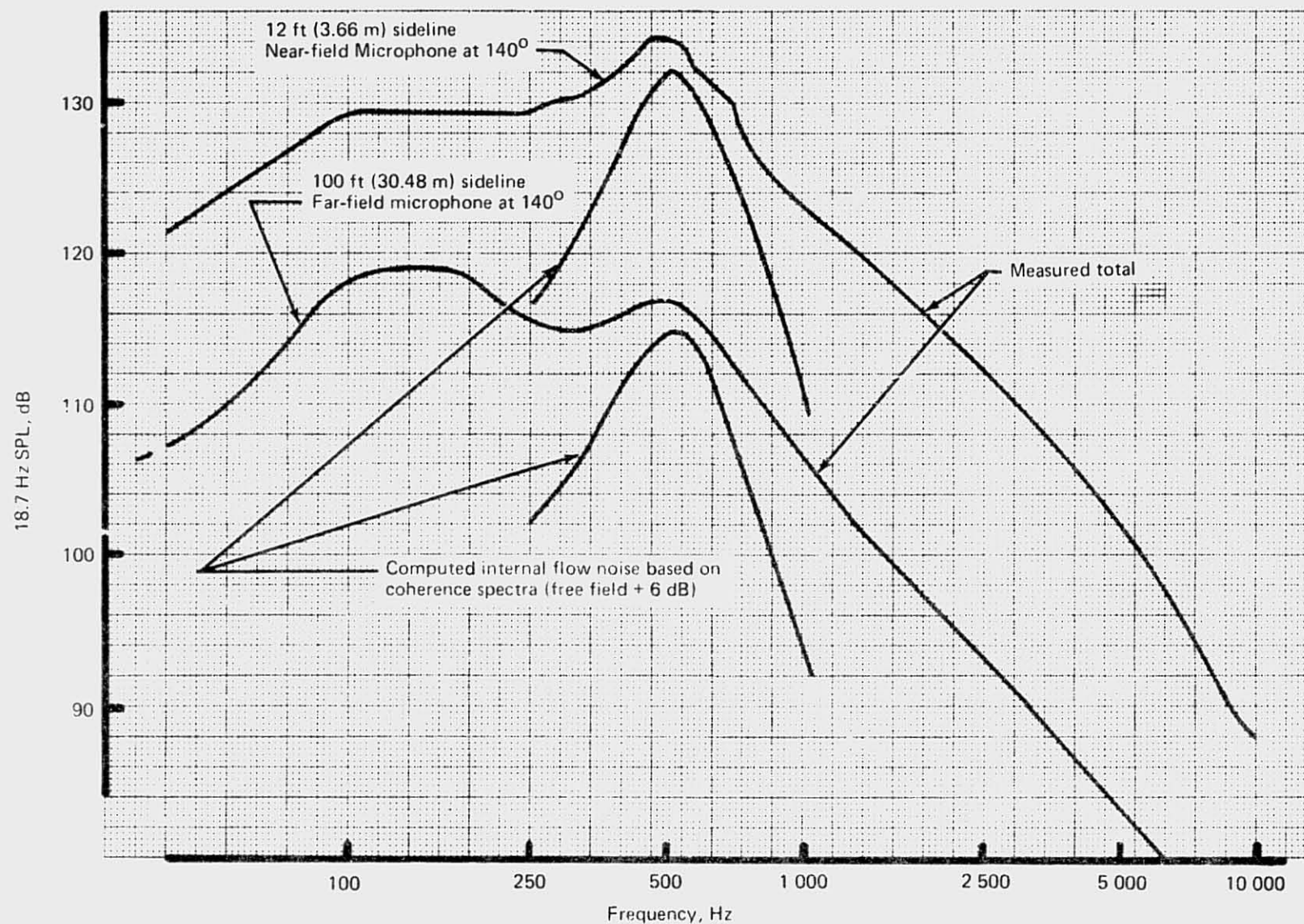


Figure 159.—JT8D-115 Ground Test—Sample Working Plot for Evaluation of Exhaust Duct Flow Noise,  $N_1/\sqrt{\theta_{t2}} = 7650$



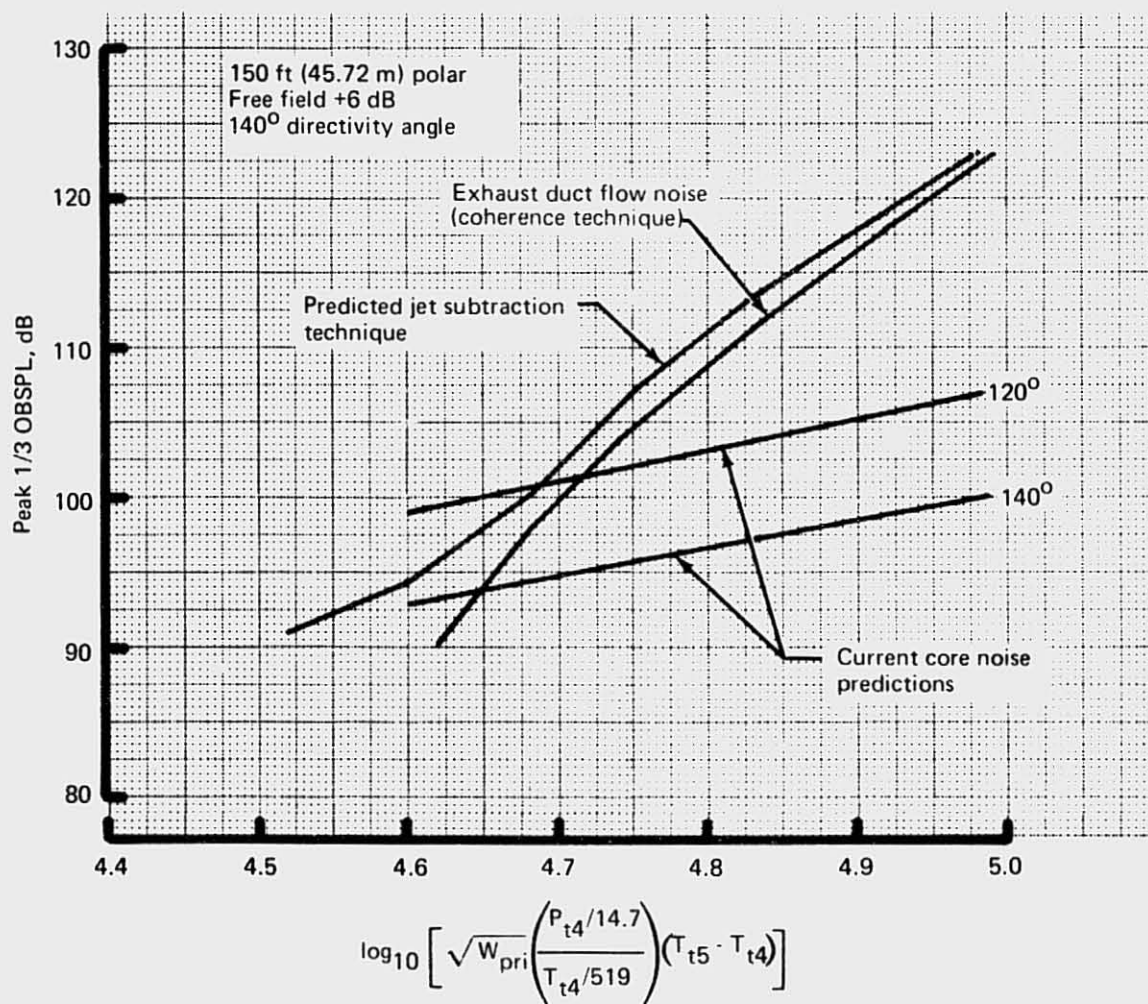


Figure 160.—JT8D-115 Ground Test—Exhaust Duct Flow Noise Basic Level

REPRODUCIBILITY OF THE  
ORIGINAL PAGE IS POOR

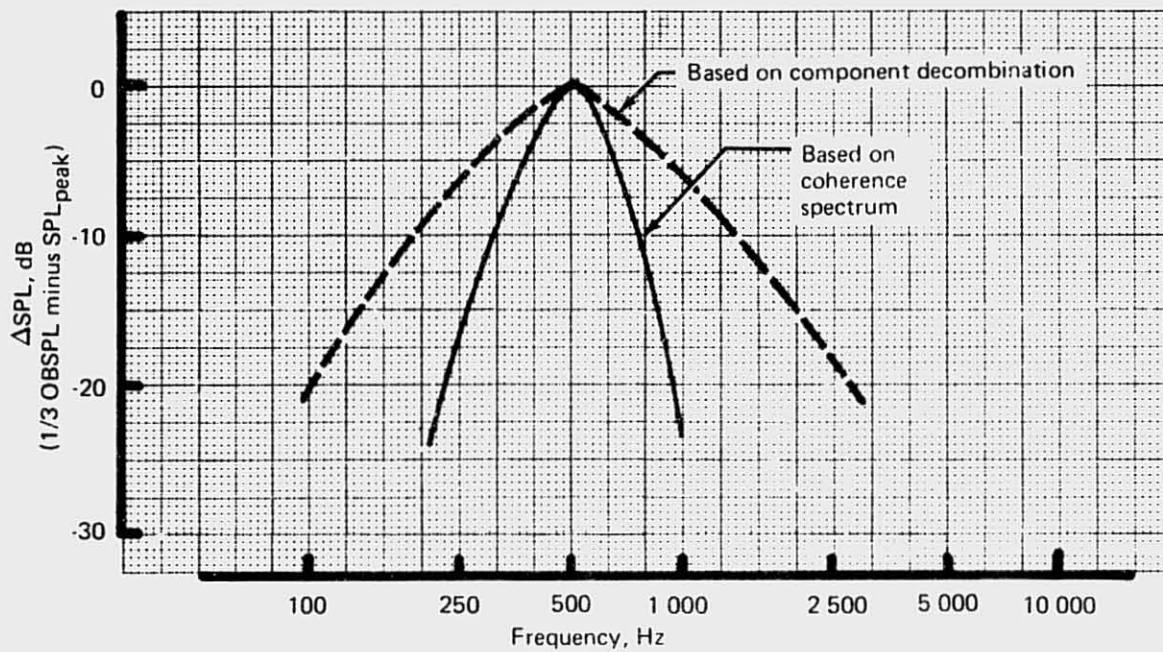


Figure 161.—JT8D-115 Ground Test—Exhaust Duct Flow Noise Spectrum Shape, Average for All Angles and Power Settings

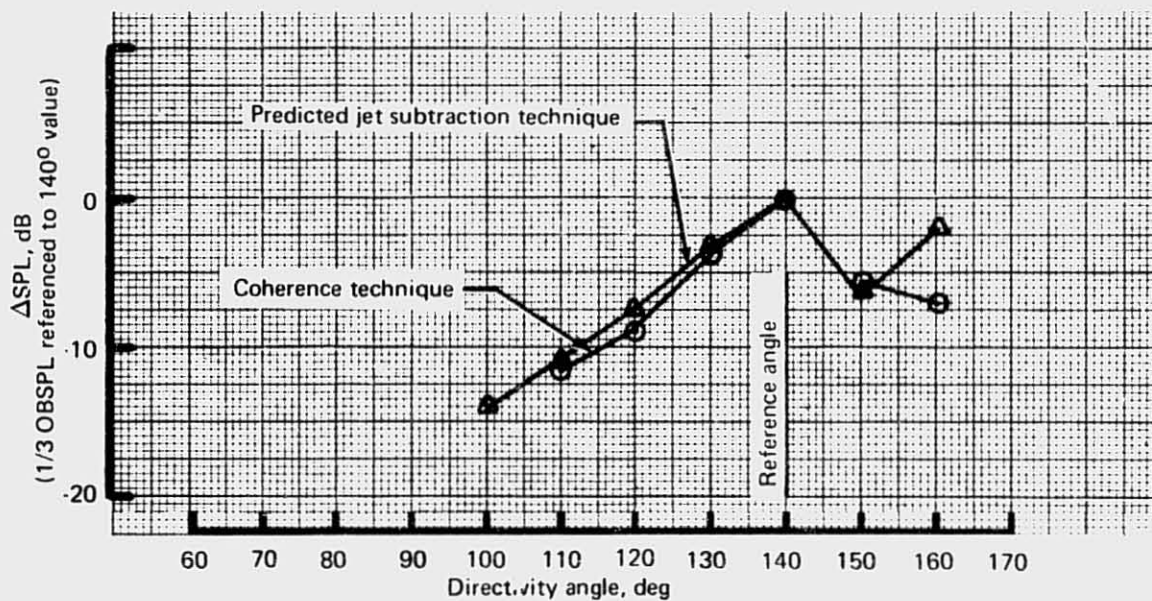


Figure 162.—JT8D 115 Ground Test—Exhaust Duct Flow Noise Directivity, Average for All Power Settings

#### 4.2.2 TOTAL STATIC ENGINE NOISE

As stated earlier in section 4.2.1, total static engine noise levels cannot be used directly for prediction of airplane flyover noise levels, and for the same reasons a direct comparison of static noise levels does not yield a valid measure of the noise differences between the JT8D-15 and -115 engines. However, total static noise levels are presented here to illustrate, on a spectral basis, the relative contribution of each component to the total measured noise level, and to evaluate the degree to which all of the measured noise is included in the prediction modules. *The reader is cautioned against drawing conclusions from these data regarding the noise benefit of the JT8D refan engine relative to the JT8D (baseline).*

A complete study of the JT8D refan engine noise benefit at airplane flight conditions is presented in Volume IV of this final report document series, "Airplane Evaluation and Analysis," NASA CR-134800 (ref. 1).

##### 4.2.2.1 JT8D-15 Engine

Measured static noise spectra for the JT8D-15 engine are presented in figures 163 and 164 along with predicted spectra for each of the noise components generated by the empirical models developed from the JT8D-15 ground test data analysis as described in section 4.2.1. Two forward-quadrant and two aft-quadrant directivity angles and two power settings (maximum power and approximate approach power) are included in these figures. The comparison between the PNL of the measured and predicted total spectra is shown numerically in the legend of each plot.

By scanning figures 163 and 164, one can see the shift in emphasis from one noise component to another with changes in directivity angle and power setting. At approach rpm ( $N_1$ ) at a  $40^\circ$  directivity angle (fig. 163a), the inlet fan tones are totally dominant over all other components. At  $60^\circ$  (fig. 163b) inlet tones are still dominant but less so than at  $40^\circ$ . At  $120^\circ$  (fig. 163c) jet noise has taken over dominance of the spectrum with a substantial contribution to the high frequencies being made by the aft-fan component. At  $140^\circ$  (fig. 163d), jet noise is totally dominant over other sources; here it can be seen that there is a substantial contribution to the measured midfrequency noise level which is not accounted for by any of the predicted components. This excess noise is attributed to the exhaust duct flow noise source which, as stated earlier, was not identified in time to be included in the empirical model. However, the effect of the exhaust duct flow noise on PNL is only about 1 PNdB at this condition. At maximum power, jet noise and inlet fan tone share dominance of the spectra in the forward quadrant (fig. 164a and b), while in the aft quadrant jet noise is totally dominant (fig. 164c and d).

In figure 164d at  $140^\circ$ , the effect of exhaust duct flow noise is again seen in the mid and high frequencies, and the measured PNL is underpredicted by 3 PNdB.

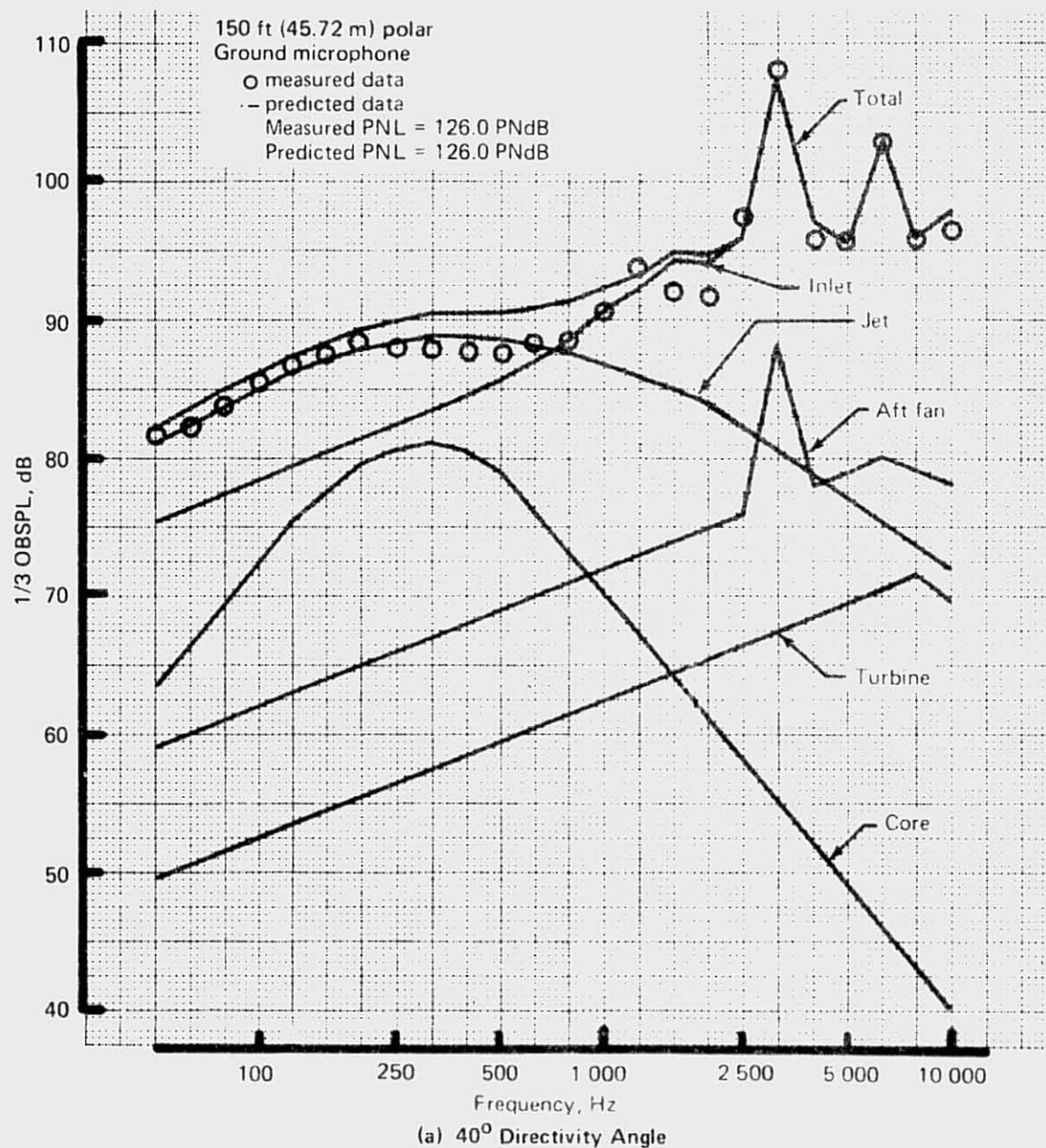


Figure 163.—JT8D-15 Ground Test—Predicted Static Component Noise Levels, Approach rpm



REPRODUCIBILITY OF  
ORIGINAL PAGE IS POOR

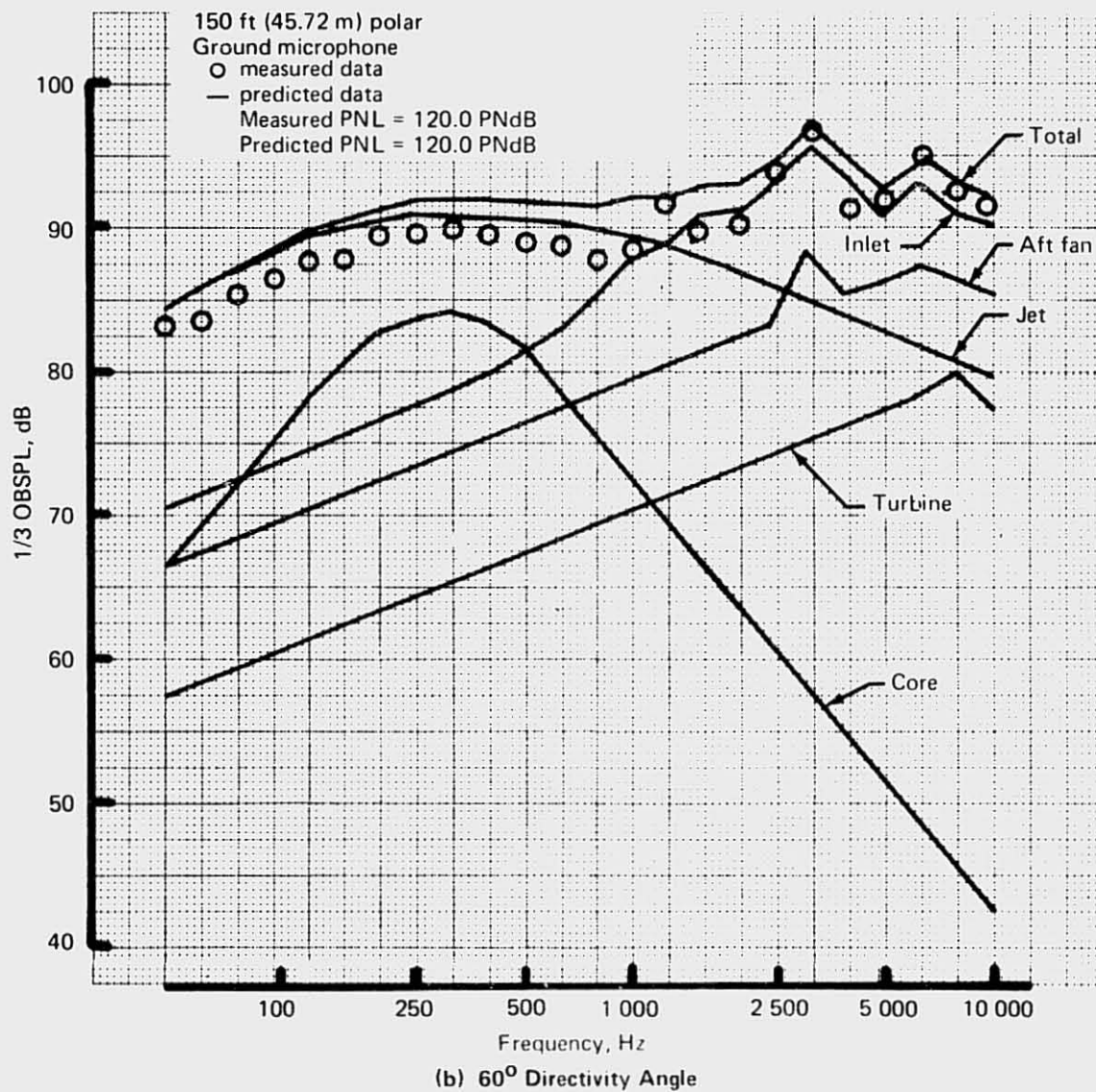


Figure 163. - (Continued)

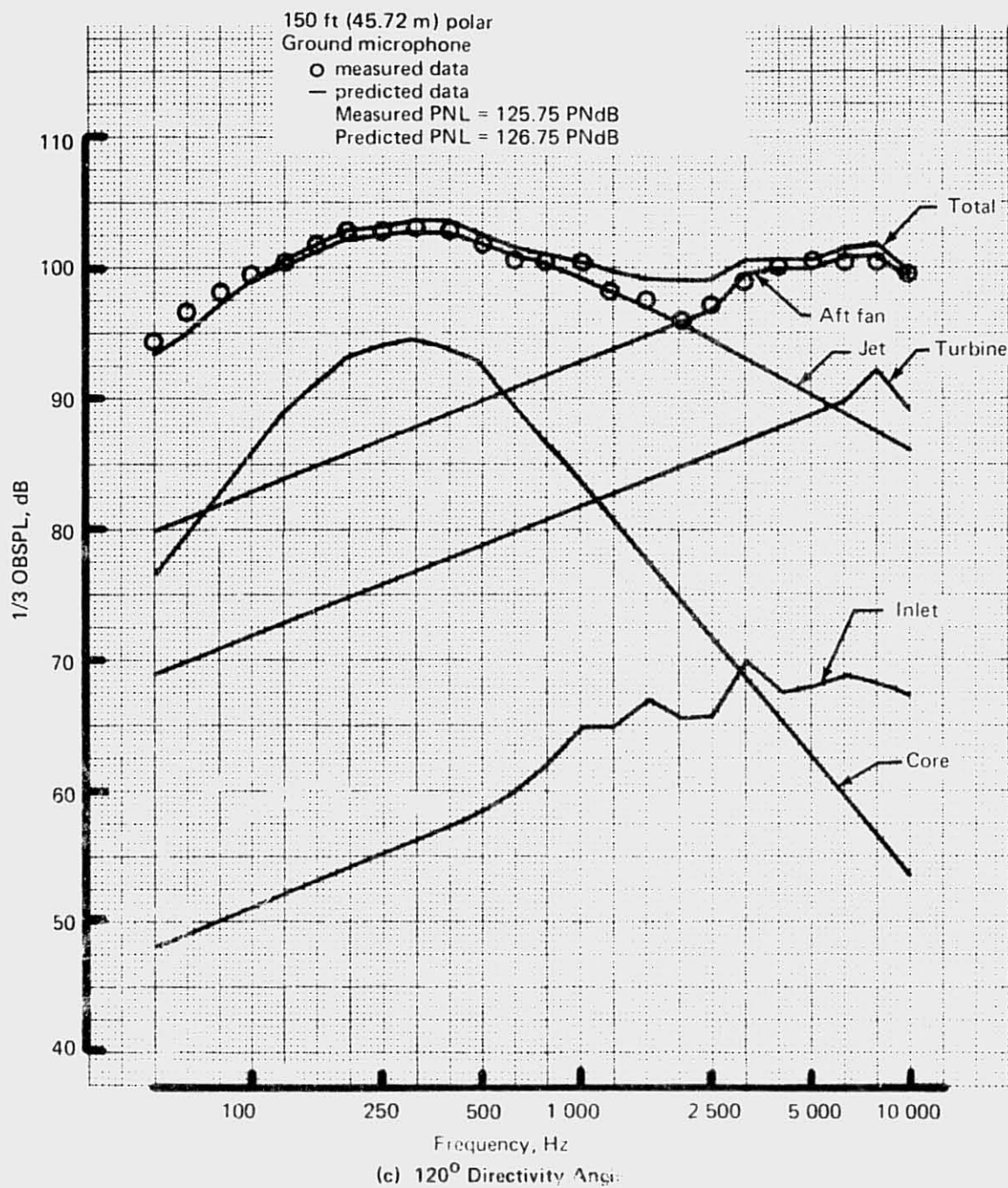


Figure 163.—(Continued)

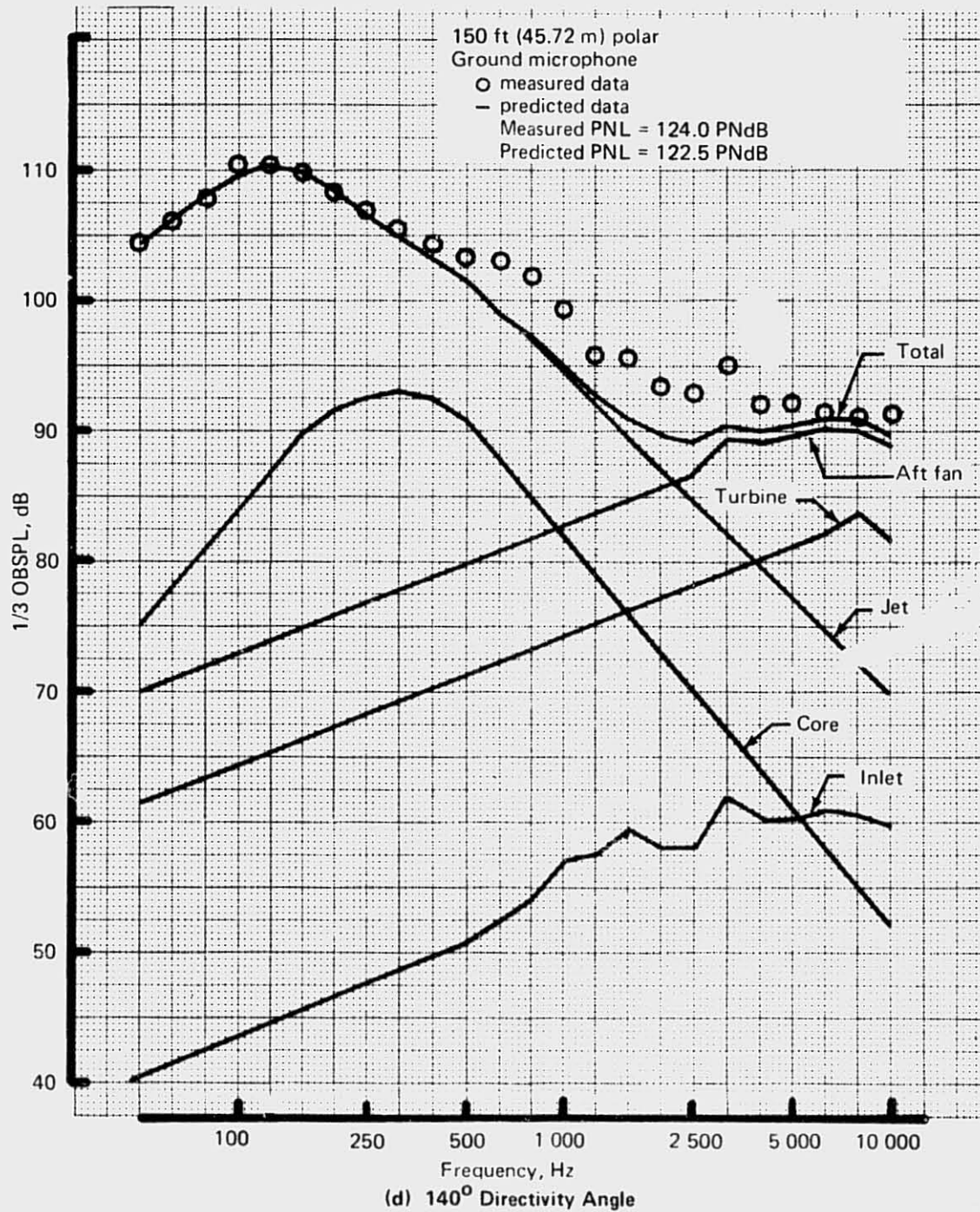


Figure 163.—(Concluded)

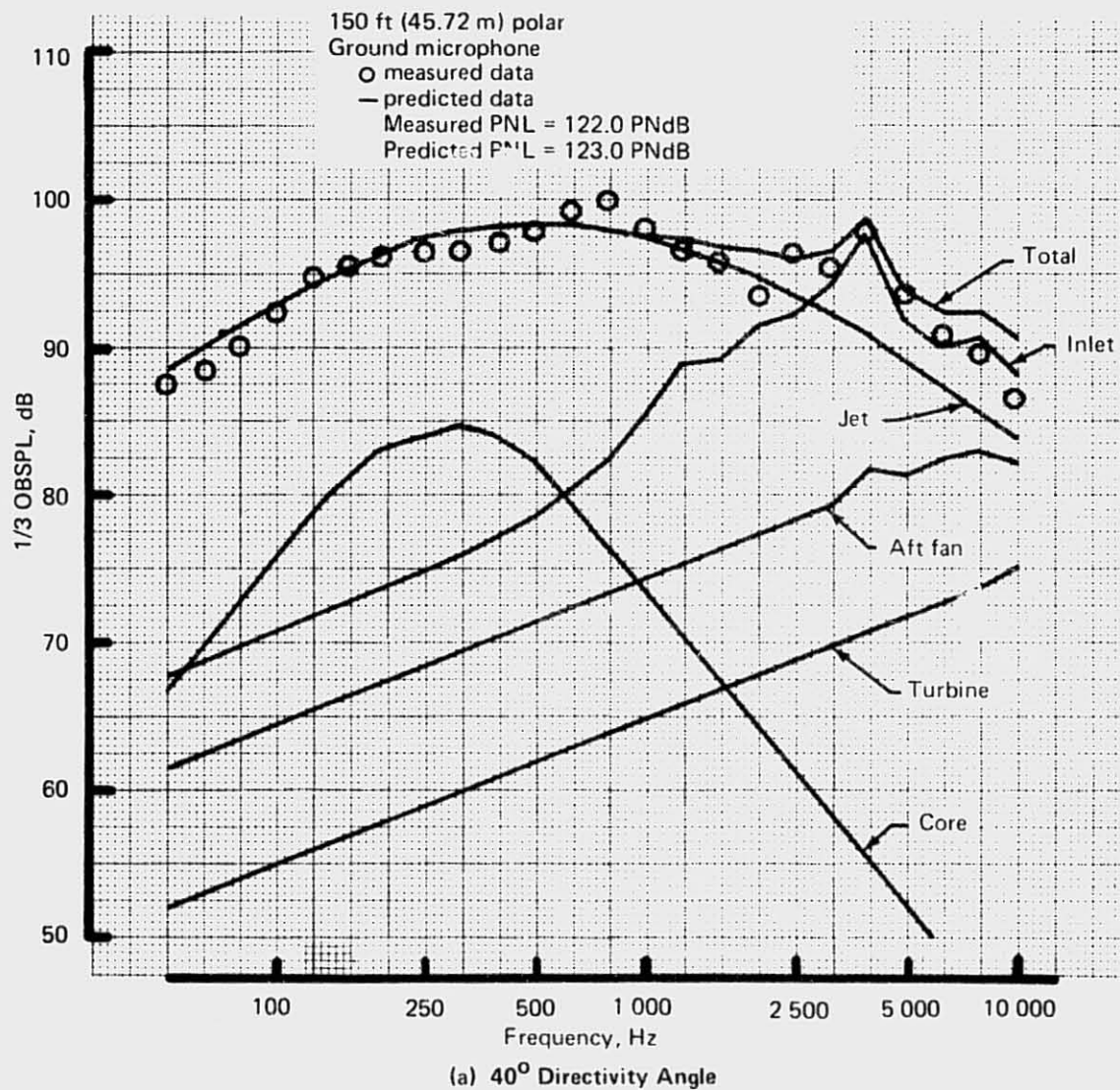


Figure 164.—JT8D-15 Ground Test—Predicted Static Component Noise Levels, Takeoff rpm



REPRODUCIBILITY OF THE  
ORIGINAL PAGE IS POOR

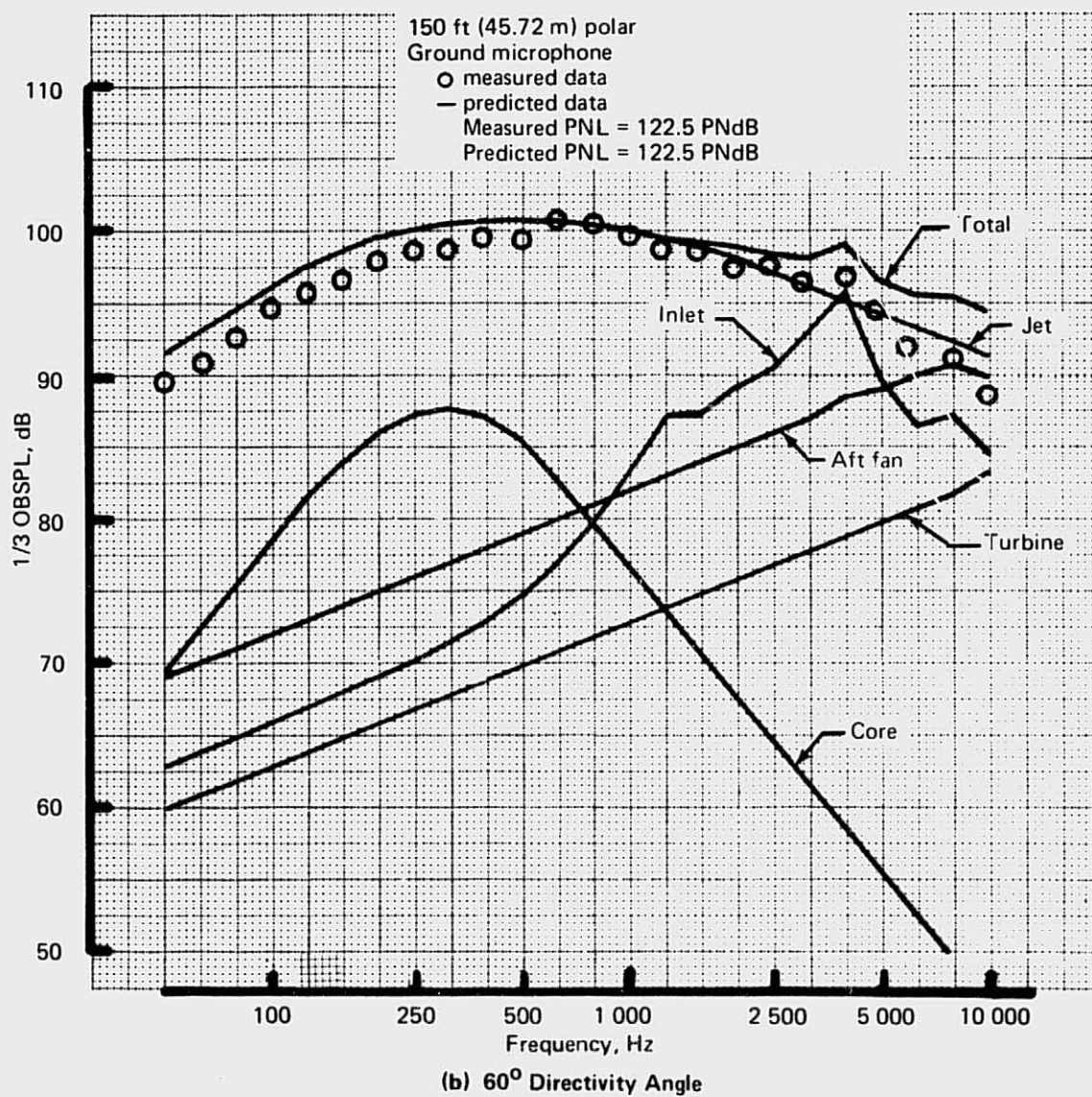
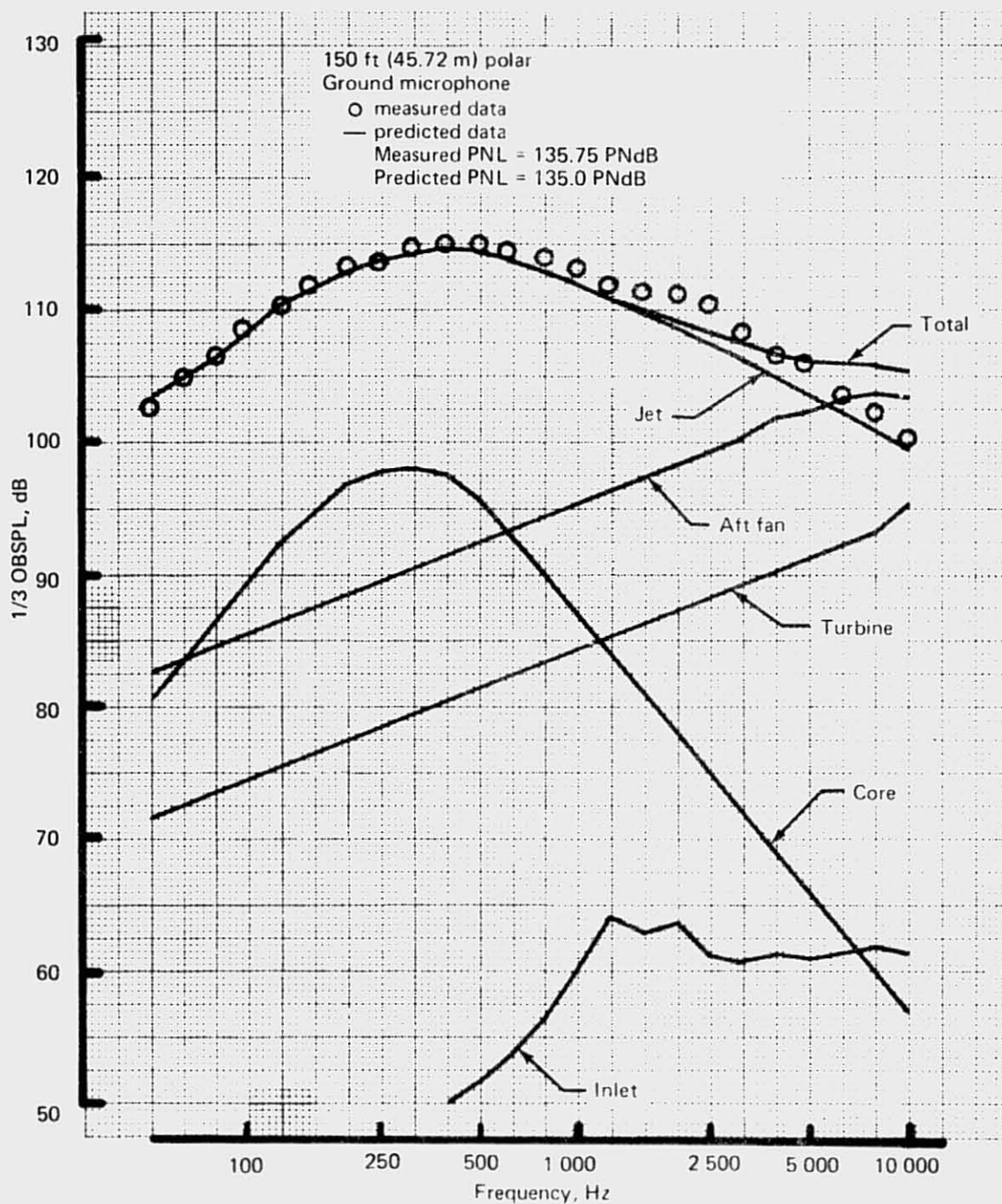
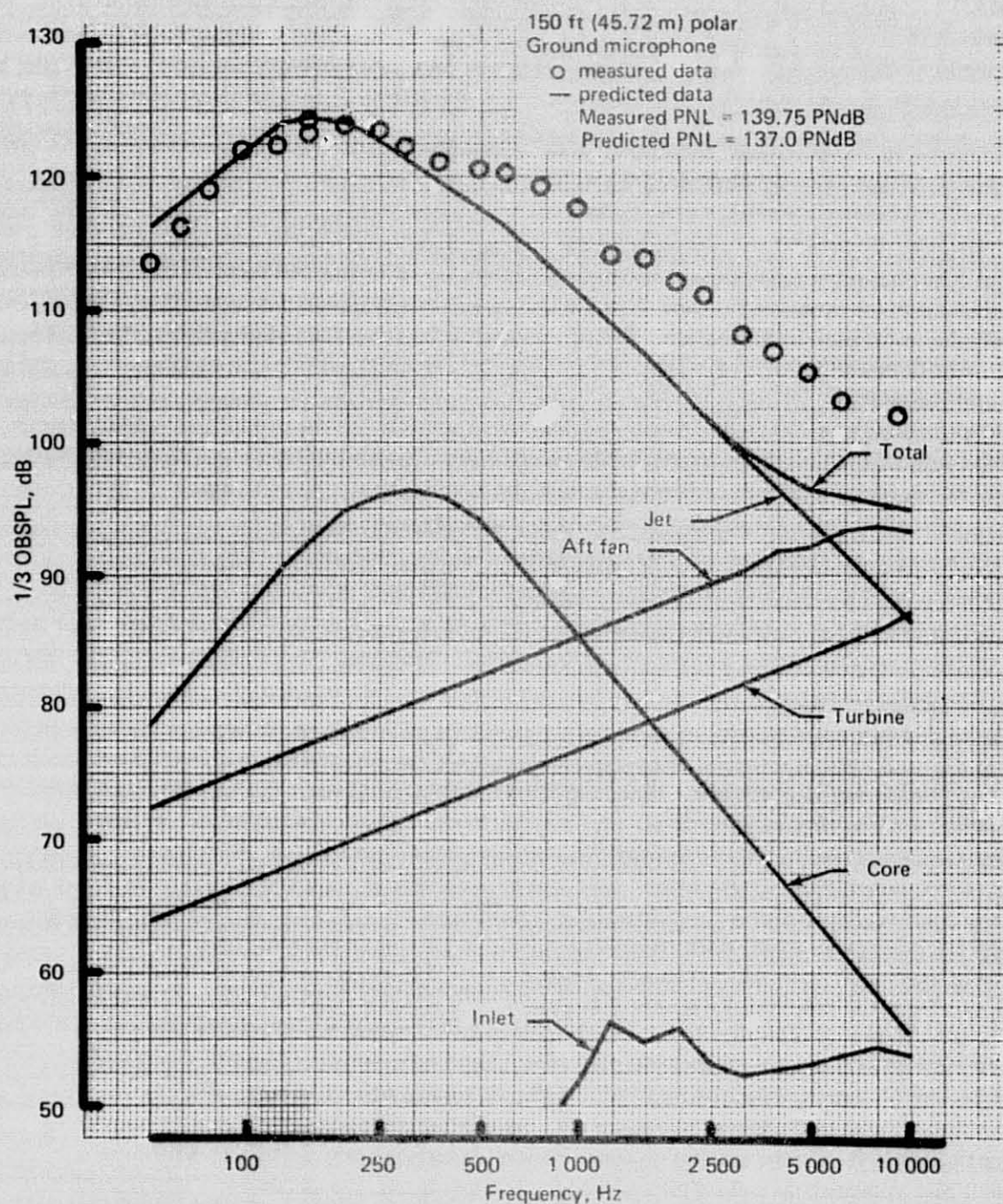


Figure 164.—(Continued)



(c) 120° Directivity Angle

Figure 164.— (Continued)



(d) 140° Directivity Angle

Figure 164.—(Concluded)



#### 4.2.2.2 JT8D-115 Engine

The JT8D-115 ground test offered a wide range of nacelle acoustic treatment configurations from which the component noise could have been extracted. The configuration chosen for this purpose included a hardwall inlet without ring and hardwall exhaust system with a fully treated fan case. Predictions for other configurations are arrived at through treatment deltas as described in section 4.2.3. The predictions presented here are compared with measured static data for this basic hardwall nacelle, and corresponding spectra are presented separately for the various treated nacelle configurations.

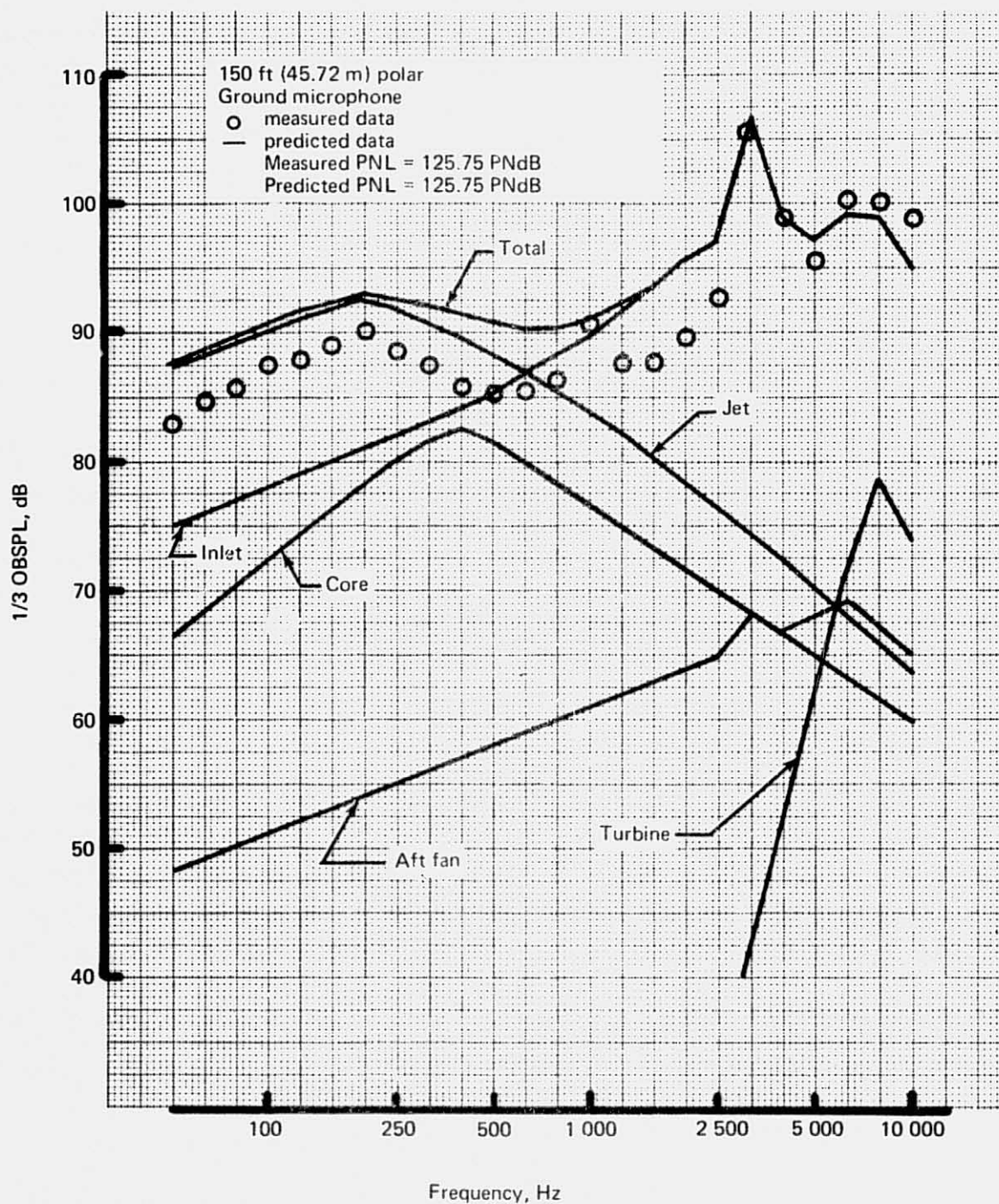
*Basic Hardwall Nacelle.*—The same set of measured total and predicted component noise spectral comparisons is presented here for the JT8D-115 engine (figs. 165 and 166) as was presented in the previous section for the JT8D-15 engine. It is important to recall that the jet and core noise predictions presented here are based on JT8D-109 engine data (as they are ultimately intended for JT8D-109 flyover noise predictions), while the measured noise and the other component spectra are from the JT8D-115 ground test. The JT8D-109 and JT8D-115 differ from each other through a "hot rematch" of the primary/secondary exhaust system; this rematch causes the JT8D-115 to have a higher primary exhaust temperature and, therefore, lower primary density than does the JT8D-109 at a given primary jet velocity. There are substantial differences in the exhaust hardware of the two engines, and primary/secondary stream mixing characteristics would be expected to differ. For these reasons, the empirical model noise levels disagree with measured JT8D-115 total noise spectra in the frequency range where jet noise is dominant. However, with only minor modifications this jet noise model could be adjusted to fit the JT8D-115 data.

By scanning figures 165 and 166, one can see the shift in emphasis from one noise component to another with changes in directivity angle and power setting. At approach rpm ( $N_1$ ) at  $40^\circ$  and  $60^\circ$  directivity angles (figs. 165a and b), the inlet-radiated fan tone overwhelms all other sources. On these figures it can be seen that the empirical model overpredicts jet noise at these angles by about 3 dB, for the reasons explained in the previous paragraph. The procedure also overpredicts inlet fan broadband noise in the frequency range 1000 to 2000 Hz. This is caused by the use of a single average broadband noise directivity, independent of power setting. However, these errors are of negligible consequence to the PNL of the spectrum, since the inlet fan tone so totally dominates the spectrum. At  $120^\circ$  (fig. 165c), jet noise has taken over dominance of the spectrum with substantial contributions from the core and turbine components. At  $140^\circ$ , jet noise is totally dominant (fig. 165d). Here it is seen that the prediction procedure overpredicts jet noise again by 2 to 3 dB. At takeoff power, jet and inlet fan noise contribute about equally to the spectra in the forward quadrant (fig. 166a and b). In the aft quadrant at  $120^\circ$  and  $140^\circ$  directivity angles, the exhaust duct flow noise source dominates the spectra (fig. 166c and d) and, consequently, the PNL is substantially underpredicted (approximately 6 PNdB). At these angles it also appears that the empirical model underpredicts jet noise slightly, although it is difficult to tell because of the influence of the exhaust duct flow noise.

*Treated Nacelle Configurations.*—Measured total JT8D-115 static engine noise spectra for the five treated refan nacelle configurations are shown in figures 167 and 168. These spectra are presented only to show the range of noise levels measured with the various

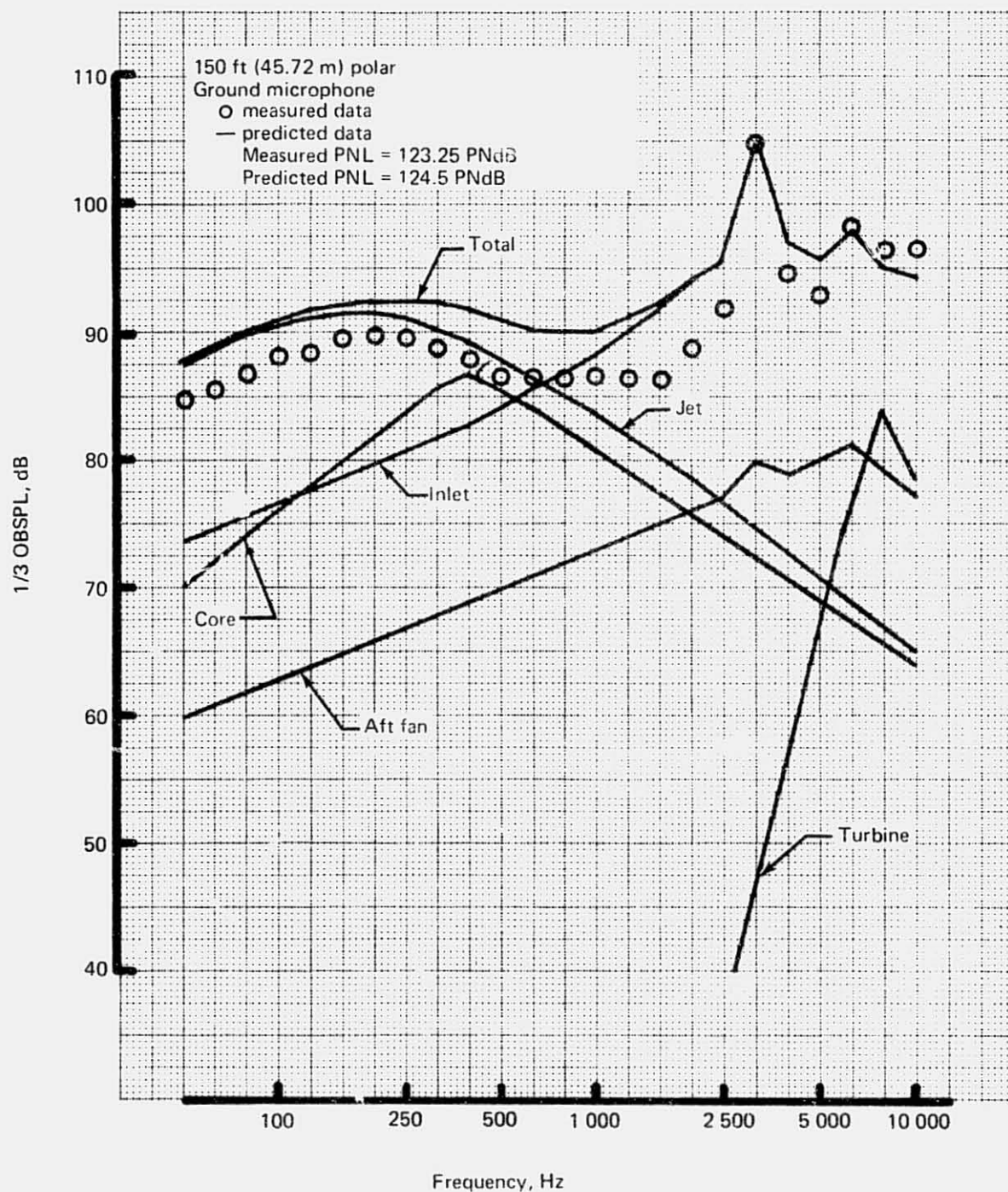


REPRODUCIBILITY OF THE  
ORIGINAL PAGE IS POOR



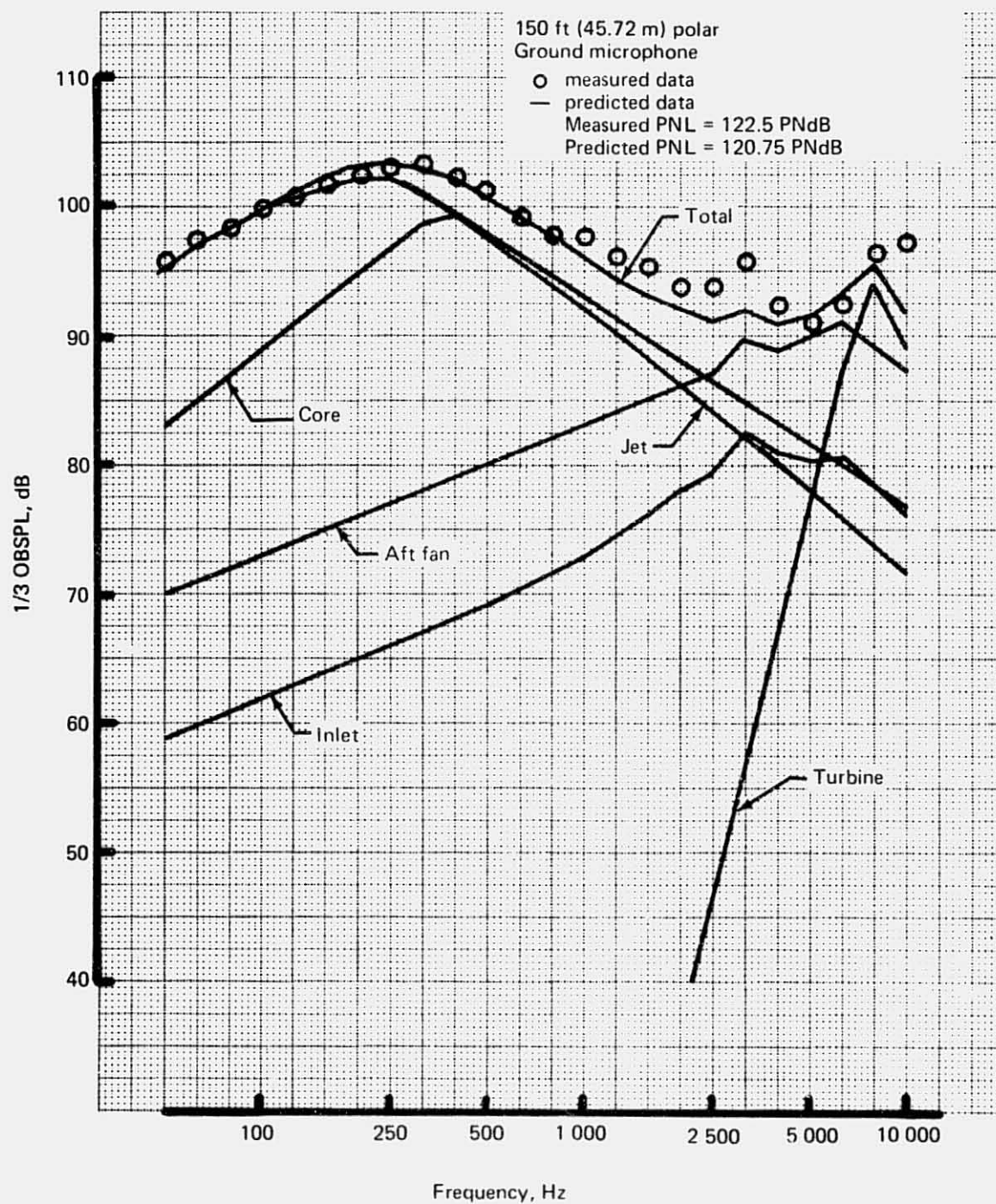
(a) 40° Directivity Angle

Figure 165.—JT8D-115 Ground Test—Predicted Static Component Noise Levels, Approach rpm



(b) 60° Directivity Angle

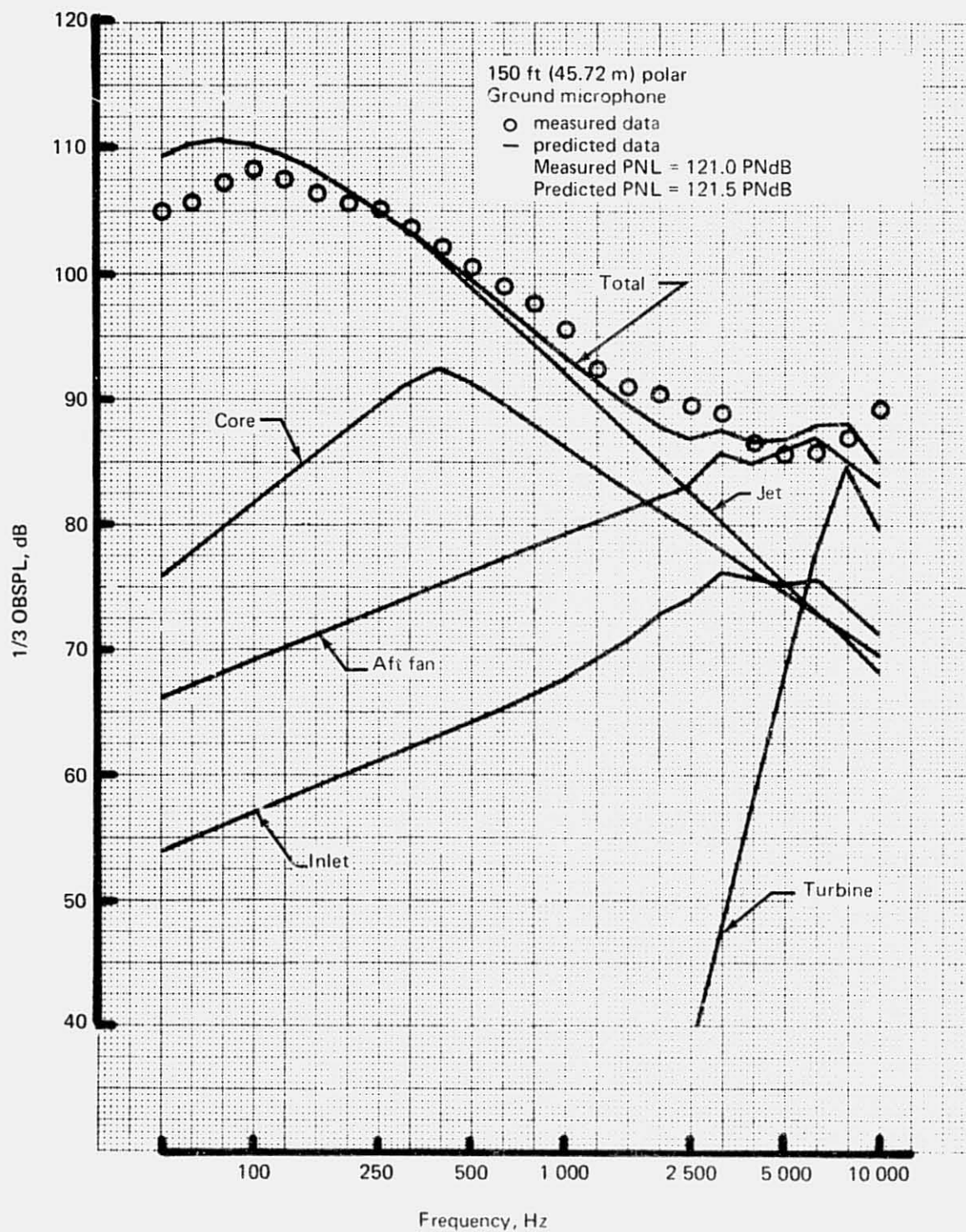
Figure 165.—(Continued)



(c) 120° Directivity Angle

Figure 165.—(Continued)





(d) 140° Directivity Angle

Figure 165.—(Concluded)



REPRODUCIBILITY OF THE  
ORIGINAL PAGE IS POOR

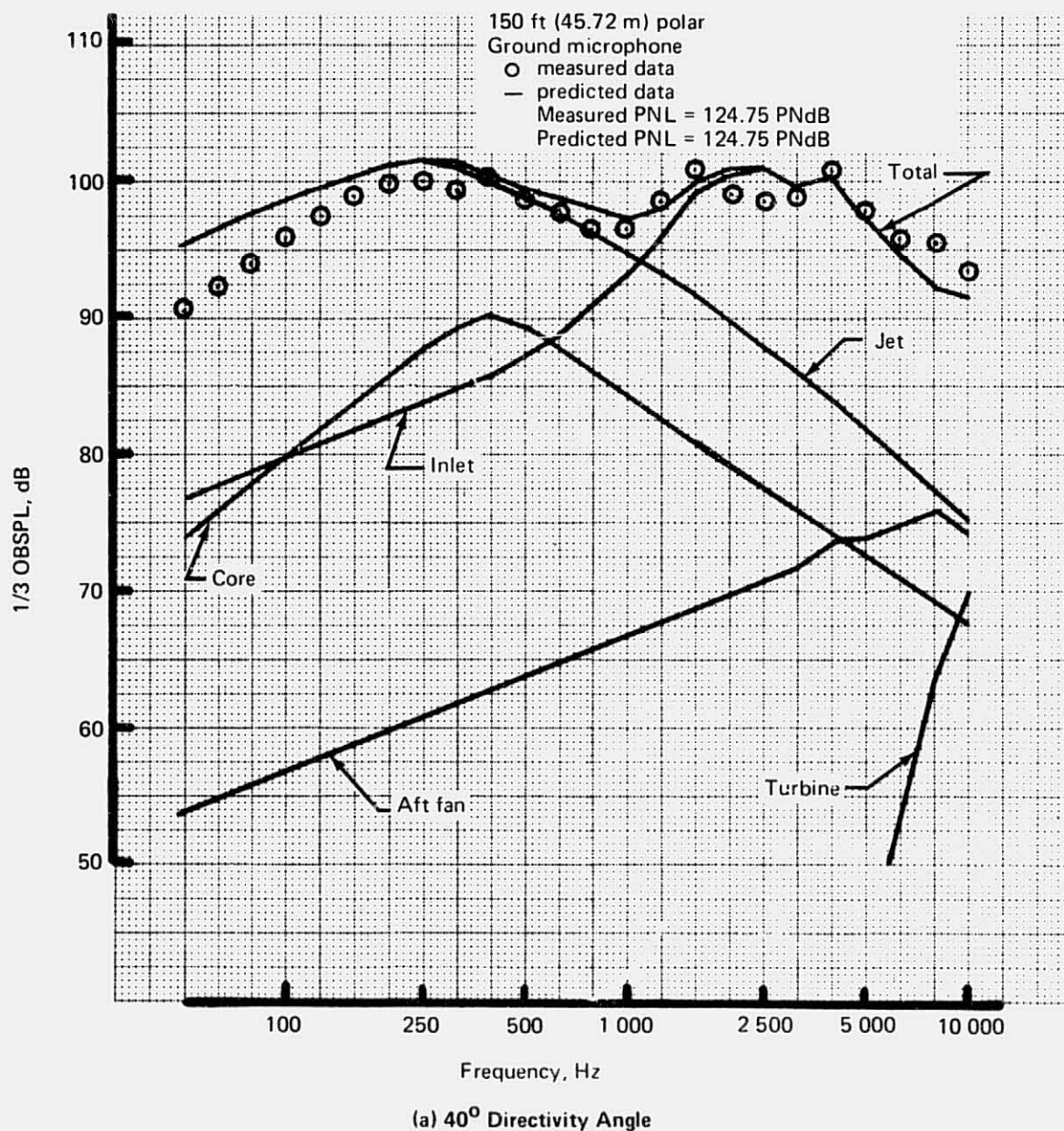
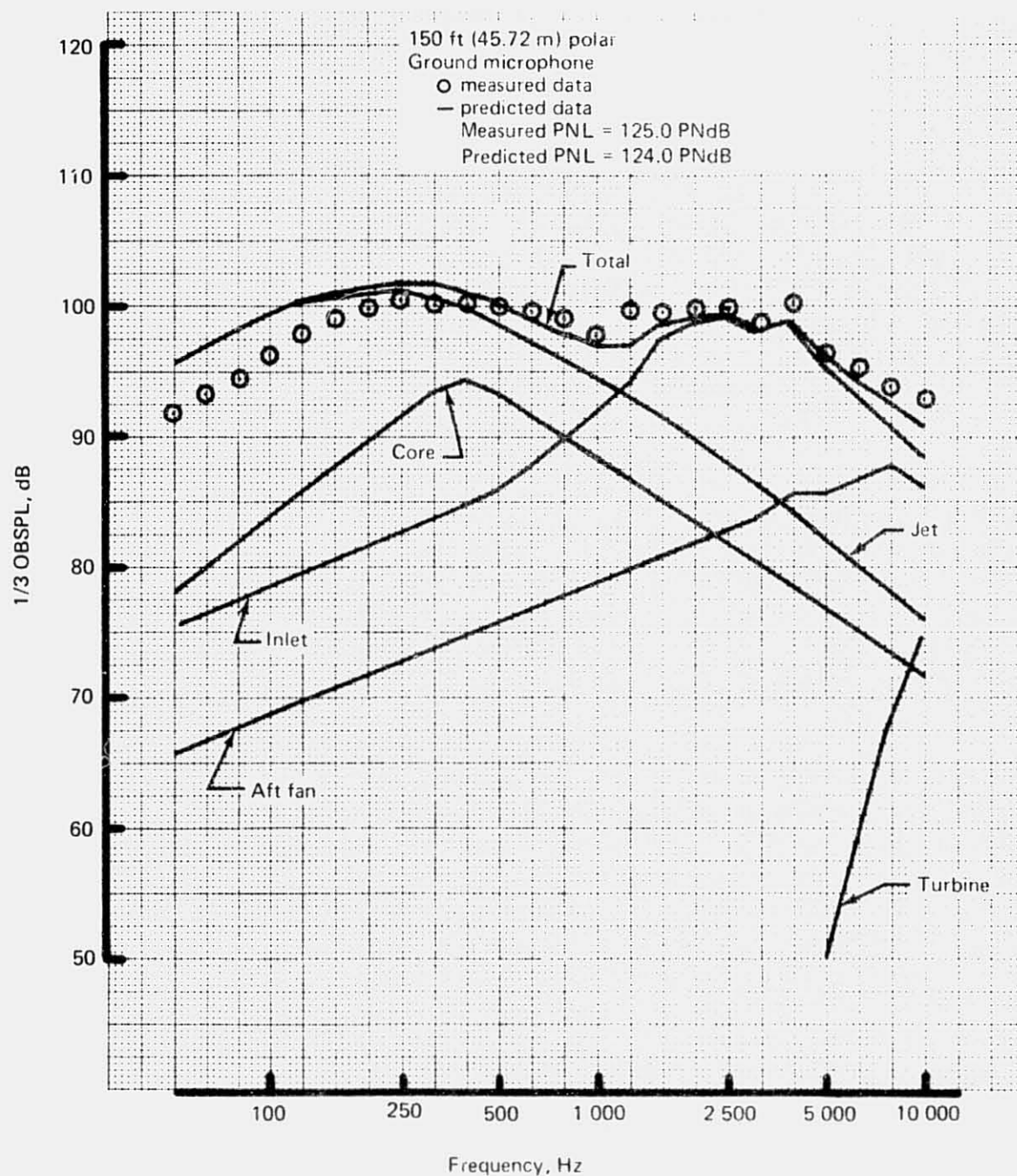
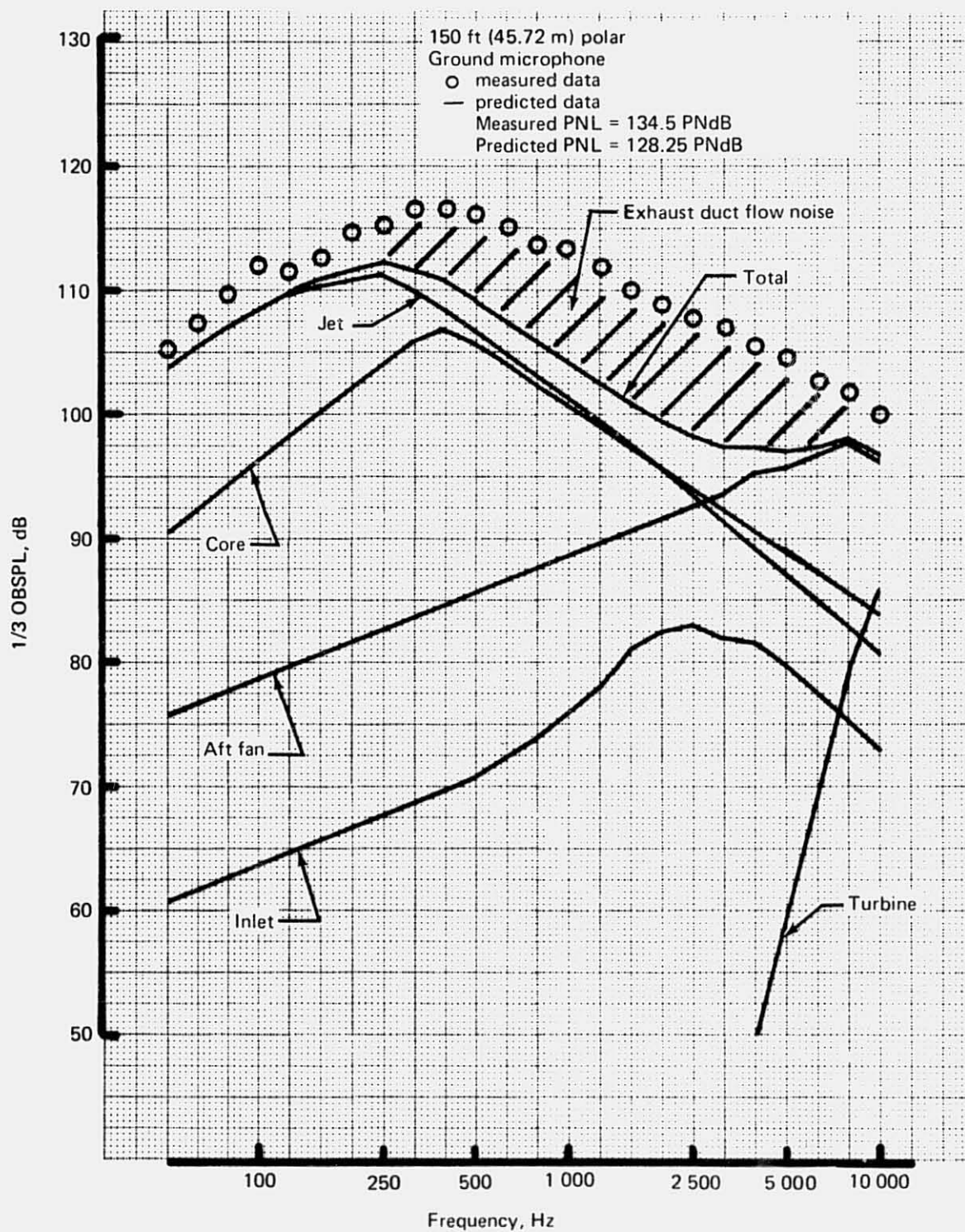


Figure 166.—JT8D-115 Ground Test—Predicted Static Component Noise Levels, Takeoff rpm



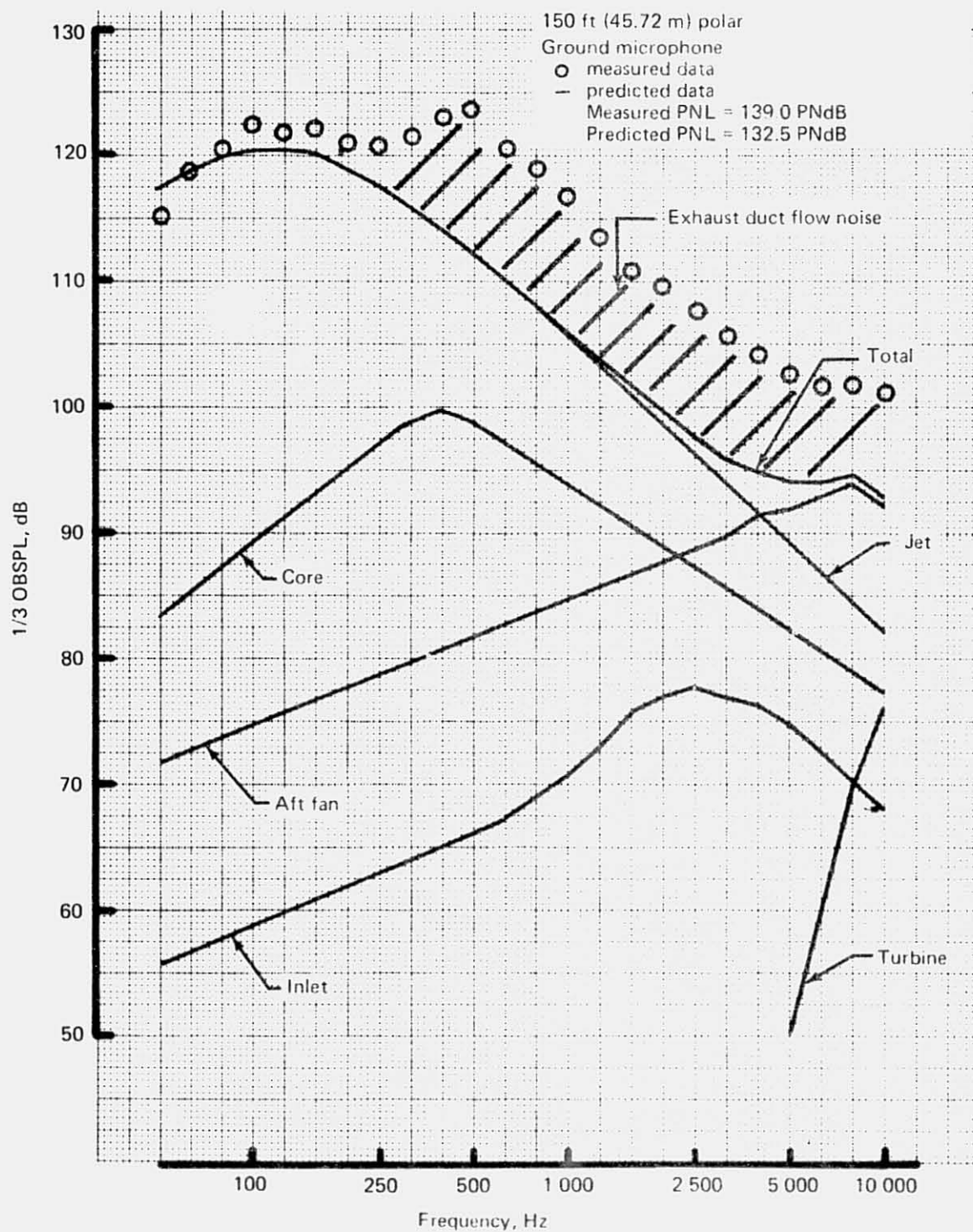
(b) 60° Directivity Angle

Figure 166.—(Continued)



(c) 120° Directivity Angle

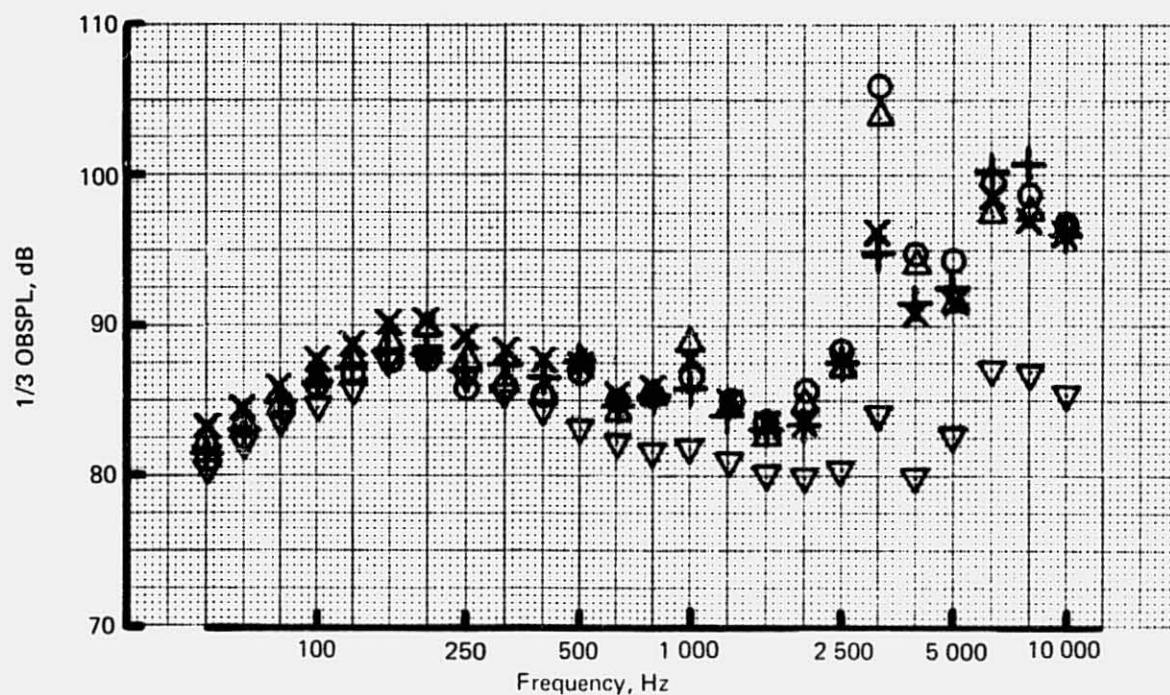
Figure 166.—(Continued)



(d) 140° Directivity Angle

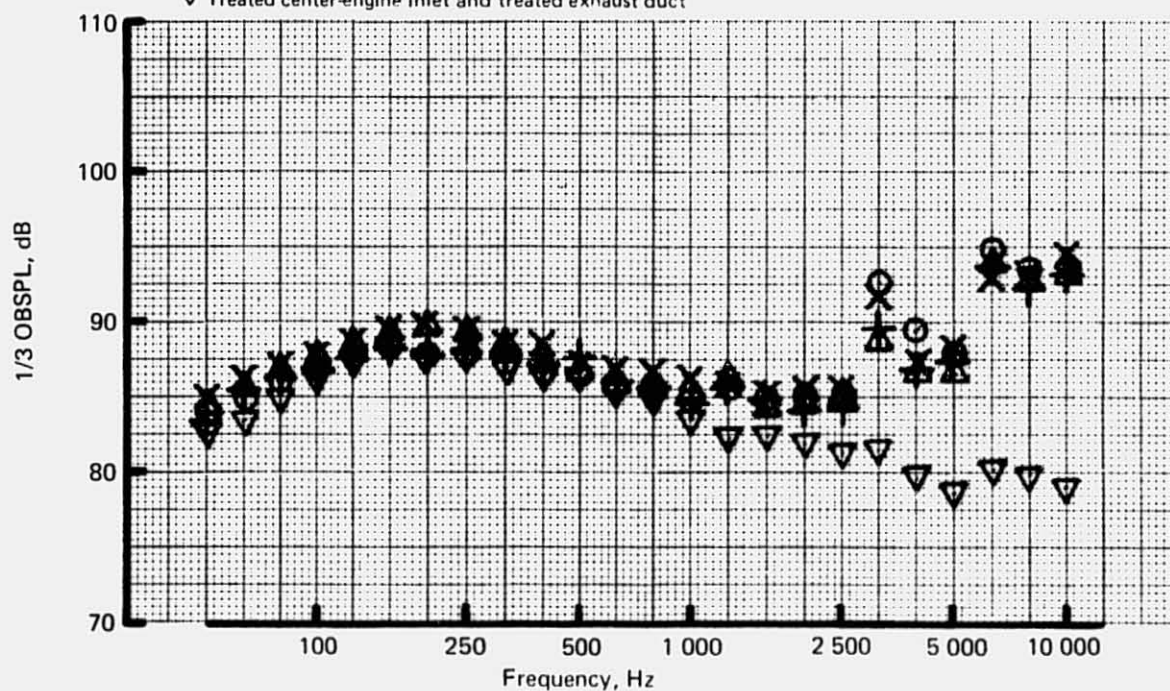
Figure 166.-(Concluded)





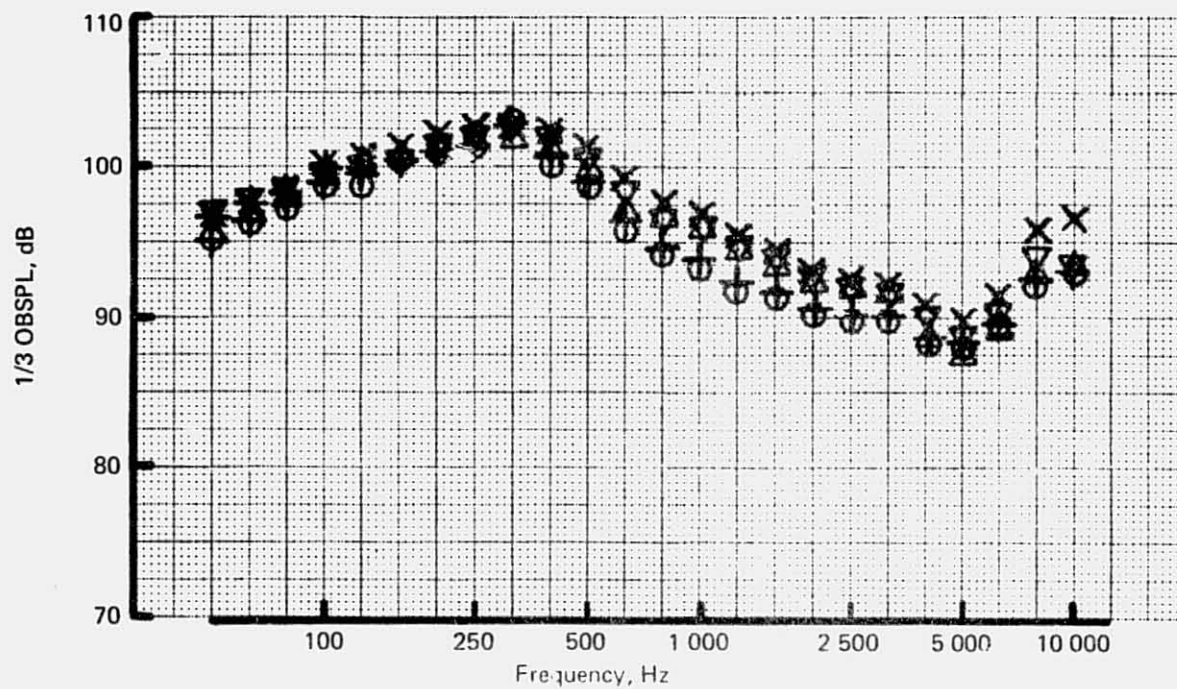
(a) 40° Directivity Angle

- X Treated side-engine inlet (with ring) and treated exhaust duct
- △ Treated side-engine inlet (without ring) and treated exhaust duct
- + Treated side-engine inlet (with ring), treated exhaust duct, and treated flow divider
- Treated side-engine inlet (without ring) treated exhaust duct, and treated flow divider
- ▽ Treated center-engine inlet and treated exhaust duct



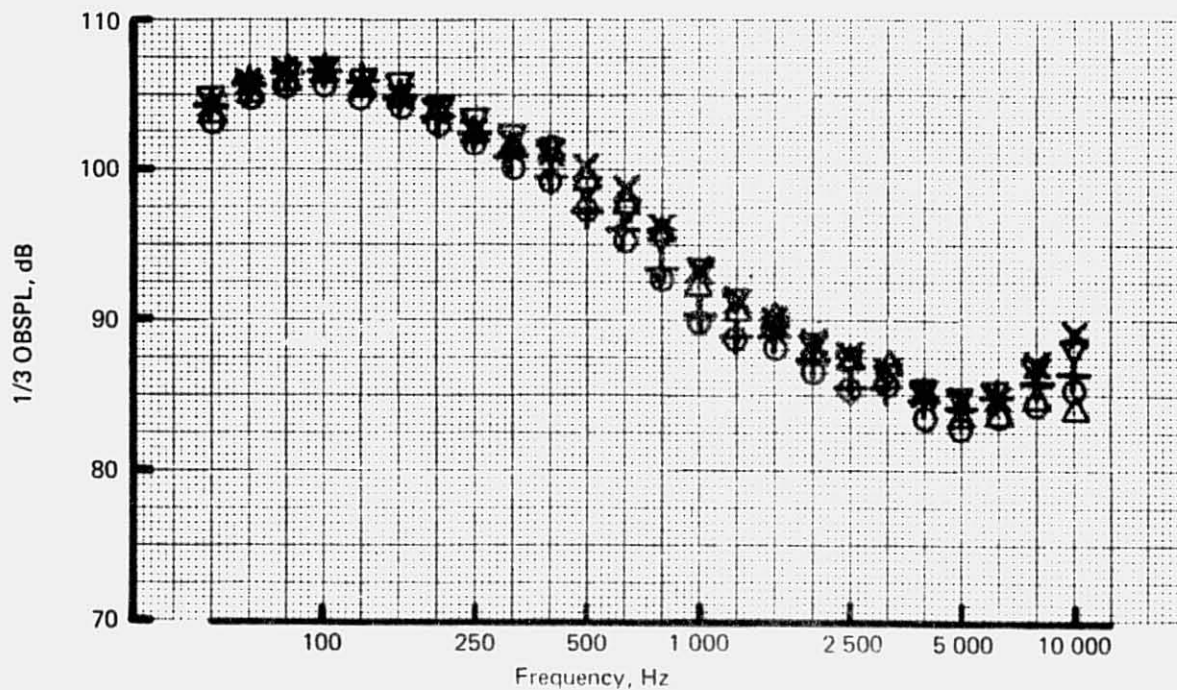
(b) 60° Directivity Angle

Figure 167.—JT8D-115 Ground Test—Total Engine Spectra for Various Nacelle Treatments: 150 ft (45.72 m) Polar, Ground Microphone, Approach rpm



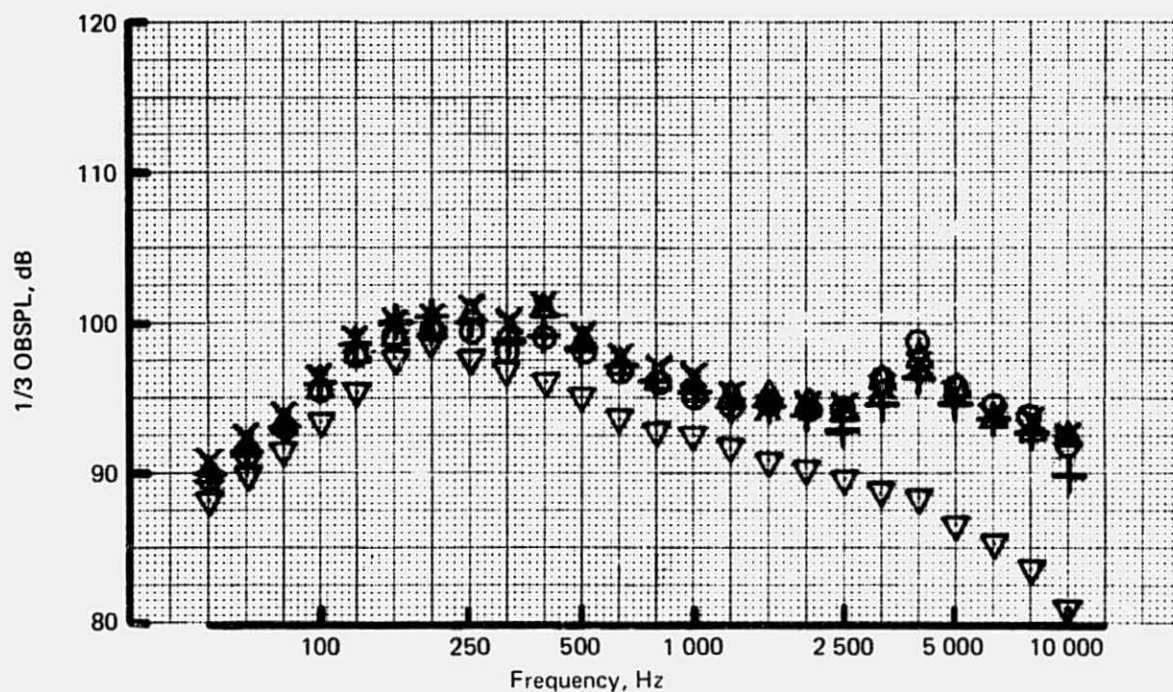
(c) 120° Directivity Angle

- X Treated side-engine inlet (with ring) and treated exhaust duct
- Δ Treated side-engine inlet (without ring) and treated exhaust duct
- + Treated side-engine inlet (with ring), treated exhaust duct, and treated flow divider
- Treated side-engine inlet (without ring) treated exhaust duct, and treated flow divider
- ▽ Treated center-engine inlet and treated exhaust duct



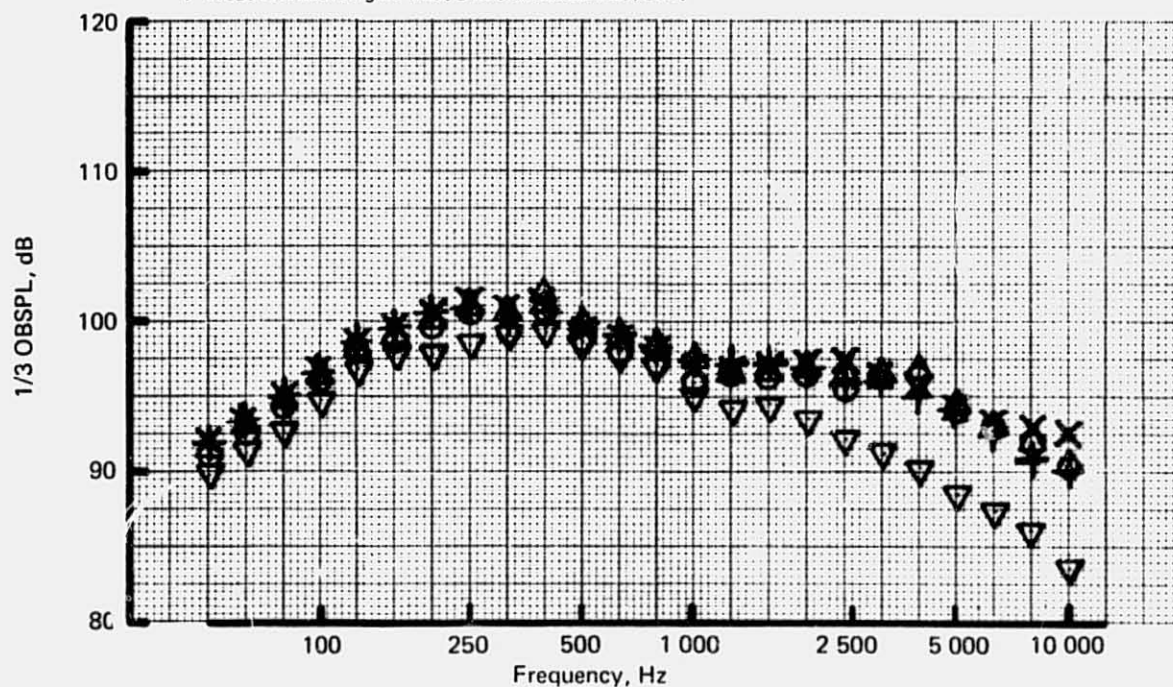
(d) 140° Directivity Angle

Figure 167.—(Concluded)



(a) 40° Directivity Angle

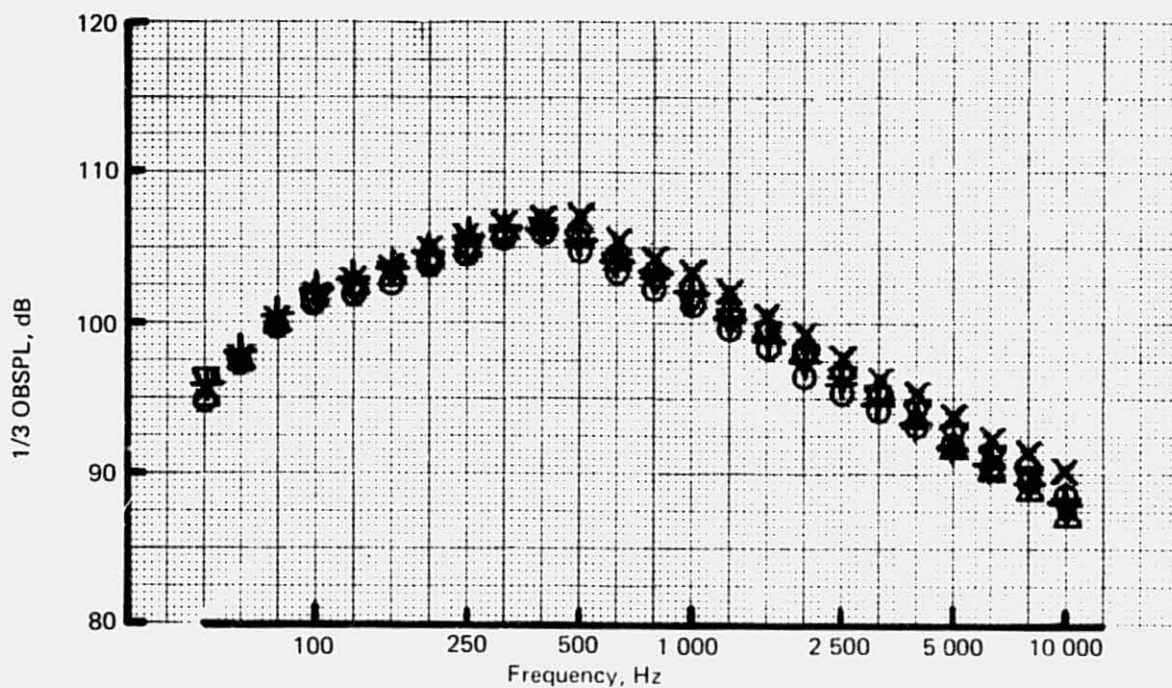
- X Treated side-engine inlet (with ring) and treated exhaust duct
- △ Treated side-engine inlet (without ring) and treated exhaust duct
- + Treated side-engine inlet (with ring), treated exhaust duct, and treated flow divider
- Treated side-engine inlet (without ring) treated exhaust duct, and treated flow divider
- ▽ Treated center-engine inlet and treated exhaust duct



(b) 60° Directivity Angle

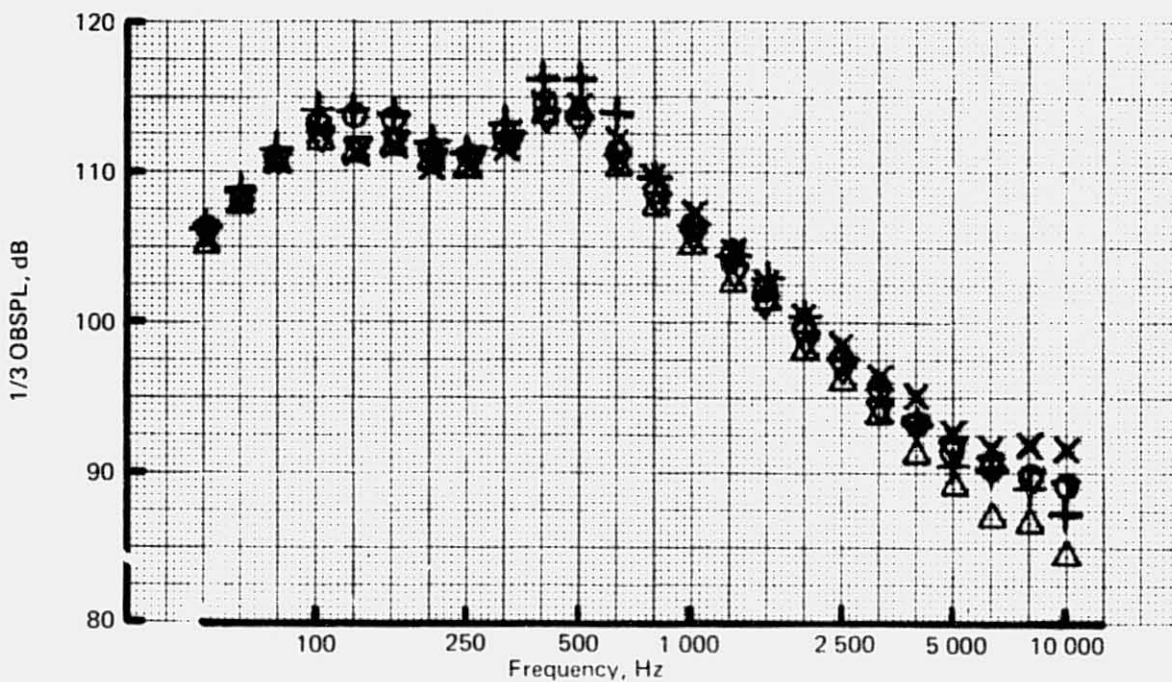
Figure 168.—JT8D-115 Ground Test—Total Engine Spectra for Various Nacelle Treatments:  
150 ft (45.72 m) Polar, Ground Plane Microphone, Takeoff rpm





(c) 120° Directivity Angle

- X Treated side-engine inlet (with ring) and treated exhaust duct
- △ Treated side-engine inlet (without ring) and treated exhaust duct
- + Treated side-engine inlet (with ring), treated exhaust duct, and treated flow divider
- Treated side-engine inlet (without ring) treated exhaust duct, and treated flow divider
- ▽ Treated center-engine inlet and treated exhaust duct



(d) 140° Directivity Angle

Figure 168.-(Concluded)



nacelle treatment configurations. The reader is cautioned that a valid evaluation of the treatment effectiveness cannot be made from this data. A complete evaluation of lining attenuation characteristics of each nacelle treatment is presented in section 4.2.3 based on analysis of source isolated noise data.

By scanning figures 167 and 168, one can see the important effects of the various nacelle acoustic treatments and the variation of these effects with directivity angle and power setting. At approach rpm in the forward quadrant (fig. 167a and b), the heavily treated center-engine inlet configuration is seen to be 12 to 15 dB below all other nacelle configurations. At the 40° directivity angle, the treated side-engine inlet with ring appears to provide approximately 10-dB reduction in the inlet fan tone compared with the side-engine inlet without ring for both exhaust configurations. However, at 60°, there is no appreciable difference between the side-engine inlet with ring and without ring. This apparent anomaly is attributed to the very large data scatter in the inlet fan tone level as discussed in section 4.2.1. In the aft quadrant (fig. 167c and d) there are few important differences among the five treatment configurations, although the two fully treated exhaust configurations do appear to have measurably lower midfrequency noise than the peripheral exhaust treatment configurations. At takeoff power in the forward quadrant (fig. 168a and b), the center-engine inlet is again well below all side-engine inlet configurations. Again only small differences are seen among the various side-engine inlet configurations. In the aft quadrant (fig. 168c and d), there are no significant differences among the five configurations within the limits of data scatter.

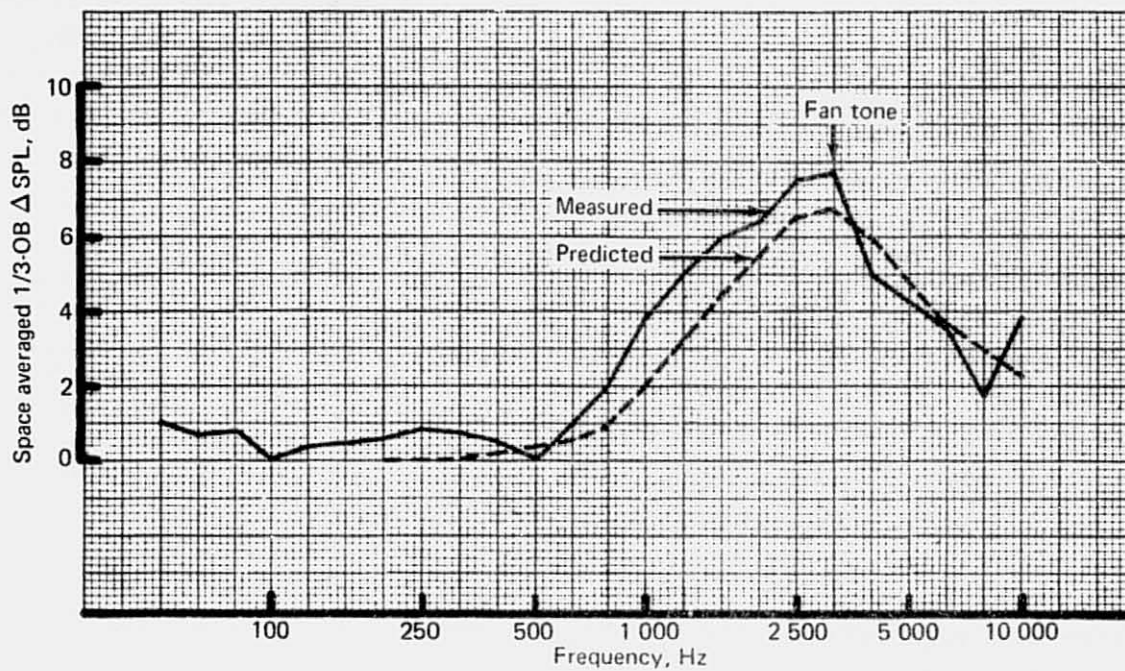
#### 4.2.3 ACOUSTIC LINING ATTENUATION

Reduction in SPL's due to acoustic linings was measured for a side-engine inlet both with and without ring, a hybrid exhaust system, and a flight-type exhaust system. These measurements were used to evaluate the effectiveness of these linings and to provide lining attenuation inputs for the flyover analysis that is presented in reference 1. To facilitate the flyover analysis objective, SPL's were also measured for a treated center duct.

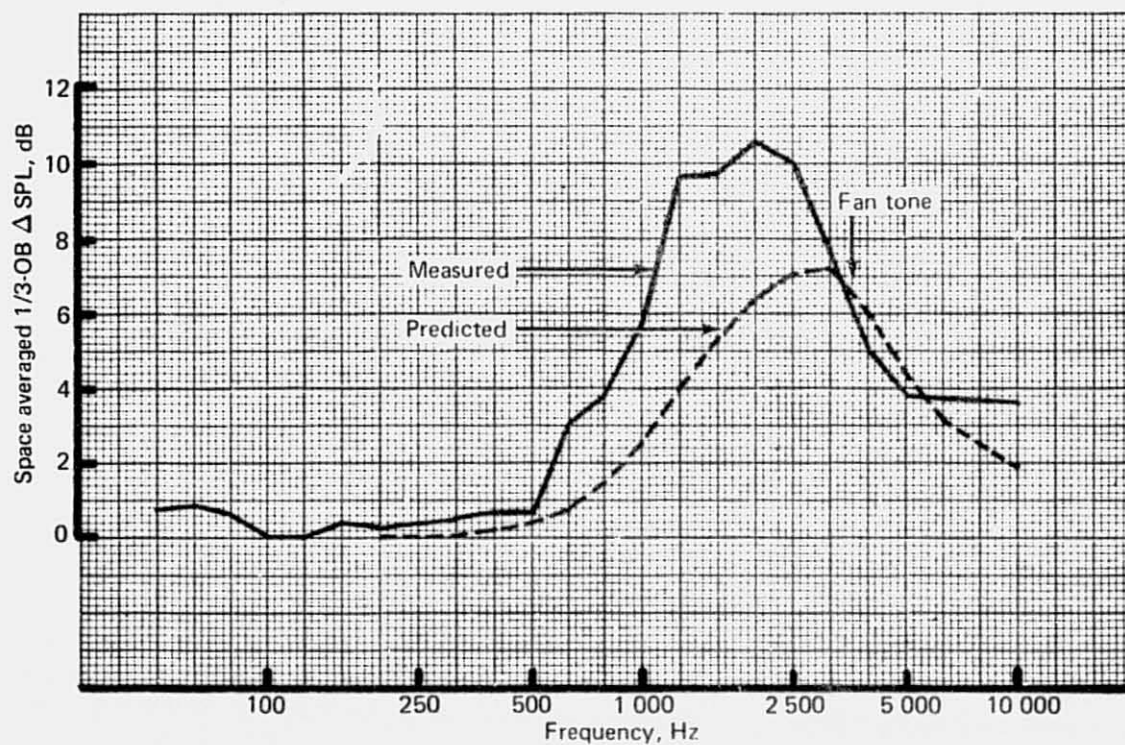
To facilitate comparison of measured SPL reductions with predicted values, the SPL values have been space averaged and compared with predicted values of power insertion loss. Space averaging was performed over a 15° to 95° arc for forward radiated noise and over an 85° to 155° arc for aft-radiated noise.

##### 4.2.3.1 Side-Engine Inlet Without Ring

Definition of the side-engine inlet (without ring) acoustic liners, as they were built for the ground test, is given in figure 15. The linings were designed to achieve optimum noise attenuation at the approach condition of the 727-200 airplane by using a cylindrical duct wave attenuation model and incorporating adjustments based on experimental (JT9D engine) data. A comparison of the predicted design point power insertion loss with the measured space average SPL reduction for the same value of corrected low rotor speed (fig. 169a) indicates that the optimum design point noise attenuation is nearly achieved or exceeded at all 1/3 OB's, and in particular, at the fan blade passing frequency.



(a) Approach rpm



(b) Cutback rpm

Figure 169.—JT8D-115 Ground Test—Measured Versus Predicted Lining Attenuation of Side-Engine Inlet Without Ring

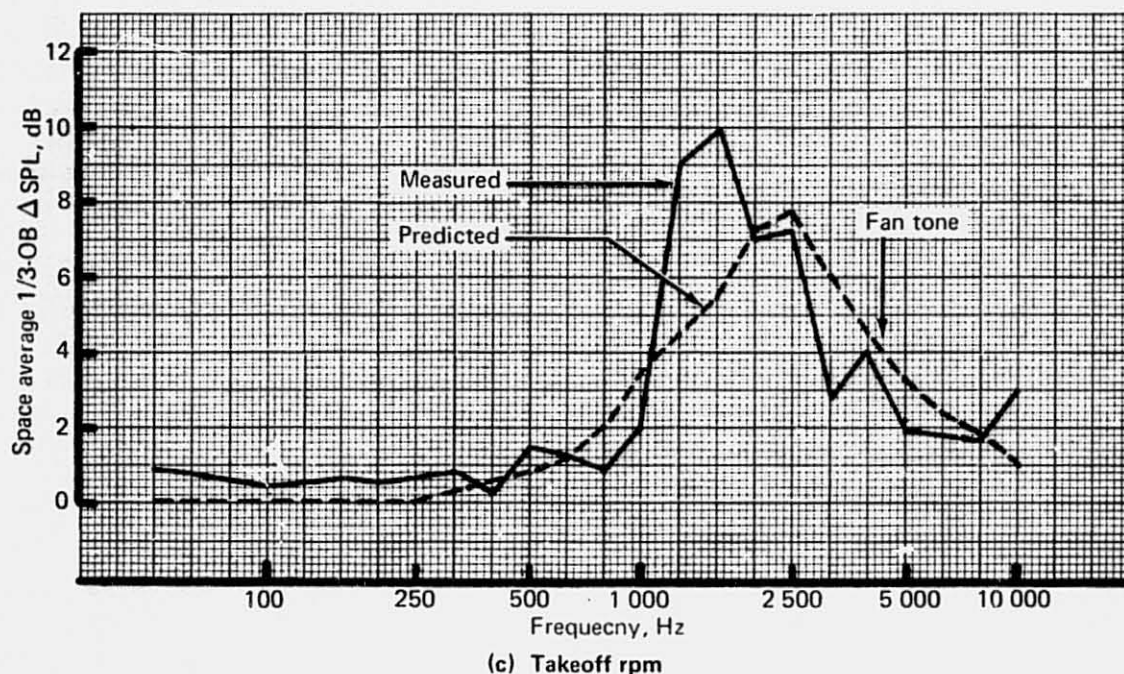


Figure 169. — (Concluded)

To see the effect of the acoustic linings at off-design power settings, the measured space averaged SPL reduction is compared to the predicted power insertion loss for corrected low speed rotor values corresponding to the 727-200 airplane cutback and takeoff conditions in figures 169b and c, respectively. While the peak measured attenuation exceeds the predicted values for both cases, these peak values occur at lower than predicted frequencies. This phenomenon is due to the tendency for linings to be more effective for the lower frequency buzzsaw noise than for the higher frequency fan tone and broadband noise.

#### 4.2.3.2 Side-Engine Inlet With Ring

Definition of the side-engine inlet (with ring) acoustic liners, as they were built for the ground test, is given in figure 16. This was a compromise design, based on incorporating a ring into the previously defined inlet without ring. With the diffuser and nose dome thus fixed, an annular duct wave attenuation program was used to optimize the lining parameters of the ring for maximum noise attenuation at the approach condition of the 727-200 airplane. The power insertion loss that was then predicted for this condition is compared with the space-averaged SPL reduction measured at the same value of corrected low rotor speed in figure 170a. This comparison indicates that the expected attenuation was very nearly achieved.



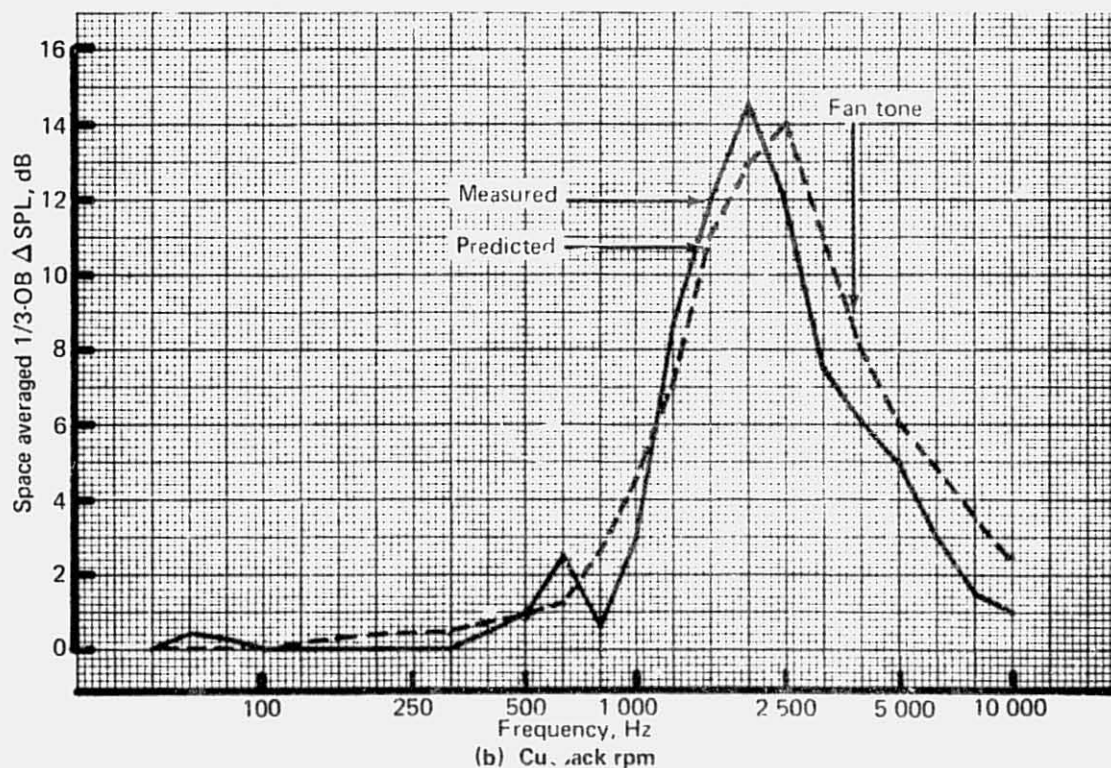
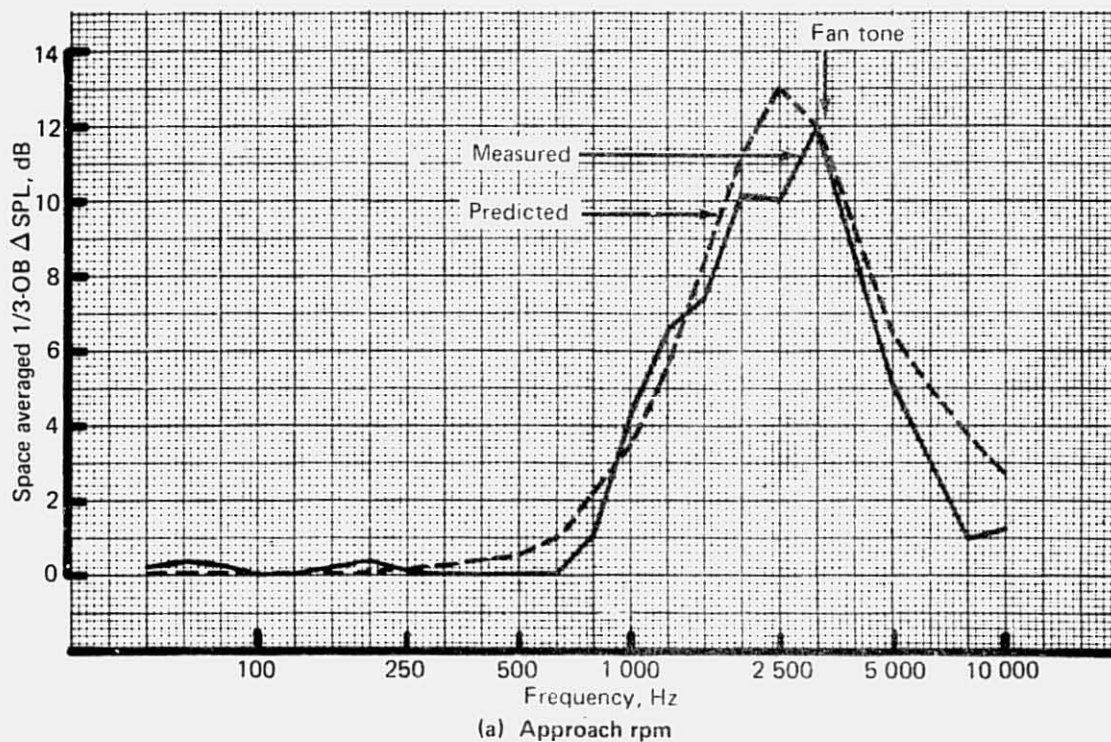


Figure 170.—JT8D-115 Ground Test—Measured Versus Predicted Lining Attenuation of Side-Engine Inlet With Ring



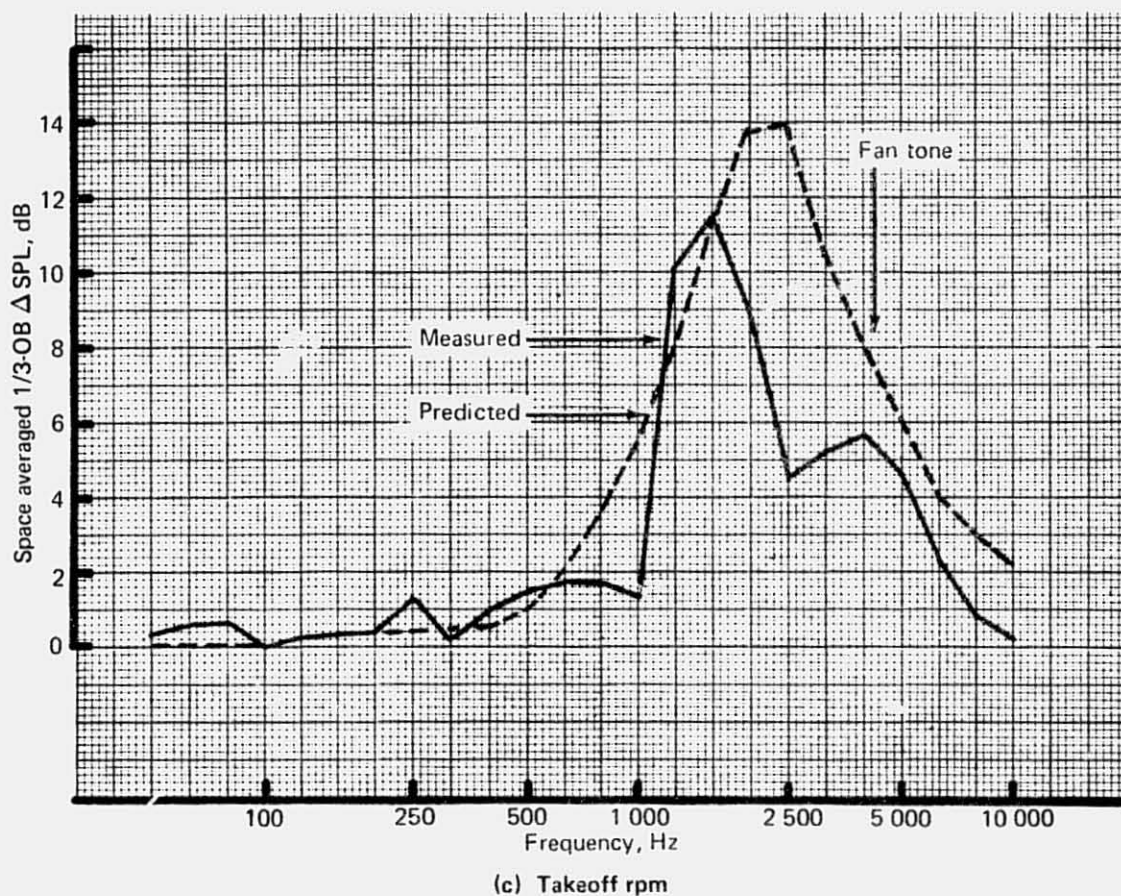


Figure 170.—(Concluded)

The effect of the acoustic linings at off-design power settings is shown in figures 170b and c, where the measured space averaged SPL reduction is compared to the predicted power insertion loss for corrected low speed rotor values corresponding to the 727-200 airplane cut-back and takeoff conditions. The tuning frequencies are seen to be below both the predicted values and the fan blade passage frequencies. Again the attenuation spectra are affected by high buzzsaw attenuation.

Directivity indices of the SPL attenuation, defined as the ratio of the SPL reduction at a given angle to the power insertion loss, have been calculated for the side-engine inlet with ring for incorporation into the flyover analysis. An average of the directivity values of the seven 1/3-OB's surrounding the fan tone (1250 to 5000 Hz) is shown in figure 171 for low speed rotor values of 4910, 5380, 5710, and 6330 rpm. The curve shown represents the values used for the flyover analysis.

It is noted that the noise reductions shown above for the inlet with ring are the differences in measured noise between the treated inlet with ring and the hardwall inlet without ring. This should have negligible effect on the space-averaged attenuation spectra, thus allowing the directivity indices that were determined above to better reflect the flyover effect of the linings since the inlet source noise is based on a ringless inlet.

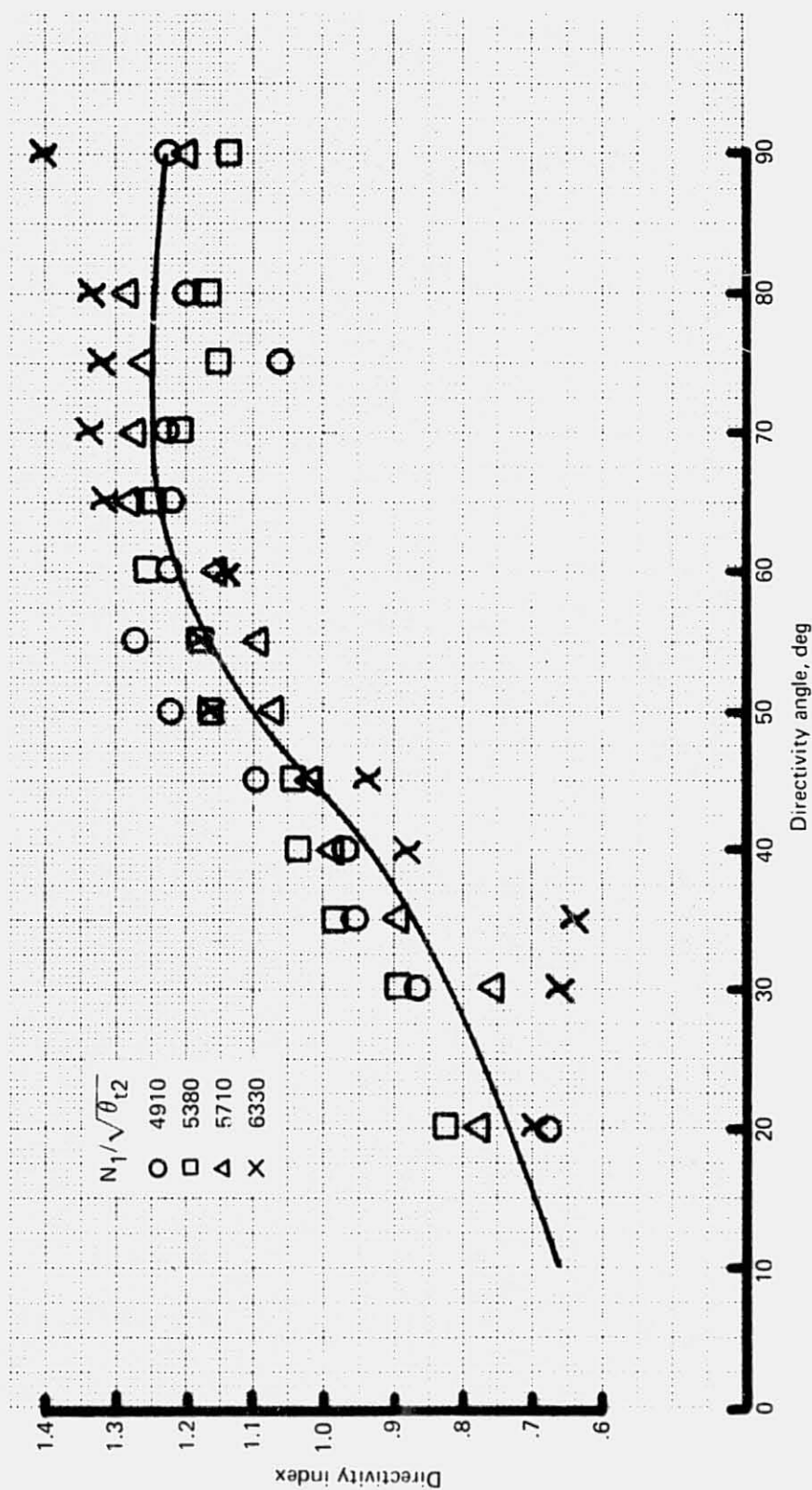


Figure 171.—JT8D-115 Ground Test—Directivity of Acoustic Lining Attenuation for Treated Side-Engine Inlet With Ring

#### 4.2.3.3 Center-Engine Inlet

The center-engine inlet acoustic liners, as they were built for the ground test, are defined in figure 17. The liners were designed to attenuate combination tones at the 727-200 airplane cruise and takeoff conditions and to provide optimum fan tone attenuation at the approach condition.

The space-averaged far-field SPL of the treated center duct is compared to that of the treated side-engine inlet with ring in figure 172 for the 727-200 airplane approach condition. This comparison indicates that the noise radiating from the treated center duct would be a negligible contributor to the total inlet community noise of the airplane, particularly when compared to the output from two side-engine inlets. Wing and fuselage shielding would be expected to further reduce the significance of the far-field noise contribution from the treated center duct.

#### 4.2.3.4 Flyover Analysis Inputs

Inlet lining attenuation spectra were determined for a variety of power settings for use in the flyover analysis that is presented in reference 1. These spectra represent the combined lining attenuation of the center-engine inlet and two side-engine inlets with rings. The attenuation spectra were determined by the parallel-duct addition of the measured space-averaged noise reduction of the center-engine inlet and side-engine inlets with rings. Equal far-field

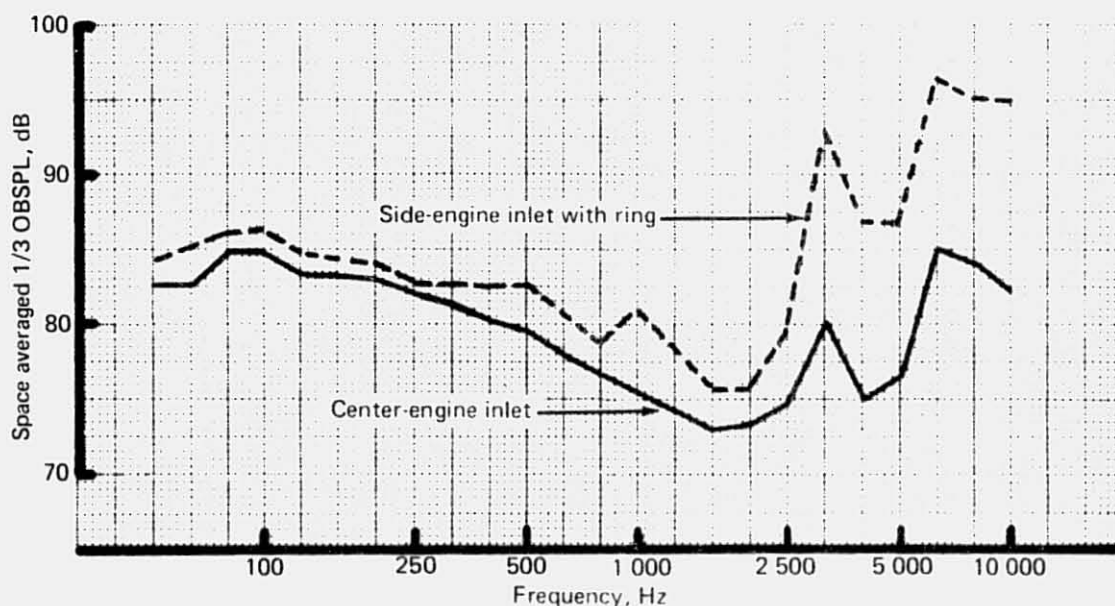


Figure 172.—JT8D-115 Ground Test—Comparison of Space Averaged SPL of Center-Engine Inlet and Side-Engine Inlet With Ring: Aft Baffled, 150 ft (45.72 m) Polar, Ground Microphones, Approach rpm

noise radiation was assumed for each of the untreated sources, each of the measured attenuation spectra were referenced to the same hardwall side-engine inlet without ring. The differences in space-average SPL values of treated center-engine inlet and the hardwall side-engine inlet without ring are shown for the three corrected low speed rotor values corresponding to the approach, cutback, and takeoff conditions of the 727-200 airplane in figure 173.

The directivity indices used in the flyover analysis are those that were determined above for the side-engine inlet with ring in figure 171. Since the contribution of the center-engine inlet noise to the total inlet noise is small, no appreciable error is incurred by not including the effects of the center-engine inlet attenuation directivity into the directivity indices.

#### 4.2.3.5 Hybrid Exhaust System

Specifications of the acoustic liners for the exhaust duct (wedge duct and nozzle) used in the hybrid configuration are those listed in figure 15. The hardwall plug and splitter used in the hybrid configuration were the reference hardware as shown in figure 9. The space-averaged SPL reduction achieved with the hybrid exhaust system is compared to the predicted power insertion loss at values of  $N_1$  corresponding to the 727-200 airplane approach, cutback, and takeoff conditions (fig. 174a, b, and c, respectively).

The disappointing noise reduction measured for the hybrid exhaust system is at least partially caused by jet noise floor. Because of this, measured attenuation directivity indices would be as much of a function of various noise sources as of the noise reduction due to the acoustic liners. Therefore, directivity indices were not determined for this exhaust system.

Additional factors that could adversely affect the measured performance of the acoustic liners include: (1) the P&WA fan case liners, which may have reduced the readily attenuable fan modes more than predicted; and (2) noise radiating from the turbine, as a result of shear layer between the primary and secondary jet streams, which might be relatively unaffected by the exhaust duct lining.

#### 4.2.3.6 Flight-Type Exhaust System

Specifications of the acoustic liners for this configuration are given in figure 15. Noise reductions reported for this exhaust system are the differences in noise between the flight-type exhaust system and the *hardwall* hybrid exhaust system. The hybrid exhaust system was made hardwall by taping over the exhaust duct (wedge duct and nozzle) treatment. The space-averaged SPL reductions thereby achieved are compared with the predicted power insertion loss at values of  $N_1$  corresponding to the 727-200 airplane approach, cutback, and takeoff conditions in figures 175a, b, and c, respectively.

The disappointing noise reduction measured for the flight-type exhaust system is at least partially caused by a noise floor at some of the microphone locations. Therefore, directivity indices were, again, not determined for this exhaust system.

The additional factors given for the possible lack of noise attenuation of the hybrid exhaust system also apply to the flight-type exhaust system.



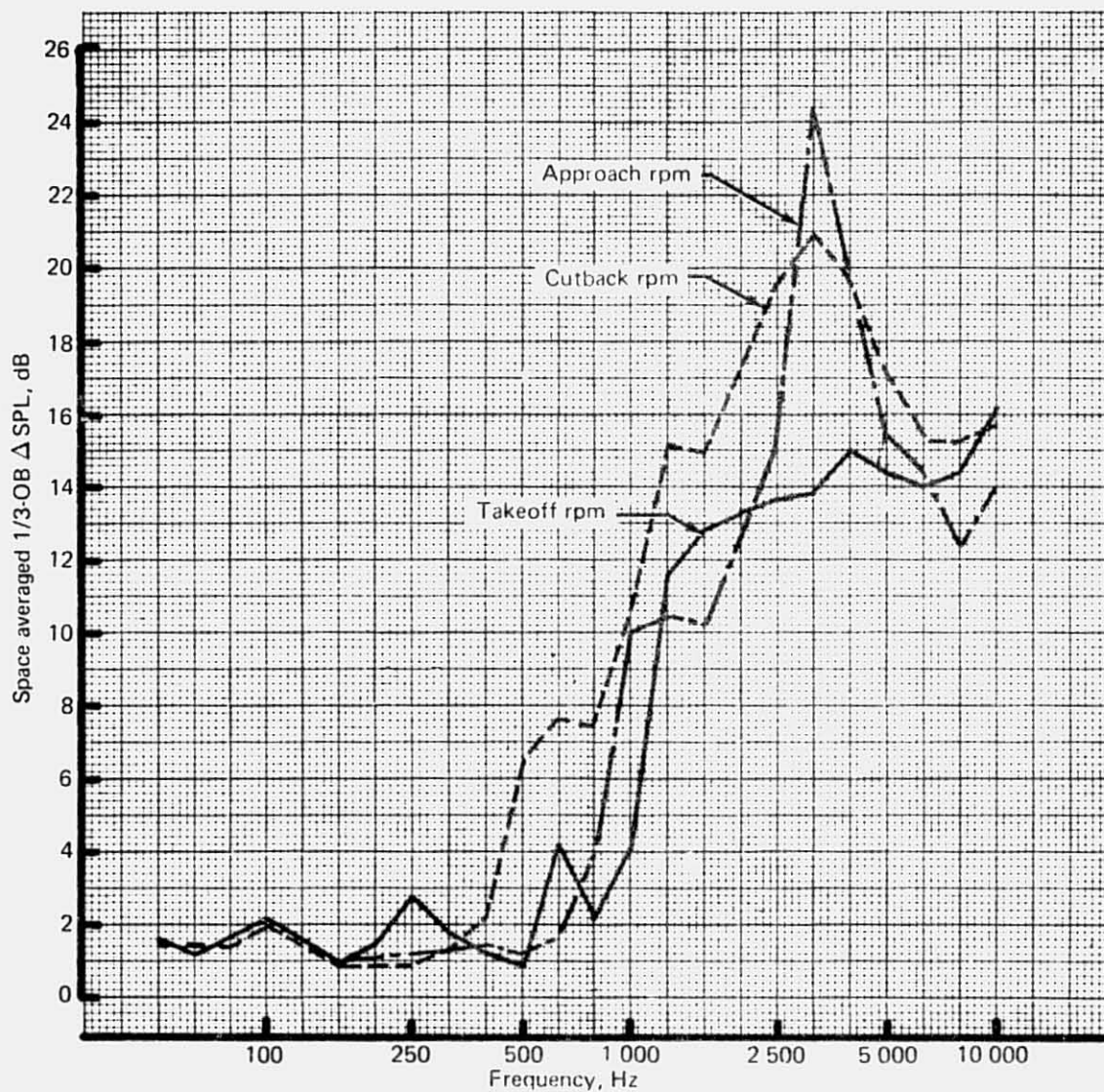


Figure 173.—JT8D-115 Ground Test—Differences in SPL Between the Hardwall Side-Engine Inlet Without Ring and the Treated Center-Engine Inlet at Approach, Cutback, and Takeoff rpm

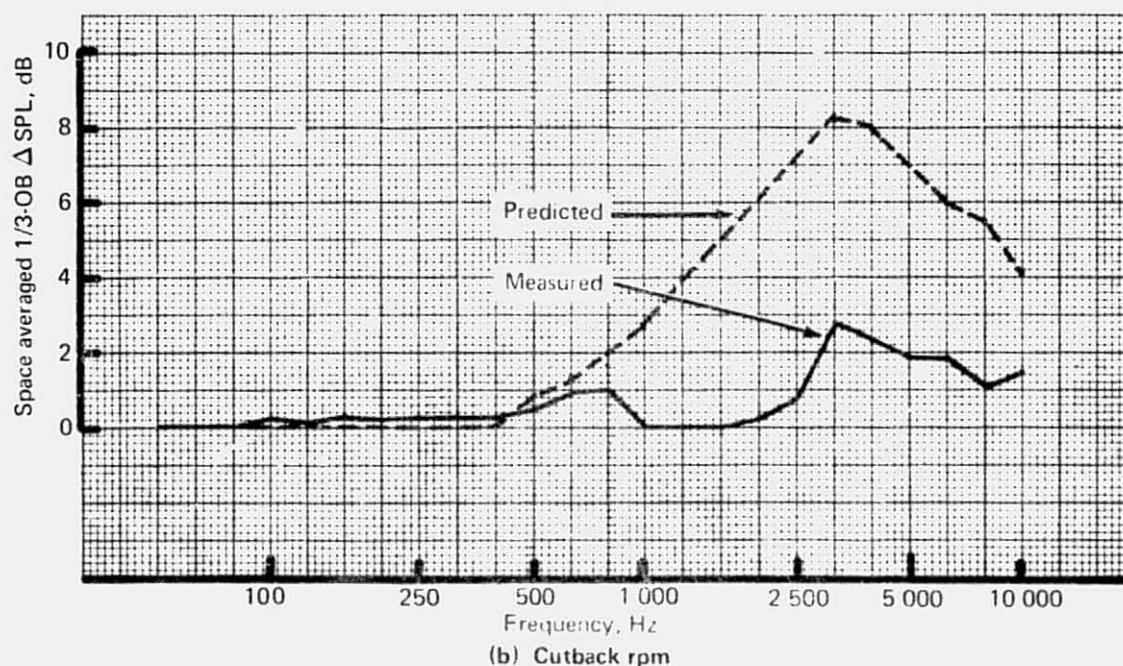
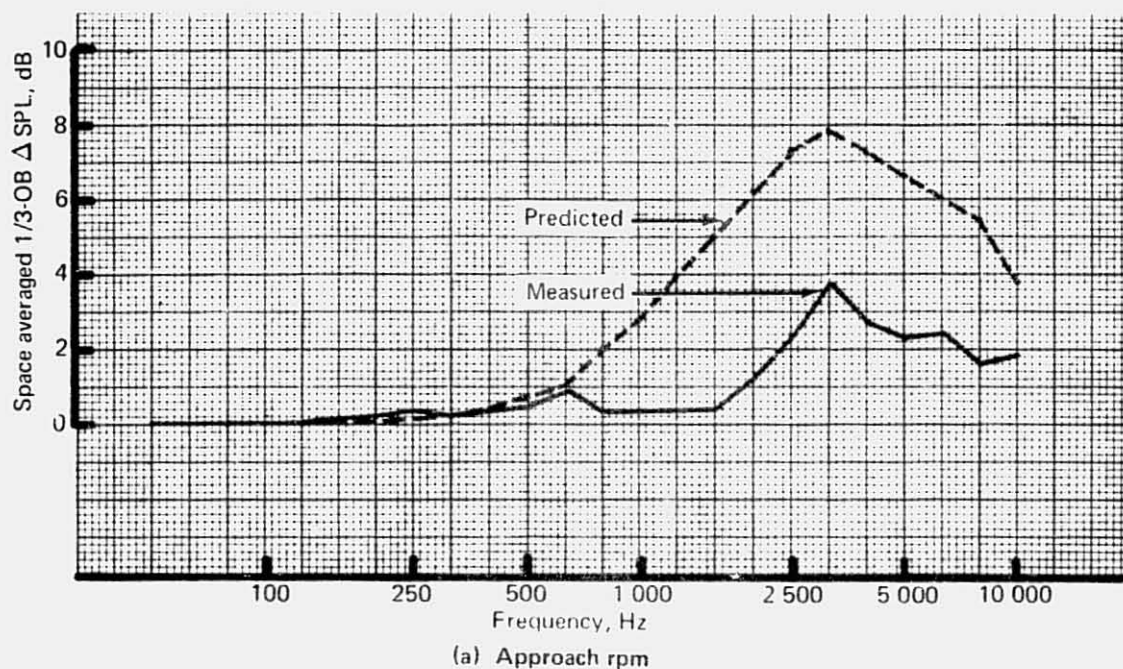


Figure 174.—JT8D-115 Ground Test—Measured Versus Predicted Lining Attenuation Spectra of Hybrid Exhaust System

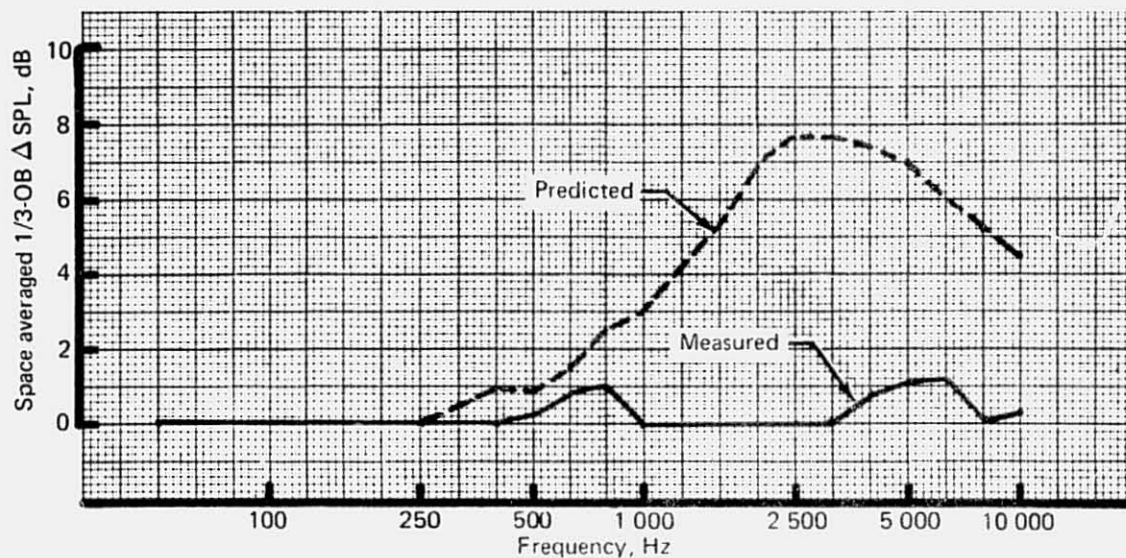


Figure 174.—(Concluded)

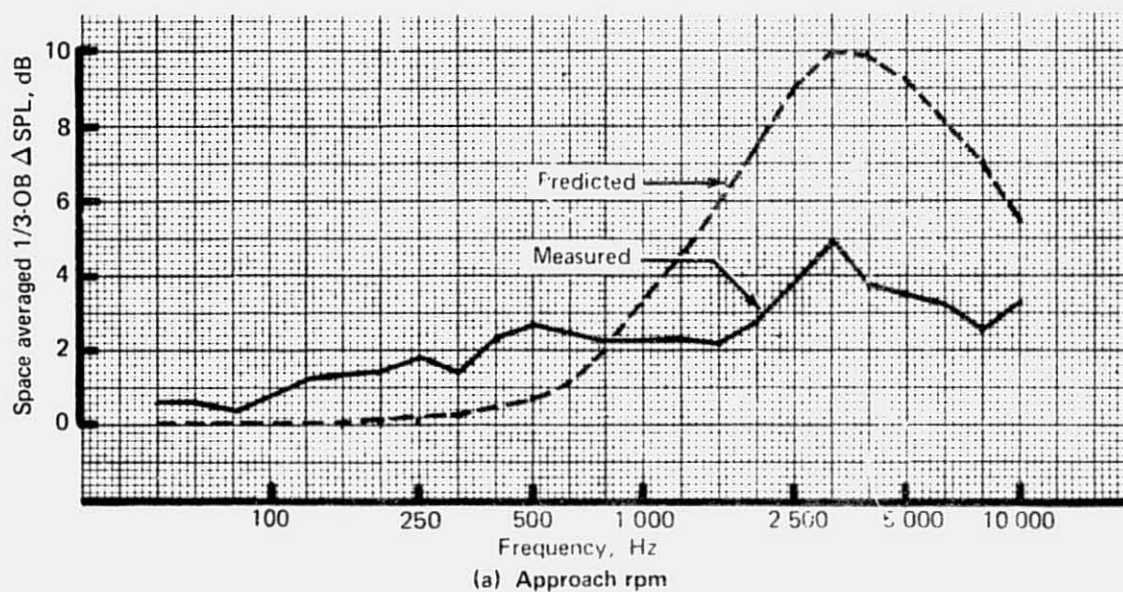


Figure 175.—J18D-115 Ground Test—Measured Versus Predicted Lining Attenuation Spectra of Flight-Type Exhaust System



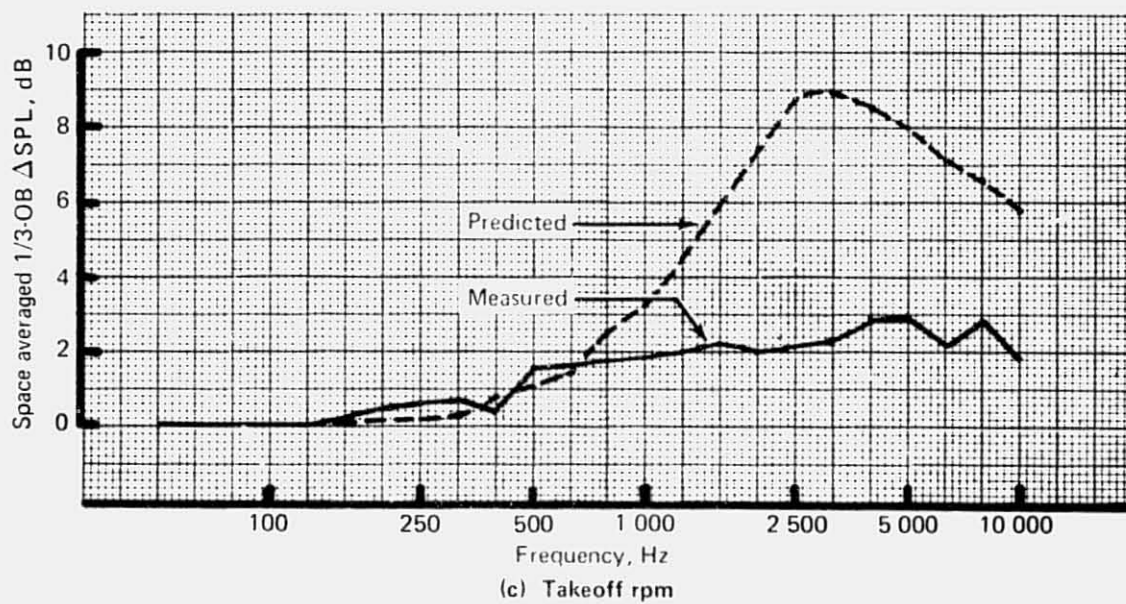
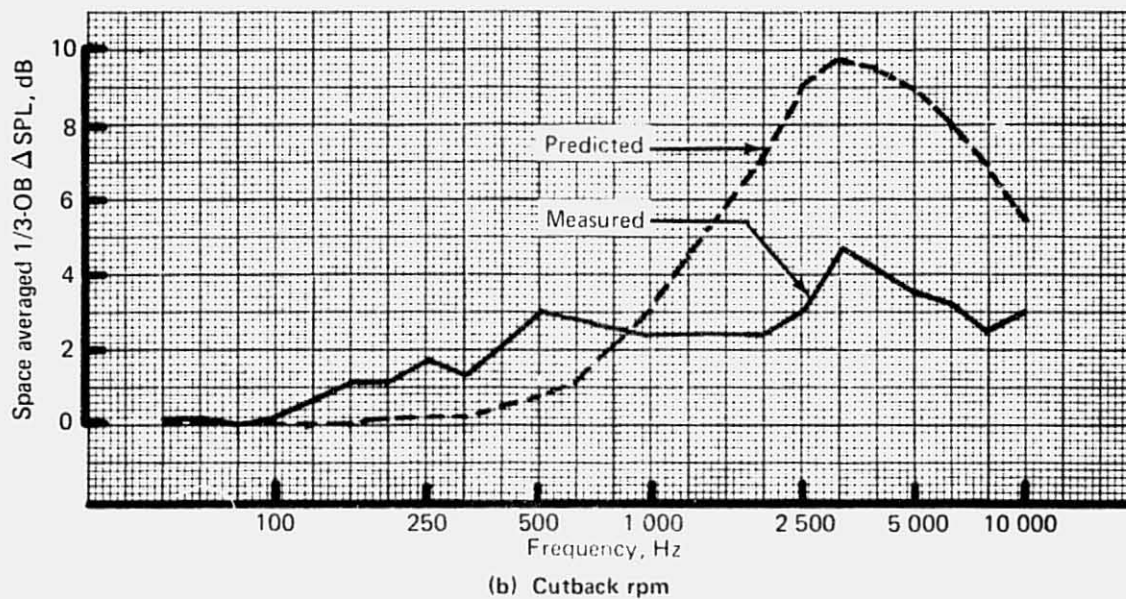


Figure 175. - (Concluded)



#### 4.2.4 INTERNAL MICROPHONE DATA

Internal microphones were used in the center-engine inlet, side-engine inlet both with and without ring, and exhaust system to allow determination of the noise spectral content, the variation of SPL's with circumferential and axial location of the treated surfaces, the variation of SPL with power setting, and the general noise levels at the treated surfaces. Radial variations of SPL's were measured for the side-engine inlet with ring to test the lining design assumption that there was zero radial gradient of the overall sound pressure level (OASPL).

##### 4.2.4.1 Center-Engine Inlet Duct

Internal microphones were mounted flush on the treated surfaces of the center-engine inlet duct at the locations indicated in figure 21. Data (averaged over three runs) of OASPL, fan tone 1/3 OBSPL and the maximum 1/3 OBSPL in the combination tone frequency range (based on spectra measured nearest the fan face) are related in table 22 for values of  $N_1$  corresponding to the approach and cutback conditions and to a higher  $N_1$  value of 6800 rpm.

It is observed that at microphone plane 1 (microphones located nearest the fan face) there is virtually no variation of OASPL with circumferential location of the microphone. There is

Table 22.—JT8D-115 Ground Test—SPL's at Various Surface Locations in the Center-Engine Inlet Duct for Various Values of  $N_1$ <sup>a</sup>

Microphone plane and clock position	Approach condition, $N_1 = 5800$ rpm			Cutback condition, $N_1 = 6300$ rpm			$N_1 = 6800$ rpm		
	OASPL	Fan tone SPL band 35	Combination tone SPL band 27	OASPL	Fan tone SPL band 36	Combination tone SPL band 27	OASPL	Fan tone SPL band 36	Combination tone SPL band 27
Plane 1 — 12	146.8	138.9	138.0	150.1	143.7	140.7	149.8	140.9	138.6
6	147.2	142.8	132.4	150.2	145.1	137.2	149.0	143.8	133.1
3	147.4	139.3	135.0	150.1	144.0	140.7	150.0	143.0	141.0
9	145.9	140.2	133.5	149.3	144.0	137.3	147.8	140.2	133.6
Plane 2 — 12	143.4	139.5	125.6	146.2	139.1	134.9	146.0	136.0	131.6
6	142.1	135.5	124.9	145.1	137.8	135.6	144.0	133.1	131.1
3	141.2	137.9	120.7	142.5	136.5	131.4	142.2	133.8	128.4
9	142.1	139.3	123.9	144.1	138.3	134.0	144.5	135.3	135.2
Plane 3 — 12 <sup>b</sup>	138.3	130.0	121.9	139.8	129.3	130.4	142.3	128.8	130.9
6	137.8	129.1	124.1	140.8	127.8	134.9	140.0	125.6	130.0
3	139.1	130.0	124.6	140.1	127.7	129.1	141.1	126.1	129.9
Plane 4 — 9	136.3	123.4	120.7	136.8	124.5	125.9	137.5	124.8	126.3
Plane 5 — 12	133.6	125.9	115.2	134.2	125.1	117.1	133.9	123.5	118.5
6	138.7	121.3	118.2	138.0	124.0	123.1	138.6	125.4	126.5
3	131.6	121.2	113.8	133.1	122.6	119.2	133.6	123.4	117.9

<sup>a</sup>Unless otherwise noted, data are the average values of three measurements.

<sup>b</sup>Data are from a single measurement.

however, some circumferential variation in the fan-tone-contained 1/3 OB and the combination-tone-contained 1/3 OB; with the fan-tone SPL being highest at the bottom microphone location and the combination-tone SPL being highest at the top microphone location. It is at least conceivable that increased turbulence near the top of the duct, due to the close proximity of the vortex generators, causes more of the total noise to be channeled into combination tone at this location.

Except at the forward most lined section, neither the OASPL nor spectral content varies excessively with circumferential location or power setting. Thus, it would not seem necessary to attempt to increase the bandwidth of the fairly sharply tuned linings except for the detuning effect of Mach Number. However, it is noted that the measured OASPL is approximately 10 dB less at each lining section than was assumed in the design of the linings. Making use of the measured values could lead to slightly improved center-engine inlet duct linings.

The OASPL is plotted as a function of the station distance from the fan face for values of  $N_1$  corresponding to approach and cutback condition and to  $N_1=6800$  rpm in figure 176. Similar plots are shown for the fan-tone SPL, and the above-selected combination-tone SPL in figures 177 and 178, respectively. It is interesting to note that in each case (OASPL, fan-tone SPL, combination-tone SPL) the total SPL reduction along the duct is relatively independent of  $N_1$ , although there is variation with  $N_1$  in the SPL reduction of individual lining sections for the fan tone and combination tone 1/3 OB's.

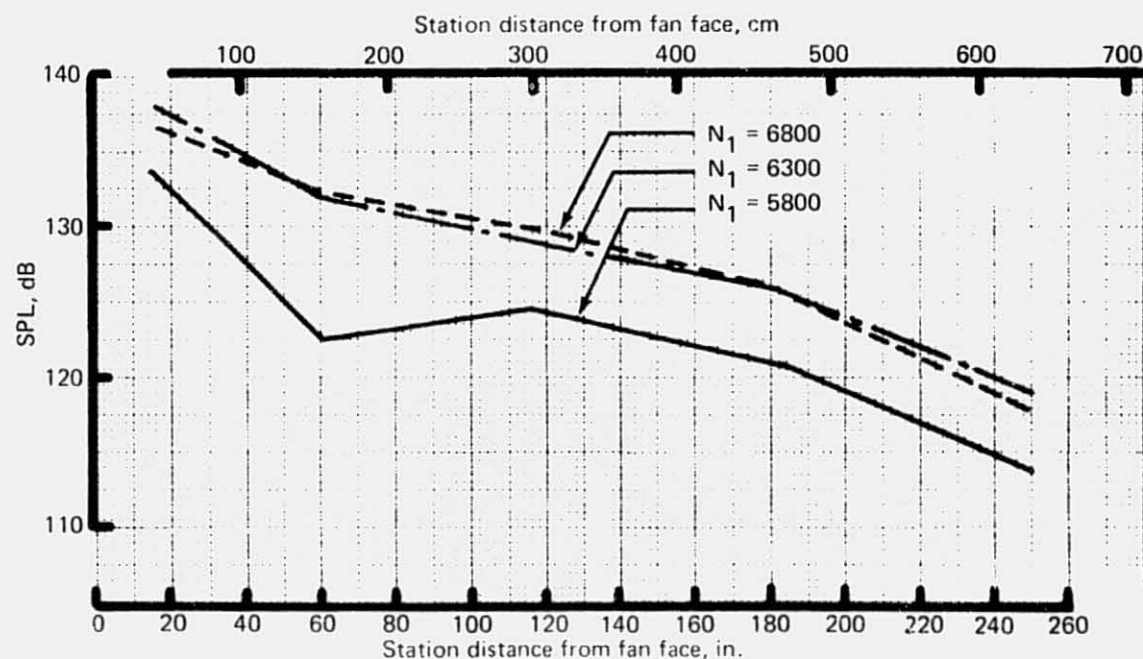


Figure 176.—JT8D-115 Ground Test—Center-Engine Inlet Internal Combination Tone SPL's

REPRODUCIBILITY OF THE  
ORIGINAL PAGE IS POOR.

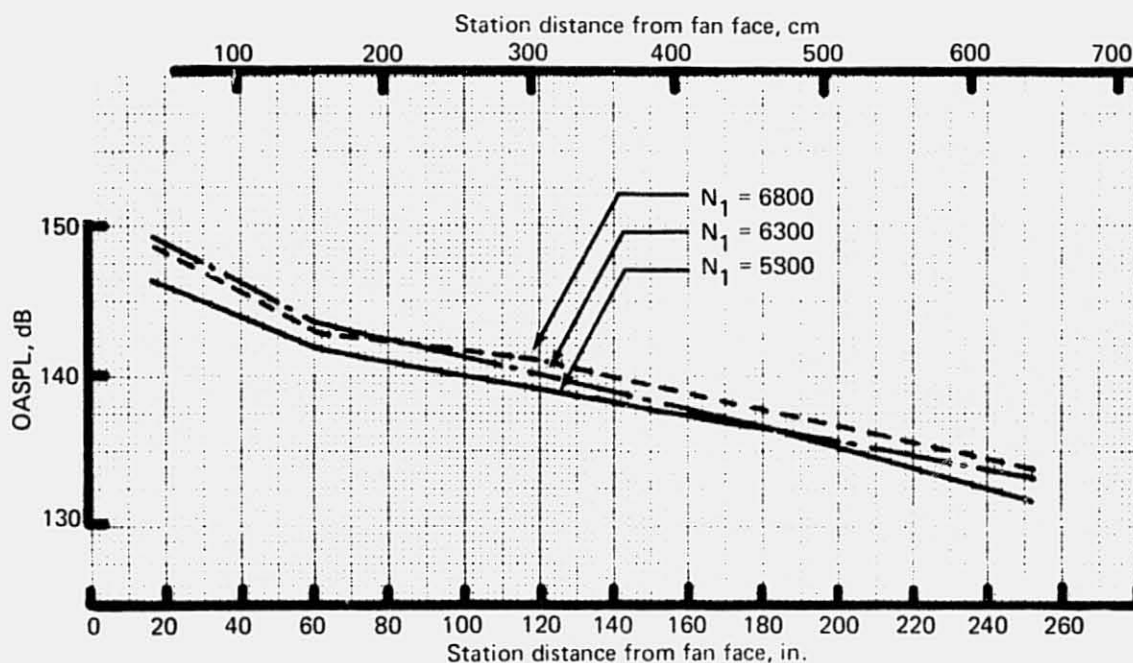


Figure 177.—JT8D-115 Ground Test—Center-Engine Inlet, Internal OASPL's

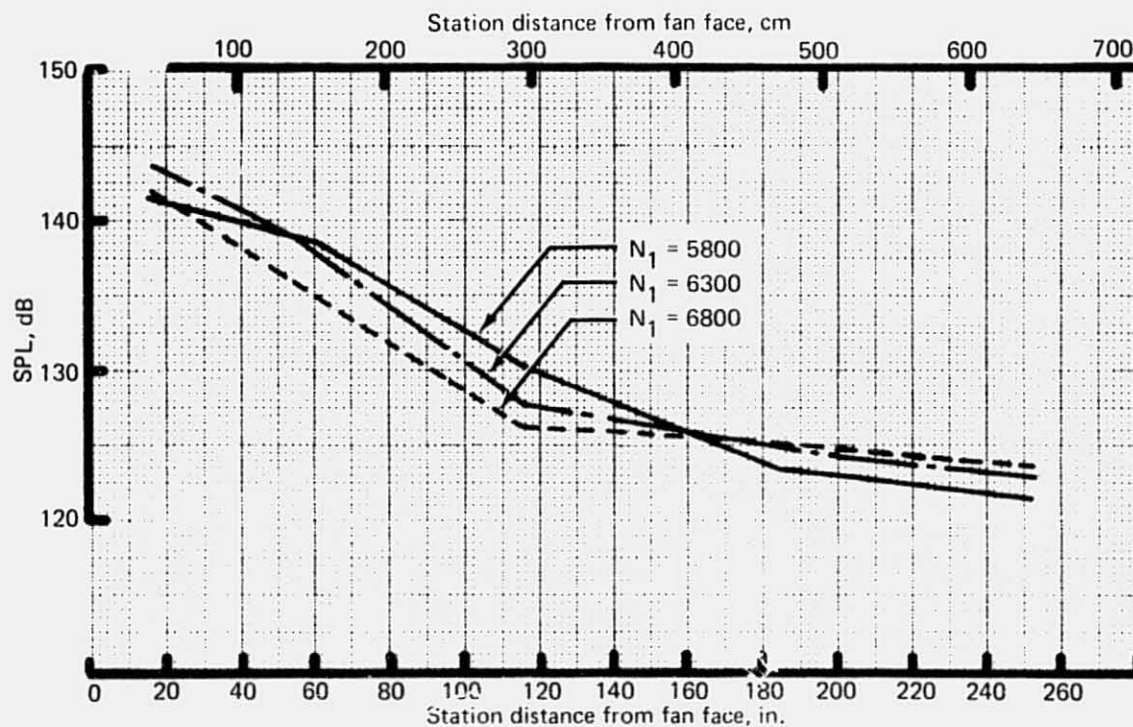


Figure 178.—JT8D-115 Ground Test—Center-Engine Inlet, Fan Tone Internal SPL's

#### 4.2.4.2 Side-Engine Inlet (With and Without Ring)

*Surface Mounted Microphones.*—Internal microphones were mounted flush on the treated surfaces of the inlet with ring at the locations that are indicated in figure 20. Microphones were identically located on the diffuser and the nose dome of the inlet without ring.

Inspection of the SPL data recorded from these microphones reveals that there is no significant variation in sound levels due to the circumferential location of the microphones, nor does the sound level differ significantly between identical locations of the inlet with and without ring. Therefore, data from all circumferential locations of the inlet both with and without ring have been averaged. These averaged values of OASPL, fan tone 1/3 OBSPL, and the 1/3 OBSPL of maximum value that lies within the combination tone frequency range (band 27) were tabulated in table 23 for values of  $N_1$  corresponding to the approach and cutback conditions and to a higher  $N_1$  value of 6800 rpm.

OASPL's at the midaxial positions at approach condition were between 5 and 10 dB below the values that were assumed for lining design purposes. A look at the combination tone 1/3 OBSPL's indicates that combination tone noise is largely confined to the outer channel of the inlet with ring. At the midaxial positions in this channel, the combination tone tends to rise above the fan tone at power settings above approach power.

Table 23.—JT8D-115 Ground Test — SPL's at Various Locations in the Side-Engine Inlet for Various Values of  $N_1$

Microphone location and station no.	Approach condition, $N_1 = 5800$ rpm			Cutback condition, $N_1 = 6300$ rpm			$N_1 = 6800$ rpm		
	OASPL	Fan tone SPL band 35	Combination tone SPL band 27	OASPL	Fan tone SPL band 35	Combination tone SPL band 27	OASPL	Fan tone SPL band 36	Combination tone SPL band 27
Diffuser									
Sta 86 in. (2.18m)	149.4	145.4	136.3	152.9	145.4	143.2	153.2	146.1	141.6
Sta 72 in. (1.88m)	145.6	131.9	127.8	149.3	139.9	141.6	148.4	139.6	138.6
Nose dome									
Sta 86 in. (2.18m)	147.0	144.3	118.2	147.4	141.5	122.7	145.9	140.5	123.7
Sta 82 in. (2.08m)	144.1	138.6	118.4	146.5	140.2	122.6	144.3	137.8	124.1
Ring outer surface									
Sta 86 in. (2.18m)	146.7	140.9	132.4	148.1	140.0	141.2	149.1	141.9	138.8
Sta 77 in. (1.96m)	141.0	129.7	137.7	143.6	133.7	139.9	144.8	130.8	139.9
Ring inner surface									
Sta 86 in. (2.18m)	146.6	141.7	122.0	146.7	138.9	126.9	147.5	140.2	129.8
Sta 77 in. (1.96m)	142.6	134.5	116.2	142.6	132.2	121.6	142.1	132.3	121.5

Note: SPL values are averaged for a number of runs including an inlet with and without ring and for all microphones that differ only by circumferential location.



*Radial Survey.*—Radial variations in SPL were measured by fitting a rake containing 10 surface microphones spaced approximately 2 in. (5.08 cm) apart into the side-engine inlet with ring. The rake was located just aft of the inlet ring at approximately the circumferential location "A" described in figure 20. Data, averaged over two runs of OASPL, fan tone 1/3 OBSPL, and the maximum valued 1/3 OBSPL that lies within the combination tone frequency range (band number 77 or 78), are plotted for the value of  $N_1$  corresponding to the approach condition in figure 179 and for the values of  $N_1$  corresponding to cutback and takeoff conditions in figures 180 and 181, respectively.

A noise gradient is observed that generally tends to increase with radius indicating that the lining attenuation of an inlet with ring should be increased by increasing the ring diameter; zero radial gradient was assumed in the current design.

Again the combination tone tends to be confined to the outer channel indicating that combination tone could be controlled with deep linings on the diffuser only. This result should be confirmed, however, by an analysis of the frequencies of combination tones.

#### 4.2.4.3 Exhaust System

Internal surface microphones were mounted in a set of three concentric rings as shown in figure 22. These rings were then mounted between the engine proper and the exhaust system, and measurements were taken using both a center-engine inlet and a side-engine inlet. In the latter case, data were obtained from only six microphones because of a microphone failure at location E3. However, the data recorded from the microphone at location E2 and also from the microphone at location E1C on the exhaust duct were suspect. Therefore, these data have not been included in the analysis.

There is no significant difference between data taken with the center-engine inlet and the side-engine inlet. Values of OASPL and of fan-tone or turbine-tone SPL at the approach condition have been averaged over four runs (two with each inlet) and are recorded in table 24.

There is no circumferential variation in OASPL and fan-tone SPL indicated by the remaining two microphones on the exhaust duct. The measured OASPL of the secondary channel is about 5 dB below the value assumed to design the linings; whereas, the measured OASPL of the primary channel is approximately equal to the value that was assumed in the design of the linings.

#### 4.2.5 DATA VALIDITY

The following sections discuss the validity of the far-field acoustic data from the standpoint of data repeatability and test technique.

##### 4.2.5.1 Data Repeatability

For purposes of examining acoustic data repeatability, one engine configuration in each test was selected for a series of repeat runs to be distributed throughout the duration of the test.

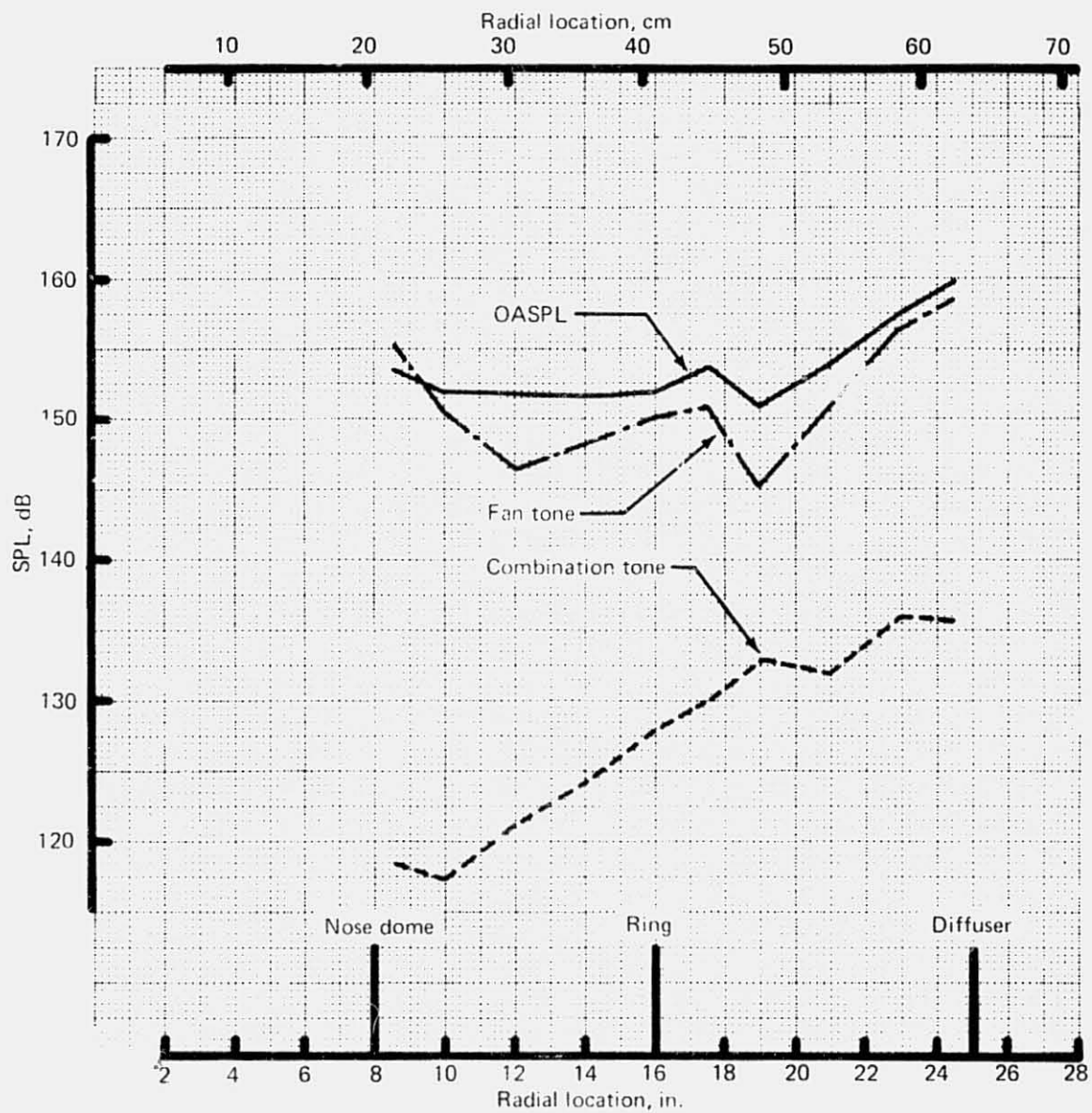


Figure 179.—JT8D-115 Ground Test—SPL Versus Radial Distance at Fan Face, Side-Engine Inlet With Ring, Approach rpm

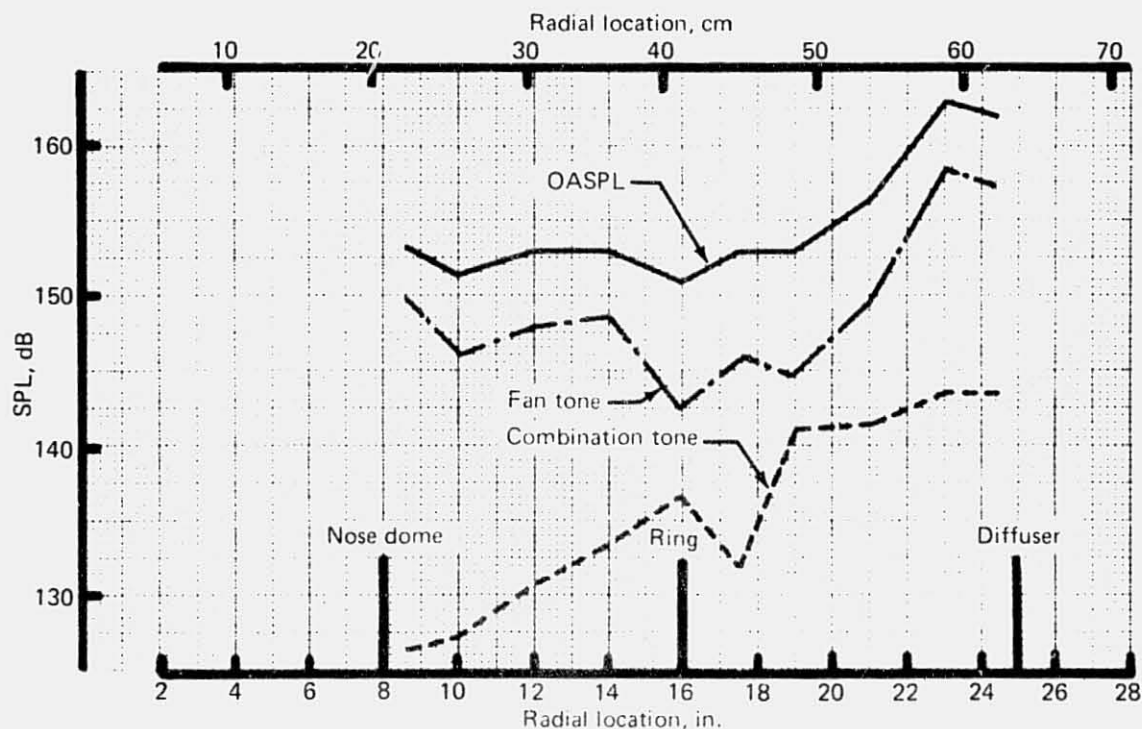


Figure 180.—JT8D-115 Ground Test—SPL Versus Radial Distance at Fan Face, Side-Engine Inlet With Ring, Cutback rpm

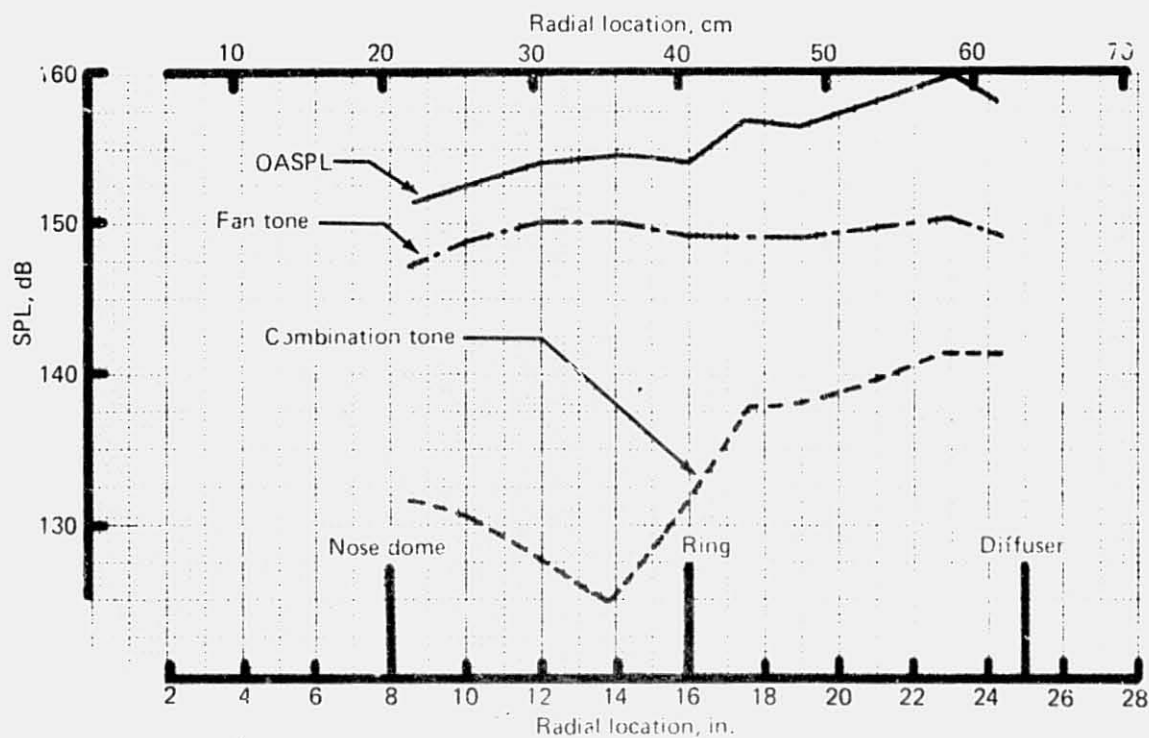


Figure 181.—JT8D-115 Ground Test—SPL Versus Radial Distance at Fan Face, Side-Engine Inlet With Ring, Takeoff rpm

**Table 24.—JT8D-115 Ground Test—SPL's at Various Surface Locations in the Exhaust System at Values of  $N_1$  Corresponding to the Approach Condition**

Microphone location	OASPL	Fantone SPL	Turbine tone SPL
Exhaust duct (wedge duct and nozzle)			
A	141.4	126.4	
B	142.4	129.1	
Splitter, fan flow side			
D	138.0	122.9	
Plug			
D	144.3		131.7

On the JT8D-15 test, the basic hardwall configuration without baffles was run a total of five times for this purpose. On the JT8D-115 test the repeatability configuration was an unbaffled engine with the treated side-engine inlet without ring and hybrid exhaust system. This configuration was run a total of nine times during the test. Both sets of repeatability data have been analyzed and show similar results, but only the JT8D-115 data are shown here because more repeat points are included. No statistical analysis of this data was conducted. The data are simply presented here to show the scatter among the repeat runs. This sets the perspective in which all ground test acoustic data must be viewed.

One-third OB spectra from selected microphones were compared for the nine repeat runs to give a band-by-band and angle-by-angle measure of the acoustic data scatter. Performance parameters for the two selected power settings are shown in table 25. Spectral plots of the repeatability data for 10 microphones and two power settings are shown in figures 182 and 183. Examining these figures, it can be seen that most of the data cluster in a scatter band of about  $\pm 1.5$  dB, with some notable exceptions. In particular, at the power settings and directivity angles where fan tones are predominant over broadband noise, the tone levels show a total scatter of up to 12 dB (figs 182c and d). It is reasonable to expect that some data scatter would occur simply because of run-to-run variations in atmospheric conditions and because of small differences in engine-operating conditions from run-to-run (variations in  $N_1$ , jet velocity, turbine exit temperature, etc.). Furthermore, the long chain of electronic equipment used to record and process the acoustic data would be expected to add some variability to the final data. A combination of these factors probably accounts for the typical scatter ( $\pm 1.5$  dB) seen in the broadband parts of figures 182 and 183. However, it is believed that the run-to-run variations in fan-tone level cannot be accounted for by these factors. Indeed, the minute-to-minute fluctuations in fan-tone level within a given run are found to be  $\pm 3$  dB or greater (fig. 184). Hence, the scatter in the fan-tone SPL is attributed primarily to fluctuations in the source itself, probably due to fluctuations in atmospheric turbulence ingested by the engine.



*Table 24.—JT8D-115 Ground Test—SPL's at Various Surface Locations in the Exhaust System at Values of  $N_1$  Corresponding to the Approach Condition*

Microphone location	OASPL	Fantone SPL	Turbine tone SPL
Exhaust duct (wedge duct and nozzle)			
A	141.4	126.4	
B	142.4	129.1	
Splitter, fan flow side			
D	136.0	122.9	
Plug			
D	144.3		131.7

On the JT8D-15 test, the basic hardwall configuration without baffles was run a total of five times for this purpose. On the JT8D-115 test the repeatability configuration was an unbaffled engine with the treated side-engine inlet without ring and hybrid exhaust system. This configuration was run a total of nine times during the test. Both sets of repeatability data have been analyzed and show similar results, but only the JT8D-115 data are shown here because more repeat points are included. No statistical analysis of this data was conducted. The data are simply presented here to show the scatter among the repeat runs. This sets the perspective in which all ground test acoustic data must be viewed.

One-third OB spectra from selected microphones were compared for the nine repeat runs to give a band-by-band and angle-by-angle measure of the acoustic data scatter. Performance parameters for the two selected power settings are shown in table 25. Spectral plots of the repeatability data for 10 microphones and two power settings are shown in figures 182 and 183. Examining these figures, it can be seen that most of the data cluster in a scatter band of about  $\pm 1.5$  dB, with some notable exceptions. In particular, at the power settings and directivity angles where fan tones are predominant over broadband noise, the tone levels show a total scatter of up to 12 dB (figs 182c and d). It is reasonable to expect that some data scatter would occur simply because of run-to-run variations in atmospheric conditions and because of small differences in engine-operating conditions from run-to-run (variations in  $N_1$ , jet velocity, turbine exit temperature, etc.). Furthermore, the long chain of electronic equipment used to record and process the acoustic data would be expected to add some variability to the final data. A combination of these factors probably accounts for the typical scatter ( $\pm 1.5$  dB) seen in the broadband parts of figures 182 and 183. However, it is believed that the run-to-run variations in fan-tone level cannot be accounted for by these factors. Indeed, the minute-to-minute fluctuations in fan-tone level within a given run are found to be  $\pm 3$  dB or greater (fig. 184). Hence, the scatter in the fan-tone SPL is attributed primarily to fluctuations in the source itself, probably due to fluctuations in atmospheric turbulence ingested by the engine.

Table 25.—JT8D-115 Ground Test—Performance Data for Selected Conditions  
from Acoustic Repeatability Runs Plotted in Figures 182 Through 184

	Run no. — Plot Symbol								
	15 +	16 X	31 Y	32 X	43 Δ	44 ⬆	93 Σ	94 ✱	113 Z
Cond 7, nominal approach rpm									
$N_1/\sqrt{\theta_{t2}}$ , RPM	5 795	5 827	5 778	5 790	5 800	5 766	5 792	5 785	5 798
$V_{pri}$ , ft/s	1 189	1 200	1 168	1 177	1 163	1 151	1 154	1 157	1 171
( $V_{pri}$ , m/s)	(362)	(366)	(356)	(359)	(354)	(351)	(352)	(353)	(360)
Thrust, lb	9 206	9 318	9 130	9 182	9 237	9 096	9 118	9 100	9 274
(Thrust, N)	(40 948)	(41 446)	(40 610)	(40 841)	(41 086)	(40 459)	(40 557)	(40 477)	(41 251)
$V_w$ , mph	4.3	4.2	5.2	7.1	3.4	5.0	2.5	2.4	14.6
( $V_w$ , m/s)	(1.9)	(1.9)	(2.3)	(3.2)	(1.5)	(2.2)	(1.1)	(1.1)	(6.5)
$N_1$ rpm	5 798	5 817	5 687	5 714	5 666	5 636	5 647	5 652	5 691
$T_{amb}$ , °F	59.7	57.1	42.8	45.6	35.3	35.9	33.4	35.4	40.0
( $T_{amb}$ , K)	(288.4)	(286.9)	(279.0)	(280.6)	(274.8)	(275.2)	(273.8)	(274.9)	(277.4)
$T_{t7}$ , °R	1 287	1 290	1 286	1 290	1 287	1 282	1 276	1 289	1 292
( $T_{t7}$ , K)	(715)	(717)	(714)	(717)	(715)	(712)	(714)	(716)	(718)
Cond 12, nominal takeoff rpm									
$N_1/\sqrt{\theta_{t2}}$ , rpm	7 520	7 569	7 623	7 615	7 617	7 613	7 592	7 604	
$V_{pri}$ , ft/s	1 759	1 760	1 752	1 752	1 737	1 736	1 727	1 737	
( $V_{pri}$ , m/s)	(536)	(536)	(534)	(534)	(529)	(529)	(526)	(529)	
Thrust, lb	17 776	17 820	17 935	17 950	18 046	18 050	17 878	18 015	
(Thrust, N)	(79 068)	(79 263)	(79 775)	(79 842)	(80 269)	(80 286)	(79 521)	(80 131)	
$V_w$ , mph	3.0	5.7	5.1	6.9	5.4	3.2	0.7	4.1	
( $V_w$ , m/s)	(1.3)	(2.5)	(2.3)	(3.1)	(2.4)	(1.4)	(0.3)	(1.8)	
$N_1$ rpm	7 524	7 536	7 514	7 516	7 449	7 445	7 409	7 438	
$T_{amb}$ , °F	59.6	54.4	44.2	45.5	36.4	36.2	34.3	36.6	
( $T_{amb}$ , K)	(288.3)	(285.4)	(279.8)	(280.5)	(275.4)	(275.3)	(274.3)	(275.6)	
$T_{t7}$ , °R	1 489	1 495	1 450	1 498	1 501	1 500	1 499	1 504	
( $T_{t7}$ , K)	(827)	(831)	(806)	(832)	(834)	(833)	(833)	(836)	

Table 25.—JT8D-115 Ground Test—Performance Data for Selected Conditions  
from Acoustic Repeatability Runs Plotted in Figures 182 Through 184

	Run no. — Plot Symbol								
	15 +	16 X	31 Y	32 X	43 Δ	44 ⬢	93 Σ	94 ✱	113 Z
Cond 7, nominal approach rpm									
$N_1/\sqrt{\theta_{t2}}$ , RPM	5 795	5 827	5 778	5 790	5 800	5 766	5 792	5 785	5 798
$V_{pri}$ , ft/s	1 189	1 200	1 168	1 177	1 163	1 151	1 154	1 157	1 171
( $V_{pri}$ , m/s)	(362)	(366)	(356)	(359)	(354)	(351)	(352)	(353)	(360)
Thrust, lb	9 206	9 318	9 130	9 182	9 237	9 096	9 118	9 100	9 274
(Thrust, N)	(40 948)	(41 446)	(40 610)	(40 841)	(41 086)	(40 459)	(40 557)	(40 477)	(41 251)
$V_w$ , mph	4.3	4.2	5.2	7.1	3.4	5.0	2.5	2.4	14.6
( $V_w$ , m/s)	(1.9)	(1.9)	(2.3)	(3.2)	(1.5)	(2.2)	(1.1)	(1.1)	(6.5)
$N_1$ rpm	5 798	5 817	5 687	5 714	5 666	5 636	5 647	5 652	5 691
$T_{amb}$ , °F	59.7	57.1	42.8	45.6	35.3	35.9	33.4	35.4	40.0
( $T_{amb}$ , K)	(288.4)	(286.9)	(279.0)	(280.6)	(274.8)	(275.2)	(273.8)	(274.9)	(277.4)
$T_{t7}$ , °R	1 287	1 290	1 286	1 290	1 287	1 282	1 276	1 289	1 292
( $T_{t7}$ , K)	(715)	(717)	(714)	(717)	(715)	(712)	(714)	(716)	(718)
Cond 12, nominal takeoff rpm									
$N_1/\sqrt{\theta_{t2}}$ , rpm	7 520	7 569	7 623	7 615	7 617	7 613	7 592	7 604	
$V_{pri}$ , ft/s	1 759	1 760	1 752	1 752	1 737	1 736	1 727	1 737	
( $V_{pri}$ , m/s)	(536)	(536)	(534)	(534)	(529)	(529)	(526)	(529)	
Thrust, lb	17 776	17 820	17 935	17 950	18 046	18 050	17 878	18 015	
(Thrust, N)	(79 068)	(79 263)	(79 775)	(79 842)	(80 269)	(80 286)	(79 521)	(80 131)	
$V_w$ , mph	3.0	5.7	5.1	6.9	5.4	3.2	0.7	4.1	
( $V_w$ , m/s)	(1.3)	(2.5)	(2.3)	(3.1)	(2.4)	(1.4)	(0.3)	(1.8)	
$N_1$ rpm	7 524	7 536	7 514	7 516	7 449	7 445	7 409	7 438	
$T_{amb}$ , °F	59.6	54.4	44.2	45.5	36.4	36.2	34.3	36.6	
( $T_{amb}$ , K)	(288.3)	(285.4)	(279.8)	(280.5)	(275.4)	(275.3)	(274.3)	(275.6)	
$T_{t7}$ , °R	1 489	1 495	1 450	1 498	1 501	1 500	1 499	1 504	
( $T_{t7}$ , K)	(827)	(831)	(806)	(832)	(834)	(833)	(833)	(836)	

REPRODUCIBILITY OF THE  
ORIGINAL PAGE IS POOR

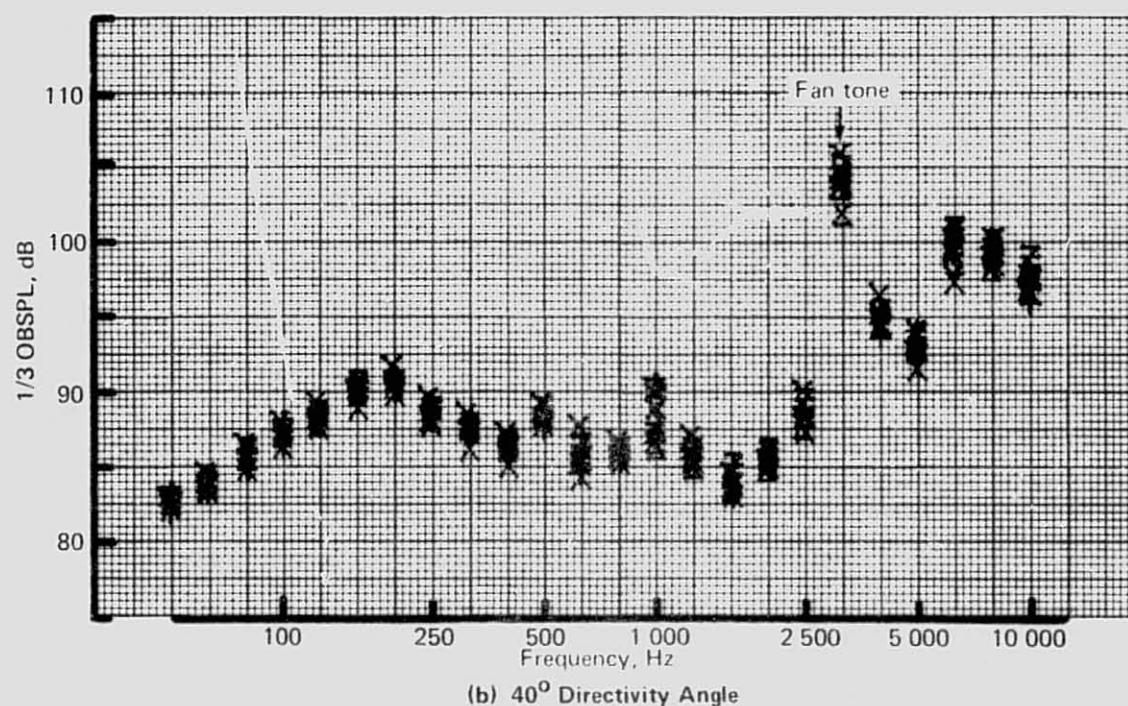
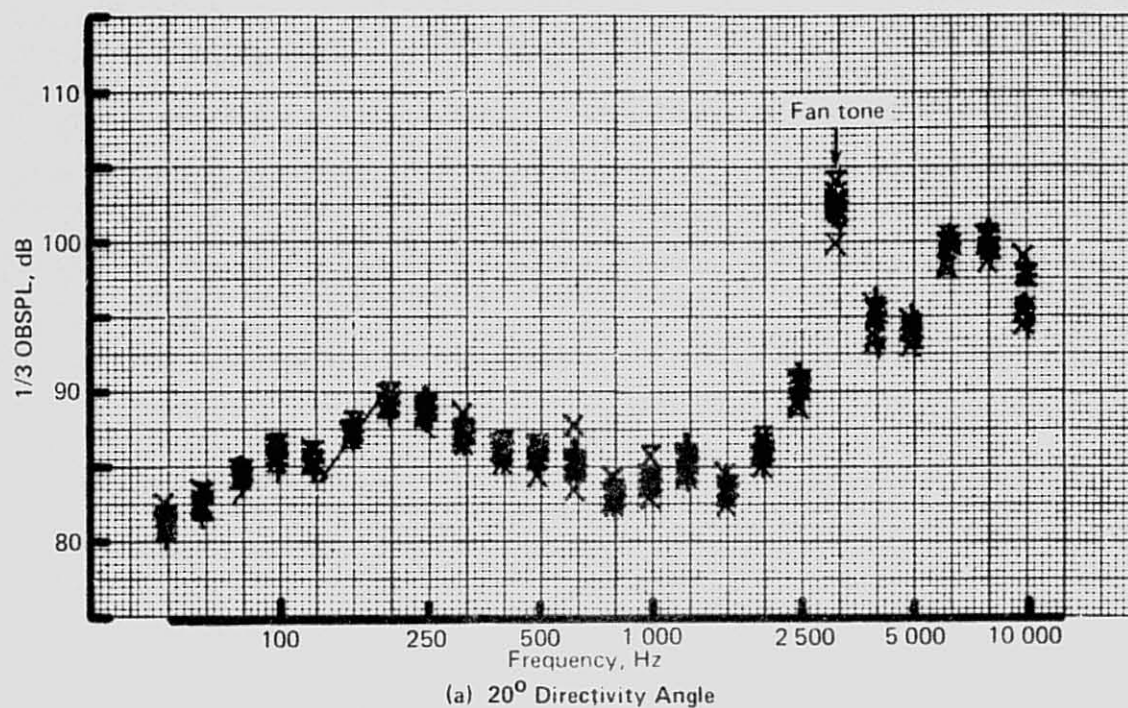


Figure 182.—JT8D-115 Ground Test—Acoustic Repeatability, Side-Engine Inlet (Without Ring) and Hybrid Exhaust System: 100 ft (30.48 m) Polar, Ground Microphones, Approach rpm



REPRODUCIBILITY OF THE  
ORIGINAL PAGE IS POOR

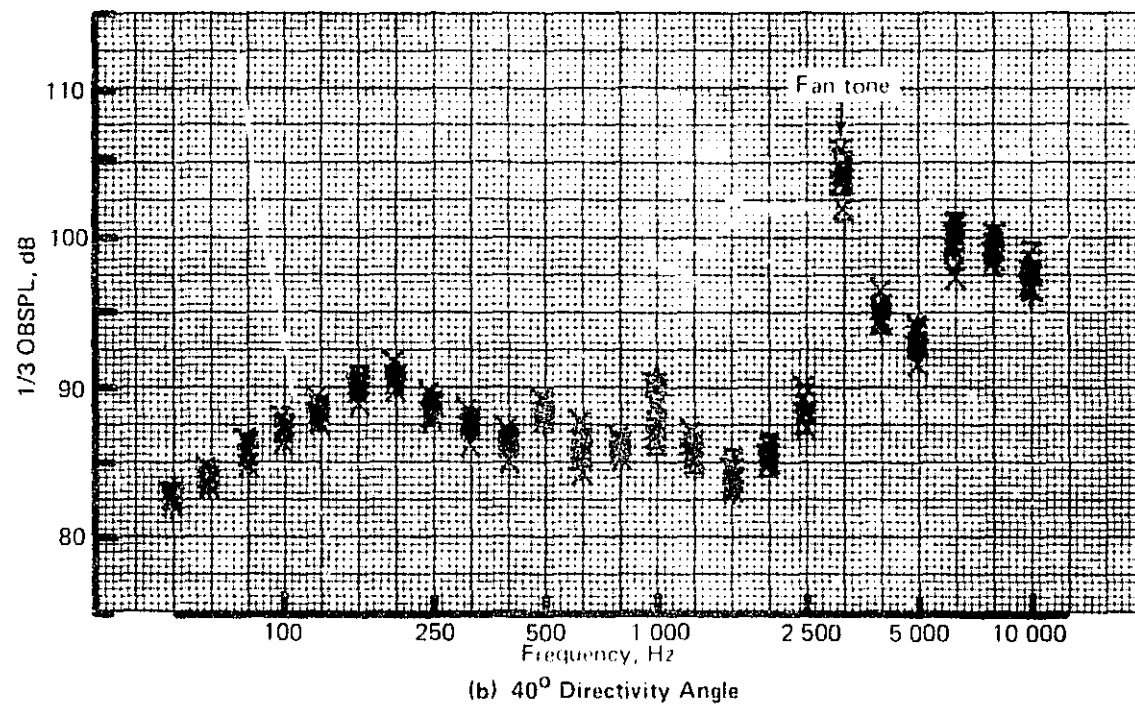
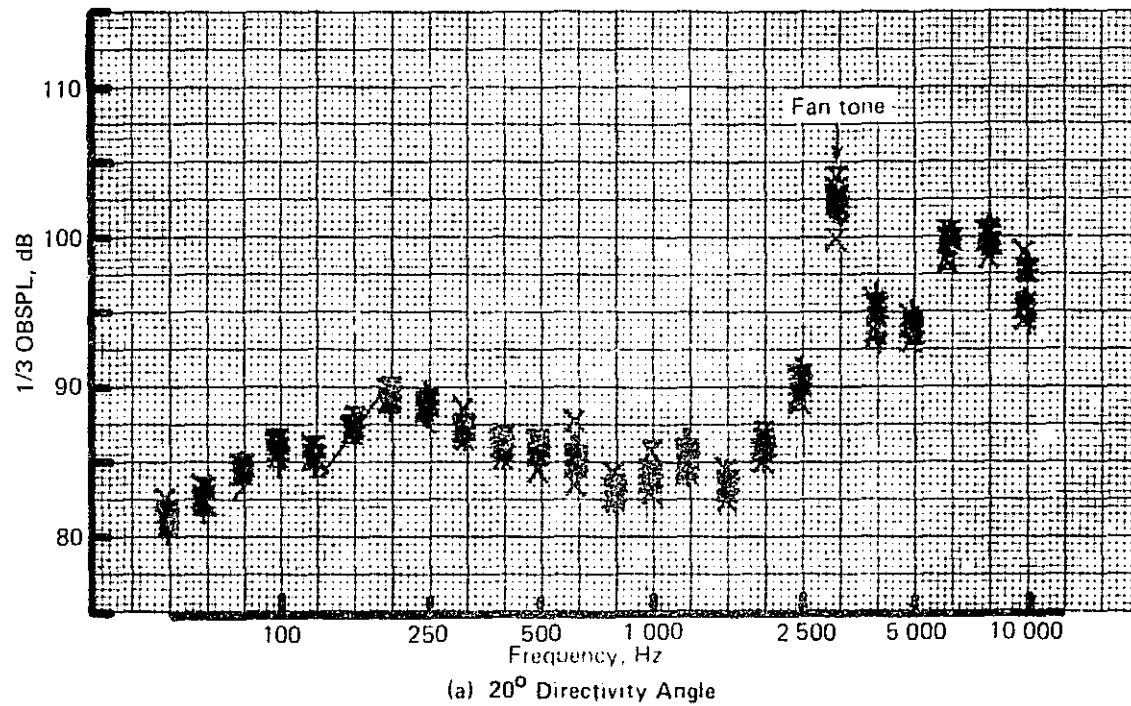


Figure 182.—JT8D-115 Ground Test—Acoustic Repeatability, Side-Engine Inlet (Without Ring) and Hybrid Exhaust System: 100 ft (30.48 m) Polar, Ground Microphones, Approach rpm

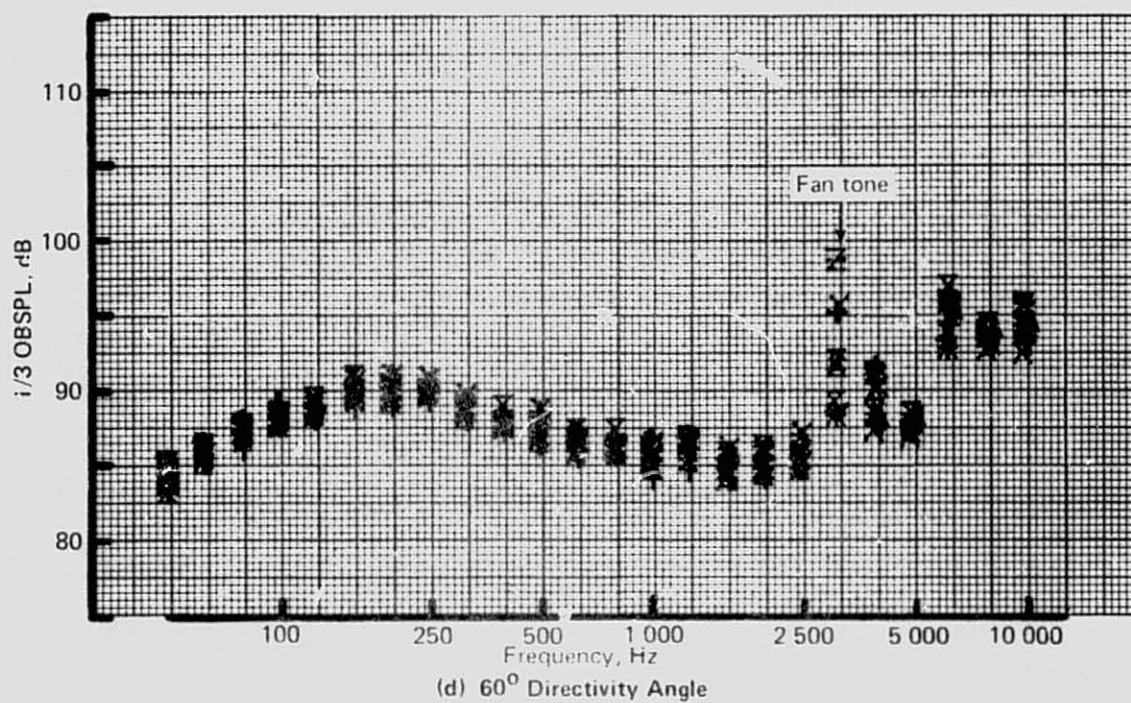
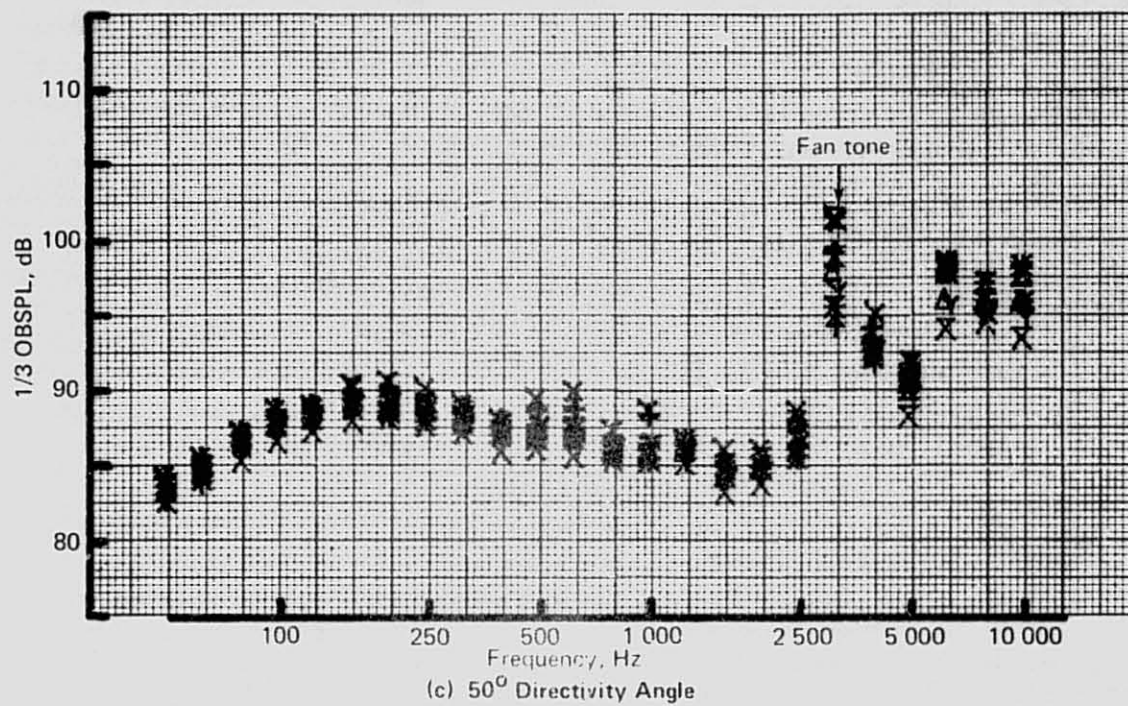


Figure 182. — (Continued)

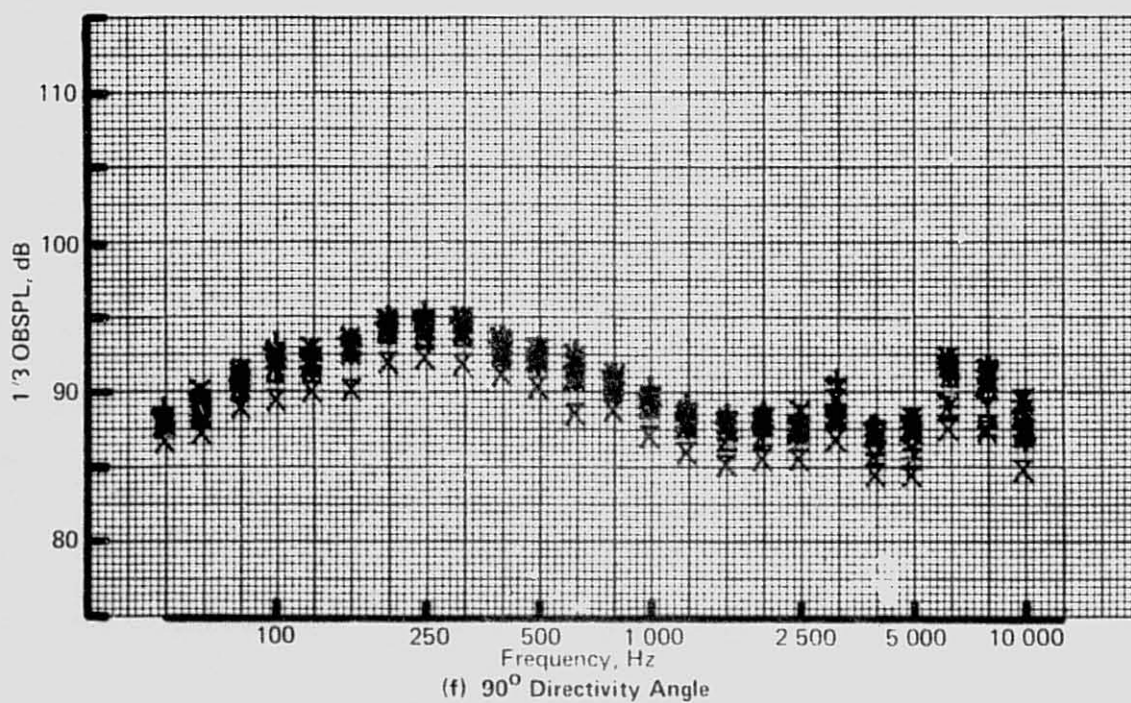
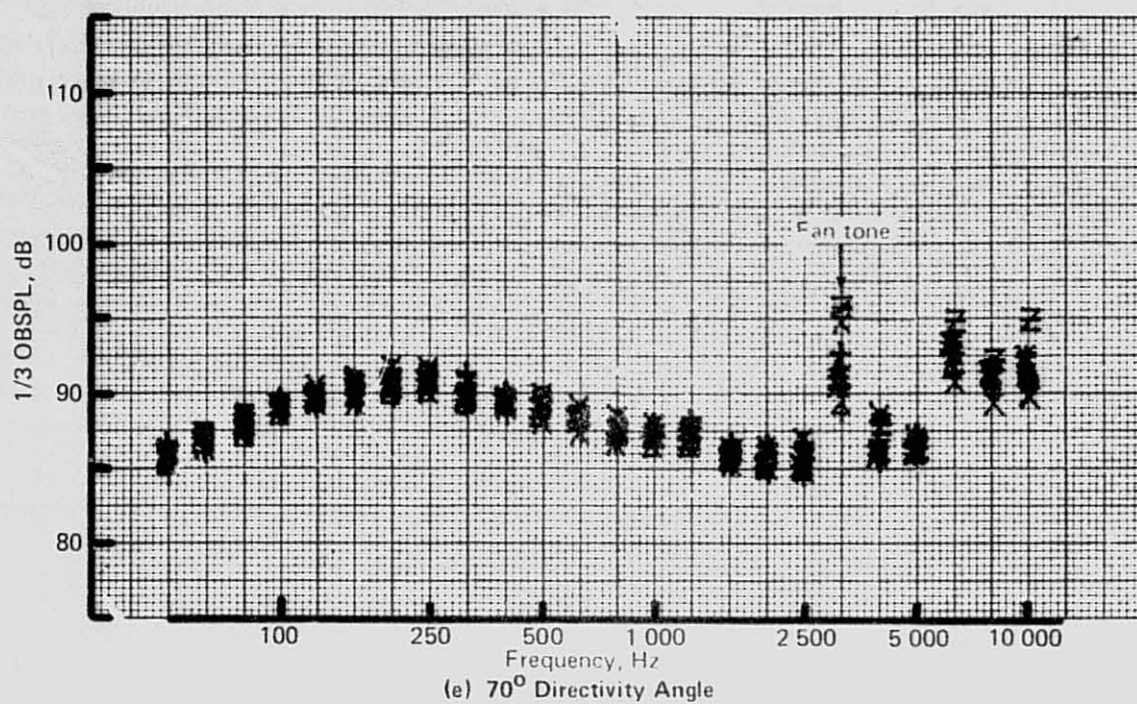


Figure 182. - (Continued)



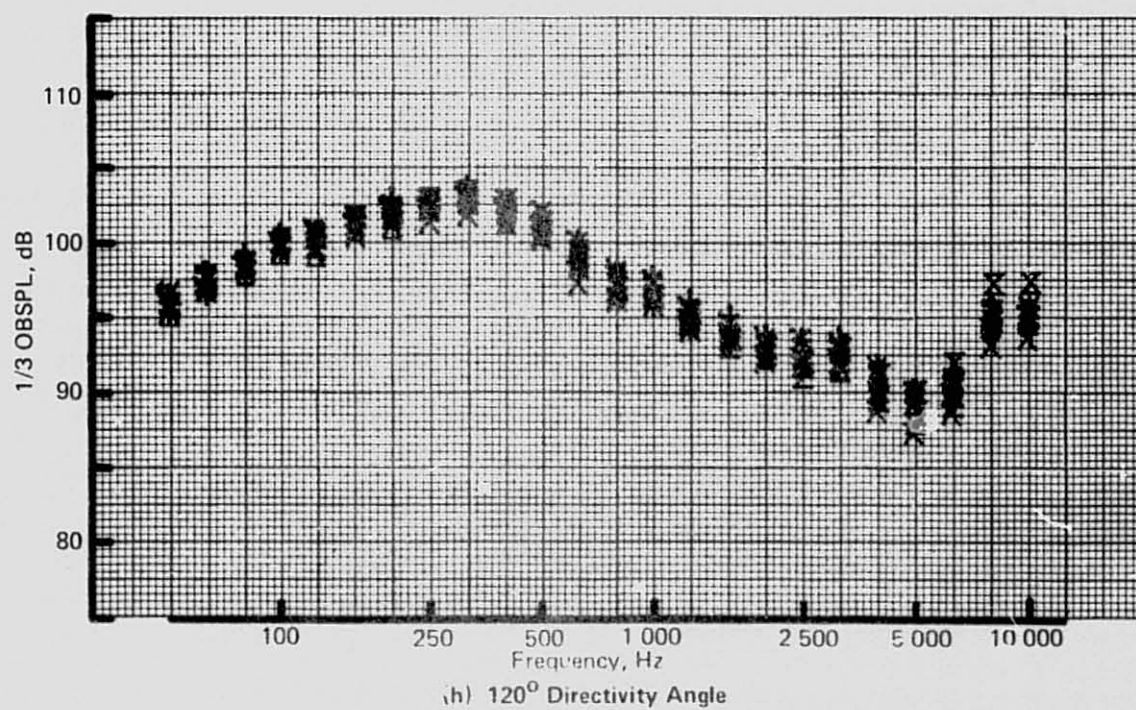
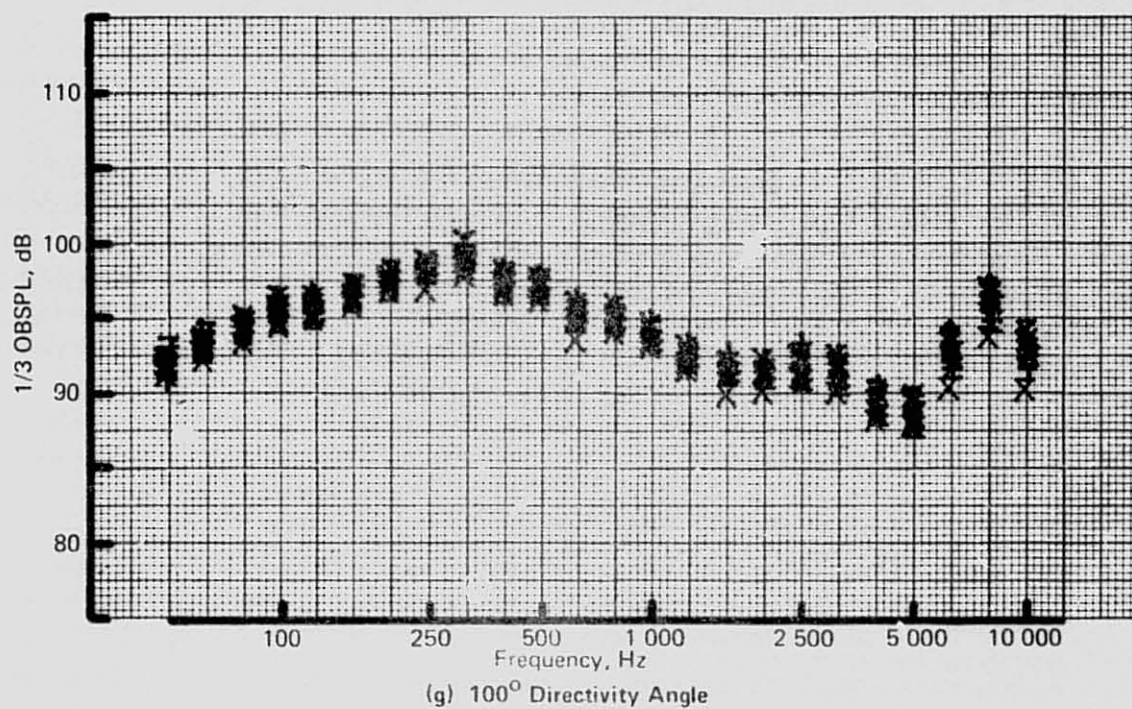


Figure 182.—(Continued)



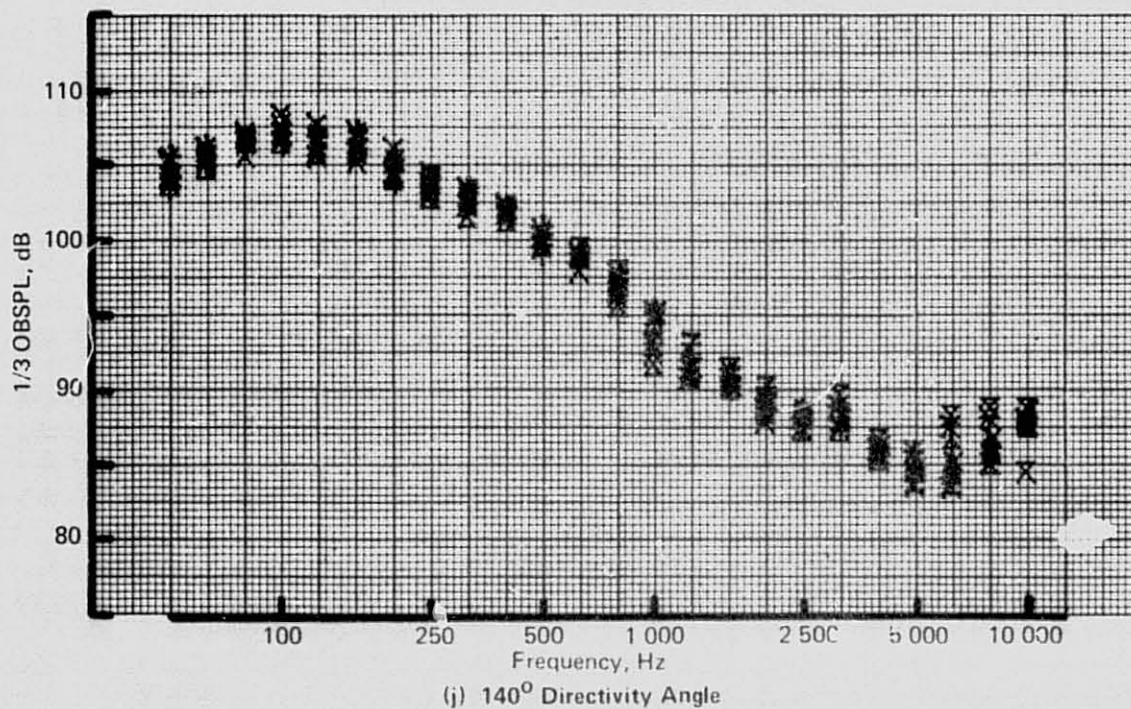
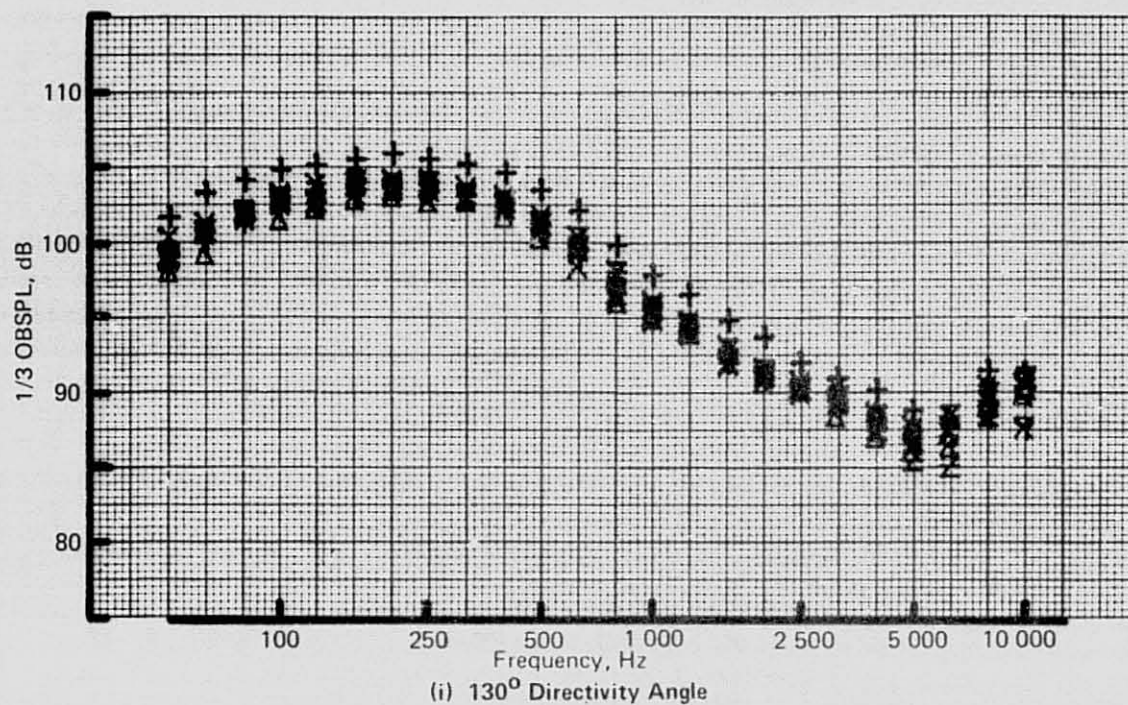
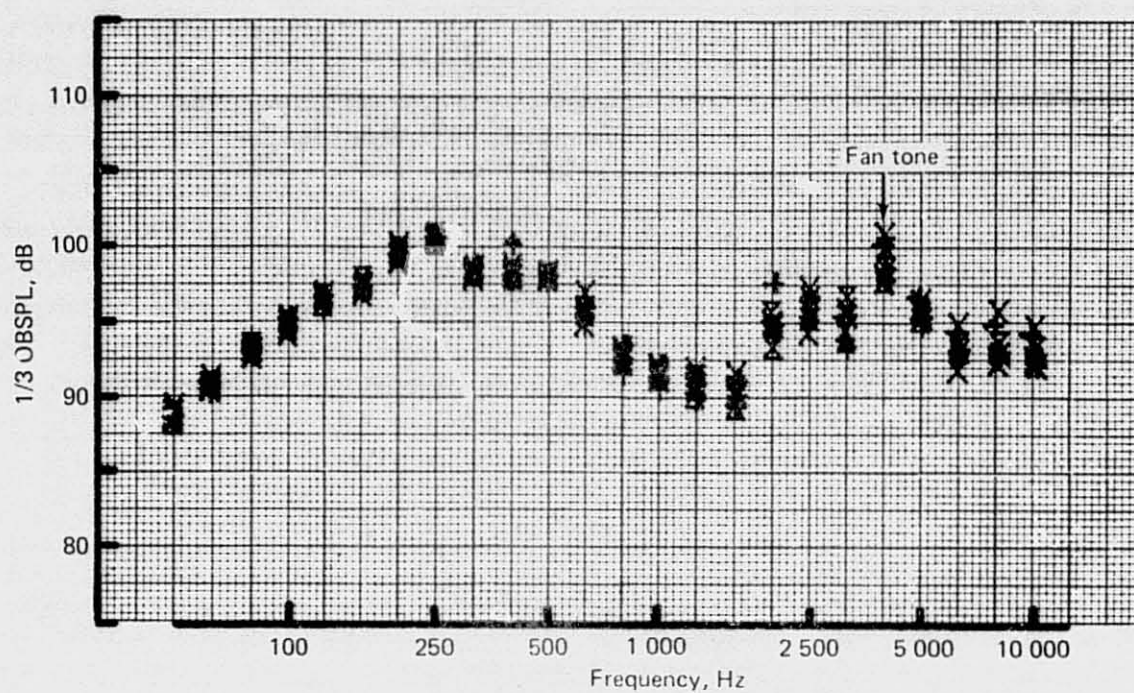
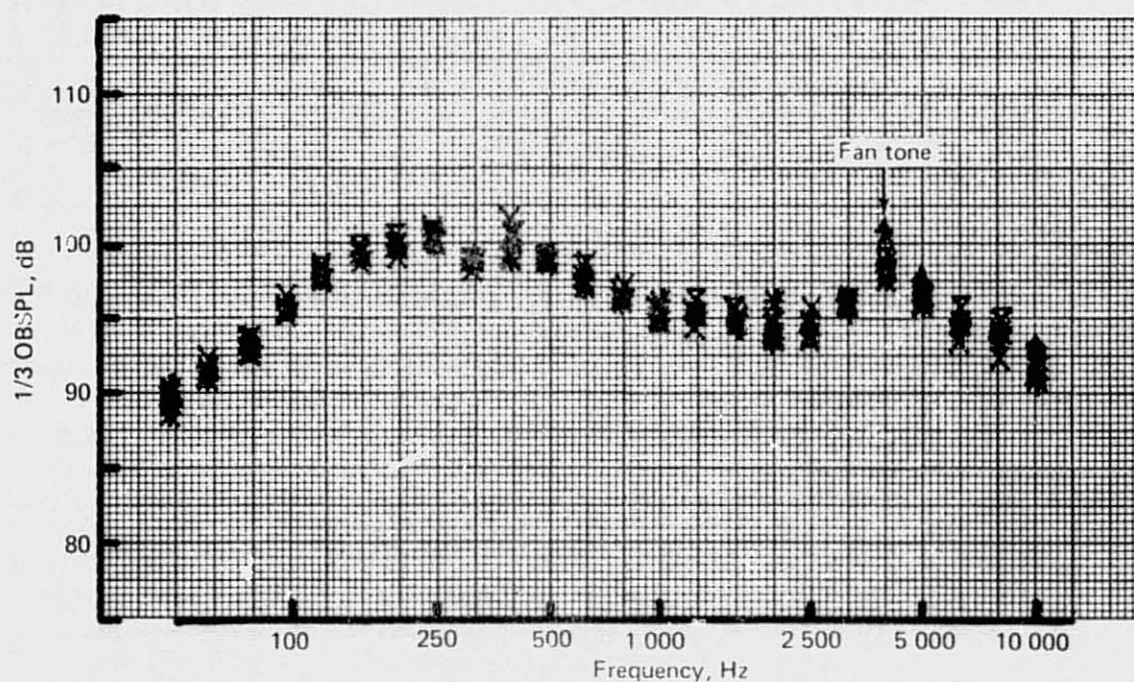


Figure 182. — (Concluded)



(a) 20° Directivity Angle

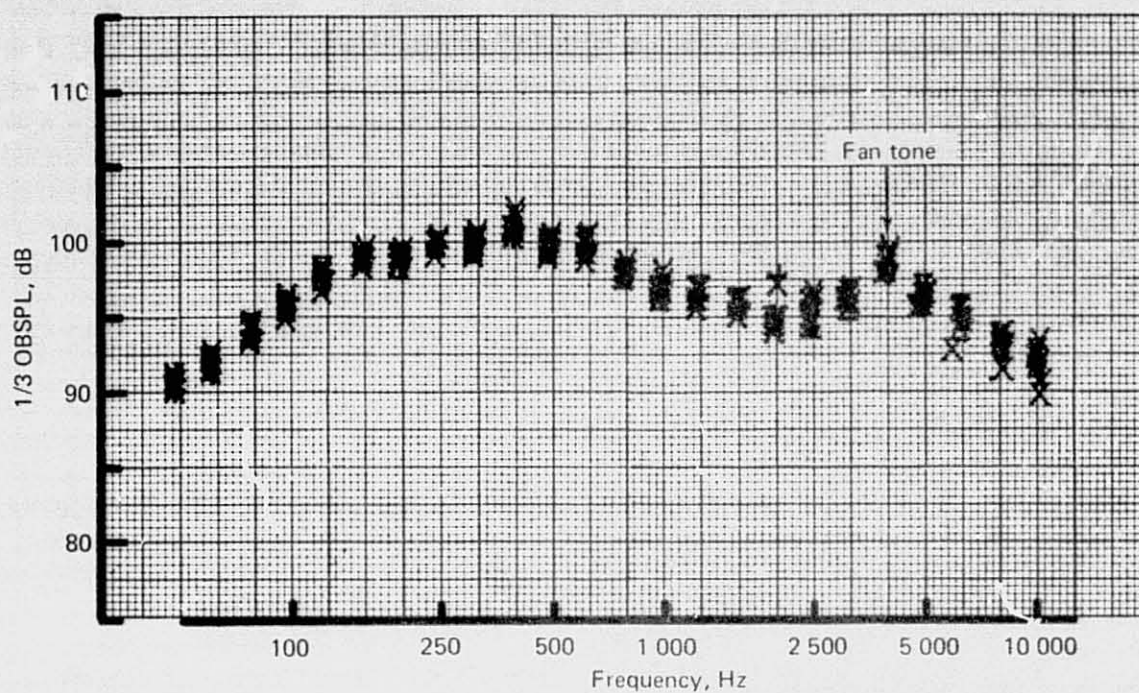


(b) 40° Directivity Angle

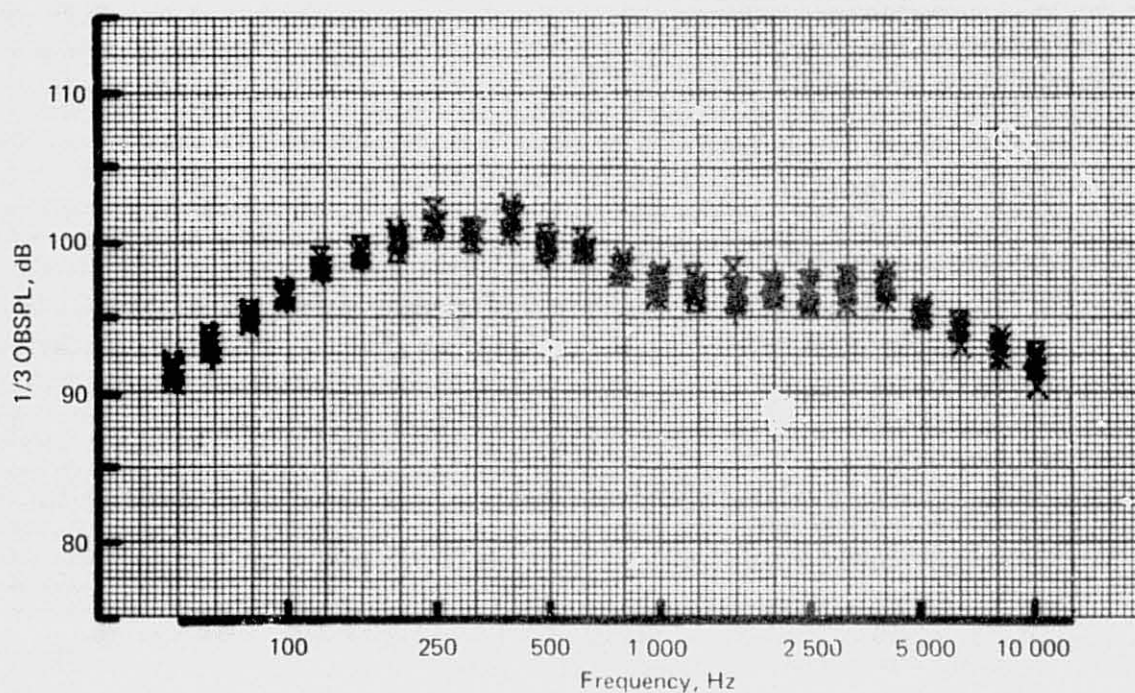
Figure 183.—JT8D-115 Ground Test—Acoustic Repeatability, Side-Engine Inlet (Without Ring) and Hybrid Exhaust System: 100 ft (30.48 m) Polar, Ground Microphones, Takeoff rpm



REPRODUCIBILITY OF THE  
ORIGINAL PAGE IS POOR

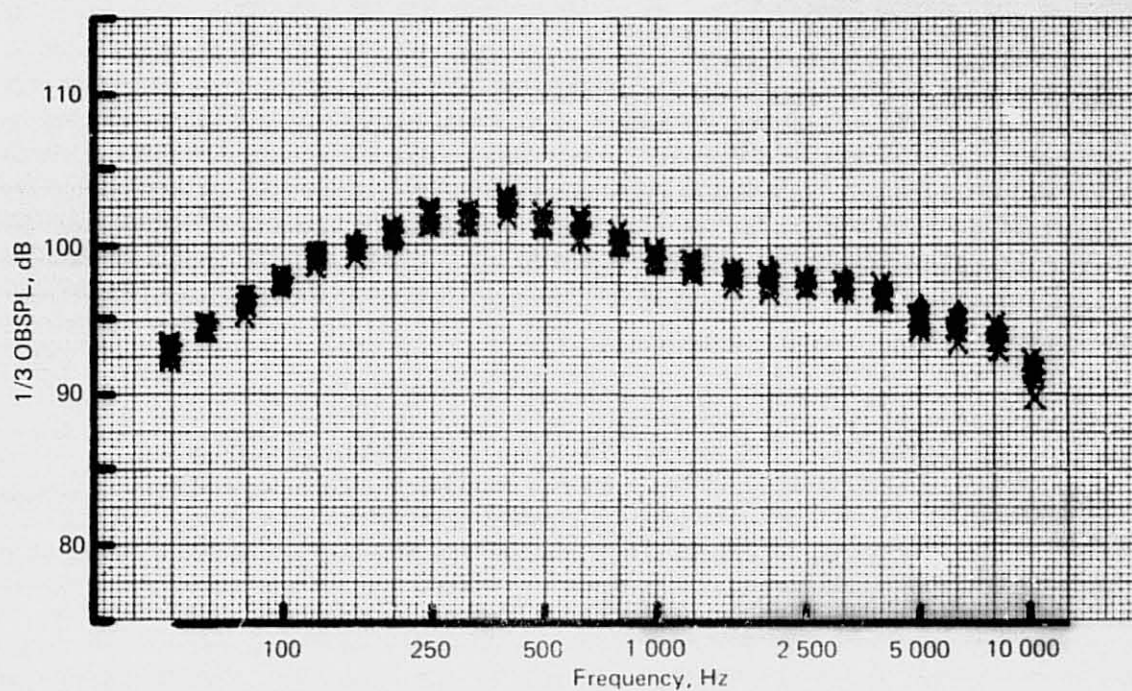


(c) 50° Directivity Angle

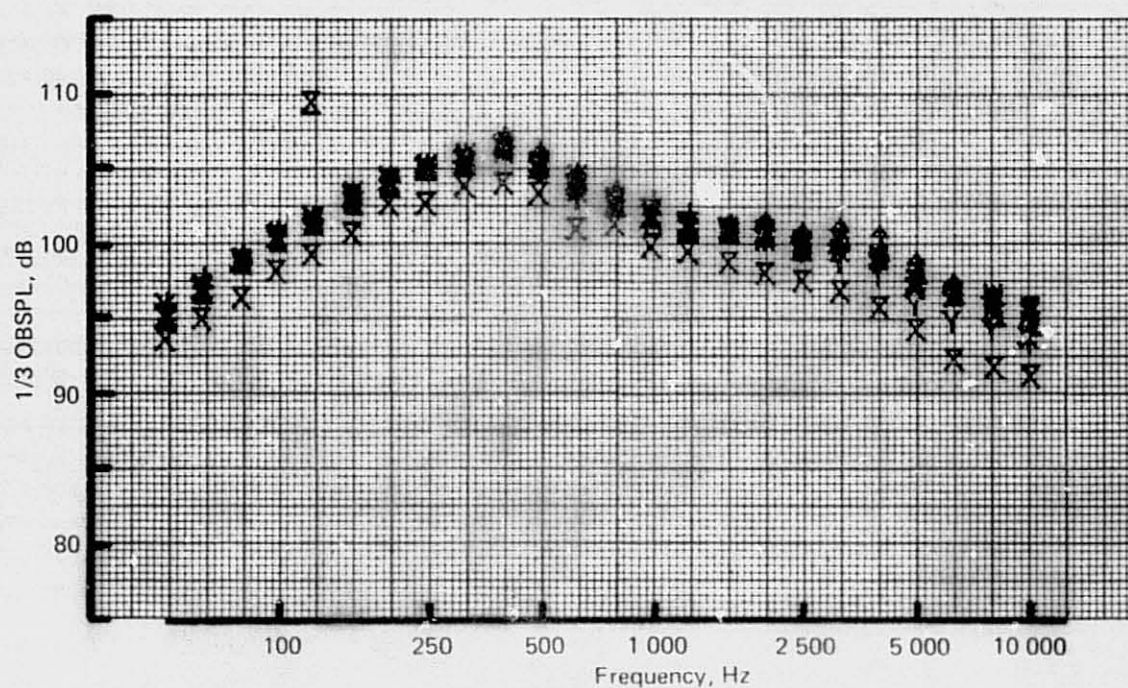


(d) 60° Directivity Angle

Figure 183.—(Continued)



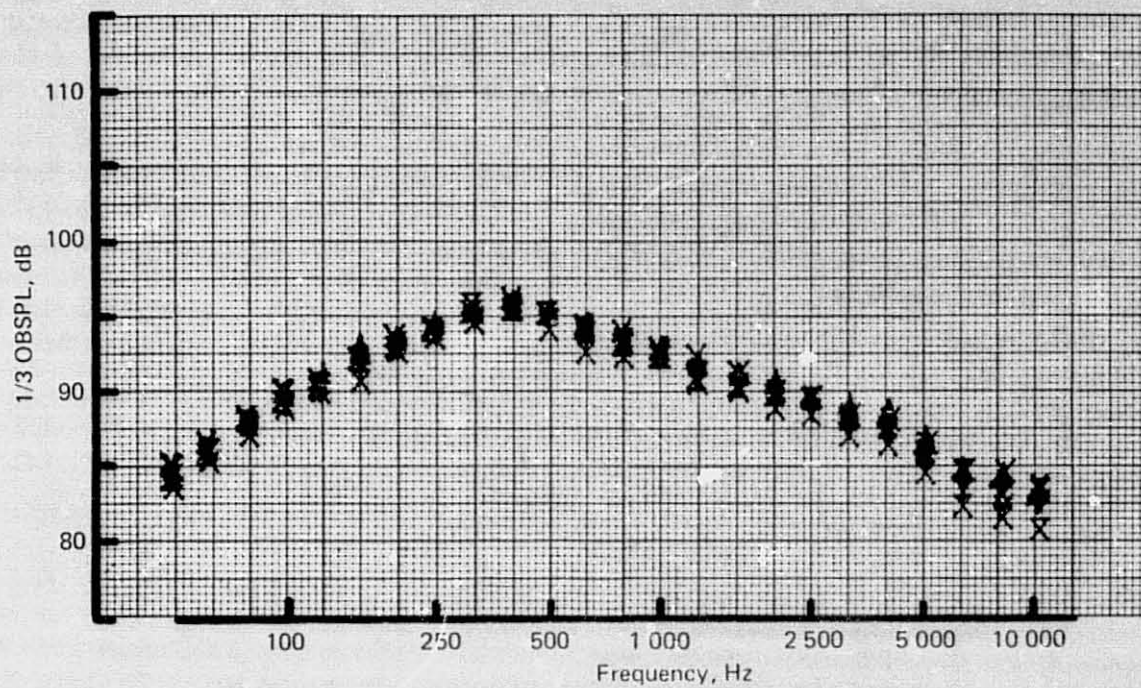
(e) 70° Directivity Angle



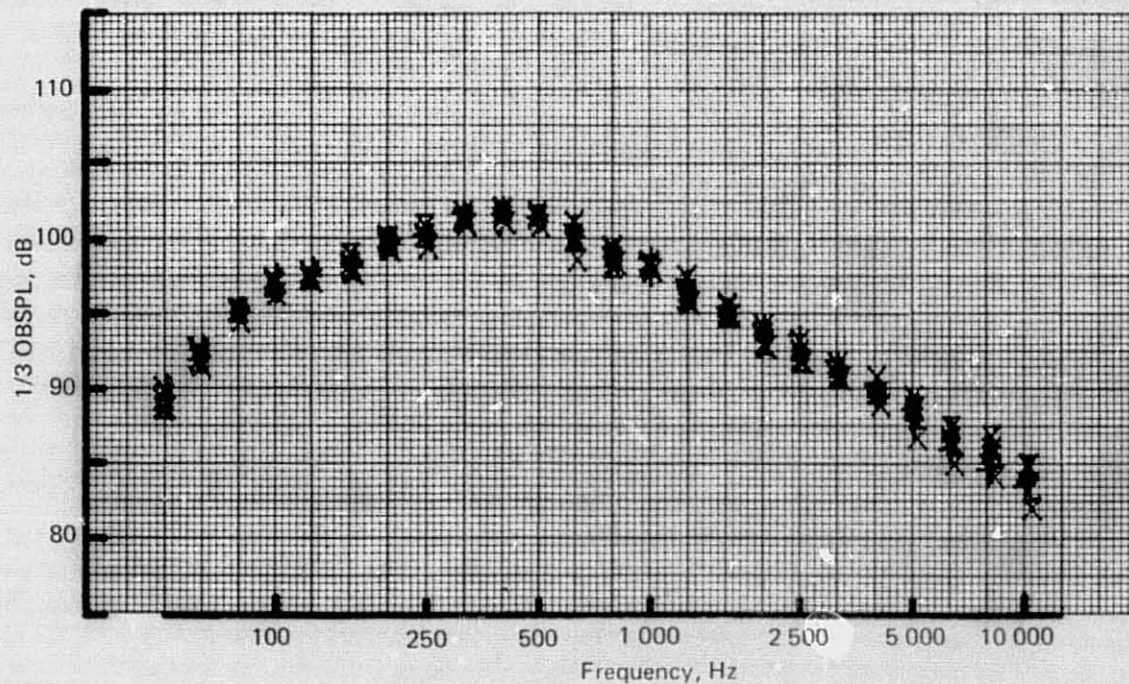
(f) 90° Directivity Angle

Figure 183.—(Continued)





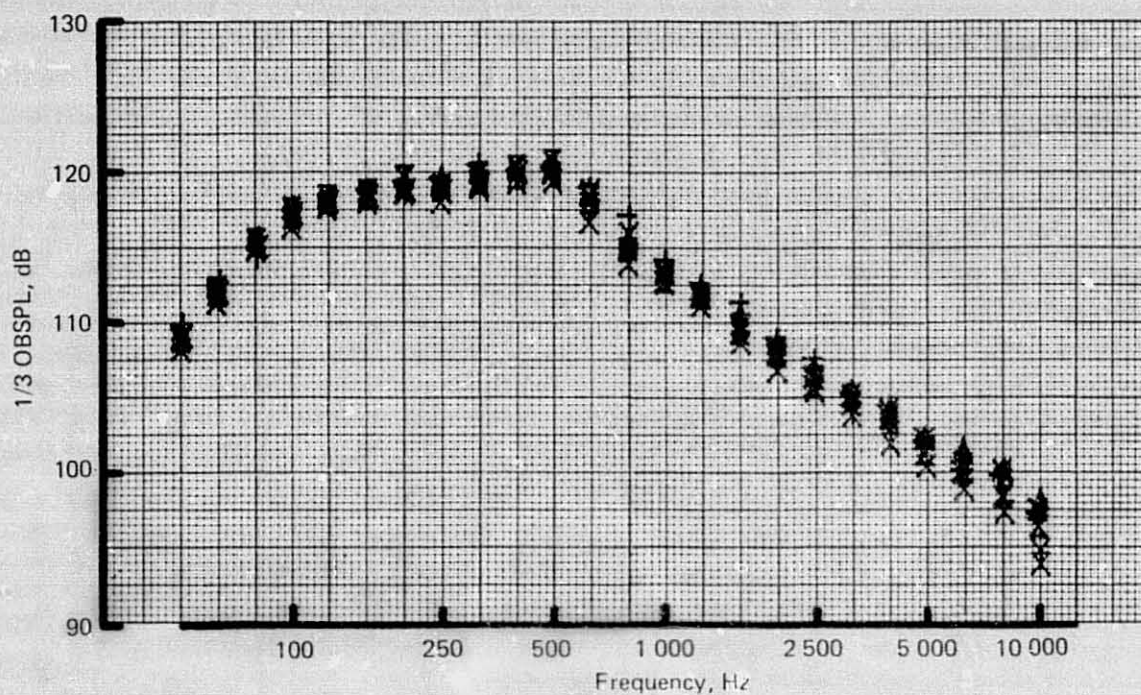
(g) 100° Directivity Angle



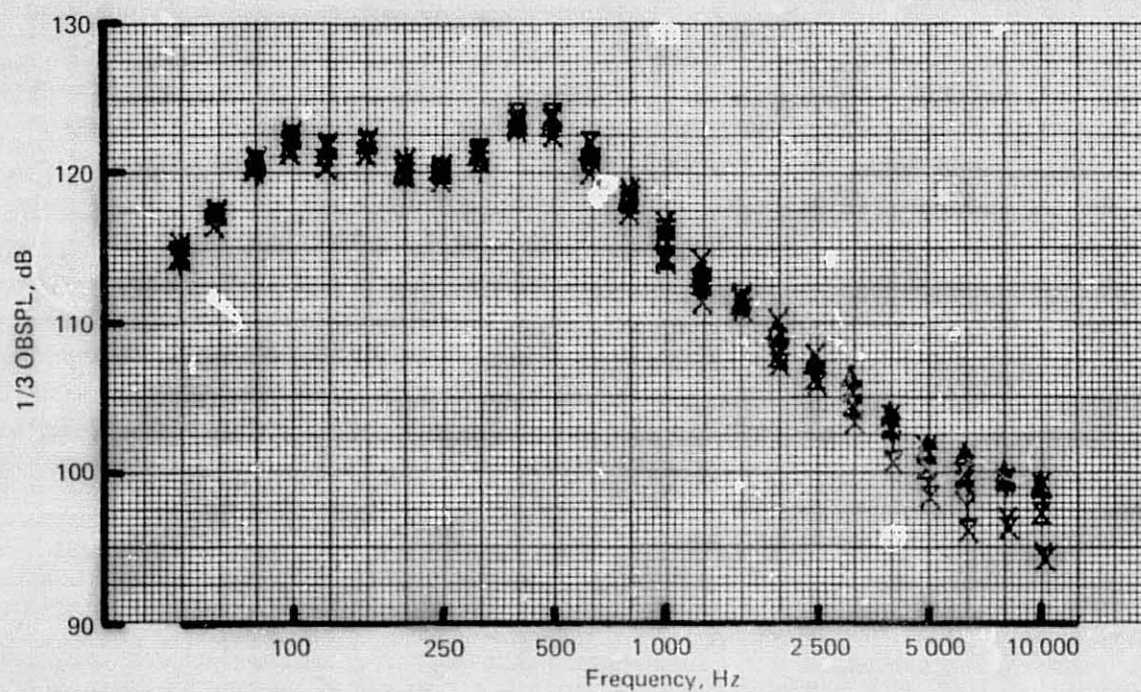
(h) 120° Directivity Angle

Figure 183.—(Continued)





(i) 130° Directivity Angle



(j) 140° Directivity Angle

Figure 183.—(Concluded)

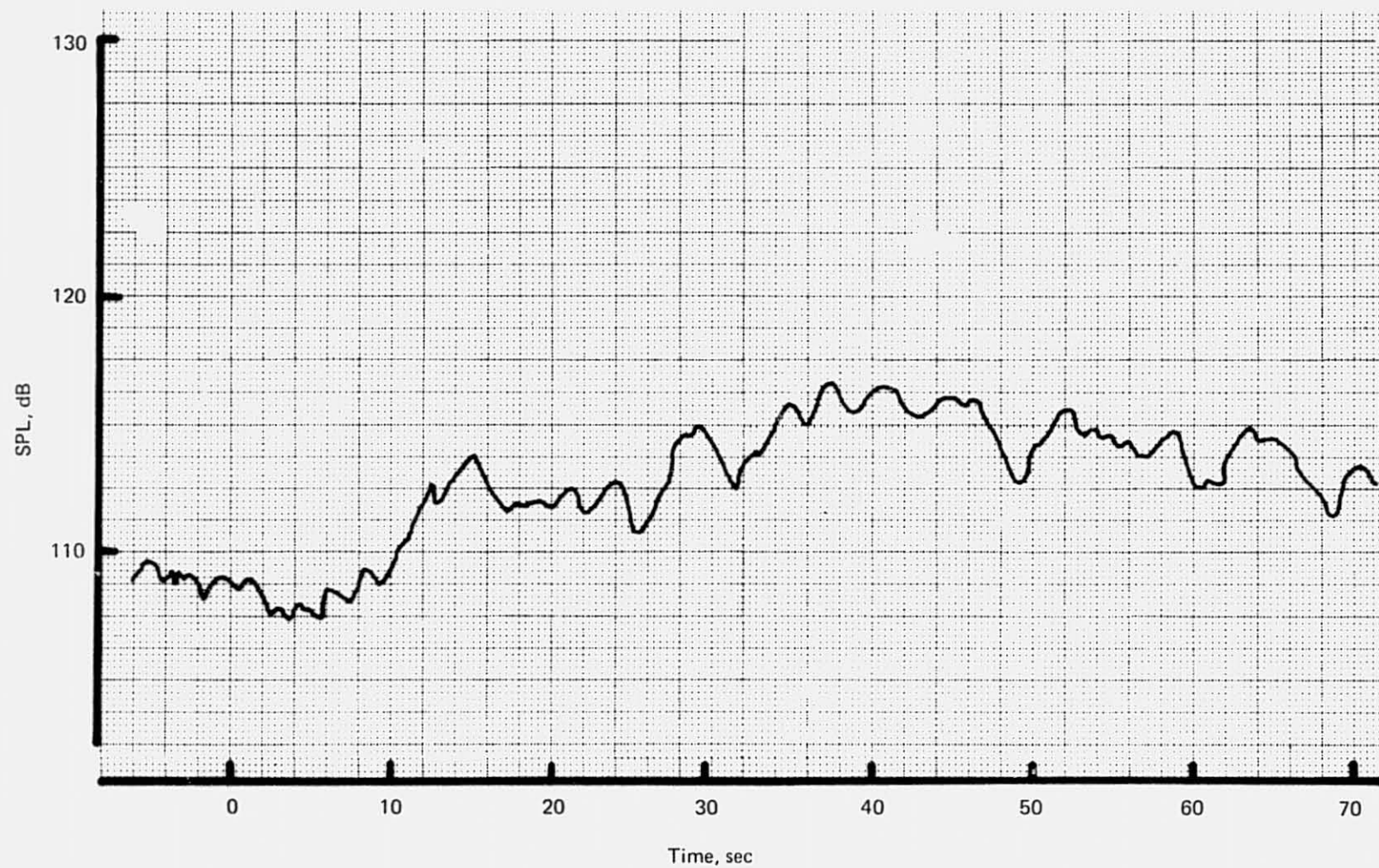


Figure 184.—JT8D-115 Ground Test—Time History of Inlet-Radiated Fan Tone Sound Pressure Level for Hardwall Side-Engine Inlet (Without Ring): 30° Directivity Angle, 100 ft (30.48 m) Polar, Ground Microphone, Approach rpm



These results have serious implications with regard to analysis of fan noise data, because an uncertainty of  $\pm 6$  dB is certainly intolerable for purposes of predicting airplane flyover noise. However, a more detailed analysis of the data shows that the fluctuations in fan-tone level at a given microphone are due more to fluctuations in the directivity pattern than to fluctuations in the source total power level. That is, the distribution of fan-tone energy among the various measurement angles is highly variable, but the total energy is much less variable, as is shown by the plot of space-averaged fan-tone SPL versus  $N_1$  for the nine repeatability runs (fig. 185). On this basis, a much higher degree of confidence may be associated with flyover noise predictions than would be implied by the fan-tone data scatter shown in figure 182c and d.

#### 4.2.5.2 Comparison of Ground-Level and Elevated Microphones

The use of surface-level microphones for acquisition of far-field acoustic data has a decided advantage over engine centerline height microphones in that the ground-level microphones eliminate the need for an interference pattern spectrum correction in the low frequency region. For this reason, ground-level microphones have been used for some time at Boardman in the aft quadrant for acquisition of jet noise data, but only elevated microphones were used in the forward quadrant. The present test used ground microphones as the primary acoustic data system in both the forward and aft quadrants, but for comparison purposes, acoustic data were also taken on three elevated microphones in each quadrant, with each elevated microphone mounted directly above a corresponding ground microphone. Comparisons of some corresponding ground and elevated microphone data taken on the JT8D-15 test are shown in figure 186.

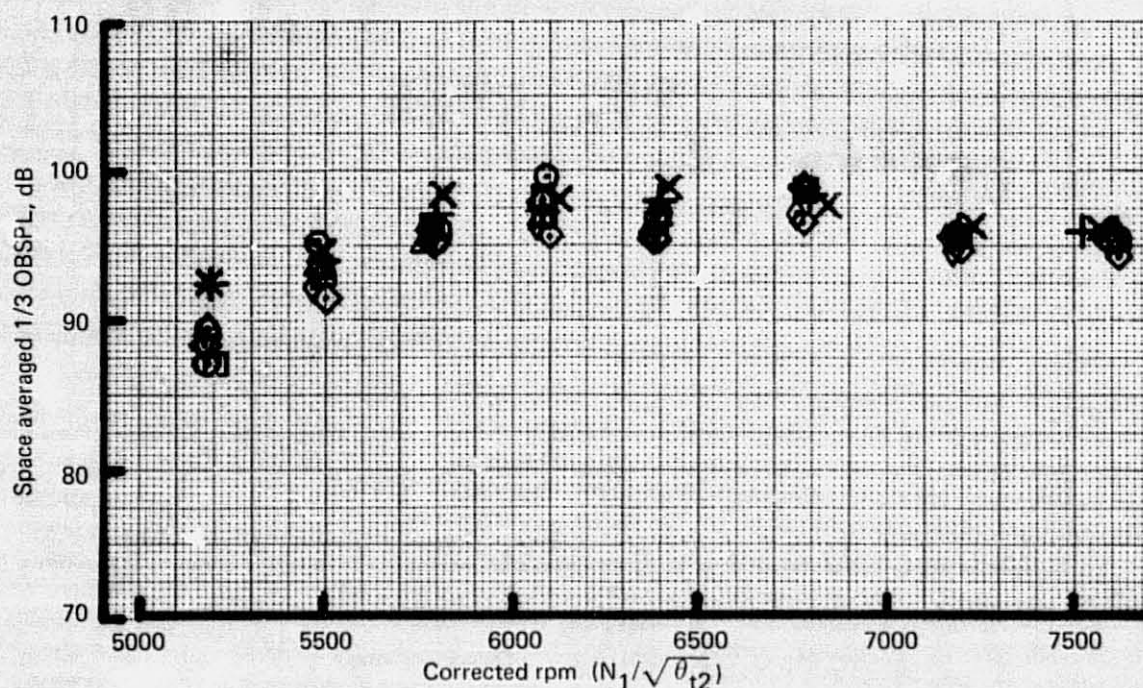


Figure 185.—JT8D-115 Ground Test—Space-Averaged Fan Tone SPL Versus  $N_1/\sqrt{\theta_{t2}}$  for Nine Repeatability Runs, Side-Engine Inlet (Without Ring), and Hybrid Exhaust System: 100 ft (30.48 m) Polar, Ground Microphones



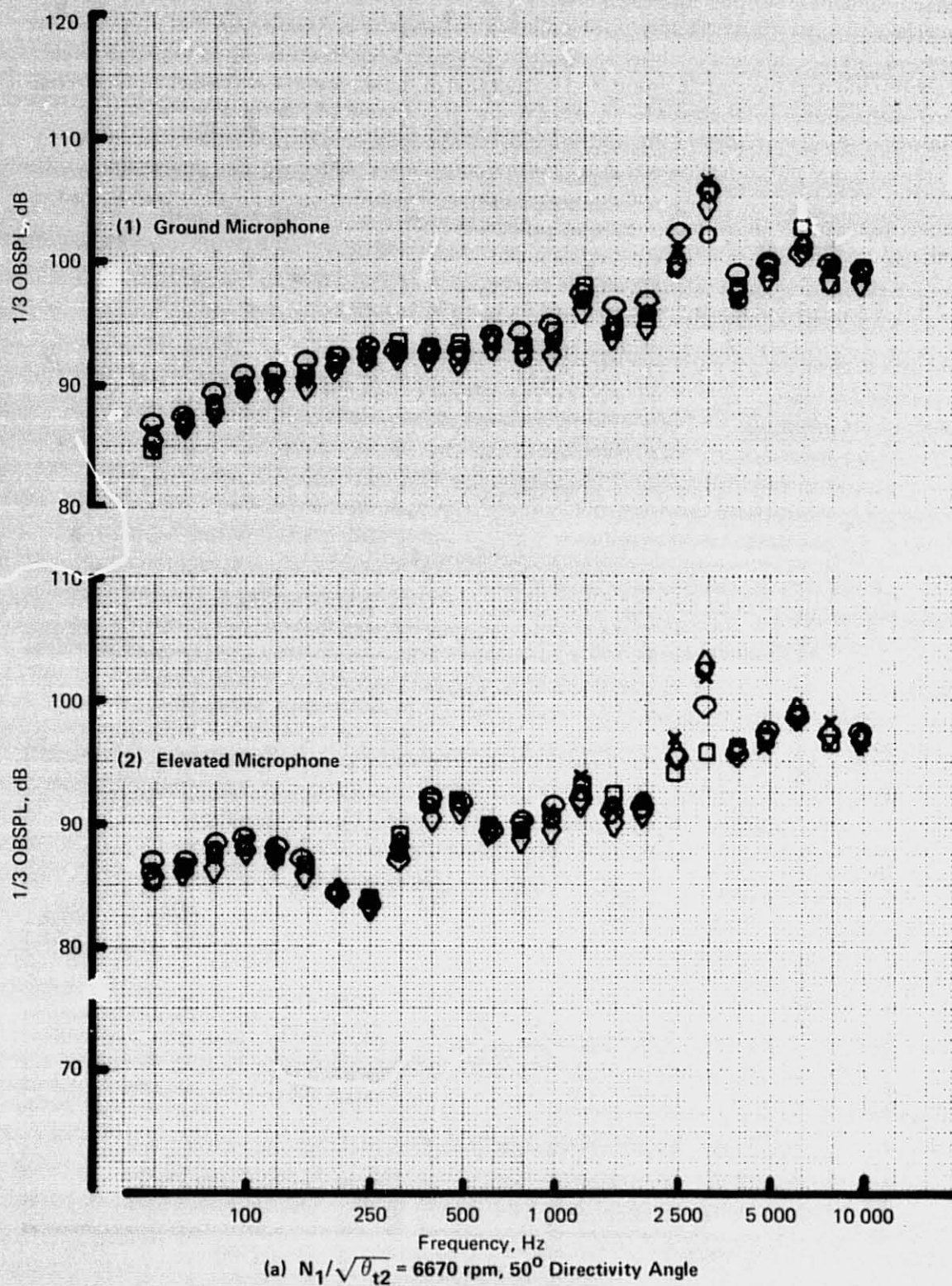
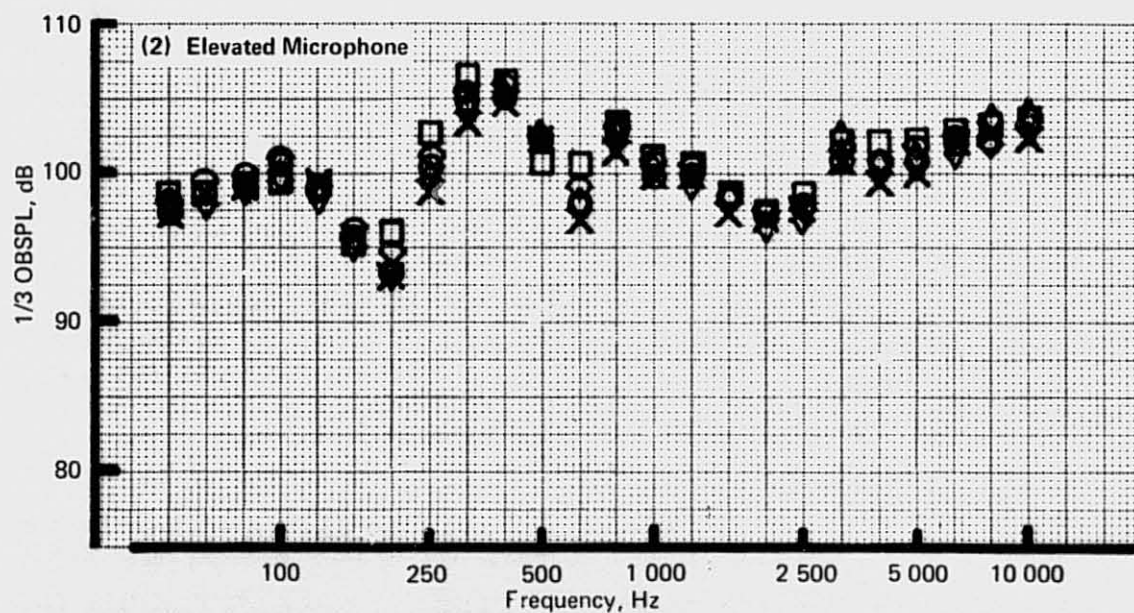
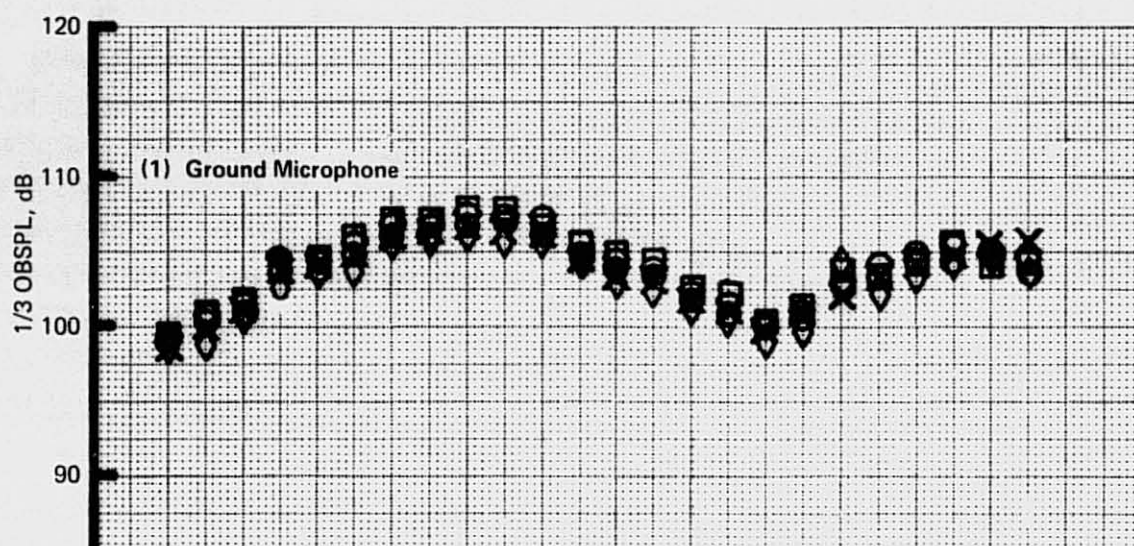


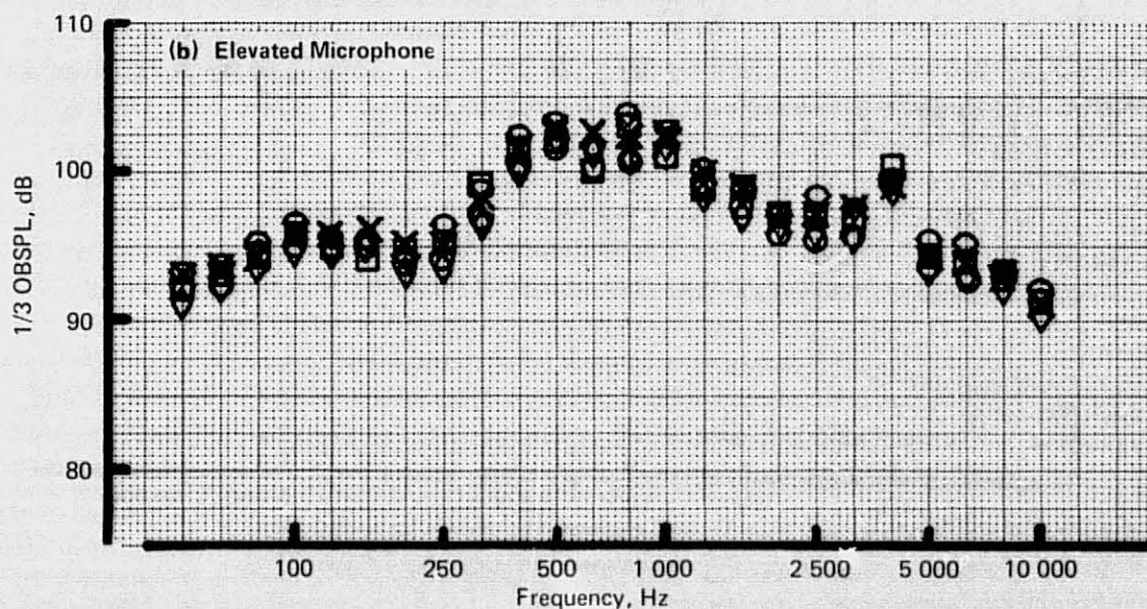
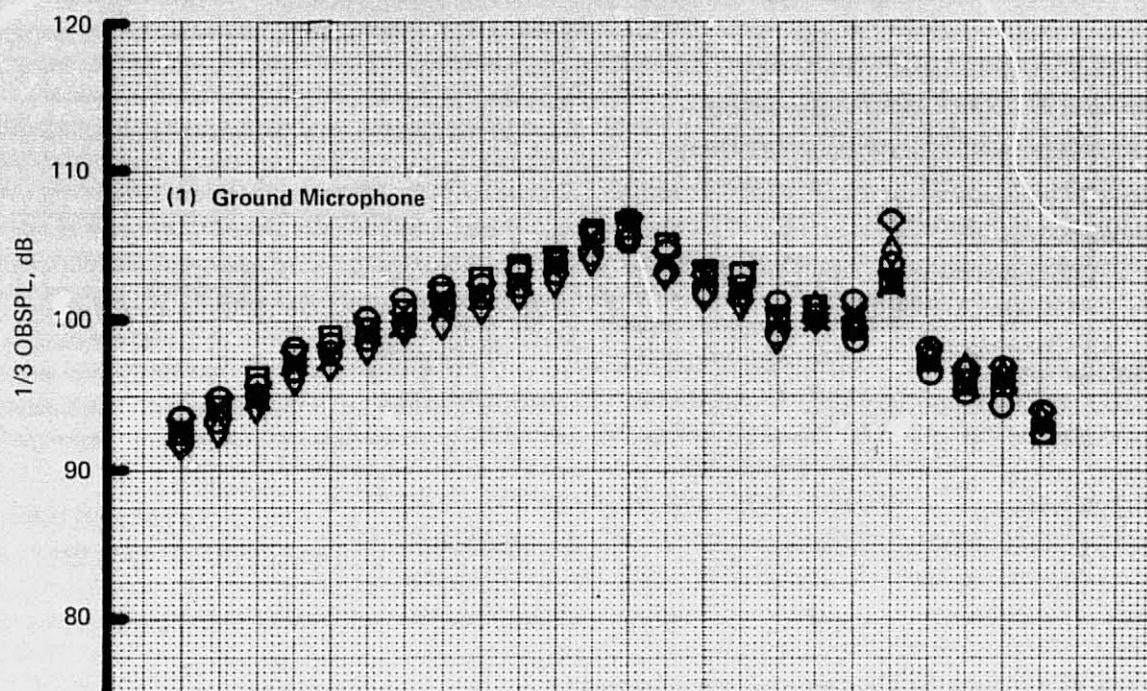
Figure 186.—JT8D-15 Ground Test—Comparison of Elevated and Ground Level Microphone Acoustic Data: 100 ft (30.48 m) Polar



(b)  $N_1/\sqrt{\theta_{t2}} = 6670 \text{ rpm}, 120^\circ \text{ Directivity Angle}$

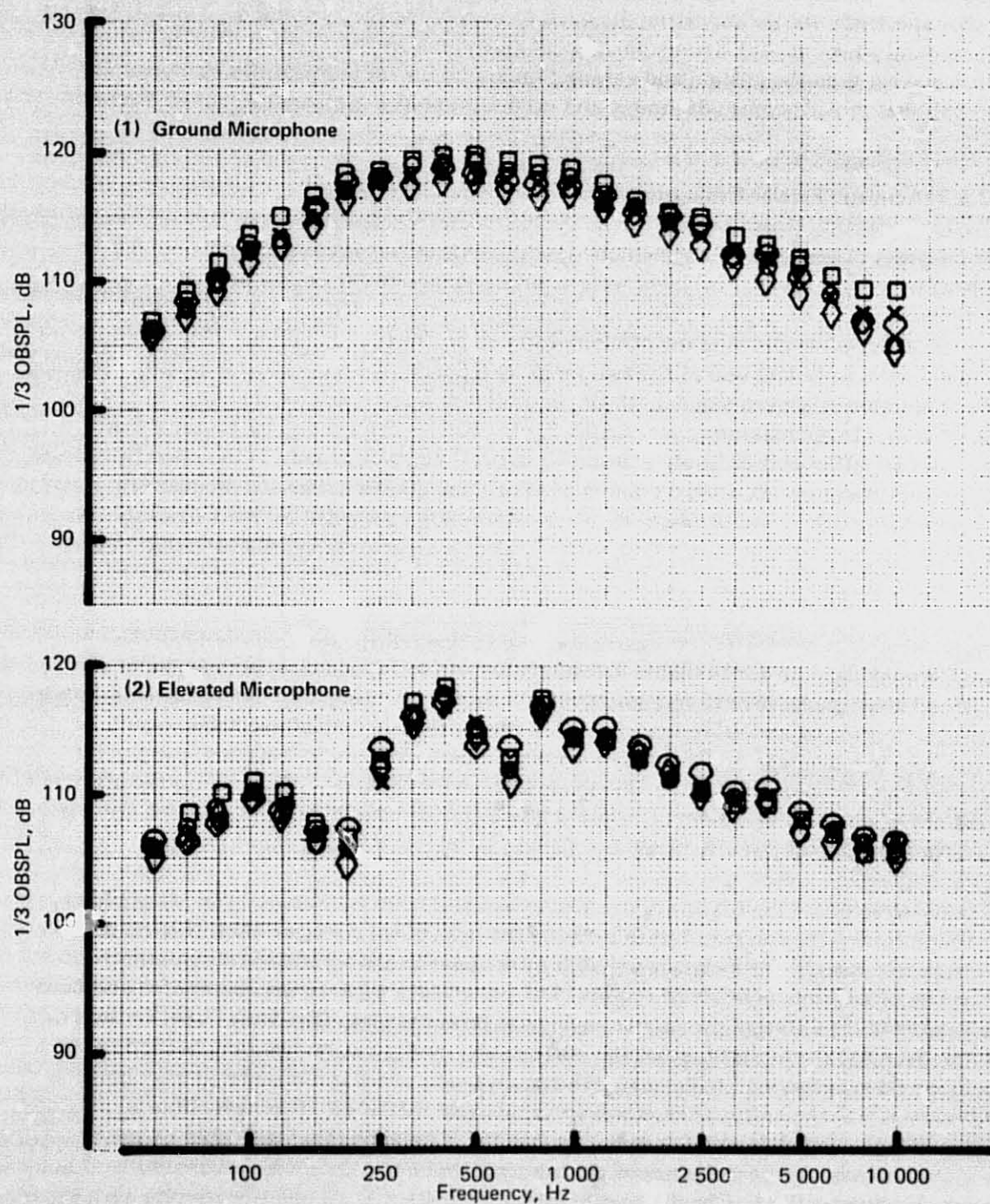
Figure 186. — (Continued)





(c)  $N_1/\sqrt{\theta_{t2}} = 8450 \text{ rpm}, 50^\circ \text{ Directivity Angle}$

Figure 186.—(Continued)



(d)  $N_1 \sqrt{\theta_{12}} = 8450 \text{ rpm}, 120^\circ \text{ Directivity Angle}$

Figure 186.—(Concluded)



Direct comparisons of mean data from ground and elevated microphones for two angles and two conditions are shown in figure 187. Examination of these spectral comparisons shows the marked improvement that the ground microphone gives in definition of the low frequency spectrum, thus, eliminating the need to correct for the "ground dip" at 200 Hz and the "ground peak" at 400 Hz. From a repeatability standpoint, there appears to be little difference between the ground and elevated microphones. It is concluded that ground microphones provide some advantages and no disadvantages compared to elevated microphones.

#### 4.2.5.3 Acoustic Barrier Evaluation

For purposes of isolation of engine noise components, seven acoustic barriers, each 8-ft (2.4-m) wide by 20-ft (6.1-m) high, were arranged alongside the engine in such a way as to shield one end of the engine (either inlet or exhaust) from radiating directly into the acoustic arena while allowing the other end to radiate freely (figs. 27 and 28). Arrangement of the barriers to isolate one of the two major component sources (inlet or exhaust) provides noise reduction at a given angle up to the limit determined by one or the other of the following limitations: (1) the maximum attenuation of the baffles determined by transmission through the baffles and diffraction around and over the baffles; and (2) the noise floor from the unbaffled source. Because a combination of these effects occurs simultaneously, it is not possible to determine precisely the exact attenuation provided by the baffles for all angles and power settings, but it is possible to place a lower limit on this attenuation and, thus, demonstrate that it is at least sufficient for the purposes of the present test.

It is reasonable to postulate some general characteristics of the attenuation phenomena which would allow an approximate determination of the baffle attenuation spectra: (1) For a given angle, the attenuation spectrum should be reasonably independent of power setting; (2) for noise radiating from the inlet, the baffle attenuation spectrum should be reasonably independent of directivity angle since the sound energy emanates essentially from a "point" source centered at the inlet; and (3) for jet noise radiating into the aft quadrant, the noise sources are distributed downstream from the nozzle, and this noise is therefore attenuated less effectively by the baffles than is the inlet noise.

In order to estimate the baffle attenuation, noise data from the forward and aft-shielded configurations were compared to those from the unshielded configuration. The reader is referred to figure 28 for a planview sketch of the inlet and aft-shielded configurations. Two sets of increments between the shielded and unshielded data were computed and have been plotted for different directivity angles and power settings (fig. 188). This method of comparison has the limitation that the baffled inlet configuration has an unbaffled exhaust so that exhaust-generated noise may influence forward quadrant noise levels and limit the extent to which the baffle attenuation spectra can be measured. It is impossible to measure the amount by which inlet noise radiating into the aft quadrant is attenuated by inlet shielding because of the influence of the aft-generated noise floor. A similar argument holds for the inlet noise floor. For this reason inlet-shielded baffle attenuation spectra have been computed only for the forward quadrant and aft-shielded spectra only for the aft quadrant. Even with this limitation, the influence of noise floor is still seen in the data, particularly that of aft noise in the forward quadrant at high power settings.

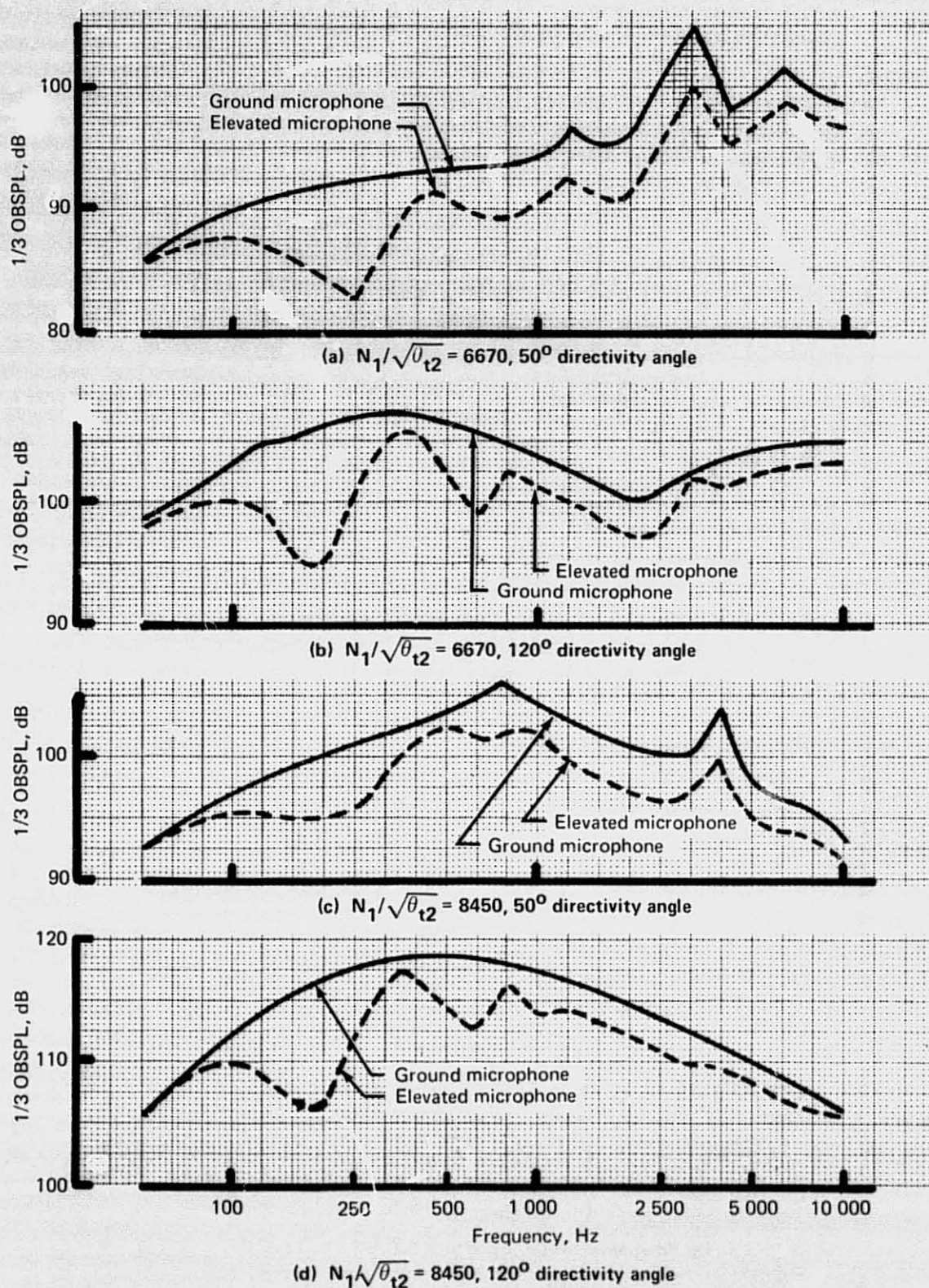
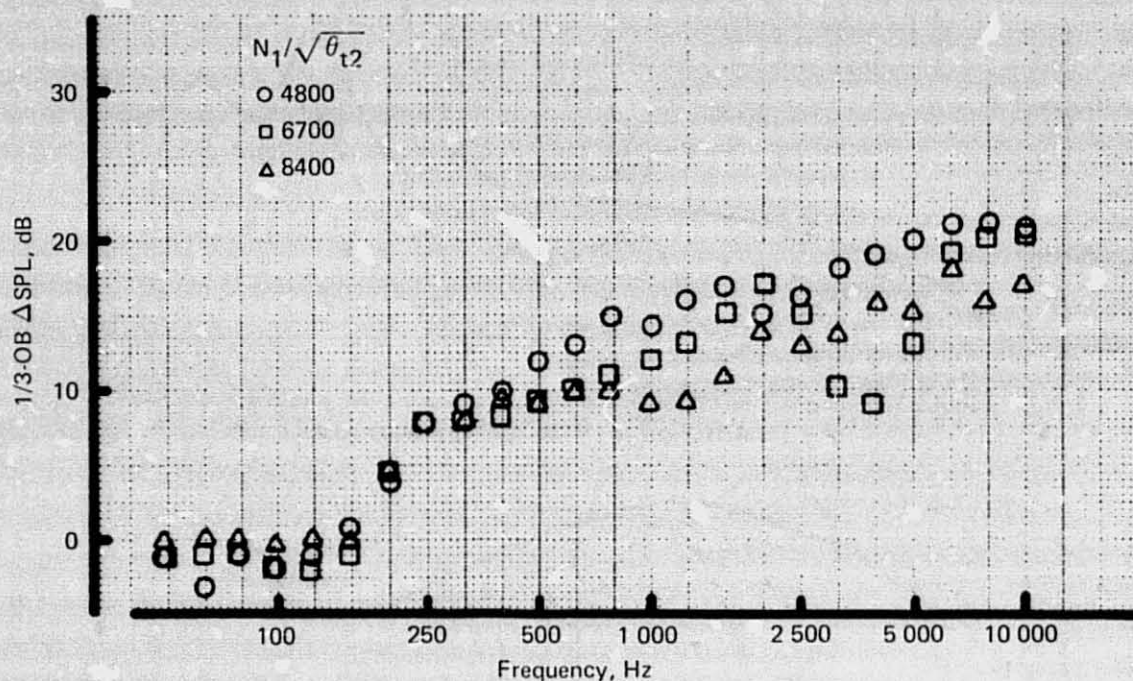
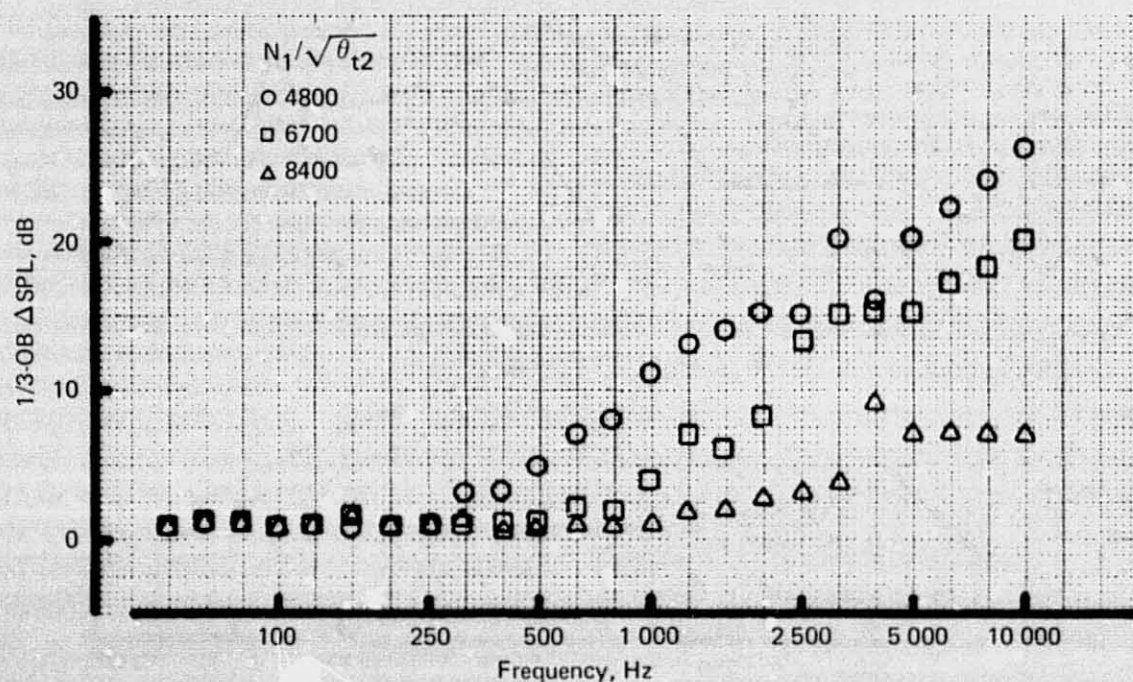


Figure 187.—JT8D-15 Ground Test—Direct Comparison of Elevated and Ground Level Microphone Spectra: 100 ft (30.48 m) Polar



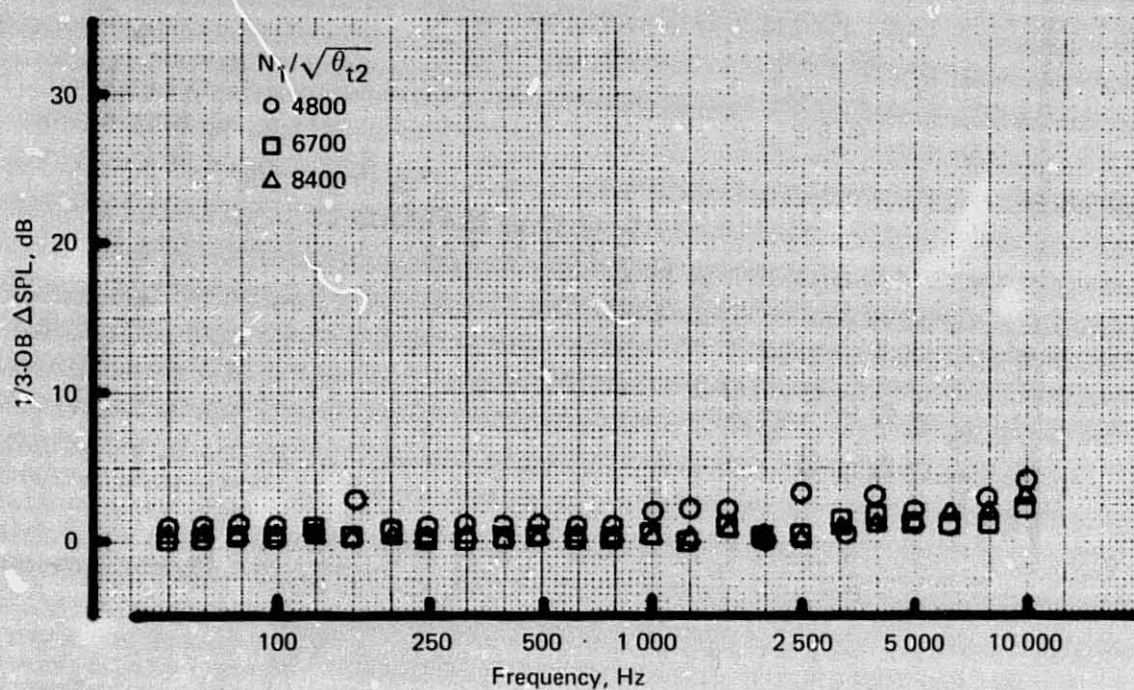


(a) Inlet-Shielded Configuration, 120° Directivity Angle

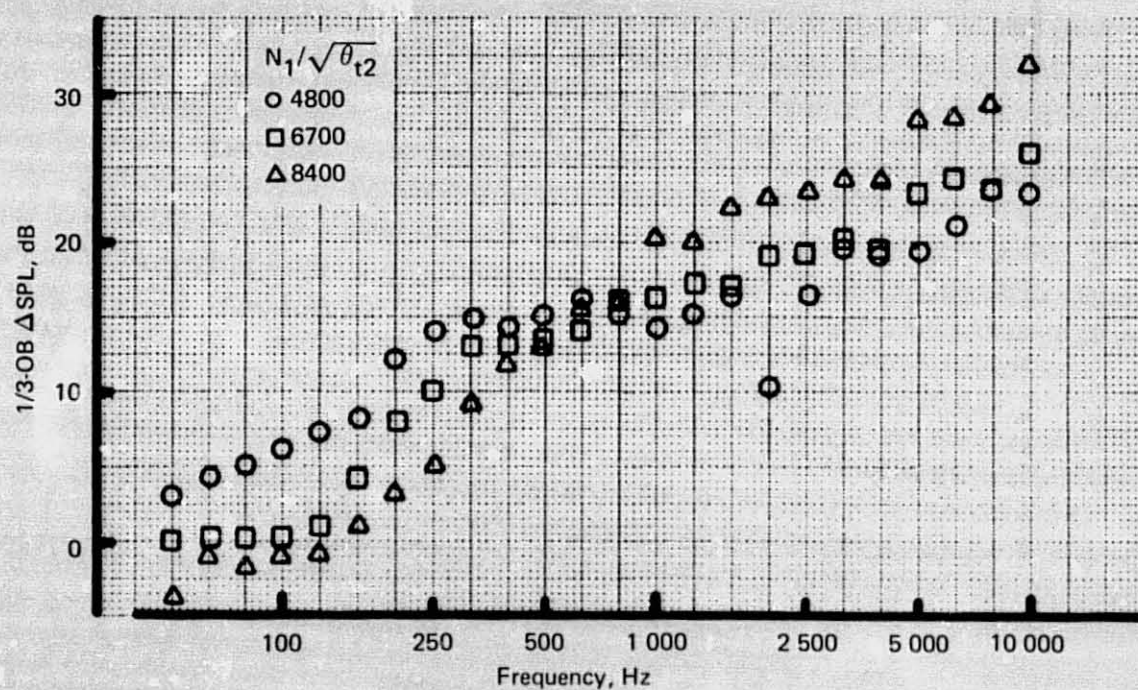


(b) Inlet-Shielded Configuration, 50° Directivity Angle

Figure 188.—JT8D-15 Ground Test—Apparent Baffle Attenuation Spectra



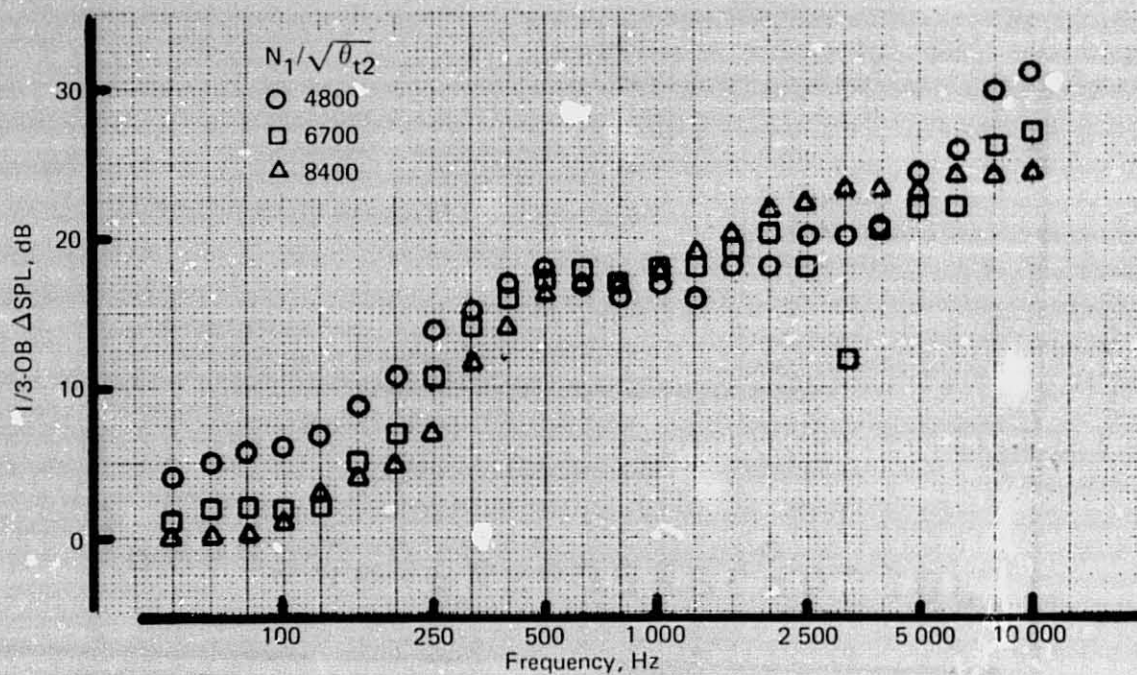
(c) Inlet-Shielded Configuration,  $80^\circ$  Directivity Angle



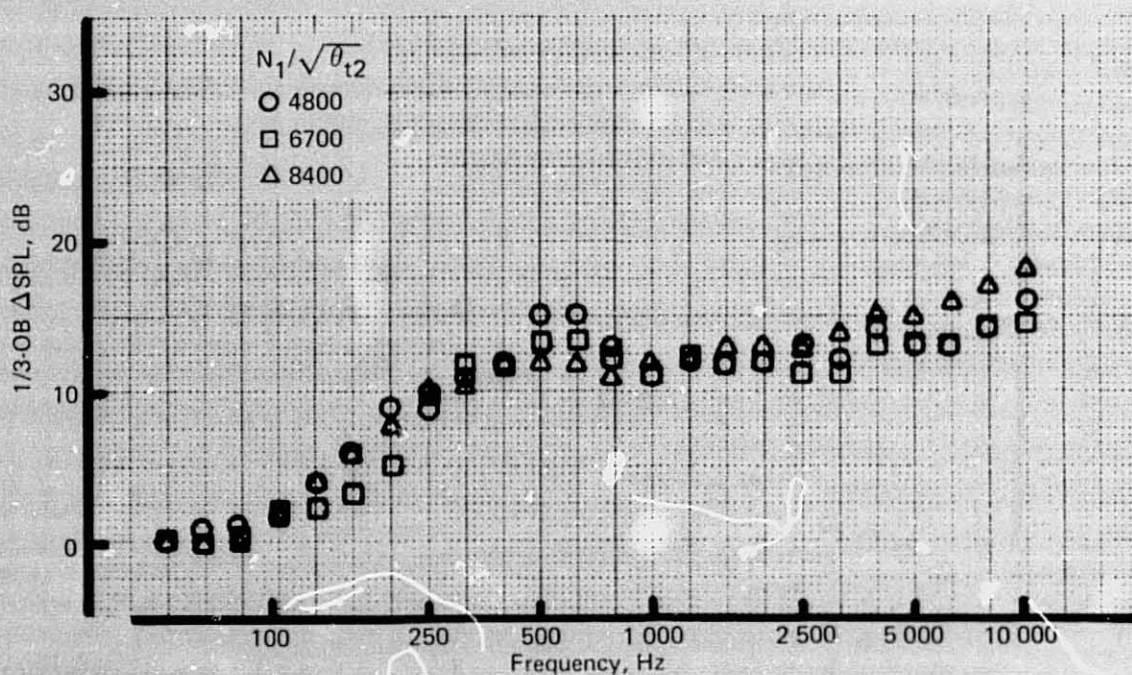
(d) Aft-Shielded Configuration,  $100^\circ$  Directivity Angle

Figure 188.—(Continued)





(e) Aft-Shielded Configuration, 120° Directivity Angle



(f) Aft-Shielded Configuration, 140° Directivity Angle

Figure 188.—(Concluded)



Recognizing that noise floor influence the data, it is possible to estimate the baffle attenuation spectra at all angles. Figures 188a through 188c show the increments between the inlet-shielded configuration and the unshielded configuration at three forward quadrant directivity angles. At the  $20^\circ$  directivity angle, where the influence of the aft-generated noise floor is expected to be minimal, the data cluster together fairly well, although somewhat less attenuation is seen at the highest power setting. It is believed that aft noise floor is just beginning to influence the attenuation data at the highest power setting. Thus, the data measured at the low power settings is probably a true measure of the baffle attenuation spectrum at the  $20^\circ$  directivity angle. The true inlet noise attenuation spectrum should not be significantly less than the  $20^\circ$  spectrum for any angle in the forward quadrant, as postulated earlier, and should not be significantly less at the most important aft quadrant angles ( $90^\circ$  through  $140^\circ$ ). At the  $50^\circ$  directivity angle (fig. 188b), the attenuation spectrum for the lowest power setting is seen to agree fairly well with that at  $20^\circ$ , but at the higher power settings, the aft noise floor is seen to have considerable influence on the data. At the  $80^\circ$  directivity angle (fig. 188c), the data at all power settings are affected by the aft noise floor.

A more accurate measure of the baffle attenuation near normal incidence is given by aft baffle data for the high power setting measurement at the  $100^\circ$  directivity angle (fig. 188d) where aft noise is totally dominant. For lower power settings, the high frequency aft-baffle attenuation is seen to diminish. This effect is attributed to the influence of inlet noise floor.

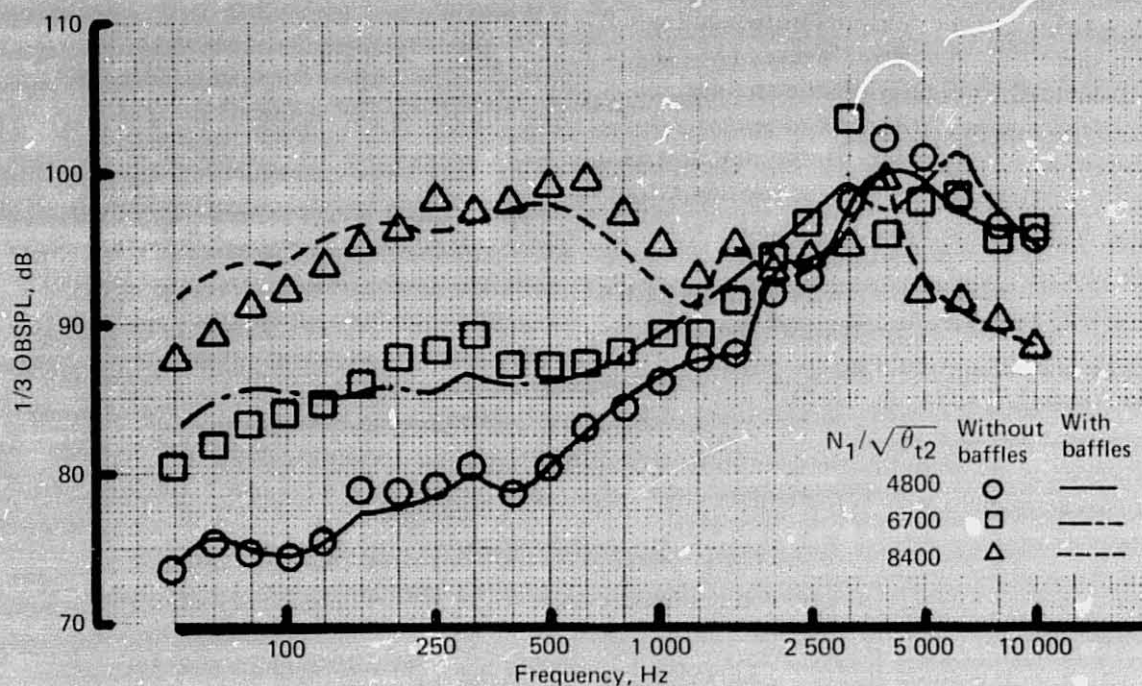
At further aft directivity angles the attenuation of aft-generated noise appears to diminish, having a peak attenuation of about 25 dB at  $120^\circ$  (fig. 188e). This is believed to be a real drop in the effectiveness of the baffles because of the substantial contribution to aft noise generated far downstream of the nozzle and the corresponding increase in diameter of the jet "cone."

As mentioned earlier, the method of comparison used to determine the attenuation spectra shown in figure 188 is suitable primarily for determination of the forward quadrant attenuation spectra for inlet-mounted barriers and the aft quadrant attenuation spectra for aft-mounted barriers. Because of noise floor problems, it is not generally possible to determine directly the attenuation of aft-radiated inlet noise by inlet-mounted baffles and vice versa.

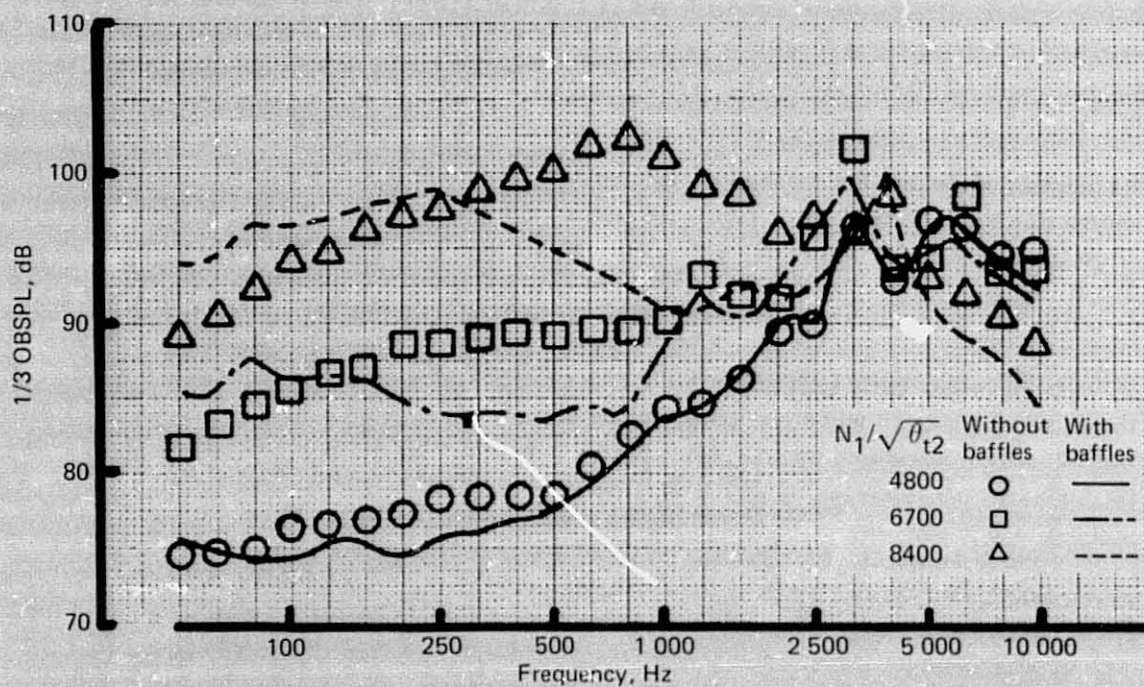
It has been observed that aft-mounted baffles produce an increase in low-frequency noise in the forward quadrant when compared to the unbaffled configuration. Comparison of forward quadrant noise spectra with no baffles and with aft baffles only (fig. 189) shows that for higher power settings the aft baffles produce an increase in SPL of up to 4 dB for frequencies below 200 Hz. This phenomenon is believed to be due to the multiple reflection of jet noise between the baffles and the stand and engine itself in such a way that the jet noise, which eventually arrives at the forward quadrant microphones, is of a higher level than the original direct wave. This effect is of small consequence, but it must be accounted for when doing the inlet fan noise analysis discussed later in this report. It is believed that the use of a set of "horse collar" baffles (not used in the present test) would have eliminated this problem.

Based on these data and the observations previously mentioned, estimates have been made of the minimum baffle attenuations for both forward and aft-shielded configurations at all directivity angles (figs. 190 and 191). While the real values of the baffle attenuations at some





(a) 20° Directivity Angle



(b) 50° Directivity Angle

Figure 189.—JT8D-15 Ground Test—Effect of Aft-Mounted Baffles on Forward Quadrant Noise: 100 ft (30.48 m) Polar, Ground Microphones

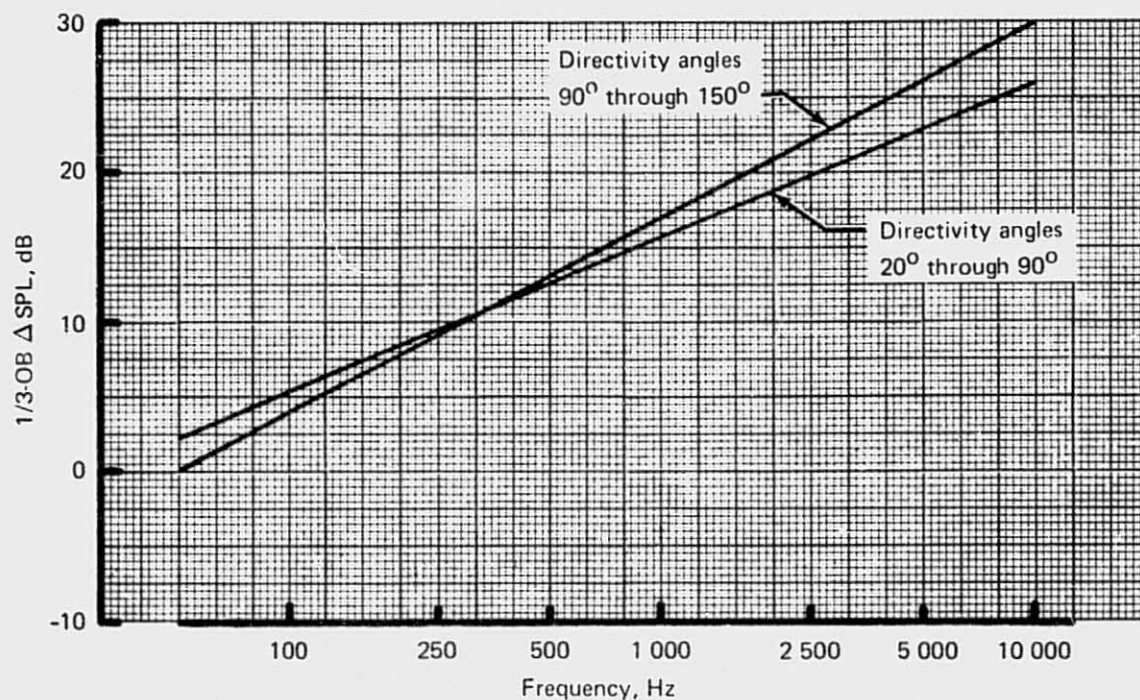


Figure 190.—JT8D-15 Ground Test—Estimated Attenuation of Inlet-Radiated Noise by Forward-Mounted Baffles, Average for All Power Settings

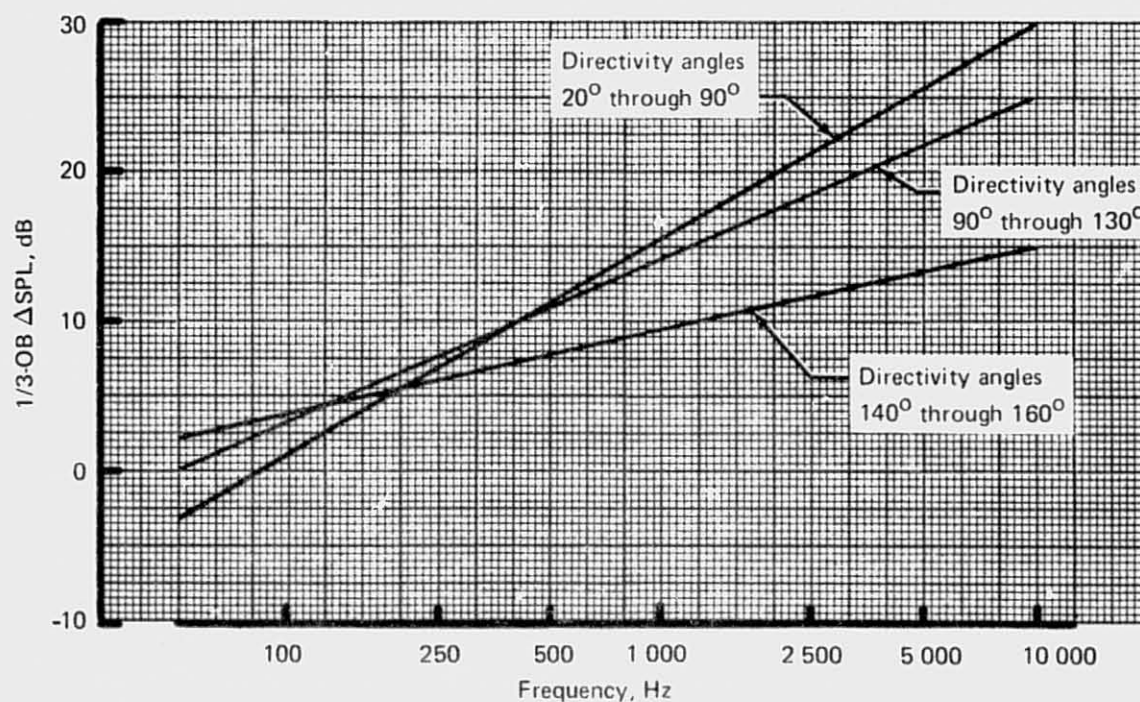


Figure 191.—JT8D-15 Ground Test—Estimated Attenuation of Discharge Radiated Noise by Aft-Mounted Baffles, Average for All Power Settings



frequencies may be substantially greater than the estimated values shown, it can be seen that for frequencies above 1000 Hz the baffle attenuations are at least sufficient to provide component noise isolation to the extent necessary to determine the absolute levels of two components in a region where there is significant contribution from both components to the total noise level.

### 4.3 STRUCTURAL

Analysis of structural data from the JT8D-115 ground test was carried out with two principal objectives: (1) interpretation of structural loads and deflection data for the center-engine inlet duct; and (2) determination of thermal stress characteristics in the exhaust duct assembly and fan/primary flow divider. The following sections describe the analysis procedures and present the results of these structural analyses.

#### 4.3.1 CENTER-ENGINE INLET DUCT

Stabilized pressures were compared to the duct model test results (ref. 4). The stabilized pressure-stress data were compared to predicted results from the structural analysis model of the center-engine inlet duct. Further evaluation of the surge conditions compared the test pressures, stress levels, and deflection time histories, illustrating the dynamic response of the duct to the surge pressure.

Test of a takeoff power condition yielded the traces shown in figures 192 through 195 (see fig. 25 for gage locations). This was a multiple peak surge condition, and for comparison, a single surge at idle power is shown in figures 196 and 197. Engine data for these conditions are shown in table 26.

The stabilized pressure data for the multiple peak surge condition at takeoff power shows fair correlation with the predicted duct internal pressure distribution. Test pressures are shown plotted together with predicted compatible duct internal pressure distribution in figure 198. Comparisons of the average test, predicted, and design pressures are shown in table 27.

Comparison of the axial and circumferential strain gage responses generally indicated a much higher response from the circumferential gages than the axial gages. Therefore, verification with the duct structural analysis was made using the circumferential gages.

The duct was designed with a clearance between the duct wall and the fin front spar fitting. This elliptical section was unrestrained or free with negative pressure and positive pressure up to 1.10 psi (7.58 kN/m<sup>2</sup>) when contact was made with the fitting. However, with increasing positive pressure, contact with the fitting restrained the duct at this cross section. These two conditions were analyzed using finite element computer techniques in the center-engine inlet duct structural analysis (ref. 1). The finite element computer program had no dynamic analysis capability, and only stabilized internal pressure conditions were considered. Therefore, predicted stresses and deflections were compared to stabilized test data only.

REPRODUCIBILITY OF THE  
ORIGINAL PAGE IS POOR

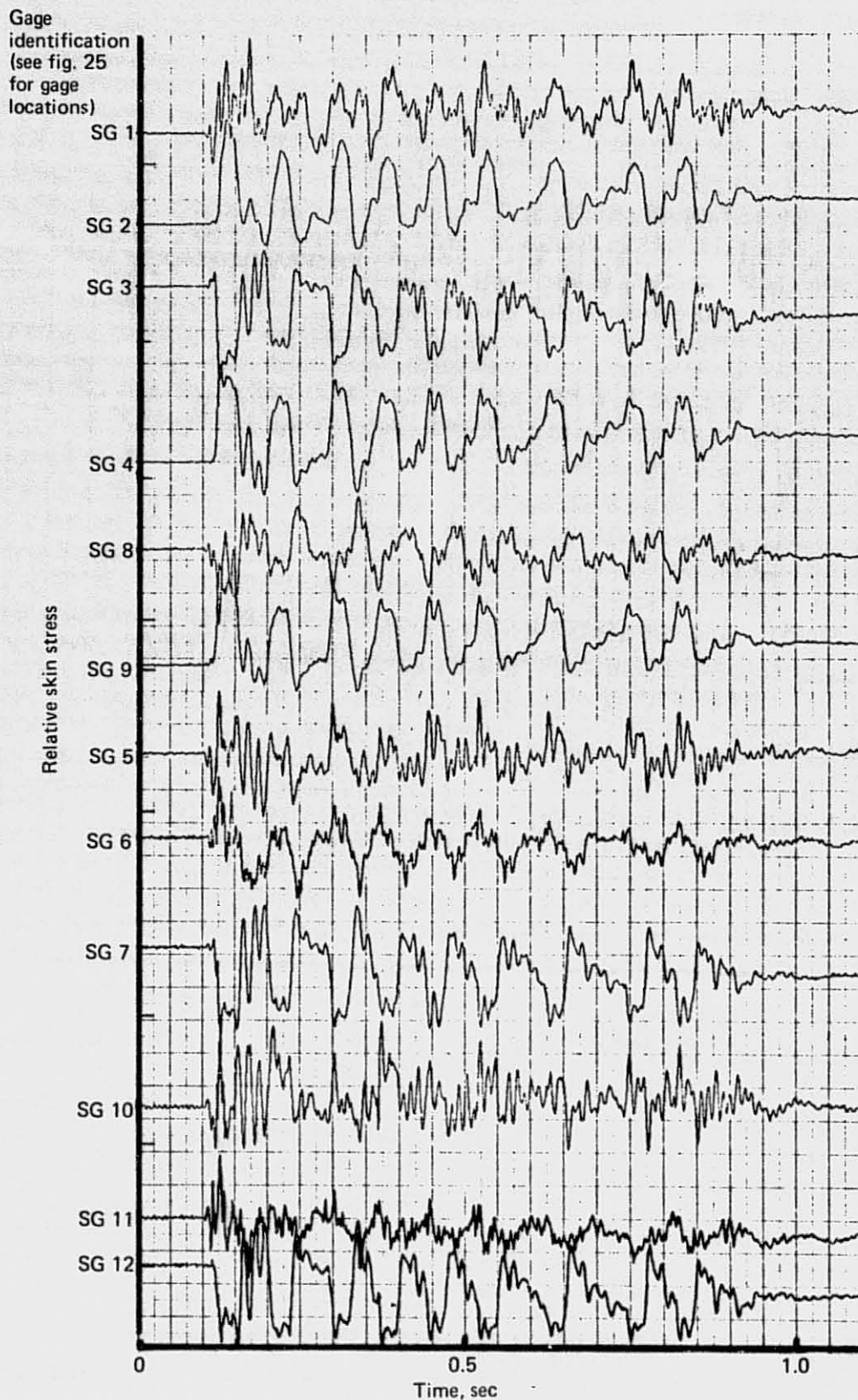


Figure 192.—JT8D-115 Ground Test—Center-Engine Inlet Duct Surge Strain Gage Trace,  
Multiple Peak Surge Condition at Takeoff Power

Gage  
identification (see fig. 25 for gage locations)

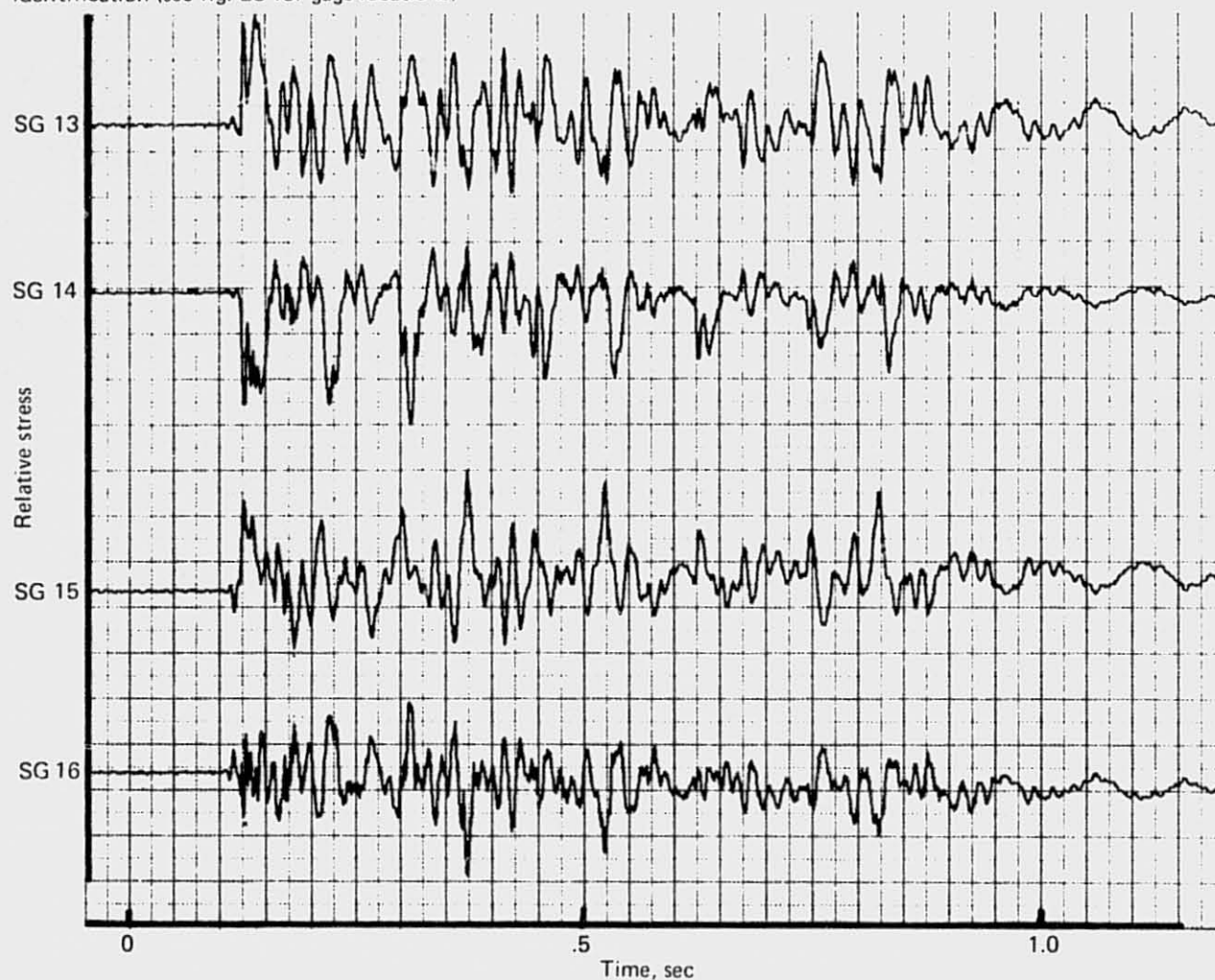


Figure 193.—JT8D-115 Ground Test—Front Spar Forging Surge Strain Gage Trace,  
Multiple Peak Surge Condition at Takeoff Power

Gage  
identification (see fig. 25 for gage locations)

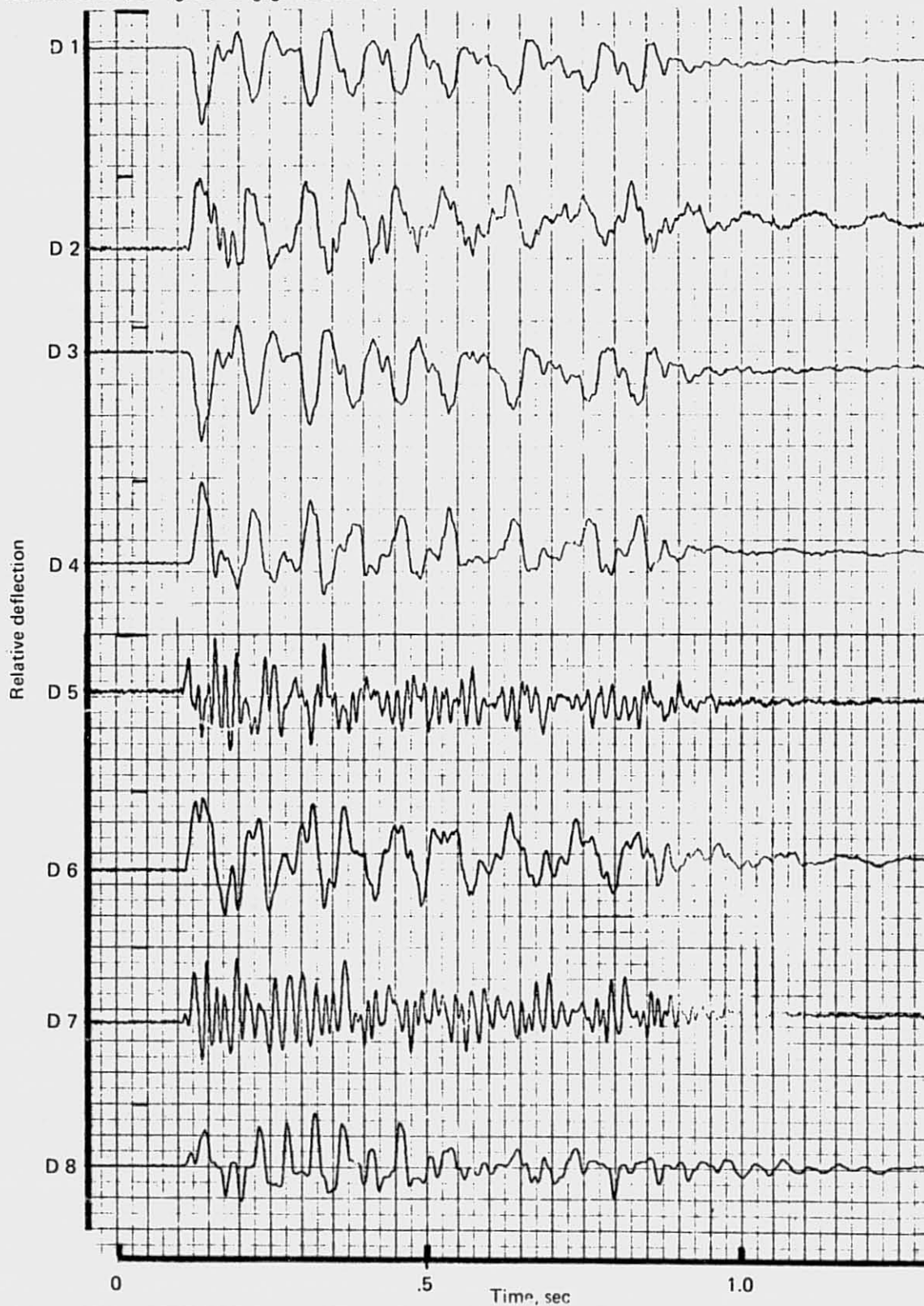


Figure 194.—JT8D-115 Ground Test—Center-Engine Inlet Duct Surge Deflection Gage Trace, Multiple Peak Surge Condition at Takeoff Power



Gage  
identification (see fig. 25 for gage locations)

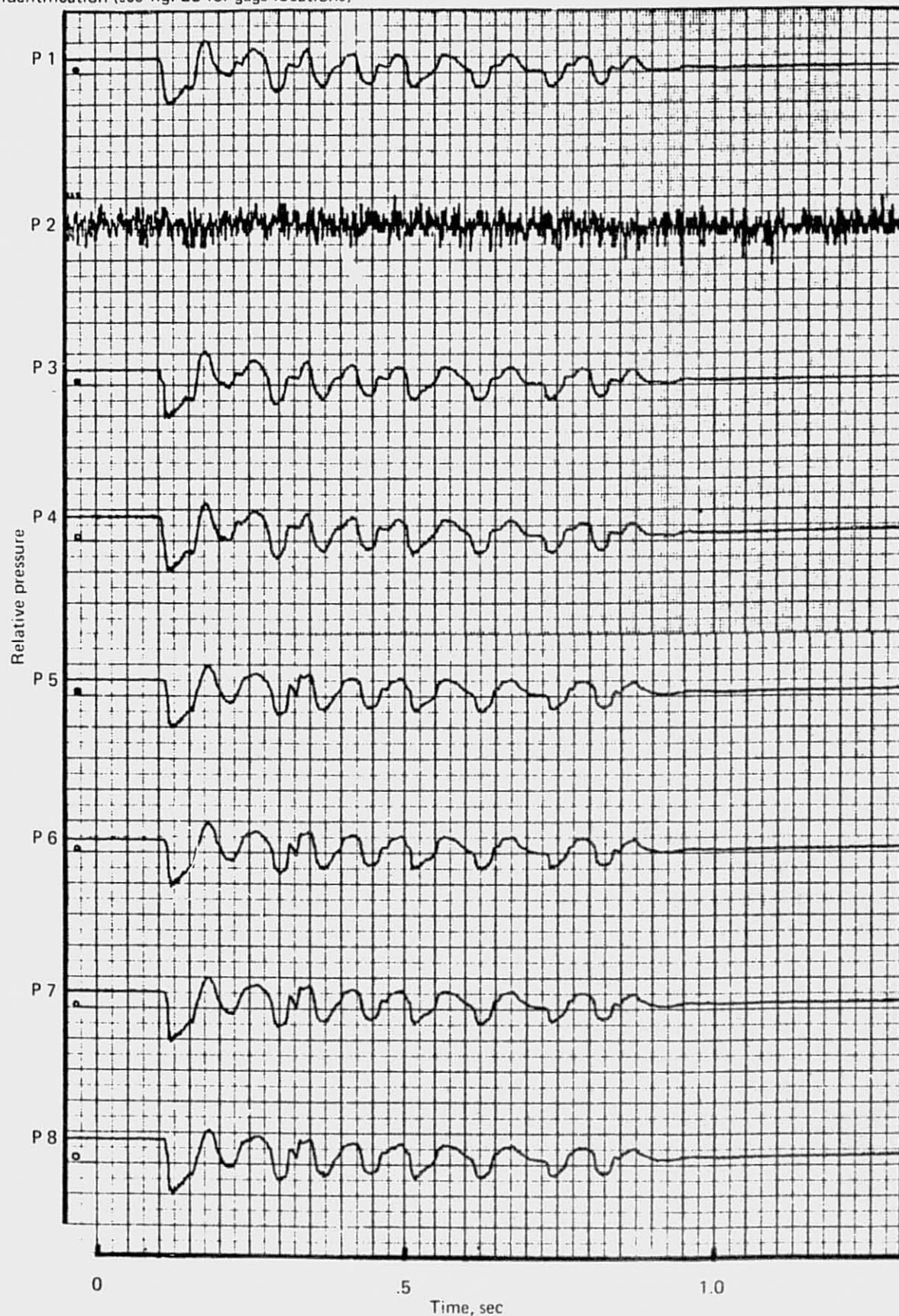


Figure 195.—JT8D-115 Ground Test—Multiple Surge Pressure Gage Traces,  
Multiple Peak Surge Condition at Takeoff Power

Gage  
identification (see fig. 25 for gage locations)

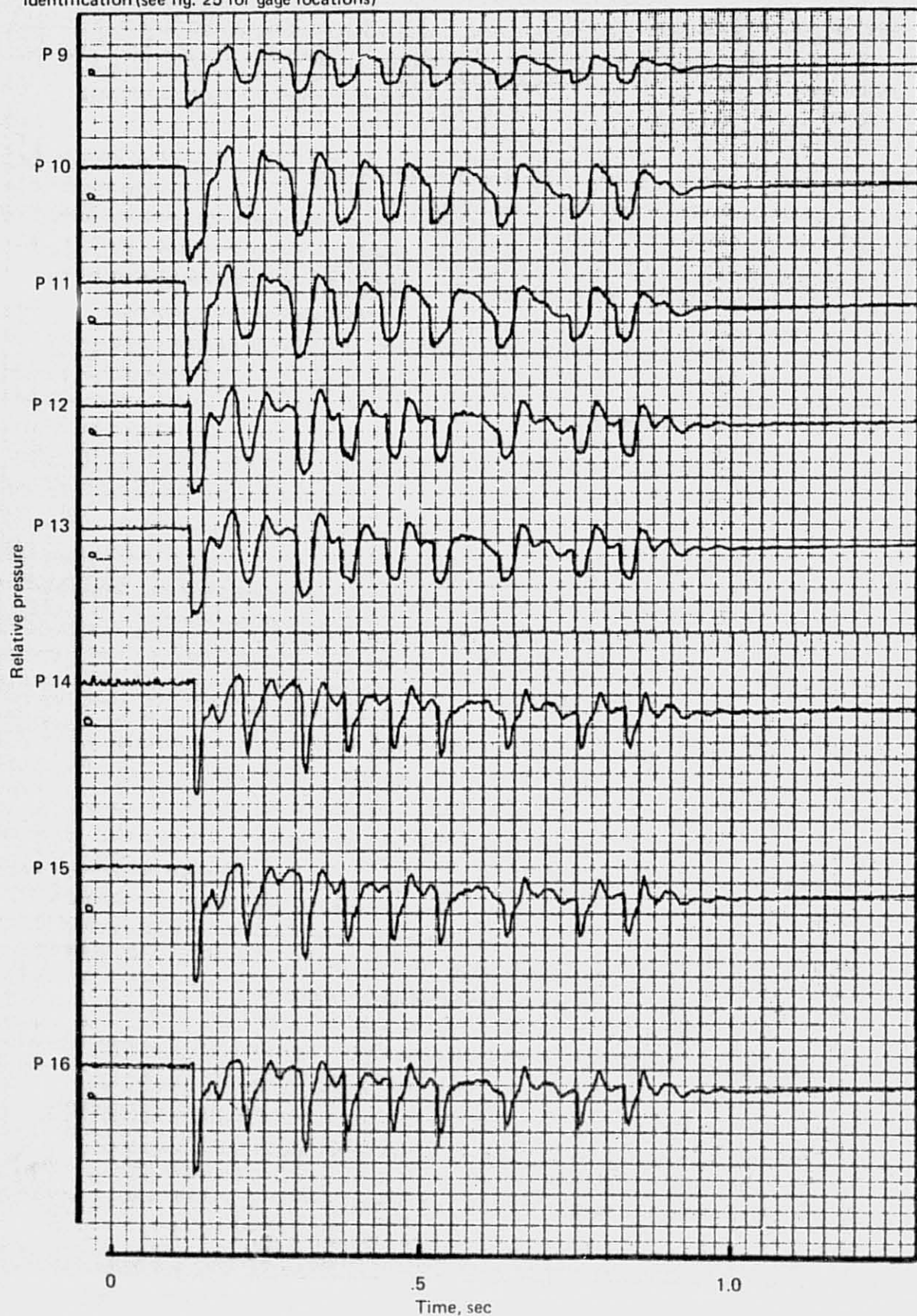


Figure 195. — (Concluded)



Gage  
identification (see fig. 25 for gage locations)

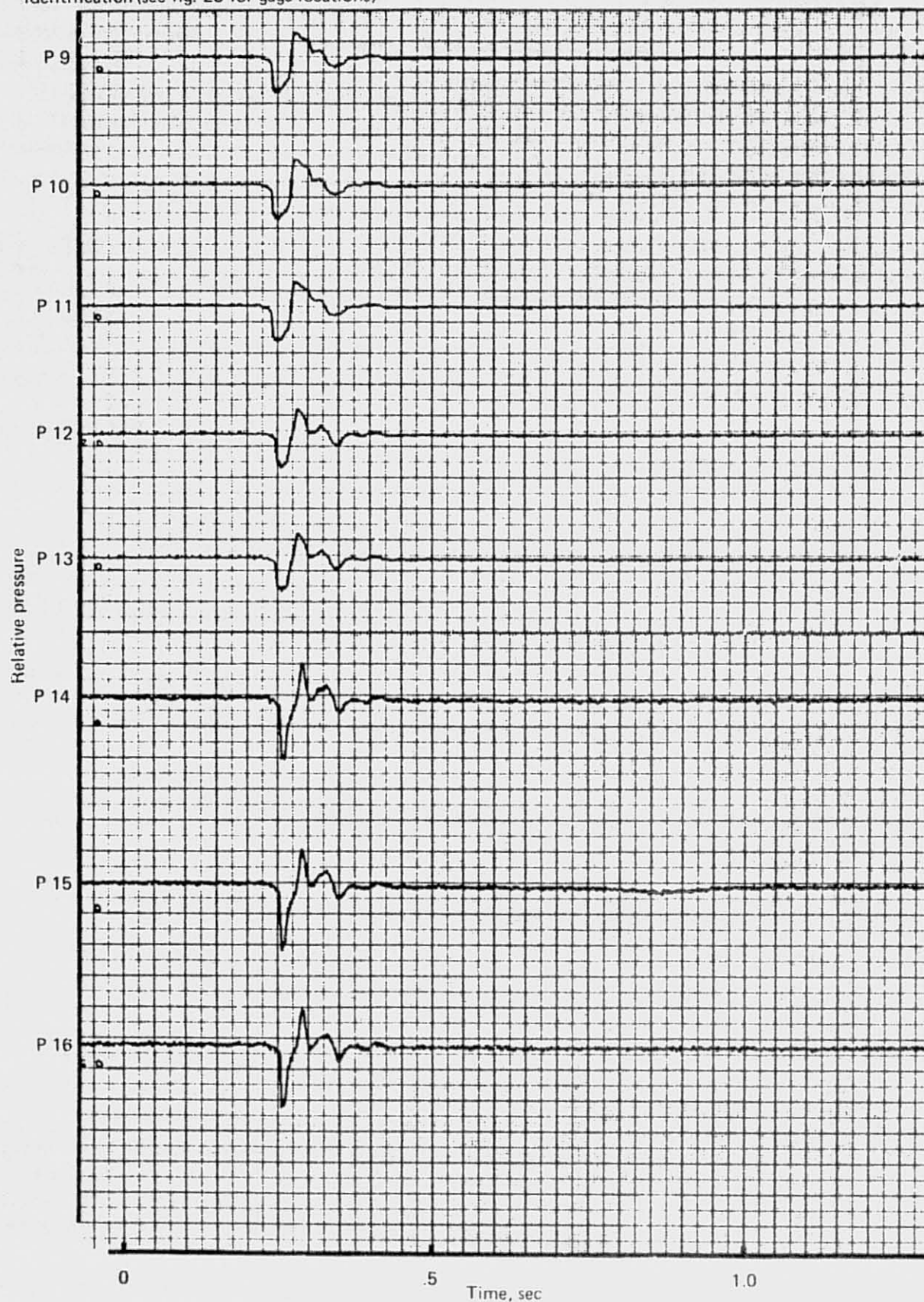


Figure 196.—JT8D-115 Ground Test—Typical Pressure Gage Traces for Single Surge Condition at Idle Power

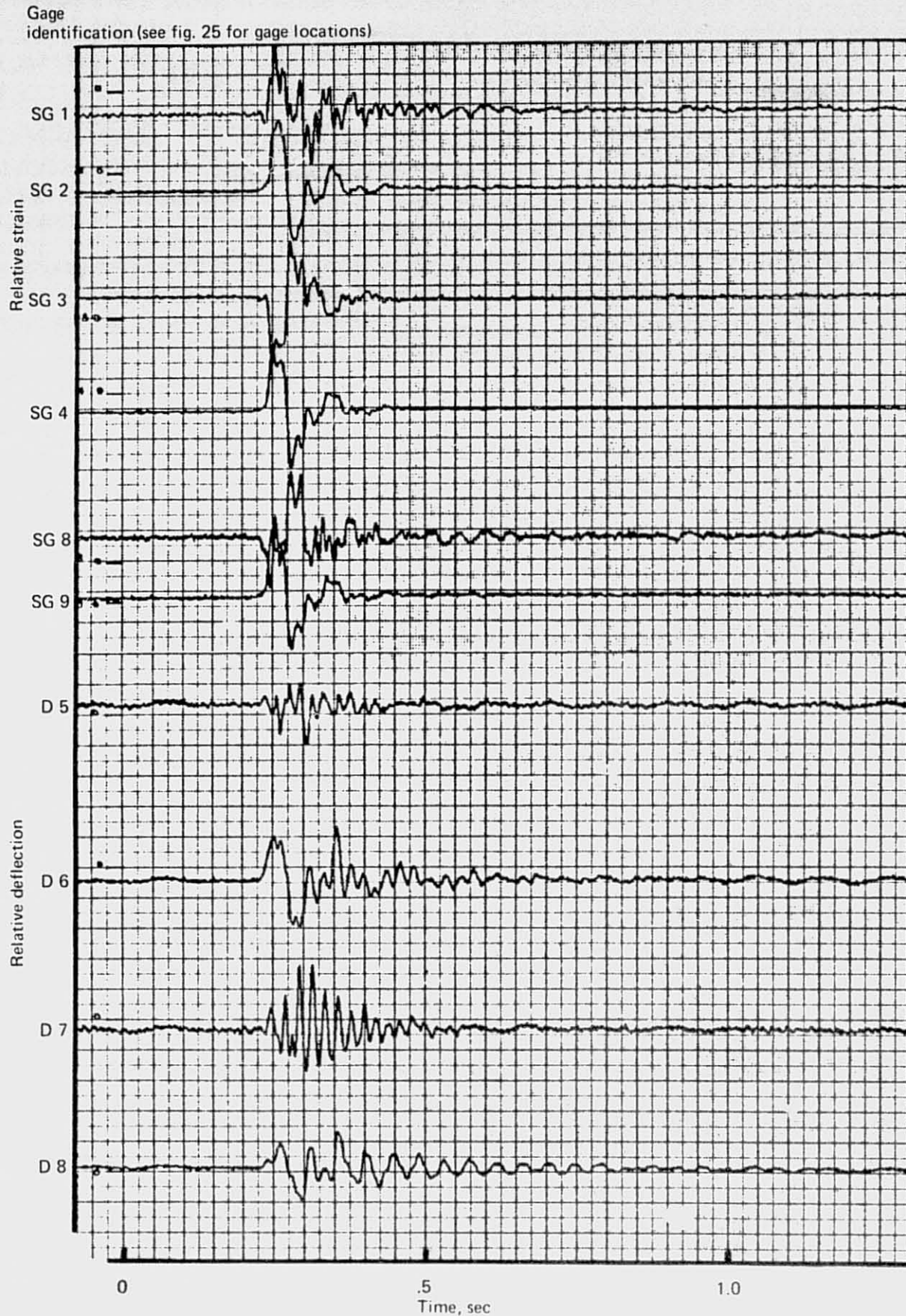


Figure 197.—JT8D-115 Ground Test—Typical Strain and Deflection Gage Traces for Single Surge Condition at Idle Power



Table 26.—JT8D-115 Ground Test—Stabilized Engine Data for Structural Runs Analyzed and Illustrated

Condition	$N_1/\sqrt{\theta_{t2}}$		Mass airflow, lb/s (kg/s)
	rpm	EPR	
Multiple peak surge—takeoff power	7390	1.90	466 (211.37)
Single surge—idle power	4835	1.22	280 (127.01)

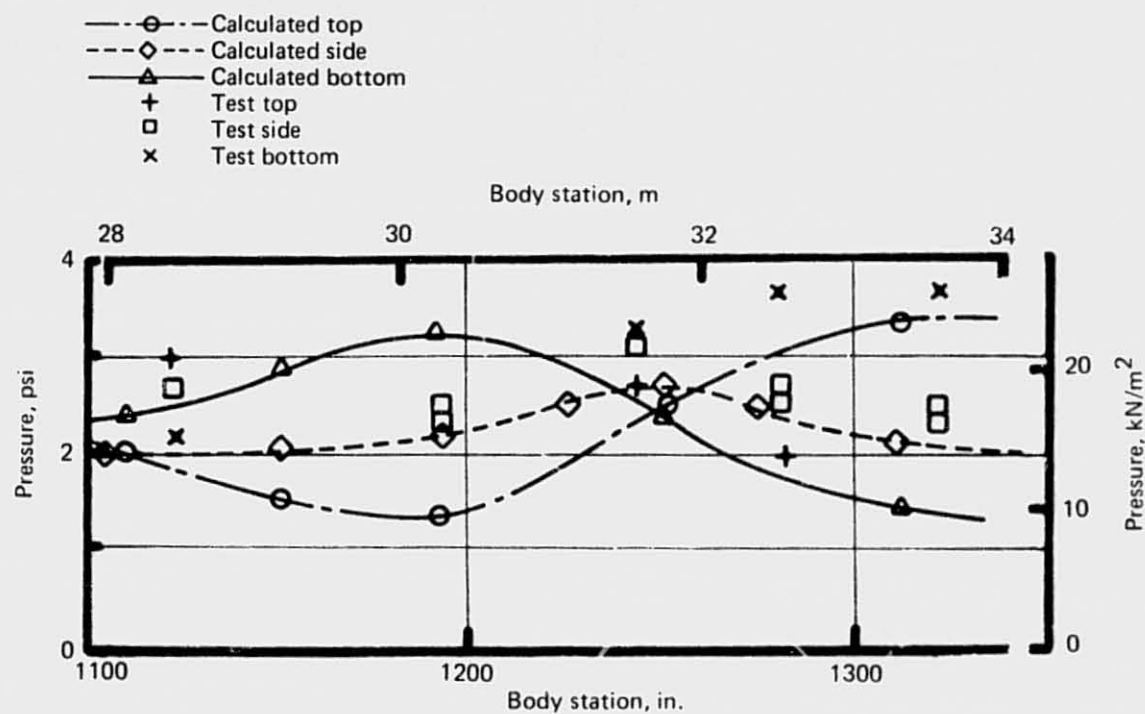


Figure 198.—JT8D-115 Ground Test—Center-Engine Inlet-Duct Pressure, Calculated and Test Data Correlation

**Table 27.—Comparison of Ground Test and Predicted and Duct Design Average Pressure for the JT8D-115 Center-Engine Inlet Duct**

Condition (takeoff power)	Test	Predicted	Design Limit
	psi (kN/m <sup>2</sup> )	psi (kN/m <sup>2</sup> )	psi (kN/m <sup>2</sup> )
Stabilized, sea level	-2.81 ( -19.374)	-2.90 ( -19.995)	-3.00 ( -20.684)
Surge minus, sea level	-4.40 ( -30.337)	-5.00 ( -34.474)	-5.00 ( -34.474)
Surge plus, sea level	+4.94 (+34.060)		
Extrapolated to altitude	+12.50 (+86.185)	+10.50 (+72.395)	+12.00 (+82.737)

The predicted stress-pressure relationship for both the free and restrained duct are shown in figures 199 and 200.

Static ground test stabilized pressures were negative, and test stresses were compared to the predicted stress levels for a free duct. Test stresses at the top, bottom, and sides of the duct compared favorably with the computed stresses. The duct was restrained by the fitting during the surge positive pressure impulse, and ignoring the oscillations, the test stress traces showed good correlation with the predicted stress levels for a restrained duct.

The duct elliptical cross section responded to the saw tooth surge pulse, (approximately 10 Hz) with a vibratory response of approximately 60 Hz, which represented a duct fundamental mode. The vibratory response predominated in the axial strain gage results, since stress levels induced by the surge pressure were low. The circumferential dynamic response of the duct to the surge pressure wave was further illustrated by plotting stress, deflection, and pressure against a common time base (fig. 201). The stress and deflection curves illustrated the duct inertial resistance to the surge pressure and the duct vibratory response superimposed on the forced response. The dynamic response of the duct is also seen by the deviation of the stress-pressure relationship from the linear stabilized pressure curves (figs. 199 and 200).

The deflections of the duct major and minor axes measured at duct section CC (fig. 25) compare reasonably well with those obtained from the structural analysis. These results are shown in table 28 for 5.0-psi (34.47-kN/m<sup>2</sup>) duct pressure.

Deflections measured at the flexible seal compare favorably with structure analysis results; however, the surge dynamic deflections were higher than predicted though still within seal design tolerances (table 28).

#### 4.3.2 EXHAUST SYSTEM

The temperature data were amplified and recorded directly onto oscillographs and also, during stabilized conditions, stored in the data system for computer reduction and printout. Correlation checks showed consistent results with both systems of data storage. Temperatures from the data system were used for comparison with the computer thermal analysis.

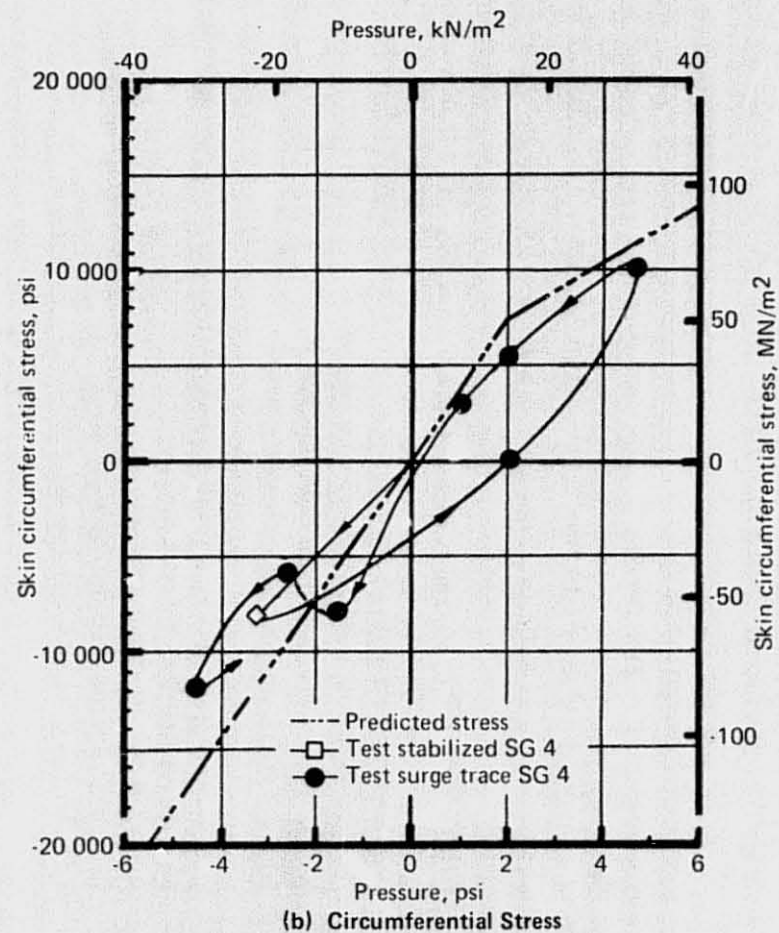
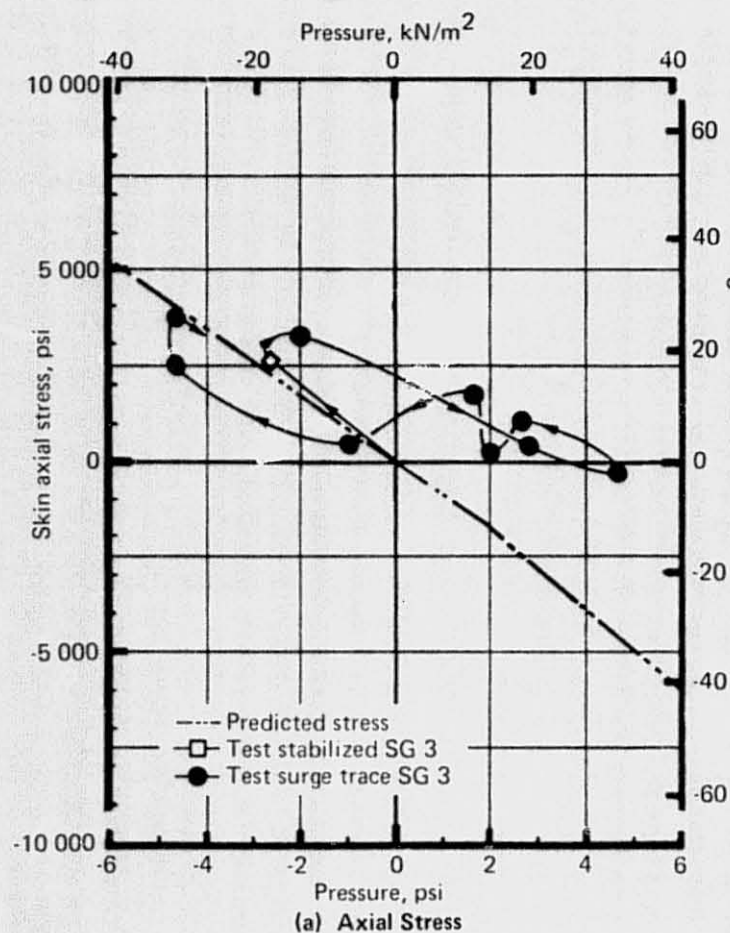
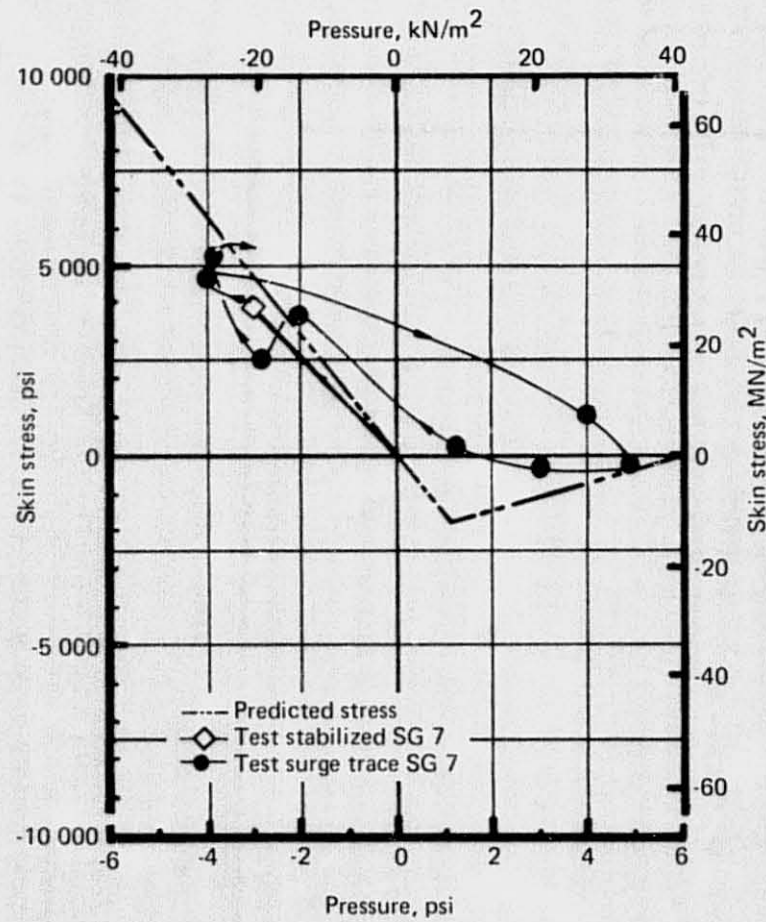
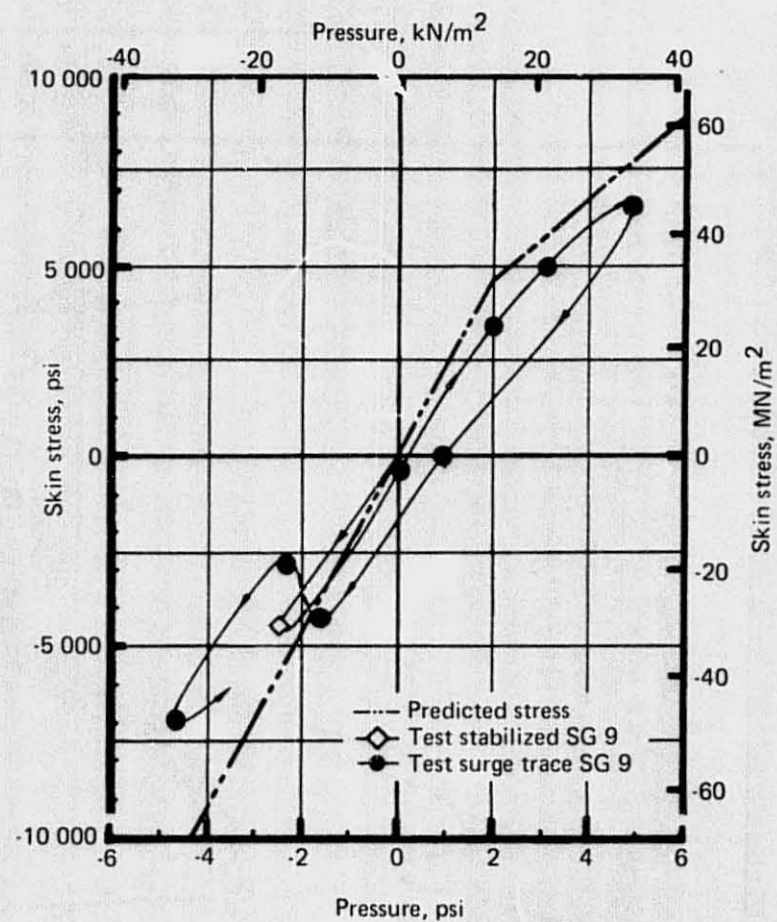


Figure 199. JT8D-115 Center-Engine Inlet Duct, Predicted, and Ground Test Gage Dynamic Response—Duct Upper Centerline Axial and Circumferential Stresses





(a) Duct Side Wall



(b) Duct Lower Centerline

Figure 200.—JT8D-115 Center-Engine Inlet Duct, Predicted, and Ground Test Gage Dynamic Response—Side and Lower Centerline Circumferential Stress



REPRODUCIBILITY OF THE  
ORIGINAL PAGE IS POOR

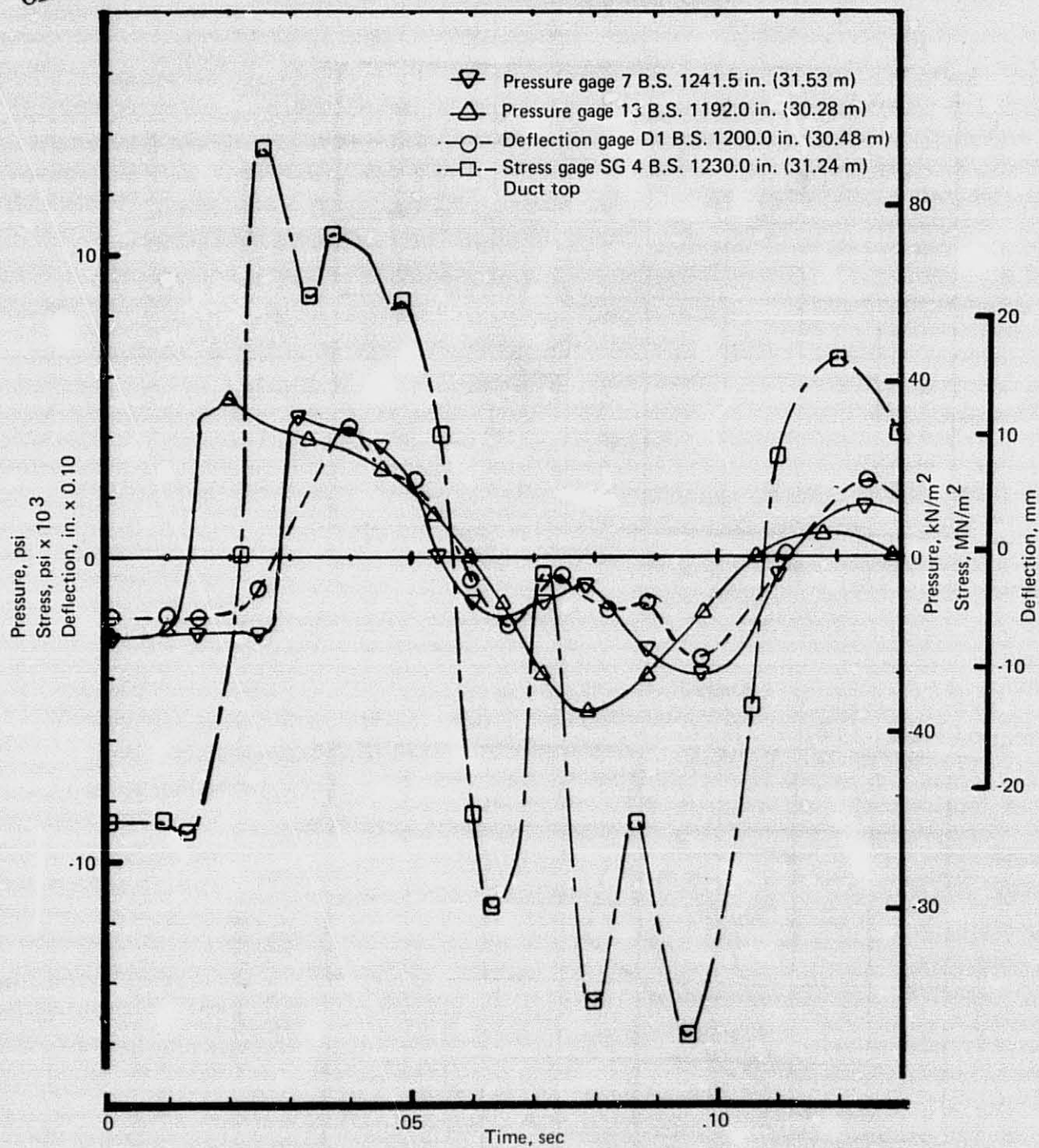


Figure 201.—Typical JT8D-115 Center-Engine Inlet Duct Surge Profile (for Multiple Peak Surge Condition at Takeoff Power) Showing Pressure, Stress and Deflection Versus Time Relationship

**Table 28.—Comparison of Ground Test and Predicted Deflection Data for the JT8D-115 Center-Engine Inlet Duct**

Load condition: Internal duct pressure + 5.0 psi (34.474 kN/m<sup>2</sup>)

Gage location <sup>a</sup>		Test result	Predicted
		in. (mm)	in. (mm)
Section AA <sup>a</sup>			
Top $\bar{C}_L$	Gage D2	-0.15 (-3.810)	-0.198 (-5.029)
Side	Gage D1 and D3	+0.42 (+10.668)	+0.376 (+9.550)
Bottom $\bar{C}_L$	Gage D4	-0.33 (-8.382)	-0.241 (-6.121)
Seal			
Top $\bar{C}_L$ vertical	Gage D5	-0.033 (-0.838)	-0.074 (-1.880)
Lower $\bar{C}_L$ vertical	Gage D7	-0.133 (-3.378)	
Average $\bar{C}_L$ vertical movement		-0.083 (-2.108)	
Top $\bar{C}_L$ horizontal	Gage D6	-0.183 (-4.648)	
Lower $\bar{C}_L$ horizontal	Gage D8	0 (0)	
Maximum dynamic deflections at seal			
Vertical		+0.330 (+8.382) -0.320 (-8.128)	±1.0 (25.40)
Horizontal		+0.860 (+21.844) -0.550 (-13.970)	±1.0 (25.40)

<sup>a</sup>See figure 25 for gage locations and description of section AA

Thermocouple locations are shown in figure 26, and engine data for the runs considered are shown in table 29.

Test temperature traces for the idle-to-takeoff and takeoff-to-idle conditions are shown in figure 202. These curves illustrate the temperature rise with increased engine power and the rapid fall in temperature of the Inconel honeycomb following power reduction.

The fan/primary flow divider temperatures for the takeoff to cruise and idle to engine shut-down are shown in figure 203.

Takeoff condition (EPR 1.96) data were used for evaluation of the fan/primary flow divider thermal analysis. Temperatures obtained from the test data storage system are compared in figure 204 with the predictions.

Primary- and fan-flow side surface temperatures showed good correlation with the analysis results, but both the Inconel and titanium honeycomb inner skin temperatures were lower than those calculated. However, review of the thermal analysis model indicated the following differences that significantly affected the calculated results for the titanium panel.

The thermal analysis was made for the original fan/primary flow divider design in which the titanium honeycomb depth was tapered. However, to facilitate manufacture, the tested assembly honeycomb was uniform in depth. This reduced the honeycomb depth and increased the air gap at the thermocouple locations. Also, the analysis used the heat transfer coefficient for perforated liquid diffusion bonded titanium honeycomb panel that was

**Table 29.—JT8D-115 Ground Test—Stabilized Engine Data for Structural  
Runs Analyzed and Illustrated**

$N_1\sqrt{\theta_{t2}}$	EPR	Temperature ambient		Temperature primary		Temperature fan	
		°F	K	°F	K	°F	K
7501	1.93	40	278	1032	829	157	343
2031	1.03	44	280	779	688	73	296
7570	1.96	44	280	1043	835	158	343
6941	1.74	44	280	956	786	144	335
7561	1.95	44	280	1044	835	159	344
2074	1.03	44	280	760	678	73	296

obtained from the titanium honeycomb acoustic lining structural and thermal tests (ref. 8). These panels had a much lower heat transfer coefficient than aluminum-brazed titanium, since aluminum is not used as the brazing material. The amount of aluminum in the honeycomb nodes varies during manufacture and also influences the heat transfer since it is the major conductor between the face sheets. The increased air gap and higher heat transfer through the titanium would result in lower temperatures consistent with the test results obtained for the titanium assembly.

Review of the thermal program input data for the Inconel assembly does not reveal any major justification for the lower inner skin temperature and, therefore, the condition of the test article and interpretation of the test thermocouple temperatures may account for the inconsistency. The Inconel assembly was repaired during manufacture because of delamination between the skin and honeycomb core. This may have been caused by insufficient braze alloy, which would have reduced conducting material and consequently the heat transfer. The resulting lack of metallic continuity where the skins were delaminated would also contribute to lower inner skin temperatures.

A further inconsistency existed in the test data. The primary flow side thermocouple 8 on the Inconel honeycomb, which was paired with thermocouple 9 on the inner skin, did not record during the test, and so only the temperature from thermocouple 16, which was located diametrically opposite, was available to establish the skin temperature and differential across the Inconel honeycomb. This may have resulted in some error caused by hot streaking in the exhaust gas primary flow. Without further test data, evaluation and analysis of the Inconel honeycomb panel are inconclusive. However, heat transfer coefficients were estimated for the tested assembly using simplified methods. The heat transfer coefficients derived from the test results are compared to the predicted coefficients in table 30.

Maximum surface temperatures recorded were less than the allowable design temperatures for the titanium and Inconel honeycomb panels (see table 31).

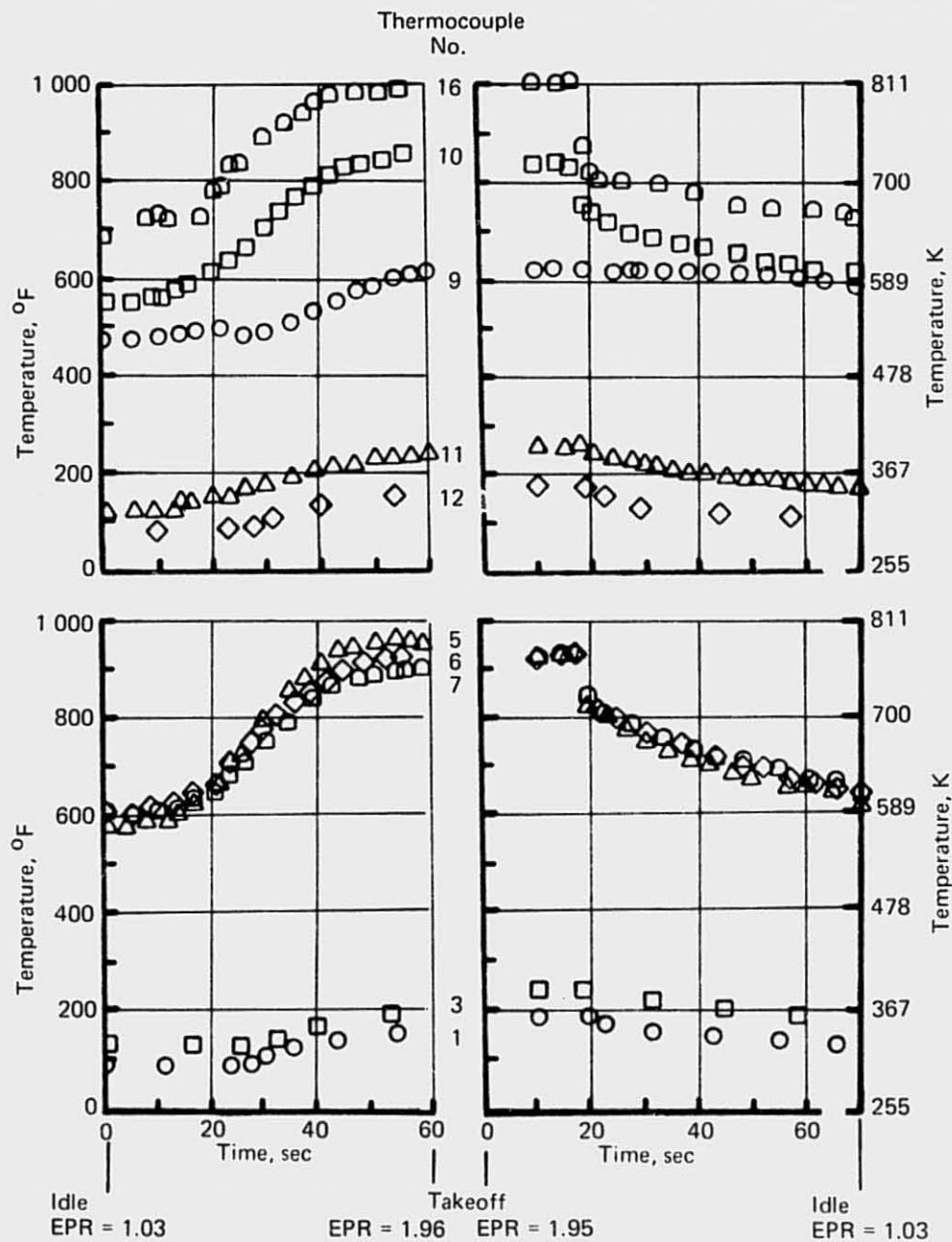
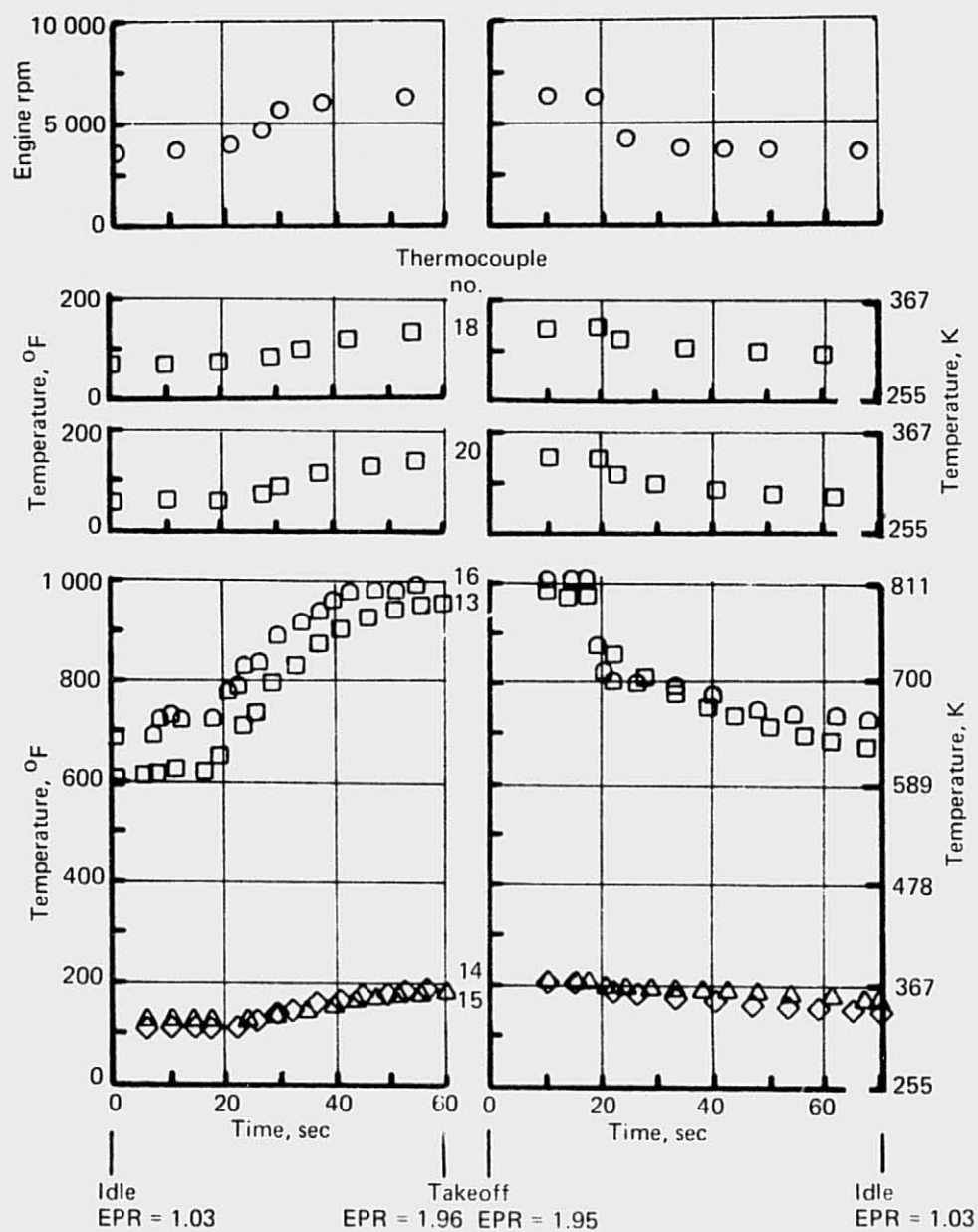


Figure 202.—JT8D-115 Ground Test—Exhaust System Assembly Thermocouple Temperature Trace—Idle to Takeoff to Idle





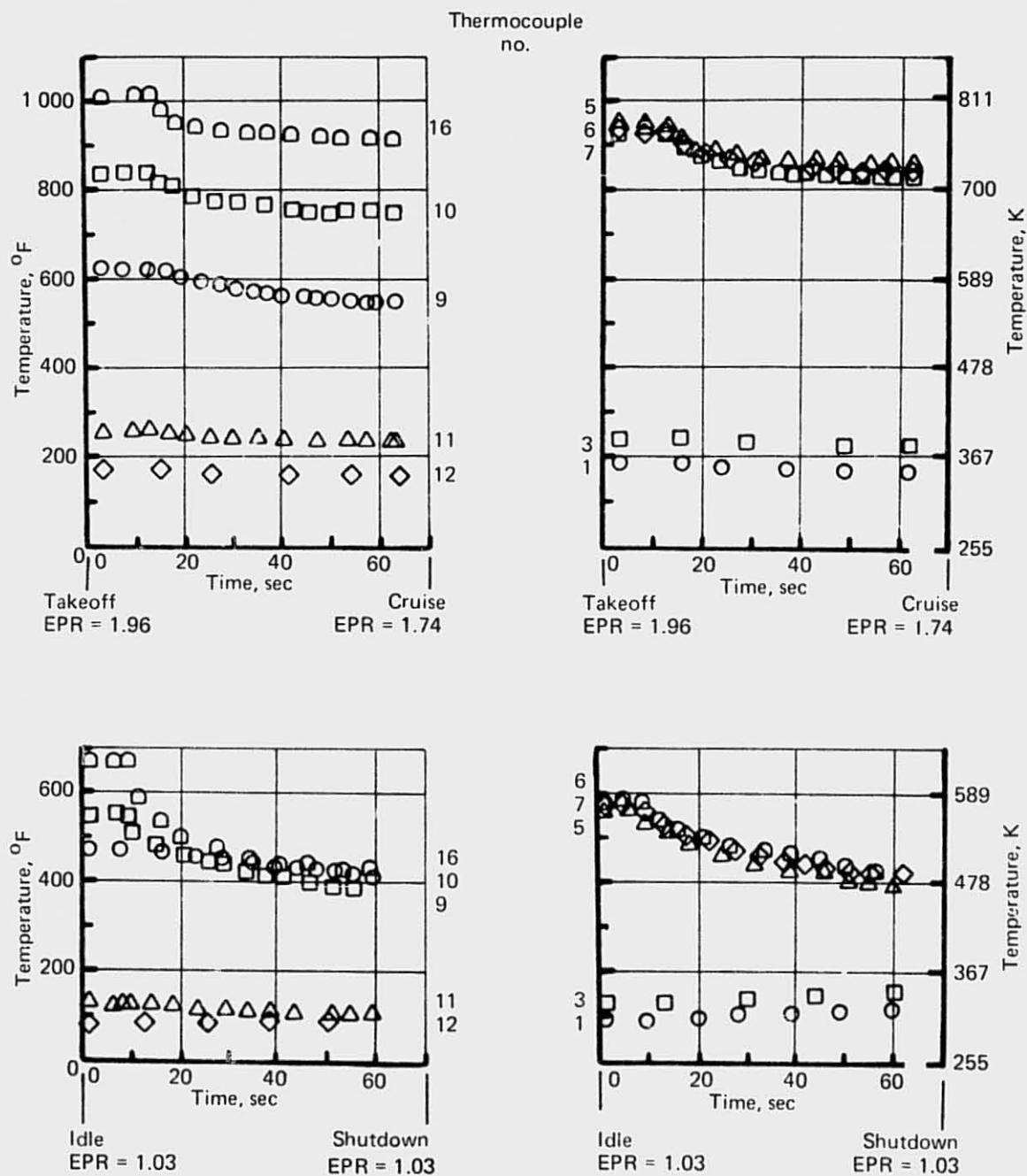


Figure 203.—JT8D-115 Ground Test—Fan/Primary Flow Divider Thermocouple Temperature Trace—Takeoff to Cruise and Idle to Engine Shutdown

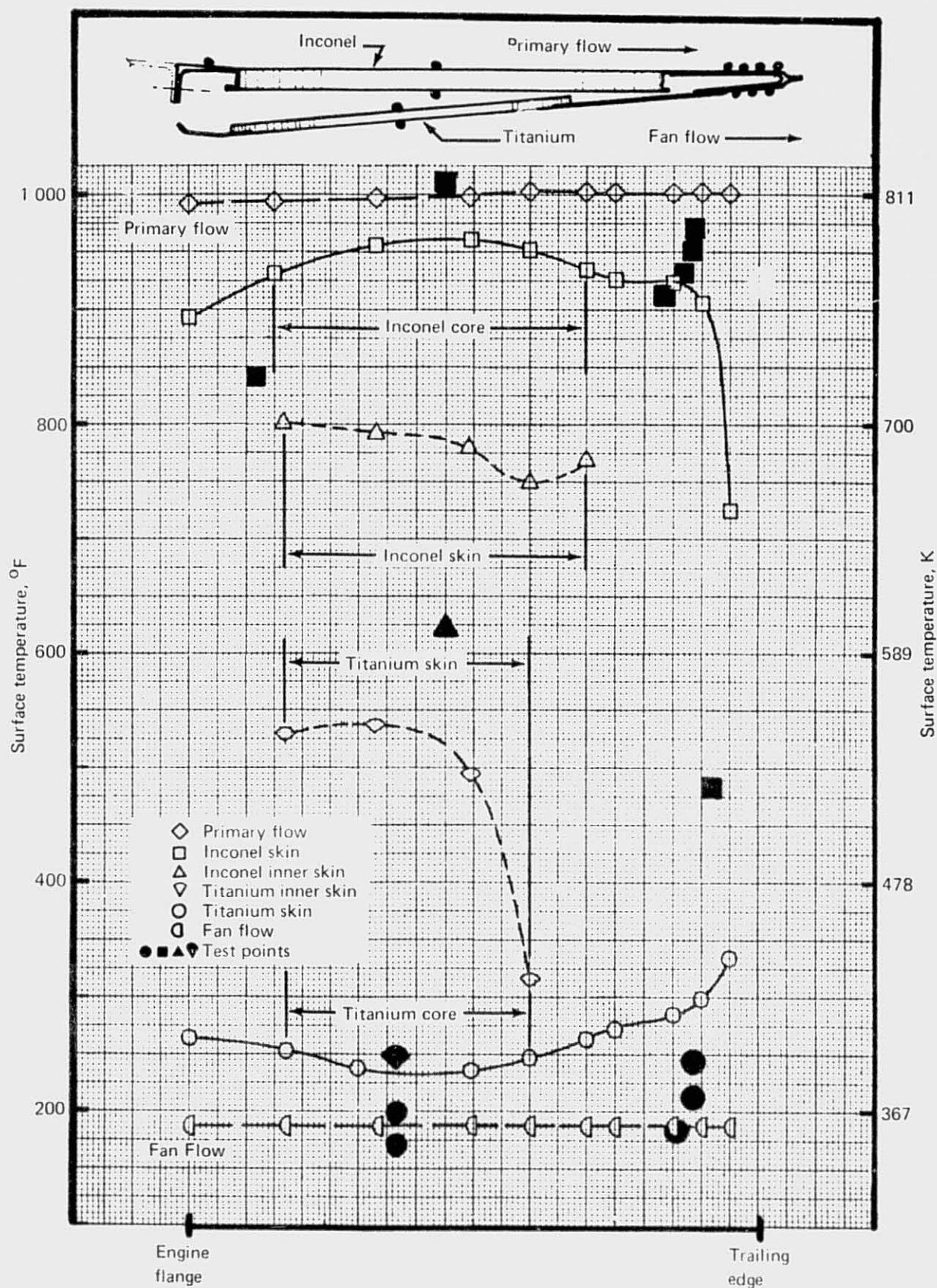


Figure 204.—JT8D-115 Ground Test—Fan/Primary Divider Temperature Test—Analysis Correlation—Engine EPR = 1.93

*Table 30.—JT8D-115 Ground Test — Comparison of  
Test and Predicted Heat Transfer Coefficients, Engine EPR = 1.96*

Item	Heat transfer coefficient					
	Test		Thermal analysis results		Predicted test configuration	
	Btu/ft <sup>2</sup> hr	W/m <sup>2</sup>	Btu/ft <sup>2</sup> hr	W/m <sup>2</sup>	Btu/ft <sup>2</sup> hr	W/m <sup>2</sup>
Titanium honeycomb	17.0	53.592	7.5	23.644	15.0	47.287
Air gap	7.3	23.013	18.0	56.745	9.0	28.372
Inconel honeycomb	3.75	11.823	13.9	43.820	13.9	43.820

*Table 31.—JT8D-115 Ground Test — Maximum Recorded Temperature on Titanium and  
Inconel Honeycomb, Engine EPR = 1.96*

Item	Thermocouple	Test temperature		Design allowable	
		°F	K	°F	K
Titanium honeycomb	11	259	399.44	800	700.00
Inconel honeycomb	16	1029	827.22	1200	922.22



## 5.0 SUMMARY OF RESULTS AND CONCLUSIONS

The JT8D-15 and JT8D-115 ground static test program provided results in the major areas of: (1) propulsion performance, including static thrust and specific fuel consumption (SFC), inlet and exhaust system component performance, and engine surge margins; (2) acoustic performance, including static component noise increments between the two engines, refan lining attenuation, and measurement repeatability; and (3) structural data, encompassing JT8D-115 center-engine inlet duct loads and deflections, and JT8D-115 exhaust system thermal environment.

The ultimate use of these results is realized in the analysis and prediction of 727 airplane performance and noise characteristics with the JT8D refan engine. The major ground test results and conclusions are presented in this section.

### 5.1 PROPULSION

The static SFC at takeoff thrust of the JT8D-115 is 12.5% to 13.2% lower than the JT8D-15 for side-engine inlets with and without a ring.

The JT8D-115 center- and side-engine inlet total pressure recoveries were found to be as predicted from model scale tests. At a corrected takeoff airflow of 470 lb/s (213 kg/s), recoveries (relative to the reference bellmouth inlet) for the center-engine inlet, the side-engine inlet with ring, the side-engine inlet without ring were 0.984, 0.9925, and 0.995, respectively.

The JT8D-115 center-engine inlet and side-engine inlet without ring gave a low pressure compressor (LPC) surge margin nearly the same as for the reference bellmouth inlet at static conditions. A 90° crosswind of 20 kn (16.3 m/s) degraded the LPC surge margin 4% relative-to-static conditions.

The flight-type exhaust system and the reference exhaust system were found to have identical gross thrust coefficients over the full range of nozzle pressure ratios from 1.2 to 1.95. The flow coefficient of the flight nozzle was found to be 0.0035 higher than that of the reference nozzle.

Statistical analysis of the propulsion performance data showed that propulsion data accuracy and repeatability were close to those anticipated: with 95% confidence, mass flow accuracy was within 0.5% of full scale and thrust accuracy within 0.25% of full scale.

### 5.2 ACOUSTIC

Analysis of component noise data showed that the fully treated JT8D-115 engine (and nacelle) produced a reduction of 6 to 7 PNdB in a weighted average value of tone corrected perceived noise level (PNLTW), relative to the JT8D-15 hardwall engine compared at equal static thrust. Separated into noise components, the JT8D-115 showed significant noise

reduction in inlet fan noise, aft fan noise, exhaust duct flow noise, turbine noise, and jet noise relative to the JT8D-15; however, core noise was increased. The jet noise reduction of 5 to 6 PNdB is due entirely to the JT8D-115 cycle modifications, while the inlet and aft-fan noise reductions are attributed primarily to acoustic lining attenuation.

The lining attenuation characteristics for the JT8D-115 inlet acoustic treatments were found to be generally as predicted. The treated side-engine inlet with ring gave an attenuation in inlet fan noise of 9.5 PNdB at approach power. However, the apparent attenuations of the exhaust system linings were disappointing. Although this is at least partially due to a noise floor, measured internal sound level data showed that the assumed sonic environment design conditions were in error in many cases. Lining redesigns based on this new sonic environment information would be expected to provide some improvement in actual lining attenuation characteristics.

Analysis of acoustic data showed that good acoustic repeatability was achieved for all noise components except inlet fan tones and buzzsaw, providing testing was restricted to accepted weather limits. The large variation in measured inlet fan tone levels is compatible with the Contractor's earlier test experience and is attributed to fluctuations in atmospheric turbulence ingested by the engine in a static mode.

### 5.3 STRUCTURAL

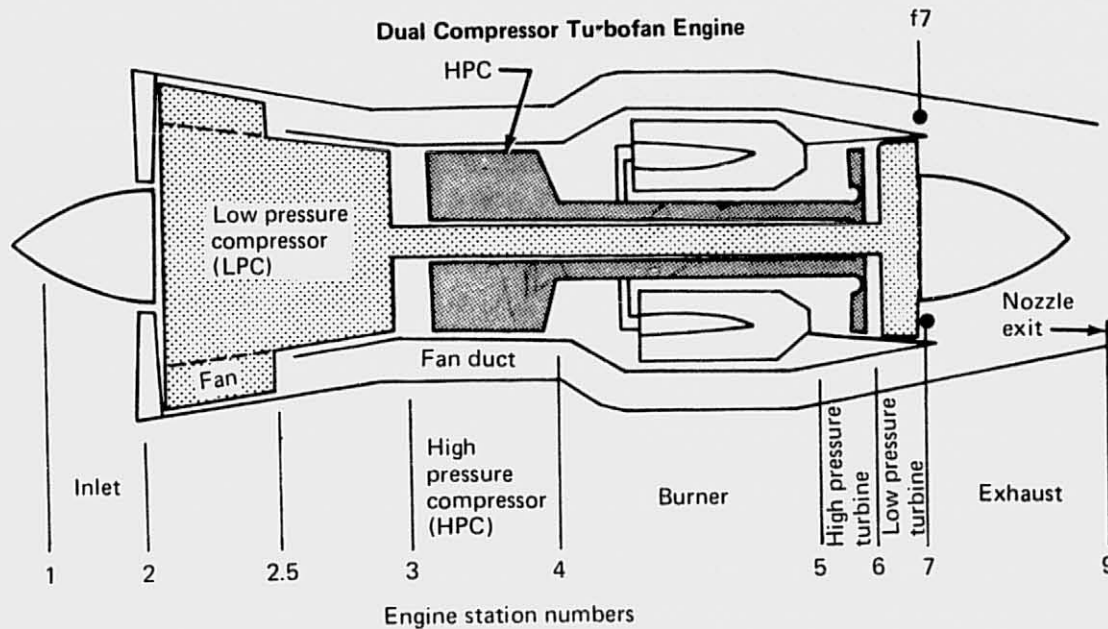
Analysis of structural test data showed that the center-engine inlet duct is subject to 3% lower stabilized pressures and up to 19% higher surge pressures than predicted by the model tests and duct flow analyses.

For the stabilized pressure conditions, the test and analysis deflections were within acceptable tolerances; however, the flexible engine seal surge deflection excursions were higher than anticipated, though still within the seal design movement envelope.

Measured exhaust system hardware temperatures were within the design structural limits. The partial loss of test data for the Inconel honeycomb assembly on the fan/primary flow divider rendered the analysis of the flow divider thermal stresses as qualitative. However, the aluminum-brazed titanium portion of the flow divider would have acceptable durability relative to the predicted thermal stresses while the brazed Inconel honeycomb portion is judged to have marginal durability. Additional testing would be required for verification of this judgment.

## APPENDIX

### SYMBOLS AND ABBREVIATIONS



A	Area
abs	Absolute
$A_F/A_P$	Fan-to-primary area ratio at mixing plane of the exhaust streams
$A_{je}$	Effective nozzle exit area
$A_j, A_g$	Nozzle exit area
Baud	Unit of communications measurement and a number of adjacent bits that contain an element of intelligence
BPF	Blade passing frequency
BPR	Bypass ratio, $W_{af}/W_{ap}$
B.S.	Body station (longitudinal location)
Btu	British thermal unit
CAR	Civil Air Regulations
$C_d$	Nozzle discharge coefficient

CDC	Control Data Corporation
$C_g$	Nozzle gross thrust coefficient
$C_L$	Centerline
cm	Centimeter
CORGE	Core noise correlation parameter, $\log \left[ \sqrt{W_{pri}} \left( \frac{P_{t4}/14.7}{T_{t4}/519} \right) (T_{t5} - T_{t4}) \right]$
$C_{Pf}$	Specific heat at constant pressure of fuel evaluated at $T_{t2}$ temperature
$C_{P2}$	Specific heat at constant pressure of air evaluated at $T_{t2}$ temperature
$C_{P7}$	Specific heat at constant pressure of air evaluated at $T_{tm7}$ temperature
$C_V$	Nozzle velocity coefficient
daN	Dekaneutron
dB	Decibel re 0.0002 $\mu$ bar
deg, °	Degree (unit of plane angular increment)
dia	Diameter
$D_w$	Wind direction
$D(\theta)$	Directivity factor
EGT	Exhaust gas temperature
EGV	Exit guide vane
EPNL	Effective perceived noise level
EPR	Engine pressure ratio, $P_{t7}/P_{t2}$
f	Frequency
FAA	Federal Aviation Administration
FAR	Federal Aviation Regulation
$F_g$	Gross thrust
$F_g/\delta_{amb}$	Corrected gross thrust



$F_n$	Net thrust
$F_n/\delta$	Corrected net thrust
$f_{\text{peak}}$	Peak frequency
FPR	Fan pressure ratio including fan exit guide vane loss, $P_{t2.5}/P_{t2}$
$F_{\text{sg}}$	Fuel specific gravity
ft	Foot, feet
fwd	Forward
$f_x, f_y$	Sound pressure functions
$^{\circ}\text{F}$	Degrees Fahrenheit
$g$	Acceleration due to gravity
gal	U. S. gallon
gpm	Gallons per minute
HPC	High pressure compressor
HP1	First turbine stage
hr	Hour
$H_v$	Fuel lower heating value
Hz	Hertz
IGV	Inlet guide vane
in.	Inch
K	Kelvin
kg	Kilogram
kHz	Kilohertz
km	Kilometer
kN	Kilonewton

kn	Knot, nautical mile per hour
KTS	KRONOS time sharing computer system
lb	Pound
loc	Location
LPC	Low pressure compressor
LP2	Second turbine stage
LP3	Third turbine stage
LP4	Fourth turbine stage
m	Meter
max	Maximum
mech	Mechanical
min	Minute
mm	Millimeter
mph	Miles per hour
N	Newton
n	Velocity exponent
$N_c$	Efficiency of combustion (assumed to be equal to 1.0)
nmi	Nautical mile
$N_1$	Mechanical low pressure compressor rotor speed
$N_1/\sqrt{\theta_{t2}}$	Corrected low pressure compressor rotor speed
$N_2$	Mechanical high pressure compressor rotor speed
OASPL	Overall sound pressure level
OB	Octave band
OBSPL	Octave band sound pressure level

O.L.	Operating line
P&WA	Pratt & Whitney Aircraft
$P_a, P_{amb}$	Ambient pressure
$P_b$	Burner static pressure
PNdB	Perceived noise in decibels
PNL	Perceived noise level
PNLT	Tone corrected perceived noise level
PNLTW	Weighted value of tone corrected perceived noise level
psi	Pounds per square inch
psig	Pounds per square inch (gage)
$P_{s2}$	Static pressure at engine station 2
$P_{s3}$	Static pressure at LPC discharge
$P_{s4}$	Static pressure at HPC discharge
$P_{tf7}$	Fan duct total pressure at engine station 7
$P_{tm7}$	Empirical mixed total pressure of $P_{t7}$ and $P_{tf7}$
$P_{tm8}$	100%-theoretical mixed total pressure
$P_{t1}$	Total pressure at inlet entrance
$P_{t2}$	Total pressure at engine station 2
$P_{t3}$	Total pressure at LPC discharge
$P_{t4}$	Total pressure at HPC discharge without bleed flow
$P_{t5}$	Total pressure at turbine inlet
$P_{t7}$	Total pressure at LP-turbine outlet
$P_{xx}, P_{yy}$	Auto power spectra
$P_{xy}(\omega)$	Cross power spectrum

$P_0$	Standard sea level day ambient pressure
$^{\circ}\text{R}$	Degrees Rankine
$r^2$	Coherence function
re	Reference value
ref	Reference
RH	Relative humidity
rms	Root mean square
rpm	Revolutions per minute
RTS	Relative fan tip Mach number
s, sec	Seconds
SDDS	Standard Digital Data System
SFC	Specific fuel consumption
SI	Système Internationale
SPL	Sound pressure level
$\text{SPL}_{\text{peak}}$	Peak sound pressure level
Sta	Station
sym	Symbol
T, t	Time
$T_a, T_{\text{amb}}$	Ambient temperature
$T_{\text{fuel}}$	Fuel temperature
TPR	Overall turbine pressure ratio, $P_{t5}/P_{t7}$
TSFC	Thrust specific fuel consumption
$T_{t7}$	Fan duct total temperature at engine station 7
$T_{tm7}$	Mixed total temperature of $T_{t7}$ and $T_{tf7}$



$T_{tm8}$	100%-theoretical mixed total temperature
$T_{t8e}$	Primary flow ideal total temperature at nozzle exit plane
typ	Typical
$T_0$	Standard sea level day ambient temperature
$T_{t2}$	Total temperature at engine station 2
$T_{t4}$	Total temperature at HPC discharge
$T_{t5}$	Total temperature at turbine inlet
$T_{t7}$	Total temperature at LP-turbine outlet
VG	Vortex generator
$V_{pri}$	Primary jet fully expanded velocity
$V_{sec}$	Secondary jet fully expanded velocity
$V_w$	Wind velocity
W	Watt
$W_a, W_{at}$	Total airflow
$W_a \sqrt{\theta_{t2}/\delta_{t2}}$	Corrected total airflow
$W_{af}$	Fan airflow
$W_{ap}$	Primary (engine) airflow
$w_f$	Engine fuel flow
$W_{pri}$	Primary jet weight flow
$W_{sec}$	Secondary jet weight flow
$\alpha$	Wind angle relative to engine centerline ( $0^\circ$ down inlet); $+\alpha$ from the acoustic field during JT8D-15 testing; $-\alpha$ from the acoustic field during JT8D-115 testing
$\gamma$	Ratio of specific heats
$\Delta$	Delta (increment of change)

$\delta_a, \delta_{amb}$	$P_{amb}/P_0$
$\delta_{t2}$	$P_{t2}/P_0$
$\delta_5$	$P_{t5}/2116$
$\theta$	Directivity angle
$\theta_{t2}$	$T_{t2}/T_0$
$\theta_5$	$T_{t5}/519$
$\sigma$	Statistical standard deviation
$\tau$	Time
$\phi_{xy}$	Cross correlation function
$\omega$	Angular frequency
%	Percent

## DEFINITIONS

Nacelle	As used in this document, the engine nacelle includes all components of an externally mounted propulsion package, including the engine plus all engine-mounted parts and accessories; the inlet, cowling, and thrust reverser (i.e., all components suspended from the engine mounts).
Strut	A structure that separates and supports the nacelle externally from the airframe, including primary and secondary structure and provisions for installation of airplane and engine systems components.
Accessories	Components required for engine operation and airplane systems components, which are mounted on the engine and strut.
Engine	The dry engine provided by P&WA.
Inlet assembly/ side-engine nose cowl	The portion of the nacelle forward of the fan case, including internal and external fairings and all components attached and normally removed with the inlet assembly/nose cowl.
Thrust reverser	The structure and mechanisms required to reverse engine thrust.
727-200	The current production model 727-200 airplane, with a BRGW of 172 500 lb (78 245 kg), which was used as the baseline in the evaluation of the refan concept.
727 refan	The 727-200 airplane equipped with JT8D-109 (refan) engines and having a BRGW of 172 500 lb (78 245 kg). This airplane/engine combination was derived through analysis.
JT8D	<p>The P&amp;WA JT8D parent engines used as the baseline in the evaluation of the refan concept included the JT8D-9 and JT8D-15 untreated engines with hardwall nacelles.</p> <ul style="list-style-type: none"><li>• The JT8D-9 was selected for use as the baseline in the analysis of the 727 refan airplane because of its wide usage in the current airplane fleet.</li><li>• The JT8D-15 engine was selected for use as the baseline in the full-scale ground tests because of its availability from the Contractor's inventory at greatly reduced program costs compared to a JT8D-9 engine.</li></ul> <p>For brevity in this final report, these parent engines will be referred to as the JT8D except when it is important to establish specific identification; then they will be referred as JT8D-9 and JT8D-15.</p>

JT8D refan	<p>The refanned P&amp;WA JT8D-100 series engines developed from JT8D parent engines during the Refan Program included the JT8D-109 and JT8D-115 engines.</p> <ul style="list-style-type: none"> <li>• The JT8D-109 is the refan derivative of the JT8D-9 engine and was used in the analysis of the 727 refan airplane.</li> <li>• The JT8D-115 was selected for full-scale ground test because of the availability of the JT8D-15 parent engine. The JT8D-115 was tested with a wide variety of nacelle hardware; therefore, the name JT8D-115 does not imply any specific nacelle but does imply peripheral engine treatment in the fan duct and fan case.</li> </ul> <p>For brevity in this final report, these refanned engines will be referred to as JT8D refan except when it is important to establish specific identification; then they will be referred to as JT8D-109 (or JT8D-109 with treated nacelle or JT8D-109 with hardwall nacelle) and JT8D-115.</p>
Reference hardware	<p>The P&amp;WA bellmouth inlet (inlet lip, diffuser, and nose dome) and exhaust system (exhaust duct, fan/primary flow divider, and plug) without acoustical treatment, which was used as a calibration reference during the full-scale ground tests.</p>
Flight-type exhaust system	<p>The Contractor's exhaust duct (wedge duct and nozzle) with peripheral acoustic treatment, fan/primary flow divider (splitter) with acoustic treatment on both the fan and primary flow sides, and plug.</p>
Hybrid exhaust system	<p>The Contractor's flight-type exhaust duct (treated wedge duct and nozzle) and the P&amp;WA reference (hardwall) fan/primary flow divider (splitter) and plug.</p>



## EQUATIONS

### GROSS THRUST:

$$\begin{aligned} F_g &= \text{Measured Thrust} + \text{Wind Correction} \\ F_g &= (F)_{\text{measured}} + W_a V_w \cos \alpha \end{aligned}$$

### CORRECTED FUEL FLOW:

$$\frac{W_f \text{ HVR}}{\delta_{t2} \text{ KC KH}} = \frac{[(W_{f1} + W_{f2}) / 2] \text{ HVR}}{\delta_{t2} \text{ KC KH}}$$

where:

$$\begin{aligned} W_{f1} &= \text{fuel flow indicated by flow meter no. 1} \\ W_{f2} &= \text{fuel flow indicated by flow meter no. 2} \\ \text{KC} &= \text{fuel flow temperature correction factor supplied by P\&WA} \\ \text{KH} &= \text{specific humidity correction factor supplied by P\&WA} \\ \text{HVR} &= \text{fuel lower heating value ratio, } H_V / H_{V0} \\ H_V &= \text{fuel lower heating value of test fuel} \\ H_{V0} &= \text{standard fuel lower heating value} \end{aligned}$$

### CORRECTED TOTAL AIRFLOW:

$$\frac{W_a \sqrt{\theta_{t2}}}{\delta_{t2}} = \text{Based on calibrated P\&WA bellmouth inlets for JT8D-15 and JT8D-115 engines. Airflow for flight-type inlets were obtained for the corrected } W_a \text{ versus correct LPC rotor speed relationship determined with P\&WA bellmouth/reference exhaust system tests.}$$

### ENGINE STATION 2 TOTAL PRESSURE:

$$P_{t2} = P_{\text{amb}} \text{ for P\&WA bellmouth inlets and the Boeing side-engine inlet (without inlet ring, with bellmouth lip); for side-engine inlet (with ring and/or production lip); } P_{t2} \text{ was determined from model test recovery curve; with inlet pressure survey rake installed, } P_{t2} \text{ is the area-weighted average of the 80 total pressure probes.}$$

EMPIRICAL MIXED TOTAL PRESSURE:

$$\begin{aligned}P_{tm7} &= (P_{t7} + 0.8 P_{tf7})/1.8 \text{ for JT8D-15 engine} \\P_{tm7} &= (P_{t7} + 1.35 P_{tf7})/2.35 \text{ for JT8D-115 engine}\end{aligned}$$

EMPIRICAL MIXED TOTAL TEMPERATURE:

$$\begin{aligned}T_{tm7} &= (T_{t7} + T_{tf7})/2.0 \text{ for JT8D-15 engine;} \\&\text{and for JT8D-115 engine, see equation (3)}\end{aligned}$$

THRUST SPECIFIC FUEL CONSUMPTION:

$$TSFC = \frac{W_f \text{ HVR}}{F_g \text{ KC KH}}$$

NOZZLE GROSS THRUST COEFFICIENT:

$$C_g = F_g / (W_{ai} V_i)$$

where:

$$\begin{aligned}W_{ai} &= \text{ideal nozzle mass flow based on } P_{tm7}, T_{tm7}, \text{ and } A_j \\V_i &= \text{ideal fully expanded jet velocity based on } P_{tm7} \text{ and } T_{tm7}\end{aligned}$$

NOZZLE DISCHARGE COEFFICIENT:

$$C_d = W_{an} / W_{ai}$$

where: nozzle airflow,  $W_{an} = W_f + W_a$

NOZZLE VELOCITY COEFFICIENT:

$$C_v = C_g / C_d$$

CERTIFICATION DISTORTION:

$$\text{Certification distortion} = (P_{t2} - P_{t \min}) / P_{t2}$$

where:  $P_{t \min}$  = lowest total pressure measured by the 80 probe rake

CERTIFICATION RECOVERY:

$$\text{Certification recovery} = P_{t2} / P_{t1}$$

where:  $P_{t2}$  = area-weighted average of the 80-probe rake

P&WA DISTORTION PARAMETERS: (Based on steady-state data for this report)

$$\text{Radial distortion} = \frac{(P_t)_{\text{max ring avg}} - (P_t)_{\text{local ring avg}}}{(P_t)_{\text{max ring avg}}}$$

where: ring averages are taken over a full  $360^\circ$

$$\text{Circumferential distortion} = \frac{(P_t)_{\text{ring avg}} - (P_t)_{\text{min sector avg}}}{(P_t)_{\text{ring avg}}}$$

where: ring averages are taken over a full  $360^\circ$  and minimum sector averages are the lowest average total pressure at a given radius for the sector of concern (either a  $60^\circ$  or  $180^\circ$  sector).

WEIGHTED AVERAGE VALUE OF TONE-CORRECTED PERCEIVED NOISE LEVEL (PNLTW)

$$\text{PNLTW} = 10 \log \sum_{i=1}^N \left\{ 10 \left[ \frac{\text{PNLT}_i}{10} \right] \sin^2 \theta_i \right\}$$

where:  $\text{PNLT}_i$  is the sideline PNLT computed from values measured at the angle  $\theta_i$ .

Table A-1.—JT8D-15 Ground Test — Engine Performance Parameters Used in Noise Analysis

$N_1/\sqrt{\theta_{t2}}$ (rpm)	EPR	$F_g/\delta$		FPR	RTS	$W_{pri}$		$V_{pri}$		$W_{sec}$		$V_{sec}$		TPR	$T_{t8e}$	
		lb	(N)			lb/s	(kg/s)	ft/s	(m/s)	lb/s	(kg/s)	ft/s	(m/s)		$^{\circ}R$	K
5000	1.19	3 600	(16 013)	1.28	0.75	84	(38.1)	800	(243.8)	113	(51.3)	640	(195.1)	4.15	1135	(630)
6000	1.34	6 000	(26 688)	1.48	0.91	90	(40.8)	1060	(323.1)	133	(60.3)	790	(240.8)	5.40	1180	(656)
6500	1.45	7 000	(31 136)	1.54	0.985	104	(47.2)	1210	(368.8)	143	(64.9)	870	(265.2)	5.95	1225	(681)
7000	1.62	9 600	(42 701)	1.69	1.07	118	(53.5)	1400	(426.7)	158	(71.7)	970	(295.7)	6.40	1315	(731)
7500	1.82	12 100	(53 821)	1.86	1.16	135	(61.2)	1610	(490.7)	169	(76.7)	1080	(329.2)	6.75	1400	(778)
8000	2.01	14 400	(64 051)	1.98	1.25	153	(69.4)	1790	(545.6)	172	(78.0)	1150	(350.5)	7.10	1480	(822)
8500	2.17	16 000	(71 168)	2.04	1.33	170	(77.1)	1910	(582.2)	165	(74.8)	1200	(365.8)	7.45	1540	(856)

Table A-2.—JT8D-115 Ground Test — Engine Performance Parameters Used in Noise Analysis

$N_1/\sqrt{\theta_{t2}}$ (rpm)	EPR	$F_g/\delta$		FPR	RTS	$W_{pri}$		$V_{pri}$		$W_{sec}$		$V_{sec}$		TPR	$T_{t8e}$		CORGE
		lb	(N)			lb/s	(kg/s)	ft/s	(m/s)	lb/s	(kg/s)	ft/s	(m/s)		$^{\circ}R$	K	
4000	1.14	3 700	(16 458)	1.14	0.78	61	(27.7)	660	(201.2)	170	(77.1)	450	(137.2)	4.05	1105	(614)	4.18
4500	1.18	4 700	(20 906)	1.18	0.88	69	(31.3)	770	(234.7)	193	(87.5)	510	(155.4)	4.6	1145	(636)	4.29
5000	1.24	6 000	(26 688)	1.225	0.975	78	(35.4)	890	(271.3)	214	(97.1)	570	(173.7)	5.1	1185	(658)	4.40
5500	1.33	7 800	(34 694)	1.295	1.08	92	(41.7)	1040	(317.0)	240	(108.9)	650	(198.1)	5.8	1240	(689)	4.53
6000	1.44	9 900	(44 035)	1.375	1.185	106	(48.1)	1200	(365.8)	265	(120.2)	725	(221.0)	6.4	1310	(728)	4.65
6500	1.58	12 400	(55 155)	1.46	1.29	122	(55.3)	1380	(420.6)	287	(130.2)	800	(243.8)	6.95	1380	(767)	4.78
7000	1.74	15 100	(67 165)	1.55	1.41	138	(62.6)	1550	(472.4)	309	(140.2)	875	(266.7)	7.35	1450	(806)	4.89
7500	1.90	17 400	(77 395)	1.63	1.52	154	(69.9)	1710	(521.2)	322	(146.1)	930	(283.5)	7.65	1530	(850)	4.97

TABLES A-1 THROUGH A-12

REPRODUCIBILITY OF THE  
ORIGINAL PAGE IS POOR



Table A-3.—JT8D-15 Ground Test — 1F1H First Fan BPF Inlet Radiated Noise at 150 ft (45.72 m) Polar

10°		20°		30°		40°		50°		60°		70°		80°		90°		100°	
FPR · 1	SPL	FPR · 1	SPL	FPR · 1	SPL	FPR · 1	SPL	FPR · 1	SPL	FPR · 1	SPL	FPR · 1	SPL	FPR · 1	SPL	FPR · 1	SPL	FPR · 1	SPL
0.02	58.9	0.02	60.9	0.02	57.2	0.02	50.9	0.02	49.9	0.02	44.9	0.02	43.9	0.02	40.2	0.02	39.3	0.02	34.9
0.115	58.9	0.10	60.9	0.07	61.6	0.068	67.9	0.068	71.4	0.068	70.9	0.068	64.9	0.068	60.9	0.068	59.4	0.068	52.9
0.21	75.9	0.20	89.9	0.21	88.4	0.12	64.9	0.12	69.9	0.12	69.4	0.12	62.4	0.12	57.9	0.12	54.9	0.12	52.9
0.32	79.9	0.26	79.9	0.26	86.9	0.26	87.4	0.215	82.7	0.26	73.9	0.17	63.9	0.26	67.9	0.215	65.9	0.185	61.9
0.38	84.9	0.32	89.9	0.35	81.9	0.32	79.9	0.26	78.9	0.32	78.9	0.38	75.9	0.375	69.4	0.32	65.9	0.32	61.9
0.50	56.9	0.50	64.9	0.50	75.9	0.50	74.9	0.50	78.9	0.50	71.9	0.50	66.9	0.50	54.9	0.50	53.9	0.50	46.9

Notes: The listed SPL values = (measured 1/3-OB levels minus 20 log D minus vane spacing correction).  
For dB levels beyond 100°, linearly extrapolate the noise levels determined for 90° and 100°.

Table A-4.—JT8D-15 Ground Test — 2F1H Second Fan BPF Inlet Radiated Noise at 150 ft (45.72 m) Polar

10°		20°		30°		40°		50°		60°		70°		80°		90°		100°	
FPR · 1	SPL	FPR · 1	SPL	FPR · 1	SPL	FPR · 1	SPL	FPR · 1	SPL	FPR · 1	SPL	FPR · 1	SPL	FPR · 1	SPL	FPR · 1	SPL	FPR · 1	SPL
0.02	60.9	0.02	61.9	0.02	61.9	0.02	58.9	0.02	64.9	0.02	63.9	0.02	58.4	0.02	58.9	0.02	55.9	0.02	51.9
0.068	60.9	0.068	61.9	0.12	74.9	0.12	77.4	0.12	74.7	0.12	60.9	0.068	50.1	0.068	45.9	0.068	46.2	0.068	43.9
0.17	69.9	0.12	74.4	0.17	65.4	0.173	67.9	0.21	61.9	0.17	58.9	0.12	54.7	0.12	50.9	0.13	50.4	0.21	41.4
0.21	69.4	0.26	68.4	0.215	65.4	0.215	72.9	0.26	60.3	0.21	58.9	0.17	53.9	0.17	52.4	0.26	48.9	0.26	46.9
0.375	62.4	0.38	62.9	0.26	71.4	0.26	62.9	0.32	64.9	0.375	54.4	0.26	55.9	0.215	48.4	0.315	43.9	0.315	41.9
0.50	43.9	0.50	43.9	0.50	48.9	0.50	57.9	0.50	52.9	0.50	48.9	0.50	46.9	0.50	42.9	0.50	43.9	0.50	37.9

Notes: The listed SPL values = (measured 1/3-OB levels minus 20 log D minus vane spacing correction).  
For dB levels beyond 100°, linearly extrapolate the noise levels determined for 90° and 100°.

Table A-5.—JT8D-15 Ground Test — 1F2H  $\Delta$  First Fan (Second-First Harmonic) Inlet Radiated at 150 ft (45.72 m) Polar

10°		20°		30°		40°		50°		60°		70°		80°		90°		100°	
FPR -1	SPL	FPR -1	SPL	FPR -1	SPL	FPR -1	SPL	FPR -1	SPL	FPR -1	SPL	FPR -1	SPL	FPR -1	SPL	FPR -1	SPL	FPR -1	SPL
0.02	+12.5	0.02	+11.5	0.02	+10.5	0.02	+7.0	0.02	+5.0	0.02	+4.5	0.02	0.0	0.02	+4.0	0.02	+7.0	0.02	-1.5
0.12	+19.0	0.068	+17.3	0.12	+2.0	0.068	-1.5	0.068	-9.5	0.068	-11.0	0.068	-9.0	0.068	-4.5	0.068	-10.0	0.12	-3.5
0.17	+11.5	0.12	+10.0	0.17	-2.0	0.12	+15.5	0.12	+0.5	0.12	-1.5	0.12	-7.0	0.17	-3.5	0.12	-2.0	0.215	-8.2
0.26	+7.0	0.17	-3.2	0.218	-7.3	0.26	-5.5	0.17	-5.5	0.17	+2.0	0.17	+2.5	0.26	-14.0	0.17	-6.8	0.26	-5.5
0.32	-5.0	0.26	-6.5	0.315	-6.7	0.375	-5.5	0.215	-1.0	0.30	-7.0	0.215	-5.5	0.32	-11.3	0.21	-12.5	0.32	-12.5
0.50	-17.0	0.50	-17.0	0.50	-17.0	0.44	-15.0	0.50	-15.0	0.50	-15.0	0.40	-17.0	0.40	-15.0	0.40	-17.0	0.50	-17.0

Notes: For 110°, 120°, 130°, and 140°, Use the Table for 100° and Apply the Increment to Previously Calculated Values for Fan Tone at Those Angles.

First fan third harmonic (1F3H) inlet noise:

- The third harmonic will necessarily be calculated after the second harmonic values have been calculated for all angles.
- All values for the third harmonic will be established as 7 dB lower than the second harmonic for same locations.

Table A-6.—JT8D-15 Ground Test — 2F2H  $\Delta$  Second Fan (Second-First Harmonic) Inlet Radiated at 150 ft (45.72 m) Polar

10°		20°		30°		40°		50°		60°		70°		80°		90°		100°	
FPR -1	SPL	FPR -1	SPL	FPR -1	SPL	FPR -1	SPL	FPR -1	SPL	FPR -1	SPL	FPR -1	SPL	FPR -1	SPL	FPR -1	SPL	FPR -1	SPL
0.02	0.0	0.02	-3.5	0.02	-6.5	0.02	-10.5	0.02	-11.0	0.02	-15.0	0.02	-14.0	0.02	-14.0	0.25	-20.0	0.02	-2.0
0.068	-8.5	0.068	-10.0	0.123	-9.5	0.068	-13.8	0.068	-11.0	0.068	-11.5	0.068	-9.0	0.068	-11.5	0.068	-16.0	0.068	-7.0
0.12	-6.0	0.12	-17.0	0.17	-7.5	0.26	-4.5	0.12	-13.4	0.12	-6.0	0.12	-10.5	0.17	-13.5	0.17	-14.0	0.17	-9.5
0.21	9.5	0.17	+2.0	0.26	-12.2	0.32	-11.0	0.17	-3.5	0.17	+2.0	0.21	-0.5	0.21	-8.0	0.21	-5.0	0.215	-12.5
0.30	-11.8	0.215	-13.5	0.32	-10.5	0.38	-13.0	0.21	0.0	0.21	+1.0	0.32	-8.0	0.32	-7.5	0.32	-6.5	0.26	-6.5
0.50	-15.0	0.40	-15.0	0.45	-15.0	0.45	-15.0	0.40	-17.0	0.44	-15.0	0.50	-15.0	0.50	-15.0	0.50	-10.0	0.50	-12.0

Notes: For 110°, 120°, 130°, and 140°, Use the Table for 100° and Apply the Delta to Previously Calculated Values for Fan Tone at These Angles.

Second fan third harmonic (2F3H) inlet noise: Calculate by application of the same method as for third harmonic of the first fan.

Table A-7.—JT8D-15 Ground Test — 1F1H + 2F1H Fans Sum-tone Inlet Radiated at 150 ft (45.72 m) Polar

10°		20°		30°		40°		50°		60°		70°		80°		90°		100°	
FPR -1	SPL	FPR -1	SPL	FPR -1	SPL	FPR -1	SPL	FPR -1	SPL	FPR -1	SPL	FPR -1	SPL	FPR -1	SPL	FPR -1	SPL	FPR -1	SPL
0.02	61.4	0.02	64.4	0.02	68.4	0.02	63.4	0.02	70.4	0.02	68.4	0.02	59.4	0.02	55.4	0.02	44.7	0.02	34.4
0.07	71.0	0.07	68.9	0.068	68.4	0.068	68.9	0.068	65.4	0.068	66.9	0.068	65.9	0.068	52.9	0.068	48.3	0.12	47.9
0.17	65.4	0.12	74.4	0.17	75.4	0.12	77.4	0.12	73.4	0.12	72.4	0.12	59.4	0.12	55.4	0.123	53.2	0.17	44.4
0.21	69.4	0.26	60.4	0.21	70.7	0.17	70.4	0.21	66.4	0.17	67.9	0.17	61.1	0.17	52.4	0.175	45.1	0.28	35.4
0.32	55.4	0.32	59.4	0.375	48.4	0.26	63.4	0.30	57.4	0.32	54.4	0.26	49.9	0.215	46.9	0.263	39.4	0.40	35.4
0.50	44.4	0.50	39.4	0.50	45.9	0.50	43.0	0.50	44.4	0.50	39.4	0.50	41.4	0.44	39.4	0.40	39.4	0.50	35.4

Notes: The listed SPL values = (measured 1/3-OB levels minus 20 log D minus average vane spacing correction for the two fans).

For dB levels beyond 100°, linearly extrapolate the noise levels determined for 90° and 100°.

Table A-8.—JT8D-15 Ground Test — 1F1H First Fan BPF Discharge-Radiated Noise at 150 ft (45.72 m) Polar

40°		50°		60°		70°		80°		90°		100°		110°		120°		130°		140°		150°		160°	
FPR-1	SPL	FPR-1	SPL	FPR-1	SPL	FPR-1	SPL	FPR-1	SPL	FPR-1	SPL	FPR-1	SPL	FPR-1	SPL	FPR-1	SPL	FPR-1	SPL	FPR-1	SPL	FPR-1	SPL	FPR-1	SPL
0.03	47.2	0.025	42.2	0.025	41.5	0.02	48.3	0.02	47.2	0.02	51.0	0.02	54.2	0.025	51.9	0.02	53.9	0.02	55.2	0.02	48.4	0.02	54.2	0.02	53.2
0.068	57.4	0.068	58.2	0.068	57.7	0.17	74.2	0.120	63.9	0.12	70.2	0.123	66.6	0.17	84.2	0.068	66.5	0.17	74.2	0.123	66.9	0.214	70.5	0.214	69.5
0.12	58.7	0.12	57.2	0.12	58.2	0.26	76.7	0.17	76.2	0.21	80.2	0.212	91.2	0.215	77.2	0.12	80.7	0.213	79.2	0.17	67.4	0.26	70.9	0.26	69.9
0.185	75.2	0.20	73.7	0.18	73.7	0.32	75.2	0.26	76.2	0.32	80.2	0.40	80.2	0.26	86.2	0.17	83.2	0.258	73.0	0.213	72.8	0.32	66.6	0.32	65.6
0.302	75.2	0.26	73.7	0.315	73.3	0.37	71.2	0.375	75.2	0.41	78.4	0.45	87.7	0.38	80.2	0.375	81.2	0.32	74.4	0.38	69.7	0.41	66.6	0.41	65.6
0.50	59.2	0.50	63.2	0.50	65.2	0.50	75.2	0.50	86.2	0.50	97.2	0.50	94.2	0.50	87.2	0.50	81.2	0.50	73.2	0.50	75.0	0.50	80.2	0.50	79.2

Note: No narrow-band data were available for 160°.

All values given here for 160° were determined by subtracting 1 dB from the levels at 150°. In turn, for 170° reduce the tone levels by 1 dB below the levels for 160°.

Decrement between 150° and 160° was estimated on the basis of comparing 1/3-OB levels. The listed SPL values = (measured 1/3-OB levels minus 10 log A minus vane spacing correction).

Table A-9.—JT8D-15 Ground Test — 2F1H Second Fan BPF Discharge-Radiated Noise at 150 ft (45.72 m) Polar

40°		50°		60°		70°		80°		90°		100°		110°		120°		130°		140°		150°		160°	
FPR-1	SPL	FPR-1	SPL	FPR-1	SPL	FPR-1	SPL	FPR-1	SPL	FPR-1	SPL	FPR-1	SPL	FPR-1	SPL	FPR-1	SPL	FPR-1	SPL	FPR-1	SPL	FPR-1	SPL	FPR-1	SPL
0.02	47.2	0.02	53.4	0.02	53.7	0.02	56.2	0.02	54.2	0.02	58.2	0.02	60.6	0.02	63.2	0.02	65.9	0.02	59.2	0.02	57.9	0.02	53.6	0.02	53.6
0.068	62.2	0.095	62.8	0.122	57.2	0.215	66.1	0.214	68.7	0.21	72.9	0.12	73.7	0.068	63.2	0.068	70.2	0.12	75.1	0.12	68.4	0.068	55.9	0.068	55.9
0.26	51.9	0.182	54.0	0.213	66.0	0.26	71.4	0.26	77.2	0.26	81.2	0.21	76.2	0.26	78.7	0.26	79.9	0.26	71.2	0.213	60.2	0.124	66.0	0.124	66.0
0.32	53.0	0.26	55.6	0.26	59.1	0.32	72.2	0.375	64.7	0.32	78.7	0.26	79.0	0.32	76.0	0.315	73.2	0.32	62.8	0.26	64.7	0.26	61.0	0.26	61.0
0.375	54.2	0.375	53.6	0.32	58.9	0.426	65.4	0.426	73.6	0.375	84.2	0.315	76.2	0.38	79.2	0.41	79.2	0.41	71.5	0.315	57.2	0.32	53.8	0.32	53.8
0.50	56.5	0.50	62.7	0.50	65.1	0.50	65.4	0.50	73.6	0.50	81.2	0.50	86.2	0.50	91.2	0.50	79.2	0.50	71.5	0.50	74.2	0.50	72.2	0.50	72.2

Notes: No narrow-band data were available for 160°.

The second fan aft tone levels for 160° were made the same as those at 150° on the basis of 1/3-OB data comparisons.

Wherever noise levels for 170° are required, the values will be considered the same as those at 160° for lack of data.

The listed SPL values = (measured 1/3-OB levels minus 10 log A minus vane spacing correction).

Table A-10.—JT8D-15 Ground Test — 1F2H ΔFirst Fan (Second-First Harmonic) Discharge-Radiated Noise at 150 ft (45.72 m) Polar

40°		50°		60°		70°		80°		90°		100°		110°		120°		130°		140°		150°		160°	
FPR-1	SPL	FPR-1	SPL	FPR-1	SPL	FPR-1	SPL	FPR-1	SPL	FPR-1	SPL	FPR-1	SPL	FPR-1	SPL	FPR-1	SPL	FPR-1	SPL	FPR-1	SPL	FPR-1	SPL	FPR-1	SPL
0.02	+3.8	0.02	+6.0	0.02	+7.3	0.02	+5.4	0.02	+7.0	0.02	+2.0	0.02	+1.0	0.02	+1.5	0.02	+5.3	0.02	+6.3	0.02	+9.8	0.02	+5.0	0.02	+5.0
0.122	+2.5	0.068	+1.5	0.122	+2.5	0.17	-1.8	0.214	-9.5	0.17	0.0	0.122	+3.6	0.12	+9.3	0.17	0.0	0.17	+6.3	0.068	+3.0	0.068	-3.5	0.068	-3.5
0.173	-10.4	0.122	+0.3	0.215	-12.7	0.26	-12.5	0.26	-7.5	0.215	-14.5	0.26	-6.7	0.214	+0.5	0.213	-8.0	0.21	-4.5	0.17	+4.4	0.172	+1.0	0.172	+1.0
0.215	-14.4	0.212	-13.2	0.26	-8.7	0.32	-12.2	0.32	-7.5	0.26	-10.2	0.32	-14.5	0.26	-8.5	0.26	-3.0	0.26	-4.5	0.213	-8.7	0.21	-7.5	0.21	-7.5
0.266	-16.8	0.26	-12.6	0.32	-10.2	0.375	-9.0	0.375	-11.7	0.32	-13.2	0.375	-7.0	0.32	-6.0	0.32	-12.8	0.32	-9.8	0.26	-11.2	0.26	-13.0	0.26	-13.0
0.50	-10.0	0.50	-9.1	0.50	-6.0	0.50	-7.8	0.50	-17.5	0.50	-13.6	0.50	-17.0	0.50	-12.5	0.50	-8.5	0.50	-11.6	0.50	-11.2	0.50	-13.0	0.50	-13.0

Note: The second harmonic trends for 150°, 160°, and 170° will all be considered the same since data were not available for 160° and 170°.



Table A-11.—JT8D-15 Ground Test — 2F2H Second Fan (Second-First Harmonic) Discharge-Radiated Noise at 150 ft (45.72 m) Polar

40°		50°		60°		70°		80°		90°		100°		110°		120°		130°		140°		150°		160°	
FPR-1	SPL	FPR-1	SPL	FPR-1	SPL	FPR-1	SPL	FPR-1	SPL	FPR-1	SPL	FPR-1	SPL	FPR-1	SPL	FPR-1	SPL	FPR-1	SPL	FPR-1	SPL	FPR-1	SPL	FPR-1	SPL
0.02	0.0	0.02	-17.0	0.02	-14.4	0.02	-10.7	0.02	-10.4	0.02	-2.5	0.02	-8.4	0.02	-12.8	0.02	-10.7	0.02	-5.0	0.02	-5.0	0.02	-4.4	0.02	-6.4
0.123	+0.8	0.17	-1.0	0.12	-1.6	0.068	-3.1	0.068	-2.6	0.122	-2.5	0.07	+0.8	0.068	-1.5	0.068	+0.5	0.17	-5.0	0.173	-5.0	0.172	-7.7	0.172	-9.7
0.173	+1.7	0.216	-12.2	0.17	-2.7	0.122	-5.9	0.12	-2.8	0.17	-11.2	0.17	-4.2	0.122	+0.2	0.17	+0.7	0.213	-0.5	0.214	-2.2	0.21	-9.5	0.21	-11.5
0.214	-9.1	0.26	-6.0	0.213	-11.3	0.17	-2.8	0.17	-0.2	0.26	-13.3	0.26	-12.6	0.26	-5.7	0.26	-10.0	0.26	-7.6	0.26	-9.4	0.26	-8.0	0.26	-10.0
0.263	-7.0	0.325	-4.8	0.26	-3.8	0.32	-15.5	0.215	-7.8	0.32	-11.5	0.32	-11.0	0.32	-4.5	0.322	-3.2	0.32	-0.5	0.32	+0.6	0.32	+1.5	0.32	-0.5
0.50	-9.8	0.50	-7.7	0.50	-6.5	0.50	-15.5	0.50	-9.7	0.50	-11.5	0.50	-11.0	0.50	-4.5	0.50	-5.7	0.50	-5.5	0.50	-4.2	0.50	-4.5	0.50	-6.5

Notes: For 160° only 1/3-OB data were available.

Based on results of the 1/3-OB data, the decrement values for 160° were simply those from 150° with an increased decrement by 2 dB.

Whenever 2F2H values are required for 170°, use the table for 160° and apply the decrement to the previously calculated 2F1H SPL level for 170°.

Table A-12.—JT8D-15 Ground Test — (1F1H + 2F1H) Fans Sum-Tone Discharge-Radiated Noise at 150 ft (45.72 m) Polar

40°		50°		60°		70°		80°		90°		100°		110°		120°		130°		140°		150°		160°	
FPR-1	SPL	FPR-1	SPL	FPR-1	SPL	FPR-1	SPL	FPR-1	SPL	FPR-1	SPL	FPR-1	SPL	FPR-1	SPL	FPR-1	SPL	FPR-1	SPL	FPR-1	SPL	FPR-1	SPL	FPR-1	SPL
0.02	47.7	0.02	47.7	0.02	49.0	0.02	46.7	0.02	43.2	0.02	52.0	0.02	55.7	0.02	59.9	0.02	63.2	0.02	65.7	0.02	60.2	0.02	53.2	0.02	52.2
0.122	59.7	0.122	58.9	0.122	62.1	0.121	63.5	0.068	66.0	0.122	72.7	0.214	80.5	0.12	77.7	0.068	77.1	0.068	73.1	0.09	63.7	0.068	58.9	0.068	57.9
0.171	56.4	0.17	55.7	0.172	58.7	0.17	62.9	0.17	68.4	0.17	69.7	0.26	71.9	0.17	70.6	0.121	84.8	0.122	72.2	0.17	58.5	0.125	63.9	0.125	62.9
0.215	51.3	0.215	51.7	0.214	60.7	0.20	68.7	0.26	64.3	0.212	73.7	0.32	71.2	0.21	72.5	0.17	71.2	0.17	65.9	0.21	63.7	0.172	55.7	0.172	54.7
0.3	48.9	0.26	49.7	0.32	58.0	0.32	55.7	0.32	63.9	0.32	70.2	0.375	67.7	0.26	71.1	0.26	80.6	0.215	70.7	0.26	59.7	0.30	55.7	0.30	54.7
0.50	43.9	0.50	49.7	0.50	51.0	0.50	55.7	0.50	58.4	0.50	62.7	0.50	61.2	0.50	72.7	0.50	62.7	0.50	56.2	0.50	53.7	0.50	55.7	0.50	54.7

Notes: Pertinent data for 160° and 170° were lacking.

All values given here for 160° were determined by subtracting 1 dB from the levels at 150°.

In turn, for 170°, reduce the tone levels by 1 dB below the levels for 160°.

The listed SPL values = (measured 1/3-OB levels minus 10 log A minus average vane spacing correction for the two fans).

## REFERENCES

1. Anon: *Phase II Program on Ground Test of Refanned JT8D Turbofan Engines and Nacelles for the 727 Airplane - Final Report: Volume IV—Airplane Evaluation and Analysis*. BCAC D6-42440-4, Boeing Commercial Airplane Company, NASA CR-134800, December 1975.
2. Mechtly, E. A.: *The International System of Units—Physical Constants and Conversion Factors*. NASA SP-7012, (revised) 1969.
3. Anon: *Phase II Program on Ground Test of Refanned JT8D Turbofan Engines and Nacelles for the 727 Airplane—Final Report: Volume II—Hardware Design and Manufacturing*. BCAC D6-42440-2, Boeing Commercial Airplane Company, NASA CR-134798, December 1975.
4. Kaldschmidt, G.; Syltebo, B. E.; and Ting, C. T.: *727 Airplane Center Duct Inlet Low-Speed Performance Confirmation Model Test for Refanned JT8D Engines - Phase II*. BCAC D6-41513, Boeing Commercial Airplane Company, NASA CR-134534, November 1973.
5. Schuehle, A. L.: *727 Airplane Side Inlet Low-Speed Performance Confirmation Model Test for Refanned JT8D Engines*. BCAC D6-41521, Boeing Commercial Airplane Company, NASA CR-134609, March 1974.
6. Haugan, W. J. and Kern, P. R. A.: *727/JT8D-100 Series Engine Exhaust System Propulsion Performance Model Test*. BCAC D6-41805, Boeing Commercial Airplane Company, NASA CR-134617, May 1974.
7. Burdsall, E.A.; Brochu, F.P.; and Scaramella, V.M.: *Results of Acoustic Testing of the JT8D-109 Refan Engines*. PWA-5298, Pratt & Whitney Aircraft, NASA CR-134875, October 1975.
8. Joynes, D. and Balut, J. P.: *Titanium Honeycomb Acoustic Lining Structural and Thermal Test Report*. BCAC D6-42352, Boeing Commercial Airplane Company, NASA CR-134783, December 1974.